Structure, Reactivity, and Solid-Gas Catalysis in Ligand-Varied Solid-State Molecular Organometallic Systems

Cameron Royle, Somerville College





A thesis submitted in partial fulfilment of the requirements for the degree of Doctor of Philosophy in Inorganic Chemistry at the University of Oxford

November 2021

Declaration

The work presented in this thesis was carried out between October 2018 and November 2021 under the supervision of Professor Andrew S. Weller at the universities of Oxford (October 2018–December 2019, *also under Professor Dermot O'Hare*) and York (secondment, January 2020–November 2021). All of the work is my own, unless otherwise stated, and has not been submitted previously for any qualification at this, or any other, institution.

Cameron Royle, Somerville College

November 2021

Acknowledgements

Andy – where else to begin? – I will be forever thankful that you made room for me inside your wonderful group and for allowing me such intellectual freedom. I have learned so very much over the last three-or-so years, especially the value of scientific rigour, as well as the value of a good garlic chicken masala at the Brunel Raj. There have been many valuable and much-appreciated life lessons besides these, but these two, I think, deserve explicit mentions. This handful of years has been a very happy time for me.

Some thanks must also go to you, Andy, for accommodating so many wonderful people in your group. To the legendary Antonio Jesús Martínez-Martínez: thank you for your patience, and the benefit of your vast knowledge. We all miss you terribly – Huelva has gained an excellent chemist. In future times of difficulty, perhaps witnessing an acetone ice-bath fire, I need only to recall your all-encompassing grin, and your becalming Spanish twang, like a fine amontillado, and all will be well.

To my countrymen, the co-habitants of 72 Alcuin: David, James and Tim. I will always cherish the time we spent watching Louis Theroux, taking advantage of David's cooking skills, and teasing Tim on the state of his room. Living there was one of the happiest times of my life – a great shame that is was cut short.

David: I have yet to meet someone with such a fine sense of humour, and such a (how to put this?) way with words, and yet balanced by such sensitivity and agelessness. Your death-wish work ethic, your monkish sense of interior design, and your self-destructive hatred of bureaucracy will be inspirations to me for decades. I treasure fond memories of your cool stoicism, on asphalt overlooked by a motorway Starbucks, watching your injured sports car leak transmission fluid.[a] P.Q. is lucky to have such an excellent *chef de cuisine* and such an upstanding friend as you.

James: I really hope you find a cure for those cheese sweats soon. Forever playing second-fiddle to you for Tim's love, I will miss your warmth, your handsome little smile, your Haribo, and your taste for cheddar cheese and gherkins, to be consumed simultaneously. There are still marks inside my car where you

[a] 'Watch this!'

wedged your bike for the journey southwards, in that uncertain March of 2020. You may escape me, but you'll never escape my nominations for lab music. And, in turn, perhaps one day I will turn to a cheeky bit of drum and bass on a Big Day™.

Tim: In the December of 2019, we loaded a van with our possessions and made the long journey northwards. We learned more about you that day than we would have in a year of close friendship, as James and I extracted from the pile a solitary wet, crumpled sock, inside a plastic bag, inside another plastic bag. We will surely miss visiting your room, dank and dark, with creased shirts stuffed haphazardly, and forgotten plates piled high. It is, perhaps, a testament to you that we gladly overlooked these things, and dearly loved you as a friend. I will greatly miss our pretentious film viewings, your love of breathy female folk artists, and watching you spill ketchup, mayonnaise, and red wine over yourself. Hopefully the next dewar of liquid nitrogen you empty triumphantly on a Friday afternoon will actually contain liquid nitrogen.[a] I toast the health of your bank balance.

No small thanks are due to the remaining members of the Weller Group. To the postdocs, Sam, Laurence, Claire, and beardy Matt: I have learned so much from you all, and it has been a pleasure to work alongside you. I'm sure I've tried the patience of each of you at least once – particularly Sam! To Alex, Ana, German Max, Kori, Joe and Helena: thank you for making the group such a privilege to be a part of. I must also take the opportunity to thank Prof. Dermot O'Hare and Dr J.-C. Buffet for accommodating me in their group during my time at Oxford.

For paving the way to a DPhil in Inorganic Chemistry(!): I cannot omit my undergraduate tutors (Profs. Andrew Goodwin, Nick Green, David Hodgson; Drs. Victor Lee, Lydia Gilday, and Andrew Seel), my Master's supervisor (Prof Simon Aldridge, also Drs. Jamie Hicks, Petra Vasko, and Xueer Zhou), my secondary school teachers (especially Julie Faux), my friends (Denis Hartmann, Group Chat) and, of course, my parents, who have encouraged me every step of the way.

[a] 'Watch this!'

Abstract

Chapter 1, Introduction: The concepts of solid-state organometallic chemistry; single-crystal to single-crystal (SC-SC) transformations; alkene isomerisation; continuous flow techniques; and *para*-hydrogen induced polarisation (PHIP) are introduced and given brief theoretical and practical backgrounds, each relevant to the following chapters.

Chapter 2: This chapter explores the successful application of P_2-type Rh-containing SMOMs in the solid-gas catalytic isomerisation of 1-butene, and describes their deployment under both batch and continuous flow conditions, achieving non-thermodynamic selectivity. In an effort to explore the chemical space, a wide variety of ligand-varied SMOMs are deployed under flow conditions: the direct tunability of solid-gas catalysis is demonstrated through ligand (R-group and tether-length) modification.

Chapter 3: The SC-SC chemistry of two related systems are described: a PONOP-bound cationic Ir-containing SMOM (in collaboration with the Diamond Light Source) and a P_2-type perfluorophenyl/Rh-containing SMOM. Remarkably, both of these systems undergo SC-SC transformations with shifts in periodic structure upon solid-state hydrogenation and desolvation respectively. These transformations are tracked with single-crystal X-ray diffractometry as well as solid-state NMR spectroscopy.

Chapter 4: This chapter explores the NMR batch-scale solid-gas catalytic hydrogenation-polarisation of unsaturated substrates with *para*-hydrogen by P_2-type Rh-containing SMOMs. Conducted in collaboration with the Centre for Hyperpolarisation in Magnetic Resonance, York (CHyM), the tunability of solid-gas catalysis is again demonstrated through ligand modification, yielding vastly different activities and rates of deactivation. The solid-gas hydrogenation mechanisms are elucidated with the assistance of D_2 gas.

Chapter 5, Experimental: The syntheses and characterisation of materials not already reported in the literature are provided, in addition to experimental methods.

Chapter 6, Future Directions: The possible future directions for these projects are described in a short epilogue.

Disclaimers

Chapter 2: This work was carried out in collaboration with Drs. Antonio Martínez-Martínez[a] and Samantha Furfari,[b] with contributions from Drs. Alexander Bukvic,[c] Dana Georgiana Crivoi,[d] and Nicholas Rees.[e] Much of the work discussed in this chapter has already been published, in *ACS Catalysis*, **2020**, *10*, 1984–1992.

Chapter 3: This work was carried out in collaboration with Dr Mark Warren and Anna Marini at the Diamond Light Source,[f] with contributions from Drs. Samantha Furfari[e] and Claire Brodie.[g]

Chapter 4: This work was carried out in collaboration with Dr Matthew Gyton[h] and Professor Simon Duckett at the Centre for Hyperpolarisation in Magnetic Resonance (CHyM), York, with contributions from Drs. Samantha Furfari[e] and Claire Brodie.[d]

This DPhil was pursued on a Clarendon Scholarship.

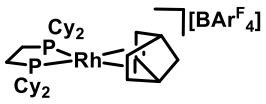
[a] Solid-gas flow work on some dcpe/dtbpe systems; some *sc*-XRD work.
[b] Solid-gas flow work on some ^{t}Bu tether-varied systems.
[c] Some *sc*-XRD work.
[d] SEM in this chapter.
[e] SSNMR in this chapter.
[f] *In situ sc*-XRD work for the pincer Ir-propene system in this chapter.
[g] Spin-lattice relaxation time (T_1) measurements.
[h] Hydrogenation-polarisation work with some dcpe systems in this chapter.

a	unit cell dimension
Å	ångströms (10^{-10} m)
ALTADENA	adiabatic longitudinal transport after dissociation engenders net alignment
app.	apparent
aq.	aqueous
Ar	aryl group
Ar^F	3,5-di(trifluoromethyl)phenyl
atm	atmosphere(s)
b	unit cell dimension
bar	10^5 Pa (gauge pressure unless otherwise stated, *i.e.* as 'bar-absolute')
BCPP	bicapped parallelepiped
br.	broad
Bu	butyl
c	unit cell dimension
C	Celsius
calc.	calculated
cat	catalyst
COD	1,5-cycloctadiene
COSY	correlation spectroscopy
Cp	*cyclo*-pentadienyl
Cy	*cyclo*-hexyl
Cyp	*cyclo*-pentyl
d	doublet
D	[bond] distance
dcpa	bis(di-*cyclo*-hexylphosphino)amine
dcpb	1,4-bis(di-*cyclo*-hexylphosphino)butane
dcpe	1,2-bis(di-*cyclo*-hexylphosphino)ethane
dcpm	bis(di-*cyclo*-hexylphosphino)methane
dcpp	1,3-bis(di-*cyclo*-hexylphosphino)propane
dcp5	1,5-bis(di-*cyclo*-hexylphosphino)pentane
dcyppb	1,4-bis(di-*cyclo*-pentylphosphino)butane
dcyppe	1,2-bis(di-*cyclo*-pentylphosphino)ethane
dcyppp	1,3-bis(di-*cyclo*-hexylphosphino)propane
deg	degree(s)
DEPT	distortionless enhancement by polarisation transfer
dibpe	1,2-bis(di-*iso*-butylphosphino)ethane
dippe	1,2-bis(di-*iso*-propylphosphino)ethane
dipp	-2,6-di(*iso*-propyl)phenyl
dippp	1,3-bis(di-*iso*-propylphosphino)propane
d_n-	degree (*n*) of deuteron substitution
dpfppe	1,2-bis(dipentafluorophenyl-phosphino)ethane
dppe	1,2-bis(diphenylphosphino)ethane
dtbpa	bis(di-*tert*-butylphosphino)amine
dtbpb	1,4-bis(di-*tert*-butylphosphino)butane
dtbpe	1,2-bis(di-*tert*-butylphosphino)ethane
dtbpp	1,3-bis(di-*tert*-butylphosphino)propane
E	*Entgegen* or energy
ΔE	change in energy
ESI	electrospray ionisation

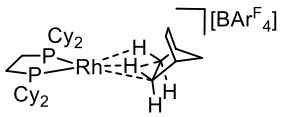
eq.	equivalent(s)
Et	ethyl
EXSY	exchange spectroscopy
FID	free induction decay
g	gram(s)
ΔG	change in Gibbs energy
GC	gas chromatography
ΔH	change in enthalpy
HETCOR	heteronuclear correlation
HMBC	heteronuclear multiple bond correlation
HP	hyperpolarised
hr	hour(s)
HSQC	heteronuclear single quantum coherence
Hz	Hertz (s^{-1})
i	*iso* or *ipso*
I	nuclear spin quantum number
^{i}Bu	*iso*-butyl
IP	initial productivity
^{i}Pr	*iso*-propyl
^{i}Pr-PONOP	-*O*,*O*-(di-*iso*-propylphosphino)-2,6-dioxypyridine
J	Joules
J	scalar coupling constant
k	kilo
k	rate constant or Boltzmann's constant
K	Kelvin
kcal	kilocalorie (= 4.184 kJ)
k_d	rate of decay
L	generic ligand or litre(s)
M	mol dm^{-3} or mega
m	multiplet, milli, or metre(s)
m	*meta*, mass, or spin projection quantum number
MaxPhos	(di-*tert*-butylphosphino)(methyl-*tert*-butylphosphino)amine
Me	methyl
mer	meridional
Mes	mesityl, -3,5-trimethylphenyl
min	minute(s)
m/*z*	mass-charge ratio
MOF	metal-organic framework
mol	mole(s)
mol%	mole-percentage
MRI	magnetic resonance imaging
MS	mass spectrometry
n	nano
NBA	norbornane
NBD	norbornadiene
NBE	norbornene
NCI	non-covalent interaction
NHC	*N*-heterocyclic carbene
NMR	nuclear magnetic resonance
o	*ortho*
O_h	octahedral
OTf	trifluoromethanesulfonate
p	pico
p	*para*, pressure, or powder
P_2	chelating *bis*-phosphine
PASADENA	*para*-hydrogen and synthesis allow dramatically enhanced nuclear alignment
Ph	phenyl
PHIP	*para*-hydrogen induced polarisation
PNL	partially negative lineshape

PˆNˆP	bis(dialkylphosphino)amine
ppm	parts-per-million
Pr	propyl
PSS	periodic structure-shifting
q	quartet
R	generic group
R	*rectus* (absolute configuration)
s	second(s) or spin quantum number
S	entropy or *sinister* (absolute configuration)
ΔS	change in entropy
SABRE	signal amplification by reversible exchange
sc	single-crystal
SC-SC	single-crystal to single-crystal
SEM	scanning electron microscopy
SHOP	Shell higher olefin process
SMOM	solid-state molecular organometallic
soln.	solution
SOMC	surface organometallic chemistry
SSNMR	solid-state nuclear magnetic resonance
t	time, tertiary
T	temperature
T_1	spin-lattice relaxation time
^{t}Bu	*tert*-butyl
THF	tetrahydrofuran
TMAB	trimethylamine-borane
tmeda	tetramethylethylene diamine
TMP	tetramethylpyrazine
TOF	turnover frequency
TON	turnover number
t^R	retention time
triphos	1,1,1-tris(diphenylphosphino-methyl)ethane
V	volume
VT	variable temperature
wt%	percentage by weight
X	generic counteranion
XantPhos	(9,9-dimethyl-9H-xanthene-4,5-diyl)bis(diphenylphosphane)
XRD	X-ray diffraction
$\|z\|$	magnitude spectrum
Z	*Zusammen* or formula units in unit cell
Z'	symmetry-independent formula units in unit cell
ZPE	zero-point energy
α	unit cell angle
β	unit cell angle or plane angle
γ	unit cell angle
δ	chemical shift (ppm)
η	degree of hapticity
θ	angle
ϑ	torsion angle
κ	degree of denticity
μ	micro, bridging group, or reduced mass
ν	[spinning] frequency
ξ	reaction coordinate
ρ	density
Σ	summation
φ	wavefunction
Ψ	overall wavefunction
$\subset$	subset (encapsulated within)

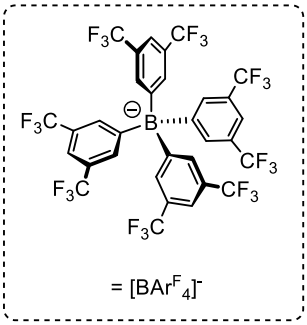
Table of Numbered Species – Note that the most important species have been highlighted in bold.

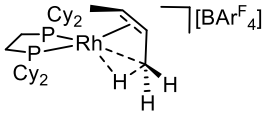


1

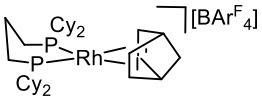


2

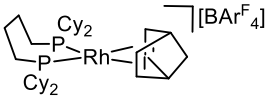




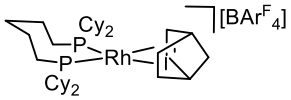
3



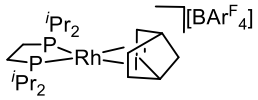
4



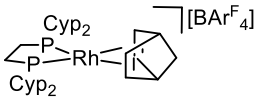
5



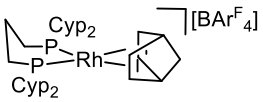
6



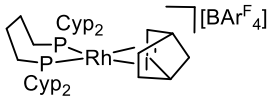
7



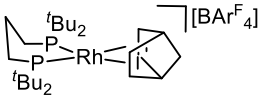
8



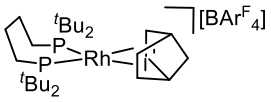
9



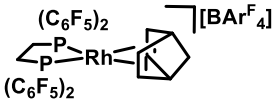
10



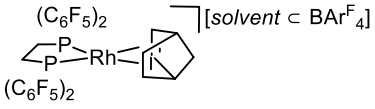
11



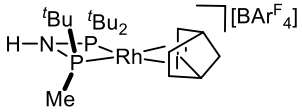
12



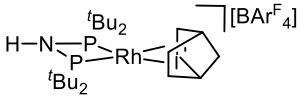
13



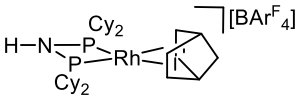
solvent = ¼CH_2Cl_2 **13-I**
none **13-II**
⅓(*n*-pentane) **13-III**



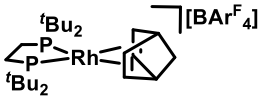
14



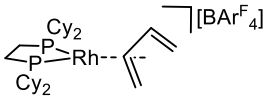
15



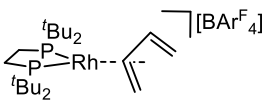
16



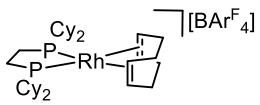
17



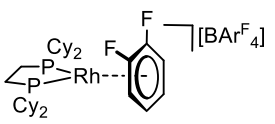
18



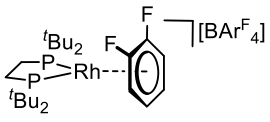
19



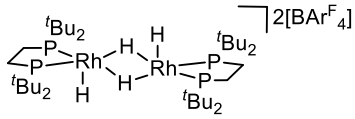
20



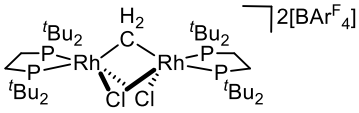
21



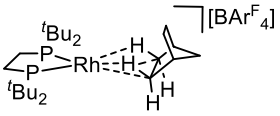
22



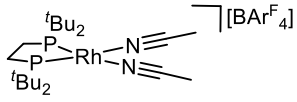
23



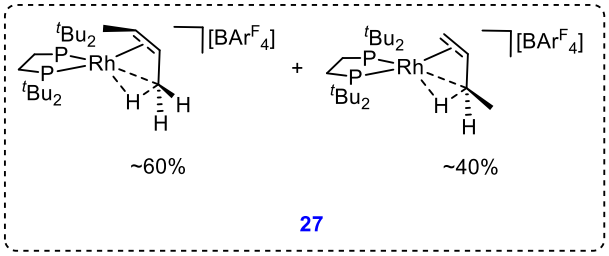
24



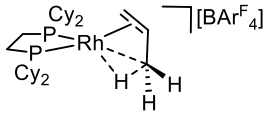
25



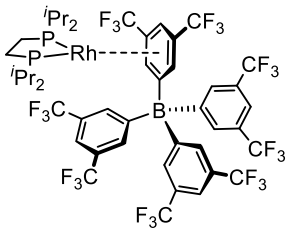
26



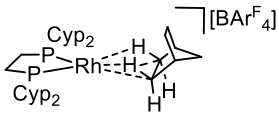
27



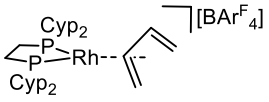
28



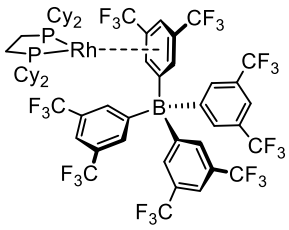
29



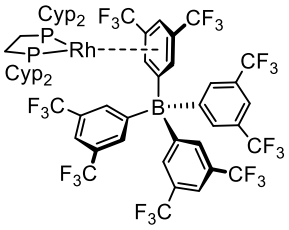
30



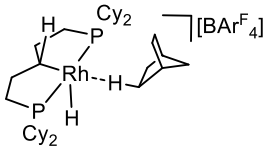
31



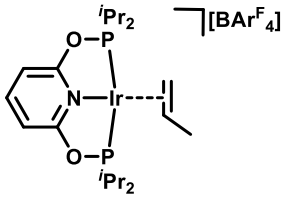
32



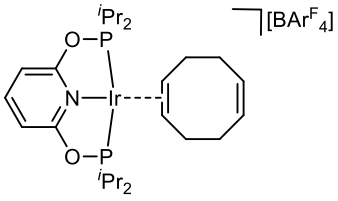
33



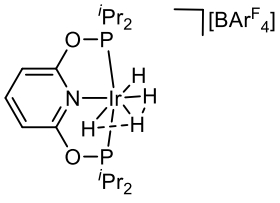
34



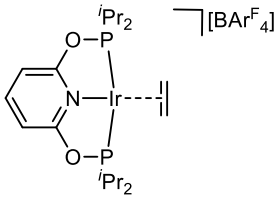
35



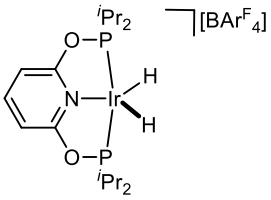
36



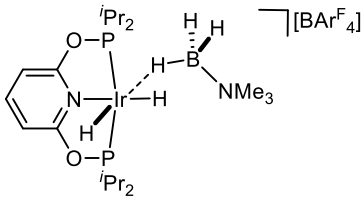
37



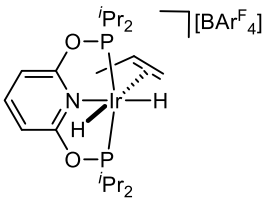
38



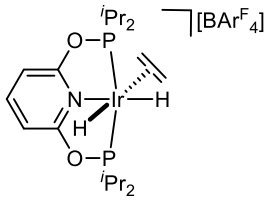
39



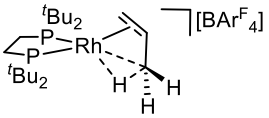
40



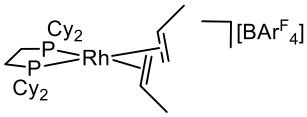
41



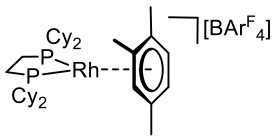
42



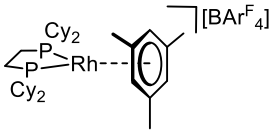
43



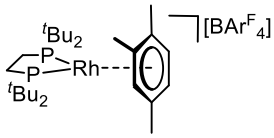
44



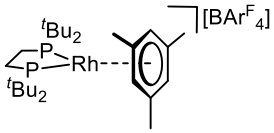
45



46



47



48

Declaration *ii*

Acknowledgements *iii*

Abstract *v*

Disclaimers *vi*

Abbreviations and Symbols *vii*

Table of Numbered Species *x*

1 Introduction

1.1 Organometallic Chemistry in the Solid-State **1**

1.1.1 Solid-State Organometallic Chemistry: Reactive Species Protection and Product Selectivity *2*

1.1.2 Single-Crystal to Single-Crystal (SC-SC) Transformations *5*

1.1.3 Polymorphism in Organometallic Crystals *14*

1.1.4 Solid-State Molecular Organometallics (SMOMs) *15*

1.1.5 'Porosity Without Pores' *20*

1.2 Alkene Isomerisation **23**

1.2.1 Mechanisms of Alkene Isomerisation *24*

1.2.2 Cis/Trans *Selectivity in Alkene Isomerisation* *27*

1.2.3 SMOMs, Solid-Gas Alkene Isomerisation, and Structure-Activity Relationships *29*

1.3 Principles of Continuous Flow Chemistry **32**

1.3.1 Selectivity Under Continuous Flow Conditions *34*

1.4 Principles of *Para*-Hydrogen Induced Polarisation (PHIP) **38**

1.4.1 Spin Isomers of the Dihydrogen Molecule *38*

1.4.2 Overview of PHIP and Relevant Spin Physics *41*

1.4.3 PHIP Experiments: Other Concerns *45*

1.4.4 Applications of PHIP in Inorganic Chemistry 47

1.4.5 Heterogeneous Hydrogenation-Polarisation 49

1.5 References **50**

2 Solid-State Molecular Organometallic Catalysts under Solid/Gas Flow Conditions: Gas-Phase Isomerisation of 1-Butene

2.1 Introduction **57**

2.2 Synthesis and Characterisation of Target SMOMs (Precursor NBD Complexes) **59**

2.2.1 Synthesis of Precursor NBD SMOMs via a Labile 1,2-difluorobenzene Complex (Protocol I) 59

2.2.2 Synthesis of Precursor NBD SMOMs Directly from [Rh(η^2,η^2-NBD)$_2$][BAr$^F{}_4$] and Chelating Bis-*Phosphine P$_2$ (Protocol II)* 60

2.2.3 Synthesis of Precursor NBD SMOMs via Halide Abstraction (Protocol III) 64

2.2.4 Overview of the Solid-State Structures of Precursor NBD SMOMs 65

2.2.5 Independent Synthesis and Characterisation of Suspected Deactivation Products as NMR References 69

2.3 Solid-Gas Catalytic Isomerisation of 1-butene with Precursor NBD SMOMs (NMR Batch Conditions) **74**

*2.3.1 Solid-Gas Reactivity of [(dcpe)Rh(η^2,η^2-NBD)][BAr$^F{}_4$] (Precursor SMOM **1**)* 74

*2.3.2 Solid-Gas Reactivity of [(dtbpe)Rh(η^2,η^2-NBD)][BAr$^F{}_4$] (Precursor SMOM **17**)* 75

*2.3.3 NMR Batch-Scale Solid-Gas Catalytic Isomerisation of 1-butene with Precursor SMOMs **1** and **17*** 84

*2.3.4 NMR Batch-Scale Solid-Gas Catalytic Isomerisation of n-butene isomers with SMOM **17** (Gas Chromatography)* 90

*2.3.5 75 mL Reactor-Scale Solid-Gas Catalytic Isomerisation of 1-butene by SMOM **17*** 97

2.3.6 Ligand and Metal Variation Under NMR Batch Conditions 98

2.4 Solid-Gas Catalytic Isomerisation of 1-butene with Precursor NBD SMOMs (Continuous Flow Conditions) **102**

2.4.1 Anatomy of Solid-Gas Flow Reactor and Samples 102

2.4.2 Solid-Gas Catalytic Isomerisation of 1-butene under Flow Conditions by SMOMs 104

*2.4.3 Precursor NBD SMOMs **1** and **17** Under Continuous Flow Conditions* 109

2.4.4 Control Experiments Under Continuous Flow Conditions: Particle Size, iso-Butene Co-Feed, Temperature, and Reproducibility 111

*2.4.5 Post-Flow Materials Characterisation, Precursor NBD SMOM **1*** 111

*2.4.6 Pre-Flow, On-Stream, and Post-Flow Materials Characterisation, Precursor NBD SMOM **17*** 112

2.4.7 The Effects of Ligand Variation Under Flow Conditions: R-Group Variation 119

2.4.8 The Effects of Ligand Variation Under Flow Conditions: Tether-Length and Identity Variation 120

2.4.9 Homogeneous Alkene Isomerisation Control Experiments 123

2.5 Conclusions **126**

2.6 References **126**

3 Single-Crystal to Single-Crystal Transformations in Solid-State Molecular Organometallics (SMOMs) with Shifts in Periodic Structure

3.1 Introduction **131**

3.2 PONOP Pincer-Iridium Solid-Gas Hydrogenation Chemistry **134**

3.2.1 Solution-Phase Synthesis and Characterisation of PONOP-Iridium(I) Precursor SMOMs [(^{i}Pr-PONOP)Ir(η^2-alkene)][$BAr^F{}_4$] (alkene = propene, ethene) Precursor SMOMs 134

3.2.2 Synthesis and Characterisation of PONOP-Iridium(III) Hydrides by Solution-Phase Hydrogenation of PONOP-Iridium(I) Alkene Complex Precursors 140

*3.2.3 PONOP-Iridium(III) Propene-Dihydride [(^{i}Pr-PONOP)IrH_2(η^2-propene)][$BAr^F{}_4$] (**41**): Solid-State and Low-Temperature Solution-Phase Synthesis* 143

*3.2.4 Propene-Dihydride **41**: Synthesis by Single-Crystal to Single-Crystal Hydrogenation* 149

*3.2.5 Propene-Dihydride **41**: Analysis of Material After H_2 Exposure with Scanning Electron Microscopy* 154

*3.2.6 PONOP-Iridium(III) Ethene-Dihydride [(^{i}Pr-PONOP)IrH_2(η^2-ethene)][$BAr^F{}_4$] (**42**): Solid-State and Low-Temperature Solution-Phase Synthesis* 156

*3.2.7 Ethene-Dihydride **42**: Recrystallisation, Solid-State Structure, and Reductive Elimination of H_2* 162

3.2.8 Probing Solid-State Redox Reversibility with D_2 167

3.3 A dpfppe-Rhodium(I) Single-Crystal to Single-Crystal Solvent De-Encapsulation **169**

*3.3.1 Solution-Phase Synthesis and Characterisation of $(C_6F_5)_2P(CH_2)_2P(C_6F_5)_2$-Rhodium(I) (dpfppe-Rhodium(I)) SMOMs **13-I,II,III*** 170

*3.3.2 CH_2Cl_2-Containing Morph **13-I**: A Single-Crystal to Single-Crystal Solvent De-Encapsulation* 177

3.4 Conclusions 181

3.5 References 181

4 Solid-Gas Catalytic Hydrogenation-Polarisation of Alkenes and Alkynes (SMOM-PHIP)

4.1 Introduction 185

4.2 Synthesis and Characterisation of a Target Propene Complex 186

4.3 Solid-Gas Hydrogenation-Polarisation of Propene by Precursor NBD SMOMs 191

4.3.1 Deactivation Routes of Propene Hydrogenation-Polarisation Catalytic Systems 195

4.3.2 Solid-Gas Propene Hydrogenation: Mechanistic Investigations with D_2 198

4.3.3 Solid-Gas PHIP with 'Normal' H_2: A Demonstration of In Situ Para-*Enrichment* 201

4.4 Solid-Gas Semihydrogenation-Polarisation of Propyne by Precursor NBD SMOMs 203

*4.4.1 Solid-State Cyclotrimerisation of Propyne by Precursor NBD SMOM **1*** 204

*4.4.2 Solid-Gas Semihydrogenation-Polarisation of Propyne by Precursor NBD SMOM **17*** 207

*4.4.3 Testing Independently-Synthesised 1,2,4-Trimethylbenzene Complex **47*** 212

4.4.4 Solid-Gas Propyne Hydrogenation: Mechanistic Investigations with D_2 213

4.5 Solid-Gas Hydrogenation-Polarisation of 1,3-Butadiene by Precursor NBD SMOMs 217

4.5.1 Solid-Gas 1,3-Butadiene Hydrogenation: Mechanistic Investigations with D_2 220

4.6 Conclusions 223

4.7 References 223

5 Experimental

5.1 Materials and Methods 225

5.2 Solution-Phase NMR Spectroscopic Data 226

5.3 Solid-State NMR Spectroscopic Data 226

5.4 Gas-Phase ^{1}H NMR Spectroscopic Data and Solid-Gas PHIP 227

5.5 Mass Spectrometric Data 228

5.6 Scanning Electron Microscopic Data 228

5.7 Powder X-ray Diffractometric Data 229

5.8 Gas Chromatographic Data 229

5.9 Elemental/CHN Microanalysis 229

5.10 Protocol for Solid-Gas Batch Experiments: Gas Analysis Sample Preparation 230

5.11 Protocol for Solid-Gas Batch Experiments: 75mL-Scale Reactor 231

5.12 Protocol for Solid-Gas Continuous Flow Experiments 232

5.13 Synthetic Procedures: Chapter 2 236

5.13.1 Synthesis of [(dcyppp)Rh(η²,η²-NBD)][BAr$^{F}_{4}$] (dcyppp = Cyp$_2$P(CH$_2$)$_3$PCyp$_2$), ***9*** 236

5.13.2 Synthesis of [(dcyppb)Rh(η²,η²-NBD)][BAr$^{F}_{4}$] (dcyppp = Cyp$_2$P(CH$_2$)$_4$PCyp$_2$), ***10*** 237

5.13.3 Synthesis of [(dtbpb)Rh(η²,η²-NBD)][BAr$^{F}_{4}$] (dtbpb = ^{t}Bu$_2$P(CH$_2$)$_4$P^{t}Bu$_2$), ***12*** 238

5.13.4 Synthesis of [((R)-MaxPhos)Rh(η²,η²-NBD)][BAr$^{F}_{4}$] (MaxPhos = HN(P^{t}Bu$_2$)(P^{t}BuMe)), ***14*** 239

5.13.5 Synthesis of [(dtbpa)Rh(η²,η²-NBD)][BAr$^{F}_{4}$] (dtbpa = HN(P^{t}Bu$_2$)$_2$), ***15*** 240

5.13.6 Syntheses of HN(PCy$_2$)$_2$ and [(dcpa)Rh(η²,η²-NBD)][BAr$^{F}_{4}$], ***16*** 241

5.13.7 Synthesis of [(dtbpe)Rh(η²,η²-NBD)][BAr$^{F}_{4}$] (dtbpe = ^{t}Bu$_2$P(CH$_2$)$_2$P^{t}Bu$_2$), ***17*** 242

5.13.8 Synthesis of [(dtbpe)Rh(η⁴-1,3-butadiene)][BAr$^{F}_{4}$], ***19*** 244

5.13.9 Independent Synthesis of [(dtbpe)Rh(η⁶-difluorobenzene)][BAr$^{F}_{4}$], ***22*** 245

5.13.10 Synthesis of {[(dtbpe)RhH(μ-H)]$_2$}[BAr$^{F}_{4}$]$_2$, ***23*** 246

5.13.11 Synthesis of [(dtbpe)Rh(μ-CH$_2$)(μ-Cl)$_2$Rh(dtbpe)][BAr$^{F}_{4}$]$_2$, ***24*** 247

5.13.12 In Situ *Solid-State Synthesis of [(dtbpe)Rh(σ-NBA)][BAr$^{F}_{4}$],* ***25*** 248

5.13.13 In Situ *Solid-State Synthesis of [(dtbpe)Rh(η²-n-butenes)][BAr$^{F}_{4}$],* ***27*** 249

5.14 Synthetic Procedures: Chapter 3 **254**

*5.14.1 Synthesis of [(^{i}Pr-PONOP)Ir(η^2-propene)][BAr^F_4], **35*** *254*

*5.14.2 Synthesis of [(^{i}Pr-PONOP)Ir(η^2-COD)][BAr^F_4], **36*** *255*

5.14.3 In Situ *NMR-Scale Synthesis of [(^{i}Pr-PONOP)IrH_4][BAr^F_4], **37*** *256*

*5.14.4 Synthesis of [(^{i}Pr-PONOP)Ir(η^2-ethene)][BAr^F_4], **38*** *257*

*5.14.5 Synthesis of [(^{i}Pr-PONOP)IrH_2][BAr^F_4], **39*** *258*

*5.14.6 Synthesis of [(^{i}Pr-PONOP)IrH_2(σ-H_3BNMe_3)][BAr^F_4], **40*** *259*

*5.14.7 Synthesis of [(^{i}Pr-PONOP)IrH_2(η^2-propene)][BAr^F_4], **41*** *260*

*5.14.8 Synthesis of [(^{i}Pr-PONOP)IrH_2(η^2-ethene)][BAr^F_4], **42*** *261*

*5.14.9 Synthesis of [(dpfppe)Rh(η^2,η^2-NBD)][BAr^F_4] Morphs (**13-I,II,III**; dpfppe = $(C_6F_5)_2P(CH_2)_2P(C_6F_5)_2$)* *263*

*5.14.10 SC-SC Reactivity of [(dtbpe)Rh(η^2,η^2-NBD)][BAr^F_4] (**13**) Morphs* *265*

5.15 Synthetic Procedures: Chapter 4 **267**

*5.15.1 Synthesis of [(dtbpe)Rh(η^2-propene)][BAr^F_4], **43*** *267*

*5.15.2 Independent Solution-Phase Synthesis of [(dtbpe)Rh(η^6-1,2,4-trimethylbenzene)][BAr^F_4], **47*** *270*

5.16 Single-Crystal X-ray Diffractometric Data **272**

5.17 References **279**

6 Future Directions

6.1 Chapter 2: Future Directions for Solid-Gas Catalytic Alkene Isomerisation **281**

6.2 Chapter 3: Future Directions Single-Crystal to Single-Crystal Transformations with Shifts in Periodic Structure **282**

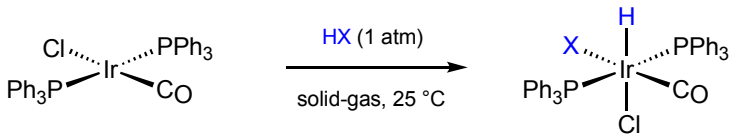
6.3 Chapter 4: Future Directions for Solid-Gas Hydrogenation-Polarisation **282**

6.4 References **282**

1 Introduction

1.1 Organometallic Chemistry in the Solid-State

While perhaps not as well established as homogeneous transition metal (TM) organometallic chemistry, a field driven in its spectacular expansion by its relationship to organometallic synthesis and homogeneous catalysis,[1] *hetero*-geneous TM organometallic chemistry has been known at least as early as 1966, when Vaska and co-workers reported the results of the exposure of solid *trans*-[Ir(Cl)(CO)(PPh_3)$_2$] to gaseous hydrogen halides to generate the *cis*-oxidative addition product. It was noted that this reaction proceeded "smoothly" in the absence of a solvent (**Scheme 1.1.1**).[2]



Scheme 1.1.1: Solid-state exposure of Vaska's complex to an atmosphere of hydrogen halide HX (X = F, Cl, Br, I). Rapid conversion to a single product was observed when X = Cl, Br; slower conversion was observed when X = F; multiple products were obtained when X = I.

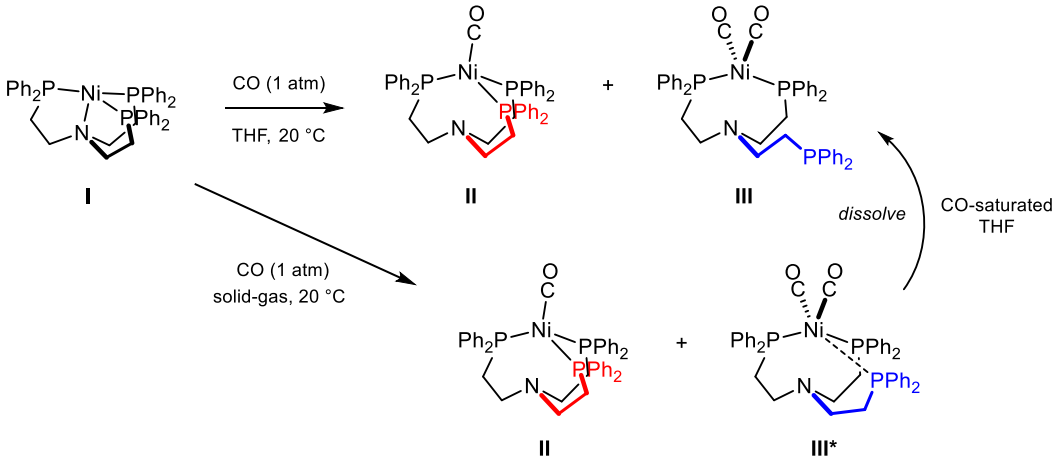
Reactions in the solid-state are proposed to occur according to the *topological principle*, which demands that such reactions occur with minimal movement to avoid lattice stress[3] and the concomitant build-up of huge pressures on the microscale.[4] The constraints imposed upon solid-state chemistry can impart both advantages and disadvantages. Translation of a reaction from solution-phase to the solid-state, for example, may result in loss of reactivity due to a reduction in conformational freedom, although evidence is available for the limited movement of some moieties inside crystal lattices of organometallic complexes.[5]

When solid-state reactivity does proceed, the removal of a solvent from the reaction eliminates issues of waste disposal, product recovery and deleterious reactivity with solvents, ensuring high atom economy – typical advantages of *heterogeneous* chemistry.[6] Solid-gas flow techniques may also be implemented, a common technique employed in heterogeneous catalysis.

1.1.1 *Solid-State Organometallic Chemistry: Reactive Species Protection and Product Selectivity*

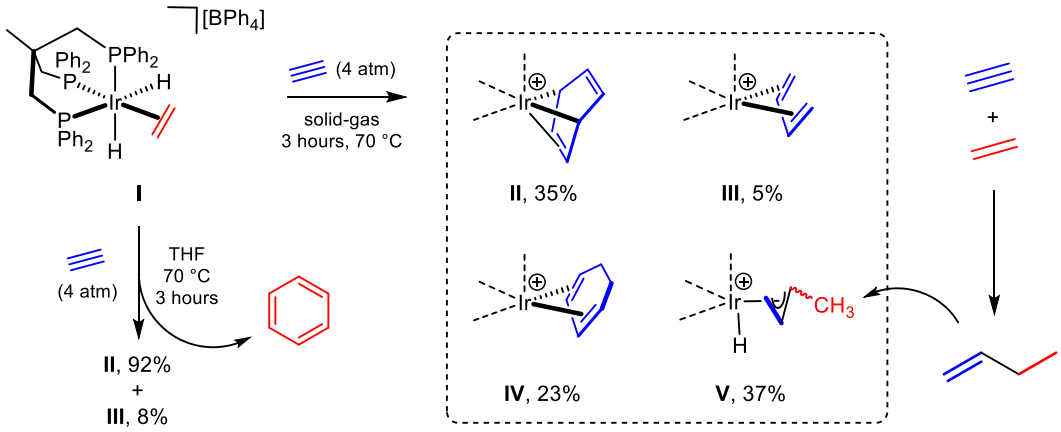
The use of precisely-defined organometallic complexes in the solid-state may allow fine-tunable[7,8] reactivity to be implemented, interrogable by the wide range of characterisation techniques available to the organometallic chemist at every stage: solution-phase and solid-state (SS-) NMR spectroscopy, single-crystal X-ray diffraction (*sc*-XRD), mass spectrometry (MS), *et cetera*. This permits meticulous investigation of mechanism, a typical advantage of *homogeneous* chemistry. In other areas of heterogeneous organometallic chemistry such as surface organometallic chemistry (SOMC), few of these characterising techniques are available (generally only SSNMR; *sc*-XRD may be available for MOFs).[9,10] If the reaction proceeds more slowly in the solid-state than in solution, this can permit careful analysis of otherwise fleeting intermediates, and the constraints imposed by the solid state may effect different product distributions.

Bianchini and colleagues reported in 1993 that treatment of a tripodal Ni(0) complex (**I**) with CO produced *bis*-carbonylated products (**III** and **III***) with distinct IR and solid-state NMR spectra, depending on whether it had been generated in solution (**III**) or in the solid-state (**III***), alongside *mono*-carbonylated **II** (**Scheme 1.1.2**).[11] Solid-state restrictions prevented the pendant phosphine in **III*** from completely leaving the metal coordination sphere in contrast to **III**; dissolving **III*** instantaneously gave rise to **III**, demonstrating the importance of the solid state in protecting this metastable arrangement of ligands.



Scheme 1.1.2: Solid-state and solution-phase exposure routes of [Ni{N(CH$_2$CH$_2$PPh$_2$)$_3$}] (**I**) to CO and their phase-dependant product distributions.

Four years later, the same group reported the isolation of the non-classical 'tetrahydride' complex [(triphos)Ir(H)$_2$(σ-H$_2$)][BPh$_4$] *via* treatment of solid [(triphos)IrH$_2$(η^2-C$_2$H$_4$)][BPh$_4$] (**Scheme 1.1.3**, **I**) with H$_2$ gas. Only solid-state techniques permitted the isolation and characterisation of this complex: THF solutions rapidly degraded to BPh$_3$, benzene, and neutral [(triphos)IrH$_3$]. While the solid 'tetrahydride' was an active catalyst for the hydrogenation of ethene, solution-phase systems showed no such catalytic activity.[12] Solid-state treatment of precursor **I** with acetylene lead to a range of alkyne dimer- and trimer-isation products (**II**-**IV**) as well as the formation of an allyl hydride (**V**), incorporating the equivalent of ethene found in precursor **I**. The product distribution (**II**-**V**) shifted when conducted in solution as ethene became able to leave the coordination sphere (required for the production of **V**), and reactivity was no longer quite so limited by the constraints of the solid-state.[13,14]

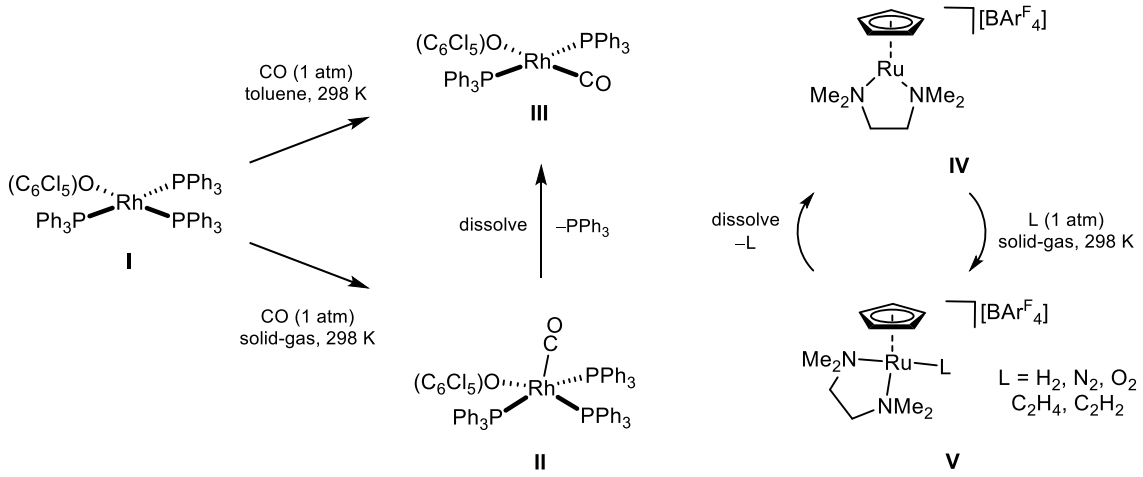


Scheme 1.1.3: Comparison of solid-gas and solution-phase acetylene dimer- and trimer-isation chemistry with [(triphos)IrH$_2$(η^2-C$_2$H$_4$)][BPh$_4$] (**I**).

Siedle and colleagues proposed that treatment of [(Ph$_3$P)$_2$Ir(η^2,η^2-COD)]$_3$[PW$_{12}$O$_{40}$] with H$_2$ in the solid-state generated coordinatively-unsaturated [(Ph$_3$P)IrH$_2$]$_3$[PW$_{12}$O$_{40}$], a solution-unstable species persistent inside the polyoxotungstate lattice. From this, further solid-gas chemistry was possible: treatment of this complex with propene gas, for example, generated the corresponding allyl hydride.[15,16]

Substitution of the large polyoxotungstate anion for smaller X = $[BF_4]^-$ or $[PF_6]^-$ resulted in the solid-state formation of dimeric, solution-characterised $[\{(Ph_3P)_2IrH\}_2(\mu\text{-}H)_3]_3[X]$ from which no further solid-state chemistry was possible. This illustrates the vital importance of both the solid-state in the stabilisation of reactive species as well as the *identity* of the anion forming this assembly. We will return to this concept, of an anionic structure-activity relationship, later in this chapter (Section 1.2.3).

Numerous additional examples of stoichiometric solid-gas organometallic reactions have been reported. Organometallic species have been employed for the stoichiometric fixation of CO_2,[17,18] O_2,[19] and N_2.[20] Penta-coordinate, solution-unstable intermediates have been described from the solid-gas exposure of certain $[(R_3P)_3Rh(OAr)]$ to CO gas (**Scheme 1.1.4**, **I-III**), in analogy to the work of Bianchini and colleagues.[21] Extensive solid-gas chemistry has also been reported for triosmium carbonyl complexes,[22,23] as well as for $[(tmeda)Ru(Cp)][BAr^F{}_4]$ (**IV**, Ar^F = -3,5-$(CF_3)_2C_6H_3$), as described by Gemel and colleagues.[20] In the latter case, some 18-electron products of solid-gas reactivity (**V**) were unstable in solution, regenerating 16-electron **IV**, and could only be characterised in the solid-state. Solid-state reactions have also been established for organic molecules,[24] including charge-transfer salts and intercalation compounds,[25] and proceed according to the same topological principle.



Scheme 1.1.4: Two further examples of phase-dependant organometallic chemistry.[20,21]

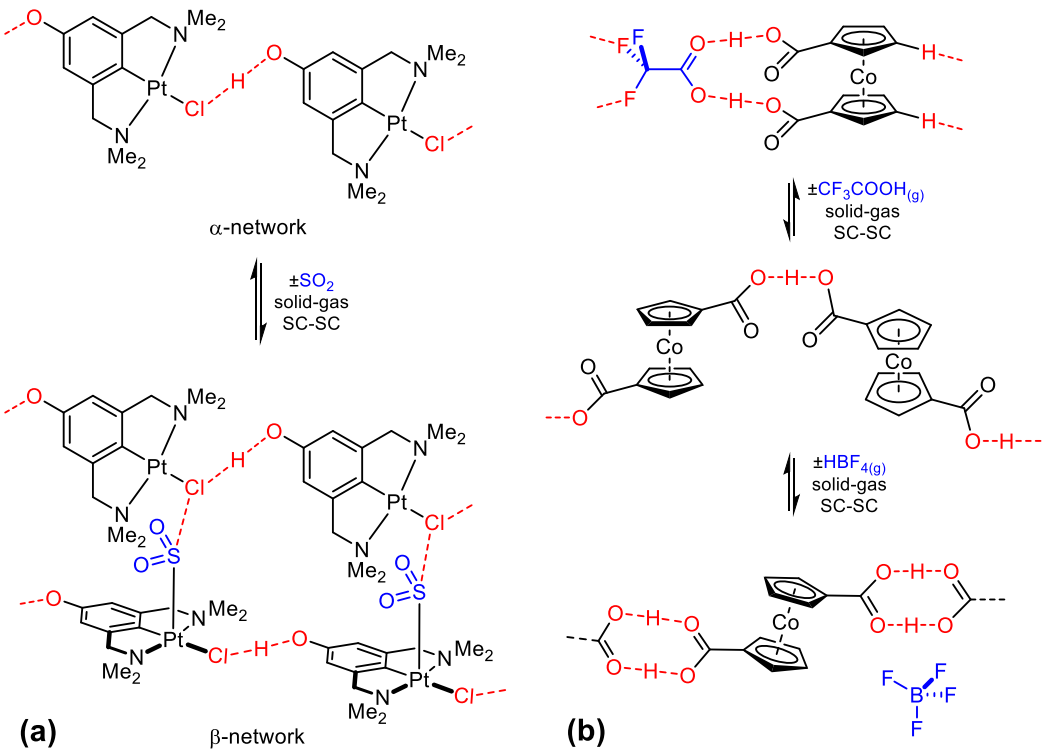
Further research on solid-gas organometallic catalysis, building on the work of Siedle and colleagues,[16] has revealed single-crystalline solid-state molecular organometallics (SMOMs) of type $[(P_2)Rh(\eta^2,\eta^2\text{-NBD})][BAr^F{}_4]$ to be viable pre-catalysts for alkene isomerisation (see Section 1.1.4). In addition, neutral PCP-type pincer-Ir(I) complexes have been deployed as solid-gas alkane dehydrogenation catalysts,[26] and the Pd(II)-triflate complex [(dppp)Pd(CH_3)(OTf)] (dppp = $Ph_2P(CH_2)_3PPh_2$, -OTf = $-O_3SCF_3$) for the rapid solid-state co-polymerisation of CO and ethene.[27]

Solid-state organometallic catalysts form a halfway-house between homogenous and heterogeneous regimes, potentially offering the advantages of both. This sub-discipline of organometallic chemistry doubtlessly has enormous potential. The solid-state platform presents both restrictions and opportunities: although necessarily limiting movement, the lattice has been shown to protect reactive, solution-unstable intermediates, a property demonstrably appealing for heterogeneous catalysis.

1.1.2 Single-Crystal to Single-Crystal (SC-SC) Transformations

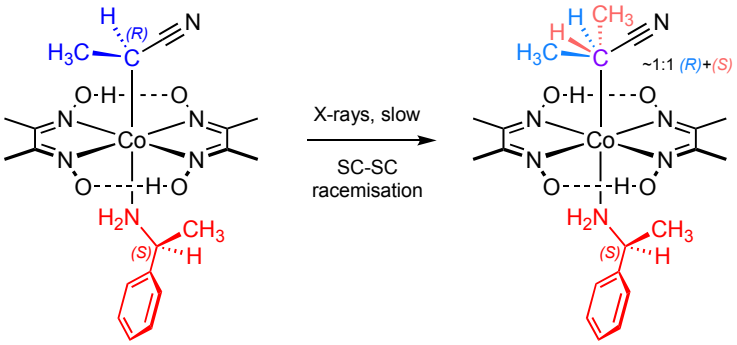
If solid-state transformations require minimal movement to avoid lattice strain, it follows that transformations that proceed with preservation of some crystalline order must be: (**i**) especially incremental, with small unit cell volume changes to prevent strain accumulation,[28,29] or otherwise (**ii**) possess a lattice tolerant to expansion, contraction, or rearrangement which would otherwise break up the lattice and yield amorphous material. This latter case, the periodic structure-shifting transformation (*i.e.* one in which the packing pattern of the parent crystal is *not* strictly preserved; 'PSS'), represents a substantially less common case of an already unusual phenomenon. Numerous cases of single-crystal to single-crystal (SC-SC) transformations are known for 3-D metal-organic frameworks (MOFs).[30–34] The rigidity of MOFs fulfils point (**i**) and their porosity is a pertinent property to gas-induced crystal-to-crystal transformations.[35,36] A remarkable example of *in crystallo* solid-gas alkene ozonolysis has been reported, the rigidity of the MOF favouring retention of crystallinity in the formation of a reactive intermediate 1,2,4-trioxolane.[37]

Examples fulfilling point (**ii**) have been described by Albrecht and colleagues[38] – an SO_2-triggered coordination switch at an NCN-Pt(II) pincer complex – and Braga and colleagues,[39] reporting solid-state protonation of a cobalt(III)ocene-centred zwitterion with vapours of acids CF_3COOH and HBF_4[40,41] (**Scheme 1.1.5a** and **b** respectively). In both cases the reversible transformations were monitored *in situ* by powder X-ray diffraction (*p*-XRD), and significant unit cell volume expansions were reported (15%; 29% and 42% respectively). While *p*-XRD evidenced the retention of long-range crystalline order across both the forward and reverse processes, these large volume expansions were apparently incompatible with retention of *single*-crystallinity, and therefore did not constitute SC-SC transformations – rather, these were polycrystal-to-polycrystal (PC-PC) only. Hydrogen-bonded networks were observed in both starting materials and products, the inherent flexibility of a hydrogen bond[42–44] apparently permitting dramatic expansion and reorganisation of the structure while retaining some form of crystalline order.[45]



Scheme 1.1.5: Solid-gas, non-periodic-structure retaining polycrystal-to-polycrystal (PC-PC) transformations monitored by *p*-XRD techniques and modulated by flexible hydrogen-bonding networks, described by Albrecht (**a**) and Braga (**b**).

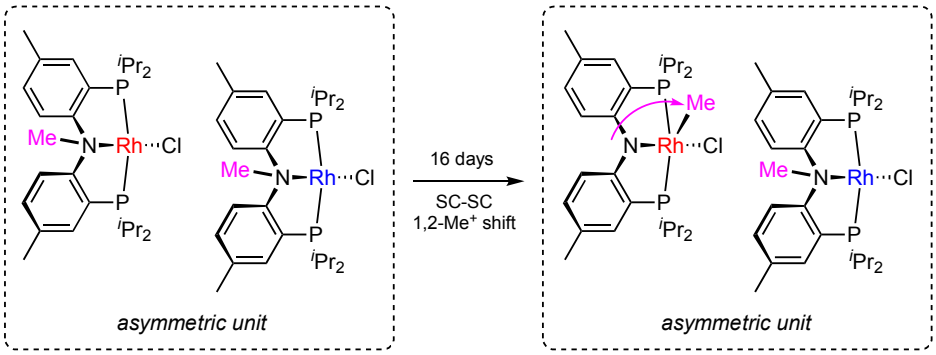
SC-SC transformations with shifts in periodic structure tend to be the exception rather than the rule. Working in 1977, Ohashi and Sasada reported that crystals of a chiral cobaloxime complex underwent racemisation under the conditions of single-crystal X-ray diffractometry (*sc*-XRD), slowly enough for multiple full dataset collections (**Scheme 1.1.6**).[46] Concomitant with the transformation was a slight (~1.3%) unit cell volume expansion, retaining the $P2_1$ space group as well as overall periodic structure. A range of cobaloximes have since demonstrated similarly incremental SC-SC chemistry.[47]



Scheme 1.1.6: X-ray induced single-crystal to single-crystal racemisation of a chiral cobaloxime.

Miniscule unit cell volume changes were also reported by Zenkina and colleagues, upon treatment of single-crystalline [*trans*-Rh(SIPr)$_2$(N$_2$)Cl] with O$_2$ gas to generate [*trans*-Rh(SIPr)$_2$(O$_2$)Cl] (~0.1% unit cell volume contraction), then with CO gas to generate [*trans*-Rh(SIPr)$_2$(CO)Cl] (~0.3% expansion).[48] Both transformations occurred with minimal change in periodic structure. The bulky -2,6-(^{i}Pr)$_2$C$_6$H$_3$-substituted NHC ligands were thought to encourage the retention of crystallinity by imparting rigidity to the structure.

SC-SC transformations do not necessarily require external inducement, be it with a gaseous reagent, reagents dissolved in a suspending liquid,[49] or by treatment with heat,[50] pressure,[51] or X-rays.[46,47] Ozerov and colleagues have reported a remarkable SC-SC transformation wherein two independent molecules of the same complex *within the same asymmetric unit* diverged in their reactivity (**Scheme 1.1.7**). Only one of these two independent amino-Rh(I) pincers underwent a 1,2-shift of a methyl group to yield the corresponding amido-Rh(III) pincer, with a unit cell volume expansion of just ~0.4%.[52]



Scheme 1.1.7: SC-SC internal oxidative addition of a C–N bond, an effective 1,2-Me^+ shift. Of two independent molecules located in the asymmetric unit, one undergoes this transformation in the solid-state.

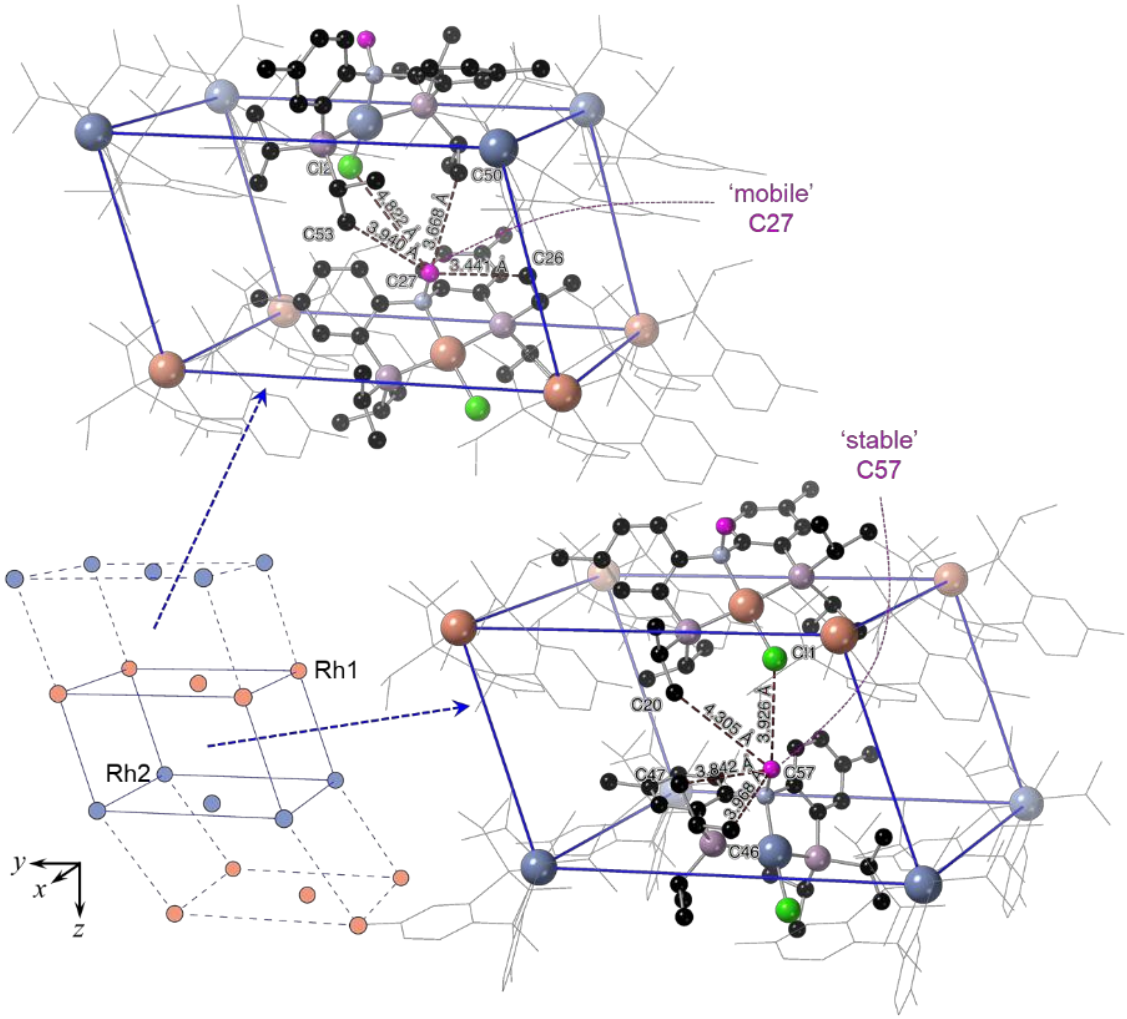
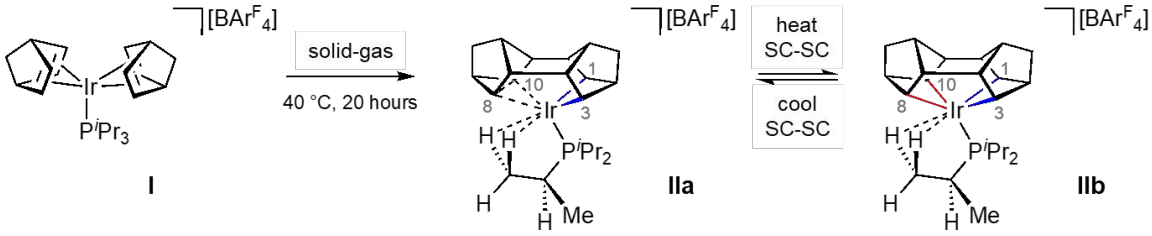


Figure 1.1.1: Solid-state packing pattern of [(P^{Me}NP)RhCl], modelled as both ball-and-stick and wireframe, demonstrating the dissimilar coordination environments about N-CH_3 (methyl carbons highlighted in magenta). Of the two independent such carbons in the asymmetric unit, 'mobile' C27 on Rh1 (**top**) undergoes slow 1,2-shift in the solid-state while 'stable' C57 on Rh2 (**bottom**) does not. Constructed from single-crystal X-ray diffraction data found in the reference.[52]

It was proposed that the dissimilar solid-state environments surrounding each molecule, namely the *micro*-environments surrounding each amine methyl group (*i.e.* the secondary coordination sphere), gave rise to dissimilar 1,2-shift activation energies. These dissimilar microenvironments are illustrated in **Figure 1.1.1**, highlighting the four nearest-neighbour atoms to the amine methyl carbon atom ('mobile' C27 on the Rh1 fragment and 'stable' C57 on the Rh2 fragment). Note, for example, the highly discrepant close-approaches of the proximal Cl atoms (4.822(8) *versus* 3.926(7) Å respectively). This demonstrates the crucial importance of the microenvironment in solid-state reactivity, a concept we will often reencounter.

Exploiting the constraining effects of the crystal lattice, Weller, Chaplin and colleagues have reported a reversible, temperature-dependant SC-SC transformation (**Figure 1.1.2**).[53]



T (K)	*D*(C8–C10) (Å)
100	1.704(5)
150	1.763(7)
200	1.806(9)
250	1.833(13)

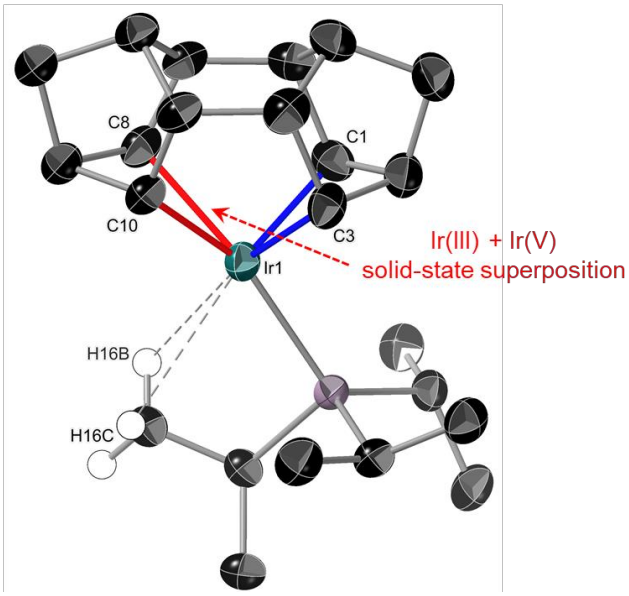


Figure 1.1.2: SC-SC reversible C-C oxidative addition in [(BINOR-S)Ir(P^{i}Pr$_3$)][BAr$^F{}_4$]. (**table**) Disordered C8–C10 bond lengths given across four temperatures. (**bottom**) Cationic fragment [(BINOR-S)Ir(P^{i}Pr$_3$)]$^+$. Anions and all H atoms omitted for clarity excepting calculated positions associated with agostic CH_3. 50% displacement ellipsoids. Constructed from *sc*-XRD data collected at 150 K found in the reference.[53]

The complex [(BINOR-S)Ir(P^iPr_3)][BAr^F_4] (**II**), a mixed C-H/C-C-agostic complex, was first generated from [(η^2,η^2-NBD)$_2$Ir(P^iPr_3)][BAr^F_4] (**I**) in the solid state. Recrystallised **II** was observed through *sc*-XRD to exist as a dynamically disordered superposition of Ir(III) (σ-C-C, **IIa**) and Ir(V) (C-C-activated, **IIb**) isomers in an SC-SC reaction. The equilibrium between **IIa** and **IIb** could be perturbed simply by changing the temperature at which the *sc*-XRD data was obtained, consistent with dynamic disorder.

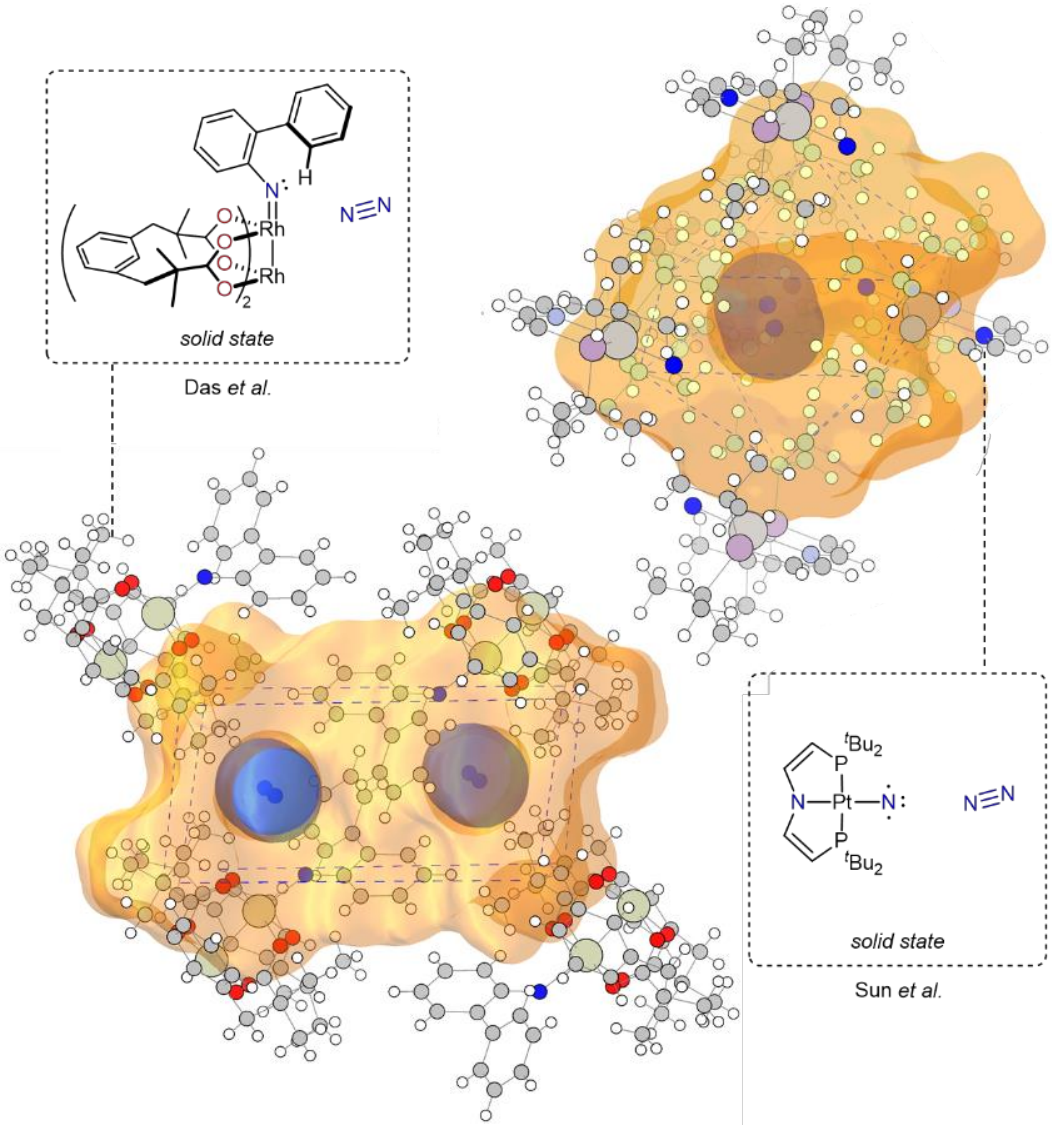


Figure 1.1.3: Cavity diagrams of SC-SC-synthesised metallonitrenes, constructed using *sc*-XRD structural data found in the references.[54,55] All species modelled as ball-and-stick. A solvent-excluded surface (probe radius 1.4 Å) in orange has been plotted around all the 'facing' atoms surrounding the photo-extruded N_2 molecules, and a complimentary surface in blue has been plotted around these sequestered molecules.

Lengthening of the C8–C10 bond was observed as the temperature was raised, with an ~8% increase in bond distance from T = 100 K to 250 K, indicating progressive C–C oxidative scission. The dynamic disorder between **IIa** and **IIb** was resolved using a two-component model, allowing the equilibrium populations at each temperature to be calculated, and the small energy span between the isomers to be quantised (ΔG_{298} = +0.09 ± 0.08 kJ mol^{-1}, Ir(III⟶V)). No solid-state equilibrium was detected for the Rh-containing congener, despite evidence for fluxionality at 298 K *via* solution-phase NMR spectrometry.[56]

In two related examples of the solid-state stabilisation of reactive intermediates, the groups of Schneider and Powers have reported the SC-SC formation of reactive nitrenes *via* photoextrusion of N_2 from azides.[54,55] Solid-state techniques were essential to allow the structural characterisation of these species, which existed in solution only transiently. In **Figure 1.1.3**, the cavities surrounding the photo-extruded N_2 molecules are shown, emphasising the protective/arresting role of the solid-state.

As we have seen thus far, SC-SC transformations can be facilitated by structures that enforce a reactive conformation,[52,53,57–61] or indeed they can be prevented by structures that deny them. Of particular note is the work of Dotson and colleagues, who have reported a series of structure-dependant SC-SC photodecarbonylations as important steps in the synthesis of various *bis-cyclo*-tryptamine alkaloids (**Figure 1.1.4**).[62] Not only did the structure-enforced conformation of the precursor determine the success of the decarbonylation, but distant substituents were reported to affect the tertiary structure and thus the topochemical[a] radical recombination trajectory. The solid-state structure was also noted to stabilise the intermediate radical pair as a local energetic minimum. Altogether, this once again demonstrates the importance of the solid-state in the stabilisation of reactive intermediates as well as its influence on product distribution: attempting the decarbonylation reaction in solution lead to a high degree of undesirable disproportionation. We have already seen how the rigid coordination sphere imposed by pincer complexes can permit SC-SC transformations (Albrecht, Ozerov, Schneider *et al*., *vide supra*). Huang, Brookhart and colleagues have also reported a remarkable set of such transformations (**Figure 1.1.5**).[63]

[a] A solid-state reaction with a pathway defined by the initial crystal structure.

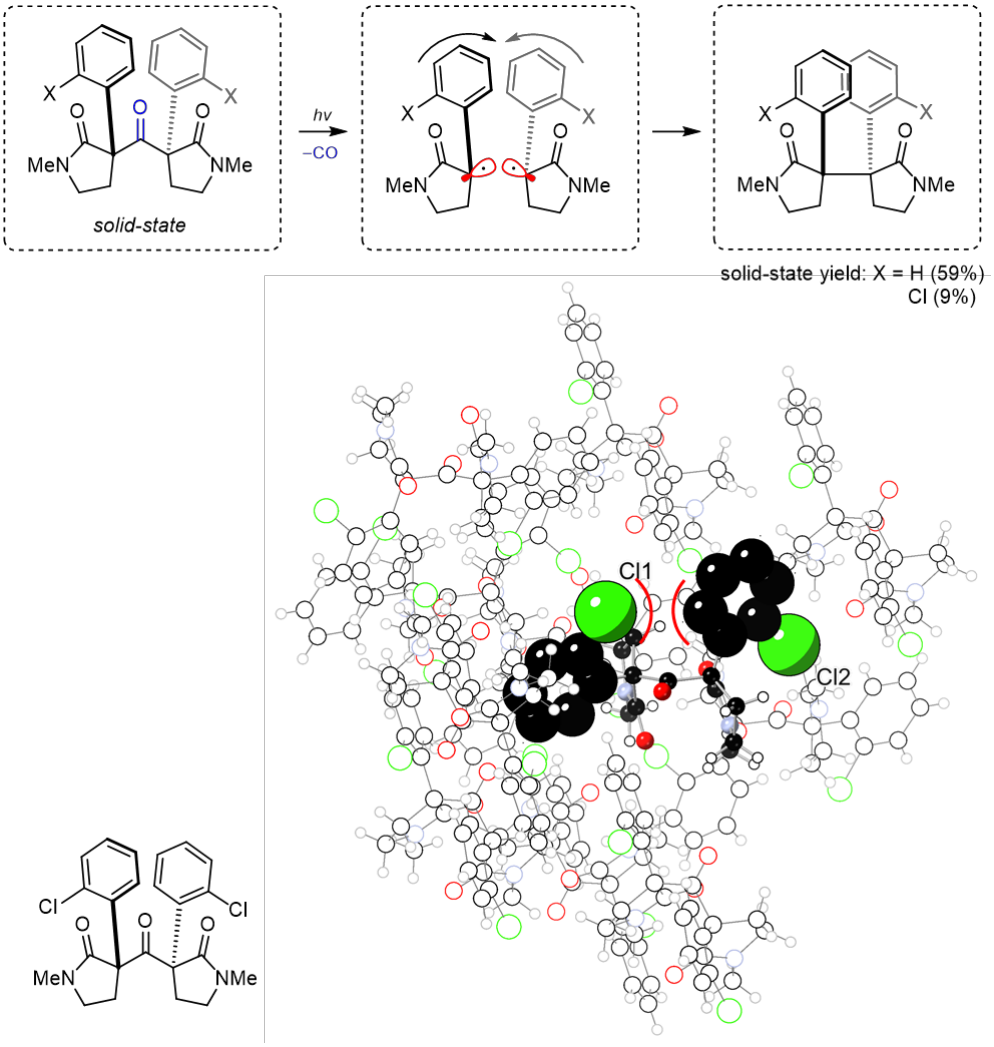


Figure 1.1.4: SC-SC photodecarbonylations described by Dotson and colleagues. The interrupted topochemical recombination trajectory intrinsic to the *ortho*-Cl structure is shown in the extended solid-state structure (constructed using *sc*-XRD data found in the reference), leading to a poor yield.[62]

Despite a non-porous structure (<6 Å^3, ~0.2% estimated free volume), small molecules (NH_3, C_2H_4, O_2, CO, H_2) were able to passivate single crystals of the labile dinitrogen complex [(Ar^{F9}-POCOP)Ir(N_2)] (Ar^{F9} = -2,4,6-$(CF_3)_3C_6H_2$) and generate the respective adducts while retaining crystallinity, with the unit cell volume varying by no more than ±0.6%. Transport throughout the crystal was proposed to occur *via* structural channels obstructed by co-crystallised toluene molecules, and catalytic hydrogenation of ethene was confirmed to be an interior process rather than a surface one. These concepts (a fluorinated ligand platform; a non-porous crystal capable of solid-gas chemistry) will also return to the discussion in later sections, particularly in Chapter 3.

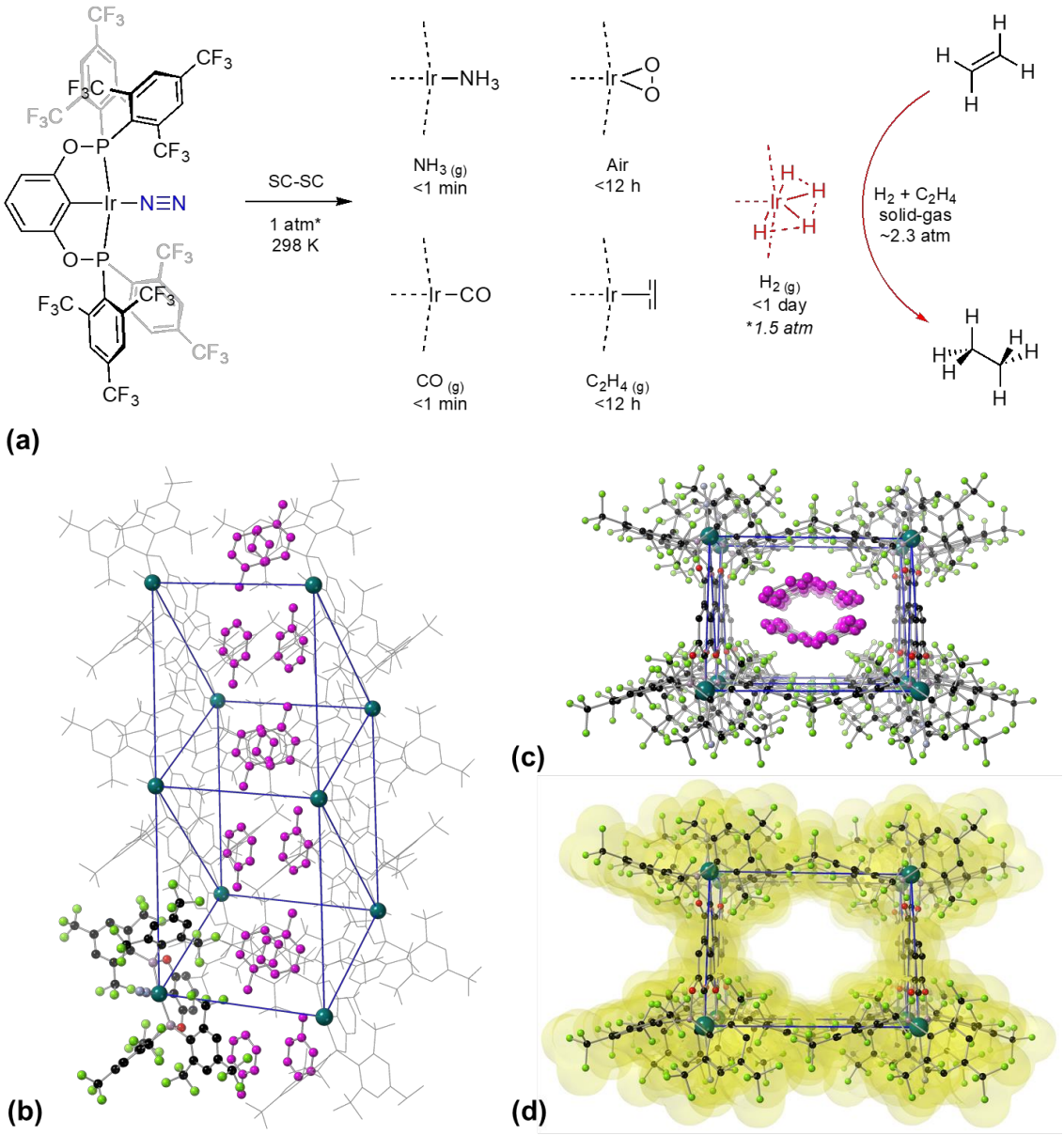
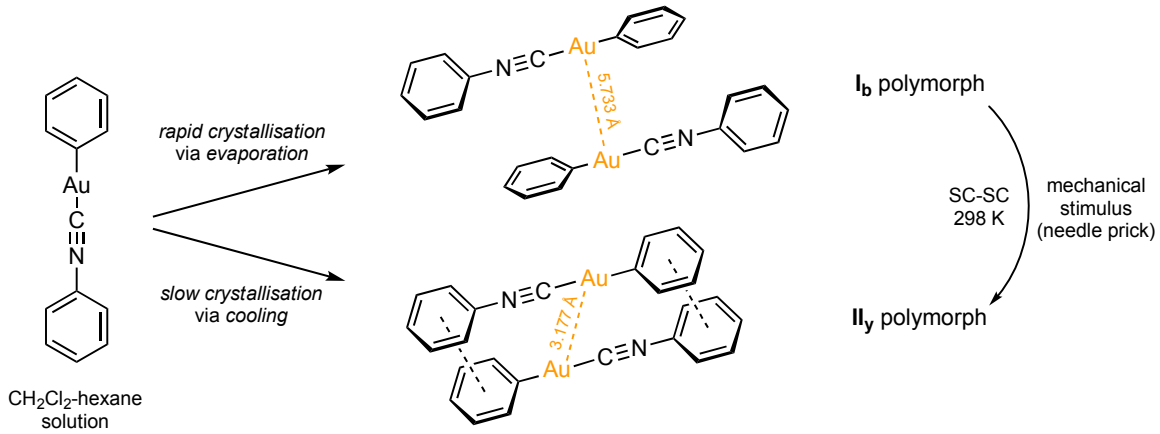


Figure 1.1.5: (**a**) Various SC-SC transformations proceeding from [(Ar^{F9}-POCOP)Ir(N_2)]. * note that H_2 gas was introduced at a higher pressure of 1.5 atm. (**b**) Solid-state packing pattern of [(Ar^{F9}-POCOP)Ir(N_2)]·(toluene)$_{2.5}$ (Ar^{F9} = -2,4,6-$(CF_3)_3C_6H_2$). Organometallic fragments modelled as both ball-and-stick and wireframe. Disordered toluene molecules modelled as ball-and-stick and highlighted in magenta. (**c**) Rotated view of (**b**), to show the structural channels. (**d**) As (**c**), with toluene molecules omitted and a van der Waals surface included (probe radius 1.4 Å). Produced from *sc*-XRD data found in the reference.[63]

1.1.3 *Polymorphism in Organometallic Crystals*

Polymorphs[64]a are well known for both inorganic[65,66] and organic[67–69] crystalline compounds, even polypeptides.[70] This is no less true for organometallic complexes:[71] conformational isomerism,[72] static and dynamic disorder,[73] and intermolecular interactions can all contribute to polymorphisms.[74–76]

While organometallic polymorph-to-polymorph transitions have been reported,[77] it is exceptionally rare that such a transition should occur in an SC-SC fashion, with an elegant example reported by Ito and colleagues (**Scheme 1.1.8**). Crystals of the metastable, monomeric $\mathbf{I}_b$ polymorph of [PhAu(CNPh)] (blue-luminescent under UV irradiation) were induced to convert to the dimeric $\mathbf{II}_y$ polymorph (yellow under UV) *via* a needle prick, promoted by the manifestation of a close aurophilic interaction.[78]



Scheme 1.1.8: Stimulus-induced polymorph-to-polymorph transition of single-crystalline [PhAu(CNPh)].

Concomitant with a closure of the intermolecular distance, a unit cell volume change of *ca.* −2.9% was noted. The small needle-prick impression, visible as a yellow-luminescent pockmark under UV irradiation, was observed to spread until this colour consumed the whole crystal. A 'domino' mechanism was envisaged, whereby the initial 'push' of the needle prick instigated a self-amplifying change throughout the solid-state assembly.

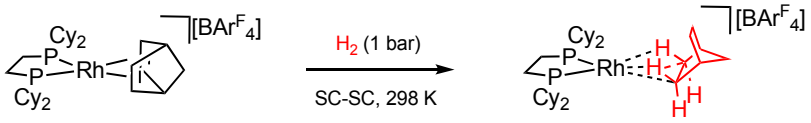
[a] Solid crystalline phases with identical chemical compositions (*i.e.* excluding isomers) but differing arrangements of atoms in the solid-state, therefore with differing intermolecular interactions and – depending on the ambient conditions – differing stabilities.

Polymorphs of [(dcpe)Rh(η^2-C_2H_4)$_2$][BAr^F_4] (dcpe = $Cy_2PCH_2CH_2PCy_2$) have been reported by Weller, Chadwick and colleagues (*vide infra*),[79] although conversion from one polymorph to the other was only possible *via* recrystallisation. Sethi and colleagues have reported a periodic structure-retaining, X-ray-induced SC-SC transformation from one polymorph of [(18-crown-6)K][$AuCl_4$] to another under the conditions of X-ray diffractometry at 110 K (~0.2% unit cell volume contraction).[80]

1.1.4 Solid-State Molecular Organometallics (SMOMs)

Solid-state molecular organometallics (SMOM) of the general formula [(P_2)Rh(η^2,η^2-alkene/s)][BAr^F_4] (P_2 = chelating *bis*-phosphine), reported by Weller and co-workers across many publications since 2012, are known to permit SC-SC transformations upon solid-gas hydrogenation, yielding remarkable σ-alkane complexes *in situ*, usually in a periodic structure-retaining fashion.[8,79,81–84] These σ-alkane complexes were sufficiently stable to permit characterisation by single-crystal X-ray/neutron diffraction techniques and solid-state NMR (SSNMR) spectroscopy.

An exemplary transformation is shown in **Scheme 1.1.9**, whereby crystals of the η^2,η^2-NBD complex [(dcpe)Rh(η^2,η^2-NBD)][BAr^F_4] were hydrogenated in the solid-state to yield the σ-NBA complex in an SC-SC fashion, with the resulting σ-NBA fragment bound to the metal through two three-centre-two-electron bonds.[82] The octahedral (O_h) packing arrangement of [BAr^F_4]$^-$ anions about cationic fragments found in the starting material was retained in the product (**Figure 1.1.6**), with a correspondingly modest unit cell volume expansion (~1.8%).



Scheme 1.1.9: SC-SC hydrogenation of SMOM [(dcpe)Rh(η^2,η^2-NBD)][BAr^F_4] to yield a σ-NBA complex.

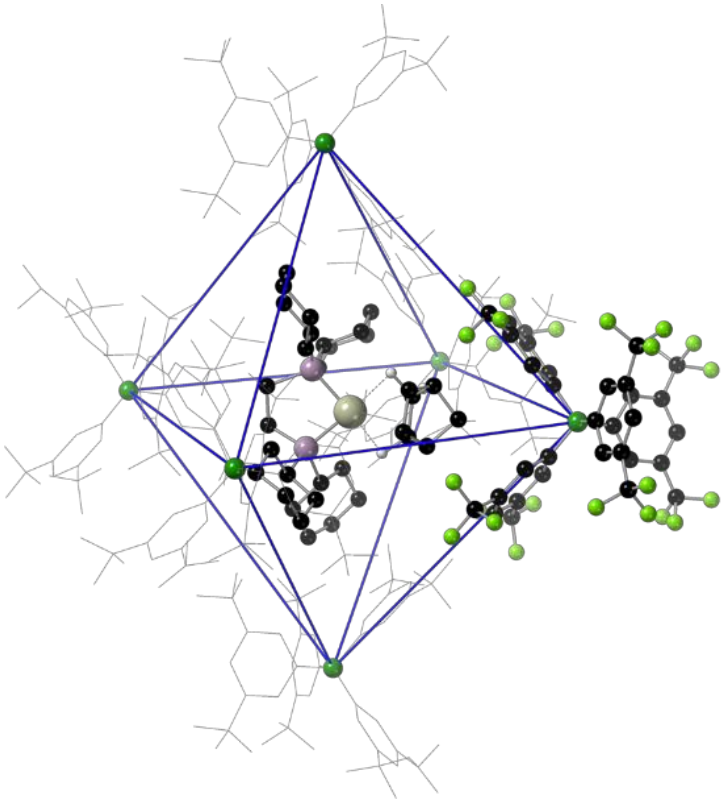


Figure 1.1.6: The near-octahedral (O_h) coordination of six $[BAr^F{}_4]^-$ anions (modelled as a mixture of ball-and-stick and wireframe with B-atom balls) about a cavity containing a $\{(dcpe)Rh\}^+$ fragment σ-bound to a molecule of norbornane (both modelled as ball-and-stick), protected inside an Ar^F-B-Ar^F 'cleft'. H atoms omitted for clarity except crystallographically-located σ-bound positions. Produced from neutron diffraction data of single-crystalline $[(dcpe)Rh(\sigma\text{-NBA})][BAr^F{}_4]$ found in the reference.[85]

Here we note once again the importance of the solid-state in stabilising a reactive species. Due to the very weak binding energy of the alkane to the metal,[86] the σ-alkane complex $[(dcpe)Rh(\sigma\text{-NBA})][BAr^F{}_4]$ was not stable in solution even at temperatures as cold as 133 K, yet was stable in the solid-state at 298 K in an argon-filled glovebox for months. It was reasoned that the $[BAr^F{}_4]^-$ anionic lattice was capable of supporting the reactive $[(P_2)Rh(\sigma\text{-NBA})]^+$ fragment in a protective microenvironment composed of $[BAr^F{}_4]^-$ anions (see **Figure 1.1.6**). Solution-phase instability is a property typical to σ-alkane complexes,[83] which are usually approached by photoextrusion of a ligand,[87] temporarily freeing up a binding site, or by metal-alkyl protonation,[88] and rarely possess lifetimes in solution on the order of seconds or longer, even at cryogenic temperatures. The reports of Weller and co-workers mark the first (and, to date, only) time solid-state techniques have been used to synthesise and characterise these reactive σ-alkane complexes.

The principle of a reactive fragment protected by an assembly of $[BAr^F_4]^-$ anions was successfully extended to the Co(I)-containing congeners, synthesised in the same way, by solid-gas hydrogenation of single-crystalline $[(P_2)Co(\eta^2,\eta^2\text{-NBD})][BAr^F_4]$ precursors.[89] The resulting high-spin $[(P_2)Co(\sigma\text{-NBA})]^+$ fragments were reactive enough to decompose in a frozen drop of oil at 100 K under *sc*-XRD conditions, but this conservative technique nonetheless permitted some structural characterisation, further highlighting the power of such solid-state techniques in supporting highly reactive species.

The weakly-bound σ-NBA ligand in $[(P_2)Rh(\sigma\text{-NBA})]^+$ (P_2 = chelating *bis*-phosphine) acts as a 'token ligand', and can easily be replaced in favour of a stronger donor in a subsequent solid-gas reaction with a small molecular reagent (*e.g.* CO, NH_3, ethene, propene, butene).[79,90] If the resulting complex is coordinatively unsaturated (*e.g. mono*-propene, *mono*-butene), the remaining coordination site may be occupied by an agostic bond that can undergo reversible C–H activation.[79] Such reversible C–H activation has also been seen in σ-NBA complexes[85] as well as in other σ-alkane complexes,[91] manifesting as H/D-exchange in the presence of a D_2 atmosphere. The importance of the property of reversible C–H activation, *especially in an allylic position*, will become apparent in the next Section, as well as in Chapter 2.

Replacement of this 'token' σ-NBA ligand in the solid-state with a stronger donor may also occur with retention of crystallinity. If it does so, this transformation generally also occurs concomitantly with retention of periodic structure. In the case of $[(dcpe)Rh(\sigma\text{-NBA})][BAr^F_4]$, itself retaining the O_h packing arrangement of the η^2,η^2-NBD precursor (**Figure 1.1.6**), action of ethene gas resulted in the formation of the *bis*-ethene complex in an SC–SC fashion, with continued retention of the O_h packing motif.[79]

However, as shown in Section 1.1.3, the products of such SC–SC transformations may be metastable polymorphs occupying structural patterns distinct from those obtained from solution methods, preserved by the solid-state nature of the chemistry. $[(dcpe)Rh(\eta^2\text{-}C_2H_4)_2][BAr^F_4]$ with an O_h arrangement of anions, as obtained by sequential exposure of $[(dcpe)Rh(\eta^2,\eta^2\text{-NBD})][BAr^F_4]$ to H_2 and ethene, was recrystallised from pentane/CH_2Cl_2 at –80 °C under an ethylene atmosphere, generating an alternative, channelled hexagonal packing motif (**Figure 1.1.7**) in a different space group ($P6_322$, *cf.* $C2/c$ of all preceding species).[79]

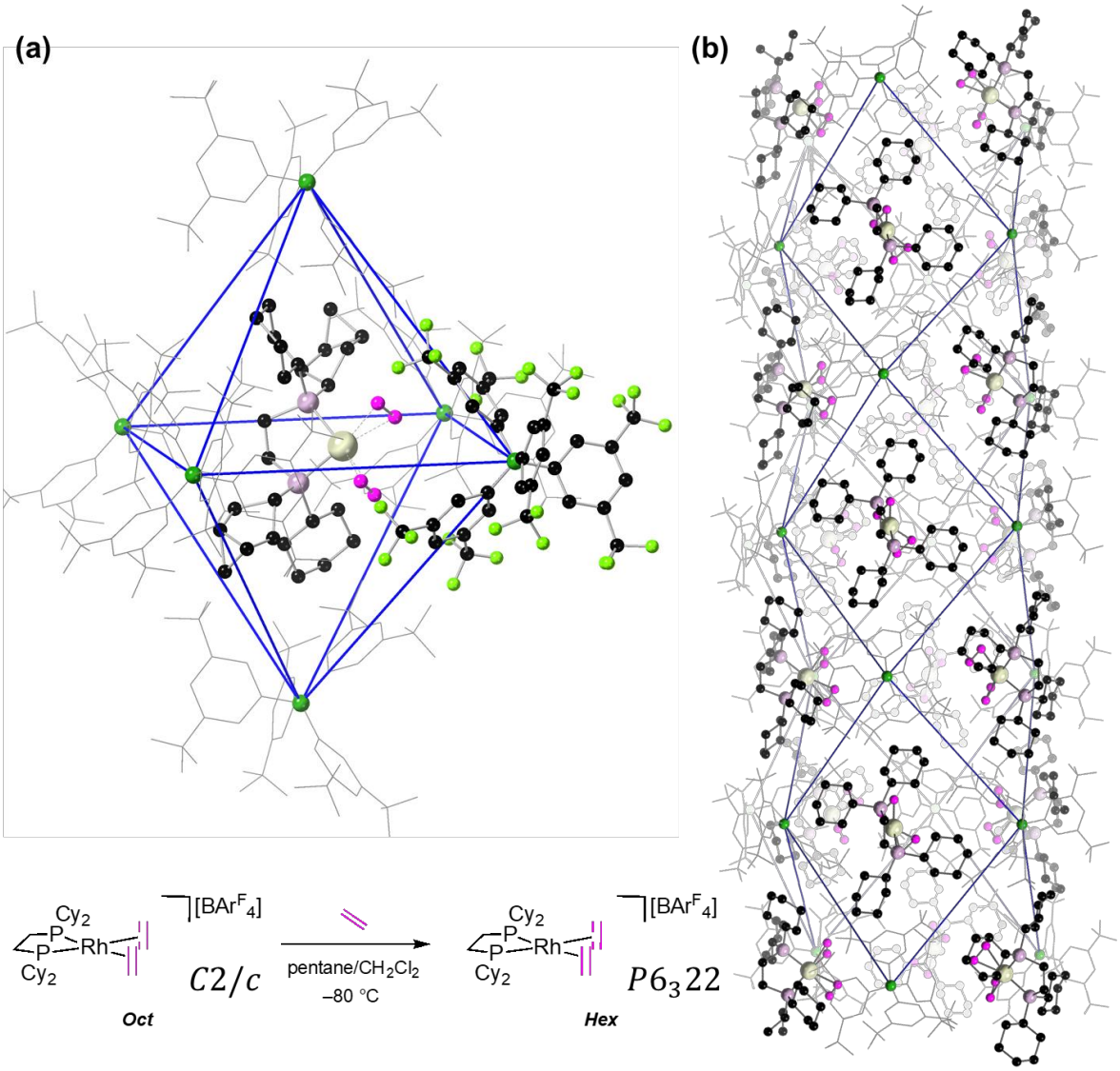
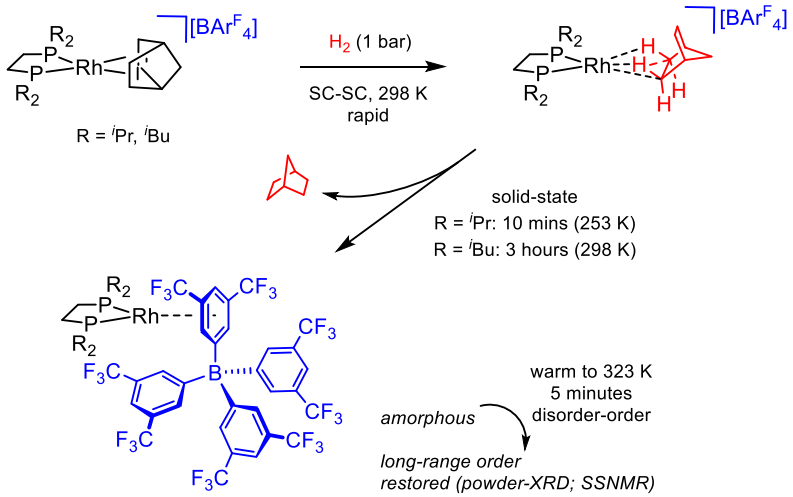


Figure 1.1.7: The (**a**) O_h and (**b**) channelled hexagonal solid-state packing patterns of $[(dcpe)Rh(\eta^2\text{-}C_2H_4)_2][BAr^F{}_4]$ polymorphs, with $[BAr^F{}_4]^-$ anions modelled as wireframes with B-atom balls and $[(dcpe)Rh(\eta^2\text{-}C_2H_4)_2]^+$ fragments modelled as ball-and-stick, with ethylene moieties highlighted in magenta. H atoms omitted for clarity. B-B nearest neighbour relationships are outlined in blue. Constructed from *sc*-XRD data found in the reference.[79]

Reflecting the plastic nature of the $[BAr^F{}_4]^-$ anionic lattice, a report on the spontaneous reordering of a SMOM has been made. Loss of weakly-bound NBA from single-crystalline $[(P_2)Rh(\sigma\text{-NBA})][BAr^F{}_4]$ (P_2 = dippe, $^iPr_2P(CH_2)_2P^iPr_2$; dibpe, $^iBu_2P(CH_2)_2P^iBu_2$) generated the corresponding Ar^F-coordinated zwitterions $[(P_2)Rh(\eta^6\text{-}Ar^F\text{-}BAr^F{}_3)]$ as amorphous solids, the structural rearrangement necessary for such a transformation leading to a complete loss of crystallinity (**Scheme 1.1.10**).[81,82]



Scheme 1.1.10: Loss of σ-bound NBA from crystalline $\{(P_2)Rh\}[BAr^F{}_4]$ resulting in the formation of an amorphous Ar^F-coordinated zwitterion.

Curiously, some restoration of crystallographic order was induced by gently warming the amorphous material to 50 °C for five minutes, *via* a disorder-order transition: the recovery of sharp peaks by *p*-XRD and solid-state NMR spectroscopy indicated the recovery of some degree of long-range crystallographic order. Such disorder-order transitions are well established for inorganics such as $[NH_4]Cl$,[92] various polymers (organic and coordination),[93,94] metals,[95] alloys,[96,97] and MOFs,[98–100] where spontaneous ordering can have a significant effect on the properties of the solid (*e.g.* conductivity, magnetism). They are, however, somewhat uncommon for discrete organometallic compounds.[101,102]

The importance of the $[BAr^F{}_4]^-$ anion array will become apparent over the course of this thesis, as further examples of order-disorder-order transitions and periodic structure-shifting SC-SC transformations are described. Critical to this discussion is the weakly-coordinating nature of the $[BAr^F{}_4]^-$ anion as well as its flexibility and plasticity in response to the stimulus of a solid-state reaction. We will now turn to how a lattice of $[BAr^F{}_4]^-$ anions can facilitate the solid-state reactivity with small molecules, even in the absence of well-defined structural channels. This property is of crucial importance in the deployment of these SMOMs as solid-gas catalysts, underlying the chemistry in both Chapters 2 and 4, and also arises in the SC-SC desolvation reaction described in the latter part of Chapter 3.

1.1.5 'Porosity Without Pores'

The CF_3 groups found in the $[BAr^F_4]^-$ anionic lattice of $[(P_2)Rh(\eta^2,\eta^2\text{-alkene/s})][BAr^F_4]$-type SMOMs ($P_2$ = chelating *bis*-phosphine) are thought to: (1) impart plasticity to the structure, allowing some degree of reorganisation, expansion or contraction; (2) facilitate small molecular reactivity as touched on above (*e.g.* with CO, NH_3, ethene, propene, butene);[79,90] and (3) prevent, due to their electron-withdrawing nature, deleterious reactivity of a metal centre with the aromatic ring, thus protecting the reactive fragment within an (almost) inert, anionic superstructure. The use of other weakly-coordinating anions in the attempted manufacture of SMOMs, such as $[Al(OC(CF_3)_3)_4]^-$,[103] yielded intractable oils that resisted attempts at crystallisation.[82,104] We have already seen how fluorinated groups have been employed successfully in solid-gas and SC-SC transformations, in the work of Gemel,[20] Chaplin,[53] and Huang *et al*.[63] Further to this, Kissel and colleagues[60] have reported the SC-SC [4+4] photodimerisation of a fluorinated derivative of triptycene, with close contacts between reactive units enforced by the crystal structure, tolerating a significant unit cell volume decrease of ~9.4% while retaining some degree of crystallinity.

Considering the van der Waals radii, these $[BAr^F_4]$-containing SMOMs are generally non-microporous materials,[105][a] with little PLATON-calculated solvent-accessible free volume.[79,106] Likewise is true for the systems described above reported by Albrecht,[38] Zenkina,[48] and Huang *et al*,[63] which all demonstrated SC-SC reactivity with various small molecules. Solid-gas, periodic structure-retaining SC-SC transformations concerning non-microporous materials have also been reported for *bis*-benzoylacetonato-copper(II) and its reversible loss of pyridine;[107] the reversible dehydration of a Cu(II)-centred metallacallixarene;[108] and the reversible uptake of vinyl bromide, methane, and CF_2Cl_2 by a polymorph of *p*-*tert*-butylcalix[4]arene, into a structure that possessed non-interconnecting voids (**Figure 1.1.8**).[109–111] Barbour has described this phenomenon as 'porosity without pores', proposing a dynamic process by which cooperation of host molecules can create transient opportunities for small-molecular trafficking.[112]

[a] A 'micropore' is defined in the IUPAC Gold Book as a structural pore with width not exceeding ~20 Å. In this instance, a non-microporous material is loosely defined as a structure lacking any significant solvent-accessible free space arranged in a manner that penetrates through the structure in an interconnecting manner to provide well-defined cross-structural channels.

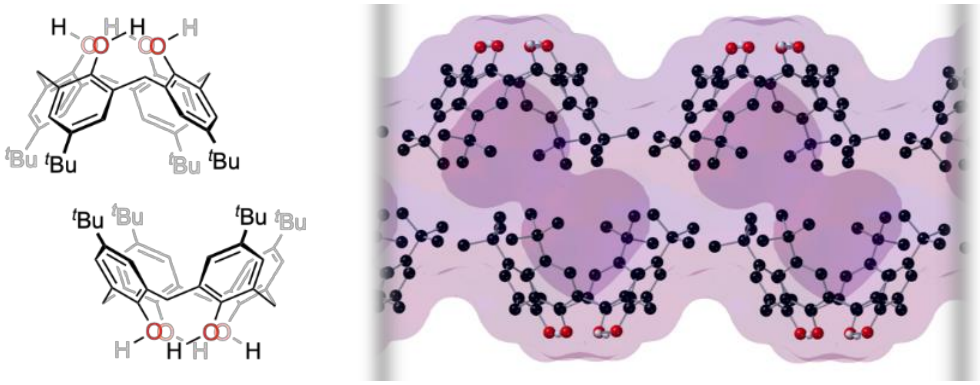


Figure 1.1.8: The solid-state packing pattern of *p-tert*-butylcalix[4]arene, modelled as ball-and-stick. H atoms omitted for clarity except those associated with -OH groups. A solvent-excluded surface (probe radius 1.4 Å) has been included, showing the non-interconnecting voids of two pairs of calixarenes. Constructed from *sc*-XRD data found in the reference.[111]

A similar explanation has been proposed by Brammer and colleagues, in studies concerning the reversible SC-SC uptake of alcohols in the non-microporous, fluorinated coordination polymer $[(CF_3CF_2CF_2COO)_4Ag_4(TMP)]_n$ (TMP = tetramethylpyrazine; ~10% unit cell volume expansion):[113,114] the cooperative motion of disordered fluoroalkyl moieties was reasoned to provide opportunities for small-molecular penetration into the lattice. The same logic may apply to the systems of Zenkina, Albrecht, Huang among others, as well as the $[(P_2)Rh(\eta^2,\eta^2\text{-alkene/s})][BAr^F{}_4]$-type SMOMs described by Weller and colleagues: a model of *solution-like* reactivity.[a]

In a study of this phenomenon, Martínez-Martínez *et al.* reported the SC-SC periodic structure-retaining uptake of xenon gas by the SMOM $[(dcpm)Rh(\eta^2,\eta^2\text{-NBD})][BAr^F{}_4]$ (dcpm = $Cy_2PCH_2PCy_2$).[115] As with the aforementioned examples, this SMOM was also essentially non-microporous in terms of its PLATON-calculated solvent-accessible free volume.[106] Successive evacuation (removal of co-crystallised CH_2Cl_2) and pressurisation under xenon gas for one week yielded single-crystalline SMOM containing xenon encapsulated inside the lattice, refining to ~50% by chemical occupancies, inside a small hydrophobic pocket (**Figure 1.1.9**) stabilised by a number of weak non-covalent interactions (NCIs). Reversible addition and removal of CH_2Cl_2 from the structure was also demonstrated.

[a] This concept is further discussed towards the end of Chapter 2 (Section 2.4.9).

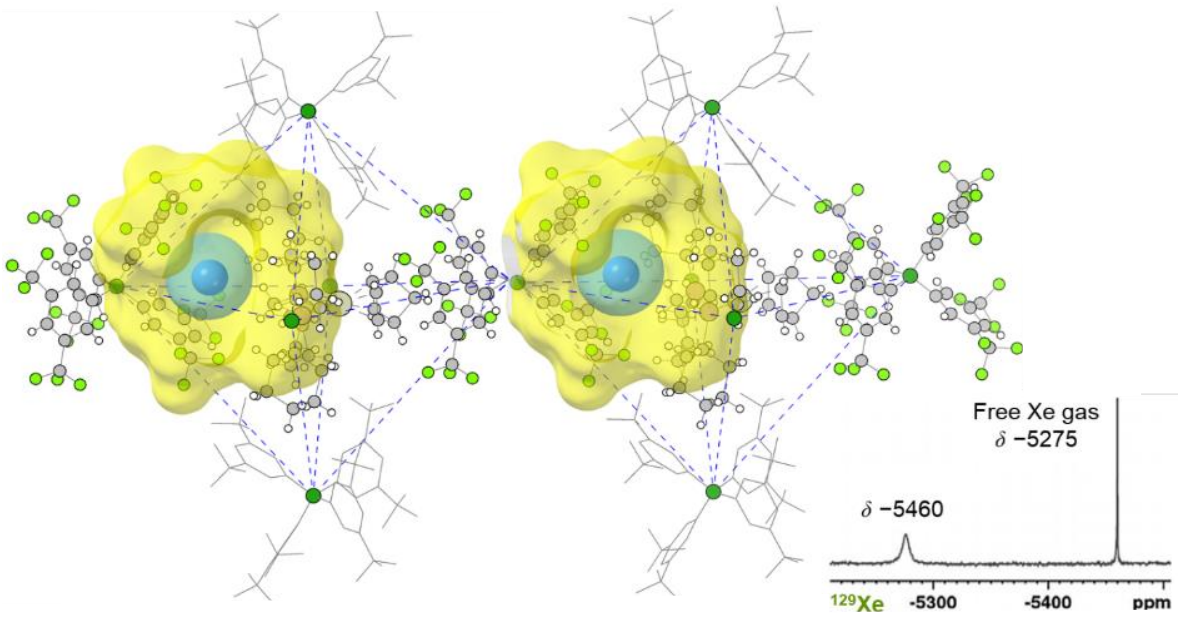


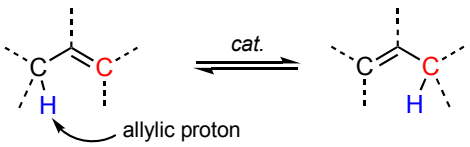
Figure 1.1.9: Two adjoining vertex-linked O_h packing motifs of six $[BAr^F{}_4]^-$ anions each (modelled as a mixture of ball-and-stick and wireframe) about cavities containing a $[(dcpm)Rh(\eta^2,\eta^2\text{-NBD})]^+$ fragment and an encapsulated xenon atom. H atoms and some anions omitted for clarity. Produced from *sc*-XRD data of single-crystalline $[(dcpe)Rh(NBA)][Xe_{0.5} \subset BAr^F{}_4]$ found in the reference.[115] A solvent-excluded surface (probe radius 1.4 Å) in yellow has been plotted around all the 'facing' atoms surrounding the crystallographically-located xenon atoms (~50% refined chemical occupancy) highlighted in blue, and a complimentary surface has been plotted around these xenon atoms. (**inset**) ^{129}Xe SSNMR spectrum of $[(dcpe)Rh(NBA)][Xe_{0.5} \subset BAr^F{}_4]$ (111 MHz, 294 K, ν = 10 kHz) in the presence of free xenon gas reproduced from the reference.[115]

The NMR-active ^{129}Xe nucleus presented an opportunity for the process to also be studied *via* SSNMR spectroscopy. At 294 K, a signal at δ –5460 was observed, corresponding to SMOM-absorbed xenon similar to that observed for MOF-absorbed xenon[116] and distinct from free xenon gas, detected at δ –5275. In line with the proposal of Brammer (*vide supra*), ^{19}F{^{1}H} SSNMR spectroscopy at 294 K revealed a broad signal at δ −63.2 ($[BAr^F{}_4]^-$ -CF_3) without ^{129}Xe coupling, suggesting rapid CF_3 rotation on the NMR timescale.

In this Section we have discussed the principles that govern solid-state organometallic chemistry – namely, the topological principle, the sequestration/stabilisation of reactive species, and the divergence between solid-state and solution-phase reactivity. We have also introduced solid-state molecular organometallics (SMOMs) as reported by Weller and colleagues, and how reactive σ-bound alkane fragments may be formed in the solid-state with retention of overall periodic structure.

We have also touched briefly on solid-state substitutions of the σ-NBA 'token ligand' by more strongly-binding alkenes, on reversible activation of C–H bonds, and on the penetration of $[BAr^F_4]^-$ anionic lattices by small molecules. We will now see how these concepts might be translated to the solid-gas isomerisation of alkenes by $\{(P_2)Rh\}[BAr^F_4]$-type SMOM catalysts (P_2 = chelating *bis*-phosphine). This will be the dominant theme of Chapter 2, in which these complexes are developed for use under continuous flow conditions.

1.2 Alkene Isomerisation



Scheme 1.2.1: Alkene isomerisation – the net migration of an allylic proton about a C=C π-bond.

An atom efficient and deceptively simple process, by which an alkene possessing at least one allylic proton is converted into its isomer (**Scheme 1.2.1**), alkene isomerisation is vital to a wide range of chemical processes: in the synthesis of certain organic compounds in which the conversion of an alkene into its isomer constitutes an important step;[117–120] and in certain industrial applications, such as the Shell Higher Olefin Process (SHOP).[121]

The isomerisation of 1-butene gas forms the first part of a process of considerable industrial importance, followed by a metathesis reaction with ethene to yield useful propene (*viz.* as the precursor to *poly*-propene).[122,123] Systems currently employed for heterogeneous 1-butene isomerisation generally catalyse the process under energy-intensive conditions, usually above 150 °C.[124] Examples that do so at 25 °C are known but scant.[125,126]

Finding a system that catalyses this process at ambient or near-ambient temperatures and pressures, with high yield and selectivity under heterogeneous conditions, remains an object of scientific interest. Deploying SMOM-type catalysts for this process will be the focus of Chapter 2.

1.2.1 Mechanisms of Alkene Isomerisation

Transition metal-catalysed alkene isomerisation is known to take place according to a range of possible mechanisms. The non-catalysed route, a concerted, suprafacial [1,3]-sigmatropic shift resulting in the transposition of the allylic proton, is symmetry-forbidden.[127] In practice, these rules are effectively relaxed in the presence of a catalyst. Acid-catalysed routes are well established, and are known to take place in solution (Brønsted and Lewis acids) or in the solid-state, on acidic surfaces (**Figure 1.2.1a**, *e.g.* on silica-alumina).[128,129] Base-catalysed routes,[130] photochemical routes with organic photosensitisers[131] and radical routes[132] have also been established.

Alkene isomerisation has been shown to proceed in the presence of an extensive range of organometallic catalysts, often dismissed as an undesirable side reaction – for example, under cracking conditions,[128] or in the presence of certain Ru-centred metathesis catalysts[117,133] or Co-centred hydroformylation catalysts.[134]

Three distinct mechanisms for the transition metal-catalysed isomerisation process have been proposed. In the presence of electrophilic metal catalysts without strongly basic ligands (*e.g.* $[Pd(NCMe)_4][BF_4]_2$[135]), the mechanism proceeds *via* a carbocationic intermediate from which a proton is eliminated (**Figure 1.2.1b**). In another, more ubiquitous mechanism, a hydride-bearing catalyst binds to an alkene, whereupon 'chain-walking' occurs *via* sequential hydride insertion and β-hydride elimination (**Figure 1.2.1c**).[117,118,136–140]

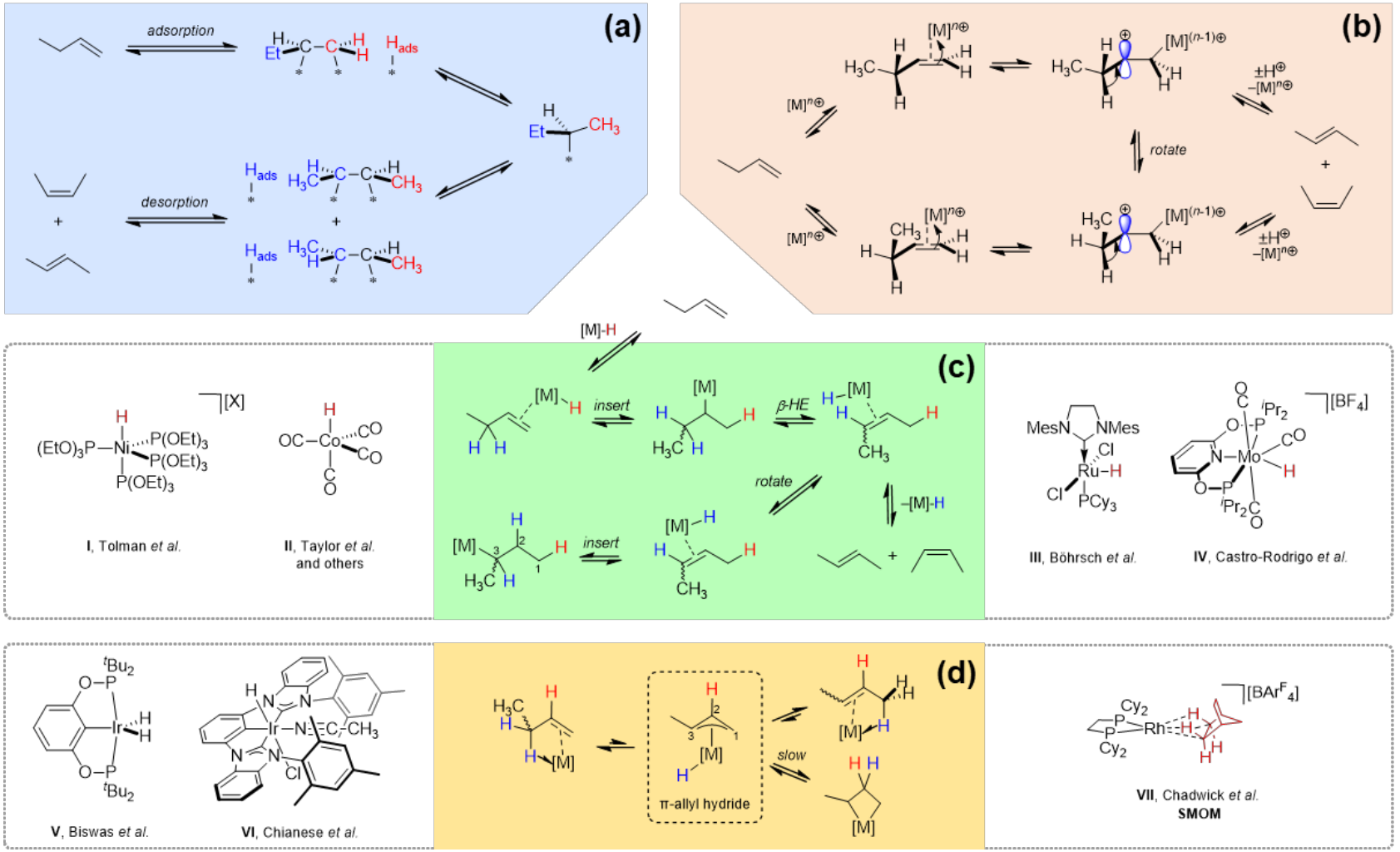
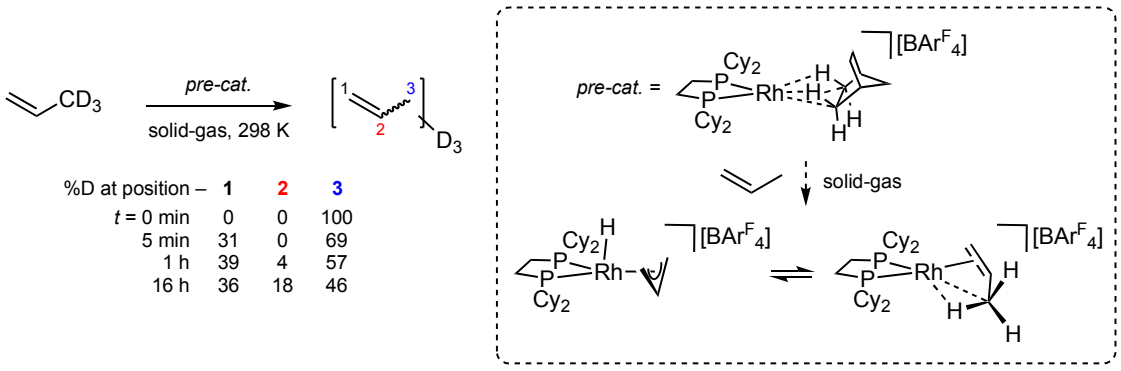


Figure 1.2.1: Mechanisms for alkene isomerisation, with 1-butene as the model alkene. (**a**) Heterogeneous acid-catalysed where * represents the surface; (**b**) Electrophilic metal-catalysed; (**c**) Metal-hydride insertion-elimination, with example catalysts **I-IV** (X = $[HSO_4]^-$, $[OTf]^-$); (**d**) π-allyl hydride, with example catalysts **V-VII**.

Another mechanism for the 1,3-shift of an allylic proton, proceeding *via* a π-allyl hydride, has been evidenced (**Figure 1.2.1d**). It has been proposed for the isomerisation of alkenes by $Fe_2(CO)_9$,[141] $Ru_3(CO)_{12}$,[142] $(Ph_3P)_3RhCl$,[143] and certain iridium-centred pincer complexes (*e.g.* **V**, **VI**).[144,145] Differentiating the insertion-elimination and π-allyl hydride mechanisms has been accomplished *via* the use of ^2H-labelled catalysts, hydride sources and substrates.[141,144,145] In the case of 1-butene, where a π-allyl hydride mechanism rapidly H/D-scrambled at the C1 (alkene CH_2) and C3 (allylic CH_2) positions only, the metal-hydride insertion-elimination mechanism was expected to rapidly scramble at all three positions.

Biswas *et al.* (**V**) were able to verify the operation of a π-allyl hydride mechanism using 3,3,3-d_3-propene (for which scrambling at only the C1 and C3 positions was observed, after ~40 hours at 333 K), and crossover experiments with *perdeutero*- and *perprotio*-propene: no intermolecular H/D scrambling was observed.[144] Chianese *et al.* (**VI**) observed similar results with d_2-4-allylbiphenyl (deuterated at the allylic position), and in crossover experiments with *perprotio*-allylbenzene.[145] Siedle and colleagues reported the generation of π-allyl hydride in a solid-gas reaction between $[(Ph_3P)_2IrH_2]_3[PW_{12}O_{40}]$ and 3,3,3-d_3-propene. Here, ^2H was also under-expressed at the central C2 position (C*1*:*2*:*3* at 1.01:0.32:1.66) on the allyl moiety.[15]

In previous work published by the Weller group, it has been reported that single-crystalline [(dcpe)Rh(σ-NBA)][BAr^F_4] (**VII**), a solid-state molecular organometallic (SMOM) produced *in situ* by solid-state hydrogenation of an η^2,η^2-NBD complex precursor (see Section 1.1.4), catalysed the solid-gas isomerisation of 1-butene at 298 K despite an absence of lattice porosity (see Section 1.1.5). The π-allyl hydride mechanism was proposed, appropriate to the 14-electron $\{(dcpe)Rh\}^+$ fragment that did not possess the metal hydride moiety necessary for the insertion-elimination mechanism.[79,104,146] Evidence for this mechanism was forthcoming *via* the use of 3,3,3-d_3-propene in conjunction with gas-phase ^2H NMR spectroscopy, for which H/D scrambling at the C2 position occurred much more slowly than for the C1 and C3 positions (**Scheme 1.2.2**).[79] Solution-phase ^1H NMR studies were undertaken after scrambling was complete (CD_2Cl_2, 193 K), in which the H-bound -CH_3, -CH_2D (two diastereomers) and -CD_2H isotopomers were all visible due to isotopic perturbation of the γ-agostic signal.



Scheme 1.2.2: Combined solid-gas alkene isomerisation and H/D scrambling in gaseous 3,3,3-d_3-propene with [(dcpe)Rh(NBA)][BAr^F_4] as pre-catalyst, forming the corresponding propene complex *in situ*. Percentage deuteration estimated (±5%) from gas-phase ^{2}H NMR spectroscopy; *cis*/*trans* ratio ~1 at $t \geq 5$ minutes, measured from gas-phase ^{1}H NMR spectroscopy.

Furthermore, solution-phase and solid-state ^{1}H and ^{31}P{^{1}H} NMR spectroscopic studies conducted on [(dcpe)Rh(η^2-h_6-propene)][BAr^F_4] evidenced a fluxional tautomerisation-isomerisation process at 298 K (see **Scheme 1.2.2**), arrested at 193 K, at which the γ-agostic η^2-bound propene complex was resolved. A similar tautomerisation-isomerisation process is described in Chapter 2 (Section 2.3.2).

1.2.2 Cis/Trans *Selectivity in Alkene Isomerisation*

Assuming that alkene isomers may bind to catalysts *reversibly* after an isomerisation reaction, a thermodynamic distribution of isomers will eventually be achieved, ultimately favouring the more stable *trans*-isomers over *cis*.[147] However, in the early stages of catalysis, under non-equilibrium conditions, it has been observed that non-thermodynamic ('kinetic') distributions of isomers may be achieved, even in the absence of directing groups. In 1972, Tolman and colleagues observed this phenomenon in the isomerisation of 1-butene with $Ni(P(OEt)_3)_4$ in the presence of H_2SO_4. The active catalyst thus generated, $HNi(P(OEt)_3)_4^+$, proceeded *via* the metal-hydride insertion-elimination mechanism.[140] While in the later stages of catalysis, a thermodynamic ratio of 2-butenes (*cis*:*trans* = ~1:3) could be observed, observations made early-on indicated a non-thermodynamic, ~1:1 ratio of 2-butenes.

A similar non-thermodynamic ratio of isomers in the early stages of catalysis was reported by Kelm and colleagues working with [$(Ph_3P)_3RhCl$], positing a π-allyl hydride mechanism.[143] More recently, Holland and colleagues observed this phenomenon of initial *cis*-selectivity with their high-spin Co(II) *β*-diketiminate system, proceeding *via* the insertion-elimination mechanism.[148] The rate-determining *β*-hydride elimination step apparently favoured the formation of *cis*- over *trans*-2-hexene, due to the imposition of the ligand scaffold. The phenomenon of initially *cis*-selective alkene isomerisation has also been observed to occur under heterogeneous solid-gas conditions. Zaera and colleagues observed initial preferential formation of *cis*- over *trans*-2-butene on Pt(0) nanoparticles, due to the imposition of the metal surface, and the resulting discrepancy in reorganisation energies.[149] More curiously, proceeding from pure 2-butene isomers, *trans*-2-butene was observed to isomerise twice as rapidly as *cis*-2-butene on the surface of tetrahedral Pt(111) nanoparticles, despite the ultimate thermodynamic preference for the *trans* isomer.

Evidence of initial *cis*-selectivity was also forthcoming in previous work by the Weller group, where *σ*-alkane complex [(dcpe)Rh(*σ*-NBA)][BAr^F_4] catalysed the heterogeneous isomerisation of 1-butene at 298 K, under NMR batch conditions.[79,104] In the early stages of catalysis, an overall conversion to 2-butenes of 96% was observed *via* gas-phase ^{1}H NMR spectroscopy, almost matching the expected thermodynamic proportion of 97.7%[147] in total, but not in detail. Analysis of the gas mixture *via* gas chromatography (GC), a technique capable of differentiating 2-butene isomers where gas-phase ^{1}H NMR spectroscopy cannot, showed a non-thermodynamic *cis*:*trans* ratio of ~1:1. The system eventually achieved the expected thermodynamic ratio of ~1:3 with a longer reaction time.

By grace of the coordination sphere's influence on the active site, certain systems have even demonstrated selectivity for terminal alkenes: Biswas and colleagues, for example, observed that their neutral pincer-ligated Ir(I) alkene isomerisation catalyst, [(^{t}Bu-POCOP)Ir(*trans*-2-hexene)], underwent rapid isomerisation to [(^{t}Bu-POCOP)Ir(1-hexene)] at 60 °C, with a calculated energy span of ~4.4 kcal mol^{-1}.[144] This reflects the difference in energy between various iterations of metal-hexene interaction rather than any thermodynamic preference for terminal over internal free alkenes.

1.2.3 SMOMs, Solid-Gas Alkene Isomerisation, and Structure-Activity Relationships

It has been shown above that stereoelectronic factors – namely, the imposition of the metal coordination sphere – can markedly affect the selectivity of an alkene isomerisation catalyst. In this section we will also demonstrate the importance of periodic structural factors – *i.e.* the anionic lattice – in solid-gas alkene isomerisation catalysed by SMOMs. To demonstrate this, the catalytic capabilities of SMOMs [(dcpe)Rh(η^2,η^2-NBD)][X] were tested, pre-hydrogenated to form the σ-NBA complex *in situ*, where X = $[BAr^F{}_4]^-$, $[BAr^{F2}{}_4]^-$, $[BAr^{Cl2}{}_4]^-$, $[BPh_4]^-$ (Ar^F = -3,5-$C_6H_4(CF_3)_2$, Ar^{F2} = -3,5-$C_6H_4F_2$, Ar^{Cl2} = -3,5-$C_6H_4Cl_2$).[104]

An obvious difference between these SMOMs in which the anion was systematically varied was their solid-state packing patterns. Where [(dcpe)Rh(η^2,η^2-NBD)][$BAr^F{}_4$] is known to possess an O_h packing motif with the cationic fragment [(dcpe)Rh(η^2,η^2-NBD)]$^+$ oriented into an Ar^F-B-Ar^F 'cleft' (refer to **Figure 1.1.6**),[82] substitution of $[BAr^F{}_4]^-$ for $[BAr^{F2}{}_4]^-$ or $[BAr^{Cl2}{}_4]^-$ lead to dramatic change in the solid-state structure. In the case of X = $[BAr^{F2}{}_4]^-$, Ar^{F2}–F $\cdots$ H–Ar^{F2} hydrogen bonds were noted, favouring a bicapped parallelepipedic (BCPP) packing motif such that two cationic fragments had 10 neighbouring anions. In the case of X = $[BAr^{Cl2}{}_4]^-$, interanionic Cl$\cdots$Cl close contacts were formed, favouring a bifastigial packing motif such that each cationic fragment had eight neighbouring anions (**Figure 1.2.2**). The change in structure for X = $[BPh_4]^-$ was more subtle. While still packing octahedrally, the cationic fragment [(dcpe)Rh(η^2,η^2-NBD)]$^+$ oriented into an inter-anionic 'channel' (an O_h 'face'), rather than a Ph-B-Ph 'cleft' (an O_h 'vertex'). The structure-organising role of inert ions (the 'anion template effect') in the solid-state has been emphasised in reports on the self-assembly of metallacyclophanes,[150] clusters,[151] and other supramolecular systems.[152]

The importance of the $[BAr^F{}_4]^-$ anion in solid-gas catalysis was demonstrated *via* systematic anion substitution, subtly altering the manifold of anion-anion and anion-cation interactions by which structure and activity are controlled. The remarkable ability of [(dcpe)Rh(σ-NBA)[$BAr^F{}_4$] to catalyse the isomerisation of alkenes in the solid-state has been discussed. 2 mg of the crystalline η^2,η^2-NBD complex in an NMR tube, after hydrogenation to form the σ-NBA complex *in situ*, achieved 96% conversion of an atmosphere of 1-butenes (1 bar) into 2-butenes at 298 K after two minutes, measured by gas-phase ^{1}H NMR spectroscopy.

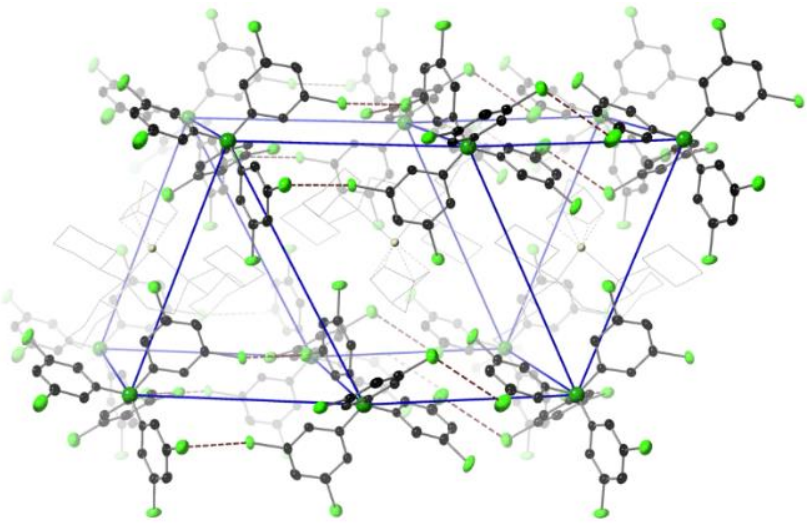


Figure 1.2.2: The bifastigial solid-state packing pattern of [(dcpe)Rh(η^2,η^2-NBD)][$BAr^{Cl2}{}_4$], constructed from *sc*-XRD data found in the reference.[104] [$BAr^{Cl2}{}_4$]$^-$ anions modelled as 50% displacement ellipsoids with B atom balls; [(dcpe)Rh(η^2,η^2-NBD)]$^+$ fragments modelled as wireframes with Rh atom balls. Cl-Cl close approaches (l < 3.8 Å) are shown as dashed lines.

Substituting X = [$BAr^F{}_4$]$^-$ for [BPh_4]$^-$ resulted in an inactive catalyst as the σ-NBA complex did not persist: the quenched, inactive Ph-coordinated zwitterion [(dcpe)Rh(η^6-Ph-BPh_3)] was formed rapidly in the solid-state. Substituting X = [$BAr^{F2}{}_4$]$^-$ or [$BAr^{Cl2}{}_4$]$^-$ still yielded active catalysts, but with stunted reactivity (72% and 88% conversion, respectively, after two minutes). The Ar-coordinated zwitterions (*e.g.* **Figure 1.2.3**) were noted to form more slowly, on a timescale on the order of hours, not seconds as for [BPh_4]$^-$ (determined *via* $^{31}P\{^1H\}$ SSNMR spectroscopy). This indicated that [$BAr^{F2}{}_4$]$^-$ and [$BAr^{Cl2}{}_4$]$^-$ also performed well as weakly-coordinating anions, albeit still inferior to [$BAr^F{}_4$]$^-$, for which the σ-NBA complex persisted for months in the solid-state at 298 K under argon. Despite reduced activity, ~1:1 *cis*:*trans* ratios were recorded for both [$BAr^{F2}{}_4$]$^-$ and [$BAr^{Cl2}{}_4$]$^-$, reflecting the early *cis*:*trans* ratio of the [$BAr^F{}_4$]$^-$ system.

This relative loss of activity in the [$BAr^{F2}{}_4$]$^-$ and [$BAr^{Cl2}{}_4$]$^-$ systems clearly demonstrated a structure-activity relationship. The blame for this discrepancy cannot have lain with solid-state quenching, due to the tardiness of this process in these systems, and instead must have lain with the more subtle, passive relationship between active site and anionic lattice: either through imposition of the structure's secondary coordination sphere upon the catalyst, or through the facilitation of molecular movement to and from active sites.

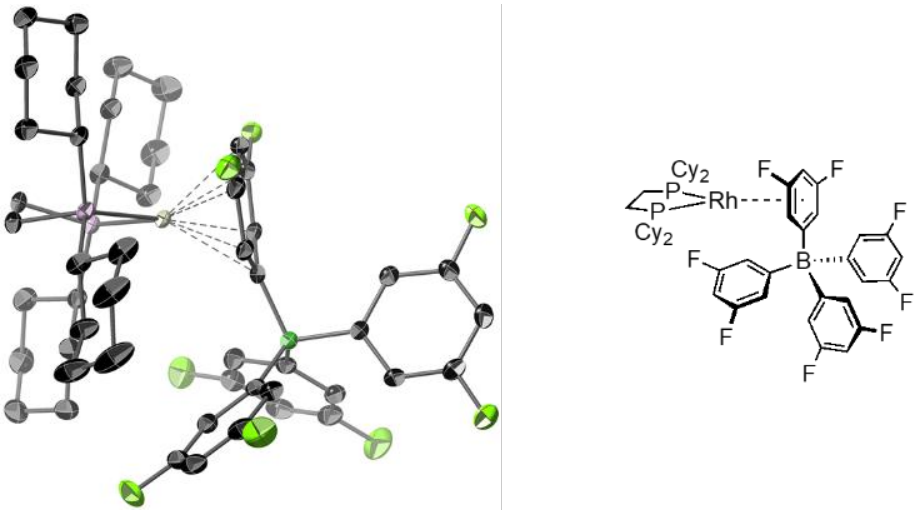


Figure 1.2.3: The zwitterionic complex [(dcpe)Rh(η^6-Ar^{F2}-BAr^{F2}_3)] as produced in the solid-state by displacement of the σ-NBA 'token ligand' and recrystallised from solution. H atoms omitted for clarity. Constructed from *sc*-XRD data found in the reference.[104]

Structure-activity relationships – including the primary, secondary and tertiary coordination environments – work holistically to promote activity and selectivity in catalysis, and are well established for enzymes[153,154] as well as certain inorganic systems such as MOFs and zeolites.[155–157] We have already encountered two polymorphs of the same SMOM, [(dcpe)Rh(η^2-C_2H_4)$_2$][BAr^F_4] (O_h $C2/c$ and hexagonal $P6_322$, **Figure 1.1.7**): structure-activity relationships in SMOMs were also illustrated for this complex, when each polymorph was tested as a solid-gas 1-butene isomerisation catalyst.[79] Where O_h $C2/c$ was essentially non-porous, hexagonal $P6_322$ was highly microporous, with cylindrical pores running through the structure and a PLATON solvent-accessible volume of ~25%.[106] The hexagonal polymorph was a considerably more active catalyst than O_h, with an apparent turnover frequency (TOF_{app}) ~60 times greater.

In this section we have discussed a wide range of possible alkene isomerisation mechanisms accessible by transition metal catalysts, and we have seen how SMOM techniques might be applied to the isomerisation process. While batch catalysis has been previously demonstrated,[79,104] including a report on a non-thermodynamic mixture of alkenes early in the experiment (see Section 1.2.2),[104] it has yet to be seen if is possible to reproduce this chemistry under industrially relevant solid-gas flow conditions. We will now discuss the principles of continuous flow techniques as a brief practical background to Chapter 2.

1.3 Principles of Continuous Flow Chemistry

Over the last 20 years, chemistry conducted under continuous flow conditions has undergone a massive expansion.[158,159] This is a testament to the wide range of synthetically powerful, industrially appealing advantages to its credit, finding application not only in the field of organic synthesis[160–162] but also in the synthesis of nanoparticles,[163] MOFs,[164] proteins,[165] and polymers,[166] as well as in heterogeneous solid-gas chemistry.[124,167,168] It is not the scope of this introduction to provide an overview to all of these fields, but rather only to focus on the core principles of continuous flow techniques, and a small number of previously reported applications pertinent to this work.

The benefits which may be afforded by conducting a reaction under continuous flow conditions, as opposed to under static batch conditions, may be summarised as follows:

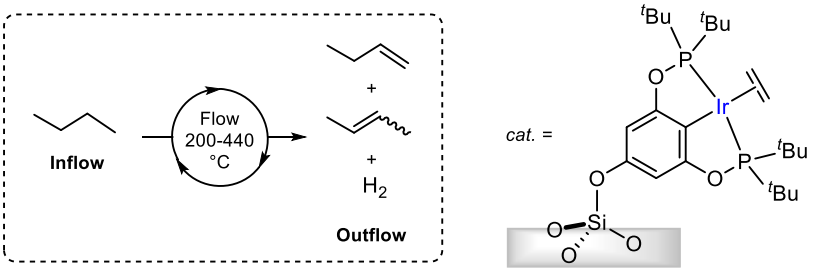
(1) Continuous flow reactors possess a much greater effective surface area than their batch reactor counterparts.[169] Not only does this lend to more effective reagent mixing, especially in multi-phase reactions (flow conditions lack a traditional 'headspace'), this also lends to more efficient heat transfer, either to the reaction or away from it, and therefore closer temperature control. This is a useful property when conducting exothermic reactions, where desired product *versus* side-product ratios can depend on careful and precise temperature control. Flow techniques can dramatically improve these ratios even when $\Delta\Delta G^{\ddagger}$ are small;[158]

(2) Although more time-consuming and costly to set up compared with traditional batch conditions, flow conditions are highly scalable, appealing to industry as a technique to undertake large-scale, continuous production;[170]

(3) Once set up, the outflow of a continuous flow experiment may be constantly monitored (solutions: *e.g.* LC-MS, TLC, NMR; gases: *e.g.* GC-MS). This property lends to the possibility of high-throughput experimentation, automation, and machine learning in conditions optimisation.

These advantages are amplified when continuous flow is applied to heterogeneous chemistry, namely solid-liquid, solid-liquid-gas, and solid-gas reactions,[171–173] where reagents or catalysts are immobilised on a solid support inside the reactor cavity. If the risk of leaching is controlled,[174] heterogeneous continuous flow conditions can impose a higher overall effective molarity of catalyst compared to heterogeneous *batch* conditions, improving reaction rates and selectivity.[175] Wasteful separation and purification steps are sidestepped,[176] and there exists the possibility of supramolecular structure- or morphology-imposed selectivity.[177,178] For heterogeneous solid-gas chemistry, disadvantaged in terms of effective molarity compared to homogeneous chemistry, there is no possibility of deleterious reactivity with a solvent and, as such, higher reaction temperatures may be contemplated. Coking may be avoided using continuous flow techniques, allowing catalysts to remain active for longer.[179]

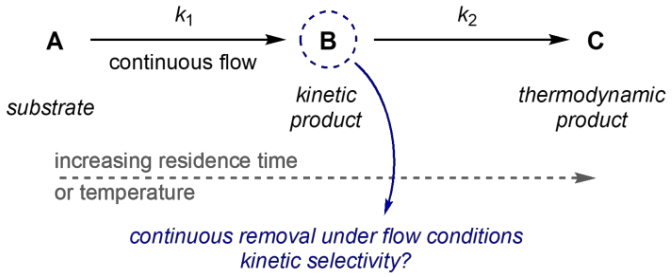
In certain cases, flow conditions may even drive a thermodynamically-uphill reaction forward, by constant removal of a gaseous product from an equilibrium process. For example, an inert gas flow might favour alkane dehydrogenation by removing any evolved H_2,[180,181] and a report of McKay and colleagues explored how this concept might translate to a SMOM.[91] Sheludko and colleagues showed that silica-supported PONOP-Ir(I) complexes catalysed alkane dehydrogenation (**Scheme 1.3.1**), with heterogeneous continuous flow conditions key in biasing the loss of H_2.[179] Flow conditions meant that once the gaseous alkene was formed it was separated from the catalyst, preventing the thermodynamically-preferable reverse reaction from taking place.



Scheme 1.3.1: Catalytic dehydrogenation of *n*-butane gas under heterogeneous continuous flow conditions by a silica-supported neutral POCOP-type iridium(I) pincer complex.

1.3.1 *Selectivity Under Continuous Flow Conditions*

Consider the simplified reaction shown in **Scheme 1.3.2.** If certain conditions are met, *e.g.* through careful control of temperature (T) and residence time in flow (t^R) under continuous flow conditions such that **B** is removed from the system before reacting further to give **C**, *non-thermodynamic* distributions of products can be obtained in the outflow. This property is significantly more difficult to replicate under batch conditions, and non-thermodynamic selectivity may be advantageous in achieving higher yields of certain isomers by simply removing the kinetic product from contact with the catalyst. This concept is especially pertinent to the chemistry discussed in the latter sections of Chapter 2, which focus on the isomerisation of 1-butene by SMOM catalysts under heterogeneous continuous flow conditions.



Scheme 1.3.2: A simplified reaction scheme outlining the possibility of kinetic selectivity under heterogeneous continuous flow conditions, where $k_1 \gtrsim k_2$.

Evidence is available for this phenomenon of kinetic selectivity under both homogeneous and heterogeneous continuous flow regimes, and for both stoichiometric and catalytic reactions. Nagaki and colleagues have reported the use of flow microreactors in controlling the selectivity of lithiation reactions: decreasing T and t^R were shown to disfavour intramolecular reactivity of 2-lithio-2′-(trimethylsilyl)biphenyl, due to the presence of a rate-determining aryl-aryl rotation for the required *cis* conformation (**Figure 1.3.1**).[182] Decreasing T has also been shown to favour *mono*-addition of various aryllithiums to difunctional electrophiles over *bis*-addition (or indeed *mono*-addition at a less electrophilic site),[183] and a carefully controlled t^R was employed to make use of transient $LiCH_2F$ in organic synthesis, produced by the lithiation of CH_2FI by MeLi *in situ* before decomposing *via* α-elimination.[184]

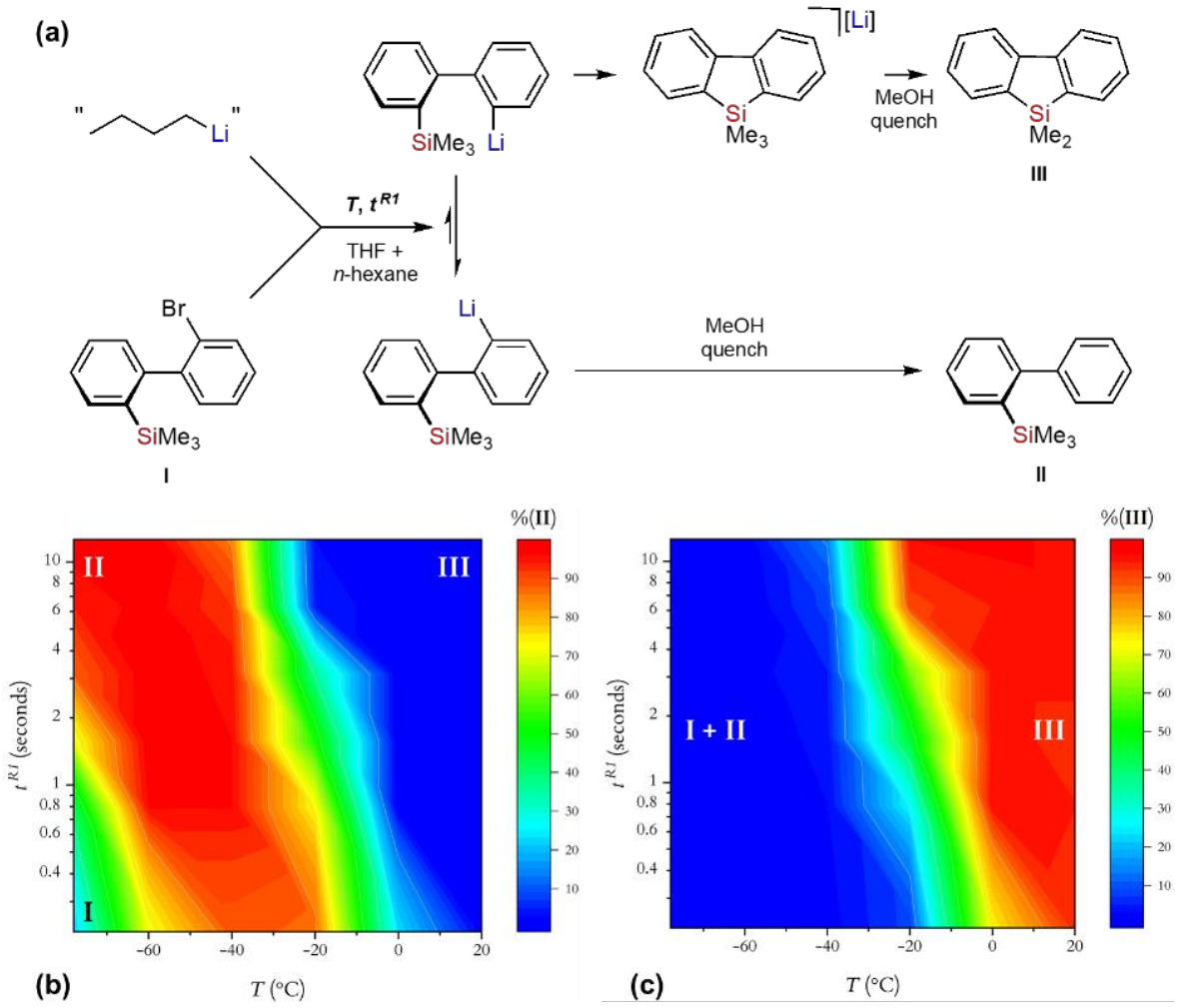


Figure 1.3.1: (**a**) The report of Nagaki and colleagues on the continuous-flow lithiation of 2-bromo-2′-(trimethylsilyl)biphenyl (**I**) followed by MeOH quenching. (**inset graphs**) Percentage yield of **II** (**b**) and **III** (**c**) in the outflow as determined by gas chromatography plotted against temperature (T) and first retention time (t^{R1}), presented as contour plots where high percentage yields are represented in red, low in blue. Constructed using data obtained from the reference.[182]

Similar reports of such kinetic selectivity under continuous flow conditions are numerous, covering topics as widespread as Staudinger cycloadditions,[185,186] photochemical alkane activation,[187,188] heterogeneous Wacker oxidations,[189] and the solid-liquid 1,4-addition of aldehydes to nitroalkenes over polypeptide-bearing resin.[190] The phenomenon of kinetic selectivity under flow conditions is also well established for supported transition-metal catalysts, particularly for solid-liquid-gas hydrogenations or solid-liquid coupling reactions.

Djakovitch and colleagues – for example – identified that their supported Pd Heck arylation catalysts favoured non-conjugated, kinetic *cyclo*-hexenyl- and *cyclo*-pentenyl-arenes at lower T, whereas raising T favoured the more stable, conjugated isomers.[191] The sequential hydrogenation/hydrogenolysis of furfural over a wide range of supported transition metals in flow was reported in detail by Garcia-Olmo and colleagues, who noted that the *mono*-hydrogenation product (furfuryl alcohol) was favoured at lower reaction temperatures.[192]

Under batch conditions, the selective hydrogenation of *bis*-alkenes (or alkynes) to *mono*-alkenes can be difficult to control, especially when the chemical environment of both π-bonds is similar. Schmidt and colleagues have described a solid-liquid hydrogenation of 1,5-cyclooctadiene, geraniol, 1-octyne and phenylacetylene over Pd nanoparticles on polyacrylic acid resin. It was identified that while more substrate was consumed with a higher residence time t^R, selectivity for the *mono*-alkene over the alkane decreased as a result.[193]

A report on the solid-gas flow hydrogenation of 1,3-cyclooctadiene in the vapour phase over Pd/Al_2O_3 has also been made by Hass and Gaube, in which the flow rate was shown to be vital in attaining good selectivity of cyclooctene (COE) over cyclooctane (COA), a key consideration being the greater binding strength of the *bis*-alkene 1,3-cyclooctadiene over the *mono*-alkene COE.[194]

At this point we can again invoke the work of Sheludko and colleagues on supported PONOP-Ir(I) complexes for catalytic alkane dehydrogenation (*vide supra*, **Scheme 1.3.1**). While dehydrogenation of gaseous *n*-butane proceeded smoothly across the temperature range, particularly for $T \geq 300$ °C, non-thermodynamic distributions of *n*-butene isomers were observed in the outflow at all tested temperatures.[179] Catalysts capable of catalytically dehydrogenating alkanes also tend to be capable of catalysing alkene isomerisation[144,195–197] – it follows that isomerisation competes with dehydrogenation, even if the initial dehydrogenation step is almost entirely selective for terminal alkenes. With the imposition of solid-gas continuous flow conditions and constant removal of the reactant gas mixture, the authors isolated non-thermodynamic mixtures of *n*-butene isomers in the outflow, favouring 1-butene (the 'kinetic' product).

As we shall see in Chapter 2, heterogeneous continuous flow techniques can be applied successfully to the solid-gas isomerisation of 1-butene by a pre-activated SMOM (also see Section 1.2.1), and, much like Sheludko and colleagues, non-thermodynamic mixtures of *n*-butenes were obtained in the outflow. The morphology of the catalyst as well as the residence time (as flow rate) and the particle size, in analogy to Sheludko, will all be shown to be important in this process.

We will now turn to the solid-gas catalytic hydrogenation of alkenes by SMOMs, a process related to (and sometimes occurring in parallel with) isomerisation. This process has already been demonstrated with normal[a] H_2.[79] We set out to extend the utility of this reaction by making use of *para*-H_2, one of two possible nuclear-spin modifications of dihydrogen that is capable of inducing significant NMR enhancement effects upon incorporation. In the proceeding Section, the principles underlying this enhancement phenomenon are outlined, highly pertinent to the work described in Chapter 4.

[a] 'Normal' refers to the ~3:1 equilibrium ratio of *ortho* and *para* H_2 nuclear spin isomers present at >250 K, reflecting the state degeneracies in the high temperature limit. The meaning of these terms will be expounded upon in the next Section. Unless otherwise specified, literature on chemistry involving H_2 gas (*e.g.* hydrogenation reactions) will have implicitly been referring to 'normal' H_2 gas (*n*-H_2).

1.4 Principles of *Para*-Hydrogen Induced Polarisation (PHIP)

The advantages posed by SMOMs for solid-gas alkene isomerisation – the preserving of a reactive, coordinatively-unsaturated intermediate in a hydrophobic pocket – may also translate to solid-gas alkene *hydrogenation*. In a previous report, various SMOMs of type [(dibpe)RhL$_2$][BAr$^F_4$] (dibpe = ^{i}Bu$_2$P(CH$_2$)$_2$P^{i}Bu$_2$) were shown to catalyse ethene hydrogenation rapidly at 298 K and at relatively low pressure (4.0 atm, unoptimised), eventually yielding the inactive Ar^F-coordinated zwitterion in the solid-state.[90]

The phenomenon of *para*-hydrogen induced polarisation (PHIP) of unsaturated substrates by means of catalytic hydrogenation is well established in the solution-phase,[198–200] giving rise to strongly emissive and/or absorptive transitions under NMR conditions with up to ~10^4 increases in signal-to-noise. This powerful NMR enhancement technique has a wealth of potential applications, from the elucidation of inorganic reaction mechanisms to medical imaging techniques.[201] In Chapter 4, we will discuss the development of PHIP chemistry in the gas phase using SMOM catalysts, in order to generate hyperpolarised gaseous hydrocarbons that may be of utility as inhalable medical contrast agents. In this section, a brief theoretical and practical background for NMR enhancement techniques involving *para*-H$_2$ is provided.

1.4.1 Spin Isomers of the Dihydrogen Molecule

For spin-½ particles ($s = ½$), two possible spin states exist: 'spin-up' ($m_s = +½$)[a] and 'spin-down' ($m_s = -½$), denoted as $|\alpha\rangle$ and $|\beta\rangle$ respectively.[202] When a nuclear spin system contains two such spins (*viz*. ^{1}H$_2$), these spins may interfere constructively or destructively, giving total nuclear spins I of either one or zero respectively. For the $I = 1$ ('triplet') case, three projections $m_I = 0, \pm 1$ exist, with three corresponding degenerate[b] wavefunctions ($|T\rangle$, **Figure 1.4.1**). Similarly, for the $I = 0$ ('singlet') case, only one projection $m_I = 0$ exists, with a sole corresponding wavefunction ($|S\rangle$, **Figure 1.4.1**).[203]

[a] m_S reflects the projection of this spin angular momentum (quantised as s) along the z-axis, which is parallel to the magnetic field.
[b] These states are degenerate only in the absence of a magnetic field.

$$|T_+\rangle = |\alpha_1\alpha_2\rangle$$

$$|T_0\rangle = \frac{1}{\sqrt{2}}(|\alpha_1\beta_2\rangle + |\beta_1\alpha_2\rangle) \qquad |S\rangle = \frac{1}{\sqrt{2}}(|\alpha_1\beta_2\rangle - |\beta_1\alpha_2\rangle)$$

$$|T_-\rangle = |\beta_1\beta_2\rangle$$

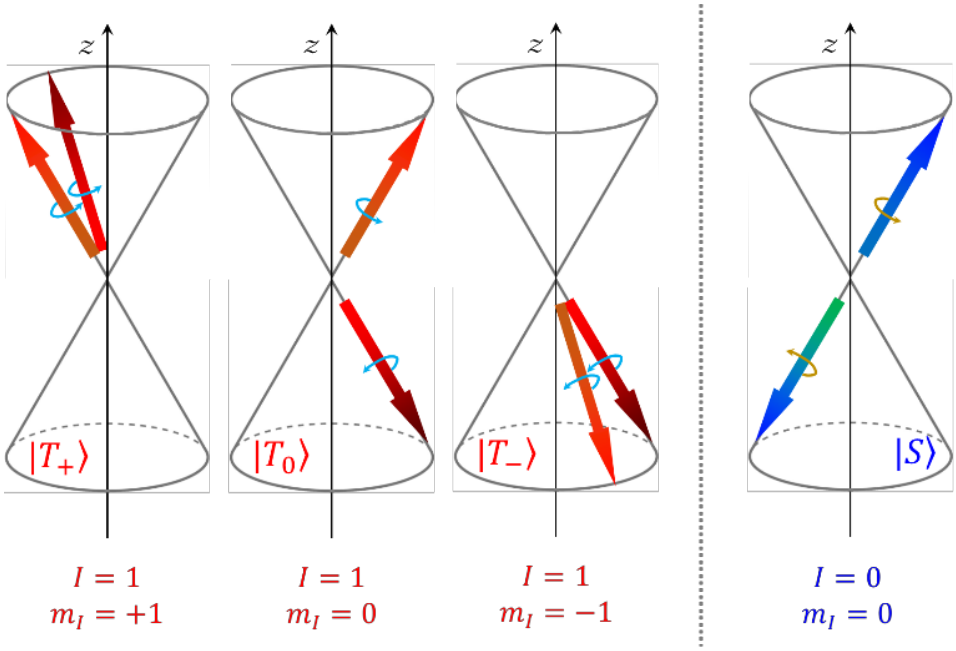


Figure 1.4.1: Simplified representation of the two ^{1}H nuclear spins found in the various spin isomers of $^1H_2$. Note that the spins are arranged in such a way that reflects the total and z-direction spin magnitudes of each isomer. Triplet wavefunctions are highlighted in red, singlet in blue. The z-axis is coincident with the magnetic field.

From here on, we will refer to the triplet states as *ortho* and the singlet state as *para*. The nuclear spin wavefunctions of the *ortho* spin isomers are symmetric (**SYM**) with respect to permutation of positions, such that $\hat{P}_{12}|T\rangle = |T\rangle$, and the *para* wavefunction is antisymmetric (**ANTI**), such that $\hat{P}_{12}|S\rangle = -|S\rangle$. States such as $|\alpha_1\beta_2\rangle$ and $|\beta_1\alpha_2\rangle$ cannot describe the intermediate-energy states as permutation of positions does not regenerate the original wavefunction, *e.g.* $\hat{P}_{12}|\alpha_1\beta_2\rangle = |\beta_1\alpha_2\rangle \neq \pm|\alpha_1\beta_2\rangle$. We therefore instead require normalised linear combinations that satisfy permutation, as given in **Figure 1.4.1**.[204]

Since the *para*-H_2 nuclear spin modification possesses no spin-allowed ($\Delta I = 0$) transitions, given only one state, *para*-H_2 is NMR-silent. *ortho*-H_2, given three states, is NMR-active.

For fermions, *i.e.* nuclei with half-integer spins, the Pauli exclusion principle requires the overall wavefunction Ψ_{total}, given in **Equation 1.1**, to be **ANTI** with respect to permutation of positions.

$$\Psi_{total} = \varphi_{trans}\,\varphi_{rot}\,\varphi_{vib}\,\varphi_{elec}\,\varphi_{nuc} \qquad \textbf{1.1}$$

Considering the nuclear spin (φ_{nuc}), rotational (φ_{rot}), vibronic (φ_{vib}), translational (φ_{trans}) and electronic (φ_{elec}) components of this overall wavefunction, we note that φ_{vib}, φ_{trans} and φ_{elec} are all **SYM** for $^1H_2$. The three *ortho* (**SYM**) nuclear spin states φ_{nuc} must therefore be paired with **ANTI** rotational states φ_{rot}, *i.e.* with spatial symmetry described by $J = \text{odd}$, to produce an **ANTI** total wavefunction Ψ_{total}. Conversely, the *para* (**ANTI**) nuclear spin state must be paired with **SYM** rotational states, *i.e.* $J = \text{even}$, including zero. The three-dimensional rotational partition function of H_2, q_{rot}, is given in **Equation 1.2**:

$$q_{rot} = \underbrace{\frac{3}{2}\cdot\sum_{J=1,3\ldots}(2J+1)e^{-E_J/kT}}_{ortho} + \underbrace{\frac{1}{2}\cdot\sum_{J=0,2\ldots}(2J+1)e^{-E_J/kT}}_{para} \qquad \textbf{1.2}$$

Here, a factor of ½ has been included to account for the ∞C_2 symmetry of the H_2 molecule, and the rotational energy $E_J \propto J(J+1)$. Note that the state degeneracies $(2J+1)$ have been included as prefactors. From this, we can deduce that the populations of the *ortho* and *para* states must be temperature dependent. In the high temperature limit (for $^1H_2$, $T > 250$ K), the partition function collapses to a 3:1 *ortho*:*para* ratio, reflecting only the state degeneracies.

Samples of room-temperature, equilibrium $^1H_2$ (so-called *normal*-H_2, with *ortho*:*para* ~ 3:1) are metastable when cooled. The singlet-triplet transition is forbidden by symmetry ($\Delta I = 0$), hence $J = \text{odd} \leftrightarrow$ even may not occur rapidly in the absence of a catalyst (usually activated charcoal or a paramagnetic material). This perturbs the system by eliminating its inherent symmetry, thereby catalysing the approach to equilibrium. In the *low* temperature limit, the ~120 cm^{-1} $J = 0 \rightarrow 1$ energy span cannot be crossed: only the $J = 0$ ground state should be populated, and the content of the *para*-H_2 spin isomer approaches 100%. 25 K is predicted to be sufficiently cold for ~98% *para*-H_2 conversion in the presence of a suitable catalyst.[204,205]

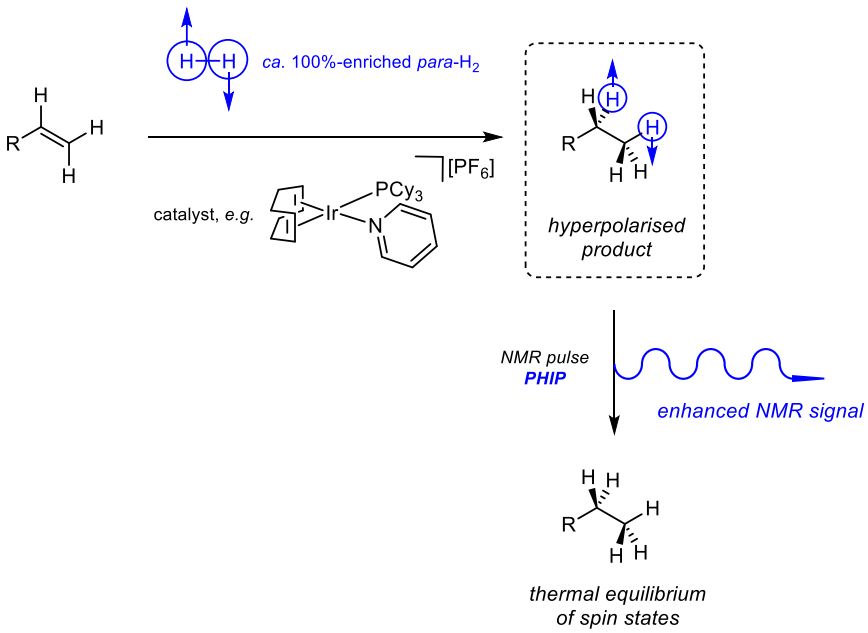
Removed from contact with this catalyst, samples of ~100% *para*-H_2 become metastable once more upon warming, taking hours or even days to reach equilibrium at 298 K. Note that this logic, of *ortho* and *para* spin states in a two-spin system, also applies to symmetric 2 × spin-½ molecules such as $^{12}C_2{}^1H_2$ and $^1H_2{}^{16}O$,[206] and higher-spin analogues of dihydrogen (*i.e.* $^2H_2$, where for a deuteron $s = 1$).[207]

1.4.2 Overview of PHIP and Relevant Spin Physics

To illustrate the PHIP phenomenon, we can use the incorporation of *para*-H_2 across a vinyl moiety, considering only five ^{1}H nuclei (vinyl + H_2) for the sake of simplicity. In the product, under normal NMR conditions, the CH_3 group of its ethyl moiety has eight possible nuclear spin states. In the absence of a magnetic field these states are degenerate, but when $\boldsymbol{B} > 0$, these states are Zeeman-split, and populate according to a Boltzmann distribution, where the state population $p_i \propto \exp(-E_i/kT)$ and therefore the population ratio between two states $p_i/p_j \propto \exp(-\Delta E/kT)$. A 90° radio-frequency pulse converts magnetisation in the z-direction into Zeeman-only transverse (x,y) magnetisation, generating a detectable free induction decay (FID) as this x,y-magnetisation evolves and decays.

Since the energy difference between these eight CH_3 states is very small even under standard NMR conditions, the population ratio between two given states is close to unity and so the population *difference* is also small. An NMR signal arises from the difference between the energy absorbed by spins transitioning from a lower state to a higher one and the energy emitted by spins transitioning from a higher state to a lower one, such that the signal intensity is directly proportional to the population difference. These eight CH_3 states interact with the adjacent CH_2 group in the ethyl moiety, for which four states exist (*cf.* $^1H_2$), two of which (*cf.* $|S\rangle$ and $|T_0\rangle$) are degenerate, giving rise to the classical 1:2:1 binomial triplet. In the reverse case, the four possible nuclear spin states of the CH_2 interact with the eight spin states of the CH_3, of which six are triply degenerate, giving rise to the classical 1:3:3:1 quartet.

We note that the generation of classical NMR signals relies on a Boltzmann population of spin states, where state populations are discriminated only on the basis of a state's energy, the temperature at which the experiment is conducted, and the static magnetic field strength. If the *opposing* spins of a *para*-H_2 molecule are incorporated into this vinyl moiety to yield an ethyl moiety, the signal patterns of those positions affected will no longer exhibit classical binomial multiplets due to the perturbation of the normal, thermal Boltzmann distribution (**Scheme 1.4.1**).[208] The population differences underpinning NMR spectroscopy, and their corresponding signal intensities, are now much greater than Boltzmann statistics might predict.



Scheme 1.4.1: The conceptual underpinnings of *para*-hydrogen induced polarisation (PHIP).

Incorporation of *para*-H_2 can generate complex, unusual resonances, especially when combined with the complicating effects of relaxation in the product molecule (regenerating an interfering classical multiplet at the same chemical shift) and imperfect pulse angles (due to an inhomogeneous magnetic field at the extremities of the coil). Enhancements on account of *para*-H_2 incorporation are referred to as *Para*-Hydrogen Induced Polarisations (PHIPs), which may be on the order of a 10^2-10^4 signal-to-noise boost in the affected ^{1}H positions.[198,205] Such enhancements are reminiscent of those observed for radical recombination reactions, which occur under the same Pauli principle constraints.[209]

A rigorous handling of the spin physics behind this phenomenon is beyond the scope of this thesis, and is covered in exhaustive detail in other publications.[210,211] Suffice to say, that by incorporating enriched *para*-hydrogen ($I = 0$) into this vinyl moiety ($I_{\text{max}} = {}^{3}/_{2}$), certain nuclear spin states in the product molecule (*i.e.* $I_{\text{max}} = {}^{5}/_{2}$) cannot be populated due to the conservation of spin angular momentum. This includes the lowest- and highest-energy spin states which will be of maximum spin multiplicity, and one unit of spin angular momentum greater than the lowest- and highest-energy spin states in the substrate.

Ethene $^{12}C_2{}^{1}H_4$, as a further example, possesses five quintet ($I = 2$) nuclear spin states, including the lowest- and highest-energy states $|\alpha_1\alpha_2\alpha_3\alpha_4\rangle$ and $|\beta_1\beta_2\beta_3\beta_4\rangle$. None of these are accessible from acetylene $^{12}C_2{}^{1}H_2$ ($I = 0, 1$, *cf.* $^{1}H_2$) by incorporating *para*-H_2 ($I = 0$).[212] This results in the over-population of certain nuclear spin states in the product molecule, and zero-population of the 'forbidden' states, giving rise to enhanced-intensity transitions (emissive and absorptive) from populated states, and absent transitions from unpopulated ones. Per molecule of *para*-H_2, this non-Boltzmann population of states is short-lived and does not last beyond a single pulse, whereafter thermal equilibrium of spin states is restored.[200]

We have assumed thus far that a magnetic field is absent (or, rather, only the Earth's weak ambient magnetic field is present). In a simple AX spin system, *e.g.* a metal hydride $[M]^{1}H_2$ with inequivalent hydrides $^{1}H_A$ and $^{1}H_X$, only one pure singlet state with opposed spins $|\alpha_A\beta_X\rangle$ survives upon incorporation of *para*-H_2, arising directly from the singlet state $|T_0\rangle$ (**Figure 1.4.1**). This effect is known as Adiabatic Longitudinal Transport After Dissociation Engenders Nuclear Alignment (ALTADENA), wherein the reaction occurs outside the spectrometer before prompt transfer to the probe.[198–200,213]

ALTADENA permits only two of the four available NMR transitions, one strongly absorptive (**2**) and one strongly emissive (**3**), and omitting two others that would have otherwise contributed to a pair of doublets. Note that now the incorporated protons from *para*-H_2 are chemically inequivalent, singlet-triplet transitions are now allowed.

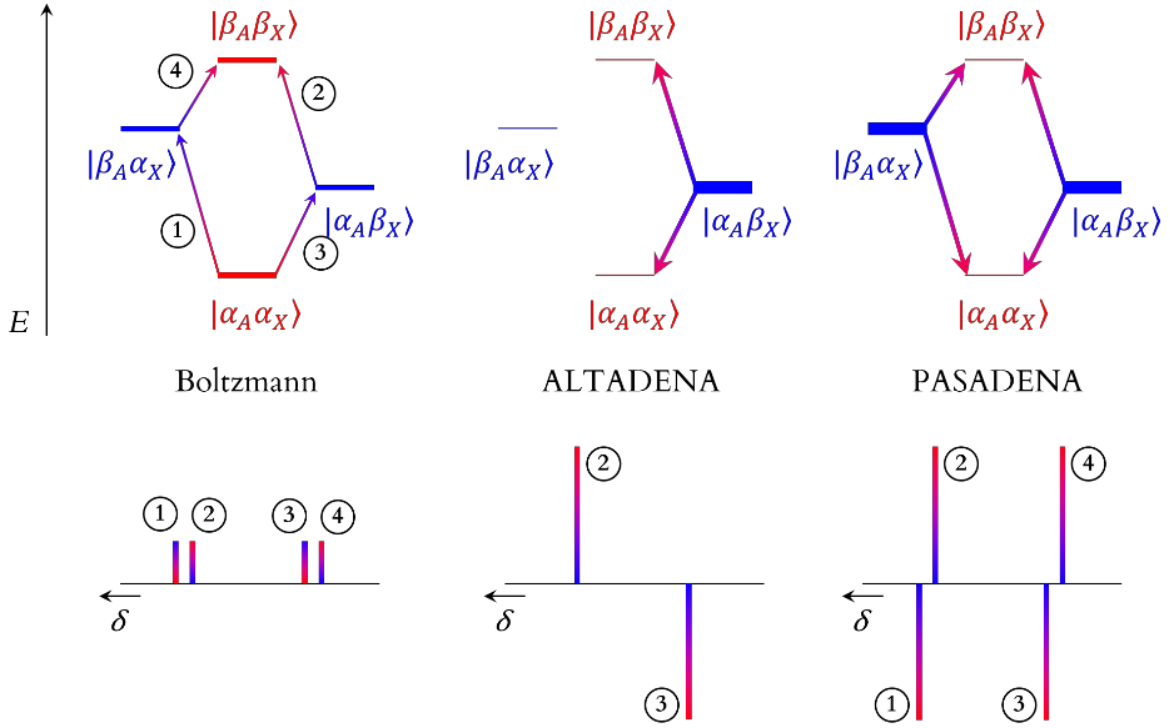


Figure 1.4.2: Simplified energy level diagram of AX nuclear spin states and the transitions between them (1-4) assuming $J_{AX} < 0$, adapted from the reference.[198] Relative spin state population and transition intensity indicated by line thickness. Since $J_{AX} \neq 0$, singlet-triplet transitions are possible.

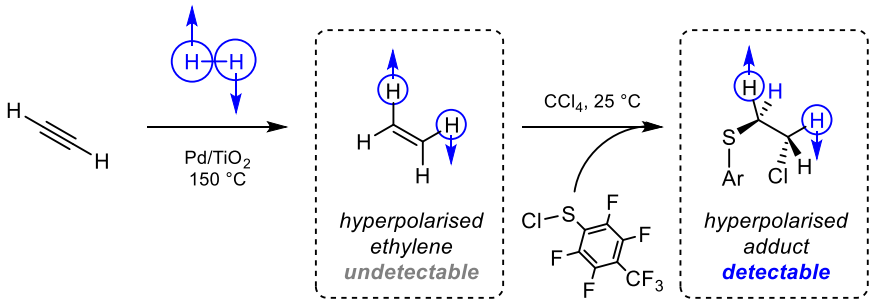
If a strong magnetic field is present, *i.e.* inside an NMR spectrometer, states with opposed spins $|\alpha_A\beta_X\rangle$ and $|\beta_A\alpha_X\rangle$ both survive upon *para*-H_2 incorporation onto the metal. This is effect is known as *Para*-hydrogen and Synthesis Allow Dramatically Enhanced Nuclear Alignment (PASADENA), and in a simple AX spin system the two previously omitted transitions (**1** and **4**) become possible, one strongly absorptive and one strongly emissive in addition to those observed for ALTADENA (**Figure 1.4.2**).

Typically, a NMR pulse angle θ of 90° is required to obtain the maximum signal, by fully converting any magnetisation in the z-direction into the x,y-plane, whereupon the magnetisation may process and freely decay, generating a signal. This remains true for ALTADENA but not PASADENA, where an NMR pulse angle θ of 45° is needed to obtain maximum signal.[214,215]

1.4.3 PHIP Experiments: Other Concerns

In addition to the aforementioned concerns over magnetic field strength and pulse angle, a number of other considerations are important to note.

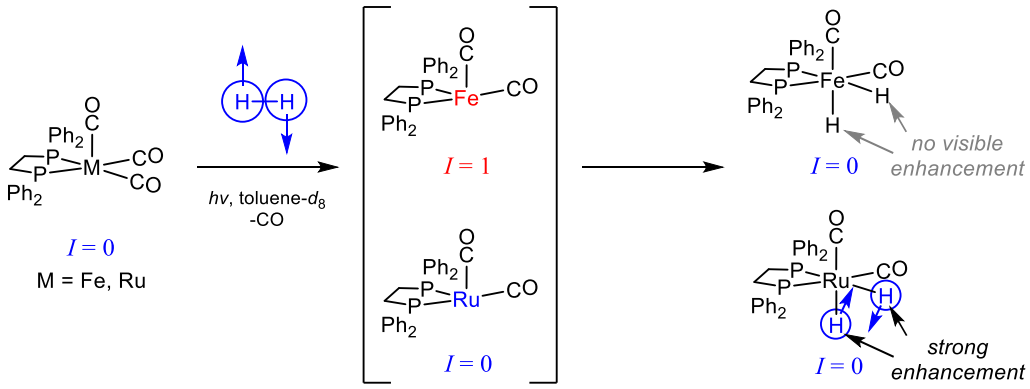
Symmetry breaking: The use of a precursor containing an asymmetrical π-bond, *e.g.* propene or styrene, allows PHIP effect to be detected. If a molecule of *para*-H_2 is incorporated across a *symmetrical* π-bond, *e.g.* across acetylene or ethene, the effect is undetectable as the opposing spins end up in magnetically equivalent positions.[212] Generally, when the coupling information for each ^1H derived from *para*-H_2 is identical, the static field Hamiltonian allows no mixing of different spin multiplicities. No singlet-triplet transitions are therefore possible, and no polarisation is observable *via* NMR.[216] The resulting nuclear spin isomers can, however, be frozen out by further reaction (*e.g.* **Scheme 1.4.2**) followed by prompt spectroscopic analysis, necessary to compensate for the relatively rapid relaxation of C_{sp3}-H protons.



Scheme 1.4.2: Rapid addition of a strong electrophile across hyperpolarised *HP*-ethene (produced by *para*-hydrogenation of acetylene) allows detection of this hyperpolarisation by ^1H NMR spectroscopy.[212]

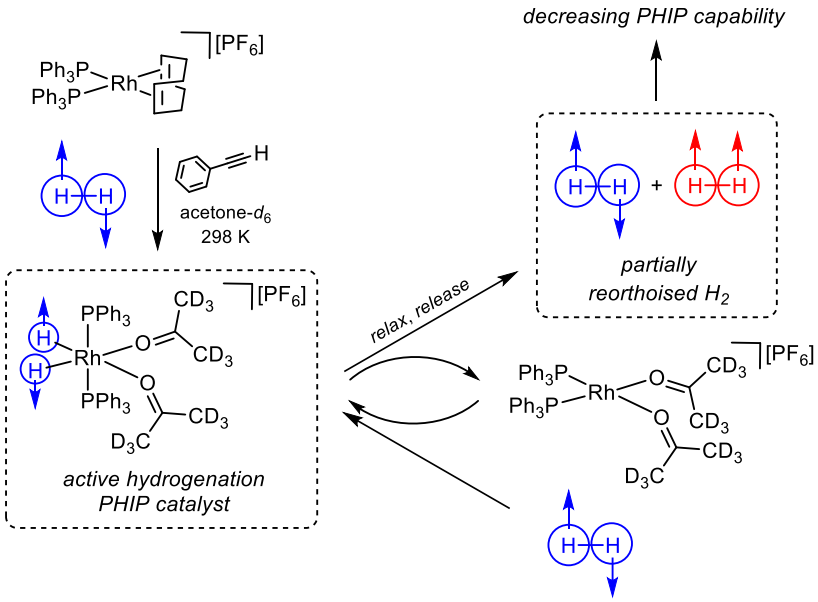
This is generalisable to most systems. For enhanced signals to be observed, under ALTADENA or PASADENA conditions, symmetry-breaking over the course of the reaction is necessary. Exceptions arise in the case of asymmetrical isotopologues (*e.g.* ^{13}C replacing ^{12}C in $^{12}C^{13}C^1H_4$); in certain molecules where avoided crossings are present at certain magnetic field strengths;[217] and in mechanisms where symmetrical precursors (*e.g. cyclo*-propane) give rise to asymmetrical intermediates (*e.g.* propene) during the hydrogenation reaction.[218]

Spin-order preservation: For enhancement to be visible, spin correlation must be preserved throughout the incorporation reaction *and* this reaction must occur more rapidly than the incorporated nuclei relax, otherwise only spin states at thermal equilibrium will be registered by the NMR experiment. During the dwell time of these polarised nuclei on a given metal centre, assuming magnetic inequivalence, some degree of nuclear singlet-triplet mixing $|S\rangle \rightarrow |T_0\rangle$ is possible.[219] Furthermore, rapidly relaxing ^{1}H nuclei such as dihydrogen complexes should not demonstrate PHIP, although one example was recently reported by the Weller group: a PONOP-type pincer-rhodium(I) dihydrogen complex undergoing slow exchange with an atmosphere of *para*-H_2.[220] Metal centres with paramagnetic $(I > 0)$ ground states will quench any polarisation due to accelerated relaxation. The photochemical reaction between [(dppe)M(CO)$_3$] (dppe = $Ph_2P(CH_2)_2PPh_2$) and *para*-H_2 resulted in PHIP at the metal hydride positions for M = Ru but *not* M = Fe, on account of the triplet ground state of the intermediate [(dppe)Fe(CO)$_2$] (**Scheme 1.4.3**).[221]



Scheme 1.4.3: The disruption of spin-order preservation by paramagnetic [(dppe)Fe(CO)$_2$].[221]

Competitive 'reorthoisation': In the absence of any substrate, a metal centre which can reversibly associate with H_2 and draw these protons into different chemical environments, thus allowing nuclear spin states to mix, will encourage the restoration of thermodynamic equilibrium in atmospheres of initially pure *para*-H_2 (or, indeed, any non-equilibrium mixture of *ortho*- and *para*-H_2).[222] This 'reorthoisation' reaction will compete with any PHIP reactions, such that an atmosphere of *para*-H_2 is steadily consumed and its ability to provide enhancement is progressively curtailed (*e.g.* **Scheme 1.4.4**).[223]



Scheme 1.4.4: An example of the problems posed by metal-H_2 interactions leading to quenching of *para*-enriched H_2 atmospheres.

Therefore, careful choices of catalyst/substrate concentrations and *para*-H_2 pressures are vital, and experiments often require multiple *para*-H_2 recharges before optimal conditions can be achieved and recorded. Some systems have been developed which allow a constant purge of *para*-H_2 *in operando*, allowing the problem of competitive reorthoisation to be sidestepped.[224] Theoretically, a catalyst capable of rapid reorthoisation of *para*-H_2 at high temperature should be capable of the reverse at low temperature, under conditions which favour a high proportion of *para*-H_2 in an equilibrium mixture.

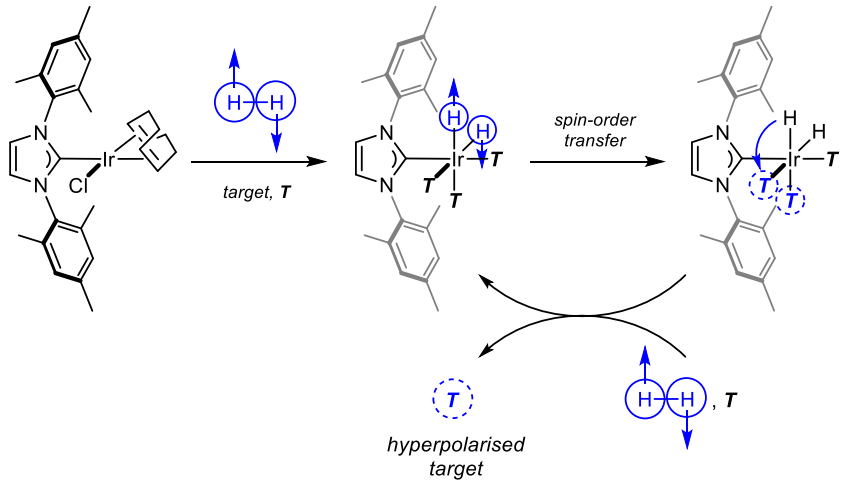
1.4.4 Applications of PHIP in Inorganic Chemistry

The extensive and growing gamut of *para*-hydrogen induced polarisation (PHIP) applications has been covered in a series of detailed reviews[198–200] – on this occasion, a brief summary will suffice. PHIP has been used since 1987 to interrogate the mechanisms of hydrogenation reactions by metalorganic catalysts. Not only it is possible to polarise the hydrogenation *products* by means of *para*-H_2 incorporation: low-concentration, transient hydrogenation *intermediates*, such as metal hydrides, can be enhanced and tempted out from the baseline.

Any ^{1}H positions on a substrate undergoing rapid exchange with polarised metal hydrides may also demonstrate PHIP.[225] EXSY experiments can even track the transfer of magnetisation from *para*-H_2, through a transient intermediate, into a product molecule.[226]

PHIPs are not necessarily limited to ^{1}H manifolds (with spin-lattice relaxation times (T_1) on the order of seconds), nor to the products of hydrogenation reactions. Coupled spin-½ heteronuclei can experience second-hand polarisation due to spin-order transfer.[216] These nuclei may be found either in the hydrogenation substrate or the catalyst ligand sphere: such transfer may lead to the advantageous uptake of polarisation by nuclei with much longer T_1 times, giving rise to longer-lived polarisation effects. ^{13}C (T_1 *O* 10s of seconds) and ^{15}N (T_1 *O* 100s of seconds) PHIPs are particularly noteworthy in the solution-phase, finding application in contrast agents for medical imaging and pharmaceuticals.[227–231] PHIPs of other traditionally insensitive spin-½ nuclei, such as ^{29}Si, ^{89}Y, ^{103}Rh, and ^{109}Ag, have also been reported.[232–235]

Polarisation can also occur across a metal centre, from metal-hydride to ligand. Rhodium- or iridium-centred catalysts which can both coordinate a target ligand (*e.g.* a drug molecule such as nicotine) *and* reversibly bind/oxidatively incorporate H_2 allow spin-order transfer from incorporated *para*-H_2 to the target, *via* coherent spin-order evolution (*J*-coupling). This Signal Amplification by Reversible Exchange (SABRE, **Scheme 1.4.5**) has been applied to a vast range of substrates.[205,236]



Scheme 1.4.5: An example of SABRE, conducted on a target ligand *T* by an iridium-centred catalyst.

SABRE can sometimes lead to misleading observations, particularly when the polarised substrate is the ^{1}H manifold of an alkene or alkyne, as it may be mistaken for metal hydride insertion–elimination for the manner in which the substrate is polarised. D_2 can be used to differentiate between SABRE and reversible insertion–elimination, where the latter gives rise to deuterium incorporation into the substrate and the former does not (see Section 4.4.4).[237]

1.4.5 Heterogeneous Hydrogenation-Polarisation

Most publications on PHIP to date, including those where the target molecule is a gas under standard conditions, report homogeneous conditions, either by direct *para*-H_2 incorporation or by SABRE.[205] Reports of heterogeneous polarisation, however, have been made,[238] making use of both supported metals[239–241] and immobilised metalorganic catalysts.[242] Typically, elevated temperatures have been required to give rise to efficient heterogeneous PHIP, with immobilised catalysts requiring at least 70 °C and supported metals at least 100 °C, with many reports as high as 600 °C. To the best of the author's knowledge, no reports have yet been made of heterogeneous PHIP at ambient temperature.

We have discussed the utility of polarised heteronuclei on the basis of a long solution-phase T_1 time compared to ^{1}H, a potentially powerful property in the context of biomedicine (*e.g.* injectable contrast agents for medical imaging).[243] Under heterogeneous conditions, however, the reverse is true: heteronuclei adopt T_1 times on the order of 1–10s of milliseconds in the gas-phase at ambient pressure.[244–246] Here, ^{1}H has the advantage, with hyperpolarised C_{sp3}–^{1}H possessing a T_1 time on the order of 100–1,000s of milliseconds at ambient pressure, long enough for potential clinical relevance.[247–249] Non-toxic polarised gases/volatiles such as hyperpolarised propane (*HP*-propane) have therefore garnered interest as inhalable contrast agents.[250] Even so, the T_1 time of *HP*-propane is still somewhat short, but can be extended through deuteration, low magnetic field strengths, and reversible dissolution.[247,251–253]

Fast T_1 relaxation times arise from local magnetic field fluctuations generated by rapid gas-phase rotation.[254] It may be possible to stymy this spin-rotation interaction by employing a gaseous alkyne (*i.e.* propyne) in the generation of *HP*-propene,[242,255,256] a molecule with fewer degrees of rotation freedom and a longer T_1 time at the C_{sp2}–^{1}H positions compared to the C_{sp3}–^{1}H positions of *HP*-propane.[201,257] We will explore this possibility in Chapter 4.

1.5 References

[1] J. F. Hartwig, *Organotransition Metal Chemistry: From Bonding to Catalysis*, John Wiley & Sons, Ltd, Sausalito, **2010**.

[2] L. Vaska, *Journal of the American Chemical Society* **1966**, *88*, 5325–5327.

[3] G. M. J. Schmidt, M. D. Cohen, *J. Chem. Soc* **1964**, 1996–2000.

[4] T. Luty, C. J. Eckhardt, *Journal of the American Chemical Society* **1995**, *117*, 2441–2452.

[5] D. Braga, *Chemical Reviews* **1992**, *92*, 633–665.

[6] C. Copéret, M. Chabanas, R. Petroff Saint-Arroman, J.-M. Basset, *Angewandte Chemie International Edition* **2003**, *42*, 156–181.

[7] A. J. Martínez-Martínez, C. G. Royle, S. K. Furfari, K. Suriye, A. S. Weller, *ACS Catalysis* **2020**, *10*, 1984–1992.

[8] A. J. Martínez-Martínez, B. E. Tegner, A. I. McKay, A. J. Bukvic, N. H. Rees, G. J. Tizzard, S. J. Coles, M. R. Warren, S. A. Macgregor, A. S. Weller, *Journal of the American Chemical Society* **2018**, *140*, 14958–14970.

[9] C. Copéret, A. Fedorov, P. A. Zhizhko, *Catalysis Letters* **2017**, *147*, 2247–2259.

[10] J.-P. Zhang, P.-Q. Liao, H.-L. Zhou, R.-B. Lin, X.-M. Chen, *Chemical Society Reviews* **2014**, *43*, 5789–5814.

[11] C. Bianchini, F. Zanobini, S. Aime, R. Gobetto, R. Psaro, L. Sordelli, *Organometallics* **1993**, *12*, 4757–4763.

[12] C. Bianchini, S. Moneti, M. Peruzzini, F. Vizza, *Inorganic Chemistry* **1997**, *36*, 5818–5825.

[13] C. Bianchini, E. Farnetti, M. Graziani, J. Kaspar, F. Vizza, *Journal of the American Chemical Society* **1993**, *115*, 1753–1759.

[14] C. Bianchini, P. Frediani, M. Graziani, J. Kaspar, A. Meli, M. Peruzzini, F. Vizza, *Organometallics* **1993**, *12*, 2886–2887.

[15] A. R. Siedle, R. A. Newmark, K. A. Brown-Wensley, R. P. Skarjune, L. C. Haddad, K. O. Hodgson, A. L. Roe, *Organometallics* **1988**, 7, 2078–2079.

[16] A. R. Siedle, R. A. Newmark, *Organometallics* **1989**, *8*, 1442–1450.

[17] B. J. Truscott, D. J. Nelson, A. M. Z. Slawin, S. P. Nolan, *Chemical Communications* **2014**, *50*, 286–288.

[18] B. R. Flynn, L. Vaska, *Journal of the Chemical Society, Chemical Communications* **1974**, 703–704.

[19] S. Dürr, B. Zarzycki, D. Ertler, I. Ivanović-Burmazović, U. Radius, *Organometallics* **2012**, *31*, 1730–1742.

[20] C. Gemel, J. C. Huffman, K. G. Caulton, K. Mauthner, K. Kirchner, *Journal of Organometallic Chemistry* **2000**, *593–594*, 342–353.

[21] K. Osakada, H. Ishii, *Inorganica Chimica Acta* **2004**, *357*, 3007–3013.

[22] S. Aime, W. Dastru, R. Gobetto, J. Krause, E. Sappa, *Organometallics* **1995**, *14*, 3224–3228.

[23] S. Aime, W. Dastru, R. Gobetto, A. J. Arce, *Organometallics* **1994**, *13*, 4232–4236.

[24] D. Braga, F. Grepioni, *Angewandte Chemie International Edition* **2004**, *43*, 4002–4011.

[25] M. L. H. Green, J. Qin, D. O'Hare, *Journal of Organometallic Chemistry* **1988**, *358*, 375–388.

[26] A. Kumar, T. Zhou, T. J. Emge, O. Mironov, R. J. Saxton, K. Krogh-Jespersen, A. S. Goldman, *Journal of the American Chemical Society* **2015**, *137*, 9894–9911.

[27] W. P. Mul, H. Oosterbeek, G. A. Beitel, G.-J. Kramer, E. Drent, *Angewandte Chemie International Edition* **2000**, *39*, 1848–1851.

[28] I. Halasz, *Crystal Growth & Design* **2010**, *10*, 2817–2823.

[29] K. A. Reid, D. C. Powers, *Chemical Communications* **2021**, *57*, 4993–5003.

[30] S. M. Neville, G. J. Halder, K. W. Chapman, M. B. Duriska, P. D. Southon, J. D. Cashion, J.-F. Létard, B. Moubaraki, K. S. Murray, C. J. Kepert, *Journal of the American Chemical Society* **2008**, *130*, 2869–2876.

[31] X. Li, H. Xu, F. Kong, R. Wang, *Angewandte Chemie International Edition* **2013**, *52*, 13769–13773.

[32] T. K. Maji, G. Mostafa, R. Matsuda, S. Kitagawa, *Journal of the American Chemical Society* **2005**, *127*, 17152–17153.

[33] C.-D. Wu, W. Lin, *Angewandte Chemie International Edition* **2005**, *44*, 1958–1961.

[34] M.-H. Zeng, Q.-X. Wang, Y.-X. Tan, S. Hu, H.-X. Zhao, L.-S. Long, M. Kurmoo, *Journal of the American Chemical Society* **2010**, *132*, 2561–2563.

[35] H. J. Park, M. P. Suh, *Chemistry – A European Journal* **2008**, *14*, 8812–8821.

[36] H. J. Park, Y. E. Cheon, M. P. Suh, *Chemistry – A European Journal* **2010**, *16*, 11662–11669.

[37] J. Albalad, H. Xu, F. Gándara, M. Haouas, C. Martineau-Corcos, R. Mas-Ballesté, S. A. Barnett, J. Juanhuix, I. Imaz, D. Maspoch, *Journal of the American Chemical Society* **2018**, *140*, 2028–2031.

[38] M. Albrecht, M. Lutz, A. L. Spek, G. van Koten, *Nature* **2000**, *406*, 970–974.

[39] D. Braga, G. Cojazzi, D. Emiliani, L. Maini, F. Grepioni, *Organometallics* **2002**, *21*, 1315–1318.

[40] D. Braga, L. Maini, M. Polito, M. Rossini, F. Grepioni, *Chemistry – A European Journal* **2000**, *6*, 4227–4235.

[41] D. Braga, S. L. Giaffreda, F. Grepioni, L. Maini, M. Polito, *Coordination Chemistry Reviews* **2006**, *250*, 1267–1285.

[42] D. Braga, F. Grepioni, K. Biradha, V. R. Pedireddi, G. R. Desiraju, *Journal of the American Chemical Society* **1995**, *117*, 3156–3166.

[43] X. Zhang, T. Chen, H.-J. Yan, D. Wang, Q.-H. Fan, L.-J. Wan, K. Ghosh, H.-B. Yang, P. J. Stang, *ACS Nano* **2010**, *4*, 5685–5692.

[44] D. Krishna Kumar, A. Das, P. Dastidar, *New Journal of Chemistry* **2006**, *30*, 1267–1275.

[45] D. Braga, F. Grepioni, M. Polito, M. R. Chierotti, S. Ellena, R. Gobetto, *Organometallics* **2006**, *25*, 4627–4633.

[46] Y. Ohashi, Y. Sasada, *Nature* **1977**, *267*, 142–144.

[47] A. Sekine, H. Tatsuki, Y. Ohashi, *Journal of Organometallic Chemistry* **1997**, *536–537*, 389–398.

[48] O. v Zenkina, E. C. Keske, R. Wang, C. M. Crudden, *Angewandte Chemie International Edition* **2011**, *50*, 8100–8104.

[49] X.-Z. Song, S.-Y. Song, S.-N. Zhao, Z.-M. Hao, M. Zhu, X. Meng, L.-L. Wu, H.-J. Zhang, *Advanced Functional Materials* **2014**, *24*, 4034–4041.

[50] J. Sun, F. Dai, W. Yuan, W. Bi, X. Zhao, W. Sun, D. Sun, *Angewandte Chemie International Edition* **2011**, *50*, 7061–7064.

[51] R. Moret, P. Launois, T. Wågberg, B. Sundqvist, V. Agafonov, V. A. Davydov, A. v Rakhmanina, *The European Physical Journal B - Condensed Matter and Complex Systems* **2004**, *37*, 25–37.

[52] O. Ozerov, C. Guo, V. A. Papkov, B. M. Foxman, *Journal of the American Chemical Society* **2004**, *126*, 4792–4793.

[53] A. B. Chaplin, J. C. Green, A. S. Weller, *Journal of the American Chemical Society* **2011**, *133*, 13162–13168.

[54] J. Sun, J. Abbenseth, H. Verplancke, M. Diefenbach, B. de Bruin, D. Hunger, C. Würtele, J. van Slageren, M. C. Holthausen, S. Schneider, *Nature Chemistry* **2020**, *12*, 1054–1059.

[55] A. Das, C.-H. Wang, G. P. van Trieste, C.-J. Sun, Y.-S. Chen, J. H. Reibenspies, D. C. Powers, *Journal of the American Chemical Society* **2020**, *142*, 19862–19867.

[56] S. K. Brayshaw, J. C. Green, G. Kociok-Köhn, E. L. Sceats, A. S. Weller, *Angewandte Chemie International Edition* **2006**, *45*, 452–456.

[57] Q. Chu, D. C. Swenson, L. R. MacGillivray, *Angewandte Chemie International Edition* **2005**, *44*, 3569–3572.

[58] E. J. Miller, T. B. Brill, A. L. Rheingold, W. C. Fultz, *Journal of the American Chemical Society* **1983**, *105*, 7580–7584.

[59] T. N. Hoheisel, S. Schrettl, R. Marty, T. K. Todorova, C. Corminboeuf, A. Sienkiewicz, R. Scopelliti, W. B. Schweizer, H. Frauenrath, *Nature Chemistry* **2013**, *5*, 327–334.

[60] P. Kissel, D. J. Murray, W. J. Wulftange, V. J. Catalano, B. T. King, *Nature Chemistry* **2014**, *6*, 774–778.

[61] Q.-H. Guo, M. Jia, Z. Liu, Y. Qiu, H. Chen, D. Shen, X. Zhang, Q. Tu, M. R. Ryder, H. Chen, P. Li, Y. Xu, P. Li, Z. Chen, G. S. Shekhawat, V. P. Dravid, R. Q. Snurr, D. Philp, A. C.-H. Sue, O. K. Farha, M. Rolandi, J. F. Stoddart, *Journal of the American Chemical Society* **2020**, *142*, 6180–6187.

[62] J. J. Dotson, I. Liepuoniute, J. L. Bachman, V. M. Hipwell, S. I. Khan, K. N. Houk, N. K. Garg, M. A. Garcia-Garibay, *Journal of the American Chemical Society* **2021**, *143*, 4043–4054.

[63] Z. Huang, P. S. White, M. Brookhart, *Nature* **2010**, *465*, 598–601.

[64] J.-P. Brog, C.-L. Chanez, A. Crochet, K. M. Fromm, *RSC Advances* **2013**, *3*, 16905–16931.

[65] S. R. Dickinson, G. E. Henderson, K. M. McGrath, *Journal of Crystal Growth* **2002**, *244*, 369–378.

[66] J. Graetz, J. J. Reilly, J. G. Kulleck, R. C. Bowman, *Journal of Alloys and Compounds* **2007**, *446–447*, 271–275.

[67] S. Roy, A. Nangia, *Crystal Growth & Design* **2007**, 7, 2047–2058.

[68] M. Svärd, F. L. Nordström, T. Jasnobulka, Å. C. Rasmuson, *Crystal Growth & Design* **2010**, *10*, 195–204.

[69] J. Sarma, G. R. Desiraju, *Crystal Engineering: The Design and Application of Fundamental Solids* **1999**, 325–356.

[70] W. Qiang, K. Kelley, R. Tycko, *Journal of the American Chemical Society* **2013**, *135*, 6860–6871.

[71] D. Braga, F. Grepioni, *Chemical Society Reviews* **2000**, *29*, 229–238.

[72] D. Braga, F. Grepioni, P. J. Dyson, B. F. G. Johnson, P. Frediani, M. Bianchi, F. Piacenti, *Journal of the Chemical Society, Dalton Transactions* **1992**, 2565–2571.

[73] D. Braga, M. Polito, D. D'Addario, F. Grepioni, *Crystal Growth & Design* **2004**, *4*, 1109–1112.

[74] S. J. la Placa, W. C. Hamilton, J. A. Ibers, A. Davison, *Inorganic Chemistry* **1969**, *8*, 1928–1935.

[75] D. Braga, P. de Leonardis, F. Grepioni, E. Tedesco, M. J. Calhorda, *Inorganic Chemistry* **1998**, *37*, 3337–3348.

[76] R. Boese, A. J. Downs, T. M. Greene, A. W. Hall, C. A. Morrison, S. Parsons, *Organometallics* **2003**, *22*, 2450–2457.

[77] D. Braga, F. Grepioni, L. Maini, M. Polito, in *Molecular Networks* (Ed.: M.W. Hosseini), Springer

Berlin Heidelberg, Berlin, Heidelberg, **2009**, pp. 87–95.
[78] H. Ito, M. Muromoto, S. Kurenuma, S. Ishizaka, N. Kitamura, H. Sato, T. Seki, *Nature Communications* **2013**, *4*, 2009.
[79] F. M. Chadwick, A. I. McKay, A. J. Martinez-Martinez, N. H. Rees, T. Krämer, S. A. Macgregor, A. S. Weller, *Chemical Science* **2017**, *8*, 6014–6029.
[80] N. K. Sethi, A. C. Whitwood, D. W. Bruce, *Inorganic Chemistry* **2018**, *57*, 13524–13532.
[81] S. D. Pike, A. L. Thompson, A. G. Algarra, D. C. Apperley, S. A. Macgregor, A. S. Weller, *Science* **2012**, *337*, 1648–1651.
[82] S. D. Pike, F. M. Chadwick, N. H. Rees, M. P. Scott, A. S. Weller, T. Krämer, S. A. Macgregor, *Journal of the American Chemical Society* **2015**, *137*, 820–833.
[83] A. S. Weller, F. M. Chadwick, A. I. McKay, in *Advances in Organometallic Chemistry* (Ed.: P.J. Pérez), Academic Press, **2016**, pp. 223–276.
[84] A. I. McKay, T. Krämer, N. H. Rees, A. L. Thompson, K. E. Christensen, S. A. Macgregor, A. S. Weller, *Organometallics* **2017**, *36*, 22–25.
[85] F. M. Chadwick, T. Krämer, T. Gutmann, N. H. Rees, A. L. Thompson, A. J. Edwards, G. Buntkowsky, S. A. Macgregor, A. S. Weller, *Journal of the American Chemical Society* **2016**, *138*, 13369–13378.
[86] R. H. Crabtree, *Chemical Reviews* **1985**, *85*, 245–269.
[87] J. A. Calladine, S. B. Duckett, M. W. George, S. L. Matthews, R. N. Perutz, O. Torres, K. Q. Vuong, *Journal of the American Chemical Society* **2011**, *133*, 2303–2310.
[88] W. H. Bernskoetter, C. K. Schauer, K. I. Goldberg, M. Brookhart, *Science* **2009**, *326*, 553–556.
[89] T. M. Boyd, B. E. Tegner, G. J. Tizzard, A. J. Martínez-Martínez, S. E. Neale, M. A. Hayward, S. J. Coles, S. A. Macgregor, A. S. Weller, *Angewandte Chemie International Edition* **2020**, *59*, 6177–6181.
[90] S. D. Pike, T. Krämer, N. H. Rees, Stuart. A. Macgregor, A. S. Weller, *Organometallics* **2015**, *34*, 1487–1497.
[91] A. I. McKay, A. J. Bukvic, B. E. Tegner, A. L. Burnage, A. J. Martínez-Martínez, N. H. Rees, S. A. Macgregor, A. S. Weller, *Journal of the American Chemical Society* **2019**, *141*, 11700–11712.
[92] C. H. Wang, R. B. Wright, *The Journal of Chemical Physics* **1973**, *58*, 1411–1419.
[93] H. H. Winter, D. B. Scott, W. Gronski, S. Okamoto, T. Hashimoto, *Macromolecules* **1993**, *26*, 7236–7244.
[94] W. X. C. Oliveira, M. A. Ribeiro, C. B. Pinheiro, W. C. Nunes, M. Julve, Y. Journaux, H. O. Stumpf, C. L. M. Pereira, *European Journal of Inorganic Chemistry* **2012**, *2012*, 5685–5693.
[95] K. S. Suslick, S.-B. Choe, A. A. Cichowlas, M. W. Grinstaff, *Nature* **1991**, *353*, 414–416.
[96] F.-W. Ling, E. A. Starke, in *Advances in X-Ray Analysis: Volume 15* (Eds.: K.F.J. Heinrich, C.S. Barrett, J.B. Newkirk, C.O. Ruud), Springer US, Boston, MA, **1972**, pp. 319–329.
[97] N. W. Lord, *The Journal of Chemical Physics* **1953**, *21*, 692–699.
[98] G.-C. Xu, X.-M. Ma, L. Zhang, Z.-M. Wang, S. Gao, *Journal of the American Chemical Society* **2010**, *132*, 9588–9590.
[99] I. E. Collings, M. Bykov, E. Bykova, M. Hanfland, S. van Smaalen, L. Dubrovinsky, N. Dubrovinskaia, *CrystEngComm* **2018**, *20*, 3512–3521.
[100] Z. Zhang, W. Li, M. A. Carpenter, C. J. Howard, A. K. Cheetham, *CrystEngComm* **2015**, *17*, 370–374.
[101] R. Świetlik, D. Jankowski, M. Fourmigué, K. Yakushi, *Vibrational Spectroscopy* **2011**, *55*, 195–200.
[102] X. Helluy, A. Sebald, *Applied Organometallic Chemistry* **2003**, *17*, 42–51.
[103] I. Krossing, I. Raabe, *Angewandte Chemie International Edition* **2004**, *43*, 2066–2090.
[104] A. I. McKay, A. J. Martínez-Martínez, H. J. Griffiths, N. H. Rees, J. B. Waters, A. S. Weller, T. Krämer, S. A. Macgregor, *Organometallics* **2018**, *37*, 3524–3532.
[105] V. Gold, K. Loening, A. McNaught, P. Shemi 2nd, *Aufl. Research Triangle Park, NC: International Union of Pure and Applied Chemistry (IUPAC)* **2019**, M03906.
[106] A. L. Spek, *Utrecht University: The Netherlands* **2005**.
[107] A. Lennartson, M. Håkansson, S. Jagner, *New Journal of Chemistry* **2007**, *31*, 344–347.
[108] C. D. Ene, A. M. Madalan, C. Maxim, B. Jurca, N. Avarvari, M. Andruh, *Journal of the American Chemical Society* **2009**, *131*, 4586–4587.
[109] J. L. Atwood, L. J. Barbour, A. Jerga, B. L. Schottel, *Science* **2002**, *298*, 1000.
[110] J. L. Atwood, L. J. Barbour, A. Jerga, *Science* **2002**, *296*, 2367.
[111] J. L. Atwood, L. J. Barbour, G. O. Lloyd, P. K. Thallapally, *Chemical Communications* **2004**, 922–923.
[112] L. J. Barbour, *Chemical Communications* **2006**, 1163–1168.
[113] S. Libri, M. Mahler, G. Mínguez Espallargas, D. C. N. G. Singh, J. Soleimannejad, H. Adams, M. D. Burgard, N. P. Rath, M. Brunelli, L. Brammer, *Angewandte Chemie International Edition* **2008**, *47*, 1693–1697.
[114] I. J. Vitórica-Yrezábal, G. Mínguez Espallargas, J. Soleimannejad, A. J. Florence, A. J. Fletcher, L. Brammer, *Chemical Science* **2013**, *4*, 696–708.
[115] A. J. Martínez-Martínez, N. H. Rees, A. S. Weller, *Angewandte Chemie International Edition* **2019**, *58*, 16873–16877.
[116] H. C. Hoffmann, B. Assfour, F. Epperlein, N. Klein, S. Paasch, I. Senkovska, S. Kaskel, G. Seifert, E. Brunner, *Journal of the American Chemical Society* **2011**, *133*, 8681–8690.
[117] T. J. Donohoe, T. J. C. O'Riordan, C. P. Rosa, *Angewandte Chemie International Edition* **2009**, *48*, 1014–1017.
[118] V. Böhrsch, S. Blechert, *Chemical Communications* **2006**, 1968–1970.
[119] H. Li, C. Mazet, *Accounts of Chemical Research* **2016**, *49*, 1232–1241.
[120] E. Larionov, H. Li, C. Mazet, *Chemical Communications* **2014**, *50*, 9816–9826.
[121] W. Keim, *Angewandte Chemie International Edition* **2013**, *52*, 12492–12496.
[122] M. Ghashghaee, *Reviews in Chemical Engineering* **2018**, *34*, 595–655.
[123] V. Blay, E. Epelde, R. Miravalles, L. A. Perea, *Catalysis Reviews* **2018**, *60*, 278–335.

[124] J. J. H. B. Sattler, J. Ruiz-Martinez, E. Santillan-Jimenez, B. M. Weckhuysen, *Chemical Reviews* **2014**, *114*, 10613–10653.

[125] K. Hashimoto, Y. Masuda, H. Kominami, *ACS Catalysis* **2013**, *3*, 1349–1355.

[126] Y. Li, C. Ma, H. Yang, Z. Zhang, X. Zhang, N. Qiao, J. Wang, Z. Hao, *Chemical Engineering Journal* **2016**, *299*, 1–7.

[127] F. D. Mango, in *Advances in Catalysis* (Eds.: D.D. Eley, H. Pines, P.B. Weisz), Academic Press, **1969**, pp. 291–325.

[128] H. N. Dunning, *Industrial & Engineering Chemistry* **1953**, *45*, 551–564.

[129] V. B. Kazansky, in *Studies in Surface Science and Catalysis* (Eds.: J.C. Jansen, M. Stöcker, H.G. Karge, J. Weitkamp), Elsevier, **1994**, pp. 251–272.

[130] A. J. Hubert, H. Reimlinger, *Synthesis* **1969**, *1969*, 97–112.

[131] G. S. Hammond, Jack. Saltiel, A. A. Lamola, N. J. Turro, J. S. Bradshaw, D. O. Cowan, R. C. Counsell, Volker. Vogt, Christopher. Dalton, *Journal of the American Chemical Society* **1964**, *86*, 3197–3217.

[132] S. W. M. Crossley, F. Barabé, R. A. Shenvi, *Journal of the American Chemical Society* **2014**, *136*, 16788–16791.

[133] S. H. Hong, D. P. Sanders, C. W. Lee, R. H. Grubbs, *Journal of the American Chemical Society* **2005**, *127*, 17160–17161.

[134] C. P. Casey, C. R. Cyr, *Journal of the American Chemical Society* **1971**, *93*, 1280–1282.

[135] A. Sen, T. W. Lai, *Inorganic Chemistry* **1981**, *20*, 4036–4038.

[136] D. McGrath, R. H. Grubbs, *Organometallics* **1994**, *13*, 224–235.

[137] J. L. Garnett, M. A. Long, K. B. Peterson, *Australian Journal of Chemistry* **1974**, *27*, 1823–1825.

[138] P. Taylor, M. Orchin, *Journal of the American Chemical Society* **1971**, *93*, 6504–6506.

[139] C. A. Tolman, *Journal of the American Chemical Society* **1970**, *92*, 4217–4222.

[140] C. A. Tolman, *Journal of the American Chemical Society* **1972**, *94*, 2994–2999.

[141] C. P. Casey, C. R. Cyr, *Journal of the American Chemical Society* **1973**, *95*, 2248–2253.

[142] A. Sivaramakrishna, P. Mushonga, I. L. Rogers, F. Zheng, R. J. Haines, E. Nordlander, J. R. Moss, *Polyhedron* **2008**, *27*, 1911–1916.

[143] M. Tuner, J. Jouanne, H.-D. Brauer, H. Kelm, *Journal of Molecular Catalysis* **1979**, *5*, 433–445.

[144] S. Biswas, Z. Huang, Y. Choliy, D. Y. Wang, M. Brookhart, K. Krogh-Jespersen, A. S. Goldman, *Journal of the American Chemical Society* **2012**, *134*, 13276–13295.

[145] S. M. M. Knapp, S. E. Shaner, D. Kim, D. Y. Shopov, J. A. Tendler, D. M. Pudalov, A. R. Chianese, *Organometallics* **2014**, *33*, 473–484.

[146] A. J. Martínez-Martínez, C. G. Royle, S. K. Furfari, K. Suriye, A. S. Weller, *ACS Catalysis* **2020**, *10*, 1984–1992.

[147] J. G. Aston, G. Szasz, H. W. Woolley, F. G. Brickwedde, *The Journal of Chemical Physics* **1946**, *14*, 67–79.

[148] C. Chen, T. R. Dugan, W. W. Brennessel, D. J. Weix, P. L. Holland, *Journal of the American Chemical Society* **2014**, *136*, 945–955.

[149] I. Lee, F. Delbecq, R. Morales, M. A. Albiter, F. Zaera, *Nature Materials* **2009**, *8*, 132–138.

[150] C. S. Campos-Fernández, B. L. Schottel, H. T. Chifotides, J. K. Bera, J. Bacsa, J. M. Koomen, D. H. Russell, K. R. Dunbar, *Journal of the American Chemical Society* **2005**, *127*, 12909–12923.

[151] D. Rais, J. Yau, D. M. P. Mingos, R. Vilar, A. J. P. White, D. J. Williams, *Angewandte Chemie International Edition* **2001**, *40*, 3464–3467.

[152] H. T. Chifotides, K. R. Dunbar, *Accounts of Chemical Research* **2013**, *46*, 894–906.

[153] M. Zhao, H.-B. Wang, L.-N. Ji, Z.-W. Mao, *Chemical Society Reviews* **2013**, *42*, 8360–8375.

[154] L. Lancaster, W. Abdallah, S. Banta, I. Wheeldon, *Chemical Society Reviews* **2018**, *47*, 5177–5186.

[155] R. Alamillo, A. J. Crisci, J. M. R. Gallo, S. L. Scott, J. A. Dumesic, *Angewandte Chemie International Edition* **2013**, *52*, 10349–10351.

[156] W. Shi, L. Cao, H. Zhang, X. Zhou, B. An, Z. Lin, R. Dai, J. Li, C. Wang, W. Lin, *Angewandte Chemie International Edition* **2017**, *56*, 9704–9709.

[157] Y. Chai, S. Liu, Z.-J. Zhao, J. Gong, W. Dai, G. Wu, N. Guan, L. Li, *ACS Catalysis* **2018**, *8*, 8578–8589.

[158] M. B. Plutschack, B. Pieber, K. Gilmore, P. H. Seeberger, *Chemical Reviews* **2017**, *117*, 11796–11893.

[159] J. Wegner, S. Ceylan, A. Kirschning, *Chemical Communications* **2011**, *47*, 4583–4592.

[160] J. Britton, C. L. Raston, *Chemical Society Reviews* **2017**, *46*, 1250–1271.

[161] D. Webb, T. F. Jamison, *Chemical Science* **2010**, *1*, 675–680.

[162] J. C. Pastre, D. L. Browne, S. v Ley, *Chemical Society Reviews* **2013**, *42*, 8849–8869.

[163] T. Maki, J.-I. Kitada, K. Mae, *Chemical Engineering & Technology* **2013**, *36*, 1027–1032.

[164] F. Carraro, J. Williams, M. Linares-Moreau, C. Parise, W. Liang, H. Amenitsch, C. Doonan, C. O. Kappe, P. Falcaro, *Angewandte Chemie International Edition* **2020**, *59*, 8123–8127.

[165] N. Hartrampf, A. Saebi, M. Poskus, Z. P. Gates, A. J. Callahan, A. E. Cowfer, S. Hanna, S. Antilla, C. K. Schissel, A. J. Quartararo, X. Ye, A. J. Mijalis, M. D. Simon, A. Loas, S. Liu, C. Jessen, T. E. Nielsen, B. L. Pentelute, *Science* **2020**, *368*, 980.

[166] M. Seo, Z. Nie, S. Xu, M. Mok, P. C. Lewis, R. Graham, E. Kumacheva, *Langmuir* **2005**, *21*, 11614–11622.

[167] A. T. Ashcroft, A. K. Cheetham, J. S. Foord, M. L. H. Green, C. P. Grey, A. J. Murrell, P. D. F. Vernon, *Nature* **1990**, *344*, 319–321.

[168] M. Hunger, M. Seiler, T. Horvath, *Catalysis Letters* **1999**, *57*, 199–204.

[169] C. J. Mallia, I. R. Baxendale, *Organic Process Research & Development* **2016**, *20*, 327–360.

[170] A. C. Gutierrez, T. F. Jamison, *Organic Letters* **2011**, *13*, 6414–6417.

[171] S. v Ley, I. R. Baxendale, R. N. Bream, P. S. Jackson, A. G. Leach, D. A. Longbottom, M. Nesi, J. S. Scott, R. I. Storer, S. J. Taylor, *Journal of the Chemical Society, Perkin Transactions 1* **2000**, 3815–4195.

[172] A. Tanimu, S. Jaenicke, K. Alhooshani, *Chemical Engineering Journal* **2017**, *327*, 792–821.
[173] M. Irfan, T. N. Glasnov, C. O. Kappe, *ChemSusChem* **2011**, *4*, 300–316.
[174] D. Cantillo, C. O. Kappe, *ChemCatChem* **2014**, *6*, 3286–3305.
[175] B. Egle, J. Muñoz, N. Alonso, W. de Borggraeve, A. de la Hoz, A. Díaz-Ortiz, J. Alcázar, *Journal of Flow Chemistry* **2013**, *4*, 22–25.
[176] A. Kirschning, W. Solodenko, K. Mennecke, *Chemistry – A European Journal* **2006**, *12*, 5972–5990.
[177] V. Pascanu, P. R. Hansen, A. Bermejo Gómez, C. Ayats, A. E. Platero-Prats, M. J. Johansson, M. À. Pericàs, B. Martín-Matute, *ChemSusChem* **2015**, *8*, 123–130.
[178] R. Porta, M. Benaglia, V. Chiroli, F. Coccia, A. Puglisi, *Israel Journal of Chemistry* **2014**, *54*, 381–394.
[179] B. Sheludko, M. T. Cunningham, A. S. Goldman, F. E. Celik, *ACS Catalysis* **2018**, *8*, 7828–7841.
[180] T. Aoki, R. H. Crabtree, *Organometallics* **1993**, *12*, 294–298.
[181] T. Fujii, Y. Saito, *Journal of the Chemical Society, Chemical Communications* **1990**, 757–758.
[182] A. Nagaki, S. Kim, N. Miuchi, H. Yamashita, K. Hirose, J. Yoshida, *Organic Chemistry Frontiers* **2016**, *3*, 1250–1253.
[183] A. Nagaki, K. Imai, S. Ishiuchi, J. Yoshida, *Angewandte Chemie International Edition* **2015**, *54*, 1914–1918.
[184] A. Nagaki, M. Colella, A. Tota, Y. Takahashi, R. Higuma, L. Degennaro, R. Luisi, *Angewandte Chemie International Edition* **2020**, *59*, 10924–10928.
[185] A. Giovine, B. Musio, L. Degennaro, A. Falcicchio, A. Nagaki, J. Yoshida, R. Luisi, *Chemistry – A European Journal* **2013**, *19*, 1872–1876.
[186] B. Musio, F. Mariani, E. P. Śliwiński, M. A. Kabeshov, H. Odajima, S. v Ley, *Synthesis* **2016**, *48*, 3515–3526.
[187] F. Bonassi, D. Ravelli, S. Protti, M. Fagnoni, *Advanced Synthesis & Catalysis* **2015**, *357*, 3687–3695.
[188] H. Deng, Q. Zhou, J. Wu, *Angewandte Chemie International Edition* **2018**, *57*, 12661–12665.
[189] S. L. Bourne, S. v Ley, *Advanced Synthesis & Catalysis* **2013**, *355*, 1905–1910.
[190] S. B. Ötvös, I. M. Mándity, F. Fülöp, *ChemSusChem* **2012**, *5*, 266–269.
[191] L. Djakovitch, M. Wagner, C. G. Hartung, M. Beller, K. Koehler, *Journal of Molecular Catalysis A: Chemical* **2004**, *219*, 121–130.
[192] A. J. Garcia-Olmo, A. Yepez, A. M. Balu, A. A. Romero, Y. Li, R. Luque, *Catalysis Science & Technology* **2016**, *6*, 4705–4711.
[193] A. Schmidt, R. Haidar, R. Schomäcker, *Catalysis Today* **2005**, *104*, 305–312.
[194] T. Hass, J. Gaube, *Chemical Engineering & Technology* **1989**, *12*, 45–53.
[195] F. Liu, A. S. Goldman, *Chemical Communications* **1999**, 655–656.
[196] D. Morales-Morales, R. Redón, C. Yung, C. M. Jensen, *Inorganica Chimica Acta* **2004**, *357*, 2953–2956.
[197] X. Jia, Z. Huang, *Nature Chemistry* **2016**, *8*, 157–161.
[198] S. B. Duckett, N. J. Wood, *Coordination Chemistry Reviews* **2008**, *252*, 2278–2291.
[199] D. Blazina, S. B. Duckett, J. P. Dunne, C. Godard, *Dalton Transactions* **2004**, 2601–2609.
[200] S. B. Duckett, C. J. Sleigh, *Progress in Nuclear Magnetic Resonance Spectroscopy* **1999**, *34*, 71–92.
[201] K. v Kovtunov, A. S. Romanov, O. G. Salnikov, D. A. Barskiy, E. Y. Chekmenev, I. v Koptyug, *Tomography* **2016**, *2*, 49–55.
[202] P. W. Atkins, Julio. de Paula, *Atkins' Physical Chemistry*, Oxford University Press, Oxford; New York, **2006**.
[203] G. Colonna, A. D'Angola, M. Capitelli, *International Journal of Hydrogen Energy* **2012**, *37*, 9656–9668.
[204] J. Y.-C. Chen, Y. Li, M. Frunzi, X. Lei, Y. Murata, R. G. Lawler, N. J. Turro, *Philosophical Transactions of the Royal Society A: Mathematical, Physical and Engineering Sciences* **2013**, *371*, 20110628.
[205] K. v Kovtunov, I. v Koptyug, M. Fekete, S. B. Duckett, T. Theis, B. Joalland, E. Y. Chekmenev, *Angewandte Chemie International Edition* **2020**, *59*, 17788–17797.
[206] V. I. Tikhonov, A. A. Volkov, *Science* **2002**, *296*, 2363–2363.
[207] F. G. Brickwedde, R. B. Scott, H. S. Taylor, *The Journal of Chemical Physics* **1935**, *3*, 653–660.
[208] M. G. Pravica, D. P. Weitekamp, *Chemical Physics Letters* **1988**, *145*, 255–258.
[209] R. G. Lawler, *Journal of the American Chemical Society* **1967**, *89*, 5519–5521.
[210] C. Bowers, Parahydrogen and Synthesis Allow Dramatically Enhanced Nuclear Alignment, **1991**.
[211] O. W. Sørensen, *Progress in Nuclear Magnetic Resonance Spectroscopy* **1989**, *21*, 503–569.
[212] V. v Zhivonitko, K. v Kovtunov, P. L. Chapovsky, I. v Koptyug, *Angewandte Chemie International Edition* **2013**, *52*, 13251–13255.
[213] G. Buntkowsky, J. Bargon, H.-H. Limbach, *Journal of the American Chemical Society* **1996**, *118*, 8677–8683.
[214] J. Natterer, J. Bargon, *Progress in Nuclear Magnetic Resonance Spectroscopy* **1997**, *31*, 293–315.
[215] S. Bouguet-Bonnet, F. Reineri, D. Canet, *The Journal of chemical physics* **2009**, *130*, 234507.
[216] S. Bär, T. Lange, D. Leibfritz, J. Hennig, D. von Elverfeldt, J.-B. Hövener, *Journal of Magnetic Resonance* **2012**, *225*, 25–35.
[217] M. B. Franzoni, L. Buljubasich, H. W. Spiess, K. Münnemann, *Journal of the American Chemical Society* **2012**, *134*, 10393–10396.
[218] Y. Du, R. Behera, R. v Maligal-Ganesh, M. Chen, E. Y. Chekmenev, W. Huang, C. R. Bowers, *The Journal of Physical Chemistry C* **2020**, *124*, 8304–8309.
[219] P. Kating, A. Wandelt, R. Selke, J. Bargon, *The Journal of Physical Chemistry* **1993**, *97*, 13313–13317.
[220] A. Johnson, C. G. Royle, C. N. Brodie, A. J. Martínez-Martínez, S. B. Duckett, A. S. Weller, *Inorganic Chemistry* **2021**, *60*, 13903–13912.
[221] D. Schott, P. Callaghan, J. Dunne, S. B. Duckett, C. Godard, J. M. Goicoechea, J. N. Harvey, John. P. Lowe, R. J. Mawby, G. Müller, R. N. Perutz, R. Poli,

M. K. Whittlesey, *Dalton Transactions* **2004**, 3218–3224.
[222] G. Buntkowsky, B. Walaszek, A. Adamczyk, Y. Xu, H.-H. Limbach, B. Chaudret, *Physical Chemistry Chemical Physics* **2006**, *8*, 1929–1935.
[223] R. U. Kirss, R. Eisenberg, *Journal of Organometallic Chemistry* **1989**, *359*, C22–C26.
[224] C. R. Bowers, D. P. Weitekamp, *Journal of the American Chemical Society* **1987**, *109*, 5541–5542.
[225] A. Harthun, R. Selke, J. Bargon, *Angewandte Chemie International Edition in English* **1996**, *35*, 2505–2507.
[226] S. A. Colebrooke, S. B. Duckett, J. A. B. Lohman, *Chemical Communications* **2000**, 685–686.
[227] K. Tokmic, R. B. Greer, L. Zhu, A. R. Fout, *Journal of the American Chemical Society* **2018**, *140*, 14844–14850.
[228] F. Reineri, A. Viale, S. Ellena, D. Alberti, T. Boi, G. B. Giovenzana, R. Gobetto, S. S. D. Premkumar, S. Aime, *Journal of the American Chemical Society* **2012**, *134*, 11146–11152.
[229] R. v Shchepin, A. M. Coffey, K. W. Waddell, E. Y. Chekmenev, *The Journal of Physical Chemistry Letters* **2012**, *3*, 3281–3285.
[230] P. Bhattacharya, E. Y. Chekmenev, W. F. Reynolds, S. Wagner, N. Zacharias, H. R. Chan, R. Bünger, B. D. Ross, *NMR in Biomedicine* **2011**, *24*, 1023–1028.
[231] J. McCormick, S. Korchak, S. Mamone, Y. N. Ertas, Z. Liu, L. Verlinsky, S. Wagner, S. Glöggler, L.-S. Bouchard, *Angewandte Chemie International Edition* **2018**, *57*, 10692–10696.
[232] S. B. Duckett, G. K. Barlow, M. G. Partridge, B. A. Messerle, *Journal of the Chemical Society, Dalton Transactions* **1995**, 3427–3429.
[233] S. Ellena, A. Viale, R. Gobetto, S. Aime, *Magnetic Resonance in Chemistry* **2012**, *50*, 529–533.
[234] P. Niedbalski, A. Kiswandhi, C. Parish, Q. Wang, F. Khashami, L. Lumata, *The Journal of Physical Chemistry Letters* **2018**, *9*, 5481–5489.
[235] B. J. Tickner, G. J. Stasiuk, S. B. Duckett, G. Angelovski, *Chemical Society Reviews* **2020**, *49*, 6169–6185.
[236] S. Lehmkuhl, M. Emondts, L. Schubert, P. Spannring, J. Klankermayer, B. Blümich, P. P. M. Schleker, *ChemPhysChem* **2017**, *18*, 2426–2429.
[237] S. Aime, D. Canet, W. Dastrù, R. Gobetto, F. Reineri, A. Viale, *The Journal of Physical Chemistry A* **2001**, *105*, 6305–6310.
[238] K. v Kovtunov, V. v Zhivonitko, I. v Skovpin, D. A. Barskiy, I. v Koptyug, in (Ed.: L.T. Kuhn), Springer Berlin Heidelberg, Berlin, Heidelberg, **2013**, pp. 123–180.
[239] K. v Kovtunov, D. A. Barskiy, O. G. Salnikov, A. K. Khudorozhkov, V. I. Bukhtiyarov, I. P. Prosvirin, I. v Koptyug, *Chemical Communications* **2014**, *50*, 875–878.
[240] K. V. Kovtunov, I. E. Beck, V. I. Bukhtiyarov, I. V. Koptyug, *Angewandte Chemie International Edition* **2008**, *47*, 1492–1495.
[241] V. v Zhivonitko, K. v Kovtunov, I. E. Beck, A. B. Ayupov, V. I. Bukhtiyarov, I. v Koptyug, *The Journal of Physical Chemistry C* **2011**, *115*, 13386–13391.
[242] K. v Kovtunov, V. v Zhivonitko, A. Corma, I. v Koptyug, *The Journal of Physical Chemistry Letters* **2010**, *1*, 1705–1708.
[243] J. Kurhanewicz, D. B. Vigneron, K. Brindle, E. Y. Chekmenev, A. Comment, C. H. Cunningham, R. J. DeBerardinis, G. G. Green, M. O. Leach, S. S. Rajan, R. R. Rizi, B. D. Ross, W. S. Warren, C. R. Malloy, *Neoplasia* **2011**, *13*, 81–97.
[244] C. J. Jameson, A. K. Jameson, N. C. Smith, *The Journal of Chemical Physics* **1987**, *86*, 6833–6838.
[245] P. Etesse, J. A. Zega, R. Kobayashi, *The Journal of Chemical Physics* **1992**, *97*, 2022–2029.
[246] D. O. Kuethe, A. Caprihan, H. M. Gach, I. J. Lowe, E. Fukushima, *Journal of Applied Physiology* **2000**, *88*, 2279–2286.
[247] K. v Kovtunov, M. L. Truong, D. A. Barskiy, O. G. Salnikov, V. I. Bukhtiyarov, A. M. Coffey, K. W. Waddell, I. v Koptyug, E. Y. Chekmenev, *The Journal of Physical Chemistry C* **2014**, *118*, 28234–28243.
[248] D. A. Barskiy, O. G. Salnikov, K. v Kovtunov, I. v Koptyug, *The Journal of Physical Chemistry A* **2015**, *119*, 996–1006.
[249] D. A. Barskiy, K. v Kovtunov, E. Y. Gerasimov, M. A. Phipps, O. G. Salnikov, A. M. Coffey, L. M. Kovtunova, I. P. Prosvirin, V. I. Bukhtiyarov, I. v Koptyug, E. Y. Chekmenev, *The Journal of Physical Chemistry C* **2017**, *121*, 10038–10046.
[250] B. Joalland, N. M. Ariyasingha, H. R. Younes, S. Nantogma, O. G. Salnikov, N. v Chukanov, K. v Kovtunov, I. v Koptyug, J. G. Gelovani, E. Y. Chekmenev, *Chemistry – A European Journal* **2021**, *27*, 2774–2781.
[251] D. B. Burueva, A. S. Romanov, O. G. Salnikov, V. v Zhivonitko, Y.-W. Chen, D. A. Barskiy, E. Y. Chekmenev, D. W. Hwang, K. v Kovtunov, I. v Koptyug, *The Journal of Physical Chemistry C* **2017**, *121*, 4481–4487.
[252] N. M. Ariyasingha, O. G. Salnikov, K. v Kovtunov, L. M. Kovtunova, V. I. Bukhtiyarov, B. M. Goodson, M. S. Rosen, I. v Koptyug, J. G. Gelovani, E. Y. Chekmenev, *The Journal of Physical Chemistry C* **2019**, *123*, 11734–11744.
[253] O. G. Salnikov, D. A. Barskiy, A. M. Coffey, K. v Kovtunov, I. v Koptyug, E. Y. Chekmenev, *ChemPhysChem* **2016**, *17*, 3395–3398.
[254] R. E. D. McClung, *eMagRes* **2007**.
[255] E. W. Zhao, Y. Xin, H. E. Hagelin-Weaver, C. R. Bowers, *ChemCatChem* **2016**, *8*, 2197–2201.
[256] O. G. Salnikov, D. A. Barskiy, D. B. Burueva, Y. K. Gulyaeva, B. S. Balzhinimaev, K. v Kovtunov, I. v Koptyug, *Applied Magnetic Resonance* **2014**, *45*, 1051–1061.
[257] A. E. Khudozhitkov, S. S. Arzumanov, D. I. Kolokolov, D. Freude, A. G. Stepanov, *Physical Chemistry Chemical Physics* **2020**, *22*, 5976–5984.

This page intentionally left blank.

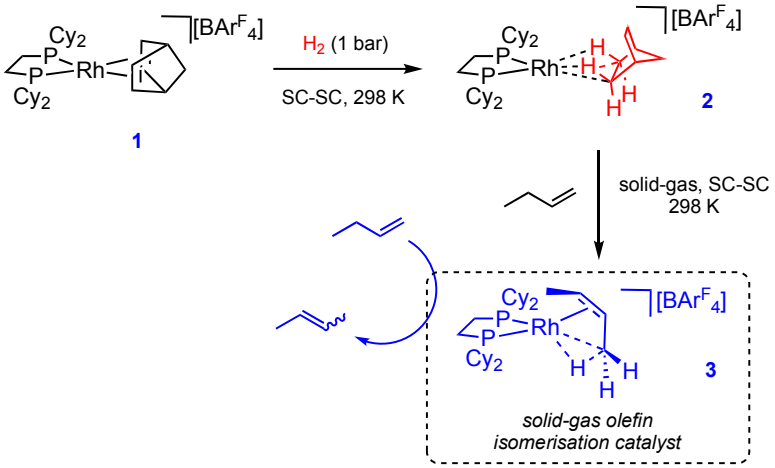
2 Solid-State Molecular Organometallic Catalysis under Solid/Gas Flow Conditions: Gas-Phase Isomerisation of 1-Butene

2.1 Introduction

A solid-state molecular organometallic complex (SMOM) of formula [(dcpe)Rh(η^2,η^2-NBD)][$BAr^F{}_4$] (**1**, dcpe = $Cy_2P(CH_2)_2PCy_2$, NBD = norbornadiene) has been shown to catalyse the isomerisation of 1-butene, after pre-hydrogenation to yield the σ-NBA complex (**2**; **Scheme 2.1.1**) from which the 'token' NBA ligand was easily displaced, ultimately yielding *cis*-2-butene complex **3** at the catalytic resting state.[1,2] In a closed system, the proportion of *n*-butene isomers tended towards a thermodynamic distribution of isomers (~21% *cis*-, ~77% *trans*-2-butene, and ~2% 1-butene at 298.16 K)[3] over the course of 60 minutes, although initial isomerisation to 2-butenes (~96%) occurred in just two minutes. An apparent turnover number (TON_{app})[4,5][a] of ~45 and apparent turnover frequency (TOF_{app}) of ~1500 hr^{-1} were measured (2 mg catalyst, 1.0 bar, 298 K). Non-thermodynamic distributions of *n*-butenes, with larger proportions of *cis*, were observed in the early stages of catalysis (**Figure 2.1.1**). This was proposed to be due to a higher barrier to loss of *trans*-2-butene from {(dcpe)Rh}[$BAr^F{}_4$] compared to the *cis* isomer.[6]

The deployment of this chemistry under industrially-appealing solid-gas flow conditions was considered as a means of obtaining 2-butenes in both high yield and potentially with non-equilibrium selectivity. This may be important in that higher, non-thermodynamic proportions of either isomer might be achieved – particularly the less stable *cis* isomer, which has been observed to be more reactive under conditions of metathesis,[7,8] hydrogenation[9] and co-polymerisation.[10] The reactivity of this isomer under metathesis conditions is potentially relevant to the manufacture of propylene, *via* metathesis of ethylene and one equivalent of 2-butene. Kinetic selectivity under flow conditions was introduced in Section 1.3.1.

[a] $TON_{app} = n^*/n_{cat}$, where n^* is the number of moles of converted substrate and n_{cat} is the number of moles of catalyst. 'Apparent' assumes all sites are participating, equally active, and equally accessible. $TOF_{app} = TON_{app}/t$, where t is time.



Scheme 2.1.1: Catalytic solid-gas isomerisation of 1-butene to 2-butenes by a pre-hydrogenated SMOM [(dcpe)Rh(η^2,η^2-NBD)][BAr^F_4] (1), *via* an *in situ*-generated *cis*-2-butene complex (3).

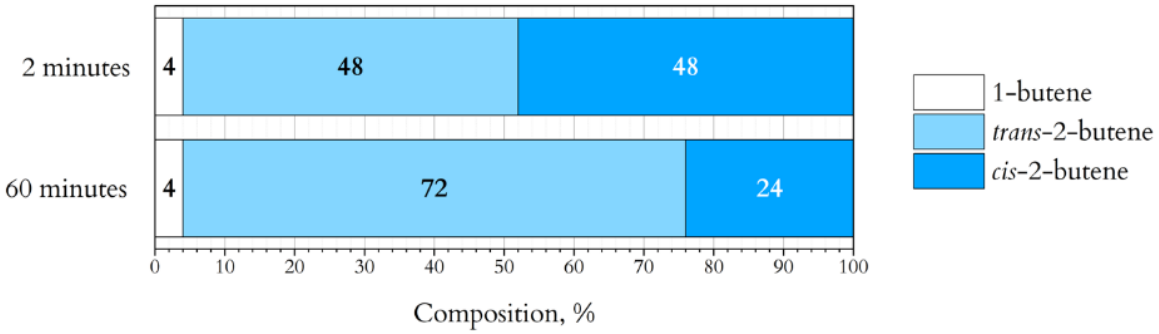


Figure 2.1.1: Conversion of 1-butene to a mixture of *n*-butenes over time (2 minutes, 60 minutes) by powdered and pre-hydrogenated single-crystalline samples of SMOM 1 (2 mg) within a high-pressure NMR tube. Proportions of each *n*-butene isomer as calculated from gas chromatography (GC) analysis. Data obtained from the reference.[6]

R_2P-E-PR_2 = P_2 chelate variation was planned, in R-group identity, tether identity (E = $(CH_2)_n$, NH), and tether length *n* (E = $(CH_2)_n$ only), such that the influence of the chelating *bis*-phosphine in the activity and selectivity of the SMOM in 1-butene solid-gas isomerisation could be explored in detail. In this Chapter, SMOM pre-catalysts for solid-gas 1-butene isomerisation were first tested under batch conditions at 1.0 bar operating pressure before a limited number of promising systems were tested under flow conditions as proofs-of-concept, the first time such SMOMs have been deployed under such conditions.[2]

2.2 Synthesis and Characterisation of Target SMOMs (Precursor NBD Complexes)

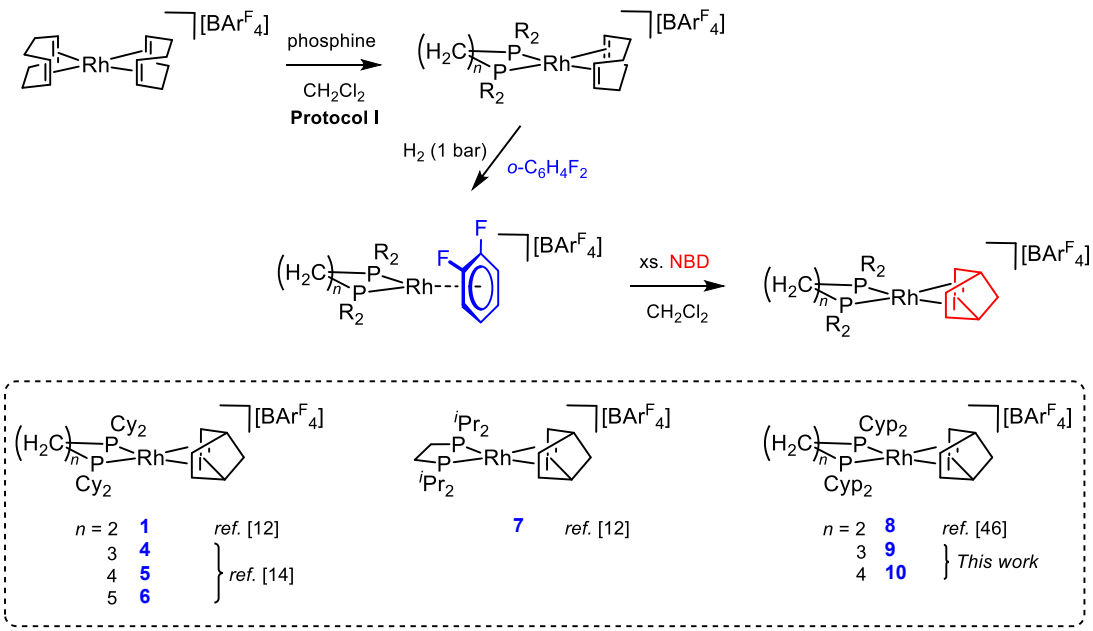
In order to generate the σ-alkane complexes of formula $[(P_2)Rh(\sigma\text{-NBA})][BAr^F{}_4]$, where the weakly-bound alkane acts as a 'token ligand' to be substituted for the substrate 1-butene gas, the precursor η^2,η^2-NBD complexes must be first synthesised and crystallised.

Three protocols were employed in the synthesis of target SMOMs $[(P_2)Rh(\eta^2,\eta^2\text{-NBD})][BAr^F{}_4]$: (I) from a labile[11] 1,2-difluorobenzene complex $[(P_2)Rh(\eta^6\text{-1,2,-difluorobenzene})][BAr^F{}_4]$; (II) from direct combination of $[Rh(\eta^2,\eta^2\text{-NBD})_2][BAr^F{}_4]$ and one equivalent of *bis*-phosphine P_2; and (III) from halide abstraction of $[(P_2)RhCl]_2$ by $Na[BAr^F{}_4]$ in the presence of excess NBD. All η^2,η^2-NBD complexes in question, irrespective of the protocol used, were produced in near-quantitative yields and isolated as single-crystalline materials that were characterised by solution-phase NMR spectroscopy, single-crystal X-ray diffraction (*sc*-XRD), mass spectrometry, and elemental microanalysis to confirm their purity. In this sub-chapter we will focus on the solid-state structures of these precursor η^2,η^2-NBD SMOMs (Section 2.2.4); most of these complexes are unremarkable as characterised by solution-phase NMR spectroscopy.

2.2.1 Synthesis of Precursor NBD SMOMs via *a Labile 1,2-difluorobenzene Complex (Protocol I)*

For *bis*-phosphines $R_2P(CH_2)_nPR_2$ where R is a primary or secondary alkyl group (*e.g.* R = Cy, Cyp, ^{i}Pr, ^{i}Bu), a route to SMOMs $[(P_2)Rh(\eta^2,\eta^2\text{-NBD})][BAr^F{}_4]$ has already been reported in the literature.[1,12–14] This route proceeds *via* the η^2,η^2-COD complex $[(P_2)Rh(\eta^2,\eta^2\text{-COD})][BAr^F{}_4]$ which, upon addition of H_2 gas in 1,2-difluorobenzene, liberated cyclooctane and yielded the corresponding labile 1,2-difluorobenzene complex.[a] Addition of neat NBD to this complex (formed *in situ*) yielded the corresponding η^2,η^2-NBD complexes, which were then recrystallised in near-quantitative yields by slow diffusion of pentane into CH_2Cl_2 solutions at 298 K (**Scheme 2.2.1**).

[a] In previous syntheses, fluorobenzene has sometimes been used in the place of 1,2-difluorobenzene, with no deleterious effect on yield or product purity.

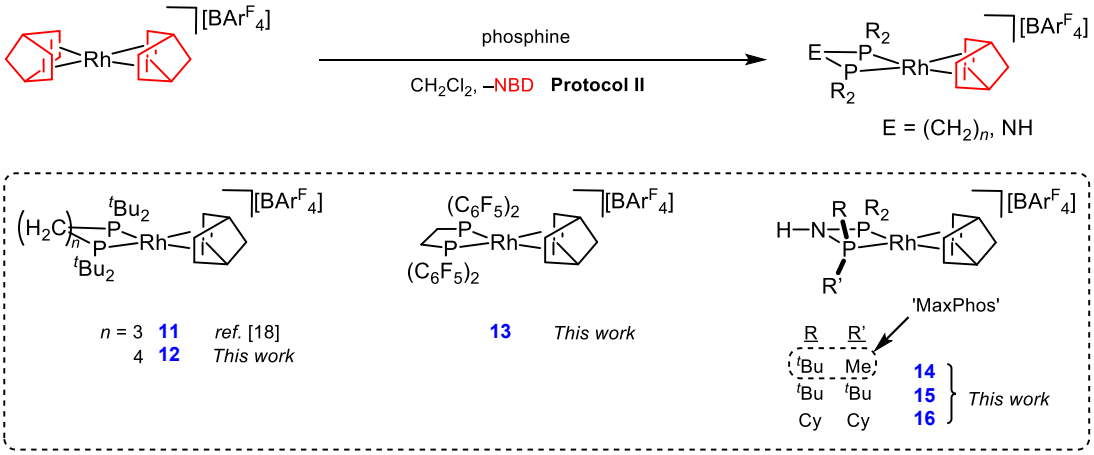


Scheme 2.2.1: Synthesis of SMOMs **1** and **4**–**10** *via* intermediate η^2,η^2-COD and 1,2-difluorobenzene complexes (Protocol I).

This indirect route was intended to avoid the formation of $[(P_2)_2Rh]^+$ that may have arisen from the direct addition of *bis*-phosphine $R_2P(CH_2)_nPR_2$ to $[Rh(\eta^2,\eta^2\text{-NBD})_2][BAr^F{}_4]$ (Protocol II, *vide infra*). It has often found in the Weller Group that $[(P_2)_2Rh][BAr^F{}_4]$ contaminants are notoriously difficult to separate from the target complexes $[(P_2)Rh(\eta^2,\eta^2\text{-NBD})][BAr^F{}_4]$. Of the η^2,η^2-NBD SMOMs synthesised by this protocol, two are new to this work, where P_2 = dcyppp = $Cyp_2P(CH_2)_3PCyp_2$ (**9**) and dcyppb = $Cyp_2P(CH_2)_4PCyp_2$ (**10**). Ligands $Cyp_2P(CH_2)_{3\text{-}4}PCyp_2$ have seen limited study in homogeneous organometallic chemistry, in a handful of palladium-catalysed reactions.[15,16] The solution-phase NMR spectra of complexes **9** and **10** were generally unremarkable.

2.2.2 *Synthesis of Precursor NBD SMOMs Directly from $[Rh(\eta^2,\eta^2\text{-NBD})_2][BAr^F{}_4]$ and Chelating* Bis-*Phosphine P_2 (Protocol II)*

A more direct route in SMOM synthesis was also employed, proceeding from the *bis*-NBD complex $[Rh(\eta^2,\eta^2\text{-NBD})_2][BAr^F{}_4]$[17] and one equivalent of *bis*-phosphine (**Scheme 2.2.2**).



Scheme 2.2.2: Synthesis of SMOMs **11**-**16** directly from $[Rh(\eta^2,\eta^2\text{-NBD})_2][BAr^F{}_4]$ (Protocol II).

With tertiary alkyl (*i.e.* ^{t}Bu) and C_6F_5 R-groups, satisfactory SMOM purities were achieved (>99.5%). However, secondary alkyl R-groups produced undesirable complexes of type $[Rh(P_2)_2][BAr^F{}_4]$ (*ca.* 1–5%) as side-products, and such impurities were detected *via* both $^{31}P\{^1H\}$ NMR spectroscopy and mass spectrometry. In these cases, the indirect route described in Section 2.2.1 was used instead. The direct route also proceeded in sufficient purity for the *bis*-phosphine amides $HN(PR_2)_2$. As in Section 2.2.1, all examples of η^2,η^2-NBD complexes were obtained as single-crystalline material in near-quantitative yields from slow diffusion of pentane into CH_2Cl_2 solutions at 298 K.

Ligands of the type ^{t}Bu$_2$P(CH$_2$)$_n$P^{t}Bu$_2$ (n = 1-4)[18] have been used in nickel and platinum catalysis, due to the ability of the sterically-demanding, powerfully electron-donating[19,20] ^{t}Bu groups to stabilise low-coordinate metal centres (*viz.* Ni(0), Pt(0)) and promote bond activation.[21–25] Catalysts of type $\{(^tBu_2P(CH_2)_nP^tBu_2)Rh\}^+$ have been employed for purposes as diverse as hydroacylation,[26] hydrosilylation,[27] and chalcogen extrusion.[28] Ligands of type $(C_6F_5)_2P(CH_2)_nP(C_6F_5)_2$ (n = 1-4) have also seen extensive study, including their use in Pd-catalysed ethylene dimerization[29] and aryl-aryl coupling,[30] in Rh-catalysed hydroformylation,[31] and in Ir-catalysed hydroacylation,[32] where the electron-withdrawing C_6F_5 groups were of especial interest.

The precursor SMOM [(dpfppe)Rh(η^2,η^2-NBD)][BAr^F_4] (dpfppe = $(C_6F_5)_2P(CH_2)_2P(C_6F_5)_2$; **13**) was pursued in this work due to the electron-withdrawing nature of the phosphine, in contrast to the other precursor η^2,η^2-NBD SMOMs investigated, as well as due to a desire to extend the structural properties imparted by the fluorinated anions (plasticity, tolerance to reorganisation – see Introduction[a]) onto the ligand itself. Fluorinated species (ligands, anions) in single-crystal to single-crystal (SC-SC) transformations have been successfully deployed in the past despite an absence of lattice porosity.[33–36] The NMR-active ^{19}F nuclei present on the pendant perfluorophenyl groups were also of interest as NMR spectroscopic handles. As crystallised from a layered mixture of CH_2Cl_2 and pentane, SMOM **13** co-crystallised with CH_2Cl_2 in the lattice. Once removed from the crystallisation solvent mixture and exposed to dynamic vacuum, this material underwent loss of CH_2Cl_2 from the lattice in an SC-SC process concomitant with a shift in periodic structure, yielding a non-solvent containing crystal. This transformation, alongside other solvent-containing structures of SMOM **13**, is discussed in detail in Chapter 3 (also see the Experimental for that chapter). When referring to SMOM **13**, in this Chapter this will indicate *only* non-solvent containing material as obtained by loss of CH_2Cl_2.[b] It is this material that will be used in the catalytic studies presented in this Chapter.

All SMOMs assessed for solid-gas reactivity to date have possessed simple aliphatic tethers connecting the chelating phosphines. In order to probe the electronic influence of the tethering atom, a bridging nitrogen was employed in three bis(dialkylphosphino)amine-type (PˆNˆP) ligands $HN(PR_2)_2$ (**Figure 2.2.1**).

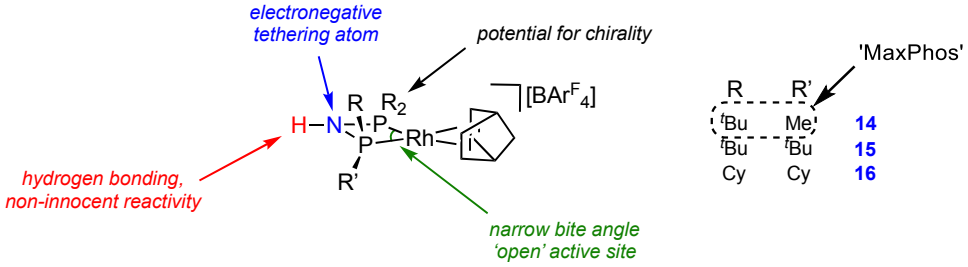
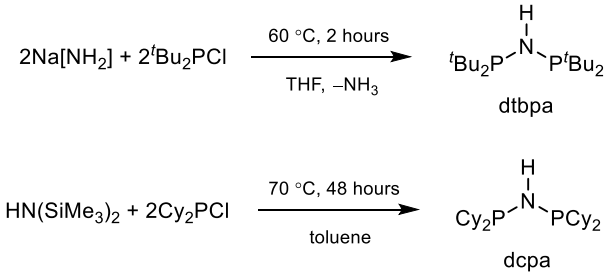


Figure 2.2.1: PˆNˆP-type precursor η^2,η^2-NBD SMOMs **14**–**16** studied in this work.

[a] Sections 1.1.2–1.1.5
[b] SMOM **13** in this Chapter equates to the structure ('morph') **13-II**$_{SCSC}$ in Chapter 3.

P^N^P-type ligands have been deployed for an immense range of applications in homogeneous catalysis. Noting a considerable scope for R-group variation at both the P and N positions, alongside the unique electronic properties of the N-atom tether, a comparatively simple synthesis, the potential for a non-symmetric coordination sphere, and a narrow P-M-P bite angle yielding a relatively unhindered active site,[37] these applications have included the polymerisation[38] or tetramerisation[39,40] of ethylene, in luminescent 'A-frame' complexes of the coinage metals,[41] and asymmetric synthesis.[42] For the intended solid-gas catalytic application, R-group tunability, an open active site at the metal, and N-H hydrogen-bonding potential[a] from the backbone, were all considered especially appealing properties.

Three P^N^P-type SMOMs **14**-**16** were synthesised as proofs-of-concept (see **Scheme 2.2.2**). The SMOM [((*R*)-MaxPhos)Rh(η^2,η^2-NBD)][BAr^F_4] (**14**; MaxPhos = ^{t}Bu$_2$P(NH)P(Me)(^{t}Bu)) was synthesised to probe the effects of a non-symmetrical active site on catalysis. The related [((*R*)-MaxPhos)Rh(η^2,η^2-L_2)][BF_4] (L_2 = COD, NBD) complexes are known, having been employed in Rh-catalysed asymmetric hydrogenations.[43] The syntheses of [(HN(PR_2)$_2$)Rh(η^2,η^2-NBD)][BAr^F_4] proceeded as in **Scheme 2.2.2**, by direct combination of [Rh(η^2,η^2-NBD)$_2$][BAr^F_4] and one equivalent of HN(PR_2)$_2$, followed by recrystallisation from CH_2Cl_2 and pentane at 298 K, then characterisation by solution-phase methods. The synthesis of chelate dtbpa = HN(P^{t}Bu$_2$)$_2$ from Na[NH_2] and ^{t}Bu$_2$PCl has been previously described.[44] Synthesis of chelate dcpa = HN(PCy_2)$_2$ proceeded from HN($SiMe_3$)$_2$ (**Scheme 2.2.3**).



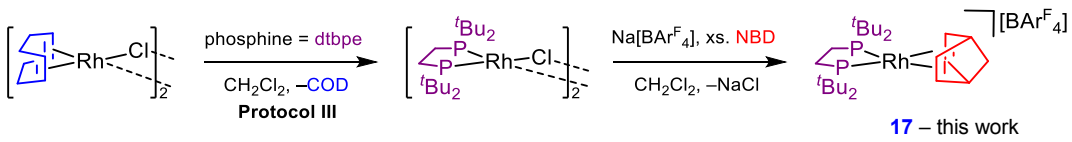
Scheme 2.2.3: Synthetic strategies for P^N^P-type HN(PR_2)$_2$ phosphines dtbpa and dcpa, used in the synthesis of SMOMs **15** and **16** respectively.

[a] See Introduction (Section 1.1.2), where hydrogen-bonded networks are noted to be particularly tolerant to lattice expansion/contraction/reorganisation (see **Scheme 1.1.5**).

The solution-phase NMR spectroscopic data for SMOM **14** are analogous to that of the known complexes [((*R*)-MaxPhos)Rh(η^2,η^2-COD,NBD)][BF_4].[43] By ^{1}H NMR spectroscopy, three signals corresponding to NBD alkene CH were resolved in a 2:1:1 integral ratio (δ 5.48, 5.69, 5.88), the result of the asymmetry of the chelate. This 2:1:1 ratio is likely due to a coincidence, as the lack of an effective mirror plane in this system would be expected to produce *four* alkene CH signals in a 1:1:1:1 integral ratio. Similarly, ^{1}H NMR spectroscopy revealed single bridging CH_2 (δ 1.46) and bridgehead CH (δ 4.13) resonances, and ^{13}C{^{1}H} NMR spectroscopy revealed three alkene CH multiplets (δ 85.0, 89.5, 92.0) instead of four. Two ^{31}P{^{1}H} resonances were observed as doublets-of-doublets (δ 57.9 ($^1J_{PRh}$ = 141 Hz), 81.6 ($^1J_{PRh}$ = 138 Hz); $^2J_{PP}$ = 53 Hz) in a 1:1 integral ratio. By comparison, SMOMs **15** and **16** produced simpler solution-phase NMR spectra due to their symmetric chelates, with only one alkene CH environment each resolved *via* ^{1}H and ^{13}C{^{1}H} NMR spectroscopy (δ_H 5.52 (**15**), 5.66 (**16**)); δ_C 84.1 (**15**), 89.1 (**16**)), and one ^{31}P environment *via* ^{31}P{^{1}H} NMR spectroscopy (δ 82.7 ($^1J_{PRh}$ = 138 Hz; **15**), 62.1 ($^1J_{PRh}$ = 137 Hz; **16**)).

2.2.3 *Synthesis of Precursor NBD SMOMs* via *Halide Abstraction (Protocol III)*

Intending to take advantage of commercially available starting materials (*i.e.* [(η^2,η^2-COD)RhCl]$_2$ and Na[BAr^F_4]), such that synthesis could be undertaken on large (>1.0 g) scale, a third protocol proceeded *via* the known *bis*-phosphine chloride dimer [(dtbpe)RhCl]$_2$ (dtbpe = ^{t}Bu$_2$P(CH$_2$)$_2$P^{t}Bu$_2$, **Scheme 2.2.4**),[45] which was generated *in situ*. This route was employed for SMOM [(dtbpe)Rh(η^2,η^2-NBD)][BAr^F_4] (**17**) in ~80% yield on a ~3.0 g scale. Direct synthesis from [Rh(η^2,η^2-NBD)$_2$][BAr^F_4] (as Protocol II, Section 2.2.2) was also a viable approach for SMOM **17**.



Scheme 2.2.4: Synthesis of precursor η^2,η^2-NBD SMOM **17** proceeding *via* halide abstraction (Protocol III).

2.2.4 Overview of the Solid-State Structures of the Precursor NBD SMOMs

The relationship between structure and activity has been discussed in the Introduction (Section 1.2.3). SMOMs of the formula [(P$_2$)Rh(η^2,η^2-NBD)][BAr$^F_4$] are known to adopt two main structure types: a so-called octahedral (O_h) motif, where six [BAr$^F_4$]$^-$ anions are arranged around one cationic fragment, and the rarer bicapped parallelepipedic (BCPP) pattern, with 10 [BAr$^F_4$]$^-$ around two cationic fragments. Most hitherto-reported SMOMs adopt the O_h structure type,[12–14,46] although two BCPP-type exceptions are known.[12,47] A brief overview of the structure types adopted by the η^2,η^2-NBD SMOMs used as pre-catalysts for solid-gas 1-butene isomerisation in this work follows, eight of which are new to this work, and most of which adopt the O_h structure type with three exceptions. An exemplar solid-state structure of one of these new η^2,η^2-NBD complexes that adopts this common O_h-type structure is shown in **Figure 2.2.2**, [(dtbpe)Rh(η^2,η^2-NBD)][BAr$^F_4$] (17).

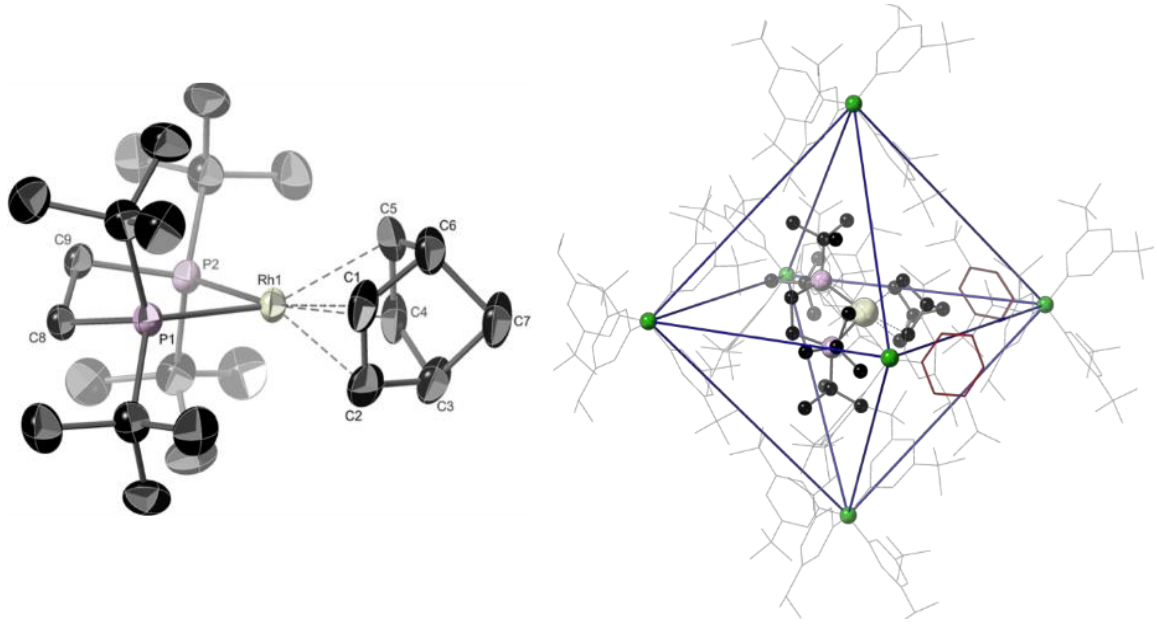


Figure 2.2.2: (**left**) Cationic fragment [(dtbpe)Rh(η^2,η^2-NBD)]$^+$ of 17. 50% displacement ellipsoids. Anions and H atoms omitted for clarity. Selected bond lengths (Å) and angles (°), where Cent is the centroid of C1–C2 and Cent' is the centroid of C4–C5: Rh1–P1, 2.3517(8); Rh1–P2, 2.3488(8); Rh1–C1, 2.195(4); Rh1–Cent, 2.082(3); Rh1–C2, 2.192(4); Rh1–C4, 2.199(4); Rh1–Cent', 2.085(3); Rh1–C5, 2.192(4); P1–Rh1–P2, 86.34(3); P1–Rh1–Cent, 102.69(10); P2–Rh1–Cent', 102.72(9); C2–Rh1–C4, 65.60(19); C1–Rh1–C5, 65.73(19). (**right**) The O_h packing environment of SMOM 17, cationic fragment [(dtbpe)Rh(η^2,η^2-NBD)]$^+$ (modelled as ball-and-stick) and its six nearest [BAr$^F_4$]$^-$ neighbours (modelled as wireframe with B atom balls). The Ar^F-B-Ar^F cleft into which the NBD moiety fits is highlighted in red. Constructed from *sc*-XRD data found in the reference.[2]

SMOM 17 shares the O_h-type packing pattern common to most SMOMs containing the $[BAr^F_4]^-$ anion, as discussed above. As reported in the solid-state structure of SMOM [(dcpe)Rh(η^2,η^2-NBD)][BAr^F_4] (1),[12] the NBD moiety of the cation [(dtbpe)Rh(η^2,η^2-NBD)]$^+$ in SMOM 17 orients into an Ar^F-B-Ar^F 'cleft'. It was suggested that this feature was partly responsible for the stability of the σ-alkane complex [(dcpe)Rh(σ-NBA)][BAr^F_4] (2), the weakly-bound NBA ligand 'protected' inside the cleft and stabilised by non-covalent interactions (NCIs), such that the σ-alkane complex was stable in the solid-state at 298 K in an argon-filled glovebox for months. These NCIs are known to be significant in the stabilisation of σ-alkane complexes of this type: of the σ-NBA binding energy in 2, as much as ~44% (14.0 of 33.1 kcal mol^{-1}) was calculated to be due to these intermolecular, microenvironmental effects.[48]

While all of the SMOMs discussed in this Section were characterised by single-crystal X-ray diffraction (*sc*-XRD), SMOM 17 was also studied by solid-state NMR spectroscopy (SSNMR): due to the uniquely high on-stream lifetime of this system (see Section 2.4.2), SSNMR information became relevant in the characterisation of on-stream and post-catalytic material (see Section 2.4.6). The virtual $^{31}P\{^1H\}$ NMR triplet at δ ~76 ($^1J_{PRh}$ ~ 140 Hz) visible in the $^{31}P\{^1H\}$ SSNMR spectrum at all temperatures (158, 183, 298 K, the latter in **Figure 2.2.3**) indicated crystallographically inequivalent ^{31}P environments in the solid-state as present in the solid-state structural solution (**Figure 2.2.2**).[2]

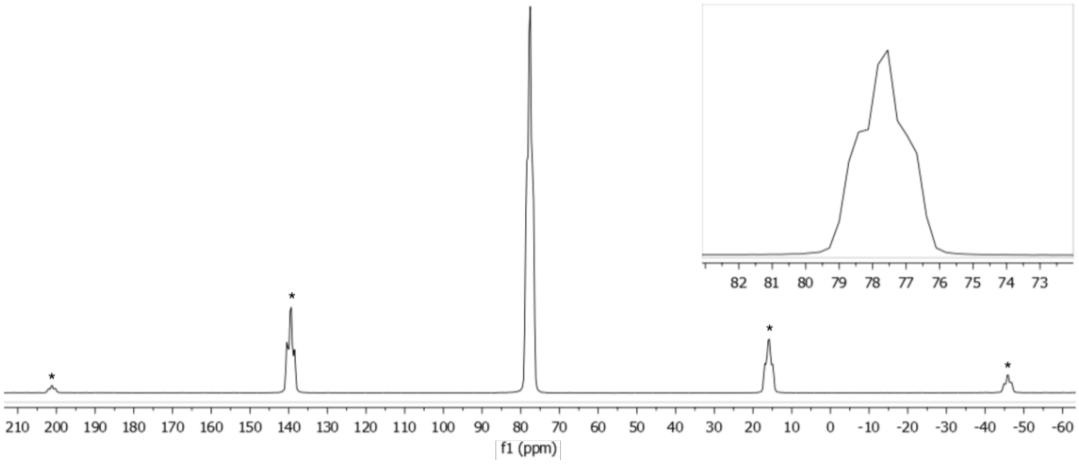


Figure 2.2.3: $^{31}P\{^1H\}$ SSNMR spectrum of SMOM 17 (161.9 MHz, 298 K, ν = 10 kHz). * indicate spinning side-bands.

The first exception to an O_h-type packing SMOM discussed here, [(L_2)Rh(η^2,η^2-NBD)][$BAr^F{}_4$] where L_2 = dippe = ^{i}Pr$_2$P(CH$_2$)$_2$P^{i}Pr$_2$ (**7**), has been previously reported to possess a bicapped parallelpipedic (BCPP) motif in the solid-state, with close C–H···F–Ar^F approaches evident (**Figure 2.2.4**).[12] Increasing the tether from two to three CH_2 moieties restored octahedral packing in the SMOM [(dippp)Rh(η^2,η^2-NBD)][$BAr^F{}_4$] where dippp = ^{i}Pr$_2$P(CH$_2$)$_3$P^{i}Pr$_2$. Clearly, solid-state packing patterns are influenced by subtle stereochemical factors, potentially giving rise to dramatic structural reorganisation between one SMOM and another.

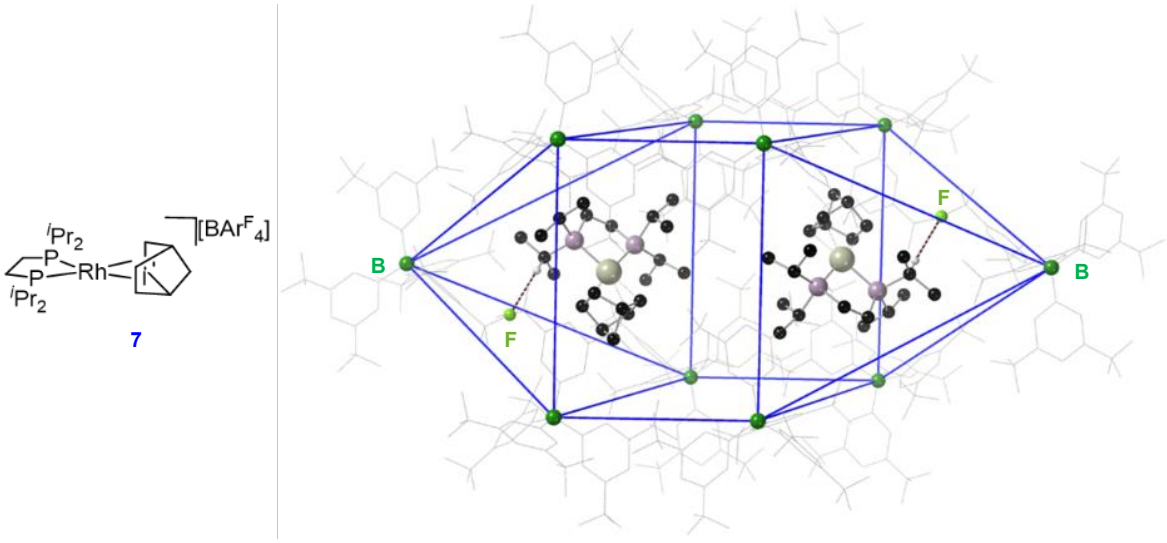


Figure 2.2.4: The bicapped parallelepipedic (BCPP) packing environment of SMOM **7**, with two cationic fragments [(dippe)Rh(η^2,η^2-NBD)]$^+$ (modelled as ball-and-stick) and their 10 nearest [$BAr^F{}_4$]$^-$ neighbours (modelled as wireframe with B atom balls). Close H···F approaches (H191–F103, 2.495(5) Å) are highlighted in red. Constructed from structural data found in the reference.[12]

As a second exception to an O_h-type packing pattern, SMOM **13**, which has already been discussed as a product of solvent loss from a precursor, departs significantly from the O_h structure type and is also best approximated as a BCPP-type structure (**Figure 2.2.5**). In a third exception, the PˆNˆP-type SMOM **14** adopts an approximately bifastigial arrangement of eight [$BAr^F{}_4$]$^-$ anions around each cationic fragment in the solid-state, with two such motifs combining to effect a buckled hexagonal prism (**Figure 2.2.6**). While a close N–H···F approach of 2.57(7) Å was observed in this structure, the related PˆNˆP-type SMOM **15** possessed a simple O_h packing motif, with no such close N–H···F approach, indicating that the NH tethering moiety does not necessarily impart an overriding influence on solid-state structure.

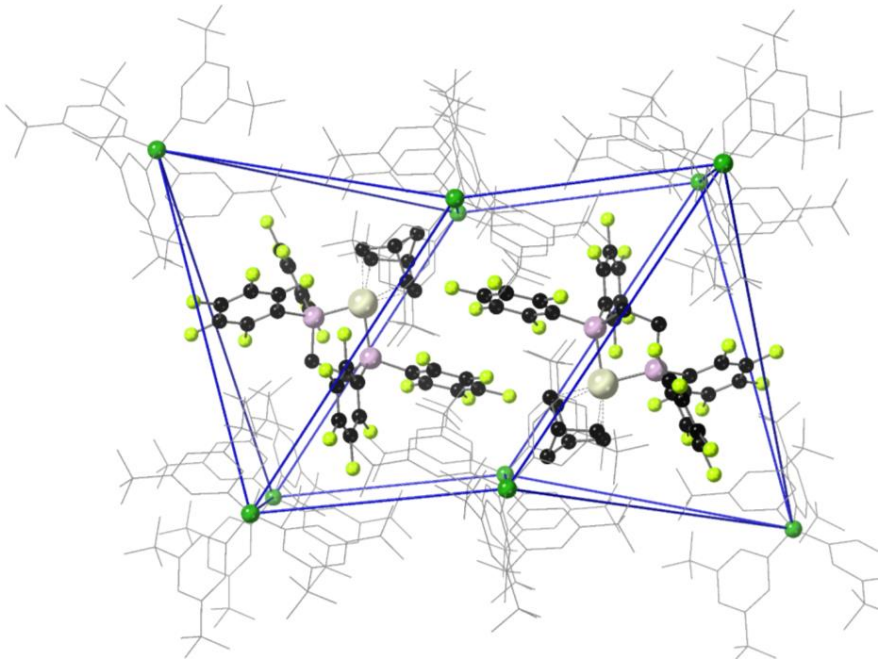


Figure 2.2.5: The bicapped parallelepipedic (BCPP) packing environment of **13**, with two cationic fragments [(dpfppe)Rh(η^2,η^2-NBD)]$^+$ (modelled as ball-and-stick) and their 10 nearest [BAr$^F_4$]$^-$ neighbours (modelled as wireframe with B atom balls).

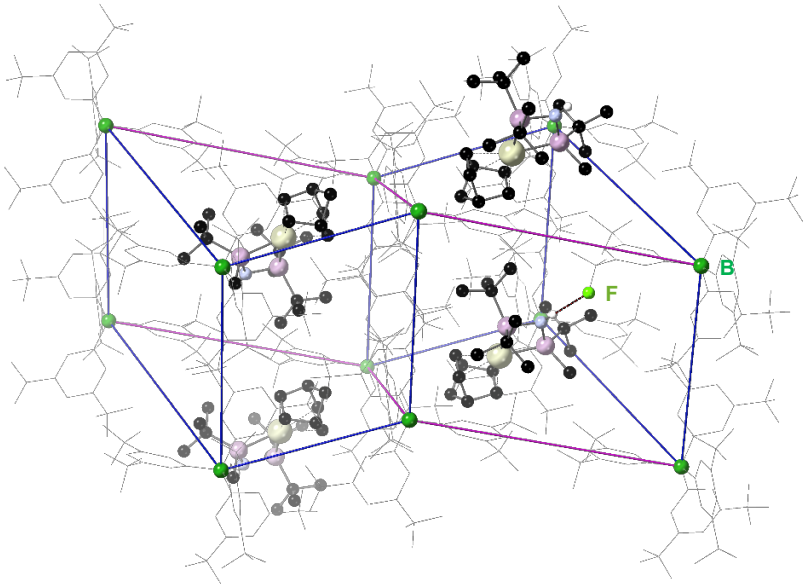
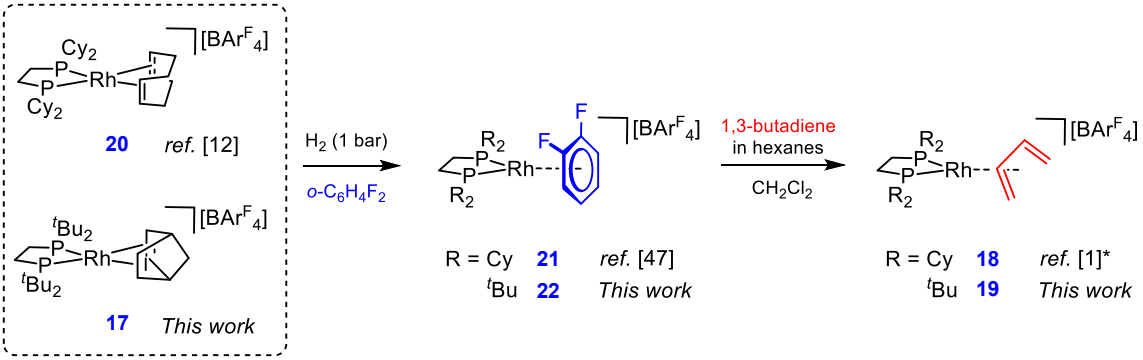


Figure 2.2.6: The buckled hexagonal prismatic coordination of 12 [BAr$^F_4$]$^-$ anions (modelled as wireframe with B-atom balls) about a cavity containing two [((*R*)-MaxPhos)Rh(η^2,η^2-NBD)]$^+$ fragments (modelled as ball-and-stick) in SMOM **14**. H atoms omitted for clarity except crystallographically-located N–H positions. A close N1–H1···F22 approach of 2.57(7) Å is indicated in red. Two additional [((*R*)-MaxPhos)Rh(η^2,η^2-NBD)]$^+$ fragments have been included outside the hexagonal prism.

2.2.5 *Independent Synthesis and Characterisation of Suspected Deactivation Products as NMR References*

The 1,3-butadiene complex [(dcpe)Rh(η^4-C_4H_6)][BAr^F_4] (**18**) is known to constitute the end-product of a deactivation pathway during solid-gas catalytic 1-butene isomerisation, *via* transfer dehydrogenation from [(dcpe)Rh(η^2-*cis*-2-butene)][BAr^F_4] (**3**).[1,2] So that the respective 1,3-butadiene complexes could be positively identified in post-catalytic material, if they were to form, complexes of formula [(P_2)Rh(η^4-C_4H_6)][BAr^F_4] where P_2 = dcpe (**18**) or dtbpe (**19**), were synthesised independently *via* a solution route from either the η^2,η^2-COD complex (dcpe, **20**) or the η^2,η^2-NBD complex (dtbpe, **17**) and characterised by both solution-phase and solid-state methods. A solution of 1,3-butadiene in hexanes was added to a CH_2Cl_2 solution of the relevant 1,2-difluorobenzene complex, followed by recrystallisation with pentane at 298 K (**Scheme 2.2.5**).



Scheme 2.2.5: Synthesis of 1,3-butadiene complexes **18** and **19** intended as an NMR spectroscopic references. *Note that a solid-gas procedure was used to generate complex **18** in the reference;[1] the solution-phase route given here was followed in this work.

One such complex, [(dcpe)Rh(η^4-C_4H_6)][BAr^F_4] (**18**), has already been described, with the authors instead making use of a solid-gas protocol for the synthesis of this complex.[1] The solid-state structure of new 1,3-butadiene complex [(dtbpe)Rh(η^4-C_4H_6)][BAr^F_4] (**19**) is shown in **Figure 2.2.7**, where a typical O_h-type structure is adopted; the two double bonds (1.337(17), 1.349(18) Å) and the single bond (1.447(15) Å) of the butadiene moiety in **19** were unambiguously differentiated by *sc*-XRD studies. By solution-phase ^{1}H NMR spectroscopy, the CH_2 and CH positions were identified at δ 2.71/4.73 and δ 5.52 respectively, each resonance integrating to 2 H relative to [BAr^F_4]$^-$.

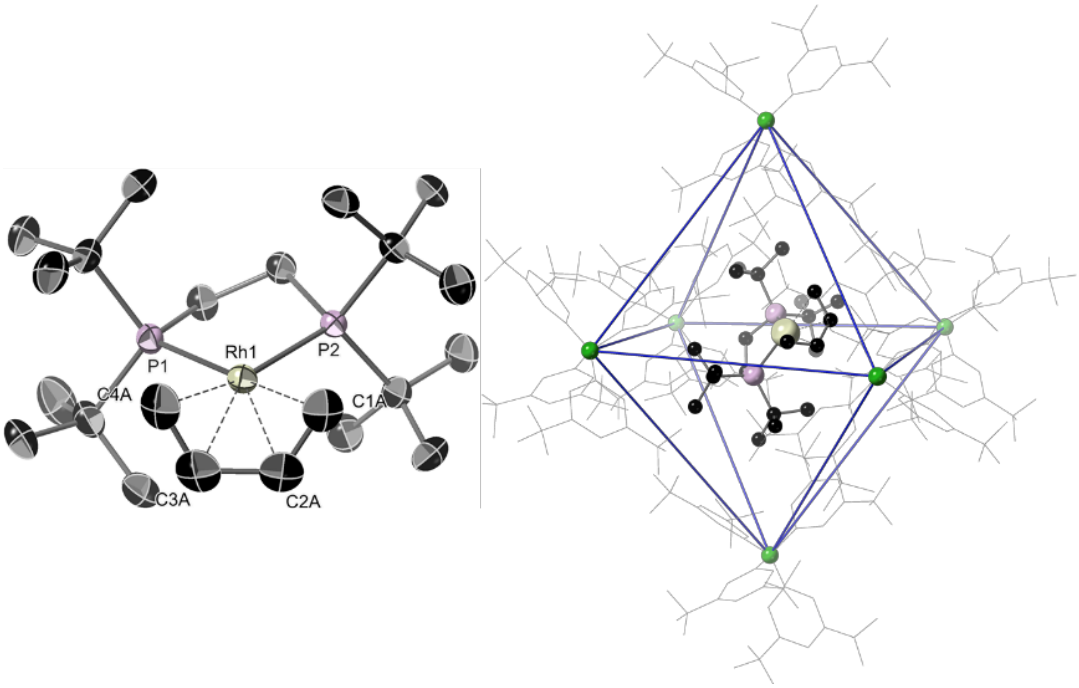
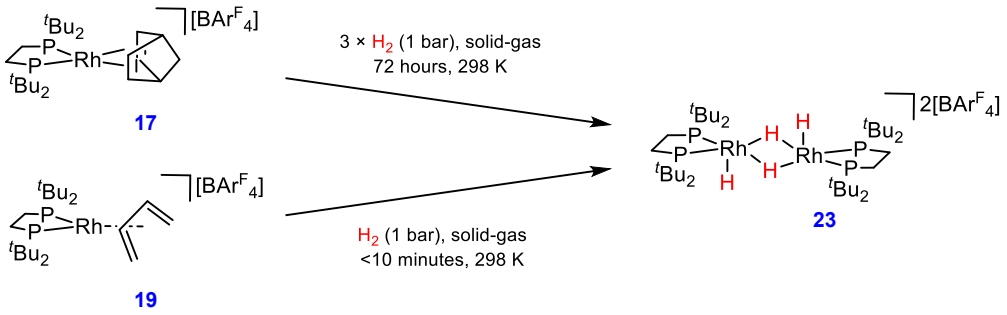


Figure 2.2.7: (**left**) Cationic fragment [(dtbpe)Rh(η^4-C_4H_6)]$^+$ of SMOM **19**. 50% displacement ellipsoids. Anions and H atoms omitted for clarity. Selected bond lengths (Å) and angles (deg): Rh1–P1, 2.3316(10); Rh1–P2, 2.3244(7); Rh1–C1B, 2.255(11); Rh1–C2B, 2.193(8); Rh1–C3B, 2.199(10); Rh1–C4B, 2.240(14); C1B–C2B, 1.337(17); C2B–C3B, 1.447(15); C3B–C4B, 1.349(18); P1–Rh1–P2, 87.06(3); C1B–C2B–C3B, 121.8(11); C2B–C3B–C4B, 119.4(10). Two cations are present in the asymmetric unit; one is shown above in which only one disordered position of butadiene is shown (58% by chemical occupancies). (**right**) The O_h packing environment of **19**, cationic fragment [(dtbpe)Rh(η^4-C_4H_6)]$^+$ (modelled as ball-and-stick) and its six nearest [BAr^F_4]$^-$ neighbours (modelled as wireframe with B atom balls).

Consistent with crystallographically inequivalent CH_2 and CH carbons, butadiene resonances in **19** observed *via* solution-phase $^{13}C\{^1H\}$ NMR spectroscopy (δ 61.9, 101.8) were observed as split by solid-state NMR methods (δ [58.9, 61.5], [99.3, 101.4]). The phenomenon of 'split' (or 'dispersed') resonances due to crystallographic inequivalence in the solid-state will re-emerge throughout this thesis.

Phosphines bearing *tert*-butyl alkyl groups are more electron-donating than their *cyclo*-hexyl-bearing counterparts. This has been experimentally shown through analysis of CO stretching frequencies in [$(R_3P)Ni(CO)_3$][19] and through NMR studies on protonated phosphines [HPR_3][CF_3COO],[49] among other corroborating studies.[20,50,51] As such, the presence of these powerfully donating ^{t}Bu groups in SMOM **17** were suspected to favour higher oxidation states at the metal centre, compared to the previously reported SMOMs with secondary alkyl R-groups (*e.g.* Cy (**1**), ^{i}Pr (**7**), Cyp (**10**)).

The identity of any solid-gas hydrogenation and deactivation products had to therefore be positively compared to (or differentiated from) a bridging Rh(III) hydride that may have arisen from H_2 oxidative addition. Such a hydride was reported for an iridium-containing congener $[(dcpe)Ir(\eta^2,\eta^2\text{-NBD})][BAr^F{}_4]$ after solid-state exposure to H_2 gas.[52] $\{[(dtbpe)Rh(H)(\mu\text{-H})]_2\}[BAr^F{}_4]_2$ (**23**) was synthesised in a similar fashion, by solid-gas hydrogenation of the η^2,η^2-NBD complex $[(dtbpe)Rh(\eta^2,\eta^2\text{-NBD})][BAr^F{}_4]$ (**17**) with three charges of H_2 gas (1 bar) over a total of 72 hours – yielding amorphous pale yellow material – followed by recrystallisation from a concentrated CH_2Cl_2 solution cooled to 2 °C under a pressure of H_2 (1 bar) (**Figure 2.2.8**). Deleterious reaction of hydride **23** with the CH_2Cl_2 solvent (*vide infra*) during recrystallisation was prevented both by the H_2 atmosphere and the sub-ambient temperature.



Scheme 2.2.6: Synthesis of bridging hydride (**23**) intended as an NMR spectroscopic reference.

Crystalline dimeric dihydride **23** was characterised by solution-phase and solid-state NMR spectroscopy and mass spectrometry. Two ^{1}H-hydride NMR signals were observed at 183 K in CD_2Cl_2 in a 1:1 integral ratio in similar positions to those reported in analogous complexes,[53]a at δ –27.6 (terminal) and –4.70 (bridging), in a 1:1 integral ratio. ^{103}Rh-^{1}H ($^1J_{HRh}$ ~ 48 Hz (terminal), 30 Hz (bridging)) and ^{31}P-^{1}H ($^2J_{HP}$ ~ 65 Hz (bridging only)) coupling were resolved at 183 K, deconvoluted *via* an ^{1}H{^{31}P} NMR experiment. Complex **23** was stable under the conditions of ESI-MS: the dication $\{[(dtbpe)Rh(H)(\mu\text{-H})]_2\}^{2+}$ was resolved with the expected *m/z* ratio for a fragment of formula $C_{36}H_{84}P_4Rh_2^{2+}$ (423.1853; calculated 423.1811).

[a] For example, $\{[(^iPr_2P(CH_2)_3P^iPr_2)Rh(H)(\mu\text{-H})]_2\}[ClO_4]_2$ was reported to give rise to hydride signals at δ –20.5 and –8.1.

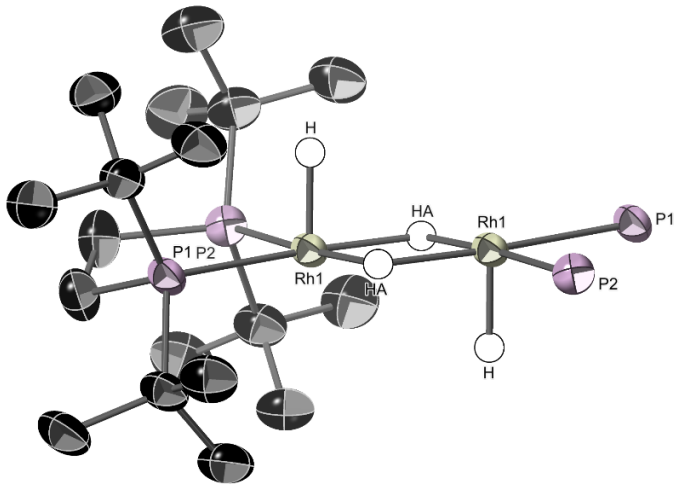
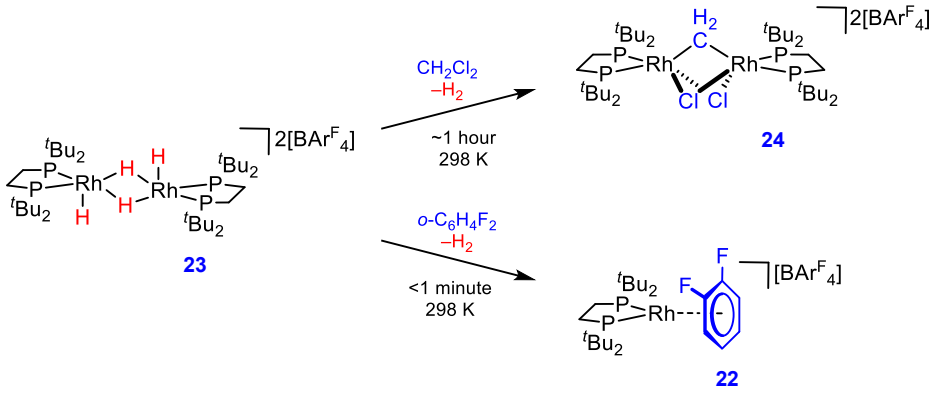


Figure 2.2.8: Major disordered component (~97% from chemical occupancies) of dicationic fragment $\{[(dtbpe)RhH(\mu\text{-}H)]_2\}^{2+}$ of bridging hydride complex **23**. 50% displacement ellipsoids. Anions, H atoms (excluding crystallographically located hydrides), and rightmost dtbpe moiety omitted for clarity. Selected bond lengths (Å) and angles (deg): Rh1–H, 1.42(4); Rh1–HA, 1.74(5); Rh1–P2, 2.2809(7); Rh1–P1, 2.2973(8); P2–Rh1–H, 92.5(16); P1–Rh1–H, 93.8(19); P2–Rh1–HA, 96.7(14); P1–Rh1–HA, 96.3(17). The alternative (~3%) disorder component is generated by a ~90° rotation of the fragment in the $(P_2)Rh(H)_2$ plane, about an axis approximately perpendicular to Rh1···Rh1 and HA···HA.

The synthesis of complex **23** was somewhat slow (~72 hours) *via* solid-state hydrogenation of the precursor η^2,η^2-NBD complex **17**, but occurred much more rapidly from the 1,3-butadiene complex **19** (<10 minutes). This may be due to the higher stability of the intermediate σ-NBA complex (*vide infra*) compared to that of the hypothetical σ-butane complex.[48] Both recrystallised and non-recrystallised[a] material were interrogated by $^{31}P\{^1H\}$ SSNMR spectroscopy, giving rise to somewhat broad resonances (δ ~120), comparing well to solution-phase $^{31}P\{^1H\}$ NMR spectroscopic data (δ 121.9 ($^2J_{PRh}$ ~ 108 Hz, $^2J_{PP'}$ ~ 20 Hz)).

Bridging hydride **23** was not indefinitely stable in CH_2Cl_2 solution at 298 K in the absence of an H_2 atmosphere, slowly reacting with the solvent over ~60 minutes to yield a C-Cl activated dimer (**24**; **Scheme 2.2.7**). This solvent activation product was amenable to recrystallisation with pentane (**Figure 2.2.9**) and full NMR characterisation at 298 K, resembling the phenomenon of CH_2Cl_2 activation reported for other *bis*-phosphine-rhodium complexes.[14,54–58] Dissolving **23** in 1,2-difluorobenzene at 298 K immediately generated the corresponding 1,2-difluorobenzene complex (**22**) and released H_2 into solution (δ_H ~4.60).

[a] *i.e.* powdered SMOMs **17** or **19** which had been exposed to H_2 gas in the solid-state but *not* recrystallised from CH_2Cl_2 under H_2.



Scheme 2.2.7: Decomposition routes of hydride **23** in CH_2Cl_2 and 1,2-difluorobenzene solution.

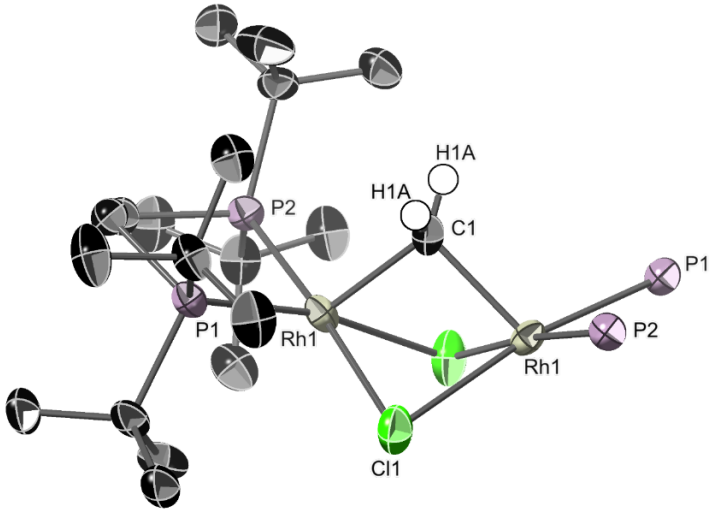


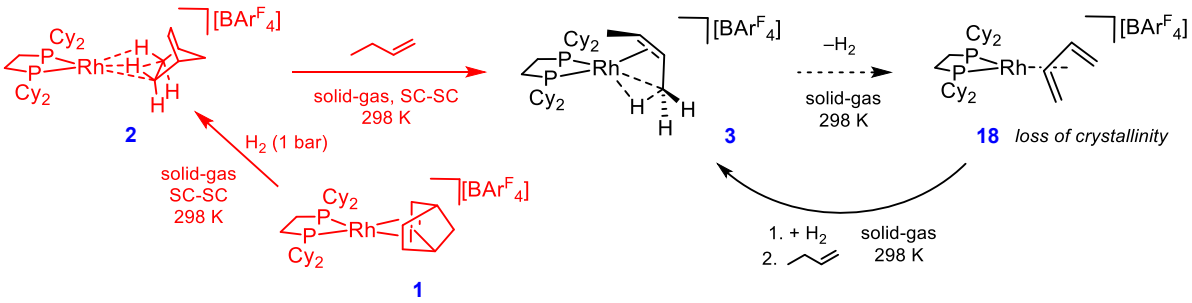
Figure 2.2.9: Dicationic fragment $[(dtbpe)Rh(\mu\text{-}CH_2)(\mu\text{-}Cl)_2Rh(dtbpe)]^{2+}$ of C-Cl activated dimer **24**. 50% displacement ellipsoids. Anions, rightmost dtbpe moiety, and H atoms omitted for clarity excepting calculated positions on bridging methylene. Selected bond lengths (Å) and angles (deg): Rh1–Rh1, 3.0312(8); Rh1–C1, 2.045(6); Rh1–Cl1, 2.4431(16); Rh1–P1, 2.3165(14); Rh1–P2, 2.3475(15); P1–Rh1–P2, 86.77(5); P1–Rh1–C1, 109.54(13); P2–Rh1–C1, 104.79(13); C1–Rh1–Cl1, 79.72(14); Rh1–Rh1–Cl1, 51.49(4); Cl1–Rh1–Cl1, 82.61(6).

2.3 Solid-Gas Catalytic Isomerisation of 1-butene with Precursor NBD SMOMs (NMR Batch Conditions)

As proofs-of-concept, pre-hydrogenated η^2,η^2-NBD SMOMs [$(P_2)Rh(\eta^2,\eta^2$-NBD)][$BAr^F{}_4$], where P_2 = dcpe = $Cy_2P(CH_2)_2PCy_2$ (**1**) and dtbpe = $^tBu_2P(CH_2)_2P^tBu_2$ (**17**), were initially tested as solid-gas 1-butene isomerisation catalysts under NMR-scale batch conditions. The differences between both the activities and the lifetimes of catalytic systems derived from SMOMs **1** and **17** under batch conditions were substantial, with SMOM **17** generally producing longer-lived and more *cis*-selective systems albeit with lower activity compared to those produced from SMOM **1**. This demonstrates the importance of the chelate P_2 in the reactivity of these SMOMs. To understand these differences, it is necessary first to briefly explore the solid-gas reactivity of these complexes with hydrogen and 1-butene *ex situ*.

2.3.1 Solid-Gas Reactivity of [(dcpe)Rh(η²,η²-NBD)][BAr$^F{}_4$] (Precursor SMOM 1)

Sequential solid-gas exposure of single-crystalline precursor η^2,η^2-NBD SMOM **1** to H_2 (yielding the intermediate σ-NBA complex (**2**) *in situ*) and then 1-butene gas has been previously reported to yield a *cis*-2-butene complex (**3**) *via* a single-crystal to single-crystal (SC–SC) solid-gas transformation (**Scheme 2.3.1**). The σ-NBA ligand, a weakly-bound 'token' ligand, was easily displaced by 1-butene and facile isomerisation of the 1-butene fragment thereafter took place *via* a π-allyl hydride intermediate.[1,14]a



Scheme 2.3.1: Solid-gas reactivity of precursor η^2,η^2-NBD SMOM **1** with H_2 and 1-butene gas, as previously reported in the reference.[1]

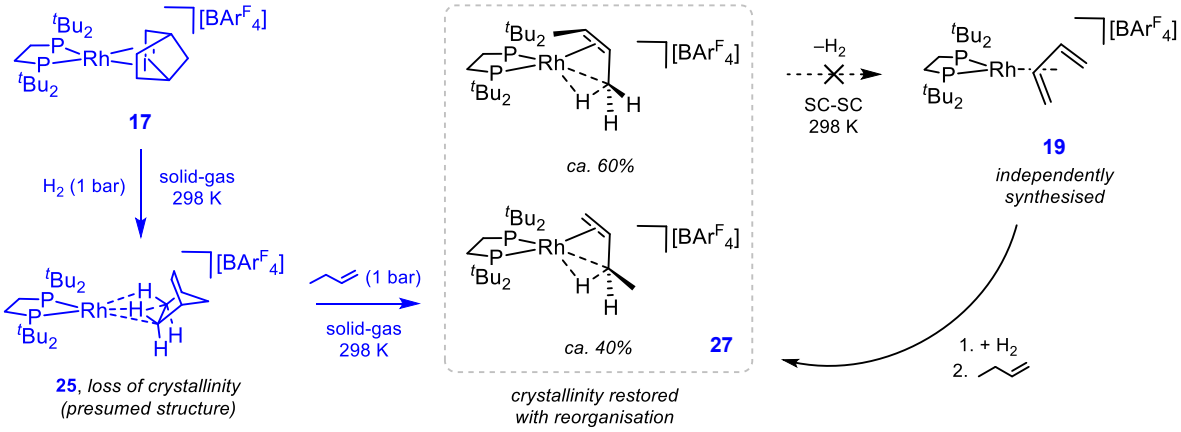
[a] See Introduction (Section 1.2.1) for a discussion of the π-allyl hydride alkene isomerisation mechanism.

In a further transformation, the *cis*-2-butene complex was reported to slowly lose one equivalent of H_2 to yield the corresponding 1,3-butadiene complex (**18**), occurring *via* a transfer dehydrogenation event involving a second molecule of butene. For the three species in the sequence (**1**, **2**, **3**) where sufficient crystallinity was retained for a structural solution, O_h-type structures were demonstrated by all three, indicating two sequential periodic structure-retaining SC-SC transformations. It is curious to note that despite the capacity of *in situ*-generated butene complex **3** for catalytic solid-gas 1-butene isomerisation into both *cis*- and *trans*-2-butene isomers, the presence of any coordinated *trans*-2-butene was *not* ascertained in the solid-state, even after thermodynamic equilibrium in the headspace atmosphere was achieved (~77% *trans*-2-butene[3]).[1,6] This apparent discrepancy, between the *trans* isomer being favoured thermodynamically in the gas-phase[3] *versus* the *cis* isomer being favoured when coordinated to the active site, is discussed further in Section 2.3.3. There, we reason that this selectivity is due to steric occlusion at the metal, destabilising any metal-bound *trans* isomer relative to *cis*.

2.3.2 Solid-Gas Reactivity of [(dtbpe)Rh(η²,η²-NBD)][BAr$^F_4$] (Precursor SMOM 17)

Precursor η^2,η^2-NBD SMOM **17** crystallised from CH_2Cl_2 and pentane into an O_h-type structure (**Figure 2.2.2**), much like precursor **1**. Upon solid-gas exposure of precursor SMOM **17** to H_2 gas (1.0 bar) at 298 K, the σ-NBA complex (**25**) was produced, with conversion surpassing 95% after 20 minutes (**Scheme 2.3.2**).[2] This was confirmed by quenching with CD_3CN and interrogating the resulting solution by ^1H and $^{31}P\{^1H\}$ NMR spectrometry for the presence of free NBA, unconverted complex **17** (~5% after 20 minutes), and the quenching product [(dtbpe)Rh(NCCD$_3$)$_2$][BAr$^F_4$] (*d*$_6$-**26**), using the known complex [(dtbpe)Rh(NCCH$_3$)$_2$][OTf] as a $^{31}P\{^1H\}$ NMR reference (δ 110.0, $^1J_{PRh}$ = 181 Hz (CD_3CN, 298 K)) (**Figure 2.3.1** and **Figure 2.3.2**).[45]

This transformation was also monitored *in situ* by $^{31}P\{^1H\}$ SSNMR spectroscopy (**Figure 2.3.3**), with a slightly longer hydrogenation time of 50 minutes to account for the area of contact between material packed inside the 4.0 mm zirconia solid-state rotor and the H_2 atmosphere.



Scheme 2.3.2: Solid-gas reactivity of precursor η^2,η^2-NBD SMOM **17** with H_2 and 1-butene gas, new to this work.

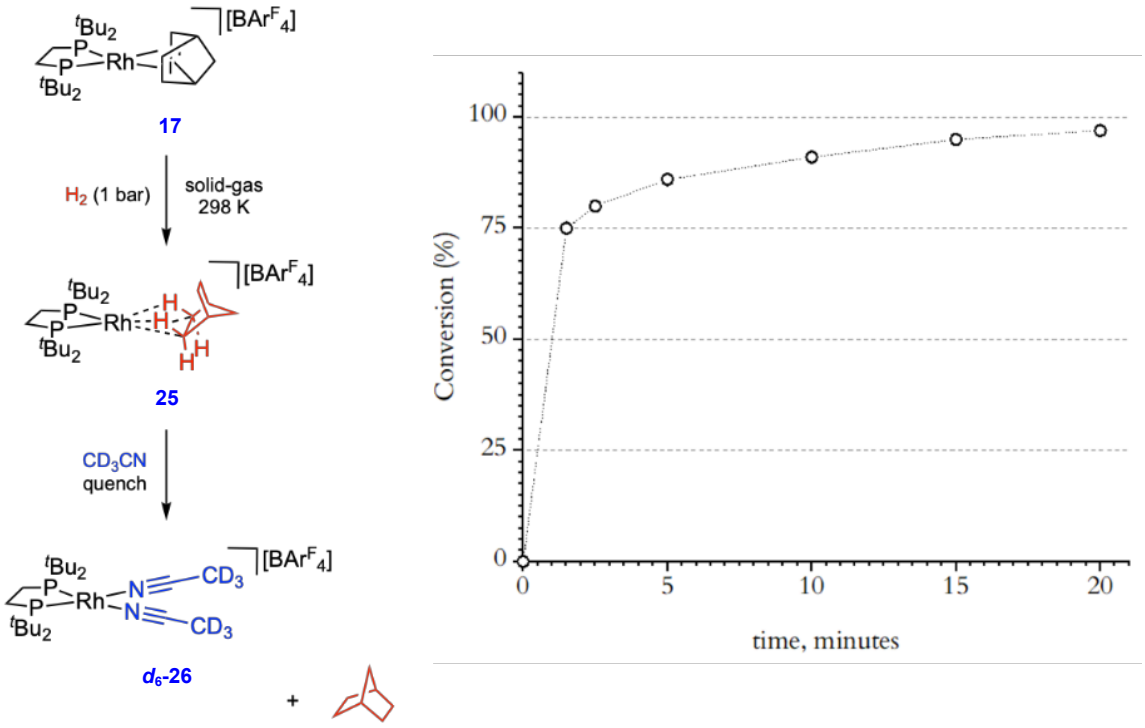


Figure 2.3.1: Ratio of quenching product *bis*-d_3-acetonitrile complex d_6-**26** (as a proxy for the proposed σ-NBA complex **25**) at time *t versus* unreacted η^2,η^2-NBD complex **17**, computed from ^{1}H NMR integrals.

The $^{31}P\{^1H\}$ SSNMR spectrum of the initial η^2,η^2-NBD SMOM (**17**) gave rise to a signal composed of two overlapping doublets at δ 77.7 ($^1J_{PRh}$ ~ 140 Hz – **Figure 2.2.3** and **Figure 2.3.3–A1**). Unexpectedly, solid-state hydrogenation of SMOM **17** did *not* proceed with maintenance of crystallinity as it did for **1**.

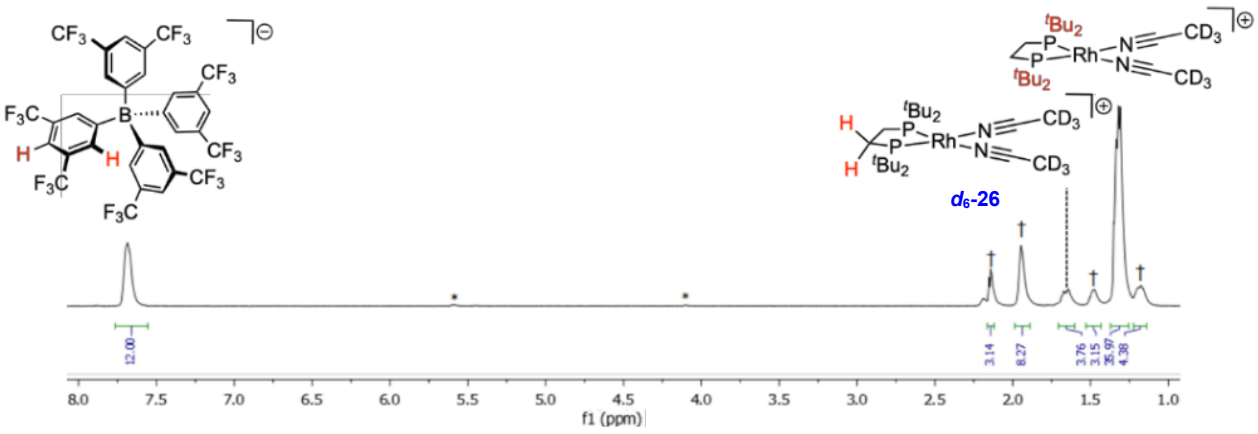


Figure 2.3.2: Exemplar ^{1}H NMR spectrum after quenching with CD_3CN at hydrogenation time t = 20 minutes (CD_3CN, 298 K). *corresponds to unreacted NBD complex (17, ~5%), and † to free NBA. δ ~2.15 is coincident with an HDO impurity and δ ~1.95 is coincident with the solvent peak. Integrals are calculated relative to the $[BAr^F_4]^-$ peak, set to 12.0 H.

Bragg reflections were observed to disappear promptly upon exposure of SMOM 17 to H_2 (**Figure 2.3.3**; **A2,3⟶B2,3**) despite the retention of a sharp, well-defined $^{31}P\{^{1}H\}$ SSNMR spectrum (**A1⟶B1**). This suggests the material lost long-range order but did not become completely amorphous: *sc*-XRD studies on the proposed σ-NBA complex 25 were therefore unsuccessful, and no direct structural evidence for a σ-NBA complex was available.

For the proposed σ-NBA complex (25; **B1**), a pair of overlapping doublets was observed with an increased ^{103}Rh–^{31}P coupling constant (δ 125.8, J_{PRh} ~ 190 Hz) relative to the precursor η^2,η^2-NBD complex 17 (δ 77.7, J_{PRh} ~ 140 Hz) and distinct from the $^{31}P\{^{1}H\}$ SSNMR spectra obtained for both recrystallised and *in situ*-generated bridging hydride 23, δ ~120. This increased ^{103}Rh–^{31}P coupling constant was indicative of a weaker ligand *trans* to the ^{31}P donor atoms (*i.e.* NBA *cf.* NBD),[59,60] corroborating the results of previous solid-state η^2,η^2-NBD → σ-NBA hydrogenations tracked by $^{31}P\{^{1}H\}$ SSNMR spectroscopy.[12–14,46] Unfortunately, solid-state ^{13}C-^{1}H HETCOR experiments conducted at 158 K were unable to unambiguously confirm the presence of a C-H σ-interaction, where such studies were successful for 2[12] and other σ-NBA complexes derived *via* the solid-state hydrogenation of η^2,η^2-NBD SMOM precursors.[14,46]

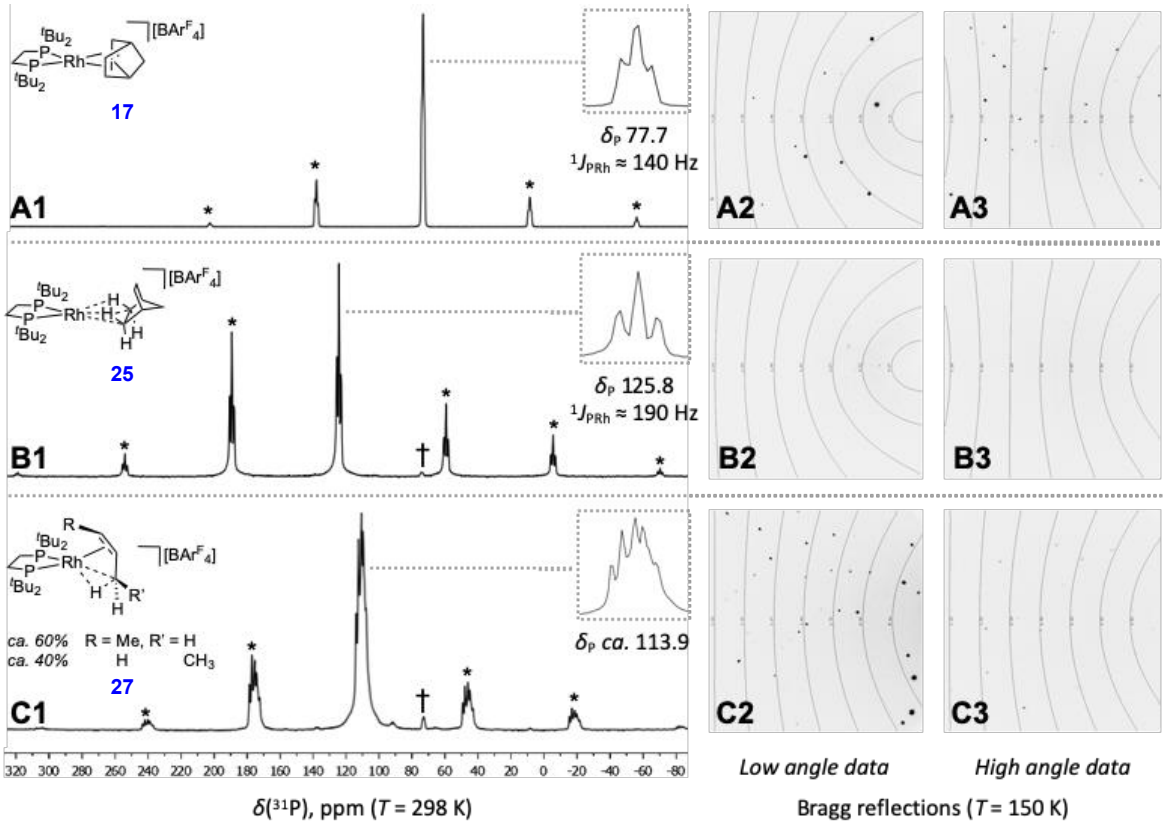


Figure 2.3.3: $^{31}P\{^{1}H\}$ SSNMR spectra (161.4 MHz, 298 K, ν = 10 kHz) of complexes 17 (**A1**), 25 (**B1**), and 27 (**C1**), compared with frames demonstrative of the loss of Bragg reflections from complex 17 (**A2-3**) to 25 (**B2-3**), and their restoration in 27 (**C2-3**). * indicates spinning side-bands. † indicates unreacted 17.

Long-term exposure of SMOM 17 to H_2 gas (~72 hours) *did* result in the formation of the hydride 23 (see Section 2.2.5), confirmed *via* $^{31}P\{^{1}H\}$ solution-phase and solid-state NMR spectroscopy, and accompanied by a solid colour change from deep red-brown to pale yellow. Significantly, solid-gas exposure of [(dtbpe)Rh(σ-NBA)][BAr^F_4] (25) to 1-butene gas (1 bar, 48 hours) was observed to *restore* the sample's Bragg reflections (**B2,3→C2,3**), indicating the return of long-range order. This remarkable order-disorder-order transformation permitted *sc*-XRD studies to take place on the resulting [(dtbpe)Rh(*n*-butenes)][BAr^F_4] (27), a solid-state mixture of isomers (**Figure 2.3.4**). Also noteworthy was that the order-disorder-order transformation resulted in solid-state structural reorganisation, from an originally O_h packing motif (**Figure 2.2.2**) to a bicapped parallelepiped (BCPP). Order-disorder-transitions have been established for a number of inorganic systems – *e.g.* superconductors,[61] PbI_2 crystals,[62] MOFs,[63] metal nanoparticles,[64–67] and enzymes ('order' refers to folding in enzymatic domains)[68,69] – but is rare for organometallic systems.

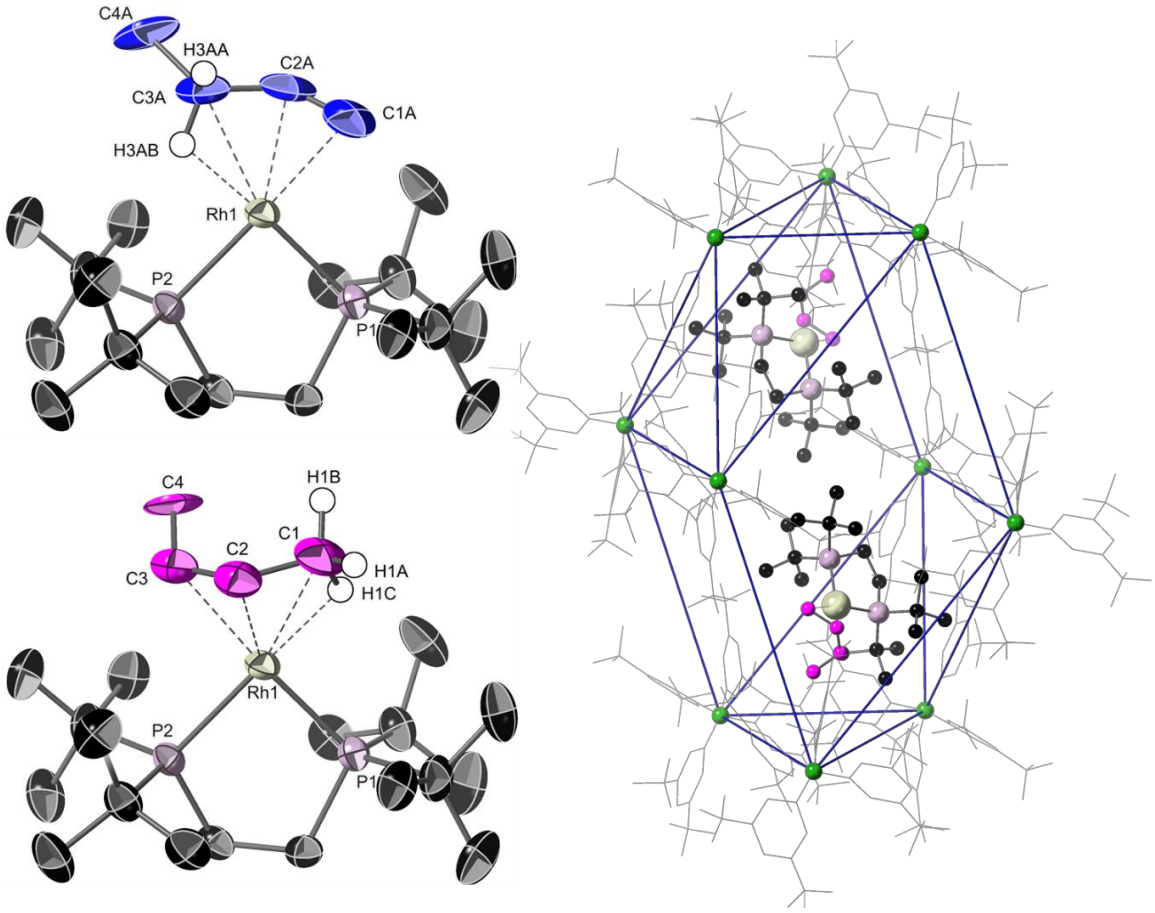


Figure 2.3.4: (**left**) Cationic fragments [(dtbpe)Rh(1-butene)]$^+$ (*ca.* 40%, by chemical occupancy, 1-butene in blue) and [(dtbpe)Rh(*cis*-2-butene)]$^+$ (*ca.* 60%, 2-butene in magenta) (**top** and **bottom** respectively) of [(dtbpe)Rh(*n*-butenes)][BAr$^F{}_4$] (27). 50% displacement ellipsoids. Anions and H atoms omitted for clarity excepting calculated H atoms associated with agostic positions. Selected bond lengths (Å) and angles (deg), where Cent1 is the centroid of C1A–C2A and Cent2 is the centroid of C2–C3: Rh1–P1, 2.2652(9); Rh1–P2, 2.2616(8); Rh1–H3AB, 1.8146(4); Rh1–H1C, 1.8953(3); Rh1–C1, 2.418(9); Rh1–C2, 2.167(7); Rh1–C3, 2.356(10); Rh1–C1A, 2.250(10); Rh1–C2A, 2.155(7); Rh1–C3A, 2.349(9); Rh1–Cent1, 2.095(7); Rh1–Cent2, 2.161(6); C1–C2, 1.475(13); C2–C3, 1.346(12); C3–C4, 1.467(14); C1A–C2A, 1.362(13); C2A–C3A, 1.525(15); C3A–C4A, 1.541(18); P2–Rh1–C2, 117.26(19); P2–Rh1–Cent2, 106.99(17); P2–Rh1–C3, 96.6(3); P1–Rh1–C2A, 119.8(2); P1–Rh1–Cent1, 108.6(2); P1–Rh1–C1A, 96.8(3); C1–C2–C3, 125.4(7); C2–C3–C4, 123.0(10); C1A–C2A–C3A, 120.6(9); C2A–C3A–C4A, 112.6(10). (**right**) The BCPP packing environment of 27, two cationic fragments [(dtbpe)Rh(*cis*-2-butene)]$^+$ (modelled as ball-and-stick) and their 10 nearest [BAr$^F{}_4$]$^-$ neighbours (modelled as wireframe with B atom balls).

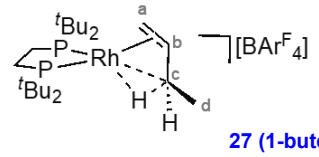
Spontaneous reordering has previously been observed in a SMOM: a disorder-order transition from amorphous Ar^F-coordinated zwitterions [(dibpe, dippe)Rh(η^6-Ar^F-BAr$^F{}_3$)] (dibpe = ^{i}Bu$_2$P(CH$_2$)$_2$P^{i}Bu$_2$, dippe = ^{i}Pr$_2$P(CH$_2$)$_2$P^{i}Pr$_2$) as formed by solid-state displacement of σ-NBA, where some return of long-range order was evidenced by powder X-ray diffraction (*p*-XRD) after gentle heating of the solids (also see **Scheme 1.1.10** and accompanying text).[12,13]

It is unclear why long-range order was lost so dramatically upon hydrogenation of precursor SMOM 17 when it was not for 1. Steric hindrance at the active site seems unlikely to be the reason, as the SMOM [(dtbpp)Rh(η^2,η^2-NBD)][BAr^F_4] (11, dtbpp = $^tBu_2P(CH_2)_3P^tBu_2$, also O_h-type structure) possesses active sites with even greater steric hindrance than SMOM 17 due to a wider bite angle, and yet is still known to give rise to the corresponding σ-NBA complex upon solid-state hydrogenation in an SC-SC fashion, albeit with loss of crystallographic order over time.[18]

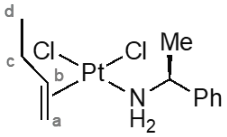
It is possible that loss of long-range order occurred due to a small percentage of sites forming the dimeric Rh(III) hydride (23). The Ir-centred congener [(dtbpe)Ir(η^2,η^2-NBD)][BAr^F_4][52] also lost crystallinity upon solid-state hydrogenation to yield the bridging hydride {[(dtbpe)Ir(H)(μ-H)]$_2$}[BAr^F_4]$_2$. Solid-state formation of dimers would require significant solid-state movement of both anions and cations, in events sufficiently disruptive to the overall structure to eliminate periodicity. It is also possible that the formation of σ-NBA complex 25 forced a non-correlated movement of the [BAr^F_4]$^-$ aryl rings of the Ar^F-B-Ar^F 'cleft' into which the C_7 moiety of this complex was oriented, shown in **Figure 2.2.2**.

Two superpositioned components were resolved in the resulting [(dtbpe)Rh(*n*-butenes)][BAr^F_4] (27) (**Figure 2.3.4**), where '*n*-butenes' corresponded to 1-butene (~40% from chemical occupancies) and *cis*-2-butene (~60%), with each butene fragment bound through the alkene and a γ-agostic interaction with no further disorder. The restoration of crystallinity was sufficient (R_1 ~ 4.1%), notwithstanding the order-disorder-order transition, such that a discussion of bond lengths and angles is appropriate. Numerous examples of crystallographically-characterised *n*-butene complexes have been reported, including examples of metal-coordinated 1-butene,[70–73] *cis*-2-butene,[1,74–81] and *trans*-2-butene.[82–84] However, only one of these examples also includes a γ-agostic interaction: the aforementioned [(dcpe)Rh(*cis*-2-butene)][BAr^F_4] (3), generated *via* an SC-SC reaction from the σ-NBA precursor (2).[1] To the author's knowledge, [(dtbpe)Rh(*n*-butenes)][BAr^F_4] (27) is the first example of a crystallographically-characterised 1-butene complex coordinated to rhodium. Pertinent bond lengths and angles for 27 are summarised in **Table 2.3.1**, compared with those observed for unbound 1-butene and *cis*-2-butene.[85–87]

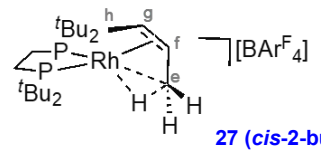
Unfortunately, no detailed comparison of bond metrics with [(dcpe)Rh(*cis*-2-butene)][BAr^F_4] (**3**) is possible, due to the insufficient quality of data reported for this complex (R_1 > 12%): each successive SC-SC transformation was observed to result in a decrease in data quality, in this case only sufficient to confirm connectivity.[1] This is also the case for the related γ-agostic-bound [(dcpe)Rh(propene)][BAr^F_4] (**28**). In contrast, in the case of [(dtbpe)Rh(*n*-butenes)][BAr^F_4] (**27**), the quality of the data was remarkably good and sufficiently so for a discussion of bond lengths and angles to be appropriate. Although a great number of complexes containing C–H agostic interactions to rhodium have been reported,[13,88–92] the bond metrics associated with the agostic position are highly dependent on position (*i.e.* γ-agostic *versus* β, δ, ε), the coordination environment of the metal, and the nature of the tether. No other structurally-characterised examples of rhodium γ-agostic interactions have been reported.



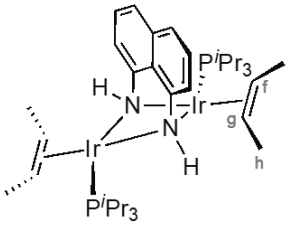
27 (1-butene)



I



27 (*cis*-2-butene)



II

D/Å, θ,ϑ/deg	**27**	*Unbound*	**I**	**II**
$D(C_a–C_b)$ C=C	1.362(13)	1.336	1.349(8)	–
$\theta(C_a–C_b–C_c)$	120.6(9)	126.7	121.0(8)	–
$\theta(C_b–C_c–C_d)$	112.6(10)	114.8	105.6(2)	–
$D(M–C_a)$	2.250(10)	–	2.163(8)	–
$D(M–C_b)$	2.155(7)	–	2.173(10)	–
$D(M–C_c)$ agostic	2.349(9)	–	–	–
$D(C_f–C_g)$ C=C	1.346(12)	1.339	–	1.416(5)
$\theta(C_e–C_f–C_g)$	125.4(7)	123.0	–	–
$\theta(C_f–C_g–C_h)$	123.0(10)	123.0	–	121.5(4)
$D(M–C_f)$	2.167(7)	–	–	2.111(4)
$D(M–C_g)$	2.356(10)	–	–	2.158(4)
$D(M–C_e)$ agostic	2.418(9)	–	–	–
$\vartheta(C_e–C_f–C_g–C_h)$	21.9(12)	0.0	–	8.6(5)

Table 2.3.1: Selected bond length and angle metrics (distance *D* in Å; bond angle θ and torsion angle ϑ in degrees) associated with [(dtbpe)Rh(*n*-butenes)][BAr^F_4] (**27**). Metrics associated with free ('unbound') 1-butene and *cis*-2-butene,[85–87] and comparison complexes **I**[70] and **II**,[74] have also been included.

The sole example of a late transition metal 1-butene complex to have been crystallographically characterised was reported by Pedone and colleagues, *cis*-[Cl_2Pt(1-butene)((*S*)-H_2NCHMePh)] (**I**).[70] This complex, alongside *cis*-2-butene bound to an binuclear iridium complex (**II**) reported by Jiménez and colleagues,[74] is included in **Table 2.3.1** for the purpose of comparison. Neither **I** nor **II** contain an agostic interaction. Consistent with π-backbonding, the C_{sp2}–C_{sp2} (**C=C**) bonds in 27 appeared lengthened *cf.* free butenes. C_{sp2}–C_{sp2}–$C_{agostic}$ bond angle compressions *cf.* free butenes were also observed within the sterically crowded coordination sphere of 27 – also reflected in the torsion angle ϑ, severely distorted from coplanar (21.9(12)°). The effect of the crowded metal coordination sphere in {(dtbpe)Rh}[BAr^F_4], referenced here, will be shown to be critically important in solid-gas catalytic selectivity in Section 2.3.4.

The presence of both coordinated 1-butene and *cis*-2-butene in 27 was confirmed *via* solution-phase and solid-state NMR studies. ^{1}H NMR signals belonging to both isomers were observed at low temperature (183 K, **Figure 2.3.5**). In the case of 1-butene in 27, resonances in the expected integral ratios according to its solid-state population (~40%) were resolved, corresponding to agostic C–H (δ 0.05; 1 H × 40% = 0.4 H) with a characteristic upfield shift,[93] one 1-butene spectator CH_3 signal (δ 1.45; 3 H × 40% = 1.2 H), and all three alkene CH signals (δ 3.37 (d, J_{HH} = 14.0 Hz; 1 H × 40% = 0.4 H), 4.74 (m; 0.4 H), 4.86 (d, J_{HH} = 7.5 Hz; 0.4 H)) linked unambiguously by a ^{1}H-COSY experiment. Attempting to obtain this data at 298 K in CD_2Cl_2 resulted in the rapid formation of the solvent activation product (d_2-24). If 1,2-difluorobenzene was used as a solvent, formation of the 1,2-difluorobenzene complex (22) was rapid at all temperatures 183–298 K.

In the case of *cis*-2-butene (~60%) in 27, signals were resolved for allylic CH_3 (δ 0.41; 6 H × 60% = ~3.6 H), ^{t}Bu CH_3 (δ 1.99; $^3J_{HP}$ ~ 13.2 Hz; 36 H × 60% = ~22 H), and alkene CH (δ ~5.32, obscured by *protio*-solvent but indicated by ^{1}H-COSY). Only individual signals were resolved in the ^{1}H solution-phase NMR spectrum for the *cis*-2-butene component's allylic, alkene, and ^{t}Bu CH_3 signals where greater complexity was expected due to the asymmetry imposed on the *cis*-2-butene fragment, with one methyl agostically bound and the other spectating, indicating a fluxional *cis*-2-butene component even at 183 K.

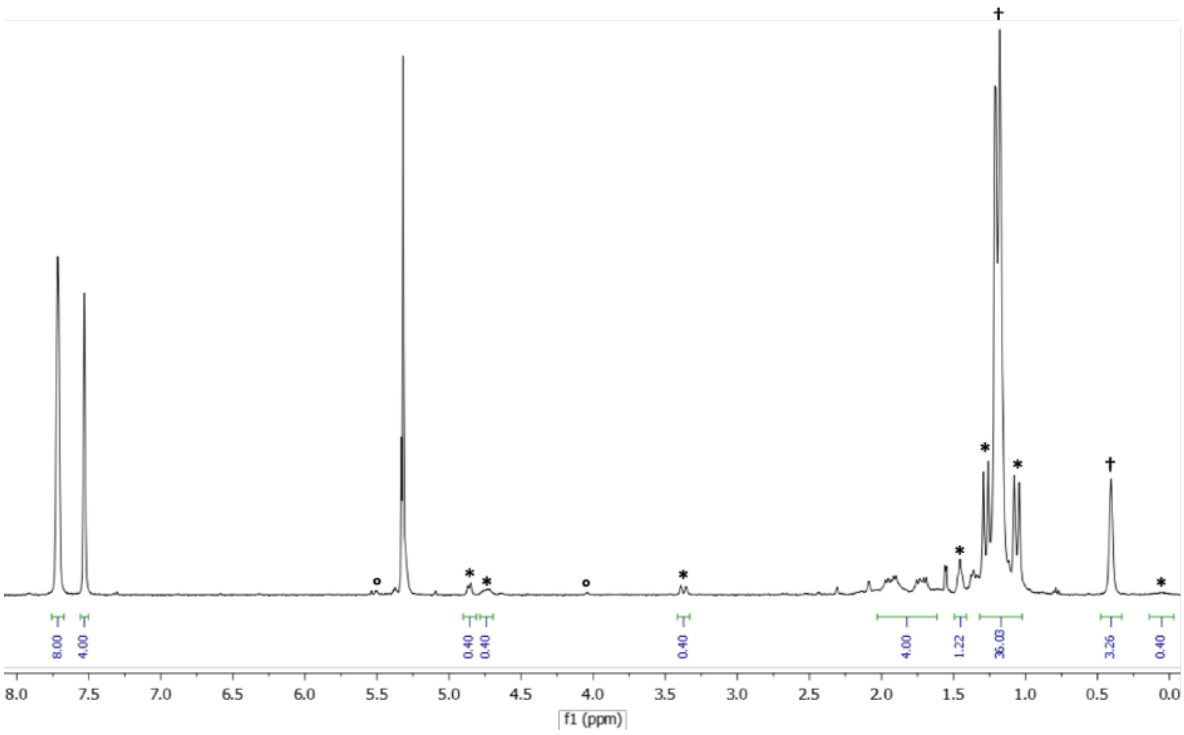
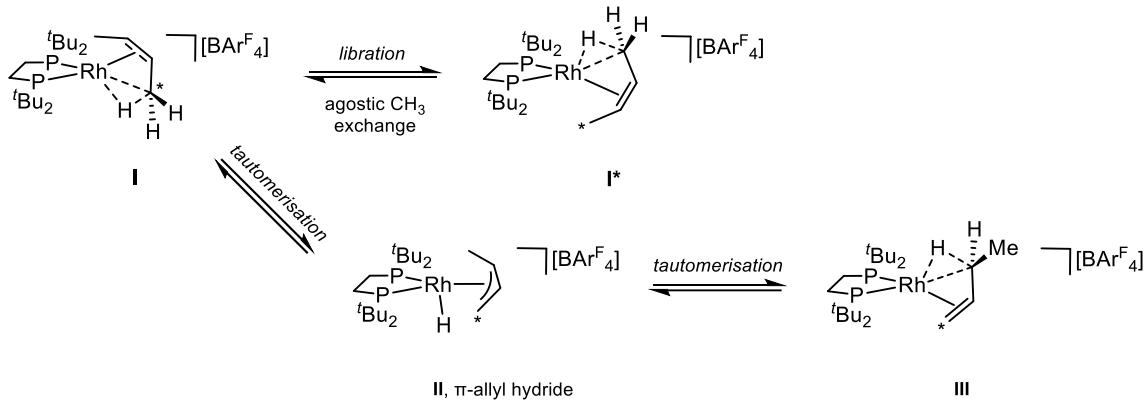


Figure 2.3.5: ^{1}H NMR spectrum of 27 (400 MHz, CD_2Cl_2, 183 K). * corresponds to [(dtbpe)Rh(1-butene)]$^+$ (~40%); † corresponds to [(dtbpe)Rh(*cis*-2-butene)]$^+$ (~60%). ° corresponds to unreacted 17 (<4%).

We reasoned that this fluxionality arose due to rapid libration/tautomerisation-isomerisation [a] (**Scheme 2.3.3**). Similar phenomena have been reported for both [(dcpe)Rh(propene)][BAr$^F_4$] (28) and [(dcpe)Rh(*cis*-2-butene)][BAr$^F_4$] (3), and studied through both experiment and computation.[1]



Scheme 2.3.3: Possible origins of fluxionality in [(dtbpe)Rh(*cis*-2-butene)]$^+$ in 27: a libration (**I→I***) involving exchange of agostic CH_3 groups, and a tautomerisation-isomerisation (**I→II→III**).

[a] See Introduction, Section 1.2.1, for a discussion on the π-allyl hydride mechanism for alkene isomerisation.

Only one alkene carbon for 27 was confidently resolved in the $^{13}C\{^{1}H\}$ solution-phase NMR spectrum at 183 K (δ 90.2, isomer identity unknown), and alkene carbons only appeared by $^{13}C\{^{1}H\}$ SSNMR spectroscopy upon cooling to 183 K (δ ~63, ~89, 90.5), indicating that this proposed libration/isomerisation fluxional process was also likely occurring in the solid-state.

Crystalline samples of [(dcpe)Rh(*cis*-2-butene)][BAr^F_4] (3) are known to dehydrogenate over 48 hours under an atmosphere of *n*-butenes to yield the 1,3-butadiene complex [(dcpe)Rh(η^4-C_4H_6)][BAr^F_4] (18).[1] This was *not* observed for [(dtbpe)Rh(*n*-butenes)][BAr^F_4] (27), wherefrom no evidence of a solid-state dehydrogenation product was obtained, *i.e.* the corresponding 1,3-butadiene complex (19), as we shall see. We will discuss the possible reasons for this in the following Section.

2.3.3 NMR Batch-Scale Solid-Gas Catalytic Isomerisation of 1-butene with Precursor SMOMs 1 and 17

Having established the *ex situ* solid-gas chemistry of precursor η^2,η^2-NBD SMOMs 1 and 17 with H_2 and 1-butene gas, we may now turn to solid-gas isomerisation catalysis under NMR batch conditions, using these same SMOMs as proofs-of-concept. Samples of finely powdered precursor SMOM (1 or 17, 2 mg, ~1.3-1.5 μmol) were introduced to high-pressure NMR tubes fitted with Young's taps (controlled atmosphere valves; V ~ 2 mL). The tubes were evacuated ($p < 10^{-2}$ mbar), repressurised with H_2 (1 bar), sealed, and left for 10 minutes at 298 K, generating the corresponding σ-NBA complexes *in situ* (*vide supra*), which were not isolated.

Following this, the tubes were evacuated a second time and repressurised with 1-butene (1 bar, ~90 μmol), after which gas-phase ^{1}H NMR spectroscopic analysis commenced immediately such that 10 spectra were obtained every 51 seconds over the course of 510 seconds (**Figure 2.3.6a**). 1-butene:2-butene ratios were measured by integration of signals at δ 8.08 (2-butene alkene CH) *versus* δ 7.50 + 7.60 (1-butene alkene CH_2). Gas-phase ^{1}H NMR spectroscopy was incapable of differentiating *cis*- and *trans*-2-butene isomers; this was accomplished instead by gas chromatography (GC; *vide infra*, Section 2.3.4 onwards).

After a set of 10 spectra had been obtained, the tubes were evacuated and recharged with 1-butene (1 bar) prior to gas-phase ^{1}H NMR studies recommenced. Sample re-hydrogenations, where necessary, were achieved by evacuating the atmosphere of *n*-butenes, re-exposing to H_2 for 10 minutes (1 bar), and finally evacuation and repressurisation with 1-butene (1 bar) before recommencing gas-phase ^{1}H NMR.

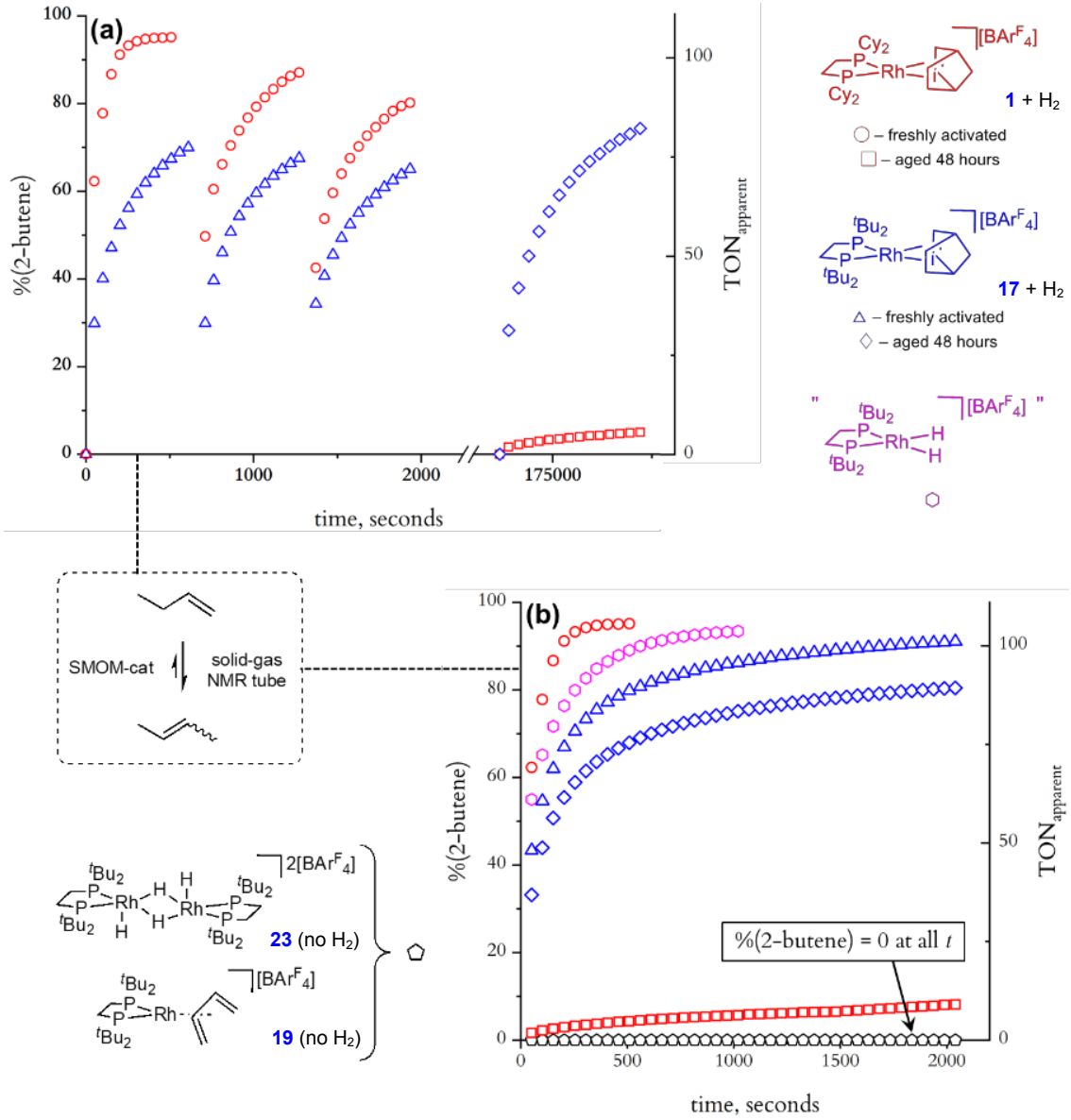


Figure 2.3.6: Conversion of initial 1-butene gas into 2-butenes by powdered and pre-hydrogenated SMOM samples (2 mg, ~1.5 mol%) in a high-pressure NMR tube. p = 1 bar, T = 298 K, V_{NMR} = ~2 mL (~90 μmol 1-butene). Percentages computed from gas-phase ^{1}H NMR integrals. 100% conversion approximates to an apparent TON of 110. (**a**) Experiment conducted with multiple charges of 1-butene, with a 48-hour ageing period following the third charge. (**b**) Experiment conducted with a single charge of 1-butene, compared with samples aged under an *n*-butenes atmosphere for 48 hours before the introduction of a second charge, as well as samples of 1,3-butadiene complex **19**, dimeric hydride **23**, and an *in situ* hydride (see text).

In order to probe degrees of deactivation by transfer dehydrogenation under a butene atmosphere, samples which had been aged for 48 hours under butene after hydrogenation and those which had not were compared as solid-gas isomerisation catalysts over a longer period, such that gas-phase ^{1}H NMR spectra were obtained every 51 seconds for a maximum of 2040 seconds (40 spectra, **Figure 2.3.6b**). These data were compared to that obtained for crystalline 1,3-butadiene complex **18** and dimeric hydride **23** (both possible deactivation products synthesised in Section 2.2.5), in addition to hydride generated *in situ*.[a]

Gram-for-gram, the catalytic systems derived from precursor SMOM **17** appeared initially lower in activity compared to SMOM **1**, which steadily deteriorated in activity across its three initial charges of 1-butene (**Figure 2.3.6a**). For SMOM **1**, apparent[94] turnover numbers (TON_{app}) obtained after 200 seconds dropped from 95 (86%) to 72 (65%) to 68 (62%), corresponding to average apparent turnover frequencies ($\langle TOF_{app} \rangle$) of ~1,710, ~1,300, and ~1,220 hr^{-1}. The decrease in activity for catalytic systems derived from precursor SMOM **1** was especially apparent after a 48-hour ageing period (TON_{app} ~ 2 (2%), $\langle TOF_{app} \rangle$ ~ 40 hr^{-1}) (**Figure 2.3.6a**, fourth charge).

Pre-catalyst SMOM **17**, while less active initially, more closely maintained its activity across the three initial charges (t = 200 seconds: TON_{app} ~ 52 (47%), 51 (46%), 50 (45%); $\langle TOF_{app} \rangle$ ~ 940, 920, 900 hr^{-1}) as well as the 48-hour ageing period (TON_{app} ~ 48 (44%), $\langle TOF_{app} \rangle$ ~860 hr^{-1}).

After repeating these experiments with a longer reaction time (**Figure 2.3.6b**), it was apparent that catalytic systems derived from SMOM **17** were only gradually deactivating across the 48-hour ageing period under a butene atmosphere (t = 200 seconds fresh/aged: TON_{app} ~ 70/63 (64/57%), $\langle TOF_{app} \rangle$ ~1,260/1,130 hr^{-1}), compared to the much more dramatic drop in activity observed for SMOM **1** across the same 48-hour period (t = 200 seconds fresh/aged: TON_{app} ~ 95/2 (86/2%), $\langle TOF_{app} \rangle$ ~1,710/40 hr^{-1}). The slight differences observed in TON_{app} between experiment sets may be due to weighing discrepancies due to the small (2 mg) masses involved as well as small differences in ambient temperature, gauge pressure, and sample grinding.

[a] *In situ* hydride **23** was obtained from solid-state hydrogenation (1 bar, 10 minutes) of powdered 1,3-butadiene complex **19**. Complete conversion to the hydride after this time was confirmed by distilling CD_2Cl_2 onto the sample and interrogating the resulting solution by solution-phase ^{1}H and ^{31}P{^{1}H} NMR spectroscopy.

Both the independently prepared crystalline 1,3-butadiene complex (**19**, without pre-hydrogenation) and the bridging hydride (**23**) proved completely inactive under NMR batch conditions (**Figure 2.3.6b**). The inactivity of 1,3-butadiene complex **19** aligns with previous observations of the dcpe analogue **18**, a deactivation product obtained by transfer dehydrogenation from the corresponding *cis*-2-butene complex **3** (Section 2.3.1).[1] The inactivity of these 1,3-butadiene complexes likely stems from the butadiene ligand (a bidentate ligand benefitting from the chelate effect[95,96]) being bound too strongly to the metal centre to be displaced by butene. 1,3-butadiene has been observed in the past to poison systems for alkene isomerisation both homogeneous[97] and heterogeneous.[98] Note that the precursor η^2,η^2-NBD SMOMs **1** and **17** were also inactive with respect to solid-gas 1-butene isomerisation without a pre-hydrogenation step.

In contrast to the recrystallised dimeric hydride **23**, however, *in situ*-generated hydride (see footnote, p. 86) proved *active*, its catalytic activity surpassing even that of precursor SMOM **17**. It seems likely, therefore, that *in situ*-generation of this hydride initially produced monomeric "[(dtbpe)Rh(H)$_2$][BAr$^F_4$]", in analogy to Siedle and colleagues,[99] where the activity of some metal centres had not yet been quenched by solid-state dimerisation. Why *in situ* hydride should be even more active than precursor SMOM **17** is unclear, and may be due to micro-cracking upon hydrogenation (*vide infra*), exposing more of the catalyst surface.

The differences between both the activities and the lifetimes of catalytic systems obtained from precursor SMOMs **1** and **17** under NMR batch conditions were substantial, illustrating the critical influence of the chelating *bis*-phosphine over catalytic lifetime and activity. In order to understand these differences, it is necessary to revisit the *ex situ* solid-gas reactivity of these complexes with H_2 and 1-butene, which we have already covered in Sections 2.3.1 and 2.3.2. The formation of *cyclo*-hexyl-bearing 1,3-butadiene complex **18** under NMR batch conditions from pre-catalyst SMOM **1** was confirmed by evacuation of the *n*-butenes atmosphere and dissolving post-catalytic material in CD_2Cl_2 at 183 K,[a] followed by $^{31}P\{^1H\}$ NMR spectroscopic studies and identification based on literature values (δ_P 81.0, $^1J_{PRh}$ = 170 Hz).[1]

[a] SMOM **1** and its corresponding 1,3-butadiene complex (**18**) are both known to be indefinitely stable in CD_2Cl_2 solution at 298 K, whereas a temperature of 183 K is required to prevent decomposition of the *cis*-2-butene complex (**3**). σ-NBA complex **2** is not known to be solution-stable (see Section 1.1.4).

ESI-MS studies conducted on dilute CH_2Cl_2 solutions of post-catalytic material revealed a mass peak at *m*/*z* 616.2830, comparing well to the calculated mass peak for complex **18** (*m*/*z* 616.2834) with the correct isotopic distribution. Post-catalytic material was therefore confirmed to be exclusively the 1,3-butadiene complex (**18**), in agreement with established chemistry.

Also aligning with chemistry previously established in Section 2.3.2, post-catalytic samples proceeding from pre-catalyst SMOM **17** did *not* contain any 1,3-butadiene complex (**19**). This was positively ascertained by ESI-MS and solution-phase $^{31}P\{^1H\}$ NMR spectroscopy. Complex **19**, normally stable in CD_2Cl_2 at 298 K, was *not* identified as per the NMR standard, independently synthesised in Section 2.2.5 (*m*/*z* 475.2124; δ_P 97.8, $^1J_{PRh}$ = 173 Hz). Instead, an intractable mixture of products was observed in addition to *n*-butenes complex **27**, converging on the C–Cl activated dimer **24** as described above after 24 hours at 183 K, and immediately at 298 K. This behaviour is the same as that of the *n*-butenes complex **27**, and is consistent with the absence of the 1,3-butadiene complex **19**. This phenomenon, of an intractable mixture of products not apparently containing any 1,3-butadiene complex **19**, was also observed for catalytic systems under continuous flow conditions and is discussed in greater detail in Section 2.4.6.

We have established that the discrepant activities and lifetimes of catalytic systems derived from precursor η^2,η^2-NBD SMOMs **1** and **17** under NMR batch conditions depended on the formation of a 1,3-butadiene complex, ultimately obtained from **1** but *not* from **17**, such that catalytic systems derived from the latter SMOM deactivated considerably more slowly than those derived from the former. We will now attempt to explain this discrepancy in deactivation route.

Both precursor SMOMs **1** and **17** are known to possess O_h-type structures (Section 2.2.4), with similar dimensions on the nanoscale (average O_h side lengths/B···B distances of ~13.3[12] and ~12.8 Å respectively). Cations $[(P_2)Rh(\eta^2,\eta^2\text{-NBD})]^+$ were oriented similarly with respect to the packing motif, such that the η^2,η^2-NBD moiety in both **1** and **17** was directed into a $[BAr^F_4]^-$ Ar^F-B-Ar^F 'cleft'.[12] We can therefore deduce that the gross microenvironments imposed on the cations were initially similar, and that the explanation for any discrepancy in deactivation route likely lies elsewhere.

SMOM 1, upon hydrogenation and exposure to 1-butene, retained this O_h motif but SMOM 17 did not, rearranging to give a BCPP motif (**Figure 2.3.4**) and thus translating the fragment {(dtbpe)Rh}$^+$ into a markedly different microenvironment. Additionally, more severe steric constraint is present about the active site of SMOM 17 compared to 1 (visualised by steric topography in **Figure 2.3.7**), since the latter's *cyclo*-hexyl groups largely orient away from the active site. This steric constraint may hinder the coordination of exogeneous butene to {(dtbpe)Rh}$^+$ and subsequent transfer dehydrogenation – requiring the interception of a π-allyl hydride intermediate by one molecule of butene followed by the elimination of butane – and therefore reduce the relative rate of deactivation by this mechanism (**Scheme 2.3.4**).

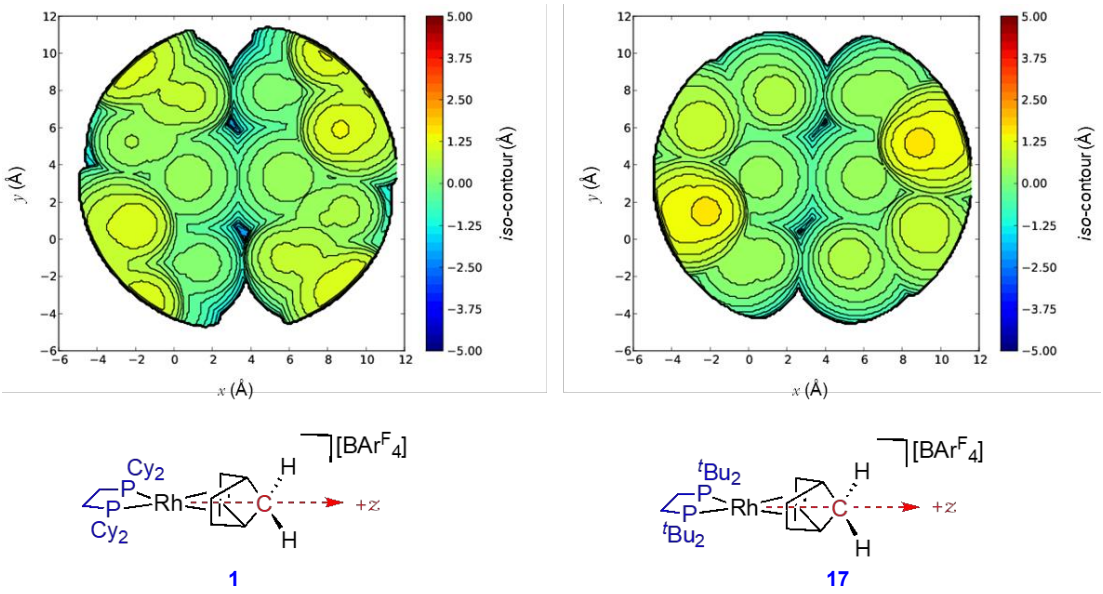
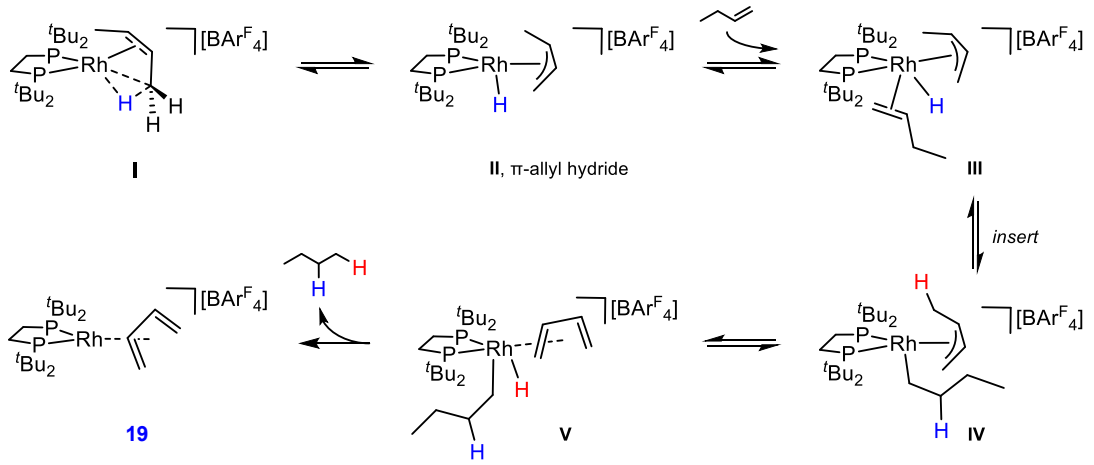


Figure 2.3.7: Steric topography maps of *bis*-phosphine ligands dcpe (**left**) and dtbpe (**right**) bound to {Rh(η^2,η^2-NBD)}$^+$ fragments, with positional information from *sc*-XRD data.[2,12] Only the ligands (in blue) have been considered in the definition of the catalytic pocket. Maps viewed down the *z*-axis, defined as the axis subtended between the Rh and NBD bridging C atoms. Orange indicates more steric hindrance; blue less. Constructed with SambVca 2.1.[100] Sphere radius 5.0 Å; atomic radius scaling factor 1.17.

Greater steric constraint may also be responsible for the reduced activity of catalytic systems derived from SMOM 17 compared to 1, reducing the accessibility of the active site to substrate molecules. Differing microenvironments may also have played a role in the discrepant longevity and activity of these systems, although the steric influence of the chelate was likely of overriding importance, given the discussion above.



Scheme 2.3.4: Proposed mechanism for transfer dehydrogenation of [(dtbpe)Rh(*n*-butenes)][BAr$^{F}_{4}$] (27) by hydride capture with exogeneous butene, ultimately yielding 1,3-butadiene complex 19, in analogy to established chemistry for SMOM 1. In this example, the initial state is given as [(dtbpe)Rh(*cis*-2-butene)]$^{+}$ (**I**), but could equally progress from [(dtbpe)Rh(1-butene)]$^{+}$ or [(dtbpe)Rh(*trans*-2-butene)]$^{+}$.

Having established the central role of the chelate R-group identity in influencing both catalytic lifetime and activity, interest moved to the ratio of *cis*- to *trans*-2-butene isomers in the headspace, how the identity of the chelating *bis*-phosphine might affect it, and how these systems might tolerate a scaled-up version of the NMR batch conditions: from a 2 mL system to a 75 mL system, in anticipation of a more industrially oriented, flow-based application.

2.3.4 NMR Batch-Scale Solid-Gas Isomerisation of n*-butene Isomers with SMOM 17 (Gas Chromatography)*

Non-thermodynamic ratios[a] of *n*-butenes in the early stages of the solid-gas catalytic isomerisation of 1-butene have been reported for catalytic systems derived from precursor SMOM 1 (see Section 2.1, **Figure 2.1.1**).[6] As this phenomenon of kinetic *cis*-selectivity is important in our discussion of catalytic systems derived from precursor SMOM 17, and re-emerges under continuous flow conditions, in this Section we will first discuss its origin in detail using model data from a previous report (SMOM 1),[1] and then turn to a catalytic system derived from SMOM 17.

[a] In the Introduction to this Chapter (**Figure 2.1.1**), we noted that a catalytic system derived from SMOM 1 gave rise to a 1-butene:*cis*:*trans*-2-butene ratio of 4:24:72 after 60 minutes (close to thermodynamic 2:21:77) and 4:48:48 after two minutes, the same conversion to 2-butenes but with an exaggerated *cis*-2-butene proportion (doubly over-expressed).

As we have seen, exposure of pre-hydrogenated SMOM 1 to 1-butene yielded exclusively [(dcpe)Rh(*cis*-2-butene)][BAr^F_4] (3) by *sc*-XRD as a resting state. Calculated in gas-phase, the [(dcpe)Rh(*cis*-2-butene)]$^+$ fragment was only 0.3 kcal mol^{-1} more stable than [(dcpe)Rh(*trans*-2-butene)]$^+$. In the solid-state, this energy span expanded to a significant 11.4 kcal mol^{-1}, demonstrating the critical importance of the microenvironment in discriminating between metal-bound butene isomers.[1]

Solid-state energy differences, however, do not tell the whole story. The $\Delta E_{C/T}$ of 11.4 kcal mol^{-1} between bound 2-butenes bound to {(dcpe)Rh}[BAr^F_4] explains why only coordinated *cis*-2-butene was observed as the *resting state* by *sc*-XRD, but fails to explain why *cis*-2-butene was initially dominant in the butenes *atmosphere*. The relative stability of [(dcpe)Rh(*cis*-2-butene)]$^+$ might imply that coordinated *cis*-2-butene requires a greater energy input than coordinated *trans*-2-butene to be displaced, and should therefore be kinetically *disadvantaged* in the butenes atmosphere. In conjunction with literature values for the energy difference between 1-butene and *cis*-2-butene (~1.3 kcal mol^{-1}) and *cis*- and *trans*-2-butene (~0.8 kcal mol^{-1}),[3,101] kinetic *cis*-selectivity can be explained with the assistance of an energy level diagram as in **Figure 2.3.8**. It should also be noted that these energy differences provided for the free *n*-butenes refer only to the gas-phase at 1.0 atm and 298.16 K – they may well have been different inside the SMOM lattice.

The loss of *trans*-2-butene from [(dcpe)Rh(*trans*-2-butene)][BAr^F_4] (**IV**) is shown to be more favourable than loss of *cis*-2-butene from the observed resting state [(dcpe)Rh(*cis*-2-butene)][BAr^F_4] (**III**) such that $\Delta E^{\ddagger}_{trans} < \Delta E^{\ddagger}_{cis}$ as indicated. However, the pathway of isomerisation proceeding from resting state **III** *followed by* loss of *trans*-2-butene ($\Delta E^{\ddagger}_{trans} + \Delta E_{C/T}$) represents a higher energy span than simple loss of *cis*-2-butene ($\Delta E^{\ddagger}_{cis}$) from resting state **III**, such that $\left[\Delta E^{\ddagger}_{trans} + \Delta E_{C/T}\right] > \Delta E^{\ddagger}_{cis}$. The loss of *cis*-2-butene from the lattice was therefore kinetically advantaged, and this isomer dominated in the early stages of catalysis.

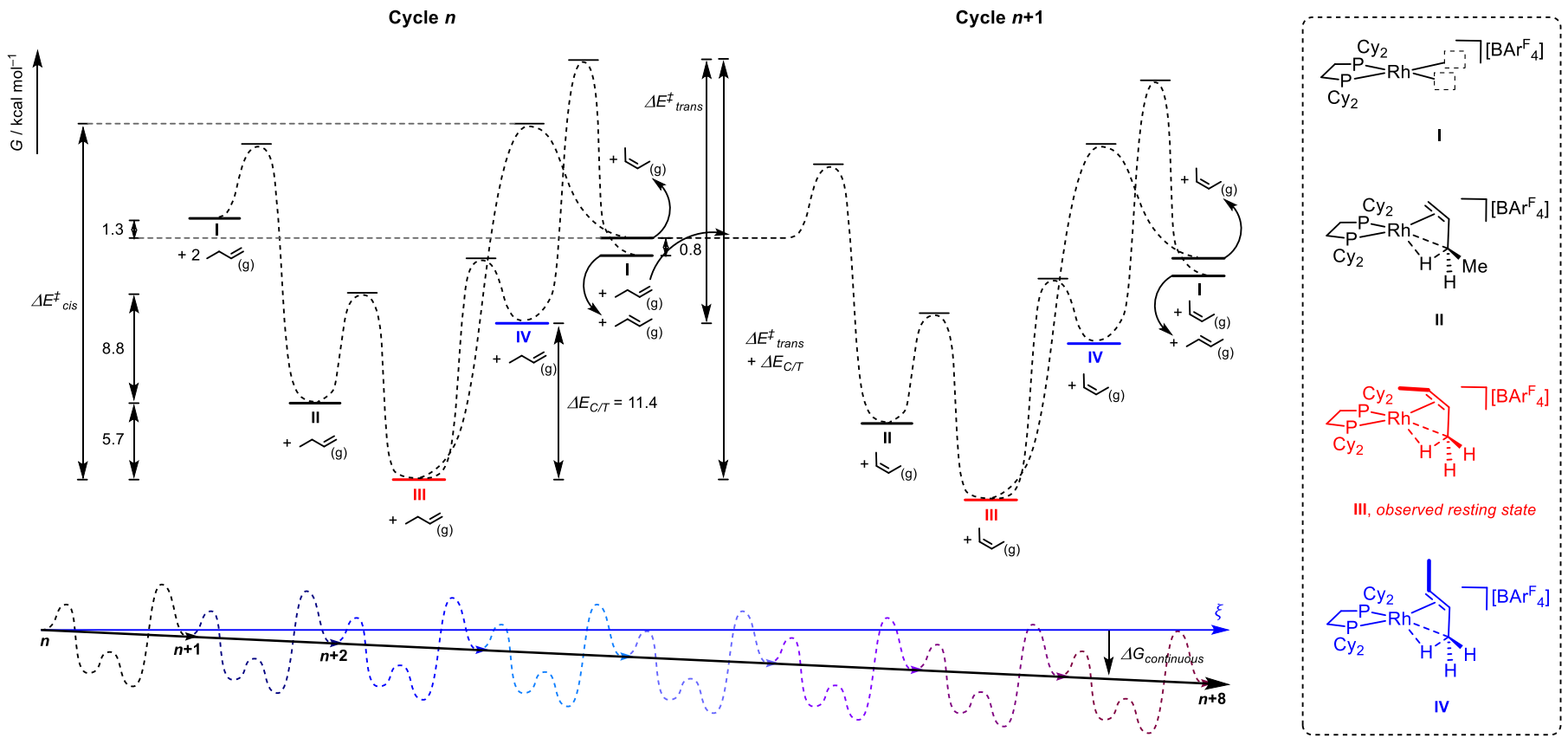


Figure 2.3.8: Energy level diagram representing the isomerisation of 1-butene bound to {(dcpe)Rh}[BAr^F_4] (**I**) and the subsequent release of 2-butene isomers. Unless specified, barriers are of unknown height and assumed to be accessible; known barriers are marked according to data retrieved from the reference.[1] Two cycles of the process are shown to demonstrate the continuous free energy output, $\Delta G_{continuous}$,[4] equal to ~1.3 kcal mol^{-1} multiplied by the number of cycles. The product of the first cycle shown (*n*) is assumed to be *cis*-2-butene, in common with the kinetic *cis*-selectivity observed under both batch and flow conditions.

We were interested to see whether the change in ligand from P_2 = dcpe to the more sterically demanding dtbpe would affect this kinetic *cis*-selectivity.[a] Samples of finely powdered precursor SMOM 17 (2 mg) were introduced to high-pressure NMR tubes fitted with Young's taps (controlled atmosphere valves). The contents of the tubes were hydrogenated (1 bar, 10 minutes) before exposure to a pure *n*-butene isomer atmosphere (1 bar: 1-butene, *cis*-2-butene, *trans*-2-butene) for a specified time *t* (2 minutes and 24 hours, constructing non-equilibrium and equilibrium conditions respectively). After exposure time *t* had elapsed, the *n*-butenes atmosphere was withdrawn into a heavy-walled ampoule under static vacuum (V ~ 50 mL) and diluted ~100-fold with argon[6] such that the sample could be analysed by gas chromatography (GC) in order to probe *cis*/*trans* selectivity (**Figure 2.3.9**).

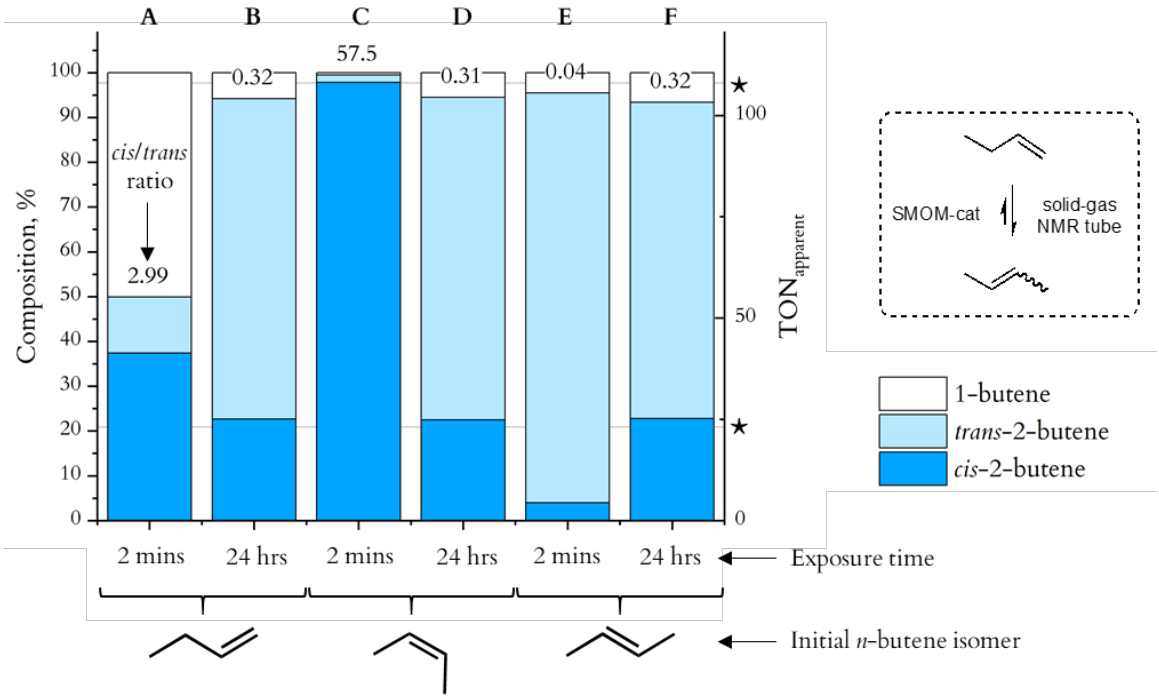


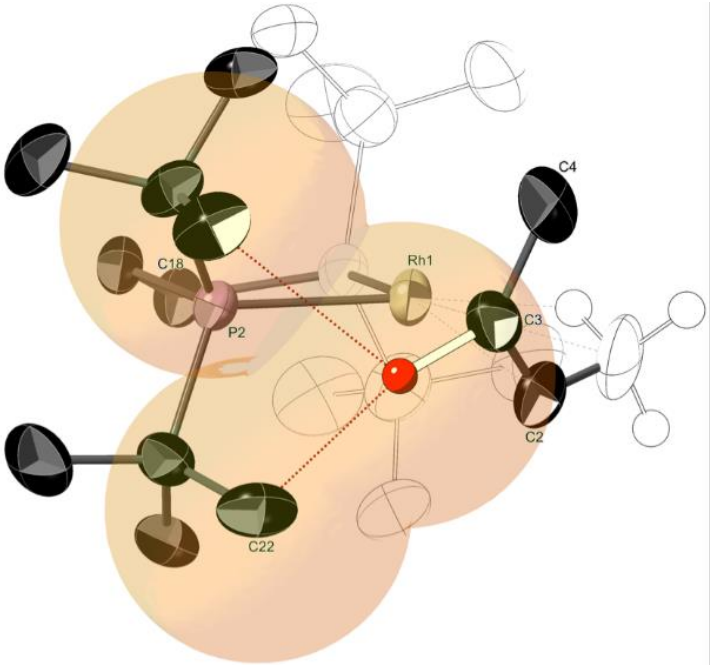
Figure 2.3.9: Conversion of the starting pure *n*-butene isomer (1-butene, *cis*-2-butene, *trans*-2-butene) to a mixture of *n*-butenes over time (2 minutes, 24 hours) by powdered and pre-hydrogenated single crystalline samples of SMOM 17 (2 mg, ~1.5 mol%) within a high-pressure NMR tube. Ratio of *n*-butenes detailed as calculated from GC data. Reference lines (indicated by asterisks) are provided for the expected thermodynamic proportions of each isomer (~2:77:21, 1-butene:*trans*:*cis*-2-butene). p = 1 bar, T = 298 K, V_{NMR} = 2 mL (~90 μmol *n*-butene).

[a] See Introduction (Section 1.3.1), for a discussion on kinetic selectivity under continuous flow conditions.

Gas-phase ^{1}H NMR spectroscopy is incapable of distinguishing between 2-butene isomers, but was used in conjunction with GC as in Section 2.3.3 to confirm the ratio of 1- to 2-butene. On this scale, t = 24 hours (**B**, **D**, **F**) proved to be sufficient time for the sample of pre-hydrogenated SMOM **17** to achieve an approximately thermodynamic distribution of *n*-butenes regardless of the starting butene. Starting from pure 1-butene, a reaction time of only two minutes (**A**) resulted in incomplete conversion to 2-butenes (49.9%) with non-equilibrium proportions of *cis*- (37.4%) and *trans*-2-butene (12.5%), indicating strong kinetic *cis*-selectivity (*cis*/*trans* = 2.99, with *cis* ~11 times overexpressed compared to equilibrium). This kinetic *cis*-selectivity was stronger still compared to precursor SMOM **1** under the same conditions, achieving a ratio of ~1.0 after two minutes (~4 times overexpressed).[6]

Kinetic dominance of the *cis* isomer in the gas-phase was reflected when pure *cis*- (**C**, **D**) and *trans*-2-butene (**E**, **F**) were used as the initial *n*-butene isomer. The rate of conversion from either 2-butene towards thermodynamic equilibrium was slow compared to 1-butene, although conversion from pure *trans*-2-butene was more rapid: 4.0% 1-butene and 4.5% *cis*-2-butene were generated from pure *trans*-2-butene after two minutes (**E**), where from *cis*-2-butene only 0.5% 1-butene and 1.7% *trans*-2-butene were generated in the same time (**C**). A parallel observation was made by Zaera and colleagues, who noted that *trans*-2-butene isomerised twice as rapidly as *cis*-2-butene on the surface of tetrahedral Pt(111) nanoparticles.[102]

It is possible to explain this kinetic *cis*-selectivity through close inspection of the crystal structure of the active catalyst (resting state), *i.e.* the *n*-butenes complex (**27**). In **Figure 2.3.10**, a hypothetical *trans* carbon atom has been placed onto the [(dtbpe)Rh(*cis*-2-butene)]$^+$ fragment and, as a consequence of the geometry imposed by the γ-agostic interaction, this hypothetical *trans* carbon would be sterically hindered by the nearby ^{t}Bu CH_3 groups, with close C···C approaches of ~2.3 and ~2.7 Å (the van der Waals radius of a rapidly rotating methyl group is ~2.0 Å[103]). Therefore, we argue that the *cis*-2-butene complex was significantly more stable than the *trans*-2-butene complex, as confirmed for P_2 = dcpe computationally (*vide supra*).[1] Consequently, *trans*-2-butene was *not* observed bound to {(dtbpe)Rh}[BAr^F_4] in the solid-state structure (**Figure 2.3.4**), conforming with [(dcpe)Rh(*cis*-2-butene)][BAr^F_4] (**3**; Section 2.3.1).



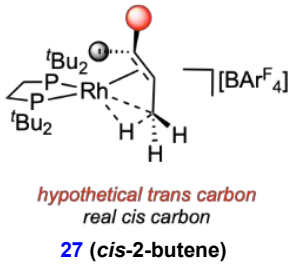


Figure 2.3.10: Cationic fragment [(dtbpe)Rh(*cis*-2-butene)]$^+$ in [(dtbpe)Rh(*n*-butenes)][BAr$^F_4$] (27), previously provided in **Figure 2.3.4**. 50% displacement ellipsoids. Anions and H atoms omitted for clarity excepting calculated H atoms associated with agostic positions. A hypothetical *trans* carbon atom has been highlighted in red, placed according to the C3–C4 bond length (*ca.* 1.47 Å) and C2–C3–C4 angle (*ca.* 123°) so as to be coplanar with C2–C3–C4. The van der Waals surfaces for C18, C22, and the hypothetical position have been provided (probe radius 1.4 Å), and their close approaches (*ca.* 2.3 and 2.7 Å) outlined in red.

We infer that the 1-butene-containing fragment [(dtbpe)Rh(1-butene)]$^+$ was also more stable than [(dtbpe)Rh(*trans*-2-butene)]$^+$ inside the [BAr$^F_4$]$^-$ lattice and only slightly less-so than [(dtbpe)Rh(*cis*-2-butene)]$^+$,[a] hence the solid-state proportions of ~40% coordinated 1-butene and ~60% *cis*-2-butene, with *trans*-2-butene absent (confirmed by solution-phase ^{1}H NMR spectroscopy, *vide supra*). The appearance of 1-butene in the solid-state suggested that it was energetically favourable, despite the lower degree of substitution on the alkene, to orient some of the hydrocarbon fragment *away* from the active site to prevent steric destabilisation. The greater kinetic dominance of *cis*-2-butene in catalytic systems derived from precursor SMOM 17 compared to SMOM 1 can again be explained with the aid of an energy level diagram (**Figure 2.3.11**, modified from **Figure 2.3.8**).

[a] Assuming coordinated *n*-butene isomers freely interconvert.

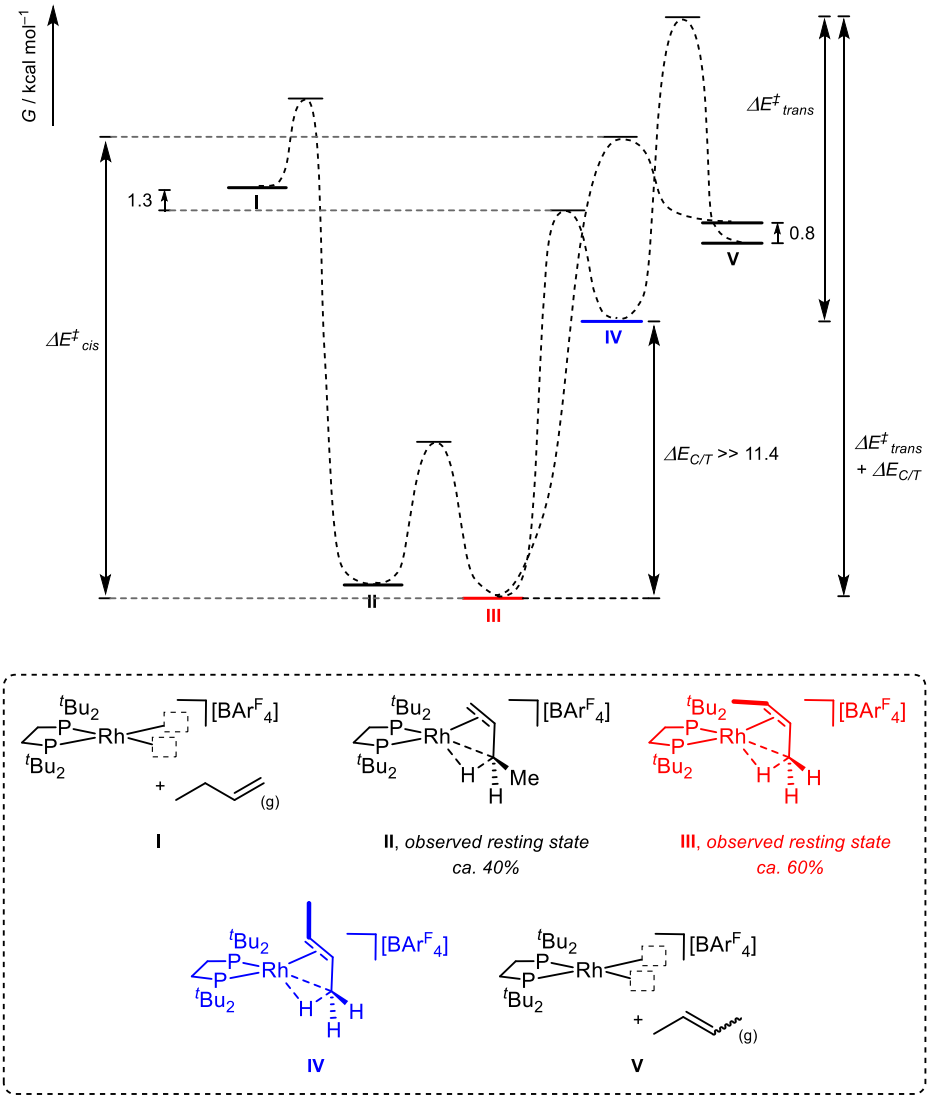


Figure 2.3.11: Energy level diagram representing the isomerisation of 1-butene bound to {(dtbpe)Rh}[BAr^F_4] and the subsequent release of 2-butene. All barriers are of unknown height and assumed to be accessible. Single catalytic cycle modified from **Figure 2.3.8**.

If we note the increased steric hindrance around the active site (1→17), as argued above, we can assume that [(P_2)Rh(*trans*-2-butene)]$^+$ (**III**) will be destabilised relative to [(P_2)Rh(*cis*-2-butene)]$^+$ (**II**), *i.e.* $\Delta E_{C/T}$ increases *cf.* **Figure 2.3.8**. Noting the presence of [(dtbpe)Rh(1-butene)][BAr^F_4] (**I**, ~40%) in the solid-state, it follows that this fragment is similar in energy to isomeric **II** in this environment. With the increase in $\Delta E_{C/T}$ relative to **Figure 2.3.8**, the difference between $[\Delta E^{\ddagger}_{trans} + \Delta E_{C/T}]$ and $\Delta E^{\ddagger}_{cis}$ also increases relative to **Figure 2.3.8**, further favouring *cis*-2-butene under kinetic conditions. This assumes the barriers to loss of alkene remain similar – likely, as these are dominated by the secondary and tertiary microenvironments.

The increased *cis*-selectivity of catalytic systems derived from precursor SMOM 17 relative to 1 was also demonstrated under continuous flow conditions (Section 2.4.2). In contrast to NMR batch conditions, continuous flow conditions continuously refresh the 1-butene atmosphere, so that a high proportion of substrate 1-butene is always available to the catalyst. To simulate this, NMR batch conditions were scaled up, from an NMR tube (V ~ 2 mL) to a bespoke glass-walled reactor vessel (V ~ 75 mL), in order to provide a more considerable excess of 1-butene substrate.

2.3.5 75 mL Reactor-Scale Solid-Gas Catalytic Isomerisation of 1-butene by SMOM 17

On the 75 mL reactor-scale, GC was again used to probe the conversion and selectivity of 1-butene to 2-butenes by a pre-hydrogenated single crystal of precursor η^2,η^2-NBD SMOM 17 (~1 mg) (**Figure 2.3.12**). The pre-hydrogenated crystal was exposed to an atmosphere of 1-butene (1.4 bar). After this time, an aliquot of gas was removed into a high-pressure NMR tube to be analysed by gas-phase ^{1}H NMR spectroscopy and GC as above, before the vessel atmosphere of 1-butene was recharged. In total, the pre-hydrogenated single crystal was exposed to four charges of 1-butene gas over 4 × 24 hours.

Upon scaling up the process, the massive increase in available 1-butene (~1.5 → ~0.02 mol% pre-catalyst) prevented the achievement of thermodynamic equilibrium even after 24 hours (first charge). A clear bias towards *cis*-2-butene was observed, congruent with the kinetic *cis*-selectivity observed under NMR batch conditions (*vide supra*). With the significant decrease in catalytic activity on subsequent charges even higher *cis*/*trans* ratios were recorded, as this decrease in activity disfavoured the subsequent isomerisation step of kinetically favoured *cis*-2-butene to the *trans* isomer. Over four charges and 96 hours, this system achieved a total TON_{app} of ~10,000, ~6,800 of which was achieved on the first charge (the maximum possible on one charge would be ~10,000). The initially well-defined crystal appeared to have lost its definition after 96 hours, and was beginning to seep into the glass frit onto which it had been mounted.

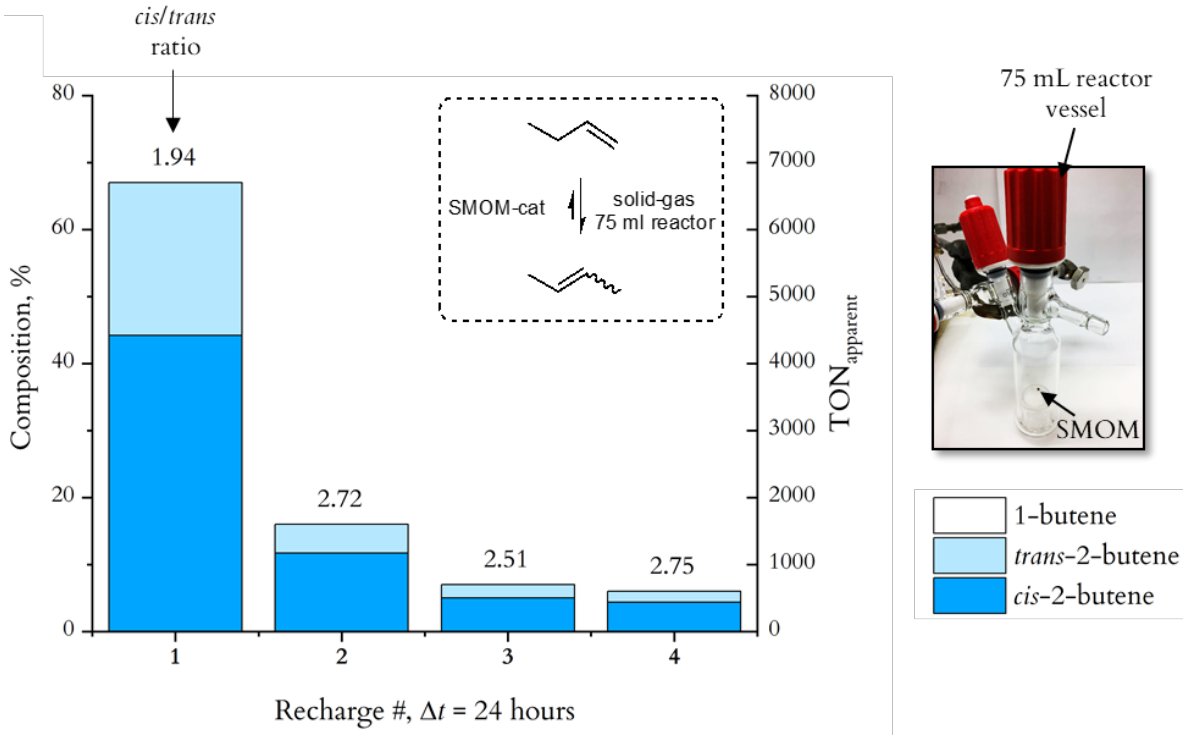


Figure 2.3.12: Conversion of 1-butene to 2-butenes after 24-hour periods by a pre-hydrogenated single crystal of SMOM 17 (~1 mg, ~0.02 mol%) within a bespoke glass-walled reactor vessel. Proportions of each 2-butene as calculated from GC analysis. p = 1.4 bar, T = 298 K, V ~ 75 mL (~4,250 μmol 1-butene). (**inset**) A photograph of the bespoke glass-walled reactor vessel.

Many of the phenomena described in this Section – *viz*. kinetic *cis*-selectivity as well as loss of crystal definition – are also noted under continuous flow conditions, and will be explored in Section 2.4. First, however, we will briefly cover the consequences of further ligand variation under NMR batch conditions. Such variation will be handled in greater detail under continuous flow conditions.

2.3.6 Ligand and Metal Variation Under NMR Batch Conditions

Up to this point, we have demonstrated the critical importance of the chelate in solid-gas catalysis by comparing two examples of pre-catalysts, η^2,η^2-NBD SMOMs 1 and 17. Here, we briefly turn our attention to wider exploration of the chemical space, by further variation of the chelating *bis*-phosphine (R-group identity), and the effects of such variations on catalyst activity and lifetime.

The results obtained for precursor η^2,η^2-NBD SMOMs [(P_2)Rh(η^2,η^2-NBD)][$BAr^F{}_4$] where P_2 = dippe = $^iPr_2P(CH_2)_2P^iPr_2$ (7) and P_2 = dcyppe = $Cyp_2P(CH_2)_2PCyp_2$ (8) are shown in **Figure 2.3.13**. To avoid a lengthy discussion of ligand variation under NMR batch conditions when the more industrially-relevant flow conditions are yet to be explored, this section will focus only on these two examples.

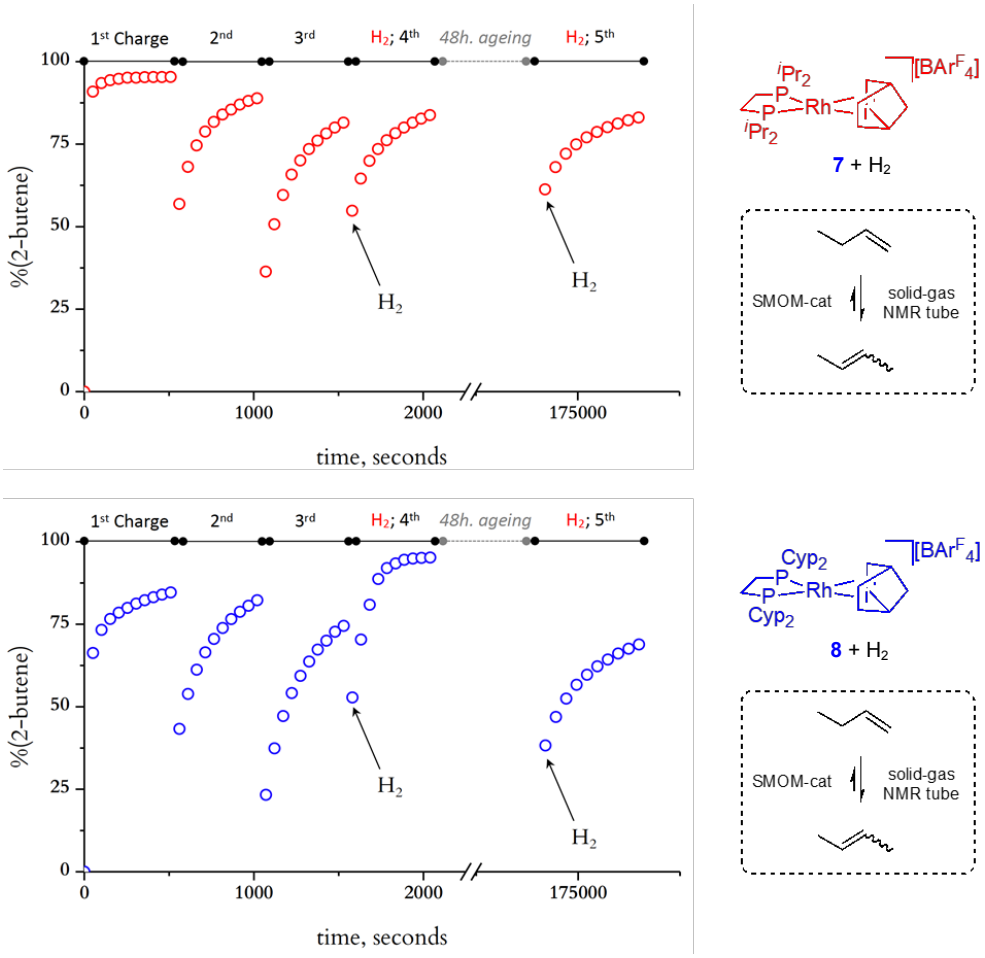
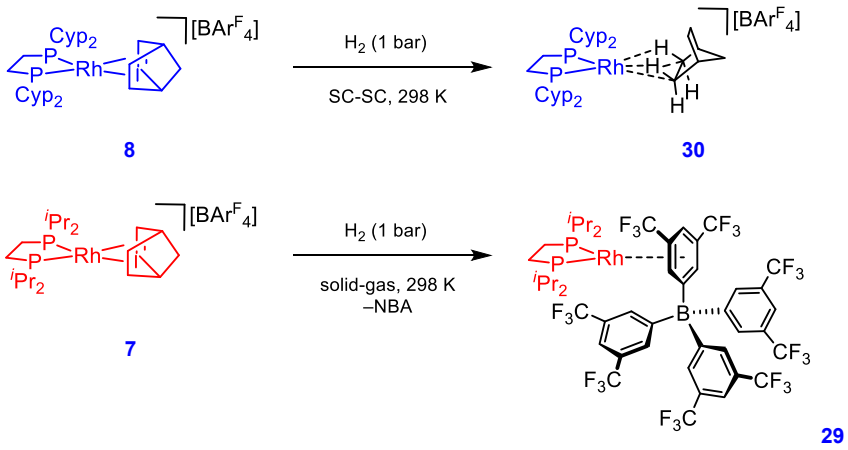


Figure 2.3.13: Conversion of initial pure 1-butene gas into 2-butenes by powdered and pre-hydrogenated SMOM samples (7 and 8, 2 mg) in a high-pressure NMR tube. p = 1 bar, T = 298 K, V_{NMR} ~ 2 mL (~900 μmol 1-butene). Percentages computed from gas-phase ^{1}H NMR integrals. 100% conversion to 2-butenes approximates to a TON_{app} of 110.

NMR-scale batch conditions were used for SMOMs 7 and 8 as in Section 2.3.3. Both SMOMs and their solid-state structures have been previously reported.[12,46] The unusual BCPP structure type [(dippe)Rh(η^2,η^2-NBD)][$BAr^F{}_4$] (8) was discussed in Section 2.2.4; upon hydrogenation, crystals of SMOM 8 almost immediately yielded the Ar^F-coordinated zwitterion (29, **Scheme 2.3.5**).[12]

Recall that SMOMs **1**, **8** and **17** all possessed O_h-type structures, and the respective cationic fragments oriented similarly in the solid-state, into $[BAr^F{}_4]^-$ Ar^F-B-Ar^F 'clefts' (recall **Figure 2.2.2**). The σ-NBA complex **30** generated from [(dcyppe)Rh(η^2,η^2-NBD)][$BAr^F{}_4$] (**8**) was reportedly relatively stable, with formation of the corresponding Ar^F-coordinated zwitterion occurring over 100 hours at 298 K in the solid-state, or rapidly under H_2 in a C_6HF_5 slurry.[46]



Scheme 2.3.5: Solid-gas hydrogenation products of SMOMs **7** and **8**, yielding a single-crystalline σ-NBA complex and an amorphous Ar^F-coordinated zwitterionic complex respectively, as previously reported in the reference.[12]

The solid-state stability of *cyclo*-pentyl-bearing σ-NBA complex **30** is intermediate between those derived from SMOMs **7** (<15 minutes at 298 K) and **1** (months),[12] correlating with the steric bulk of the R-group on the chelate. We can therefore assume, under NMR batch conditions, that the pre-hydrogenation step for SMOM **7** largely generated the Ar^F-coordinated zwitterion (**30**) *in situ*, while for SMOM **8**, the corresponding σ-NBA complex **29** was generated (**Scheme 2.3.5**). After sample hydrogenation (10 minutes, 1.0 bar) and exposure to 1-butene (1.0 bar), activity was observed to decline in both systems across three initial charges of 1-butene, and (in the case of **8** only) was recoverable, both after three charges and 48 hours of ageing under *n*-butenes, with the action of H_2. Given the unusual BCPP-type structure of SMOM **7**, we note that the O_h packing motif was not necessarily a prerequisite for catalytic activity.

With the subtle stereoelectronic modification in R-group from R = *cyclo*-hexyl to *cyclo*-pentyl (**1** → **8**), initial activity under NMR batch conditions was not observed to change significantly, initially surpassing 65% after 51 seconds (TON_{app} ~ 72, TOF_{app} ~ 5,000 hr^{-1}) – *cf.* SMOM **1**, surpassing 62% in the same time. *Cyclo*-hexyl and *cyclo*-pentyl have similar stereoelectronic profiles, hence the similar TOF_{app} – a reality reflected in the similar Tolman parameters for PCy_3 and $PCyp_3$.[104] Solution-phase NMR analysis of post-catalytic material (pre-catalyst SMOM **8**) revealed the presence of a 1,3-butadiene complex (**31**) after 48 hours' ageing under a butene atmosphere. ^{1}H NMR signals corresponding to the 1,3-butadiene moiety (δ 2.86, 4.55, 5.44; 1:1:1 integral ratio) compared remarkably well to those of the dcpe analogue (**18**: δ 2.83, 4.51, 5.47; 1:1:1), as did the ^{103}Rh-^{31}P coupling constant ($^1J_{PRh}$ = 169 Hz in both cases).

It is unclear why SMOM **7** displayed such superlative initial activity, surpassing 90% conversion after just 51 seconds (TON_{app} ~ 100, TOF_{app} ~ 7,000 hr^{-1}). Post-catalytic material, when dissolved in CD_2Cl_2 at 183 K revealed only the Ar^F-coordinated zwitterion **29** (δ_P 100.6 ($^1J_{PRh}$ = 202 Hz); δ_F −58.8, −61.0, 1:3 integral ratio), comparing well to the previous report.[12] We have discussed above how the Ar^F-coordinated zwitterion **29** was probably formed in the solid-state after 10 minutes' exposure to H_2. Independent solution-phase synthesis[12] and deployment of this zwitterion under these NMR batch conditions resulted in no measurable conversion. Further experiments are needed to conclusively identify both the active catalyst and the deactivation product (*e.g.* solid-state NMR spectroscopy).

Having shown that numerous SMOMs of the general formula $[(P_2)Rh(\eta^2,\eta^2\text{-NBD})][BAr^F{}_4]$ constituted promising pre-catalysts for the solid-gas isomerisation of 1-butene under batch conditions, attention will now shift to the industrially appealing setting of a solid-gas flow reactor, the first time such systems have been tested under heterogeneous continuous flow conditions.

2.4 Solid-Gas Catalytic Isomerisation of 1-butene with Precursor NBD SMOMs (Continuous Flow Conditions)

Two candidates, precursor η^2,η^2-NBD SMOMs **1** and **17**, were first tested under solid-gas continuous flow conditions as proofs-of-concept, to demonstrate how in-flow catalyst performance may be tuned by simple R-group modification on the chelate. The results corresponding to other R- and tether-varied precursor SMOMs under the same conditions are then presented, in order to explore chemical space and the effects of such changes on activity and selectivity under continuous flow conditions. We have already discussed how flow techniques can be employed to achieve non-thermodynamic selectivities,[a] and were eager to see whether this phenomenon – positively identified above under batch conditions (Sections 2.3.4 and 2.3.5) and in a previous report with pre-catalyst SMOM **1**[6] – could be translated to continuous flow conditions, such that a non-thermodynamic distribution of *n*-butenes might be captured in the outflow.

2.4.1 Anatomy of Solid-Gas Flow Reactor and Samples

Samples intended for testing under flow conditions were prepared by finely powdering the appropriate catalyst or pre-catalyst with the action of a metal spatula inside a glass vial, and filtering the resulting powder through 150 μm Endecott sieves before further grinding for no more than 60 seconds. The final, extremely fine powder was then introduced to a stainless-steel column, pre-loaded with a glass wool plug (~100 mg). Each load of powder (2-3 mg) was then followed by a further glass wool plug (~30 mg).[2] This was repeated 5-7 times until a specified total pre-catalyst weight was achieved, intending to prevent the catalyst dislodging from the column and to improve dispersion, the degree of which will be shown to be crucial in determining activity in flow. In order to maintain a temperature of 298 K, ethylene glycol was passed through the space between the inner and outer steel jackets of the column, and kept at 298 K by a temperature-controlled circulation pump. Sealed at each end using two-way gas-tight Swagelock valves, the pre-loaded column was then fitted to a bespoke continuous gas-flow reactor (**Figure 2.4.1**).

[a] See Introduction, Section 1.3.1.

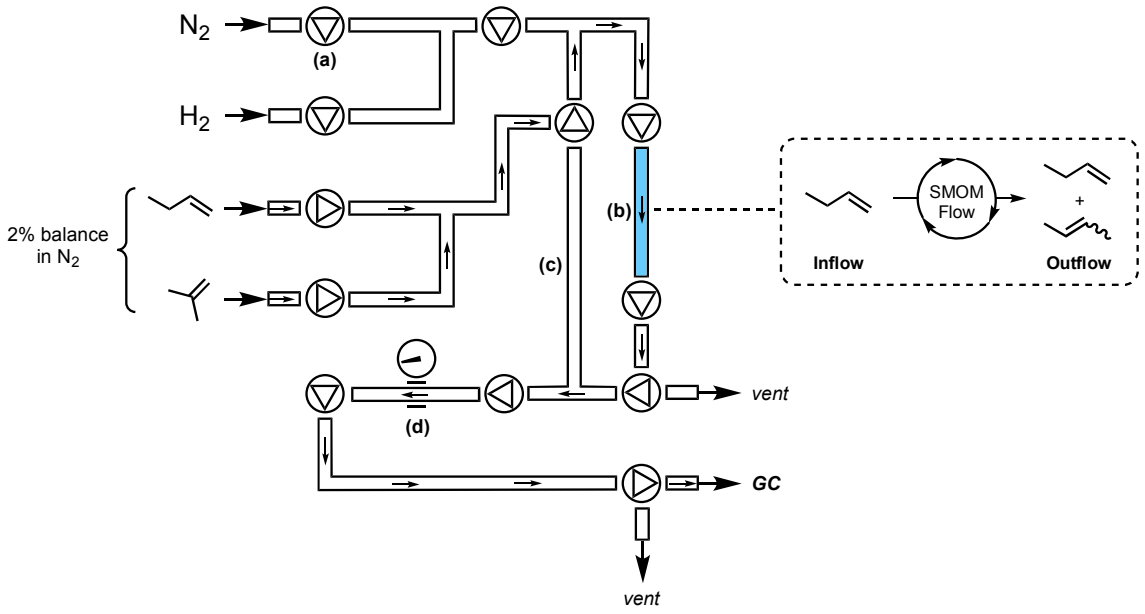


Figure 2.4.1: Simplified schematic of the flow reactor setup, shown operating under gas-flow conditions: a butenes (1-butene + *iso*-butene) gas mixture passing *via* a pre-loaded column, over active catalyst, to be analysed *via* gas chromatography. (**a**) A gas-tight Swagelock valve. (**b**) Stainless steel column pre-loaded with catalyst/pre-catalyst dispersed on glass wool, fitted at each end with gas-tight Swagelock valves. (**c**) Column bypass. (**d**) Regulated loop, intended to establish a pressure of H_2 during hydrogenation of pre-catalyst.

Four different gas feeds could be passed through this column, controlled by mass-flow meters: N_2, H_2, 1-butene (2% balance in N_2) and *iso*-butene (2% balance in N_2), all of which were first passed through silica drying columns to prevent water entering the system. N_2 (typically set to 50 mL min^{-1}), was used to purge the system before and after hydrogenation. Hydrogenations in-flow were achieved by pressurising the system with H_2 to 1.0 bar by passing a flow (typically set to 100 mL min^{-1}) *via* a loop fitted with a regulator. The butenes gas mixture utilised was typically 6.4 mL min^{-1} 1-butene combined with 1.2 mL min^{-1} *iso*-butene (both 2% balance in N_2).

The presence of *iso*-butene in these experiments was intended to simulate its presence in the C_4 feed of a cracker,[105] such that the results of these experiments would be more industrially relevant. The outflow, having passed *via* the pre-loaded column, was then passed *via* a gas chromatograph before venting. Gas aliquots were taken every 15 minutes for GC analysis, wherefrom the ratio of 1-butene:*cis*-2-butene:*trans*-2-butene at different time points was determined.

At the conclusion of a flow experiment, the columns could be sealed against the air using the attached Swagelocks, then removed and unpacked inside a glove-box under an argon atmosphere, permitting post-catalytic material to be interrogated in detail (*i.e.* solid-state and solution-phase NMR spectroscopy, scanning electron microscopy, powder X-ray diffraction, and further catalysis under batch conditions). Catalyst/pre-catalyst masses were carefully selected such that initial conversion to 2-butenes registered in the range ~40-90%. If initial conversion surpassed ~90%, an inaccurate view of the catalyst's decay profile was risked, due to the presence of a 'thermodynamic ceiling' at ~97% conversion. For more detail on valid assessments of catalyst stability under flow conditions, see Scott's excellent editorial on the matter.[106]

2.4.2 Solid-Gas Catalytic Isomerisation of 1-butene Under Flow Conditions by SMOMs

The results of these experiments are presented on the proceeding pages. **Figure 2.4.2** and **Figure 2.4.3** summarise the results pertaining to R-group and tether-varied η^2,η^2-NBD SMOMs (1, 4-17) acting as pre-catalysts. All hydrogenations were accomplished by pressurising the system to 1.0 bar of H_2 for 10 minutes, after the system had been purged with H_2 at a flow rate of 100 mL min^{-1} for five minutes. Metrics of SMOMs operating under flow conditions (**Figure 2.4.2** and **Figure 2.4.3**) are summarised in **Table 2.4.1**.

Figure 2.4.4 summarises the results of the various control experiments making use of the two SMOMs used in the preceding section as proofs-of-concept (1 and 17): the importance of particle size (*i.e.* the effectiveness of sieving, pre-catalyst SMOM 1), an *iso*-butene co-feed (17); different masses of pre-catalyst SMOM (17); a large number (*i.e.* six) of hydrogenation 'reactivation' events over a long experiment (*i.e.* >50 hours, 1); and temperature control (*i.e.* 298, 293, 288, 283[a] K, 17). Reproducibility was also demonstrated: three operators conducted flow experiments on three separate batches of catalyst (1). The results of these control experiments are discussed in Section 2.4.4.

[a] Below this temperature, the condensation of butenes was expected to become problematic, hence no temperatures lower than this were explored.

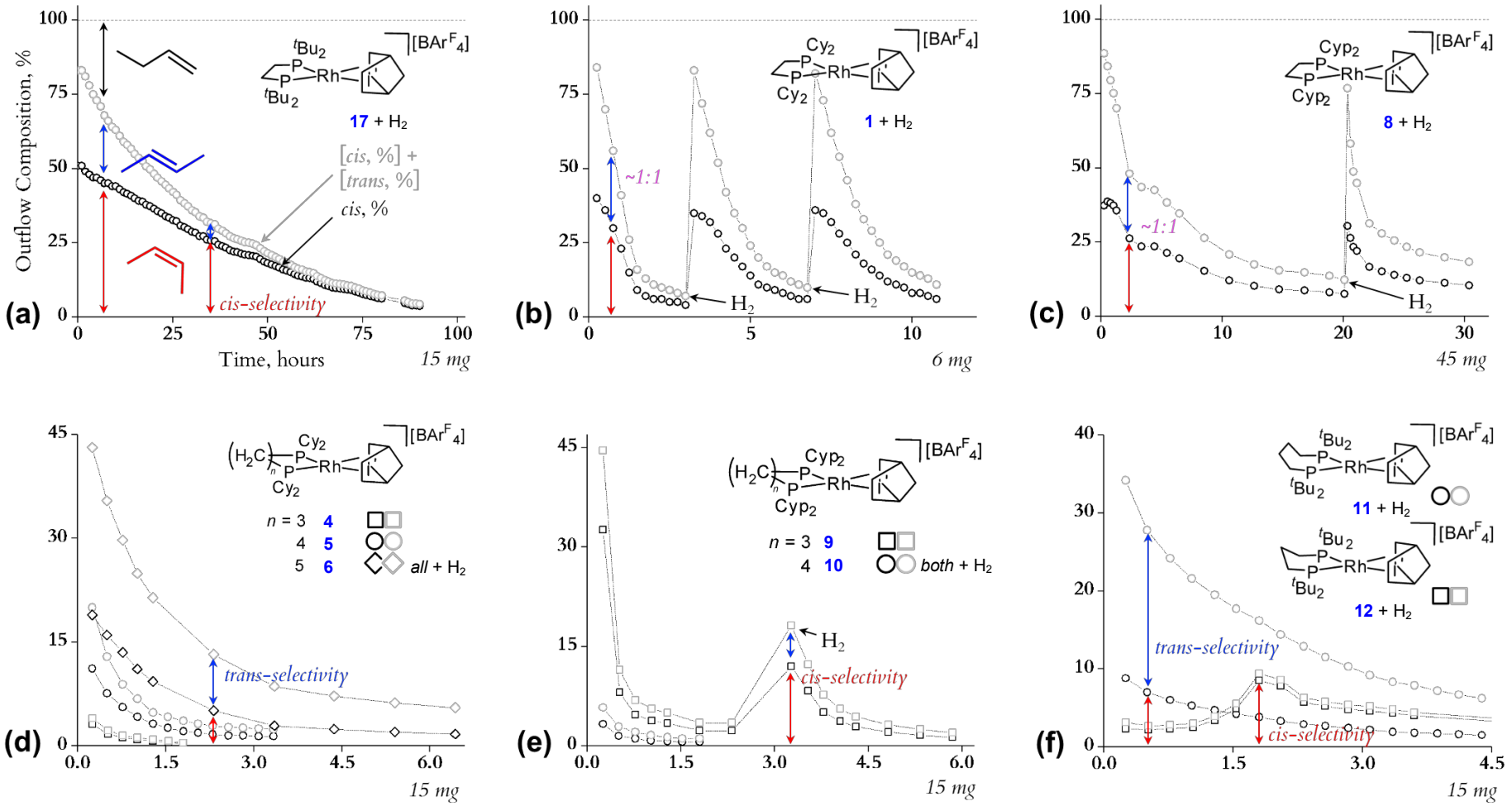


Figure 2.4.2: On-stream catalytic performance of 1-butene isomerisation catalysis under solid-gas flow conditions by R-group- and tether-varied SMOMs as indicated. p = 1 bar, T = 298 K, and pre-catalyst masses indicated. 1-butene (2% balance in N_2, 6.4 mL min^{-1}) + 15% *iso*-butene (2% balance in N_2, 1.2 mL min^{-1}) co-feed (*ca.* 0.3 mmol min^{-1}). Data plotted are total 2-butenes and *cis*-2-butene only (GC conversions).

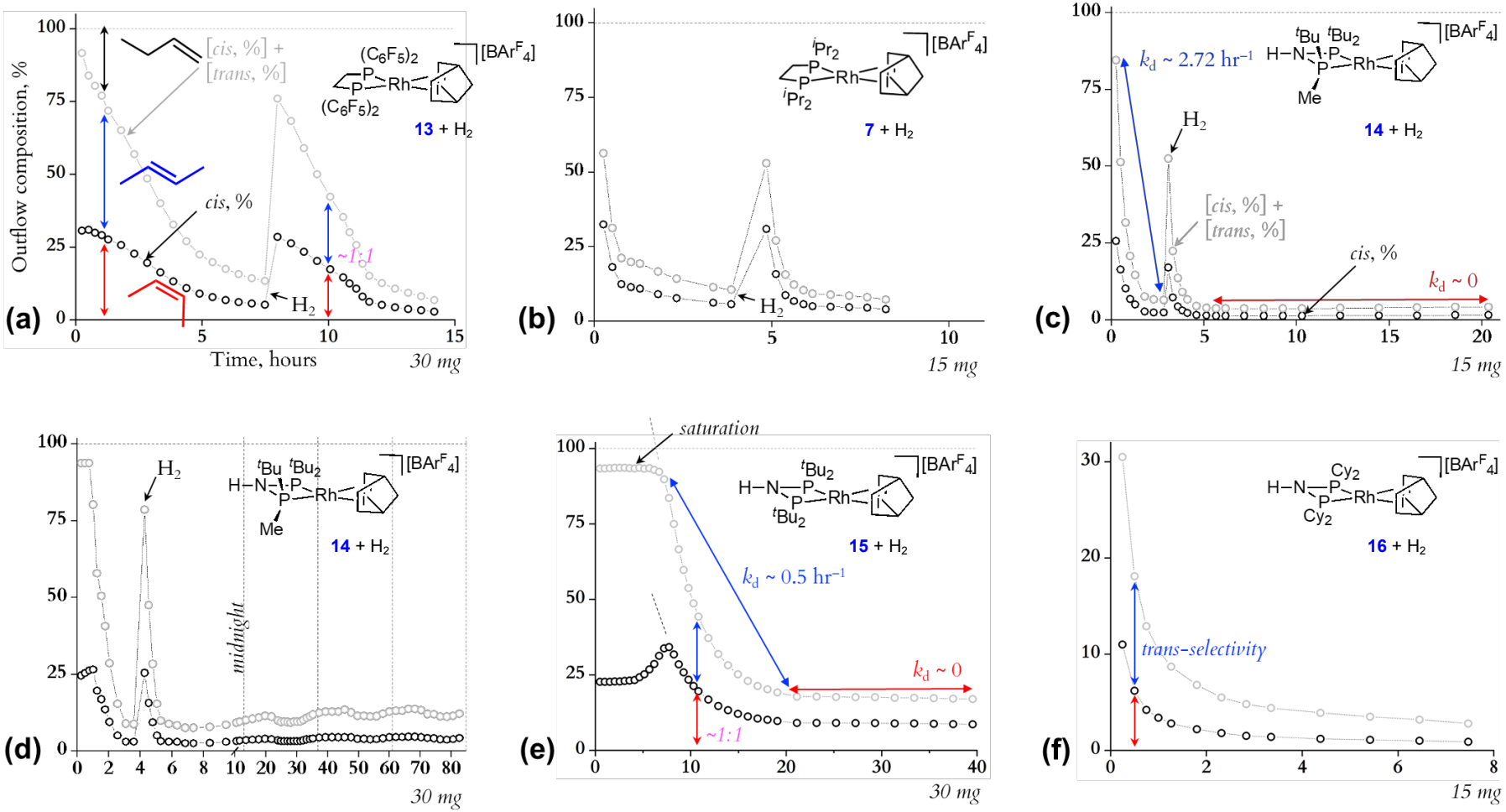


Figure 2.4.3: On-stream catalytic performance of 1-butene isomerisation catalysis under solid-gas flow conditions by R-group- and tether-varied SMOMs as indicated, including PˆNˆP-type SMOMs (**c**-**f**). p = 1 bar, T = 298 K, and pre-catalyst masses indicated. 1-butene (2% balance in N_2, 6.4 mL min^{-1}) + 15% *iso*-butene (2% balance in N_2, 1.2 mL min^{-1}) co-feed (*ca.* 0.3 mmol min^{-1}). Data plotted are total 2-butenes and *cis*-2-butene only (GC conversions). Note that (**d**) lacks temperature control.

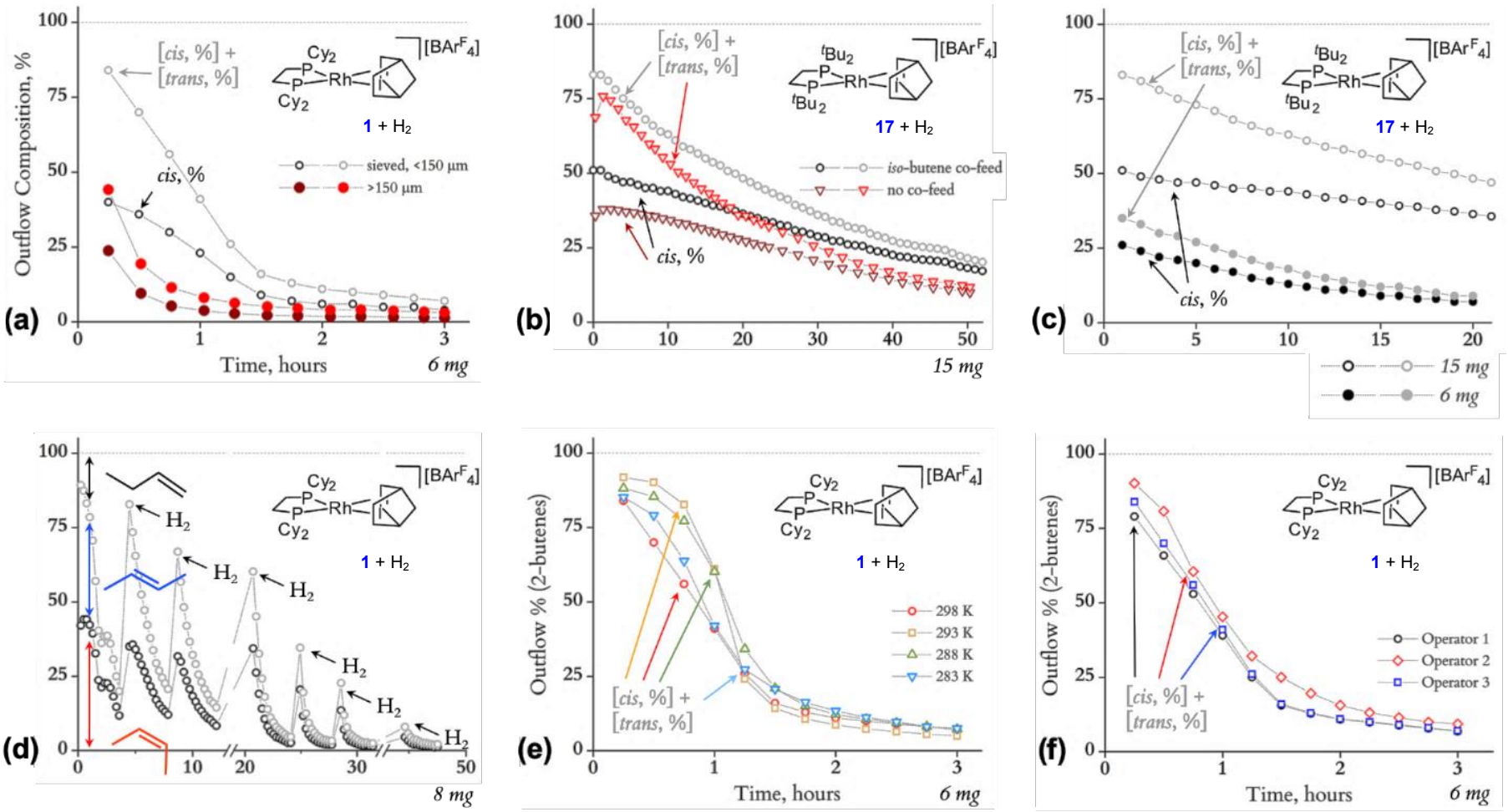


Figure 2.4.4: Control experiments for on-stream catalytic performance of 1-butene isomerisation catalysis under solid-gas flow conditions by SMOMs as indicated: (**a**) the effectiveness of particle sieving; (**b**) the impact of the *iso*-butene co-feed; (**c**) mass = 6 mg *versus* 15 mg; (**d**) a long-term flow experiment with six re-hydrogenation events; (**e**) variable temperature; (**f**) different operators. p = 1 bar, T = 298 K, and pre-catalyst masses indicated. 1-butene (2% balance in N_2, 6.4 mL min^{-1}) + 15% *iso*-butene (2% balance in N_2, 1.2 mL min^{-1}) co-feed (*ca.* 0.3 mmol min^{-1}). Data plotted are total 2-butenes and *cis*-2-butene only (GC conversions).

Precursor SMOM	WHSV (hr^{-1})[a]	k_d (hr^{-1})[b]	*cis*/*trans* ratio[c]	IP_{app} ($mol_{1\text{-butene}}\ mol_{cat}^{-1}\ hr^{-1}$)[d]
1	2.99	1.42 (2.16–0.51)	0.91–1.3	66.5
17 (15 mg)	1.19	0.08	1.6–5.3	24.4
4[e]	1.19	~1.30	~3.4–3.0	~1.3
5	1.19	0.40	1.3–1.4	6.4
6	1.19	0.40	0.78–0.45	14.0
7	1.19	0.34 (2.03–0.26)	1.37–1.21	15.9
8	0.40	0.20 (0.92–0.10)	0.73–1.7	9.0
9	1.19	1.35 (7.30–0.61)	2.7–1.92	13.8
10[e]	1.19	~0.95	~1.3–1.2	~1.8
11[e]	1.19	–	~2.9–6.0	~1.2
12	1.19	0.47	0.35–0.32	10.2
13	0.60	0.57	0.50–0.63	17.7
14 (15 mg)	1.19	2.72	0.44–0.56	23.8
15	0.60	0.50	0.69–1.02	26.1
16	1.19	0.36	0.56–0.47	9.6

Table 2.4.1: Selected metrics derived from the results of solid-gas catalytic isomerisation of 1-butene by pre-catalyst SMOMs under flow conditions. [a]Weight hour space velocity $WHSV = m_{1\text{-butene}} \div [m_{cat} \cdot t]$. [b]Decay rate $k_d = t \cdot [[\ln(1 - x_{end}) \div x_{end}] - [\ln(1 - x_{start}) \div x_{start}]$, where x is the proportion of 2-butenes in the outflow (0–1), assuming a first order deactivation process.[107] Where decay profiles are severely staggered, two extreme decay rates are also given. If an experiment includes a re-hydrogenation event, k_d refers to data points before the first such event. [c]If an experiment includes a re-hydrogenation event, *cis*/*trans* ratios refer to the range observed before the first such event. [d]Initial apparent productivity $IP_{app} = f_{1\text{-butene}} \div n_{cat}$, where $f_{1\text{-butene}}$ is a flow rate expressed as mol hr^{-1} and n_{cat} is catalyst/pre-catalyst molarity. [e]As a consequence of these systems' low activity, calculated metrics are likely to be less accurate.

We will now discuss portions of these data in detail. As we began our study of catalytic systems under NMR batch conditions by comparing precursor η^2,η^2-NBD SMOMs **1** and **17** as two proofs-of-concept, so too we shall begin by comparing the on-stream activity, lifetime, *cis*/*trans* selectivity, and H_2-revivability of catalytic systems derived from these two SMOMs under heterogeneous continuous flow conditions.

2.4.3 *Precursor NBD SMOMs 1 and 17 Under Continuous Flow Conditions*

In order to achieve approximately the same conversion to 2-butenes at the first data point (~80% at t = 15 minutes, refer to **Figure 2.4.2a,b**), 6 mg of precursor η^2,η^2-NBD SMOM **1** was required (obtaining an initial productivity of 66.5 $mol_{1\text{-butene}}$ mol_{cat}^{-1} hr^{-1}) compared to 15 mg of **17** (24.4 $mol_{1\text{-butene}}$ mol_{cat}^{-1} hr^{-1}). This agrees with the difference in activities observed under NMR batch conditions in Section 2.3.3, where it was argued that this was due to increased steric constraint at the {(dtbpe)Rh}$^+$ active site.

Proceeding from approximately the same initial conversion, **1** remained on-stream for ~3 hours before conversion dropped below 5%, while **17** remained on-stream for ~90 hours, with first-order decay constants of k_d = 1.42 and 0.08 hr^{-1} respectively. This is congruent with observations in-batch of the catalytic longevity of **17** compared to **1**, argued in Section 2.3.3 to also be a result of a more sterically constrained active site. It was also noted that the decay trend for **17** was relatively smooth, whereas the same trend for system **1** appeared staggered into two distinct regimes with distinct decay rates ($k_{d,1}$ ~ 2.16 hr^{-1}, $k_{d,2}$ ~ 0.51 hr^{-1}). Since **1** was highly active and deactivated rapidly, it is possible this was due to an inwardly creeping 'shell' of deactivation product 1,3-butadiene complex **18** forming on microcrystallites: if the catalytic process was primarily a surface effect (*vide infra*), then the onset of deactivation will have seemed rapid.

In terms of 2-butene isomer selectivity, both systems observed non-thermodynamic selectivity of 2-butenes across each experiment, with a bias in favour of *cis*-2-butene (recall that the thermodynamic *cis*:*trans* ratio is ~1:3[3]). System **1** initially demonstrated a *cis*:*trans* ratio of ~1:1.1, increasing over the course of the experiment to ~1.3:1, while **17** initially demonstrated ~1.6:1, increasing to ~5.3:1. Under solid-gas continuous flow conditions, system **17** was considerably more *cis*-selective than **1**, according with observations of kinetic *cis*-selectivity made in the preceding Sections and also attributed to steric hindrance at the active site. The *cis*:*trans* ratio observed in the outflow for system **1** did not vary significantly, and was never recorded outside the range of 1-1.3:1. In the outflow for system **17**, however, this ratio was seen to increase dramatically over the course of catalysis (1.6-5.3:1). We reason that is a result of deteriorating catalyst activity further disfavouring the subsequent *cis*- to *trans*-2-butene isomerisation reaction.

This phenomenon may also be linked to a shift in catalyst morphology over the course of the experiment (*vide infra*), and mirrors the results of the 75 mL reactor experiment (Section 2.3.5), where an increasing *cis*:*trans* ratio was observed and a change in catalyst morphology across the 96-hour experiment was visible with the naked eye.

The *cis*:*trans* ratio could also be affected by catalyst loading. When the loading of precursor η^2,η^2-NBD SMOM **17** was decreased from 15 mg to 6 mg (**Figure 2.4.4c**, to match **1** in **Figure 2.4.2b**), the expected ~60% drop in initial conversion (82-32% 2-butenes, −61%) was observed, with almost indistinguishable initial productivity (24.4, 25.7 $mol_{1\text{-butene}}\ mol_{cat}\ hr^{-1}$). Now, an increased initial *cis*:*trans* ratio of ~3:1 was measured (compare ~1.6:1 in **Figure 2.4.2a**), ostensibly due to a reduced catalyst residence time t^R on account of the lower catalyst loading, further favouring the kinetic *cis* isomer by reducing the probability of a successful subsequent *cis*→*trans* isomerisation reaction.

The deactivation product of catalytic system **1** under NMR batch conditions (Section 2.3.3), the corresponding 1,3-butadiene complex (**18**), existed as a 'dormant' state under both batch and flow conditions. This meant that activity could be restored by re-exposure to H_2 gas (**Figure 2.4.2b**). An experiment with six re-hydrogenations across a longer time range for system **1** was also conducted (**Figure 2.4.4d**), demonstrating that system **1** could not be reactivated indefinitely. Reactivation of catalysts with H_2 has been established for supported metal catalysts,[108] but, to the knowledge of the author, is otherwise unprecedented for organometallic systems under these conditions.

Catalytic systems derived from SMOM **17**, however, did *not* reactivate upon re-exposure to H_2, suggesting that **17** did not deactivate under flow conditions to yield the corresponding 1,3-butadiene complex (**19**); this assertion is proved in Section 2.4.6, and aligns with chemistry already established under batch conditions. Note that pre-hydrogenated samples of this 1,3-butadiene complex, independently prepared, were shown to be *active* under batch conditions in Section 2.3.3, generating hydride **23** *in situ* (see footnote, p. 86).

2.4.4 *Control Experiments Under Continuous Flow Conditions: Particle Size,* iso*-Butene Co-Feed, Temperature, and Reproducibility*

Experiments conducted with material left over after sieving (17 only, **Figure 2.4.4a**), such that particle sizes were ≥150 μm, showed a much-reduced initial productivity under the same conditions compared to **Figure 2.4.2a** (13.0 *versus* 24.4 $mol_{1\text{-butene}}\ mol_{cat}^{-1}\ hr^{-1}$), with a lower *cis*-2-butene selectivity (*cis*:*trans* = 1.2 *versus* 1.6), and a higher decay rate (1.07 *versus* 0.08 hr^{-1}), indicating the importance of particle size/morphology in catalytic activity and selectivity. This phenomenon has been reported for the Pd-nanoparticle-catalysed isomerisation of butenes,[102,109] pointing towards a surface process.

Flow experiments with and without the 15% *iso*-butene co-feed were conducted in order to simulate its presence in the C_4 feed of a cracker[105] (SMOM 17, **Figure 2.4.4b**): no significant difference in decay rate or selectivity was observed, indicating that *iso*-butene did not significantly compete for coordination at the active site with *n*-butene isomers. In order to study the effect of temperature under continuous flow conditions, experiments were conducted with precursor η^2,η^2-NBD SMOM 1 at 283, 288, 293 and 298 K (**Figure 2.4.4e**), having little noticeable effect on the decay profile or the initial productivity. Reproducibility was demonstrated with three repeated catalytic runs with precursor η^2,η^2-NBD SMOM 1, each with three different operators and three different, separately-prepared batches of catalyst (**Figure 2.4.4f**). Initial conversion varied by no more than ±3%, with practically indistinguishable decay profiles.

Having observed the behaviour of pre-catalyst SMOMs 1 and 17 as solid-gas alkene isomerisation catalysts under continuous flow conditions, attention turned to the respective in-flow deactivation processes. This necessitated characterisation of the material left over after a continuous solid-gas flow experiment.

2.4.5 *Post-Flow Materials Characterisation, Precursor NBD SMOM 1*

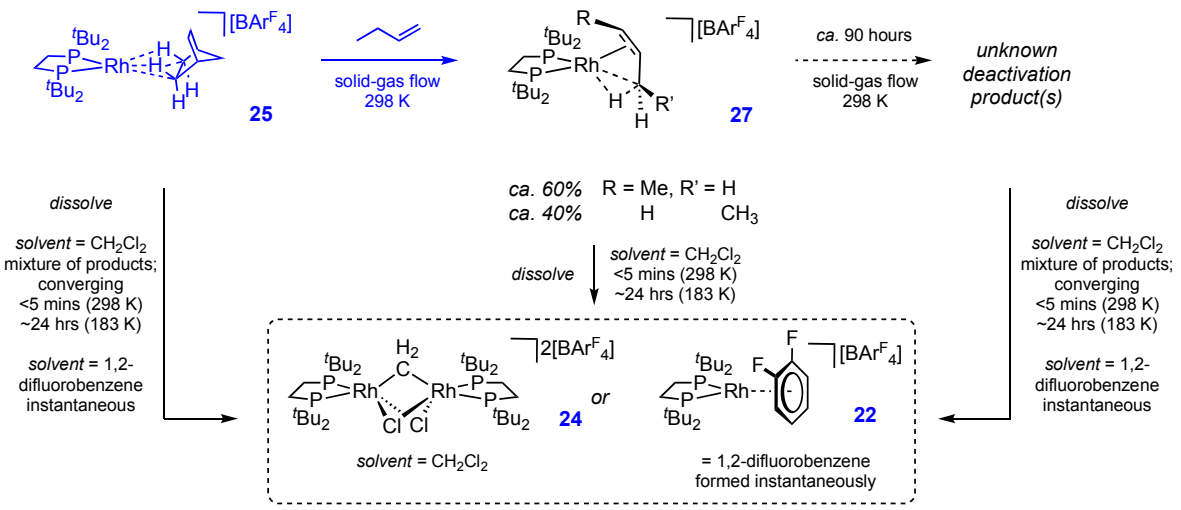
Once catalytic activity in flow was observed to drop below 5% conversion, columns that had been pre-loaded with SMOM 1 as pre-catalyst were purged with N_2, Swagelock-sealed, and unpacked inside a glovebox under an argon atmosphere.

The initially pale orange organometallic/glass wool mixture had reddened considerably over the course of the catalysis, superficially indicating the formation of the inactive 1,3-butadiene complex (**18**). This was confirmed by loading post-catalytic material, into NMR tubes fitted with Young's taps. CD_2Cl_2 was then distilled into the headspaces of these tubes, dissolving any organometallic complexes dispersed onto the glass wool and thus permitting solution-phase NMR spectroscopic analysis. $^{31}P\{^1H\}$ NMR spectroscopy, in both the solution-phase and the solid-state (organometallic/glass wool mixture), confirmed the presence of 1,3-butadiene complex **18** (δ_{soln} 80.9, $^1J_{PRh}$ = 170 Hz (CD_2Cl_2, 298 K); δ_{SS} 80.0 (ν = 10 kHz, 298 K)), consistent with observations under batch conditions (Section 2.3.3) and with literature spectroscopic data.[1]

Post-catalytic material obtained after a prolonged experiment (**Figure 2.4.4d**) was also analysed by solution-phase NMR spectroscopy, and contained 1,3-butadiene complex **18** in addition to a small amount (~10%) of the Ar^F-coordinated zwitterion **32**[12] and a host of unidentified decomposition products. The formation of deactivation products in the solid-state *other* than the 1,3-butadiene complex (**18**) that did not respond to reactivation by exposure to H_2 may explain the slow but irreversible loss of activity observed over ~45 hours; physical deformation (*vide infra*) may also have contributed. Attempts to synthesise zwitterion **32** in the past have been met only with qualified success: significant partial decomposition was observed when σ-NBA complex **2** was taken up in CH_2Cl_2.[12]

2.4.6 Pre-Flow, On-Stream, and Post-Flow Materials Characterisation, Precursor NBD SMOM 17

The same procedure as in Section 2.4.5 was also conducted for columns that had been pre-loaded with SMOM **17**, hydrogenated, and then exposed to flow conditions for both one hour ('on-stream') and 100 hours ('post-flow'). The initially pale-orange organometallic/glass wool mixture was noted to have darkened (on-stream) and then lightened, to a pale-yellow colour (post-flow). Post-flow material yielded the 1,2-difluorobenzene complex **22** when dissolved in 1,2-difluorobenzene at 298 K or reacted to yield the Cl-bridged dimer **24** when dissolved in CD_2Cl_2 at 298 K, in common with the solution-phase chemistry of both the σ-NBA (**25**) and *n*-butenes (**27**) complexes (**Scheme 2.4.1**).



Scheme 2.4.1: Solution-phase behaviour of post-flow catalytic material (system 17) and its precursors generated *in situ* in the solid state, the σ-NBA complex (25) and the butenes complex (27), to instantaneously yield the 1,2-difluorobenzene complex (22) when dissolved in 1,2-difluorobenzene, and ultimately yielding the C-Cl activated dimer (24) when dissolved in CH_2Cl_2.

This indicates that a ligand bound strongly to the {(dtbpe)Rh}$^+$ fragment, such as 1,3-butadiene, was *not* formed as the ultimate deactivation product in post-flow material. A solid-state deactivation product corresponding to a weakly-bound Ar^F-coordinated zwitterion of formula [(dtbpe)Rh(η^6-Ar^F-BAr$^F_3$)] may be tentatively suggested. However, no direct solution-phase NMR spectroscopic evidence was forthcoming for this hypothesis even at 183 K: it is possible that the sterically-demanding and powerfully electron-donating ^{t}Bu groups favour rapid dissociation of [BAr$^F_4$]$^-$ and CD_2Cl_2 activation respectively upon dissolution. In CD_2Cl_2, this decomposition occurred immediately at 298 K but more slowly at 183 K (**Figure 2.4.5**). In the case of post-flow material, a mixture of products was identified in solution at 183 K before converging on the Cl-bridged dimer 24 over 24 hours. Excepting the butenes complex 27, none of these peaks were positively identified, and none corresponded to the 1,3-butadiene complex (19).

Solution-phase characterisation routes having thus proved inconclusive, $^{31}P\{^1H\}$ SSNMR spectroscopic techniques were employed on on-stream and post-flow material. For material pre-hydrogenated and exposed to flow conditions for just one hour ('on-stream'), the σ-NBA complex (25) and a small amount of *n*-butenes complex (~10%, 27) were positively identified (**Figure 2.4.6a**).

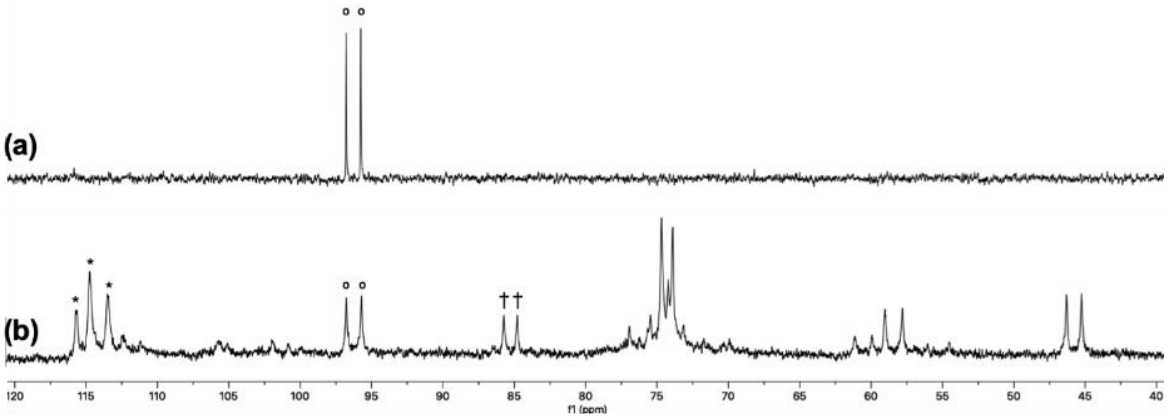


Figure 2.4.5: $^{31}P\{^{1}H\}$ NMR spectrum (161.99 MHz) of post-flow organometallic/glass wool mixture (system 17) redissolved in CH_2Cl_2 at (**a**) 298 K, (**b**) 183 K after five minutes. *indicates signals identified as the butenes complex 27. †indicates signals identified as unreacted η^2,η^2-NBD complex 17. °indicates signals identified as the C-Cl activated dimer 25. All other signals not positively identified.

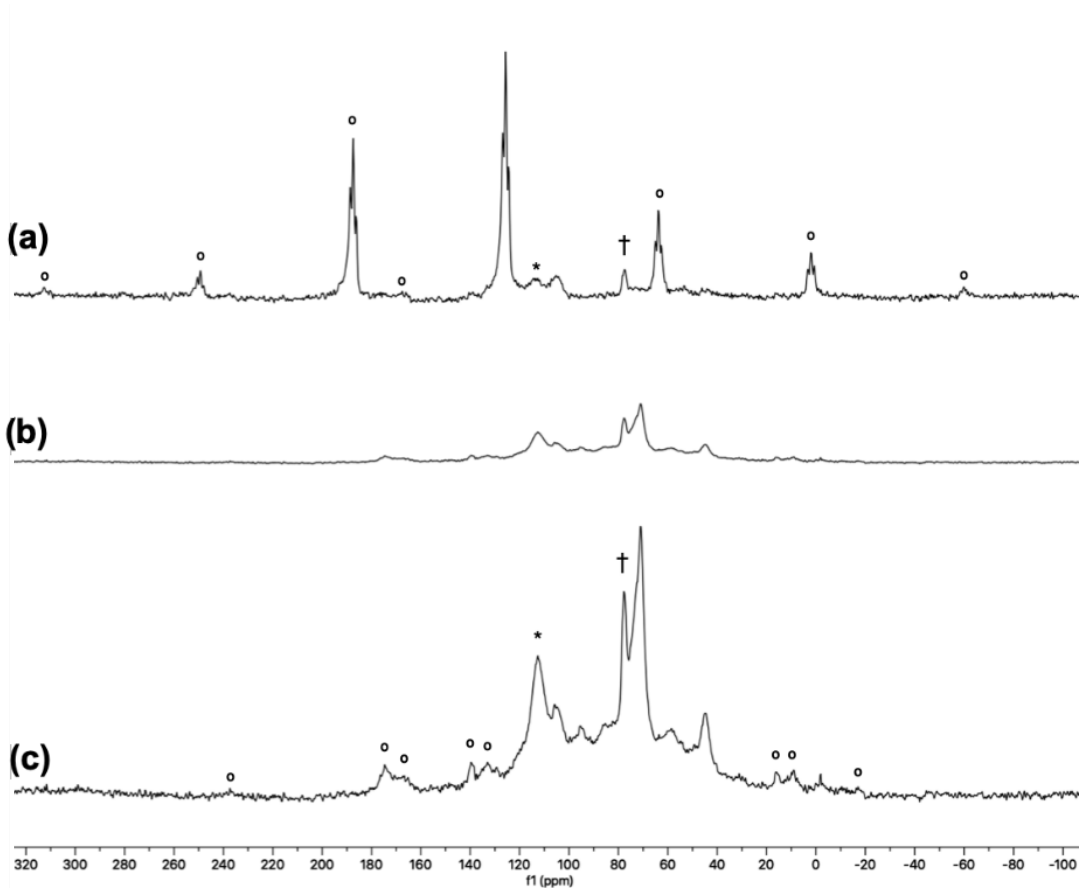


Figure 2.4.6: $^{31}P\{^{1}H\}$ SSNMR (162.03 MHz, 298 K, ν = 10 kHz) spectra of (**a**) 'on-stream' (one hour) organometallic/glass wool mixture and (**b**) 'post-flow' (100 hours) material with the same receiver gain, expanded in (**c**). *indicates signals identified as the *n*-butenes complex 27. †indicates signals identified as unreacted η^2,η^2-NBD complex 17. °indicates spinning side-bands. All other signals not positively identified.

This indicated that the formation of the butenes complex 27 was slow on the timescale of catalysis, and that catalysis was probably a surface or near-surface process (on-stream conversion was above 80% at this stage). This evokes the results of the particle-size control experiment (**Figure 2.4.4a**), where larger particle size and hence poorer surface-area-to-volume ratio lent to a lower initial productivity, suggesting a surface or near-surface process. For material pre-hydrogenated and exposed to flow conditions for 100 hours ('post-flow'), a range of broad, low intensity peaks were observed in the $^{31}P\{^{1}H\}$ SSNMR spectrum (**Figure 2.4.6b,c**). Consonant with observations in solution, resonances corresponding to the *n*-butenes complex (27) and unreacted η^2,η^2-NBD complex (17) were identified, with all other signals failing to correspond to known species. No signal belonging to the 1,3-butadiene complex (19, δ 95.5) was identified, further evidencing that deactivation *via* transfer dehydrogenation of the *n*-butenes complex (27) did not occur appreciably in this system under flow conditions.

The relative inactivity of a post-flow material sample was confirmed by re-exposing 2 mg of recouped organometallic to 1-butene (1 bar) under NMR batch conditions as in Section 2.3.3 without pre-exposure to H_2: <5% conversion to 2-butenes after 1,000 seconds was measured by gas-phase ^{1}H NMR spectroscopy.

The weakness and broadness of the SSNMR resonances in **Figure 2.4.6b** suggested the loss of long-range order in the bulk of the sample. This was confirmed *via* powder X-ray diffraction (*p*-XRD) studies and scanning electron microscopy (SEM). Diffractograms of samples of post-flow material were compared to samples of single-crystalline η^2,η^2-NBD complex 17 and samples of this complex hydrogenated and exposed to 1-butene for 96 hours in the solid-state *ex situ*, to simulate the ageing process under continuous flow conditions (**Figure 2.4.7**). Some peaks were retained in post-flow and *ex situ*-aged material compared to precursor SMOM 17, although with significant broadening/loss of information, indicating a deterioration in crystallinity/long-range order. Similar *p*-XRD studies conducted on post-flow material for system 1 indicated much the same (*i.e.* broadening and loss of information), consonant with previous observations[1] of a progressive reduction in crystallinity upon sequential generation of the 1,3-butadiene complex (1→2→3→18, Section 2.3.1).

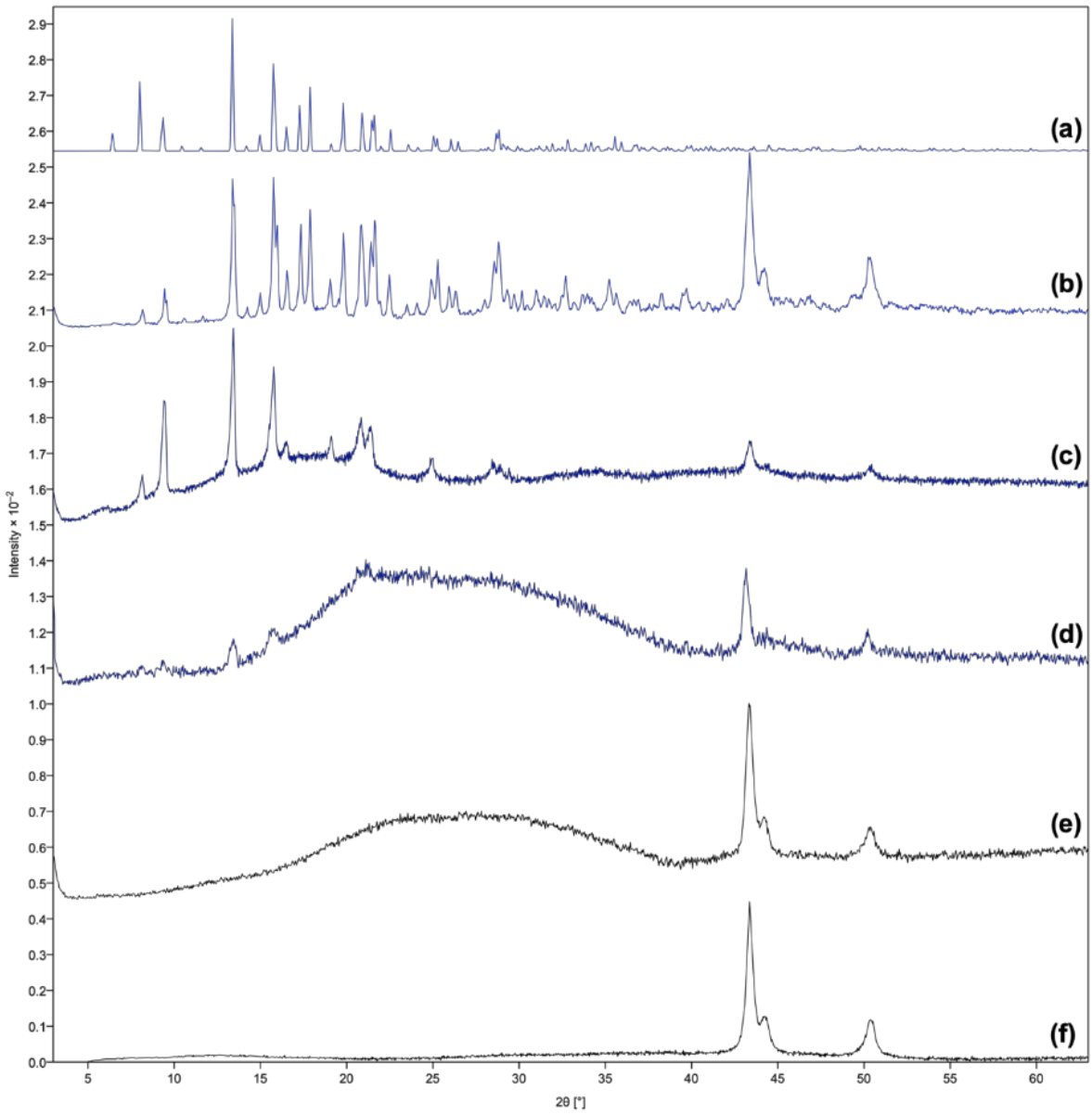


Figure 2.4.7: Powder x-ray diffractograms of η^2,η^2-NBD SMOM **17** (calculated (**a**) and measured (**b**)); (**c**) *n*-butenes complex **27** generated *ex situ* in the solid state from σ-NBA complex **25** and 1-butene gas; (**d**) 'post-flow' organometallic/glass wool mixture pre-hydrogenated and exposed to flow conditions for 100 hours; (**e**) a blank sample holder containing crushed glass wool; (**f**) a blank sample holder.

Scanning electron micrographs were taken of post-flow (100 hours), on-stream (one hour), and 'pre-flow' material (crystals of precursor SMOM **1** powdered finely and mixed with glass wool) in order to observe supported crystallites of organometallic on the microscale, and how their morphology changed (if at all) over the course of a flow experiment. Organometallic species (B, C, F, P-containing) were differentiated unambiguously from glass wool (Si, O-containing) *via* energy-dispersive X-ray spectroscopy (EDX).

Pre-flow material generally contained well-defined microcrystallites, many of them large, on the order of 5-25 μm across, with some examples as large as 50 μm across (**Figure 2.4.8**). Much the same was observed for on-stream material, though many examples of fractured/shattered microcrystallites were spotted (**Figure 2.4.9**), aligning with observations of crystal cracking upon hydrogenation under batch conditions.

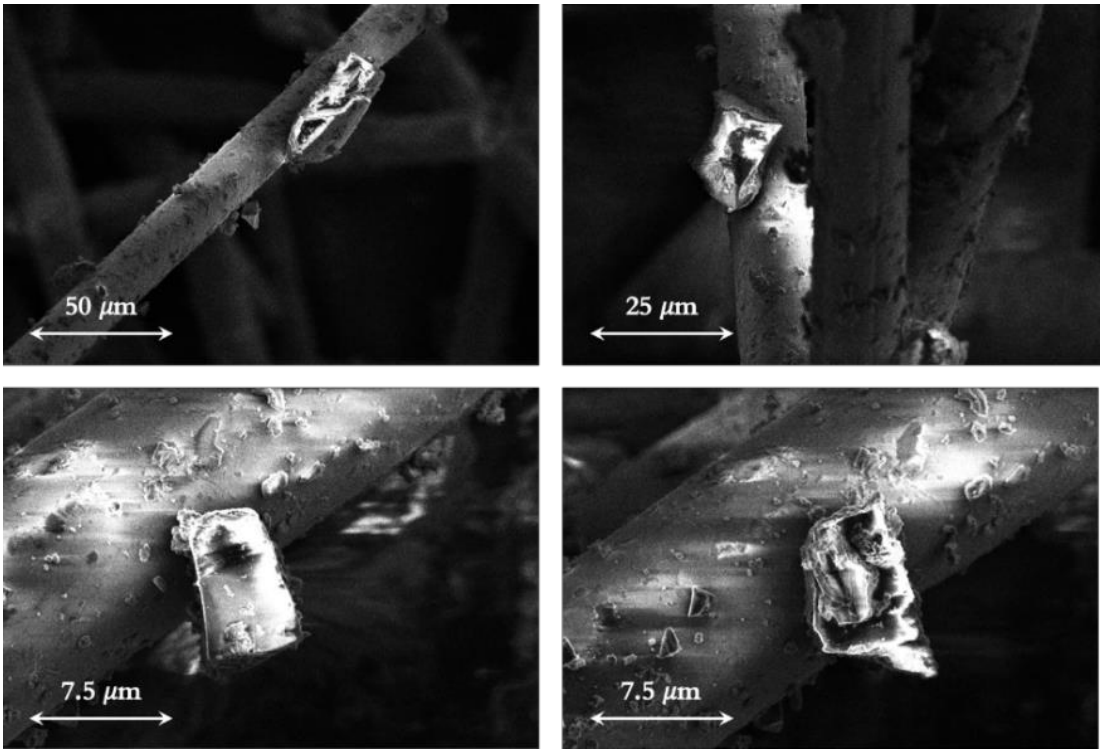


Figure 2.4.8: Scanning electron micrographs of an organometallic (17)/glass wool mixture that had not been exposed to H_2 or 1-butene gas ('pre-flow').

Post-flow material (**Figure 2.4.10**) generally contained no well-defined microcrystallites, with organometallic material largely consisting of small particles with smoothened edges, on the order of 1-5 μm across. This agreed with SSNMR and *p*-XRD observations (*vide supra*) suggesting a loss in long-range order over the course of catalysis. Loss of definition may also be linked to the increasing *cis*-selectivity observed over the course of a 100-hour experiment: if catalysis occurred as a surface or near-surface process, microcrystallite surface morphology must be essential in determining catalyst behaviour, as seen in the work of Zaera, Goetz, and colleagues.[102,109]

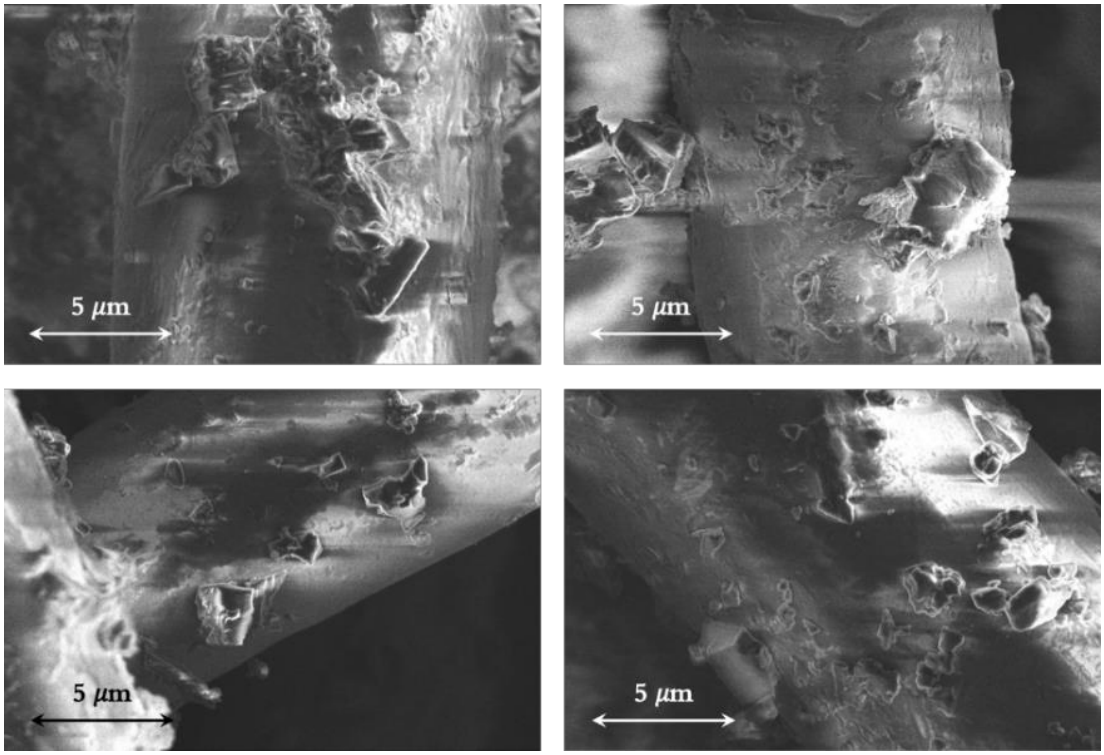


Figure 2.4.9: Scanning electron micrographs of an organometallic (17)/glass wool mixture exposed to H_2 and then 1-butene and 15% *iso*-butene (2% balance in N_2) for one hour under flow conditions ('on-stream').

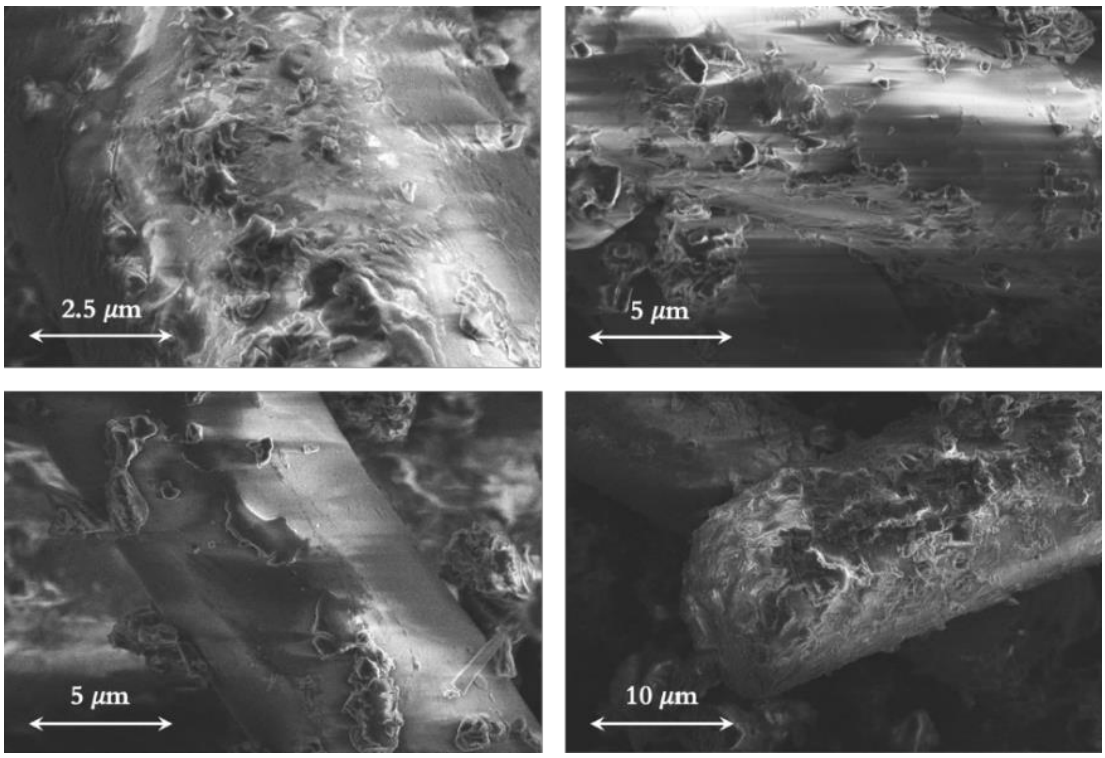
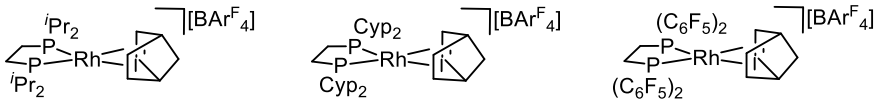


Figure 2.4.10: Scanning electron micrographs of an organometallic (17)/glass wool mixture exposed to H_2 and then 1-butene and 15% *iso*-butene (2% balance in N_2) for 100 hours under flow conditions ('post-flow').

Changes in surface morphology may occur as a result of local surface or near-surface concentrations of butenes causing crystal 'melting', as seen for precursor SMOM 17 during the 75 mL reactor experiment under batch conditions (Section 2.3.5). Taken together, these observations strongly suggest crystallinity/robustness of surface morphology – 'structural' stability – is an important factor in the catalytic behaviour of system 17 under continuous flow conditions. This acts in addition to stereoelectronic considerations – 'chemical' stability, *e.g.* formation of an 1,3-butadiene complex or an Ar^F-coordinated zwitterion – influenced by the chelating *bis*-phosphine as well as the solid-state microenvironment.[1,6]

The critical importance of *chemical* stability has been demonstrated unequivocally, *via* the comparison of pre-catalyst SMOMs 1 and 17 under batch and flow conditions. In order to further explore the influence of the chelate over catalytic activity, selectivity, and lifetime under continuous flow conditions, in the following sections the results of chelate R-group and tether length $(CH_2)_n$ variation will be discussed briefly.

2.4.7 The Effects of Ligand Variation Under Flow Conditions: R-Group Variation



7 8 13

Figure 2.4.11: R-group-varied pre-catalyst η^2,η^2-NBD SMOMs at a constant tether length, relevant to this section.

Similar catalytic activity to precursor η^2,η^2-NBD SMOM 1 for *cyclo*-pentyl-bearing SMOM 8 was observed under batch conditions in Section 2.3.6. Under continuous flow conditions, however, a dramatic discrepancy in productivity was observed (**Figure 2.4.2b,c**): in order to achieve approximately the same initial conversion of 1-butenes to 2-butenes as pre-catalyst SMOM 1 (6 mg), more than *seven* times the mass of SMOM 8 (45 mg) was required. Why such a difference should have been observed in-flow but not in-batch is unclear, especially when the two systems still deactivated in-flow to give the corresponding 1,3-butadiene complex (*vide infra*), and both generated a *cis*:*trans* ratio of ~1:1 across their lifetimes.

This suggests that NMR batch conditions do *not* constitute a reliable model for whether a certain SMOM will succeed under flow conditions; it is possible that any discrepancies, structural or stereoelectronic, giving rise to small differences in activity or selectivity in-batch, were magnified when placed under flow conditions. $^{31}P\{^{1}H\}$ NMR spectroscopic analysis of post-flow material derived from precursor η^2,η^2-NBD SMOM **8** (CD_2Cl_2, 183 K) again revealed the 1,3-butadiene complex (**31**; δ 77.0, $^{1}J_{PRh}$ = 169 Hz), in addition to ~20% of the Ar^F-coordinated zwitterion (**33**; δ 83.0, $^{1}J_{PRh}$ = 200 Hz).[46]

Iso-propyl-bearing SMOM **7** (**Figure 2.4.3b**) only achieved ~24% of the initial apparent productivity of SMOM **1** with a ~1:1 *cis*:*trans* selectivity in the outflow, similar to SMOM **1**. Post-flow $^{31}P\{^{1}H\}$ NMR spectroscopic analysis (CD_2Cl_2, 183 K) only revealed the Ar^F-coordinated zwitterion (**29**; δ 102.0, $^{1}J_{PRh}$ = 205 Hz),[12] similarly to batch conditions.

Perfluorophenyl-bearing SMOM **13** was also tested under flow conditions (**Figure 2.4.3a**) with an unusually marked preference for *trans*-2-butene across the experiment. This may be a result of the uniquely aryl-substituted chelate, in which a comparatively open, sterically unconstrained active site (*cf.* SMOMs **1** and **17**) produced a flatter energy landscape,[a] thus reducing kinetic *cis*-selectivity. The activity of pre-catalyst SMOMs **7** and **13** under continuous flow conditions, respectively with BCPP and buckled hexagonal prismatic structure types (Section 2.2.4) demonstrated that the O_h packing motif was not necessarily a prerequisite for catalytic activity.

2.4.8 *The Effects of Ligand Variation Under Flow Conditions: Tether Length and Identity Variation*

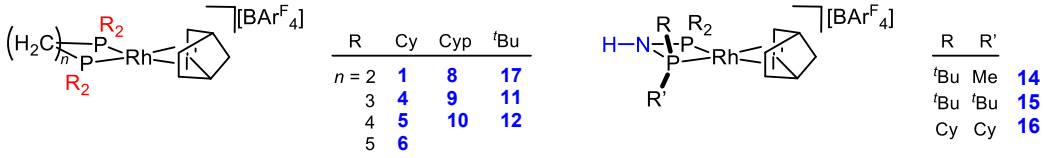
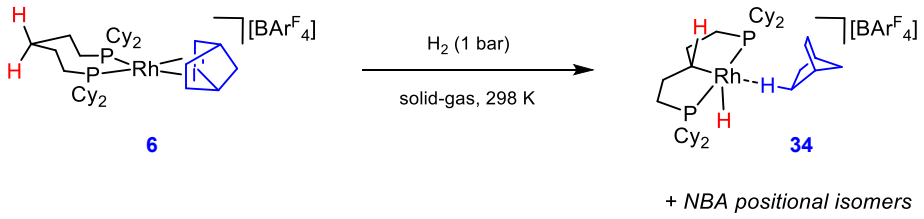


Figure 2.4.12: Chelate tether length- and identity-varied pre-catalyst η^2,η^2-NBD SMOMs relevant to this section.

[a] The solid-state structure of this SMOM is discussed in detail in Chapter 3 (Section 3.3.1).

By increasing the number of CH_2 links in the tether, widening the P-Rh-P bite angle, two principal effects result: an electronic effect, where the angle favours a certain oxidation state geometry (*e.g.* bite angles of ~109.5° favouring tetrahedral d^{10} Ni(0), ~90° favouring square-planar d^8 Ni(II)); and a steric effect, whereby a widening bite angle results in a more sterically constrained active site.[110,111] The critical effect of bite angle on SMOM solid-gas reactivity has already been documented, in a study of SMOMs $[(Cy_2P(CH_2)_nPCy_2)Rh(\eta^2,\eta^2\text{-NBD})][BAr^F_4]$ (n = 2-5) and their SC-SC hydrogenation chemistry.[14] In this report, increasing bite angle was demonstrated to increasingly favour oxidative addition at the metal.[37,111] In an extreme example, upon solid-state hydrogenation of SMOM **6**, C-H activation of the central, proximal CH_2 position occurred, reportedly yielding a Rh(III) κ^3-pincer-hydride σ-NBA complex (**34**, **Scheme 2.4.2**),[14] evidenced by both solution-phase and solid-state NMR spectroscopy.



Scheme 2.4.2: SC-SC solid-gas hydrogenation of SMOM **6** to generate a Rh(III) κ^3-pincer-hydride σ-NBA complex **34**, as related in the reference.[14]

It follows that catalytic behaviour under continuous flow conditions should also have depended on tether length. Indeed, when the chelate in the precursor η^2,η^2-NBD SMOMs was systematically varied in tether length, significant changes in catalytic system lifetime, selectivity and activity were observed. These results, pertaining to R = Cy, Cyp, and ^{t}Bu, are given in **Figure 2.4.2d-f**. SMOMs $[(R_2P(CH_2)_nPR_2)Rh(\eta^2,\eta^2\text{-NBD})][BAr^F_4]$ with tether-length n > 2 (R = Cy, ^{t}Bu) yielded markedly poorer initial productivities *cf.* n = 2 under continuous flow conditions. The disadvantage in productivity *cf.* n = 2 may be a result of increasing steric hindrance at the active site, although why initial productivity increased in the order n = 3 < 4 < 2 (R = Cy, ^{t}Bu) is not certain. The reverse was observed for R = Cyp, where initial productivity increased in the order n = 3 > 2 > 4.

Cis/*trans* selectivities were also observed to alter with tether variation. With pre-catalyst η^2,η^2-NBD SMOMs **4**, **5**, **9**, and **11**, despite poor activity, greater *cis*-selectivity was observed compared to their n = 2 counterparts, a result of increasing steric constraint at the active site with increasing bite angle (see Section 2.3.4); the sterically demanding ^{t}Bu groups in **11** produced the most powerful *cis*-selectivity.

However, SMOMs **6** and **12** observed markedly *lower cis*:*trans* ratios (~0.6 and ~0.3 respectively) compared to their n = 2 counterparts. We have discussed how SMOM **6** is known to form a pincer upon solid-state hydrogenation (**Scheme 2.4.2**).[14] Kinetic *trans*-selectivity by a pincer complex has been reported by Chianese and colleagues, with their *bis*-NHC pincer-Ir(III) complex.[112] A common feature of this report and other reports of *trans*-selective alkene isomerisation catalysts[113,114] is the arrangement of steric bulk around the metal coordination sphere in a *trans* fashion. Compared to the P_2-type SMOMs, with *cis*-ligated phosphines, it is apparent much of the steric bulk in these pincer-hydrides was pulled 'away' from the active site, suggesting a flatter energy landscape with less ingrained kinetic selectivity for either *cis* or *trans*, in common with our observations.

Aligning with reports of pincer formation upon solid-gas hydrogenation of SMOM **6**, solution-phase NMR spectroscopy conducted on SMOM **12** – first exposed to H_2 (1 bar) in the solid-state for 15 minutes followed by dissolution in CD_2Cl_2 – strongly suggested that this precursor *also* formed a κ^3-pincer-hydride in the solid-state upon hydrogenation. This hydride was located at δ −28.12 ($^1J_{HRh}$ = 63.5 Hz, $^2J_{HP}$ = ~10, ~12 Hz), and was associated with two distinct $^{31}P\{^1H\}$ environments at δ 100.0 ($^1J_{PRh}$ = 128 Hz) and −14.4 (89 Hz) ($^2J_{PP'}$ = 295 Hz).[a] The markedly upfield shift of the latter resonance is typical of strained phosphametallacyclobutanes generated by intramolecular C–H activation of alkyl groups borne by a phosphine donor.[115,116] Tracked by $^{31}P\{^1H\}$ SSNMR spectroscopy, the solid-state hydrogenation also generated two ^{31}P environments, at δ 97.6 and 49.7.[b]

[a] These resonances presumably belonged to the solvate, $[\kappa^3$-(^{t}Bu$_2$PCH$_2$CH(CH$_2$)$_2$P^{t}Bu$_2$)RhH(CD$_2$Cl$_2$)]$^+$, in analogy to the solvate $[\kappa^3$-(Cy$_2$P(CH$_2$)$_2$CH(CH$_2$)$_2$PCy$_2$)RhH(CD$_2$Cl$_2$)]$^+$ related in the reference.[14]

[b] These resonances belonged to the 'naked' $[\kappa^3$-(^{t}Bu$_2$PCH$_2$CH(CH$_2$)$_2$P^{t}Bu$_2$)RhH]$^+$ fragment. Ongoing experiments beyond the scope of this Chapter have shown that this solid-gas hydrogenation is an SC-SC transformation.

Further SSNMR experiments are necessary to confirm that this pincer motif was retained throughout the catalytic process, *i.e.* after exposure to 1-butene gas, for both SMOMs **6** and **12**.

P^N^P-type precursor SMOMs (**14–16**) were deployed under continuous flow conditions (refer to **Figure 2.4.3c–f**)[a] in a deliberate attempt to move away from P_2C_n-type SMOMs (see Chapter 6). All demonstrated mild outflow *cis*-selectivity (*cis*:*trans* ~0.5–1), aligning with a less sterically constrained[117] active site producing a flatter energy landscape with less ingrained kinetic *cis*-selectivity, similar to the pincer-type systems described above. The non-symmetric active site of precursor SMOM **14** appeared to have no significant effect on the outflow *cis*/*trans* ratio, compared to SMOMs **15** and **16**.

Curiously, catalytic systems derived from precursor SMOMs **14** and **15** did not tend to apparent productivities of zero with elapsing time, in contrast to all precursor SMOMs hitherto tested. Instead, they retained appreciable productivities (~5 $mol_{1\text{-butene}}$ mol_{cat}^{-1} hr^{-1}) and on-stream conversions (>15% at 30 mg of catalyst) after achieving $k_d \sim 0$.

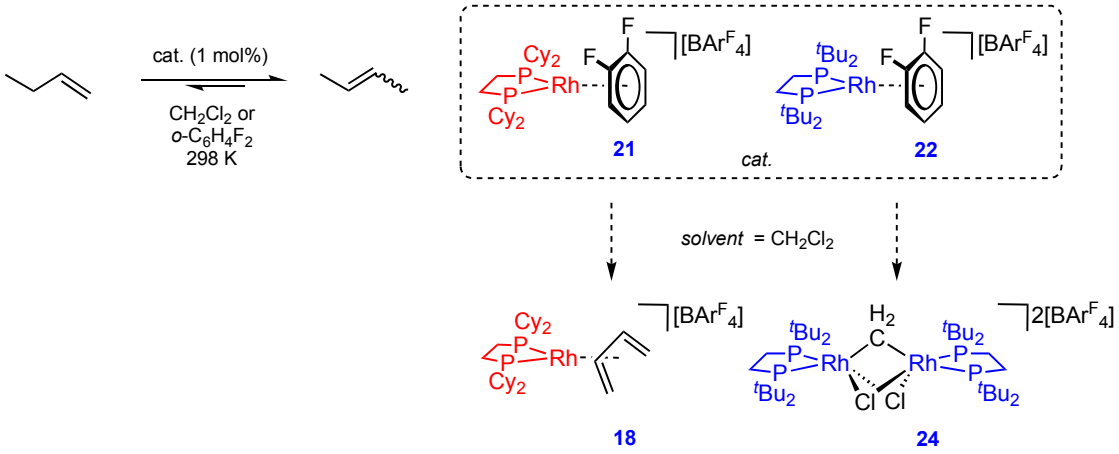
The Ar^F-coordinated zwitterion appeared to play an important role in the persistent activity of SMOMs **14** and **15**. Post-flow material and pre-hydrogenated material which had not yet been exposed to 1-butene gas were interrogated by solution-phase NMR spectroscopy at 183 K – in both cases, only the Ar^F-coordinated zwitterions were evidenced, with ^1H and $^{19}F\{^1H\}$ NMR signals consistent with symmetry-breaking on the $[BAr^F_4]^-$ anion. Whether the Ar^F-coordinated zwitterion constituted the resting state of these P^N^P-type catalytic systems has yet to be positively confirmed – SSNMR experiments on in-flow and post-flow material, in analogy to Sections 2.4.5 and 2.4.6, will shed light on this.

Throughout this work, we have emphasised the importance of the solid-state in influencing reactivity and protecting reactive species. As a control, we will now see whether alkene isomerisation catalysis also proceeds in solution, and – if it does – whether any similarities may be drawn between the heterogeneous and homogeneous catalysis regimes.

[a] Note that in **Figure 2.4.3d** and **f** an excessive loading of pre-catalyst SMOM has been employed deliberately, achieving catalytic saturation, in order to obtain a higher constant productivity when $k_d \sim 0$.

2.4.9 *Homogeneous Alkene Isomerisation Control Experiments*

η^6-1,2-difluorobenzene complexes have been exploited for their lability,[11] both in this work (Section 2.2.1) and previously, for purposes both synthetic and catalytic.[1,14,118] Intended as solution-phase analogues of precursor η^2,η^2-NBD SMOMs **1** and **17** and their corresponding σ-NBA complexes **2** and **25**, in which the weakly bound σ-NBA 'token' ligand was replaced by labile η^6-1,2-difluorobenzene, these aryl complexes **21**[47] and **22**[2] (2 mg, ~1.0 mol%) were taken in CH_2Cl_2 or 1,2-difluorobenzene solution (0.4 mL) in NMR tubes before the solutions were frozen with liquid N_2, exposed to vacuum (p < 10^{-2} mbar), thawed, and pressurised under 1-butene gas (1.0 bar) (**Scheme 2.4.3**).



Scheme 2.4.3: Solution-phase isomerisation of 1-butene (solvent = CH_2Cl_2 or 1,2-difluorobenzene), utilising 1,2-difluorobenzene complexes **21** and **22** as pre-catalysts.

In the absence of 1-butene, the 1,2-difluorobenzene complexes **21** and **22** were stable for at least 48 hours in CH_2Cl_2 at 298 K. Homogeneous 1-butene isomerisation catalysed by **21** proceeded almost instantaneously at 298 K (t < 1 minute for 97% conversion to 2-butenes with a ~1:3 *cis*:*trans* ratio, the thermodynamic limit,[3] *via* ^{1}H NMR integrals). At all time points (ranging from t = 1-90 minutes), $^{31}P\{^1H\}$ NMR signals corresponding to the 1,2-difluorobenzene (**21**; δ 98.6, >98%)[47] and *n*-butenes (**3**; δ ~97.5, <2%)[1] complexes were observed.

Signals corresponding to the 1,3-butadiene complex (**18**; δ 82.0)[1] gradually intensified over the course of the experiment, approaching a ~1:1 intensity ratio with the 1,2-difluorobenzene complex (**21**) by 90 minutes. In 1,2-difluorobenzene (otherwise under the same conditions as in CH_2Cl_2), catalysis with **21** proceeded more slowly, achieving thermodynamic equilibrium only after t ~ 5 minutes. Across a one-hour experiment, $^{31}P\{^1H\}$ NMR spectroscopy revealed only the 1,2-difluorobenzene complex (**21**; δ 98.6).[12]

Catalyst **22** produced markedly lower activity in CH_2Cl_2, achieving equilibrium only after t ~ 5 minutes. At all time points $^{31}P\{^1H\}$ NMR spectroscopy revealed only the CH_2Cl_2-activated dimer (**24**; δ 98.0),[2] aptly demonstrating the more electron-donating nature of the ligand favouring oxidative activation of CH_2Cl_2. Catalysis proceeded on a similar timescale in 1,2-difluorobenzene, achieving equilibrium at t ~ 10 minutes. The 1,2-difluorobenzene complex (**22**; δ 117.7) was visible *via* $^{31}P\{^1H\}$ NMR spectroscopy at all time points. No 1,3-butadiene complex (**19**; δ 97.8) was observed at any time point.

For {(dcpe)Rh}$^+$ and {(dtbpe)Rh}$^+$ cationic fragments, all three sets of conditions studied[a] were conducive to catalysis, and the deactivation pathway for {(dcpe)Rh}$^+$ in CH_2Cl_2 mirrored that seen in the solid-state. This suggests that chemistry taking place inside a SMOM was 'solution-like', where the inert, plastic, and flexible $[BAr^F_4]^-$ anion array substituted for a weakly-coordinating solvent, even occasioning to coordinate in an η^6 fashion under both solid-state and solution-phase conditions,[1,12,13,46] in analogy to 1,2-difluorobenzene. The influence of the solvent over catalytic activity appeared analogous to the shift in solid-gas reactivity observed with modification of the counteranion.[6]b

This concept, of 'solution-like' behaviour by $[BAr^F_4]^-$ anions, has been evidenced previously in this Chapter, in the dramatic reorganisation seen in the order-disorder-order transition proceeding from SMOM **17** (Section 2.3.2), and will re-emerge in the subsequent Chapters. In the next Chapter, for instance, the solution-like behaviour of $[BAr^F_4]^-$ anions in the solid-state will take centre-stage, as we focus on their role in facilitating SC-SC transformations involving shifts in periodic structure.

[a] Homogeneous (CH_2Cl_2/1,2-difluorobenzene); heterogeneous batch; heterogeneous continuous flow.
[b] In the Introduction (Section 1.2.3), we explored the structure-activity relationship of a SMOM by substitution of the counteranion.

2.5 Conclusions

SMOMs of the general formula [(P_2)Rh(η^2,η^2-NBD)][BAr^F_4] (P_2 = chelating *bis*-phsophine) were successfully applied as solid-gas alkene isomerisation pre-catalysts under continuous flow conditions, the first time such SMOMs have been deployed in flow. Solid-gas conditions presented the distinct advantage of pure gas recoverability – an industrially appealing property – and the use of SMOMs as precisely defined complexes permitted careful analysis of the organometallic species involved.

Non-thermodynamic *cis*-selectivity for many SMOM pre-catalysts was observed under continuous flow conditions, where the steric constraints of the chelating *bis*-phosphine were shown to be crucially important in achieving this kinetic *cis*-selectivity.

The direct tunability of solid-gas catalysis was demonstrated through R-group, tether length, and tether identity modification, correspondingly affecting activity, on-stream lifetime, and 2-butene isomer selectivity, thus controlling the catalysis through bespoke molecular design.

2.6 References

[1] F. M. Chadwick, A. I. McKay, A. J. Martinez-Martinez, N. H. Rees, T. Krämer, S. A. Macgregor, A. S. Weller, *Chemical Science* **2017**, *8*, 6014–6029.

[2] A. J. Martínez-Martínez, C. G. Royle, S. K. Furfari, K. Suriye, A. S. Weller, *ACS Catalysis* **2020**, *10*, 1984–1992.

[3] J. G. Aston, G. Szasz, H. W. Woolley, F. G. Brickwedde, *The Journal of Chemical Physics* **1946**, *14*, 67–79.

[4] R. Poli, *Comments on Inorganic Chemistry* **2009**, *30*, 177–228.

[5] S. Kozuch, J. M. L. Martin, *ACS Catalysis* **2012**, *2*, 2787–2794.

[6] A. I. McKay, A. J. Martínez-Martínez, H. J. Griffiths, N. H. Rees, J. B. Waters, A. S. Weller, T. Krämer, S. A. Macgregor, *Organometallics* **2018**, *37*, 3524–3532.

[7] N. Poovarawan, K. Suriye, S. K. N. Ayudhya, J. Punpranot, F. J. C. S. Aires, P. Praserthdam, *Catalysis Letters* **2014**, *144*, 920–927.

[8] M. Ulman, R. H. Grubbs, *Organometallics* **1998**, *17*, 2484–2489.

[9] B. Brandt, W. Ludwig, J.-H. Fischer, J. Libuda, F. Zaera, S. Schauermann, *Journal of Catalysis* **2009**, *265*, 191–198.

[10] P. Longo, F. Grisi, G. Guerra, L. Cavallo, *Macromolecules* **2000**, *33*, 4647–4659.

[11] S. D. Pike, M. R. Crimmin, A. B. Chaplin, *Chemical Communications* **2017**, *53*, 3615–3633.

[12] S. D. Pike, F. M. Chadwick, N. H. Rees, M. P. Scott, A. S. Weller, T. Krämer, S. A. Macgregor, *Journal of the American Chemical Society* **2015**, *137*, 820–833.

[13] S. D. Pike, A. L. Thompson, A. G. Algarra, D. C. Apperley, S. A. Macgregor, A. S. Weller, *Science* **2012**, *337*, 1648–1651.

[14] A. J. Martínez-Martínez, B. E. Tegner, A. I. McKay, A. J. Bukvic, N. H. Rees, G. J. Tizzard, S. J. Coles, M. R. Warren, S. A. Macgregor, A. S. Weller, *Journal of the American Chemical Society* **2018**, *140*, 14958–14970.

[15] A. Döhring, R. Goddard, G. Hopp, P. W. Jolly, N. Kokel, C. Krüger, *Inorganica Chimica Acta* **1994**, *222*, 179–192.

[16] C. F. J. Barnard, *Organic Process Research & Development* **2008**, *12*, 566–574.

[17] S. K. Brayshaw, J. C. Green, R. Edge, E. J. L. McInnes, P. R. Raithby, J. E. Warren, A. S. Weller, *Angewandte Chemie International Edition* **2007**, *46*, 7844–7848.

[18] S. K. Furfari, B. E. Tegner, A. L. Burnage, L. R. Doyle, A. J. Bukvic, S. A. Macgregor, A. S. Weller, *Chemistry – A European Journal* **2021**, *27*, 3177–3183.

[19] C. A. Tolman, *Journal of the American Chemical Society* **1970**, *92*, 2953–2956.

[20] P. Bisel, L. Al-Momani, M. Müller, *Organic & Biomolecular Chemistry* **2008**, *6*, 2655–2665.

[21] A. N. Desnoyer, J. Geng, M. W. Drover, B. O. Patrick, J. A. Love, *Chemistry – A European Journal* **2017**, *23*, 11509–11512.

[22] S. Neumann, T. W. Gerl, F. Rominger, G. Scherhag, C. Meier, M. Metz, A. Albinati, P. Hofmann, *Organometallics* **2019**, *38*, 3358–3368.

[23] R. Waterman, G. L. Hillhouse, *Journal of the American Chemical Society* **2008**, *130*, 12628–12629.

[24] M. Reinhold, J. E. McGrady, R. N. Perutz, *Journal of the American Chemical Society* **2004**, *126*, 5268–5276.

[25] D. J. Mindiola, G. L. Hillhouse, *Journal of the American Chemical Society* **2001**, *123*, 4623–4624.

[26] A. B. Chaplin, J. F. Hooper, A. S. Weller, M. C. Willis, *Journal of the American Chemical Society* **2012**, *134*, 4885–4897.

[27] M. E. Fasulo, E. Calimano, J. M. Buchanan, T. D. Tilley, *Organometallics* **2013**, *32*, 1016–1028.

[28] M. T. Whited, L. Qiu, A. J. Kosanovich, D. E. Janzen, *Inorganic Chemistry* **2015**, *54*, 3670–3679.

[29] S. Debnath, S. Basu, B. M. Schmidt, J. J. Adams, N. Arulsamy, D. M. Roddick, *Polyhedron* **2020**, *181*, 114461.

[30] R. K. Merwin, R. C. Schnabel, J. D. Koola, D. M. Roddick, *Organometallics* **1992**, *11*, 2972–2978.

[31] A. S. C. Chan, C.-C. Pai, T.-K. Yang, S.-M. Chen, *Journal of the Chemical Society, Chemical Communications* **1995**, 2031–2032.

[32] G. E. M. Crisenza, O. O. Sokolova, J. F. Bower, *Angewandte Chemie International Edition* **2015**, *54*, 14866–14870.

[33] Z. Huang, P. S. White, M. Brookhart, *Nature* **2010**, *465*, 598–601.

[34] A. J. Martínez-Martínez, N. H. Rees, A. S. Weller, *Angewandte Chemie International Edition* **2019**, *58*, 16873–16877.

[35] S. Libri, M. Mahler, G. Mínguez Espallargas, D. C. N. G. Singh, J. Soleimannejad, H. Adams, M. D. Burgard, N. P. Rath, M. Brunelli, L. Brammer, *Angewandte Chemie International Edition* **2008**, *47*, 1693–1697.

[36] I. J. Vitórica-Yrezábal, G. Mínguez Espallargas, J. Soleimannejad, A. J. Florence, A. J. Fletcher, L. Brammer, *Chemical Science* **2013**, *4*, 696–708.

[37] S. M. Mansell, *Dalton Transactions* **2017**, *46*, 15157–15174.

[38] N. A. Cooley, S. M. Green, D. F. Wass, K. Heslop, A. G. Orpen, P. G. Pringle, *Organometallics* **2001**, *20*, 4769–4771.

[39] A. J. Rucklidge, D. S. McGuinness, R. P. Tooze, A. M. Z. Slawin, J. D. A. Pelletier, M. J. Hanton, P. B. Webb, *Organometallics* **2007**, *26*, 2782–2787.

[40] A. Bollmann, K. Blann, J. T. Dixon, F. M. Hess, E. Killian, H. Maumela, D. S. McGuinness, D. H. Morgan, A. Neveling, S. Otto, M. Overett, A. M. Z. Slawin, P. Wasserscheid, S. Kuhlmann, *Journal of the American Chemical Society* **2004**, *126*, 14712–14713.

[41] V. W.-W. Yam, C.-L. Chan, C.-K. Li, K. M.-C. Wong, *Coordination Chemistry Reviews* **2001**, *216–217*, 173–194.

[42] T. Imamoto, J. Watanabe, Y. Wada, H. Masuda, H. Yamada, H. Tsuruta, S. Matsukawa, K. Yamaguchi, *Journal of the American Chemical Society* **1998**, *120*, 1635–1636.

[43] E. Cristóbal-Lecina, P. Etayo, S. Doran, M. Revés, P. Martín-Gago, A. Grabulosa, A. R. Costantino, A. Vidal-Ferran, A. Riera, X. Verdaguer, *Advanced Synthesis & Catalysis* **2014**, *356*, 795–804.

[44] J. S. Ritch, T. Chivers, D. J. Eisler, H. M. Tuononen, *Chemistry – A European Journal* **2007**, *13*, 4643–4653.

[45] M. T. Whited, A. J. Kosanovich, D. E. Janzen, *Organometallics* **2014**, *33*, 1416–1422.

[46] A. I. McKay, T. Krämer, N. H. Rees, A. L. Thompson, K. E. Christensen, S. A. Macgregor, A. S. Weller, *Organometallics* **2017**, *36*, 22–25.

[47] F. M. Chadwick, N. H. Rees, A. S. Weller, T. Krämer, M. Iannuzzi, S. A. Macgregor, *Angewandte Chemie International Edition* **2016**, *55*, 3677–3681.

[48] A. J. Bukvic, A. L. Burnage, G. J. Tizzard, A. J. Martínez-Martínez, A. I. McKay, N. H. Rees, B. E. Tegner, T. Krämer, H. Fish, M. R. Warren, S. J. Coles, S. A. Macgregor, A. S. Weller, *Journal of the American Chemical Society* **2021**, *143*, 5106–5120.

[49] T. Allman, R. G. Goel, *Canadian Journal of Chemistry* **1982**, *60*, 716–722.

[50] D. Martin, D. Moraleda, T. Achard, L. Giordano, G. Buono, *Chemistry – A European Journal* **2011**, *17*, 12729–12740.

[51] M. N. Chevykalova, L. F. Manzhukova, N. v Artemova, Yu. N. Luzikov, I. E. Nifantev, E. E. Nifantev, *Russian Chemical Bulletin* **2003**, *52*, 78–84.

[52] F. M. Chadwick, N. Olliff, A. S. Weller, *Journal of Organometallic Chemistry* **2016**, *812*, 268–271.

[53] K. Tani, E. Tanigawa, Y. Tatsuno, S. Otsuka, *Journal of Organometallic Chemistry* **1985**, *279*, 87–101.

[54] A. Mannu, H.-J. Drexler, R. Thede, M. Ferro, W. Baumann, J. Rüger, D. Heller, *Journal of Organometallic Chemistry* **2018**, *871*, 178–184.

[55] G. E. Ball, W. R. Cullen, M. D. Fryzuk, B. R. James, S. J. Rettig, *Organometallics* **1991**, *10*, 3767–3769.

[56] P. M. Scheetz, N. F. Blank, S. K. Gibbons, D. S. Glueck, A. L. Rheingold, *Inorganica Chimica Acta* **2018**, *483*, 111–115.

[57] J.-C. Choi, K. Kohno, M. Otsuka, H. Yasuda, T. Sakakura, *Organometallics* **2011**, *30*, 6060–6062.

[58] I. R. McKeer, S. J. Sherlock, M. Cowie, *Journal of Organometallic Chemistry* **1988**, *352*, 205–222.

[59] G. G. Christoph, P. Blum, W. C. Liu, A. Elia, D. W. Meek, *Inorganic Chemistry* **1979**, *18*, 894–897.

[60] T. H. Brown, P. J. Green, *Journal of the American Chemical Society* **1970**, *92*, 2359–2362.

[61] C. S. Knee, J. Holmlund, J. Andreasson, M. Käll, S. G. Eriksson, L. Börjesson, *Physical Review B* **2005**, *71*, 214518.

[62] V. A. Bibik, N. A. Davydova, *Physica Status Solidi (B)* **1989**, *151*, 733–737.

[63] P. K. Allan, B. Xiao, S. J. Teat, J. W. Knight, R. E. Morris, *Journal of the American Chemical Society* **2010**, *132*, 3605–3611.

[64] Th. Dretschkow, Th. Wandlowski, *Electrochimica Acta* **1999**, *45*, 731–740.

[65] K. Heinz, E. Lang, K. Strauss, K. Müller, *Applications of Surface Science* **1982**, *11–12*, 611–624.

[66] T. Nakagawa, H. Okuyama, M. Nishijima, T. Aruga, H. W. Yeom, E. Rotenberg, B. Krenzer, S. D. Kevan, *Physical Review B* **2003**, *67*, 241401.

[67] R. Lopez, L. C. Feldman, R. F. Haglund Jr, *Physical review letters* **2004**, *93*, 177403.

[68] R. S. Ampapathi, A. L. Creath, D. I. Lou, J. W. Craft, S. R. Blanke, G. B. Legge, *Journal of Molecular Biology* **2008**, *377*, 748–760.

[69] M. Wolf-Watz, U. Olsson, *Biophysical Journal* **2012**, *102*, 50a.

[70] C. Pedone, E. Benedetti, *Journal of Organometallic Chemistry* **1971**, *29*, 443–449.

[71] E. O. Changamu, H. B. Friedrich, M. Rademeyer, *Journal of Organometallic Chemistry* **2008**, *693*, 164–168.

[72] K. F. Hirsekorn, E. B. Hulley, P. T. Wolczanski, T. R. Cundari, *Journal of the American Chemical Society* **2008**, *130*, 1183–1196.

[73] R. Goddard, P. Binger, S. R. Hall, P. + Müller, *Acta Crystallographica Section C: Crystal Structure Communications* **1990**, *46*, 998–1001.

[74] M. V. Jiménez, E. Sola, J. Caballero, F. J. Lahoz, L. A. Oro, *Angewandte Chemie International Edition* **2002**, *41*, 1208–1211.

[75] R. R. Schrock, J. Y. Jamieson, J. P. Araujo, P. J. Bonitatebus, A. Sinha, L. P. H. Lopez, *Journal of Organometallic Chemistry* **2003**, *684*, 56–67.

[76] H. M. Pritchard, M. Etienne, L. Vendier, G. S. McGrady, *Organometallics* **2004**, *23*, 1203–1206.

[77] G. E. Herberich, U. Englert, M. Hoeveler, I. Savvopoulos, *Journal of Organometallic Chemistry* **1990**, *399*, 35–46.

[78] S. G. Ridlen, N. v Kulkarni, H. V. R. Dias, *Inorganic Chemistry* **2017**, *56*, 7237–7246.

[79] K. Miki, K. Yamatoya, N. Kasai, H. Kurosawa, A. Urabe, M. Emoto, K. Tatsumi, A. Nakamura, *Journal of the American Chemical Society* **1988**, *110*, 3191–3198.

[80] D. Steinborn, V. v Potechin, M. Gerisch, C. Bruhn, H. Schmidt, *Transition Metal Chemistry* **1999**, *24*, 67–70.

[81] C. P. Casey, T. E. Vos, J. T. Brady, R. K. Hayashi, *Organometallics* **2003**, *22*, 1183–1195.

[82] E. Benedetti, P. Corradini, C. Pedone, *Journal of Organometallic Chemistry* **1969**, *18*, 203–208.

[83] V. Albano, F. Demartin, A. de Renzi, G. Morelli, A. Saporito, *Inorganic Chemistry* **1985**, *24*, 2032–2039.

[84] V. G. Albano, F. Demartin, B. di Blasio, G. Morelli, A. Panunzi, *Gaz. Chim. Ital* **1985**, *115*, 361–364.

[85] I. W. Levin, R. A. R. Pearce, *Journal of Molecular Spectroscopy* **1974**, *49*, 91–99.

[86] K. S. Pitzer, W. D. Gwinn, *The Journal of Chemical Physics* **1942**, *10*, 428–440.

[87] M. A. Murcko, H. Castejon, K. B. Wiberg, *The Journal of Physical Chemistry* **1996**, *100*, 16162–16168.

[88] L. J. Sewell, A. B. Chaplin, J. A. B. Abdalla, A. S. Weller, *Dalton Transactions* **2010**, *39*, 7437–7439.

[89] R. Dorta, E. D. Stevens, S. P. Nolan, *Journal of the American Chemical Society* **2004**, *126*, 5054–5055.

[90] A. Vigalok, O. Uzan, L. J. W. Shimon, Y. Ben-David, J. M. L. Martin, D. Milstein, *Journal of the American Chemical Society* **1998**, *120*, 12539–12544.

[91] S. K. Brayshaw, J. C. Green, G. Kociok-Köhn, E. L. Sceats, A. S. Weller, *Angewandte Chemie International Edition* **2006**, *45*, 452–456.

[92] T. M. Douglas, A. B. Chaplin, A. S. Weller, *Organometallics* **2008**, *27*, 2918–2921.

[93] J. E. Barquera-Lozada, A. Obenhuber, C. Hauf, W. Scherer, *The Journal of Physical Chemistry A* **2013**, *117*, 4304–4315.

[94] A. B. Crooks, K.-H. Yih, L. Li, J. C. Yang, S. Özkar, R. G. Finke, *ACS Catalysis* **2015**, *5*, 3342–3353.

[95] J. J. R. Frausto da Silva, *Journal of Chemical Education* **1983**, *60*, 390.

[96] A. E. Martell, in *Werner Centennial*, American Chemical Society, **1967**, pp. 19–272.

[97] C. A. Tolman, *Journal of the American Chemical Society* **1970**, *92*, 4217–4222.

[98] G. D. Pirngruber, K. Seshan, J. A. Lercher, *Microporous and Mesoporous Materials* **2000**, *38*, 221–237.

[99] A. R. Siedle, R. A. Newmark, *Organometallics* **1989**, *8*, 1442–1450.

[100] L. Falivene, Z. Cao, A. Petta, L. Serra, A. Poater, R. Oliva, V. Scarano, L. Cavallo, *Nature Chemistry* **2019**, *11*, 872–879.

[101] T. L. Hill, *The Journal of Chemical Physics* **1948**, *16*, 938–949.

[102] I. Lee, F. Delbecq, R. Morales, M. A. Albiter, F. Zaera, *Nature Materials* **2009**, *8*, 132–138.

[103] K. Mierzejewska, M. Bochtler, H. Czapinska, *Nucleic Acids Research* **2016**, *44*, 485–495.

[104] Z. L. Niemeyer, A. Milo, D. P. Hickey, M. S. Sigman, *Nature Chemistry* **2016**, *8*, 610–617.

[105] F. Obenaus, Droste W, Neumeister J, *Ullmann's Encyclopedia of Industrial Chemistry*, J. Wiley & Sons, Ltd, **2014**.

[106] S. L. Scott, *ACS Catalysis* **2018**, *8*, 8597–8599.

[107] J. J. H. B. Sattler, J. Ruiz-Martinez, E. Santillan-Jimenez, B. M. Weckhuysen, *Chemical Reviews* **2014**, *114*, 10613–10653.

[108] J.-R. Chang, S.-L. Chang, *Journal of Catalysis* **1998**, *176*, 42–51.

[109] J. Goetz, M. A. Volpe, R. Touroude, *Journal of Catalysis* **1996**, *164*, 369–377.

[110] R. J. van Haaren, K. Goubitz, J. Fraanje, G. P. F. van Strijdonck, H. Oevering, B. Coussens, J. N. H. Reek, P. C. J. Kamer, P. W. N. M. van Leeuwen, *Inorganic Chemistry* **2001**, *40*, 3363–3372.

[111] A. D. Wilson, A. J. M. Miller, D. L. DuBois, J. A. Labinger, J. E. Bercaw, *Inorganic Chemistry* **2010**, *49*, 3918–3926.

[112] S. M. M. Knapp, S. E. Shaner, D. Kim, D. Y. Shopov, J. A. Tendler, D. M. Pudalov, A. R. Chianese, *Organometallics* **2014**, *33*, 473–484.

[113] D. Gauthier, A. T. Lindhardt, E. P. K. Olsen, J. Overgaard, T. Skrydstrup, *Journal of the American Chemical Society* **2010**, *132*, 7998–8009.

[114] Y. Wang, C. Qin, X. Jia, X. Leng, Z. Huang, *Angewandte Chemie International Edition* **2017**, *56*, 1614–1618.

[115] M. Aizenberg, D. Milstein, *Journal of the Chemical Society, Chemical Communications* **1994**, 411–412.

[116] L. A. Wickramasinghe, P. R. Sharp, *Organometallics* **2015**, *34*, 3451–3454.

[117] I. Pernik, J. F. Hooper, A. B. Chaplin, A. S. Weller, M. C. Willis, *ACS Catalysis* **2012**, *2*, 2779–2786.

[118] A. L. Colebatch, A. I. McKay, N. A. Beattie, S. A. Macgregor, A. S. Weller, *European Journal of Inorganic Chemistry* **2017**, *2017*, 4533–4540.

This page intentionally left blank.

3 Single-Crystal to Single-Crystal Transformations in Solid-State Molecular Organometallics (SMOMs) with Shifts in Periodic Structure

3.1 Introduction

In the previous chapter, SMOMs of type [(P$_2$)Rh(η^2,η^2-NBD)][BAr$^F_4$] were systematically varied *via* modification of the chelating *bis*-phosphine ligand P$_2$, and the effects of both tether length and R-group[1] variation on solid-gas alkene isomerisation catalysis were explored. Variants with iridium centres[2] were also briefly explored to little success, generating an intractable mixture of dimeric hydridic products upon solid-state hydrogenation. A ligand set capable of exacting greater control over the metal centre was necessary.

Aside from its relatively straightforward synthesis,[3] a pyridine-based PONOP-type pincer chelate 2,6-(OP^{i}Pr$_2$)C$_5$H$_3$N was targeted in this work originally for three reasons: (1) to encourage P-donor stabilisation of both low and high oxidation states; (2) its provision of a highly stable κ^3-meridional ligand scaffold; and (3) to avoid complicating cooperative ligand Milstein-type chemistry,[4–6] due to the absence of acidic CH$_2$ (PNP) or NH (PNNNP) moieties. *Iso*-propyl groups were employed to establish conformational flexibility and a sterically unconstrainted active site.[7–11] Neutral PONOP was pursued in lieu of anionic POCOP so salts analogous to [(P$_2$)Rh(η^2,η^2-NBD)][BAr$^F_4$] might be produced, and in the same way, through the presence of a flexible array of anions, permit single-crystal to single-crystal (SC-SC) solid-gas reactivity.

In the Introduction, a wealth of periodic structure-retaining SC-SC transformations were discussed, where the transition from one species to another occurred with retention of both crystallinity and packing motif, such that initial atom positions were approximately preserved in the product (apart from certain ligands directly involved in the chemical transformation, such as η^2,η^2-NBD → σ-NBA). As this project matured, focus shifted away from catalysis and onto periodic structure-shifting (PSS) SC-SC transformations where the packing pattern of the parent crystal was *not* strictly preserved but overall crystallinity *was*.

These so-called 'PSS' SC-SC transformations constitute an intriguing and substantially less common case[12–14] of the already unusual SC-SC phenomenon. Across SC-SC transformations involving SMOMs, the positions of both the cationic fragment $\{(P_2)Rh\}^+$ and the $[BAr^F{}_4]^-$ anions forming the 'microenvironment' generally have remained locked. Only a handful of exceptions have been reported, discussed below.

In the SC-SC hydrogenation of $[(dcyppe)Rh(\eta^2,\eta^2\text{-NBD})][BAr^F{}_4]$ (dcyppe = $Cyp_2P(CH_2)_2PCyp_2$; **8**), for example, the resulting $\{(dcyppe)Rh\}^+$ fragment shifted significantly from its starting position, twisting ~90° inside a static microenvironment of anions (**Figure 3.1.1**).[15] Spontaneous reordering was noted after amorphous $[(dippe)Rh(\eta^6\text{-}Ar^F\text{-}BAr^F{}_3)]$ (dippe = $^iPr_2P(CH_2)_2P^iPr_2$; **29**), generated by solid-state displacement of σ-NBA by $[BAr^F{}_4]^-$, was gently heated to 50 °C.[16] In Chapter 2,[a] a remarkable PSS order-disorder-order transition proceeding from $[(dtbpe)Rh(\eta^2,\eta^2\text{-NBD})][BAr^F{}_4]$ (dtbpe = $^tBu_2P(CH_2)_2P^tBu_2$; **17**) was discussed.[17] These exceptions reveal that these structures are not necessarily static and can exhibit considerable plasticity.

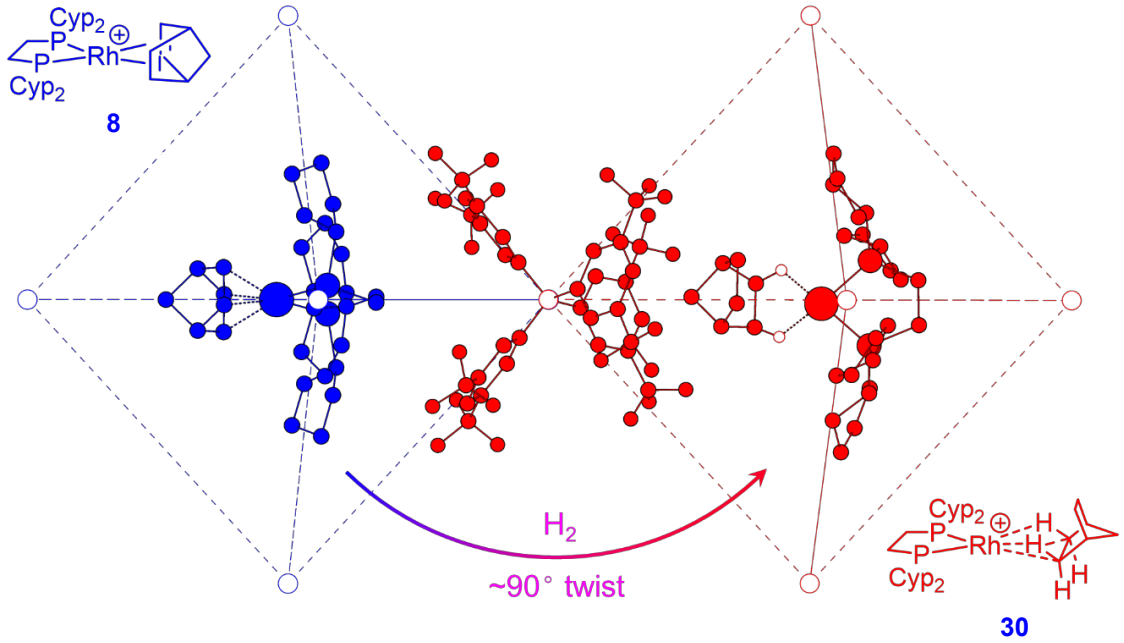


Figure 3.1.1: Two octahedral (O_h) motifs of the solid-state structure of $[(dcyppe)Rh(\eta^2,\eta^2\text{-NBD})][BAr^F{}_4]$ (**8**), viewed in the x-y plane. H atoms and anions (except one bridging) omitted for clarity. Cationic fragments rendered as ball-and-stick, with B–B 'bonds' included as dashed lines. (**left**) Cationic fragment $[(dcyppe)Rh(\eta^2,\eta^2\text{-NBD})]^+$ in blue. (**right**) Cationic fragment $[(dcyppe)Rh(\sigma\text{-NBA})]^+$ in blue, inserted into the structure and viewed in the same orientation. Constructed from structural data found in the reference.[15]

[a] Section 2.3.2

The influence of -CF_3 groups over solid-state reactivity in SMOMs was highlighted when different anions, such as $[BPh_4]^-$, were used to deleterious effect (Section 1.2.3).[18] Hydrophobic fluorinated groups (*e.g.* -CF_3, C_{arene}-F) have been reported to tolerate transformations involving significant structural change while maintaining crystallinity,[19–21] indicating a plastic quality. In the Introduction, the concept of *porosity without pores* was introduced: Brammer and colleagues have proposed a mechanism for the passage of small molecules through essentially non-porous structures involving the cooperative motion of rotating/oscillating fluoroalkyl moieties,[22,23] also manifested as disorder on the $[BAr^F_4]^-$ anions in SMOM-type solid-state structures. This mechanism was invoked by the Weller group in their study on a SMOM shown to undergo reversible, SC-SC, periodic structure-retaining encapsulation of xenon gas (Section 1.1.5).[24]

In this chapter, we will examine two different systems exhibiting periodic structure-shifting (PSS) SC-SC transformations (**Figure 3.1.2**): one H_2-induced, and another induced by loss of co-crystallised solvent molecules from the lattice. The former system (based on pincer complex **35**) is an example of a PONOP-bound iridium(I) SMOM, exploiting the exquisite stereo-electronic control and inherent thermodynamic stability of the pincer motif.[25] The latter system (based on complex **13-I**) is a more typical P_2-type rhodium(I) SMOM with a C_6F_5-bearing *bis*-phosphine chelate, approached because we were interested to explore further the implications of fluorinated groups by expanding their use onto the cation as well as the anion, anticipating greater possibilities for solid-state rearrangements.

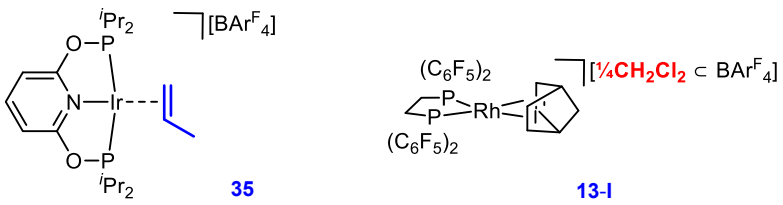


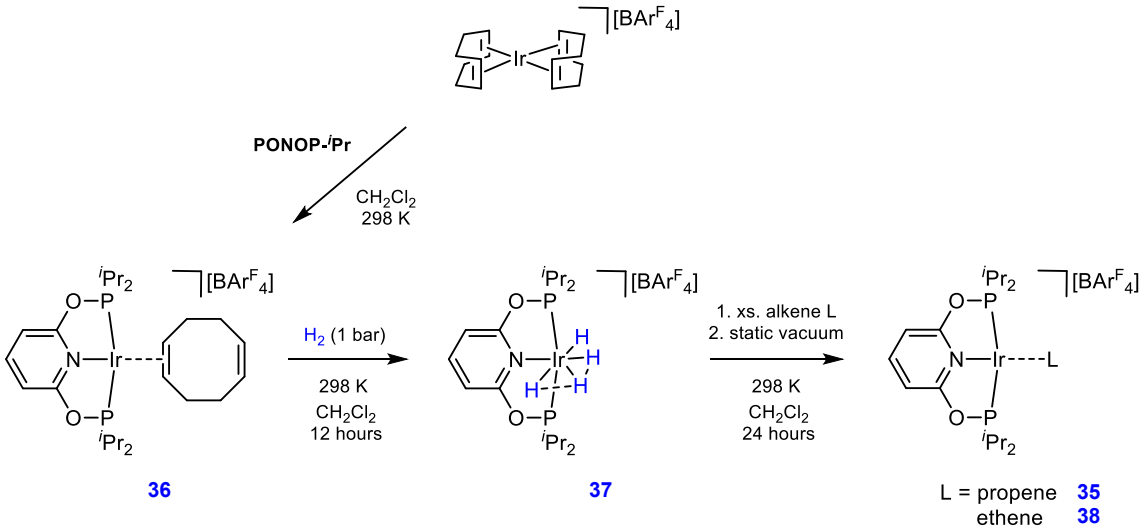
Figure 3.1.2: The two SMOMs to be examined for 'PSS' SC-SC transformations in this chapter.

Although SMOMs **35** and **13-I** are quite different in their chemical make-up, they have been grouped together in this chapter under the umbrella theme of unusual 'PSS' (periodic structure-shifting) SC-SC transformations, facilitated by flexible structures composed largely of fluorinated groups.

3.2 PONOP Pincer-Iridium Solid-Gas Hydrogenation Chemistry

3.2.1 Solution-Phase Synthesis and Characterisation of PONOP-Iridium(I) Precursor SMOMs [(ⁱPr-PONOP)Ir(η²-alkene)][BAr$^F_4$] (alkene = propene, ethene)

Before any SC-SC chemistry is discussed, the syntheses of all the SMOMs that will enter the discussion in this Chapter will be introduced. [(ⁱPr-PONOP)Ir(η^2-COD)][BAr$^F_4$] (**36**) was synthesised analogously to its Rh-containing and ⁱPr-PNP analogues:[26,27] a solution of [Ir(η^2,η^2-COD)$_2$][BAr$^F_4$][28] in CH_2Cl_2 was treated with free ligand ⁱPr-PONOP in the presence of excess COD to prevent the formation of an η^2,η^2-bridging dimer,[29] ultimately yielding analytically pure **36** after recrystallisation from CH_2Cl_2 and pentane at 298 K (**Scheme 3.2.1**). Characterising information for this synthetic intermediate is given in Chapter 5.



Scheme 3.2.1: Synthesis of new [(ⁱPr-PONOP)Ir(η^2-alkene)][BAr$^F_4$] target SMOMs **35** and **38**.

The synthesis of iridium(I) olefin complexes **35** and **38** proceeded from **36**. CH_2Cl_2 solutions of complex **36** were treated with H_2 (1 bar) at 298 K, liberating *cyclo*-octane and yielding non-classical 'tetrahydride' **37** *in situ* (*vide infra*). Five charges of alkene atmosphere (ethene or propene) were then introduced, after which the reaction mixture was exposed to multiple freeze-pump-thaw cycles to encourage egress of H_2 from solution. Single-crystalline material was obtained in near-quantitative yields (≥90%) by layering CH_2Cl_2 solutions with pentane at 298 K (**35**) or 273 K (**38**) under an N_2 atmosphere.

While most P_2-type SMOMs are known to exhibit octahedral-type (O_h) packing motifs,[a] three examples of bicapped parallelepiped-type (BCPP) have been noted,[16,18,30] where two cationic fragments are surrounded in the solid-state by 10 $[BAr^F_4]^-$ anions. Solid-state structures obtained for all iridium(I)-alkene derivatives (**35**, **36**, **38**) observed either O_h (**38**, $P2_1/c$) or BCPP (**35** and **36**, $P\bar{1}$) structure types. Interestingly, ethene complex **38** (**Figure 3.2.1**) did not share the same packing pattern as its rhodium-containing analogue (BCPP, $P\bar{1}$).[26] Crystallisation of propene complex **35** from CH_2Cl_2 yielded the solvent-containing structure **35**·½CH_2Cl_2 (O_h, $C2/c$); crystallisation from 1,2-difluorobenzene yielded a structure containing no co-crystallised solvent (BCPP, $P\bar{1}$; **Figure 3.2.2** and **Figure 3.2.3**). Altogether, this evidences the close energetic relationship between these two structure types.

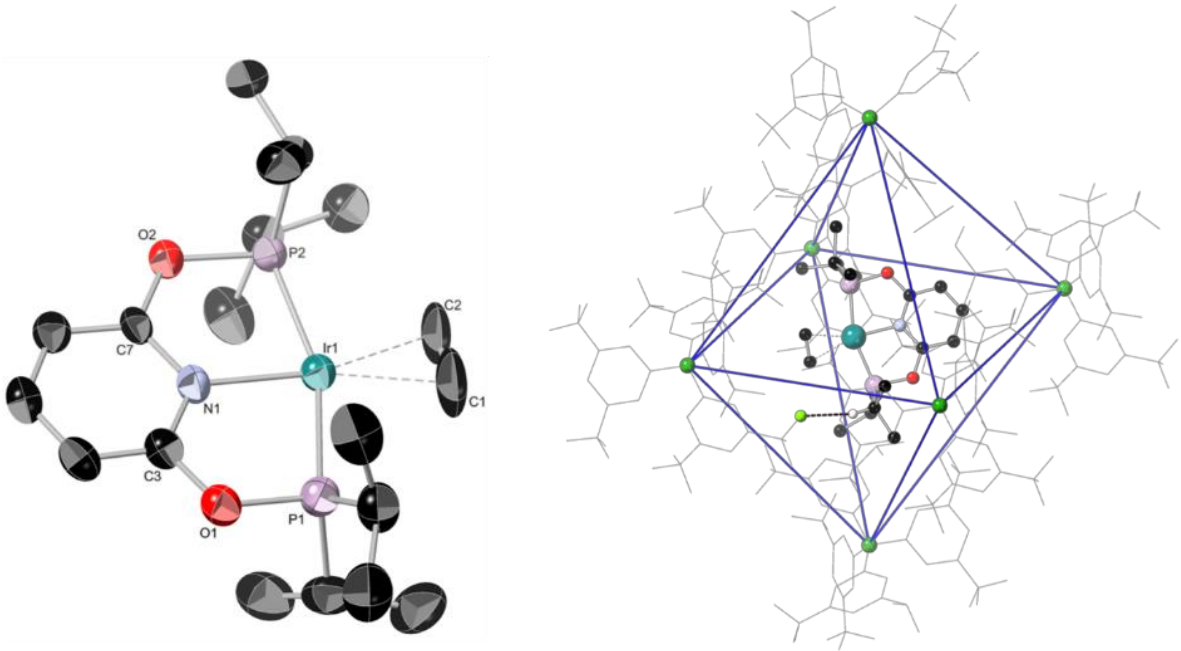


Figure 3.2.1: (**left**) Metal-containing fragment [(^{i}Pr-PONOP)Ir(η^2-C_2H_4)]$^+$ of **38**. 50% displacement ellipsoids. Anions and H atoms omitted for clarity. Selected bond lengths (Å), angles (deg), and torsion angles (deg), where Cent is the centroid of C1–C2: Ir1–P1, 2.2581(11), Ir1–P2, 2.2604(12); Ir1–N1, 2.047(3); Ir1–C1, 2.138(6); Ir1–Cent, 2.0465(2); Ir1–C2, 2.155(5); C1–C2, 1.292(8); P1–Ir1–N1, 2.047(3); P2–Ir1–N1, 80.58(10); P1–Ir1–Cent, 99.95(3); P2–Ir1–Cent, 99.58(3); P1–Ir1–Cent–C1, 23.1(8). (**right**) The octahedral (O_h) coordination of six $[BAr^F_4]^-$ anions (modelled as wireframes with B atoms balls) about a cavity containing a [(^{i}Pr-PONOP)Ir(η^2-C_2H_4)]$^+$ fragment (modelled as ball-and-stick). H atoms omitted except H8 ··· F13 close approach of 2.559(3) Å, highlighted in red.

[a] See Chapter 2 (Section 2.2.4) for a discussion of the O_h and BCPP structure types.

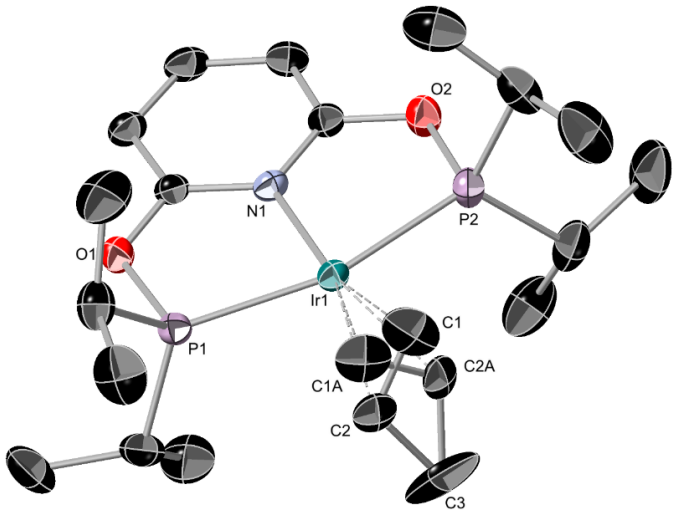


Figure 3.2.2: Metal-containing fragment [(^{i}Pr-PONOP)Ir(η^2-propene)]$^+$ of **35** as recrystallised from 1,2-difluorobenzene/pentane, with both propene ligand disorder components shown (~58:42 by chemical occupancies). 50% displacement ellipsoids. Anions and H atoms omitted for clarity. Selected bond lengths (Å), angles (deg), and torsion angles (deg), where Cent is the centroid of C1–C2 and Cent' the centroid of C1A–C2A: Ir1–P1, 2.2600(5), Ir1–P2, 2.2613(5); Ir1–N1, 2.0486(15); P1–O1, 1.6777(14); P2–O2, 1.6785(15); Ir1–C1, 2.160(5); Ir1–Cent, 2.05989(13); Ir1–C2, 2.208(4); Ir1–C1A, 2.155(6); Ir1–Cent', 2.07424(13); Ir1–C2A, 2.190(5); C1–C2, 1.369(10); C1A–C2A, 1.381(13); C2–C3, 1.512(6); C2A–C3A, 1.516(8); N1–Ir1–P1, 80.44(5); N1–Ir1–P2, 80.54(5); P1–Ir1–Cent', 97.515(13); P2–Ir1–Cent, 97.701(12); C1–C2–C3, 121.1(6); C1A–C2A–C3A, 118.1(7); P1–Ir1–Cent'–C1A, 55.3(10); P2–Ir1–Cent–C1, 65.8(8).

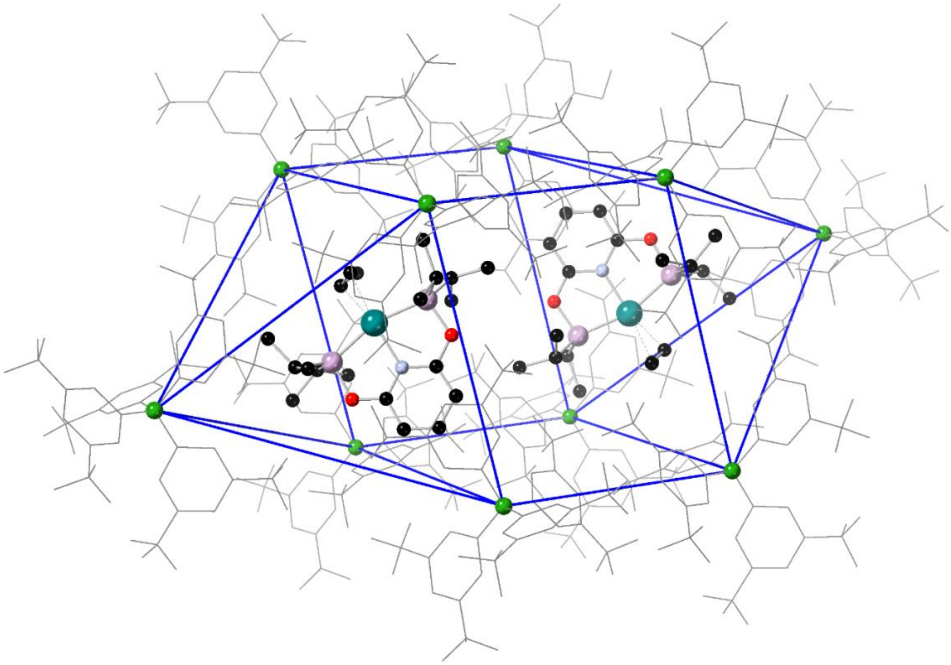


Figure 3.2.3: The bicapped parallelepipedic (BCPP) coordination of 10 [BAr$^F{}_4$]$^-$ anions (modelled as wireframes with B atoms balls) about a cavity containing two [(^{i}Pr-PONOP)Ir(η^2-propene)]$^+$ fragments (modelled as ball-and-stick) in SMOM **35**. H atoms omitted for clarity.

Two propene ligand disorder components in the solid-state structure of **35** (**Figure 3.2.2**) were related by an approximate mirror plane parallel to the Ir–N bond and perpendicular to the C_5N plane, with freely refined chemical occupancies of ~58:42. In both components, similar and unambiguous metrics were obtained, with clearly differentiated double (1.369(10), 1.381(13) Å) and single (1.512(6), 1.516(8) Å) bonds.

The average IrP_2N-alkene plane angle β in [(^{i}Pr-PONOP)Ir(η^2-alkene)][BAr^F_4] was noted to increase with increasing steric demand of the alkene substituent, rising in the order **38** (~23°), **35** (~60°), **36** (~64°). The rhodium-containing analogue of **38** was reported with β of only ~4.6°.[26]

Two general coordination modes of ethylene to {(pincer)M} (M = Rh, Ir) centres have been reported: in-plane/parallel (∥) coordination, where the π-bond runs approximately parallel to P–M–P and denotes back-donation principally from d_{xy} (where the plane x,y corresponds to the plane of {(pincer)M}), with β approaching 0°; and perpendicular (⊥) coordination, denoting back-donation principally from d_{xz} (**Figure 3.2.4**), with β approaching 90°.[31–33]

The selection of one mode over the other depends on a subtle interplay of steric and electronic effects. Increasing steric hindrance at the metal is known to favour ⊥-coordination, while E = CH_2→O substitution on the tether favours ∥-coordination by increasing the π-acidity of the P-atom donors.[32] ∥-coordination has been observed in pincers containing a strongly π-accepting boryl donor.[34–37]

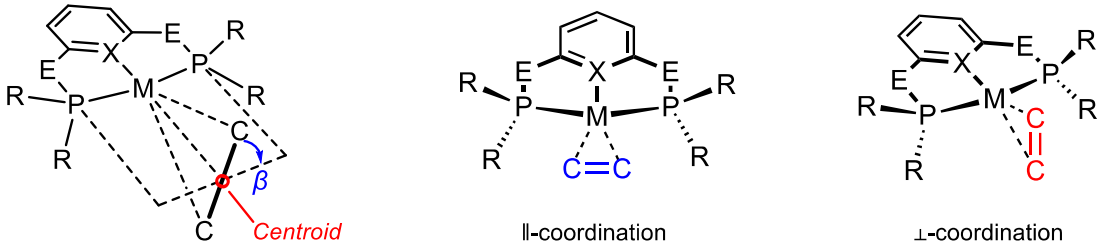


Figure 3.2.4: Definition of plane angle β for pincer-M(I) complexes (M = Rh, Ir) approximately equal to the average torsion angle between M–P and C_{alkene}–Centroid, and two extreme coordination modes of an ethene π-bond to a {(pincer)M}$^+$ (M = Rh, Ir) fragment.

We observed ∥-coordination in both **38** and its rhodium congener,[26] with average MP_2N-alkene plane angles β ~ 0.4° (M = Rh) and ~23° (M = Ir). Related complex [(^{i}Pr-PNP)Rh(η^2-C_2H_4)][BF_4], with a similar steric profile and differing only in the identity of the tethering moiety E, possessed a plane angle β ~ 74° (approaching ⊥-coordination).[6] This indicates the importance of the π-acidic phosphite donors in determining the coordination geometry.

While no disorder could be resolved on the ethene moiety in the solid-state structure of complex **38** (**Figure 3.2.1**), the C1–C2 π-bond distance of 1.292(8) Å is somewhat short compared to those found in similar [(pincer)Ir(η^2-C_2H_4)]$^+$ complexes, normally in the range 1.35–1.40 Å.[31,38,39] This indicates the possibility of some unresolved disorder similar to that observed in propene complex **35** (**Figure 3.2.2**).

As a result of the particularly high quality of the crystals of **35** as obtained from 1,2-difluorobenzene and pentane (R_1 = 1.90%, R_{int} = 1.98%), these crystals presented an ideal 'launching pad' for SC–SC reactivity, as SC–SC transformations usually result in some loss of data quality.

By solution-phase NMR spectroscopy, ethene complex **38** possessed a time-averaged C_{2v} symmetry at the metal centre, with a single alkene resonance resolved in the solution ^{1}H NMR spectrum (δ 3.09), alongside single resonances for ^{i}Pr methyl and methine protons. A single $^{31}P\{^1H\}$ NMR resonance in solution (δ 191.8) was also observed in the solid-state (δ ~194.0), although upon closer inspection satellite-like peaks together with the central 'singlet' were more accurately modelled as two doublets experiencing severe second-order coupling (δ 193.7, 194.3; $^2J_{PP'}$ ~ 300 Hz), consistent with the presence of crystallographically inequivalent phosphorus atoms in the solid-state structure (**Figure 3.2.1**).

Such solid-state splitting effects on account of crystallographic inequivalence have been noted previously by the Weller group[40] as well as in a report by Henn and colleagues on pincer-Sn(II) complexes,[41] and previously in this thesis.[a]

[a] See Chapter 2 (Section 2.2.4), where $^{31}P\{^1H\}$ SSNMR spectra were collected for {(dtbpe)Rh}$^+$-containing species **17** and **25**, giving rise to resonance manifolds incompatible with crystallographically equivalent P-donor atoms (*i.e.* not a simple doublet, rather a partially-coincident pair of ^{31}P–^{103}Rh doublets for which ^{31}P–^{31}P coupling was not resolved).

A single ethene $^{13}C\{^{1}H\}$ NMR resonance was evident in both solution (δ 37.3) and the solid-state (δ 38.4) at 298 K. Other $^{13}C\{^{1}H\}$ SSNMR resonances bore the effects of crystallographic inequivalence: C_5N *meta*-^{13}C produced a single resonance in solution at 298 K (δ 103.5) and two in the solid-state (δ 103.1, 103.6), likewise for ^{i}Pr methine (δ 30.7; *cf.* 30.2, 32.1). Note that in the latter case one would expect *four* such resonances, as all four ^{i}Pr methine ^{13}C atoms were crystallographically inequivalent. We suggest that libration of the ethene ligand gave rise to effective C_2 symmetry in the solid-state and thus coincidences in the $^{13}C\{^{1}H\}$ SSNMR spectrum. Solid-state inequivalence was also evident for *ortho*, *meta*, and *para* $[BAr^{F}_{4}]^{-}$ positions, and at least five SSNMR resonances were resolved for ^{i}Pr methyl $^{13}CH_3$ in the range δ 13–18, for which eight crystallographically distinct carbons were refined for only two observed in solution (δ 16.5, 17.1).

Propene complex **35**, with its unsymmetrical alkene ligand, produced a somewhat more complicated ^{1}H NMR spectrum (**Figure 3.2.5**) than ethene complex **38**. Alkene-associated resonances were resolved at δ 1.72 (H_D), 3.08 (H_A), 3.40 (H_B), and 4.33 (H_C), the latter a doublet of doublets of quartets of triplets.

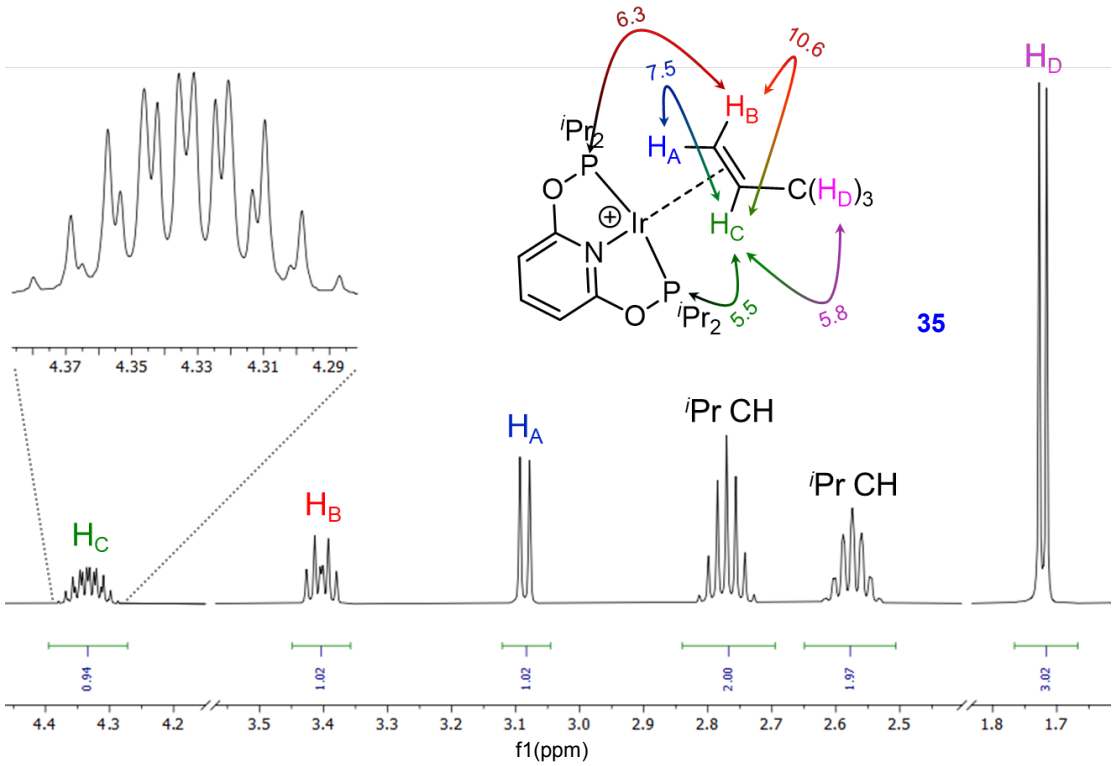


Figure 3.2.5: Sections of the ^{1}H NMR spectrum (500.23 MHz, CD_2Cl_2, 298 K) of propene complex **35**, with *J*-coupling constants labelled in Hz. Couplings to ^{31}P were differentiated with ^{31}P-decoupling experiments.

A solution-phase $^{31}P\{^{1}H\}$ NMR singlet (δ 188.6) resolved into a pair of roofed doublets in the solid-state (δ 189.5, 194.1; $^{2}J_{PP'}$ ~ 310 Hz), again reflecting inequivalence. Alkene-associated resonances also exhibited splitting in the $^{13}C\{^{1}H\}$ SSNMR spectrum, at both the methine (δ 54.8 → 56.6, 57.4; solution → solid-state) and methylene (δ 42.6 → 42.7, 44.6) positions. This evokes the solid-state structure of **35** (**Figure 3.2.2**) in which the propene ligand exhibited non-crystallographically imposed disorder over two positions.

3.2.2 Synthesis and Characterisation of PONOP-Iridium(III) Hydrides by Solution-Phase Hydrogenation of PONOP-Iridium(I) Alkene Complex Precursors

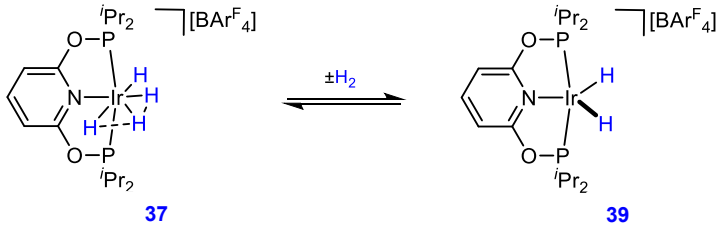
Exposure of iridium(I) alkene complexes **35**, **36**,[a] and **38** to H_2 on an NMR scale in CD_2Cl_2 solution at 298 K resulted in rapid hydrogenation of the alkene fragments to yield the 'tetrahydride' **37**, more aptly described as an iridium(III) complex [(^{i}Pr-PONOP)Ir(H)$_2$(σ-H$_2$)][BAr$^{F}_4$] possessing a highly fluxional manifold of hydrides at all surveyed temperatures (183–298 K), visible as a broad resonance (δ −8.75) integrating to 4 H relative to [BAr$^{F}_4$]$^-$. [(^{t}Bu-PONOP)Ir(H)$_2$(σ-H$_2$)][BAr$^{F}_4$], the previously reported ^{t}Bu analogue, exhibited a broad hydridic resonance at 193 K, also integrating to 4 H (δ −8.44).[42]

Spin-lattice relaxation time (T_1) measurements[43] were obtained for 'tetrahydride' **37** at 295 K (119 ± 8 ms) and 253 K (38 ± 1 ms) under a pressure of H_2 (1.5 bar).[b] The former value closely resembles values previously reported for polyhydrides of type [(^{t}Bu-PCP, POCOP)IrH$_4$] (T_1 ~ 110–130 ms) for which classical Ir(V) was calculated to be the ground state;[44] the latter value approaches the values observed for true dihydrogen complexes (T_1 < 50 ms).[26,45–47] This behaviour is reminiscent of non-classical tetrahydride [(triphos)Ir(H)$_2$(σ-H$_2$)][BPh$_4$], where a T_1 time was recorded at 273 K (145 ms) and 181 K (36 ms, the coalescence point).[48] The authors suggested a decreasing contribution of non-classical protons and an increasingly intact dihydrogen ligand with decreasing temperature, in line with other reports of such behaviour in fluxional polyhydrides by Crabtree and others.[43,49–51]

[a] Solution-phase hydrogenations of COD complex **36** on larger scales were allowed considerably longer reaction times, on the order of days (see Chapter 5), due to the formation of recalcitrant, poorly-characterised bridging dimers under such conditions.
[b] T_1 measurements were carried out by the inversion-recovery method using a standard 180°-θ-90° pulse sequence. Here, the presence of an H_2 atmosphere is required to prevent loss of H_2 (*vide infra*).

It is possible, therefore, that the various hydride/dihydrogen isomers of **37** were rapidly interconverting, permitting hydride permutation *via* a combination of σ-CAM[52] and free rotation of σ-H_2. Replacing the H_2 atmosphere with D_2 confirmed the lability of the hydrides: the 'tetradeuteride' d_4-**37** was generated, for which the solution ^{1}H NMR hydridic resonance was naturally now absent, and a new ^{2}H NMR signal was resolved (δ −8.70). Rapid H-D scrambling/permutation generated free HD (δ 4.55, $^1J_{HD}$ = 43 Hz; 298 K, CD_2Cl_2), a phenomenon also observed for Rh-centred [(^{i}Pr-PONOP)Rh(σ-H_2)][BAr^F_4].[26]

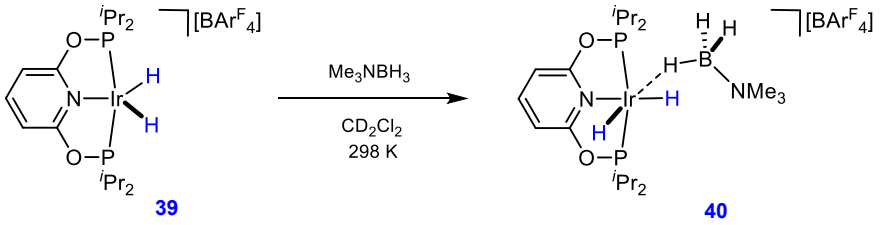
In the absence of an H_2 atmosphere, solutions of 'tetrahydride' **37** slowly lost H_2 to yield dihydride **39** (**Scheme 3.2.2**). Concomitantly, the solution ^{1}H NMR hydridic resonance shifted upfield, to δ −19.85, now integrating to 2 H relative to [BAr^F_4]$^-$ (compare the previously reported ^{t}Bu-PONOP analogue, resonating at δ −25.07).[46] A T_1 measurement at 295 K indicated classical hydrides (1870 ± 10 ms).[53–56] The solution ^{31}P{^{1}H} NMR resonance also shifted downfield, from δ 181.2 to 183.3.



Scheme 3.2.2: The equilibrium between non-classical 'tetrahydride' **37** and classical dihydride **39**.

Under the conditions of electrospray ionisation (ESI) mass spectrometry, **39** proved unstable with respect to loss of H_2: a CH_2Cl_2 solution produced mass peaks at both *m*/*z* 538.1604 (**39**, calc. 538.1616) and 536.1460 ({(^{i}Pr-PONOP)Ir}$^+$, calc. 536.1459, ~50% relative intensity).

Attempts to crystallise **37** or **39** failed, in both cases yielding pale yellow oils. Solutions of these hydrides could be evaporated to dryness *in vacuo* to yield an analytically pure pale orange solid (exclusively as dihydride **39**). Crystallisation could be induced, however, by saturating the 16-electron dihydride **39** with trimethylamine-borane (TMAB; **Scheme 3.2.3**).



Scheme 3.2.3: Synthesis of pincer-iridium(III) σ-TMAB complex **40**.

A solid sample of dihydride **39** was generated as above and combined with TMAB (~1.5 equivalents) in CD_2Cl_2 inside an NMR tube. The resulting η^1-σ-TMAB complex **40** was solution-stable as iridium(III) in the absence of an H_2 atmosphere at 298 K. Characteristic of a *cis* arrangement of hydrides, ^{1}H NMR spectroscopy revealed two resonances in a 1:1 integral ratio, at δ –20.00 (td, $^2J_{HP}$ = 17.3 Hz, $^2J_{HH}$ ~ 6 Hz), and –15.91 (td, $^2J_{HP}$ = 12.0 Hz, $^2J_{HH}$ = 6 Hz). Indicating rapid exchange between Ir–*H*–B bridging and B–*H* terminal positions at 298 K, a broad signal integrating to 3 H relative to $[BAr^F_4]^-$ was identified at δ –2.20. ^{11}B{^{1}H} NMR spectroscopy revealed a resonance at δ –14.7 (in addition to $[BAr^F_4]^-$ at δ –6.63).

A CD_2Cl_2 solution of **40** was layered with pentane inside the NMR tube, yielding a small number of high quality (R_1 = 2.6 %) colourless cuboidal crystals after one week. Both metal hydrides and borohydrides were located in the solid-state structure (**Figure 3.2.6**) and freely refined. Existing examples of iridium-bound σ-TMAB complexes are all η^2, with narrower Ir–H–B angles (~85-90°, *cf.* **40** at 134(2)°) and slightly longer σ-bound B–H bond lengths (~1.2-1.4 Å, *cf.* **40** at ~1.0-1.2 Å).[57–59]

Complex **40** marks the first example of an η^1 iridium-bound σ-borane, and it compares well metrically to the similar $[(XantPhos)RhH_2(\eta^1\text{-}\sigma\text{-TMAB})][BAr^F_4]$ as reported by Johnson and colleagues: a comparable Ir···H_{TMAB} distance (1.74(3) *versus* 1.7542(9) Å), and similar B–H bond lengths (1.26(3) *versus* 1.246(9) Å bound and ~1.05-1.10 *versus* ~0.95-1.00 Å spectating).[60]

The related σ-silane complex $[(^t$Bu-POCOP$)IrH(\sigma\text{-HSiEt}_3)][B(C_6F_5)_4]$, as reported by Brookhart and colleagues, possessed a somewhat longer σ-bound Ir–H distance, refined to 1.94(3) Å.[61]

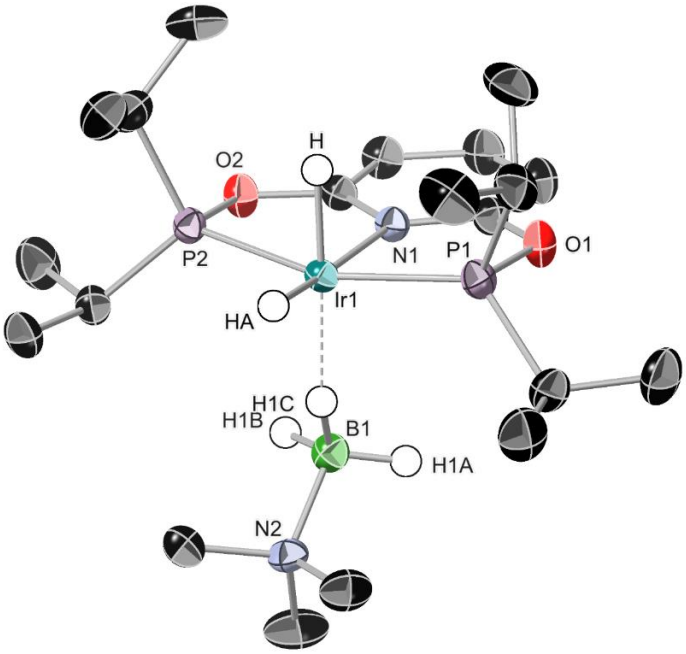
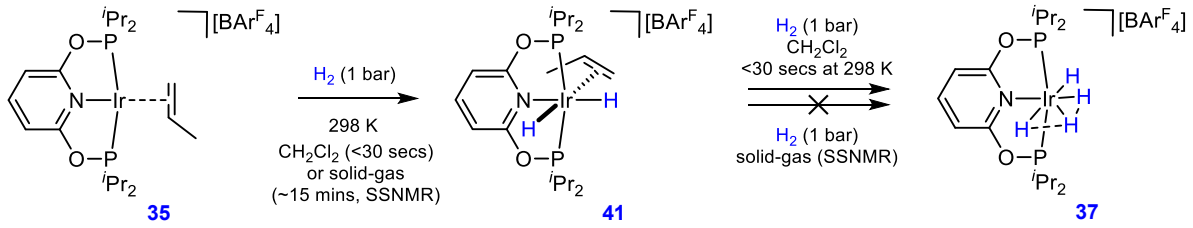


Figure 3.2.6: Cationic fragment [*cis*-(^{i}Pr-PONOP)IrH$_2$(η^1-σ-H$_3$BNMe$_3$)]$^+$ of **40**. 50% displacement ellipsoids. H atoms and anions omitted for clarity except crystallographically-located metal hydrides and borohydrides. Selected bond lengths (Å) and angles (deg): Ir1–P1, 2.2621(7); Ir1–P2, 2.2660(6); Ir1–N1, 2.103(2); Ir1–H, 1.55(2); Ir1–HA, 1.56(3); Ir1–H1C, 1.74(3); B1–H1C, 1.26(3); B1–H1A, 1.05(3); B1–H1B, 1.10(3); B1–N2, 1.617(4); P1–O1, 1.679(2); P2–O2, 1.6830(18); N1–Ir1–P1, 80.51(7); N1–Ir1–P2, 80.25(7); P1–Ir1–HA, 96.8(13); P2–Ir1–HA, 101.6(13); N1–Ir1–H, 90.7(10); H–Ir1 HA, 84.7(16); HA–Ir1–H1C, 84.1(17); N1–Ir1–H1C, 100.3(12); Ir1–H1C–B1, 134(2); N2–B1–H1C, 99.6(15).

*3.2.3 PONOP-Iridium(III) Propene-Dihydride [(^{i}Pr-PONOP)IrH$_2$(η^2-propene)][BAr$^F{}_4$] (**41**): Solid-State and Low-Temperature Solution-Phase Synthesis*

The presence of an Ir(III) alkene-dihydride as a solution-phase hydrogenation intermediate in the generation of 'tetrahydride' **37** from Ir(I) complexes **35**, **36** and **38** was suspected, in common with observations made as early as 1977 in the work of Crabtree and colleagues, investigating mechanisms of alkene hydrogenation by iridium-centred catalysts.[62] A unifying characteristic of many reported Ir(III) alkene-dihydrides is their instability with respect towards insertion-elimination or reductive elimination of H_2, such that characterisation has generally required bulky ligands or low temperatures to kinetically stabilise and characterise these reactive species.[62–67] We will now demonstrate that it is possible to use the solid-state to stabilise Ir(III) alkene-dihydrides, turning first to the hydrogenation chemistry of propene complex **35**.



Scheme 3.2.4: Synthesis of Ir(III) propene-dihydride complex **41** by both solid-state and solution routes.

Ir(I)-propene complex **35** converted promptly to Ir(III) propene-dihydride **41** upon solid-gas exposure to H_2 (**Scheme 3.2.4**), accompanied by a powder colour change from orange to white and requiring ~15 minutes' exposure inside an SSNMR rotor (**Figure 3.2.7** and **Figure 3.2.8**). Conversion was never recorded to exceed ~90% due to facile reversible loss of H_2 occurring inside the rotor, even under a gentle, brief purging flow of argon. This was visible as a powder colour *reversion* from white (pure propene-dihydride **41**) to pale pink (solid-state mixture of **41** and **35**) immediately upon removal of the H_2 atmosphere.

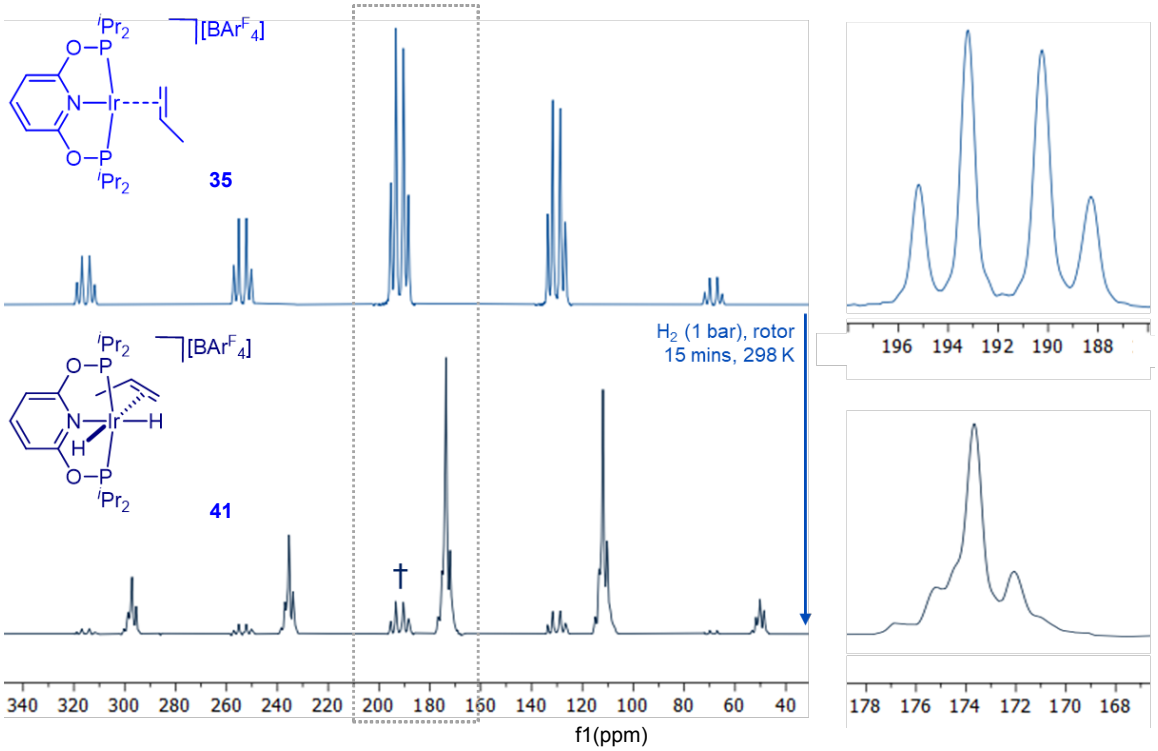


Figure 3.2.7: $^{31}P\{^1H\}$ SSNMR (162.03 MHz, 298 K, ν = 10 kHz) spectra demonstrating the *in situ* hydrogenation of propene complex **35** to yield propene-dihydride **41**. Signals outside the dotted region are spinning sidebands. † indicates incipient **35** (~10%) due to unavoidable reductive elimination of H_2 from thus-formed **41** in the rotor.

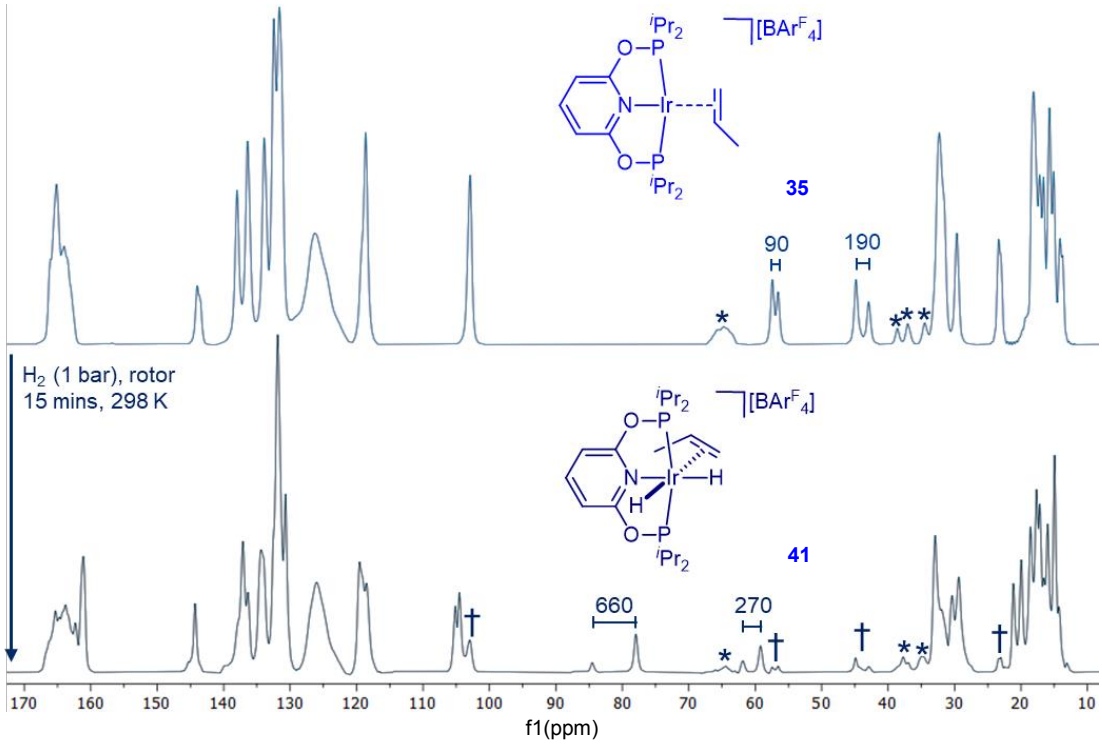


Figure 3.2.8: $^{13}C\{^{1}H\}$ SSNMR (100.66 MHz, 298 K, ν = 10 kHz) spectra demonstrating the *in situ* hydrogenation of propene complex **35** to yield propene-dihydride **41**. * indicate spinning side-bands. † indicate incipient **35** (~10%) due to unavoidable reductive elimination of H_2 from thus-formed **41** in the rotor. Signal dispersions for propene ligand *C*H and *C*H_2 resonances are indicated in Hz.

Oxidative addition of H_2 was accompanied by an upfield shift in the $^{31}P\{^{1}H\}$ SSNMR resonance (**Figure 3.2.7**), giving rise to a complex group of peaks in the region δ 169-178. Solid-state hydrogenation also occurred concomitantly with a *down*-field movement of the alkene $^{13}C\{^{1}H\}$ NMR resonances (δ [42.9, 44.8], [56.6, 57.4] → [59.2, 61.8], [77.9, 84.5]) (**Figure 3.2.8**). Note the significant signal dispersions of the resulting pairs of propene CH (~660 Hz) and CH_2 (~270 Hz) resonances compared to those in the precursor (90 and 190 Hz respectively), as well as an apparently altered solid-state ratio. For Ir(I) propene complex **35**, the ratios of resonances at δ [42.9, 44.8] and [56.6, 57.4] reflected the freely-refined chemical occupancies of the propene disorder components in the solid-state structure (~58:42; **Figure 3.2.2**), whereas for *in situ*-generated **41** this ratio appears to have changed for δ [59.2, 61.8] and [77.9, 84.5], reflecting a less balanced solid-state ratio of two components. The possible identities of these components are discussed below. The presence of two sufficiently dissimilar solid-state components may also explain the complex group of peaks observed for **41** *via* $^{31}P\{^{1}H\}$ SSNMR spectroscopy.

Changes were also noted in the $^{13}C\{^{1}H\}$ SSNMR region δ 115–140, the $[BAr^{F}_{4}]^{-}$ *ortho*, *meta*, *para*, and CF_3 positions. This was reasoned to be due to a structural modification affecting the anionic array: previous reports of SC-SC transformations within $[BAr^{F}_{4}]^{-}$ anionic microenvironments exhibited close similarity in $^{13}C\{^{1}H\}$ SSNMR $[BAr^{F}_{4}]^{-}$ region between parent and daughter samples, sometimes with the exception of the *para* position δ ~118, close-by to any modification of the cationic fragment.[16,30,40,68,69]

The process was fully reversible as verified by SSNMR spectroscopy. Exposure of *in situ*-generated **41** to dynamic vacuum for two hours regenerated indistinguishable spectra to precursor **35**. Prolonged exposure of **41** to H_2 produced no further changes by SSNMR spectroscopy after seven days, indicating that the forward hydrogenation reactivity of Ir(III) propene-dihydride **41** was successfully arrested in the solid-state.

In the *absence* of an H_2 atmosphere, propene-dihydride **41** thus generated in the solid-state was dissolved in CD_2Cl_2. Slow loss of H_2, regenerating **35**, occurred in solution at 298 K on a timescale of ~3-6 hours. This reluctance to react further (*i.e.* by insertion-elimination) without excess H_2 reflects an analogous reactivity to the coordination-assisted reductive elimination described for both Rh analogues of these systems[26] and the carbazole-based PNP-Ir pincers described by Goldman and colleagues.[67]

An equally valid solution route to the propene-dihydride **41** (and also ethene-dihydride **42**, *vide infra*) involved exposing concentrated frozen CD_2Cl_2 solutions of the alkene complex to H_2 (1 bar), shaking them while thawing (*i.e.* while still cold), and re-freezing and exposing to vacuum immediately once decolourised. This solution route was usually used for solution-phase NMR studies of the Ir(III) alkene-dihydrides, as loss of H_2 from solid-state samples would occur rapidly once the H_2 atmosphere was removed, compromising sample purity.

A downfield shift in the alkene ^{1}H resonances (δ 3.08, 3.40, 4.33 → ~3.6 (broad, overlapping CH_2), 4.84 (broad)), accompanied by significant broadening, was observed by solution-phase ^{1}H NMR spectroscopy alongside a pair of broad roofed doublets by $^{31}P\{^{1}H\}$ NMR spectroscopy (δ 188.6 (**35**) → 168.2, 170.0; $^{2}J_{PP'}$ ~ 320 Hz; whm ~ 50 Hz (**41**)). The downfield shift of the alkene $^{13}C\{^{1}H\}$ resonances observed by SSNMR spectroscopy was matched in solution (δ 42.6, 54.8 → 62.0, 82.5).

We sought to investigate the solution-phase ^{1}H and $^{31}P\{^{1}H\}$ NMR broadness of propene-dihydride **41** by progressive cooling to 185 K (**Figure 3.2.9**), hoping to arrest any fluxional processes that may have been taking place in CD_2Cl_2 solution at 298 K.

Some signals were observed to sharpen and reveal multiplicity upon cooling; others were found to broaden and divide. Protons at the alkene allylic position (H_D), for example, were initially resolved as a sharp doublet (δ 1.73, $^{3}J_{HH}$ = 6.0 Hz), broadening and splitting at 250 K, to the point of imperceptibility at 215 K and below, indicating the progressive arrestation of some fluxional process initially in the fast exchange limit. Similar behaviour was observed at the alkene methylene position (H_A + H_B), which integrated in a 2:1 ratio with the methine (H_C) position at all temperatures except 215 K, where a 1:1 ratio was observed with one proton (H_A) imperceptible at this temperature. The other proton in question (H_B) was resolved at all temperatures with a coupling constant ($^{3}J_{HH}$ = 13.8 Hz) appropriate for a *trans* relationship to the methine proton (H_C).

The broadness initially resolved at the heterocyclic *meta* position (H_m) gave way to two doublets ($^{3}J_{HH}$ = 8.2 Hz, ~1:1 integral ratio) at 250 K and below, betraying the symmetry-breaking nature of the non-symmetrical propene moiety. This occurred in parallel with sharpening and division of the ^{i}Pr methyl positions. Initially resolved as triplets (δ −11.63, −16.50; $^{2}J_{HP}$ = 18.5, ~10 Hz), the ^{1}H-hydride NMR signals (H_X + H_Y) progressively broadened with decreasing temperature, resolved as two separate signals in a ~2:1 integral ratio at 185 K. This occurred in parallel with the division of the ^{i}Pr methine signals in the same ratio as well as the $^{31}P\{^{1}H\}$ NMR signals, giving way to a singlet (δ 167.7; whm ~80 Hz; ~⅔) and a pair of roofed doublets (δ 169.7, 172.3; whm ~110 Hz; Σ ~⅓) at 185 K. We suggest these two low-temperature species corresponded to either of the parallel (∥) or perpendicular (⊥) coordination isomers (**Figure 3.2.10**), which may also correspond to the two unequal components observed in the SSNMR spectra for *in situ*-generated propene-dihydride **41** (especially $^{13}C\{^{1}H\}$, **Figure 3.2.8**). *In situ* crystallographic evidence for this isomerism is provided in the proceeding section, *i.e.* of the two distinct components observed by both solution-phase (low temperature) and solid-state NMR spectroscopy.

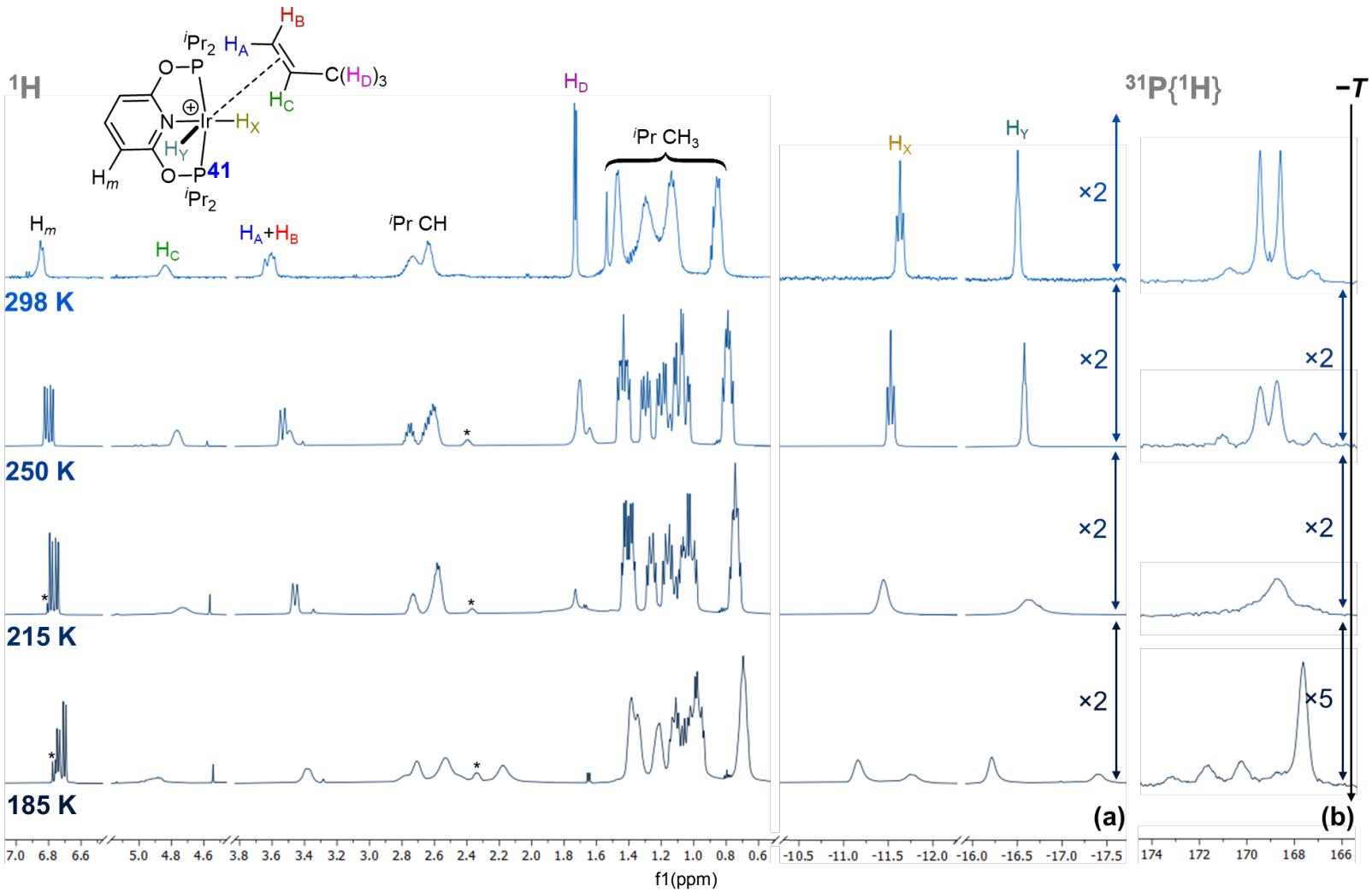


Figure 3.2.9: Sections of the variable-temperature (**a**) ^{1}H NMR (500.23 MHz, CD_2Cl_2) and (**b**) $^{31}P\{^{1}H\}$ NMR (242.96 MHz, CD_2Cl_2) spectra of propene-dihydride **41** as obtained in solution. Some sections are zoomed relative to the others as indicated. The *para* heterocyclic and $[BAr^{F}_{4}]^{-}$ ^{1}H positions are not shown as they overlap (δ ~7.73), obscuring useful details. * indicates a small impurity of non-classical tetrahydride **37** (<3%).

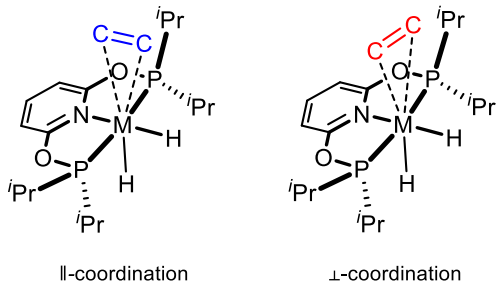


Figure 3.2.10: Two possible coordination modes of a C=C π-bond to a {*cis*-(ⁱPr-PONOP)MH_2}$^+$ fragment.

Crystals of propene-dihydride **41** were obtained by layering a concentrated CH_2Cl_2 solution with pentane at 275 K. However, due to the combination of a large unit cell (18,135.9 Å^3), poor crystal quality, high monodirectional mosaicity, and a non-straightforward structural solution ($\alpha \approx \beta \approx \gamma \approx 90°$), these data proved nonpractical for structural modelling.

*3.2.4 Propene-Dihydride **41**: Synthesis by Single-Crystal to Single-Crystal Hydrogenation*

The solid-state hydrogenation of propene complex **35** to yield propene-dihydride **41**, as tracked in the previous Section by SSNMR spectroscopy, was also followed by *sc*-XRD, taking advantage of the SC-SC nature of this transformation.

Ex situ hydrogenation of single-crystalline **35** followed by *sc*-XRD analysis initially showed that it underwent H_2 oxidative addition and an SC-SC transformation between two $P\bar{1}$ structures at 298 K. This transformation ultimately yielded propene-dihydride **41**$_{SCSC}$, with a slight change in the anionic packing pattern and unit cell volume (+1.6%), as well as a significant change in the orientation of the pincer fragment within the packing motif – specifically, an approximate 90° rotation of the PONOP chelate about the P–Ir–P axis (**Figure 3.2.11**). This indicated an SC-SC transformation in which the packing pattern of only the anions was preserved, similar to that of SMOM [(dcyppe)Rh(η^2,η^2-NBD)][BAr$^F_4$] (**8**), which was discussed in the Introduction to this Chapter.

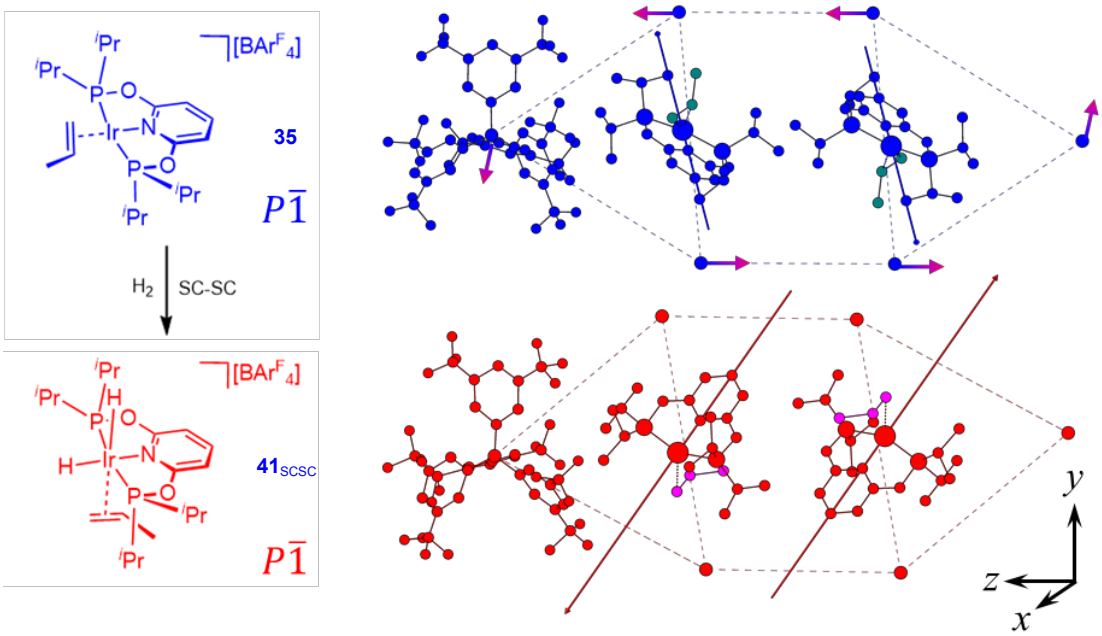


Figure 3.2.11: The bicapped parallelepipedic (BCPP) motifs of the crystal structures involved in the *ex situ* hydrogenation and *sc*-XRD analysis of the SC-SC transformation from **35** to **41**$_{SCSC}$, viewed along the same axis. Rendered in ball-and-stick, with surrounding $[BAr^F_4]^-$ anions indicated with B-atom balls connected with virtual B–B 'bonds' (nearest neighbours) as dashed lines. One $[BAr^F_4]^-$ anion is fully depicted. The apparent shifts of the surrounding $[BAr^F_4]^-$ anions from **35** to **41**$_{SCSC}$ have been indicated with arrows. Vectors have been added to highlight the orientation of the pincer fragment, along the Ir–N direction. The propene fragment is highlighted respectively in teal and magenta.

Ex situ pre-exposure of crystals of **35** to H_2, however, came with a major disadvantage. Crystals of the propene dihydride structure **41**$_{SCSC}$, thus formed, dehydrogenated in the absence of an H_2 atmosphere, visible as a crystalline colour *reversion* from colourless to orange-pink, similarly to observations made by SSNMR spectroscopy in the previous Section. Rapid transfer (<2 minutes) of crystals from under an H_2 atmosphere to the diffractometer gave rise to a structural solution of **41**$_{SCSC}$ and (reformed) **35** superposed in a solid-state ratio of ~3:1 **41**:**35** by chemical occupancies, after free refinement.

Seeking to overcome the problem of facile reductive elimination of H_2, we undertook *in situ sc*-XRD analysis using a specially-designed gas cell on the I19 beamline at the Diamond Light Source, in collaboration with Dr Mark Warren and Anna Marini. Remarkably, by monitoring the solid-state hydrogenation of single-crystalline **35** *in situ* on-beamline, evidence for an intermediate, metastable variant structure of propene-dihydride **41** was obtained, solved in the monoclinic space group $C2/c$ (**41***; **Figure 3.2.12**).

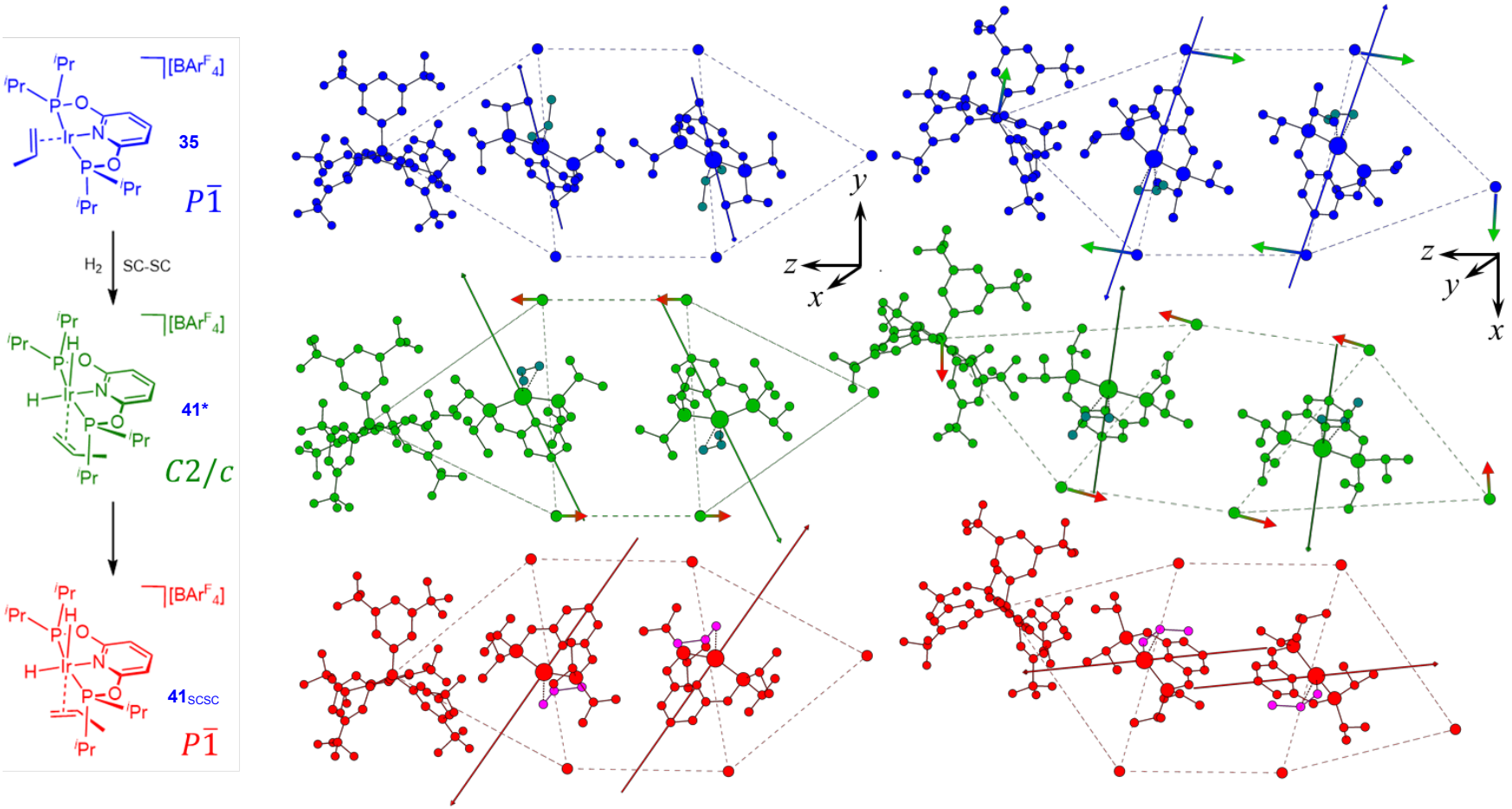


Figure 3.2.12: The bicapped parallelepipedic (BCPP) motifs of all three discrete preliminary crystal structures involved in the on-beamline SC-SC-SC transformation from **35** to **41**$_{SCSC}$ *via* **41*** viewed along two equivalent axes. Rendered in ball-and-stick, with surrounding [BAr$^F_4$]$^-$ indicated with B-atom balls connected with virtual B–B 'bonds' as dashed lines. One [BAr$^F_4$]$^-$ anion is fully depicted. The apparent shifts of the surrounding [BAr$^F_4$]$^-$ anions from one structure to the next have been indicated with arrows. Vectors have been added to highlight the orientation of the pincer fragment, along the Ir–N direction. The propene fragment is highlighted in teal (**top** and **middle**) or magenta (**bottom**).

While *Z'* remained unity, *Z* rose from 2 to 8 (**35** → **41***) – correspondingly, the unit cell volume rose by a factor of ~4.[a] The crystallographic metrics for the structures discussed in this SC-SC-SC sequence (**41*** and **41**$_{SCSC}$) obtained on the I19 beamline are summarised in **Table 3.2.1**. Note the drop in data quality,[b] approximated by the increase in the value of R_{int} – consequently, a quantitative discussion of the bond distances and angles in the SC-SC solid-state structures of **41*** and **41**$_{SCSC}$ would be inappropriate. Intermediate structure[c] **41*** possessed a different anionic packing pattern than both its $P\bar{1}$ precursor **35** and successor **41**$_{SCSC}$ (note the significantly different cell angle *α*). The changes observed in the $^{13}C\{^{1}H\}$ SSNMR $[BAr^{F}_{4}]^{-}$ region *δ* 130–140 upon solid-state hydrogenation of **35** (**Figure 3.2.8**), as discussed above, may be due to the movement of the anionic array seen across the periodic structure-shifting ('PSS') SC-SC-SC transformation **35**→**41***→**41**$_{SCSC}$.

Structure	S.G.	*a* (Å)	*b* (Å)	*c* (Å)	*α* (°)	*β* (°)	*γ* (°)	R_{int} (%)
35	$P\bar{1}$	12.0828(2)	12.3637(2)	20.0374(3)	102.664(1)	100.402(1)	90.187(1)	1.98
41*	$C2/c$	38.540(3)	12.7865(9)	23.894(2)	90	99.035(8)	90	11.7
41$_{SCSC}$	$P\bar{1}$	12.5277(19)	12.8255(17)	19.5074(17)	104.711(10)	100.421(11)	90.094(12)	10.1

Table 3.2.1: Selected crystal metrics for all preliminary structure solutions involved in the on-beamline PSS SC-SC-SC transformation proceeding from propene complex **35** to propene-dihydride **41**$_{SCSC}$ *via* metastable variant structure **41***. S.G. = space group.

Altogether, these on-beamline experiments showed that the SC-SC hydrogenation of propene complex **35** was more complex than initially thought, benefitting from the responsive, plastic nature of the $[BAr^{F}_{4}]^{-}$ anionic array, which appeared to have permitted an SC-SC transformation in which the periodic structures of *both* anions and cations shifted ('PSS'), similarly to [(dtbpe)Rh(η^2-*n*-butenes)][BAr^{F}_{4}] (**27**).[d]

[a] *Z* is the number of formula units in a unit cell; *Z'* is the number of symmetry-independent formula units in a unit cell. Structural 'buckling' in the *z*-direction, giving rise to an 'up-down' arrangement of BCPP motifs, is believed to be responsible for the shift in space group from $P\bar{1}$ to higher-symmetry $C2/c$ in **41***.

[b] Resolution drop to ~1.0 Å (**41***) then ~1.2 Å (**41**$_{SCSC}$) from <0.8 Å (**35**). This progressive drop in data quality meant that monitoring the *reverse* of this reaction by *in situ sc*-XRD, *i.e.* solid-gas reductive elimination of H_2 from **41**$_{SCSC}$ thus formed from **35**, was not feasible.

[c] Due to the dissimilar nature of the coordination of the propene ligand between **41*** and **41**$_{SCSC}$, these structures are not strictly polymorphic, despite identical connectivity between the two structures.

[d] See Chapter 2, Section 2.3.2.

Coordination of the propene moiety parallel (∥) to the Ir–N bond was observed in the ultimate $\mathbf{41}_{SCSC}$, whereas perpendicular (⊥) coordination was observed in intermediate **41*** (**Figure 3.2.13**). This evidence for two coordination isomers aligns with observations made in the previous Section, of two unequal components visible by solid-state and low-temperature solution-phase NMR spectroscopy.

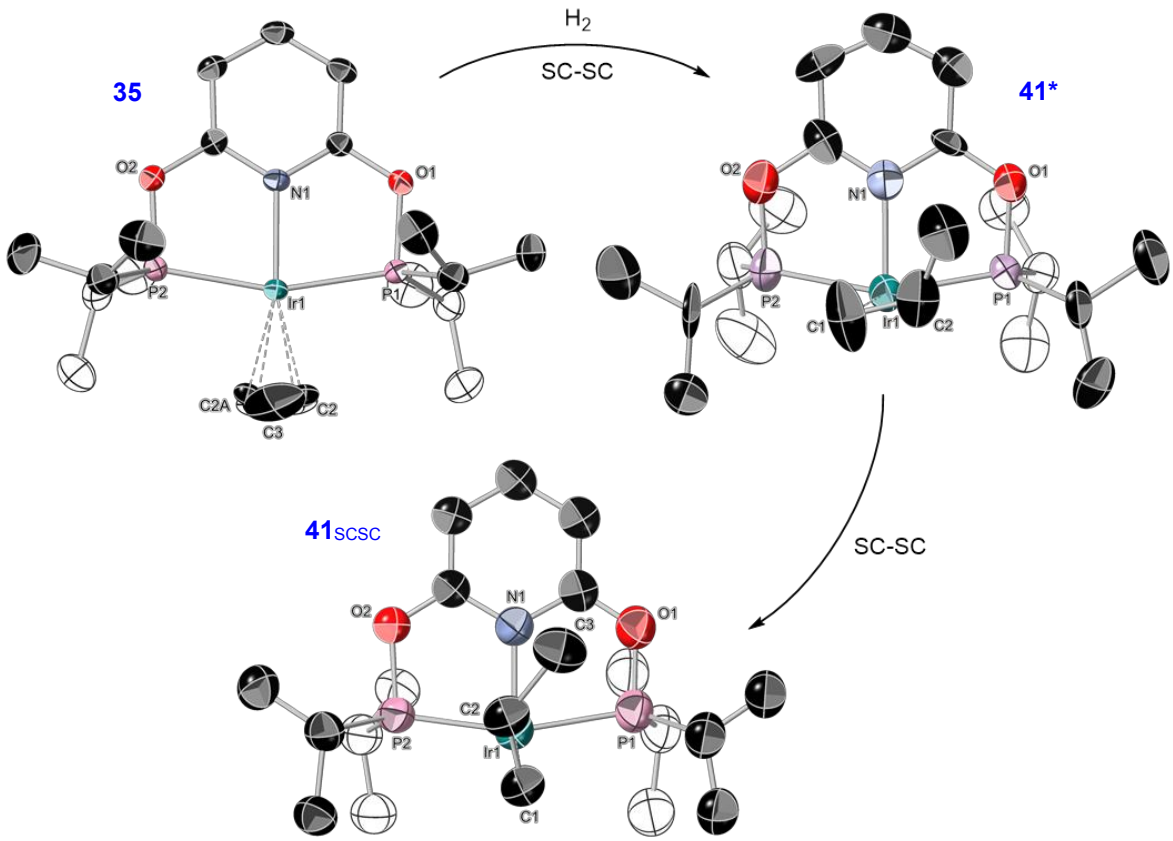


Figure 3.2.13: Solid-state structures of the isolated cations of **35**, **41***, and $\mathbf{41}_{SCSC}$. Displacement ellipsoids modelled at 50% (**35**), 35% (**41***), and 25% ($\mathbf{41}_{SCSC}$) probability levels. H atoms and anions omitted for clarity; hydrides could not be crystallographically located. *Preliminary* on-beamline data is used for **41*** and $\mathbf{41}_{SCSC}$. All three cations shown have been freely refined.

Due to the drop in data quality, disorder was not initially resolved on the propene moieties of **41*** and $\mathbf{41}_{SCSC}$ as it was for precursor **35**, and these structures as modelled in **Figure 3.2.13** appeared to entertain different alkene-face isomers. Ongoing on-beamline studies suggest that the disorder seen in precursor **35** was, in fact, preserved across the transformation to $\mathbf{41}_{SCSC}$, with the propene disorder components in the expected ~50:50 chemical occupancy ratio and an *average* near-parallel (∥) geometry of the propene ligand.

In order to verify whether any alkene-face exchange mechanism was occurring in the solid-state at 298 K, crystals of propene complex **35** were interrogated by *sc*-XRD at this temperature. The structure obtained was essentially isomorphous to that obtained at 150 K (see **Table 3.2.1**), with somewhat poorer data quality (R_1 2.19% *versus* 1.98%) and a larger unit cell volume (+4.3%). A slowly but steadily increasing unit cell volume with increasing temperature is a common observation for variable-temperature *sc*-XRD experiments, occurring as a result of intensifying bond vibrations and thus increasing equilibrium bond lengths.[70–74] The disordered propene ligand was not significantly different at 298 K, with near-identical freely-refined bond lengths and component occupancies. This strongly suggests no such alkene-face exchange mechanism was taking place in the solid-state at 298 K, consistent with the observations of dispersed alkene signals by $^{13}C\{^1H\}$ SSNMR spectroscopy.

*3.2.5 Propene-Dihydride **41**: Analysis of Material After H_2 Exposure with Scanning Electron Microscopy*

In Section 2.4.6, we showed by scanning electron microscopy (SEM) that crystallites of [(dtbpe)Rh(η^2,η^2-NBD)][BAr^F_4] (precursor SMOM **17**), which had undertaken solid-gas catalytic 1-butene isomerisation, had lost definition over the course of their lifetimes.[17] Inspection of hydrogenated crystals of propene complex **35** using simple visible-light microscopy suggested a similar phenomenon was taking place: exposure to H_2 lead to striation, splintering, and clouding of the crystal bodies. We reasoned this was due to the stress[75] rendered on the overall structure over the course of the transformation, namely by the movements undertaken by both anions and cations, resulting in the collapse of crystal domains correlating with the loss of data quality **35**→**41***→**41**$_{SCSC}$. Such a phenomenon (*i.e.* loss of crystallinity as a result of a solid-state reaction) is well documented and tends to be the rule rather than the exception, both for SMOMs, especially in the solid-state formation of Ar^F-coordinated zwitterions,[17,18,68,76] and elsewhere.[77–80] Crystal fracturing as a response to solid-state dynamical processes is also a commonly reported observation.[17,81–85]

In order to confirm this phenomenon on the micro-scale, two ~1 mg batches of fine crystalline **35** were inspected by SEM: one first exposed to five cycles of H_2 (1 bar, 15 mins) and dynamic vacuum ($p < 10^{-2}$ mbar, 60 mins) (batch **P**), and one which had not been exposed to H_2 (control batch **Q**) (**Figure 3.2.14**).

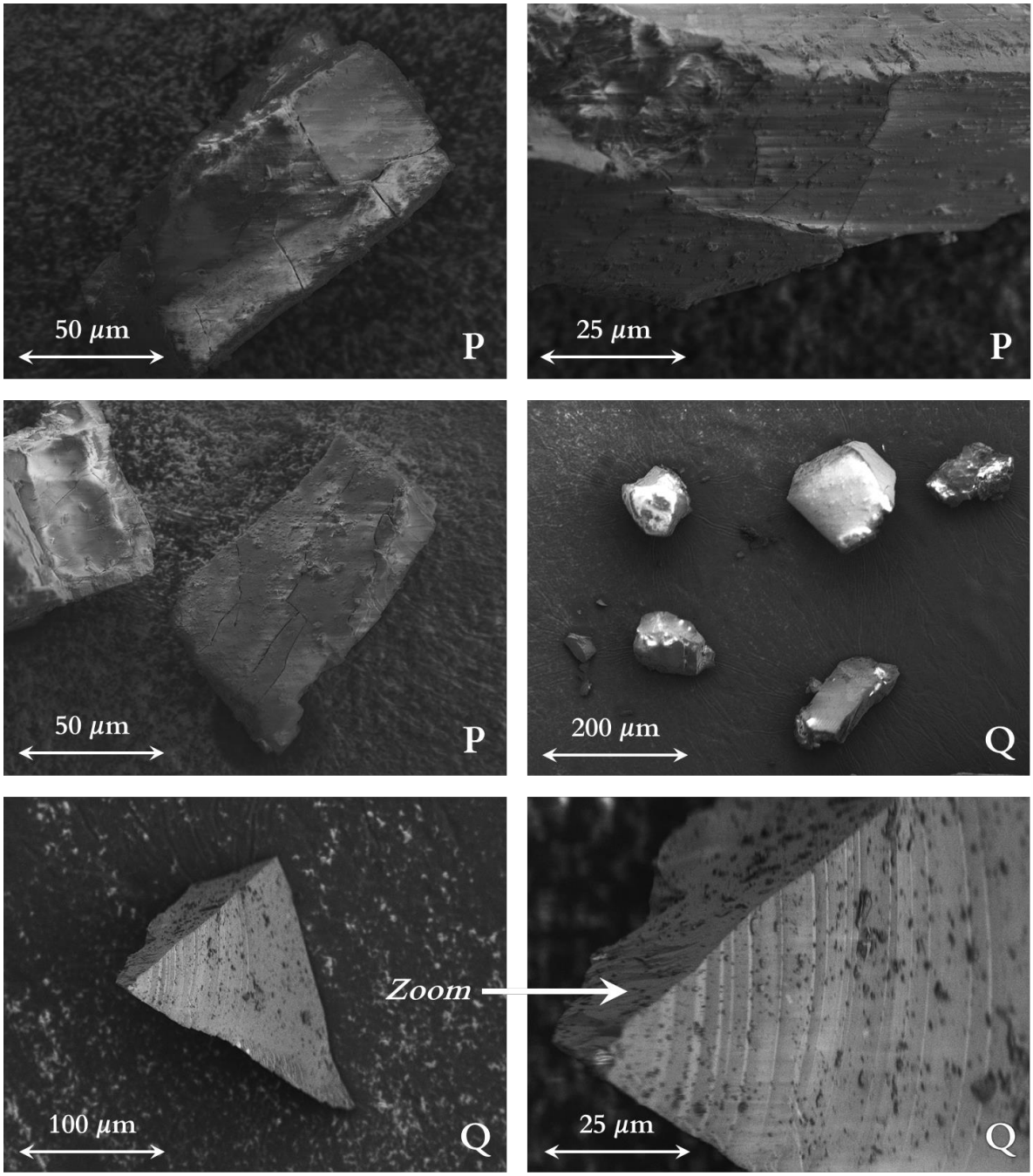


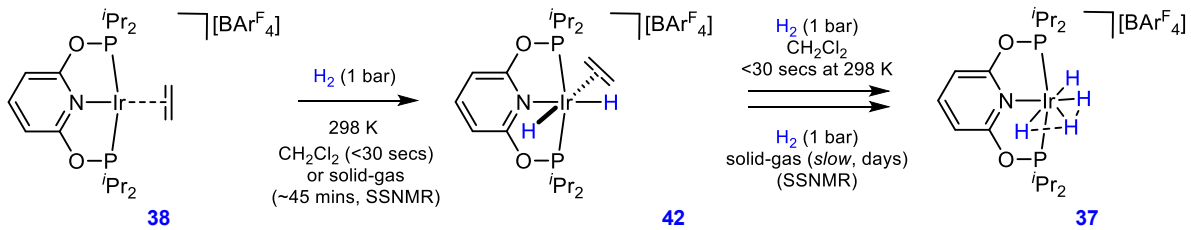
Figure 3.2.14: Scanning electron micrographs of: (**P**) fine crystals of propene complex **35** exposed to five cycles of H_2 and dynamic vacuum, generating amorphous material; (**Q**) fine crystals of pristine propene complex **35** that had not been exposed to any H_2.

Compared to those of batch **Q**, micrographs of batch **P** confirmed significant distressing of the crystal bodies, visible as cracking (surface and bulk) and obscuring/clouding of surface detail, which we equate with the progressive loss in crystallinity observed during the SC-SC-SC transformation **35**→**41***→**41**$_{SCSC}$. We interpret the high-resolution (~1-3 μm) surface features seen in the lowermost micrographs of **Figure 3.2.14** as crystal growth steps.[86–88]

*3.2.6 PONOP-Iridium(III) Ethene-Dihydride [(^{t}Pr-PONOP)IrH$_2$(η^2-ethene)][BAr$^F{}_4$] (**42**): Solid-State and Low-Temperature Solution-Phase Synthesis*

As a counterpoint to the solid-state hydrogenation chemistry of propene complex **35**, we now turn to that of the related ethene complex **38** – whose synthesis was explored in Section 3.2.1 – and its corresponding ethene-dihydride **42**. Recall that alkene complexes **35** and **38** possessed dissimilar solid-state packing motifs: where ethene complex **38** packed in an octahedral (O_h) fashion (see **Figure 3.2.1**), propene complex **35** packed in a bicapped parallelepipedic (BCPP) fashion (see **Figure 3.2.3**).[a]

As with propene-dihydride **41**, ethene-dihydride **42** was obtained in high purity using solid-state techniques. Exposure of powdered crystals of ethene complex **38** to H_2 (SSNMR rotor, 1 bar, 45 minutes, 298 K) generated **42** quantitatively and cleanly by SSNMR spectroscopy (**Scheme 3.2.5**), taking longer to completely undergo solid-gas oxidative addition of H_2 compared to its counterpart **35** (~15 minutes) but without evidence of *in situ* reductive elimination to regenerate **38** upon removal of the H_2 atmosphere and replacement with argon (without prolonged evacuation, *vide infra*).



Scheme 3.2.5: Synthesis of Ir(III) ethene-dihydride complex **42** by both solid-state and solution routes.

[a] From CH_2Cl_2 and pentane, crystals of the solvent-containing and O_h-type **35**·½CH_2Cl_2 ($C2/c$) were obtained; from 1,2-difluorobenzenea and pentane, crystals of the structure in question, BCPP-type **35** ($P\bar{1}$) were obtained, with no co-crystallised solvent.

Unlike *in situ*-generated propene-dihydride **41**, ethene-dihydride **42** showed evidence of further reactivity with prolonged H_2 exposure, as we shall see. By $^{31}P\{^1H\}$ SSNMR spectroscopy, an roofed pair of upfield doublets was initially observed upon oxidative incorporation of H_2, at δ 168.9, 172.7 ($^2J_{PP}$ ~ 340 Hz, **Figure 3.2.15a→b**), indicating that the initially inequivalent P-donor atoms in precursor **38** remained so in the product **42**, with an increased chemical shift difference ($\Delta\delta$ ~0.5 → ~4.0).

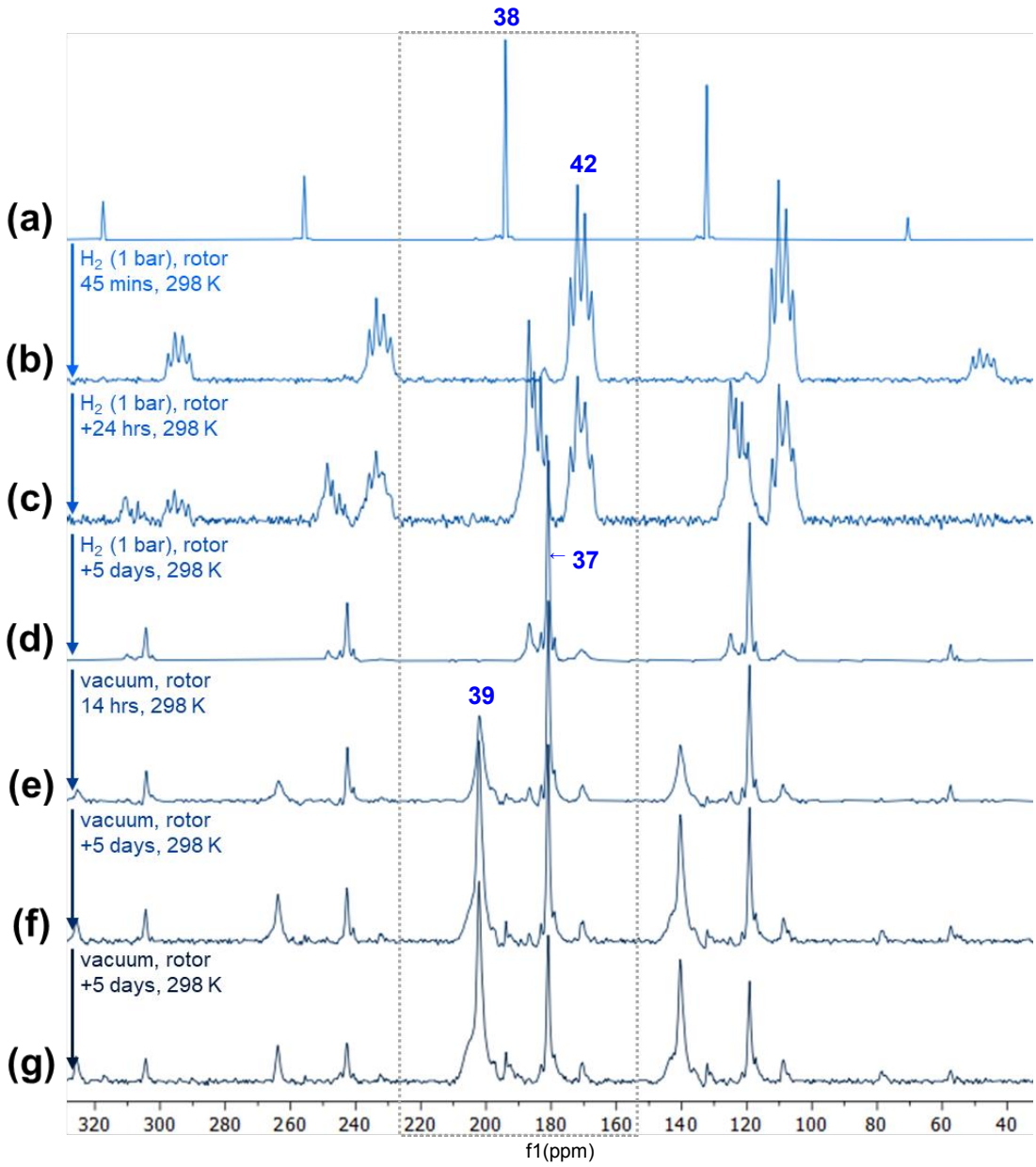


Figure 3.2.15: $^{31}P\{^1H\}$ SSNMR (162.03 MHz, 298 K, ν = 10 kHz) spectra demonstrating the progressive *in situ* hydrogenation of ethene complex **38**. Signals outside the dotted region are spinning sidebands.

Upfield shifts of $^{31}P\{^{1}H\}$ NMR signals upon reaction with H_2 have also been observed for the similar [(^{t}Bu-PONOP)Ir(η^2-C_2H_4)][BAr^F_4] (resulting in the corresponding Ir(III) ethyl-hydride),[46,89] and for [(^{t}Bu-PONOP)IrH(CH_3)][BAr^F_4] (forming a non-classical Ir(III) methyl-trihydride).[90,91] Compared to the complex group of resonances observed for *in situ*-generated **41** (**Figure 3.2.7**), the relatively simple pair of doublets observed here for **42** indicated either rapid rotation of the ethene moiety in the solid-state – allowing for rapid interconversion of ∥ and ⊥ coordination isomers analogous to those discussed for **41** – or that these coordination isomers were sufficiently indistinct so as to be coincident by $^{31}P\{^{1}H\}$ SSNMR spectroscopy. This is a significant possibility due to the intrinsic symmetry of the ethene ligand compared to propene.

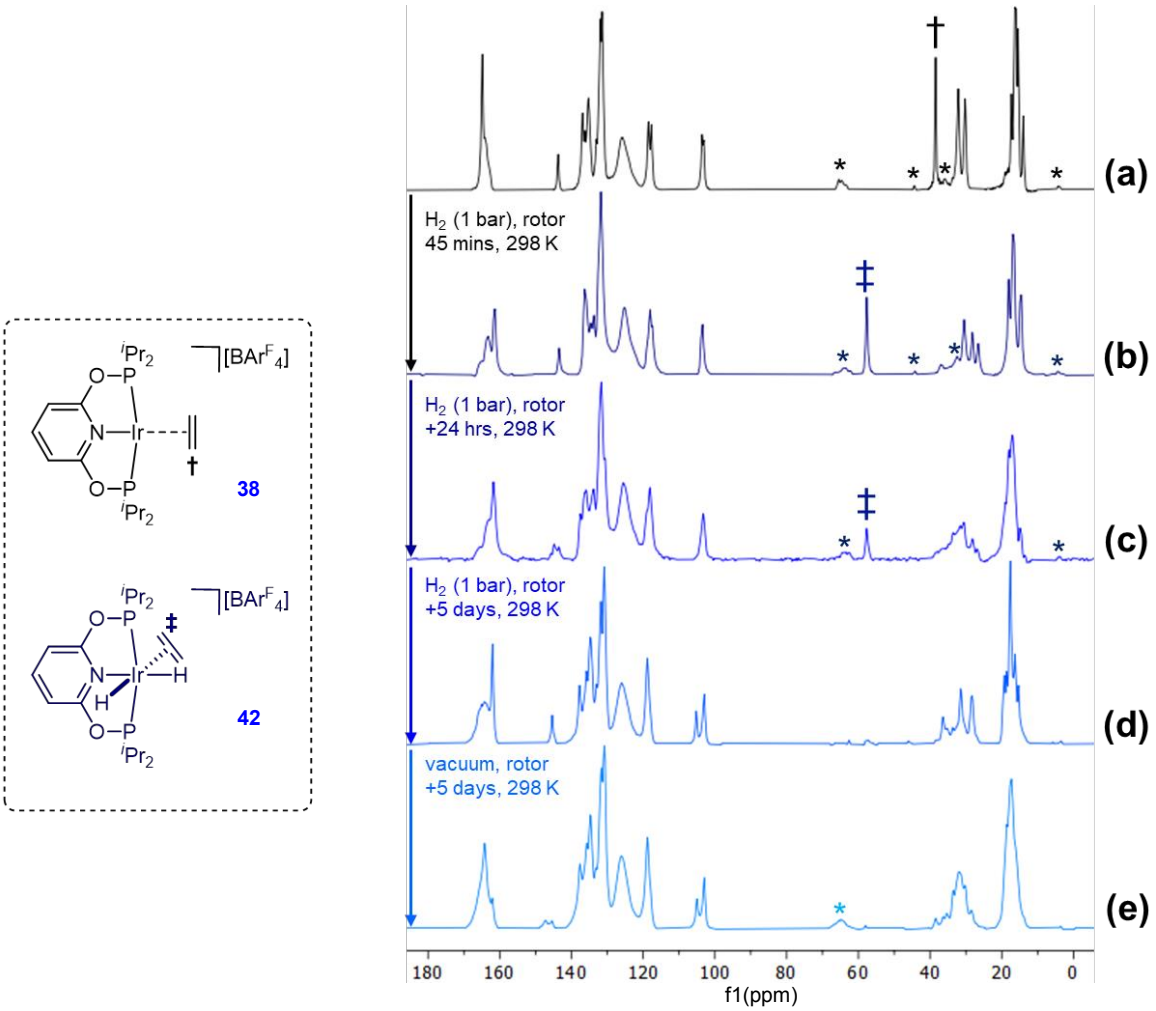


Figure 3.2.16: $^{13}C\{^{1}H\}$ SSNMR (100.66 MHz, 298 K, ν = 10 kHz) spectra demonstrating the progressive *in situ* hydrogenation of ethene complex **38** *via* the ethene-dihydride **42**. * indicate spinning side-bands.

By $^{13}C\{^1H\}$ SSNMR spectroscopy, a significant *downfield* shift in the ethene $^{13}C\{^1H\}$ resonance was observed (δ 38.4→57.7) (**Figure 3.2.16a→b**). Such a movement in the ethene resonance has also been reported in the work of Caulton and colleagues, upon the oxidative addition of H_2 to $[(PhMe_2P)_3Ir(\eta^2\text{-}C_2H_4)_2][BF_4]$ (δ_{ethene} ~27) to generate $[cis,mer\text{-}(PhMe_2P)_3IrH_2(\eta^2\text{-}C_2H_4)][BF_4]$ (δ_{ethene} 46.9).[92] Unlike propene-dihydride **41**, ethene-dihydride **42** exhibited only a single alkene $^{13}C\{^1H\}$ SSNMR resonance with no evidence of inequivalence that may have lead to visible signal dispersion, chiming with the relative simplicity of the $^{31}P\{^1H\}$ SSNMR spectrum (**Figure 3.2.15b**). At this stage, complex **38** could be regenerated by exposing the contents of the SSNMR rotor to dynamic vacuum for 24 hours to generate SSNMR spectra indistinguishable from those of the starting material, taking longer to do so than *in situ*-generated propene dihydride **41** under the same conditions (~2 hours *in situ* evacuation).

Further exposure (24 hours) of **42** to H_2 in the solid-state generated a complex set of $^{31}P\{^1H\}$ SSNMR resonances δ 80–90, concomitant with a ~50% loss in signal intensity in the roofed doublets corresponding to **42** (**Figure 3.2.15c**), as well as the $^{13}C\{^1H\}$ SSNMR ethene resonance at δ 57.7 (**Figure 3.2.16c**). These new resonances were modelled to correspond to at least two species: at δ [182.6, 185.8] ($^2J_{PP'}$ ~ 300 Hz) and ~186.7 (broad), in a population ratio of ~1:0.75. This was corroborated by the $^{13}C\{^1H\}$ SSNMR spectrum, wherein the resonance corresponding to C_5N *para*-^{13}C (**38**, δ 143.7; **42**, δ 143.4) was observed to complicate with continued H_2 exposure, with new resonances observed at δ 144.9 and 145.7.

Insufficient evidence was available for the unambiguous identification of these intermediate solid-state species, which we speculate (one or both) to be a non-classical 'ethyl-trihydride' in analogy to 'tetrahydride' **37** as well as the fluxional 'methyl-trihydride' $[(^tBu\text{-}PONOP)IrH_3(CH_3)][BAr^F{}_4]$[91] and 'silyl-trihydride' $[(^tBu\text{-}POCOP)IrH_3(SiEt_2H)]$[93] investigated by Brookhart and colleagues. Solution-phase NMR studies conducted on the rotor contents at this stage at 183 K evidenced only ethene-dihydride **42** (solution-phase metrics discussed below) and a small amount of 'tetrahydride' **37**, with no evidence for liberated H_2 in solution (δ ~4.60). Altogether, this suggested that a solution-unstable species (or set of species) isomeric to **42** had been sequestered in the solid-state.

After a further five days' exposure to H_2, a new species was observed by $^{31}P\{^1H\}$ SSNMR spectroscopy, at δ [180.3, 181.6] ($^2J_{PP'}$ ~ 320 Hz) (**Figure 3.2.15d**), still retaining the inequivalent P-donor atoms of the starting material. Due to the similarity of the average $^{31}P\{^1H\}$ SSNMR shift of the convergent species (δ_{av} 180.9) with the solution-phase $^{31}P\{^1H\}$ NMR resonance of 'tetrahydride' **37** (δ 181.2), we identified this species as **37**. Indeed, exposure of **37** thus generated in the solid-state to dynamic vacuum gradually generated a new species (**Figure 3.2.15e**), presumably *via* loss of H_2 to give a complex speculated to have been dihydride **39**, as a broad resonance at δ 202.1.

After 10 days' exposure to vacuum, these species existed in a solid-state ratio **37**:**39** of ~1:2.2 by $^{31}P\{^1H\}$ SSNMR integrals, with further prolonged evacuation leading only to decomposition. Unlike in previous stages (**Figure 3.2.16a→d**), the $^{13}C\{^1H\}$ SSNMR $[BAr^F_4]^-$ region δ 115–140 was noted to undergo no further changes during the evacuation process (**Figure 3.2.16d→e**), evidencing a minor structural modification affecting only the immediate metal coordination sphere. Solution-phase ^1H (δ −19.85) and $^{31}P\{^1H\}$ (δ 183.3) NMR analysis of the rotor contents at this stage also evidenced the solid-state formation of **39**. Curiously, the $^{31}P\{^1H\}$ SSNMR signal for provisionally-assigned **39** was markedly downfield from its solution-phase (CD_2Cl_2) measurement (δ 183.3, $\Delta\delta$ +18.8). We propose that this difference arose from the presence of transient stabilising interactions between solvent molecules and 16-electron $[(^i$Pr-PONOP)$IrH_2]^+$;[94] these interactions would have been absent in the solid-state. Two structural reports of CH_2Cl_2 coordination to unsaturated Ir(III)-hydride centres have been made.[95,96] Indeed, the $^{31}P\{^1H\}$ NMR spectrum of **39**[a] obtained in 1,2-difluorobenzene, a more weakly-coordinating solvent than CH_2Cl_2 with similar solvating properties,[97,98] revealed a shift of δ 186.5, closer to the solid-state value (δ 202.1).

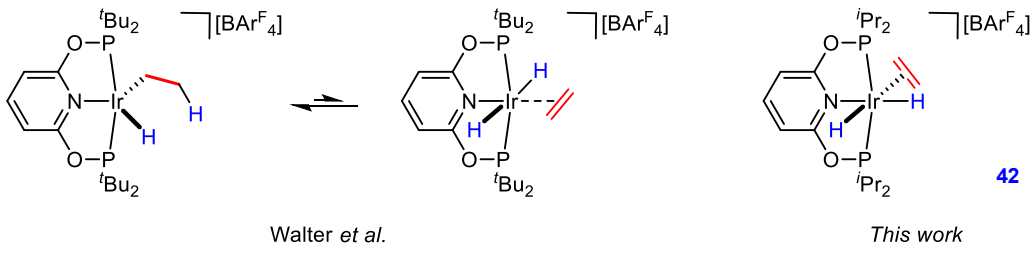
Attempts to track the solid-state transformation **38**→**42** by *sc*-XRD were not successful. While evidence for some retention of crystallinity was available upon exposure of crystals of **38** to H_2 (*i.e.* Bragg peaks dissimilar to those in the starting material were observed up to ~1.0 Å), no satisfactory structural solution of the tentatively proposed ethene-dihydride $\mathbf{42}_{SCSC}$ could be achieved.

[a] As independently synthesised *via* the solution route followed by removal of volatiles *in vacuo* described in Section 3.2.2.

In the same manner as **41**, ethene-dihydride **42** as generated in the solid-state could be dissolved in CD_2Cl_2 in the absence of an H_2 atmosphere, only slowly losing H_2 into solution to regenerate ethene complex **38**, on a timescale of ~6-12 hours at 298 K. Complex **42** was also analogously prepared, *via* the low-temperature solution-phase route as described in Section 3.2.3, allowing its synthesis to be tracked by solution-phase NMR spectroscopy in parallel with solid-state methods.

^{1}H NMR spectroscopy evidenced **42** to be a *cis*-dihydride similarly to TMAB-dihydride **40**: both hydrides were observed at 298 K as well-defined triplets (δ −16.30, $^2J_{HP}$ = 10.2 Hz; δ −9.56, $^2J_{HP}$ = 17.6 Hz), the former corresponding to the hydride *trans* to ethene. Oxidative addition of H_2 (**38**→**42**) was accompanied by a downfield shift in the solution-phase ^{1}H NMR ethylene resonances (δ 3.09 → 3.49) and an upfield shift in the ^{31}P{^{1}H} NMR resonance (δ 191.8 → [169.1, 169.3], $^2J_{PP'}$ ~ 320 Hz), comparing well to the solid-state average (δ_{av} 170.8). Solution-phase ^{13}C{^{1}H} NMR spectroscopy paralleled the changes observed in the solid-state upon oxidation, principally the downfield shift of the ethene resonance (δ 37.3 → 57.8).

It is curious to note that the ^{t}Bu-PONOP analogue of ethene-dihydride **42** possessed an ethyl-hydride ground state instead of an isomeric ethene-dihydride (**Scheme 3.2.6**).[89] This likely results from the steric constraints of the {(^{t}Bu-PONOP)Ir}$^+$ chelate. For **42**, the *cis*-ethene-dihydride isomer formed the ground state, as evidenced by both NMR spectroscopy (solid-state and solution-phase) and single-crystal X-ray diffraction studies (*vide infra*). The preference for *cis* over *trans* hydride geometry likely arose from the energetically favourable relationship between each strongly σ-donating hydride and a *trans*-located acceptor, relatively unencumbered by sterics as compared to the more severely hindered ^{t}Bu-PONOP.



Scheme 3.2.6: Juxtaposition of ^{i}Pr-PONOP-ligated ethene-dihydride **42** with its ^{t}Bu-PONOP analogue.

3.2.7 *Ethene-Dihydride 42: Recrystallisation, Solid-State Structure, and Reductive Elimination of H_2*

The reasonable solution-phase stability of **42** in the absence of H_2 (*vide supra*) was exploited to obtain crystalline material. Concentrated CH_2Cl_2 solutions were layered with pentane at 2 °C (see Section 5.14.8), and **42** crystallised as large colourless blocks suitable for *sc*-XRD studies (so-called $\mathbf{42}_{xtal}$; **Figure 3.2.17**) in addition to ~10% crystalline **38** resulting from reductive elimination of H_2, visible as smaller orange blocks from which $\mathbf{42}_{xtal}$ was easily separated by hand. To date, only one other report of an iridium ethene-dihydride structure has been published.[99]

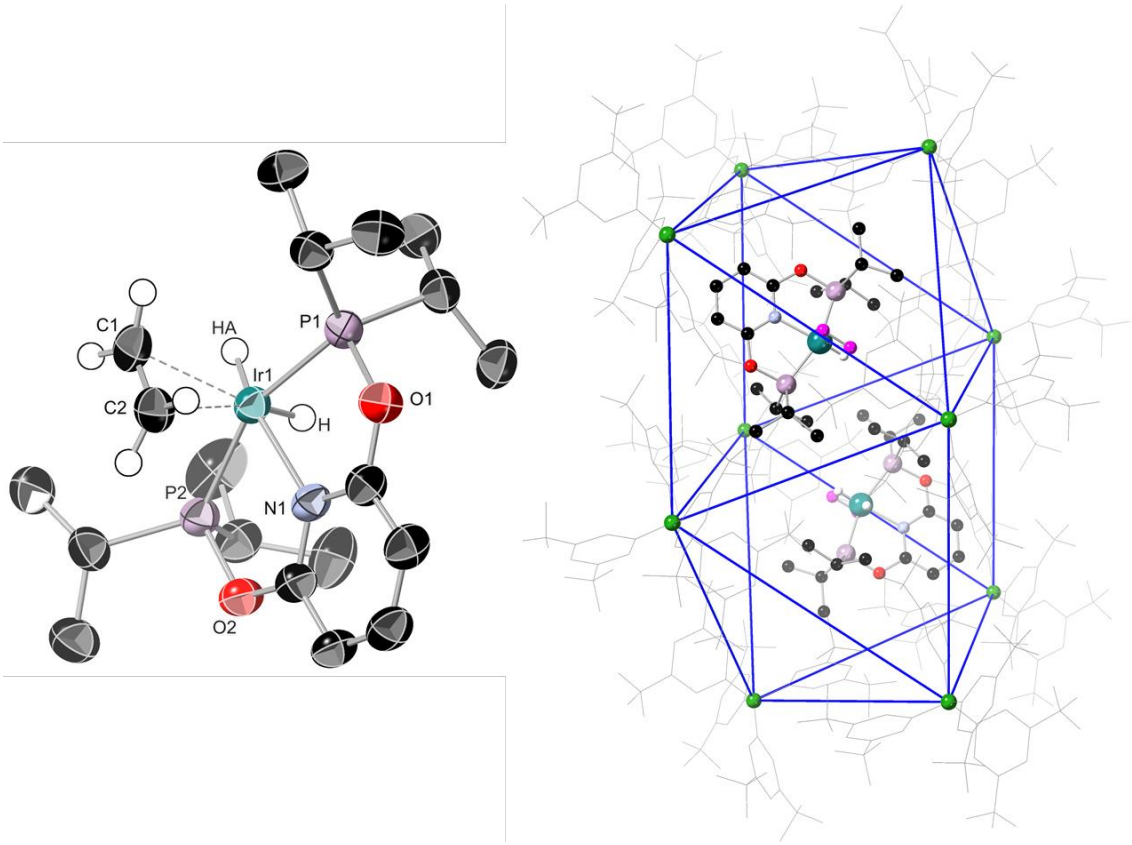
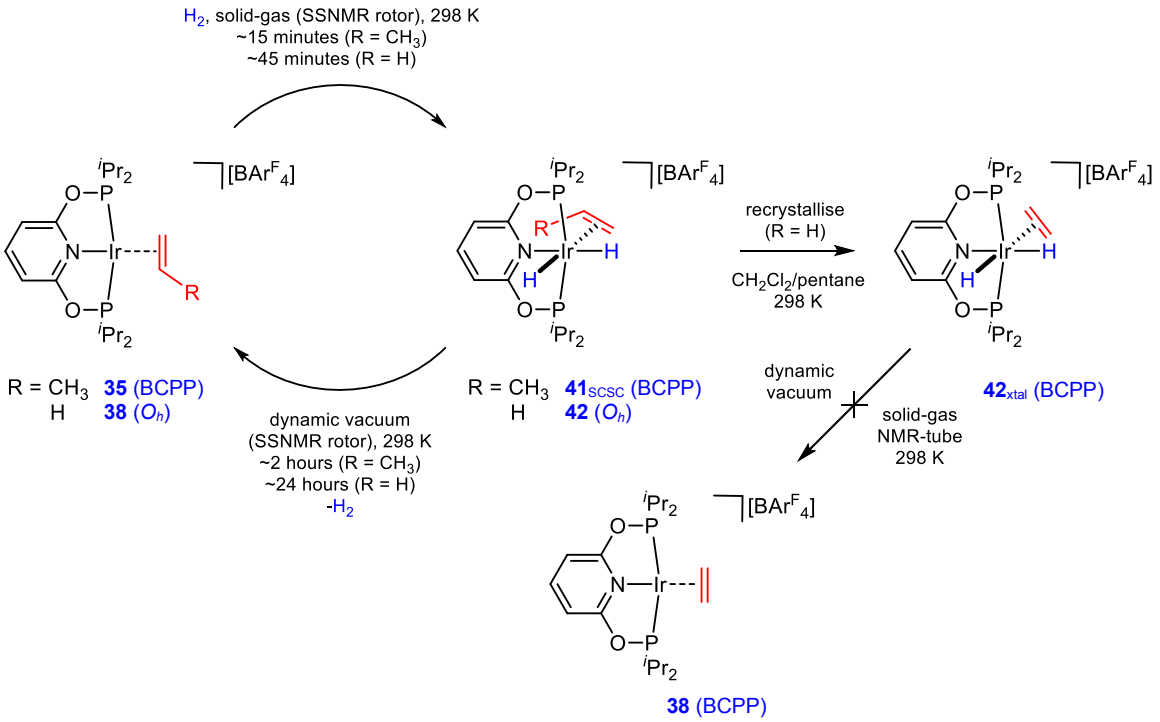


Figure 3.2.17: (**left**) Solid-state structure of $\mathbf{42}_{xtal}$, with the cationic fragment and selected H atoms shown. Anion omitted for clarity. 50% displacement ellipsoids. Selected bond lengths (Å), angles (deg), and torsion angles (deg), where Cent is the centroid of C1–C2: Ir1–N1, 2.101(3); Ir1–P1, 2.2672(10); Ir1–P2, 2.277(1); Ir1–C1, 2.266(4); Ir1–Cent, 2.17533(14); Ir1–C2, 2.289(4); C1–C2, 1.350(6); N1–Ir1–P1, 80.17(9); N1–Ir1–P2, 80.45(9); N1–Ir1–H, 88.5(15); H–Ir1–HA, 75(2); N1–Ir1–Cent, 101.91(8); N1–Ir1–C1–C2, 1.4(3). (**right**) The bicapped parallelpipedic (BCPP) coordination of 10 $[BAr^F{}_4]^-$ anions (modelled as wireframes with B atoms balls) about a cavity containing two $[(^i\text{Pr-PONOP})IrH_2(\eta^2\text{-}C_2H_4)]^+$ fragments (modelled as ball-and-stick).

While the hydrides of **42**$_{xtal}$ were crystallographically located, they freely refined with unrealistically short Ir–H distances (~1.21, ~1.09 A); a DFIX command (1.67 Å) was applied to both in order to induce a more appropriate bond length.[100] Ethene was observed to be bound parallel to the Ir–N bond (*i.e.* ∥-coordinated) with no resolved disorder. Despite a minor modification to the metal coordination sphere between **38** and **42**$_{xtal}$, the structure type shifted from O_h to BCPP, with no solvent molecules co-crystallised.

Once formed, crystals of BCPP-type ethene-dihydride **42**$_{xtal}$ did not lose H_2 under dynamic vacuum, and could be stored at 298 K under argon for months. This is in marked contrast to **42** as generated in the solid-state from O_h-type crystals of **38**. As discussed above, *in situ* SSNMR samples of **42** could be reconverted to **38** by 24 hours' exposure to dynamic vacuum at 298 K (**Scheme 3.2.7**), visibly reacquiring their original bright orange colour from the white colour of powdered **42**. The BCPP-type propene complex **35** generated the similarly BCPP-type propene-dihydride **41**$_{SCSC}$ in the solid-state upon exposure to H_2 (*vide supra*), thereafter readily losing H_2 even inside the SSNMR rotor (~2 hours under dynamic vacuum).



Scheme 3.2.7: Summarised solid-gas oxidative addition reactivity of H_2 to alkene complexes **35** and **38**, and subsequent reductive elimination, resisted by the recrystallised ethene-dihydride **42**$_{xtal}$.

In situ-generated **42** and recrystallised **42**$_{xtal}$ must be polymorphic, and where facile solid-state movement seems to be possible for the cationic fragments in habits originating from Ir(I) starting materials (either BCPP-type **35** or O_h-type **38**) – thus permitting facile solid-gas H_2 oxidative addition and reductive elimination – this seems not to be the case for BCPP-type **42**$_{xtal}$. This indicates that recrystallisation afforded the opportunity for a structure to be achieved by **42** that did not permit the solid-state reorganisation required for reductive elimination of H_2, which we theorise was due to a 'structural locking feature'. Note that **42**$_{xtal}$ possessed the highest PLATON-calculated structural void space (1008.17 Å^3),[101,102] compared to the Ir(I) complexes **38** (973.07 Å^3, *Z* scaled from 4 to 2) and **35** (994.95 Å^3).

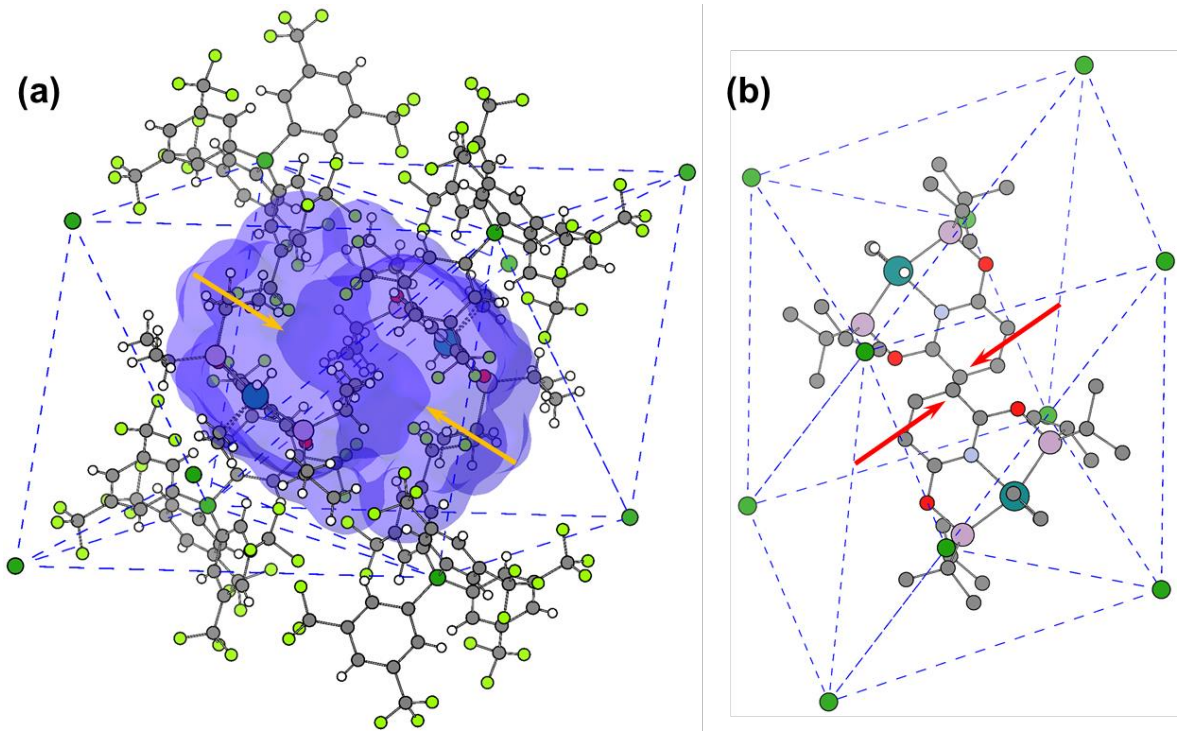


Figure 3.2.18: (**a**) BCPP motif of **42**$_{xtal}$, viewed parallel to the PONOP heterocycles. A solvent-excluded surface (probe radius 0.8 Å) has been plotted around the 'facing' atoms surrounding the 'concentration of void space' between two cationic fragments inside the BCPP motif; this void space has been highlighted with yellow arrows. Only fragments with atoms 'facing' this void space are modelled, excepting the B-atom vertices of the BCPP motif. (**b**) The BCPP motif of the solid-state structure of recrystallised ethene-dihydride **42**$_{xtal}$, modelled as ball-and-stick, reoriented to be viewed perpendicular to parallel planes containing the PONOP heterocycles. $[BAr^F_4]^-$ anions (except B-atom balls) and most H atoms have been omitted for clarity. A proposed 'structural locking feature', involving two PONOP heterocycles that would clash when undergoing ~90° rotations about their P–Ir–P axes (one into the page, one out of the page), is highlighted in red.

In the extended structure of **42**$_{xtal}$, much of this void space was concentrated into a locus between two heterocycles within the BCPP motif (inter-centroid distance ~7.14 Å), with no such concentration near the ethene ligand, or the metal coordination sphere in general (**Figure 3.2.18a**). If no void space was concentrated near the ethene moiety in **42**$_{xtal}$, then – upon reductive elimination of H_2 – a direct ~90° movement of the ethene ligand about the iridium atom into the position *trans* to $N_{pyridine}$ could not have taken place, with the ethene moiety structurally 'locked' in position.

If reductive elimination of H_2 from **42**$_{xtal}$ were to take place somehow, we can envisage the reverse of the SC-SC hydrogenation **35**→**41**$_{SCSC}$ described in Section 3.2.4 (**Figure 3.2.11**). This did not take place *via* direct ~90° movement of the propene moiety about the iridium atom into a position *cis* to $N_{pyridine}$, but rather with reorganisation of the entire structure and particularly of the cations, with effective ~90° rotations of the PONOP chelates about their P–Ir–P axes upon oxidative addition of H_2. A similar provision of void space to that seen for **42**$_{xtal}$ in **Figure 3.2.18a** was available in the reminiscent solid-state structure of **35**, *i.e.* in a locus between two heterocycles within the BCPP motif (inter-centroid distance ~10.11 Å).

If reductive elimination of H_2 from **42**$_{xtal}$ were then to take place *via* the effective ~90° rotations of the PONOP chelates about their P–Ir–P axes, in a similar manner to the oxidative addition **35**→**41**$_{SCSC}$, we can envisage an *interrupted* reorganisation, due to the two heterocycles coming into unfeasibly close proximity (**Figure 3.2.18b**).

In the solid-state structure of propene complex **35** it seems that this clash can be avoided. Although also BCPP-type, important differences exist between the structures of **35** and **42**$_{xtal}$. The PONOP intercentroid distances not only differ significantly (~10.11 *versus* ~7.14 Å), the two heterocycles within the BCPP motif are also not as closely aligned in **35** (compare **Figure 3.2.18b** and **Figure 3.2.19**). **35** possesses a much larger out-of-alignment displacement compared to **42**$_{xtal}$ (~8.9 Å *versus* ~3.3 Å in-plane PONOP intercentroid displacement), such that the cationic fragments are more well-spaced, permitting the facile ~90° rotations of PONOP chelates about P–Ir–P axes upon oxidative addition of H_2 as in Section 3.2.4.

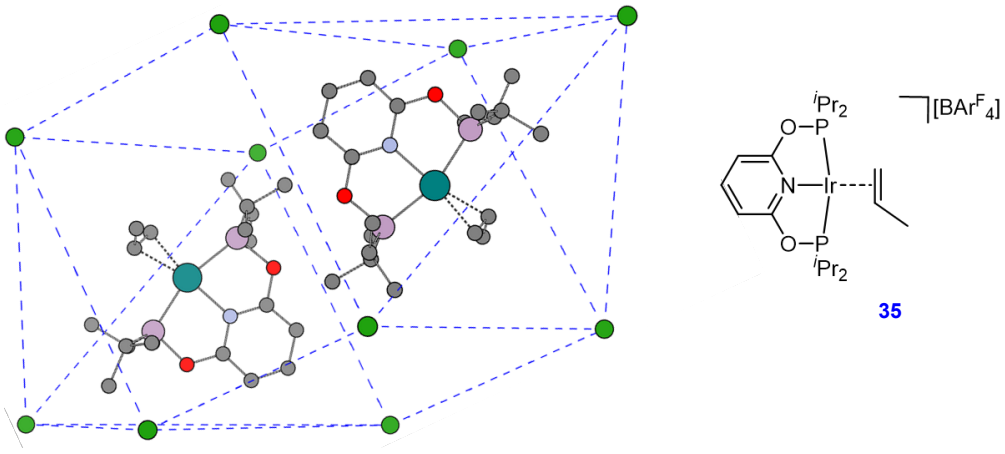
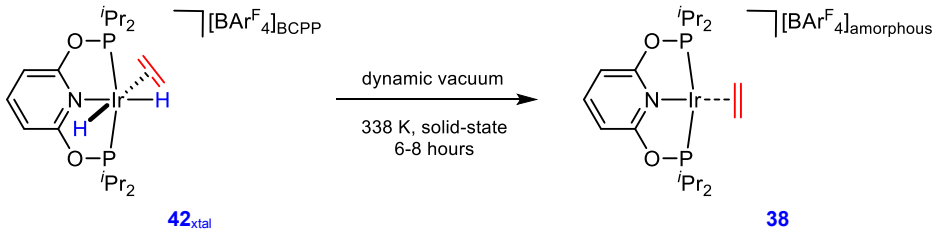


Figure 3.2.19: The BCPP motif of the solid-state structure of propene complex **35**, modelled as ball-and-stick, viewed perpendicular to parallel planes containing the PONOP heterocycles. $[BAr^F_4]^-$ anions (except B-atom balls) and H atoms have been omitted for clarity.

Since ethene complex **38** possessed an O_h-type structure, we can assume that no such structural locking feature was present in the structure of *in situ*-generated ethene-dihydride **42**, since the O_h microenvironment contained only one cation.

Reductive elimination of H_2 from $\mathbf{42}_{xtal}$ could, however, be induced by heating the crystals under a dynamic vacuum (**Scheme 3.2.8**). Colourless single crystals of $\mathbf{42}_{xtal}$ exposed to dynamic vacuum ($p < 10^{-2}$ mbar) and elevated temperature (65 °C) inside an NMR tube slowly turned orange over the course of 6-8 hours. Inspection of the crystals by visible-light microscopy revealed significant crystal clouding and pockmarking. Attempts to conduct *sc*-XRD studies on the presumed product, a BCPP-packing polymorph of ethene complex **38**, were unsuccessful: any Bragg peaks observed corresponded only to a low solid-state concentration of the starting ethene-dihydride $\mathbf{42}_{xtal}$ with an essentially identical unit cell.



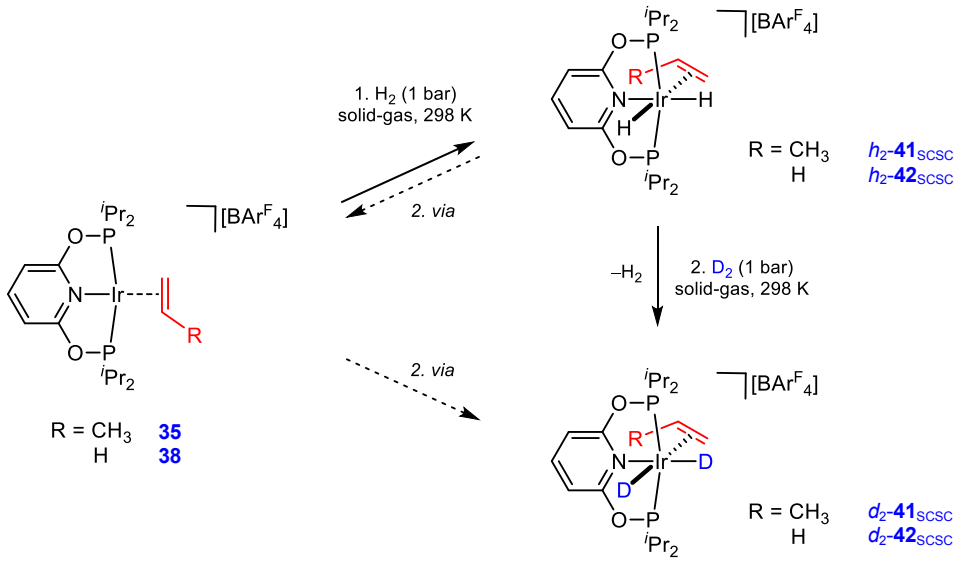
Scheme 3.2.8: Solid-state reductive elimination of H_2 from recrystallised ethene-dihydride $\mathbf{42}_{xtal}$.

Solution-phase NMR spectroscopy confirmed the regeneration of **38** in the bulk (>90% conversion), suggesting that dehydrogenation events resulted in local losses of crystalline order, giving rise to amorphous **38**, with long-range order retained by unconverted Ir(III) sites.

Divergent reactivity between organometallic crystal polymorphs has been widely attested.[103–107] An example is even available for SMOM-type systems, in the form of the O_h and hexagonal polymorphs of [(dcpe)Rh(η^2-ethene)$_2$][BAr$^F_4$]:[a] when deployed as solid-gas 1-butene isomerisation catalysts, the porous hexagonal polymorph achieved a turnover frequency ~40 times greater than the essentially non-porous O_h.[40]

3.2.8 Probing Solid-State Redox Reversibility with D_2

In order to further probe the solid-state reversibility of the oxidative addition of H_2 to alkene complexes **35** and **38**, we were curious as to whether solid-state *in situ*-generated samples of alkene-dihydrides h_2-**41**$_{SCSC}$ or h_2-**42** underwent hydride-deuteride exchange under an atmosphere of D_2 (**Scheme 3.2.9**).



Scheme 3.2.9: Solid-gas H/D-exchange at the hydride positions of *in situ*-generated h_2-**41**$_{SCSC}$ and h_2-**42**$_{SCSC}$.

[a] See Introduction (Sections 1.1.3 and 1.1.4).

To this end, a ~10 mg sample of *in situ*-generated ethene-dihydride h_2-**42**$_{SCSC}$ was cooled in liquid N_2 (to prevent loss of H_2 from the sample), briefly exposed to dynamic vacuum, and repressurised under D_2 (1 bar) for five minutes at 298 K, before cooling again in liquid N_2, replacing the atmosphere with N_2, and dissolving in CD_2Cl_2. Near-complete (<7%) loss of the ^{1}H NMR hydridic signals was observed, with the deuterides in the resulting ethene-dideuteride d_2-**42** evidenced *via* ^{2}H NMR spectroscopy (δ −9.4, −16.5).

After exposure to h_2-**42**$_{SCSC}$, the D_2 atmosphere was vacuum-transferred to another NMR tube containing CD_2Cl_2, wherein an increased concentration of H_2 (not HD)[a] was observed, indicating H_2 loss and then D_2 oxidative addition (hence **Scheme 3.2.9**), rather than a process where hydride insertion into the alkene took place followed by H/D-exchange, as this would lead to HD being observed.

Integration of the ^{1}H NMR ethene signals (4.0 H) relative to $[BAr^F_4]^-$ also confirmed the absence of an insertion-elimination shuttling mechanism that would presumably have diminished this integral. Indeed, no evidence of ^{2}H incorporation onto the alkene was noted by ^{2}H NMR spectroscopy nor by ESI-MS. Even after 60 minutes in CD_2Cl_2, solutions of d_2-**42** demonstrated no significant change in the integrals of the alkene protons or the hydride positions. Parallel results were obtained for *in situ* propene-dihydride, **41**$_{SCSC}$ (*i.e.* successful hydride H/D-exchange with a D_2 atmosphere; evolution of H_2 in lieu of HD; no evidence of insertion-elimination even after 60 minutes in CD_2Cl_2 solution).

While Rh-analogue [(^{i}Pr-PONOP)Rh(η^2-ethene)][BAr^F_4] was noted to undergo progressive ^{2}H incorporation onto the ethene ligand under a D_2 atmosphere in CD_2Cl_2 solution, this process occurred extremely slowly, over the course of five days at 298 K, and no such incorporation was noted under solid-gas conditions.[26] These extended conditions could not be reproduced for the *in situ*-generated alkene-dideuterides d_2-**41** and d_2-**42** dissolved in CD_2Cl_2, which slowly released D_2 on this timescale into solution to regenerate the respective Ir(I) alkene complexes (as the non-deuterated **35** and **38** respectively).

[a] The lecture bottle of D_2 as purchased from Sigma-Aldrich contained small impurities of both H_2 (δ 4.64) and HD (δ 4.61, $^1J_{HD}$ = 42.7 Hz), in a ~1:9 total integral ratio. Exposure to ethene-dihydride h_2-**42**$_{SCSC}$ elevated the proportion of H_2 significantly, to ~1:1, with the HD integral remaining approximately constant with respect to the solvent peak and the minor water peak.

These results could also not be reproduced for recrystallised samples of ethene-dihydride **42**$_{xtal}$. Ground crystals resisted solid-gas H/D exchange at 298 K, even given 60 minutes' exposure to D_2, where no reduction in the hydridic integrals (1.0 H each relative to $[BAr^F{}_4]^-$) was noted by solution-phase ^{1}H NMR spectroscopy. This is congruent with the observed reluctance of recrystallised **42**$_{xtal}$ to undergo solid-gas reductive elimination of H_2 due to its 'structural locking feature', discussed in the previous Section, and the comparative ease by which the solid-state *in situ*-generated alkene-dihydrides **41**$_{SCSC}$ and **42** did the same.

Having discussed the periodic structure-shifting (PSS) SC-SC hydrogenation **35**→**41***→**41**$_{SCSC}$ in detail, as well as the solid-gas hydrogenation of the similar ethene complex **38**, we now turn to a related PSS SC-SC desolvation. Both transformations were reasoned to benefit from the plastic, flexible array of $[BAr^F{}_4]^-$ anions, permitting retention of crystallinity despite a changing periodic structure.

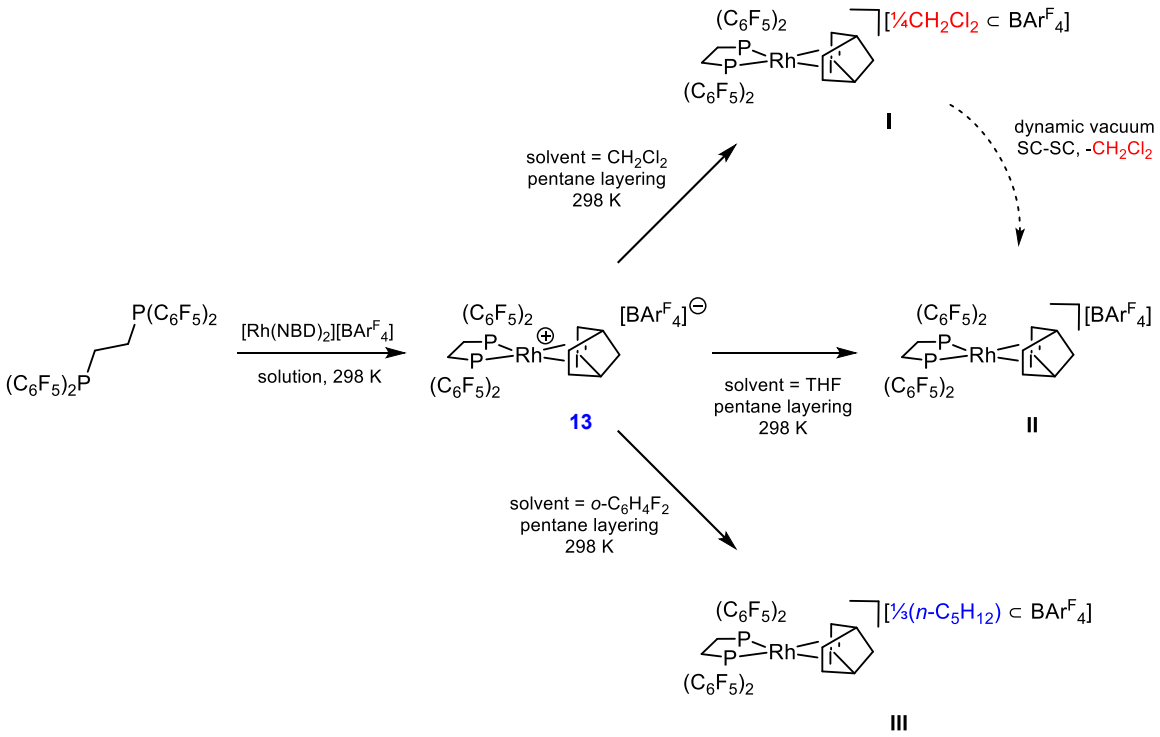
3.3 A dpfppe-Rhodium(I) Single-Crystal to Single-Crystal Solvent De-Encapsulation

In the previous Chapter, we briefly touched on the synthesis[a] of [(dpfppe)Rh(η^2,η^2-NBD)][$BAr^F{}_4$] (dpfppe = $(C_6F_5)_2P(CH_2)_2P(C_6F_5)_2$; SMOM **13**), its unusual solid-state structure,[b] and its deployment as a solid-gas pre-catalyst for 1-butene isomerisation.[c] We were interested as to whether the electron-withdrawing -C_6F_5 groups located on the chelate would have a significant effect on catalysis. Serendipitously, it was discovered that a number of solvent-containing variant structures (solvent 'morphs') could be obtained, depending on the crystallisation conditions. One of these structures, the CH_2Cl_2-containing morph **13-I**, will be shown in this Chapter to be capable of undergoing an SC-SC solvent de-encapsulation reaction with a significant change in periodic structure (periodic structure shifting, 'PSS').

[a] Section 2.2.2
[b] Section 2.2.4, specifically of the structure containing no co-crystallised solvent as obtained by loss of CH_2Cl_2 from the lattice, designated in this chapter as '**13-II**$_{SCSC}$'
[c] Sections 2.4.2 and 2.4.7

3.3.1 *Solution-Phase Synthesis and Characterisation of $(C_6F_5)_2P(CH_2)_2P(C_6F_5)_2$-Rhodium(I) (dpfppe-Rhodium(I)) SMOMs 13-I,II,III*

The solvent-containing variants of the perfluorophenylated P_2-type SMOM **13** were obtained by combination of *bis*-phosphine 'dpfppe' with one equivalent of $[Rh(\eta^2,\eta^2\text{-NBD})_2][BAr^F{}_4]$ in a certain solvent (CH_2Cl_2, THF, 1,2-difluorobenzene), followed by crystallisation *via* layering with pentane at 298 K to generate large orange prismatic crystals in all cases. Use of CH_2Cl_2 as the solvent generated the CH_2Cl_2-containing morph **13-I**, whereas use of THF generated the non-solvent-containing 'empty' morph **13-II**, and use of 1,2-difluorobenzene generated the pentane-containing morph **13-III** (**Scheme 3.3.1**). Once removed from the solvent mixture and exposed to dynamic vacuum ($p < 10^{-2}$ mbar, 10 minutes), smaller crystals (< *ca.* 1 mm × 1 mm × 1 mm) of **13-I** lost CH_2Cl_2 rapidly and irreversibly in an SC-SC fashion to generate 'empty' morph **13-II**$_{SCSC}$. Loss of CH_2Cl_2 was also observed from fine powders of **13-I**.



Scheme 3.3.1: Synthesis of various solvent-containing morphs of SMOM **13**: CH_2Cl_2-containing (**I**), non-solvent-containing ('empty', **II**), and pentane-containing (**III**).

We will discuss this SC-SC transformation in detail in the proceeding section; here, we will discuss the solution-phase NMR spectroscopic data and the solid-state structures of these morphs. Rhodium-dpfppe complexes similar to **13** have been reported, and their NMR spectroscopic data were similar.[108,109]

Loss of CH_2Cl_2 from **13-I** was confirmed by *sc*-XRD studies (unit-cell checks on multiple individual crystals) and bulk solution-phase NMR, where no *protio*-CH_2Cl_2 was evidenced by ^{1}H NMR spectroscopy, expected at δ 5.33. Larger crystals of **13-I** (greater than *ca.* 2 mm × 2 mm × 2 mm) resisted loss of CH_2Cl_2 during exposure to dynamic vacuum, with evidence for *protio*-CH_2Cl_2 by ^{1}H NMR spectroscopy: after exposing a large crystal of **13-I** (*ca.* 3 mm × 2 mm × 1 mm) to dynamic vacuum ($p < 10^{-2}$ mbar) for 60 minutes in total, a resonance at δ 5.33 was observed, integrating to 0.36 H relative to the adjacent NBD alkene peak, fixed to 4.00 H. Prolonged exposure to dynamic vacuum (8 hours in total, on a different but similarly-sized large crystal) lead to the further diminishment of this resonance, to 0.21 H.

The solid-state structure of **13-I** revealed a rhodium-containing cationic fragment $[(C_6F_5)_2P(CH_2)_2P(C_6F_5)_2Rh]^+$ located inside an approximately eight-fold coordination environment of $[BAr^F{}_4]^-$ anions, arranged in distorted gyrobifastigia[a] with two such units combining along a square face to effect a buckled hexagonal prism. This hexagonal-prismatic packing pattern is atypical for SMOM-type systems, which usually pack in an octahedral (O_h) fashion,[b] as the similar [(dpfppe)Ir(η^2,η^2-COD)][$BAr^F{}_4$] reported by Crisenza *et al.* is known to do so.[110] Some degree of π-π stacking interaction was observed between one dpfppe -C_6F_5 group (C8) and one $[BAr^F{}_4]^-$ -Ar^F group (intercentroid distance ~4.09 Å).

Assignment of n_{DCM} ~ ¼ for **13-I** was based upon the most reasonable refinement of the solid-state structure. Present in the asymmetric unit of **13-I** was an encapsulated CH_2Cl_2 molecule, refining to approximately 25% chemical occupancies. Two such sites were found close to one another in cavities of eight anionic and four cationic fragments (**Figure 3.3.1a**).

[a] A *gyrobifastigium* is composed of two triangular prisms joined on a square face and then rotated relative to one another by 90°. See **Figure 3.3.1d**.
[b] See Section 2.2.4 for a discussion on SMOM structure-types, including those of SMOM **13-II**$_{SCSC}$ (as simply 'SMOM **13**'), which packs in a hexagonal-prismatic fashion similarly to **13-I**.

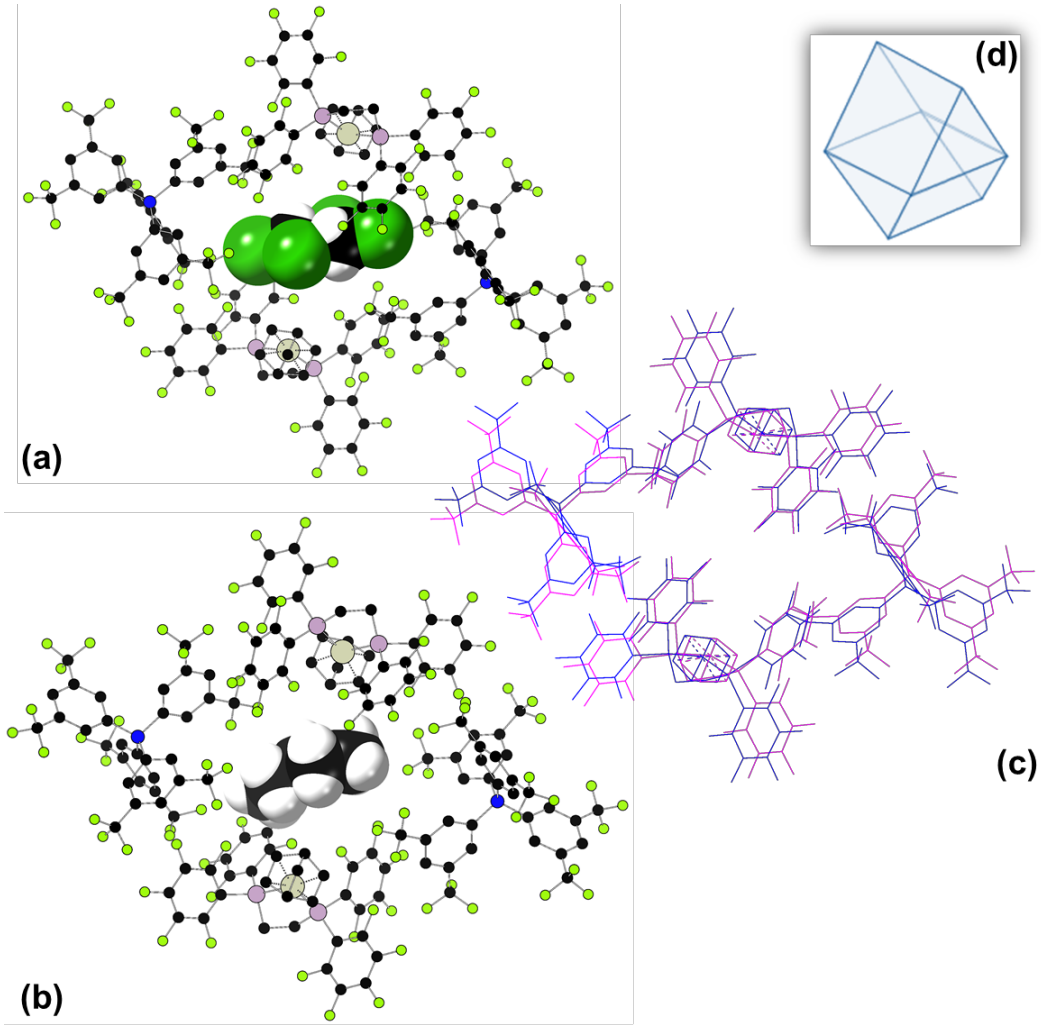


Figure 3.3.1: Sections of the solid-state structure of CH_2Cl_2-containing (**13-I**, (**a**)) and pentane-containing (**13-III**, (**b**)), showing the encapsulated solvent molecule(s) (**I**: two nearby *ca.* ¼ chemical occupancy sites; **II**: one pentane *ca.* ⅙ occupancy site), rendered as space-filling), surrounded by two cationic and two anionic fragments (rendered as ball-and-stick). (**c**) Approximate overlay of the structures in (**a**) and (**b**) minus solvent, rendered in wireframe and overlaid along approximately the same orientations, intended to show that these structures, excepting encapsulated solvent, are almost isomorphous. (**d**) A gyrobifastigium.

These cavities were interconnected by narrow cross-structural pores running in the *x*-direction, with each pair separated from the next by ~12.4 Å. These pores measured ~3.5 Å wide at their narrowest (F2···F3 separation of 3.576(3) Å, of which ~95% existed in the *y*,*z* projection). Accounting for the van der Waals radii of the fluorine atoms (~1.20 Å),[111] this diminished to ~1.1 Å, too narrow to admit CH_2Cl_2 molecules (r_{vdW}(Cl) ≈ 1.60 Å) without some flexion. Other possible routes for CH_2Cl_2 transport (*i.e.* in the *y* and *z* directions) faced greater degrees of obstruction.

Pentane-containing **13-III** (**Figure 3.3.1b**), notwithstanding encapsulated solvent, was structurally very similar to CH_2Cl_2-containing **13-I** such that these structures could not be easily told apart by *sc*-XRD unit cell checks (**Figure 3.3.1c**). $n_{pentane}$ ~ ⅓ was informed by NMR studies as well as reasonable solid-state refinement. Crystals of **13-III** of any size (including finely ground powders) did not lose pentane upon exposure to dynamic vacuum, as multiple exposures did not significantly alter the integral ratio of the pentane resonances by bulk solution-phase ^{1}H NMR spectroscopy. Pentane in **13-III** was detected at δ 0.86 (CH_3), 1.22 (CH_2), and 1.27 (CH_2), with the latter two overlapping, giving rise to two groups of resonances in a ~1:1 integral ratio. $n_{pentane}$ ~ ⅓ would be expected to give rise to pentane resonances of integral ~2.0+2.0 H relative to $[BAr^F_4]^-$. Integrals in the ranges 1.74-1.86 H and 1.87-1.99 H respectively were noted.

The absence of any solvent in the 'empty' structure **13-II** as obtained from both THF/pentane and from the SC-SC CH_2Cl_2 loss from **13-I** (as **13-II**$_{SCSC}$) was confirmed by bulk solution-phase ^{1}H NMR spectroscopy, where resonances corresponding to any of *protio*-CH_2Cl_2, pentane, and THF were not resolved. Crystals of **13-II** obtained by THF/pentane recrystallisation produced *sc*-XRD unit-cell checks indistinguishable from **13-II**$_{SCSC}$. Compared to the similar structures of **13-I** and **13-III** (**Figure 3.3.1**), that of **13-II** was notably dissimilar (**Figure 3.3.2**).

Also observed from structural refinement in all cases was an unusual coordination geometry of the η^2,η^2-NBD fragment about the Rh centre, distorted from the expected square-planar geometry seen in all previously-obtained Rh(I) SMOMs, with the η^2,η^2-NBD fragment lifted ~18° out of the P-Rh-P plane (**Figure 3.3.3**).

A CCDC search of all dppe-type complexes of {Rh,Ir(η^2,η^2-NBD)}$^+$ (dppe = $Ph_2P(CH_2)_2PPh_2$) bearing aryl groups with varying degrees of substitution indicated that these complexes generally obeyed square-planarity with respect to the centroids of the η^2,η^2-NBD alkene bonds. Deviations from this norm may take two forms: 'roll', where the η^2,η^2-NBD fragment twists about the Rh···$C_{methylene}$ axis, and 'pitch', observed here, where the alkene units are tilted out of the RhP_2 plane in the same direction.

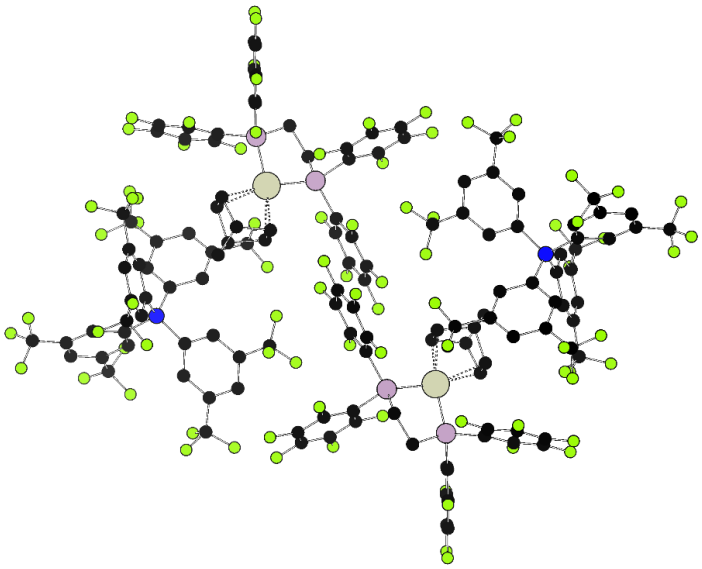


Figure 3.3.2: Section of the solid-state structure of non-solvent-containing morph **13-II** as obtained by recrystallisation from THF/pentane, rendered as ball-and-stick, oriented to show a similar profile to **Figure 3.3.1** and to emphasise the closure of the pore. An indistinguishable motif is found in the isostructural **13-II**$_{SCSC}$ as obtained by SC-SC CH_2Cl_2 loss from **13-I**.

A pitching distortion, not observed in [(dppe)Rh(η^2,η^2-NBD)]$^+$,[112] may be induced by a more sterically crowded coordination sphere[113,114] as well as by weak intramolecular dative interactions.[114,115] Two intramolecular Rh···*ortho*-F close approaches of ~3.05-3.15 Å were noted in all three structure types (indicated in red in **Figure 3.3.3**). Similar distortions from square-planarity were observed in the solid-state structures of related complexes *trans*-[(P(C_6F_5)$_3$)$_2$RhCl(CO)][116] and [(dpfppe)RhCl(PPh_3)],[117] with these 'non-primary valence interactions' occurring with Rh···*ortho*-F close approaches of ~3.06–3.09 Å. We suggest that a combination of effects, *viz.* proximal F atoms which may act as weak donors[118–120] and a crowded metal coordination sphere, induced the pitching distortion seen in all **13** solvent morphs.

The solution-phase NMR spectroscopic data obtained for all **13** solvent morphs were unremarkable and, save for encapsulated solvent discussed above, were indistinguishable by this method. $^{31}P\{^1H\}$ and $^{13}C\{^1H\}$ (**Figure 3.3.4**) SSNMR data were collected for powders of **13-II**$_{SCSC}$ and **13-III**. The presence of signals at δ_C 14.3 (pentane CH_2) and 24.0 (CH_3) in the latter and the absence of δ_C ~53.8 (CH_2Cl_2) in the former constituted important evidence for retention of pentane and loss of CH_2Cl_2 respectively.

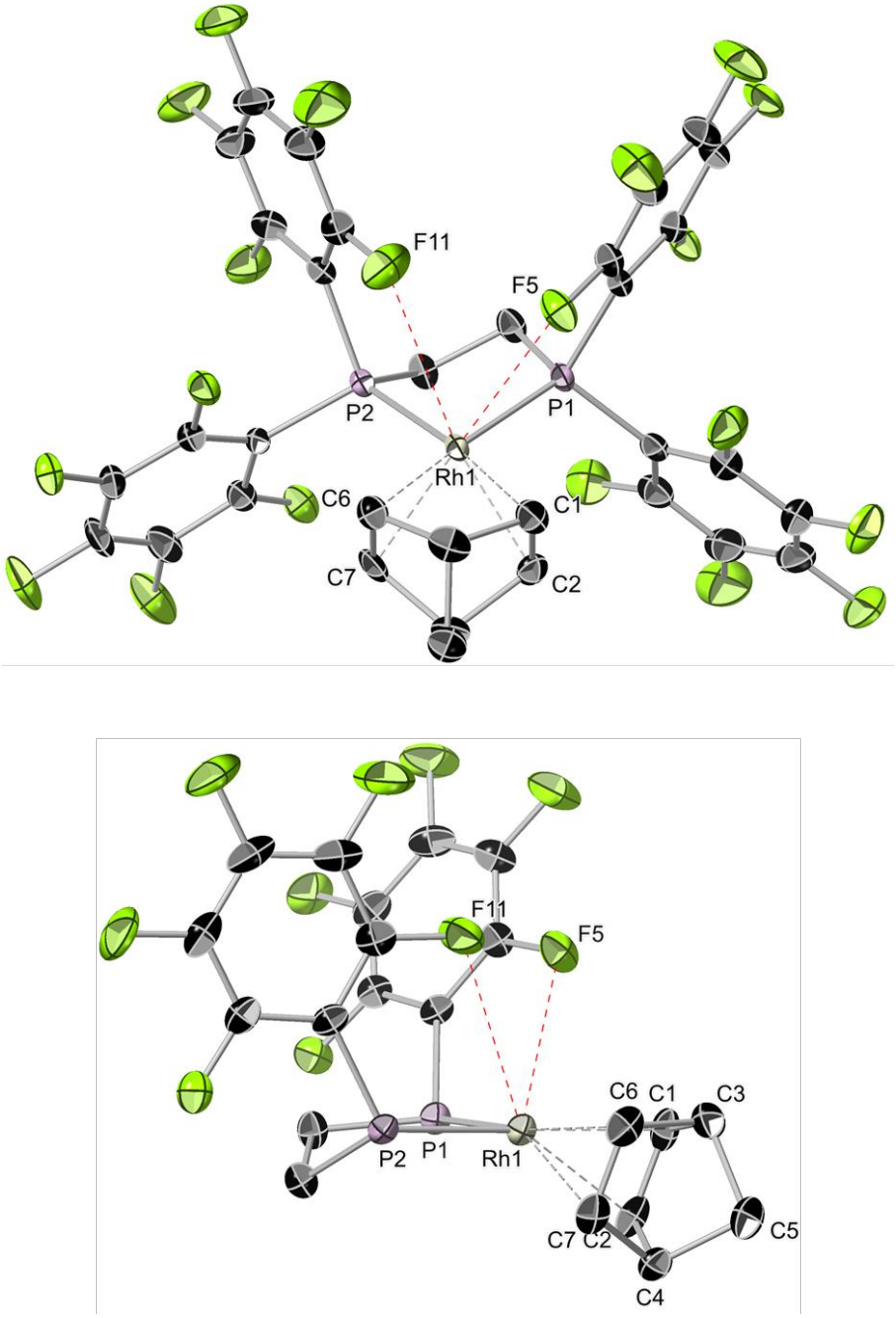


Figure 3.3.3: Two views of cationic fragment [(dpfppe)Rh(η^2,η^2-NBD)]$^+$ from the solid-state structure of **13-II** as obtained *via* recrystallisation from THF/pentane. 50% displacement ellipsoids. H-atoms, [$BAr^F{}_4$]$^-$ anions and C_6F_5 rings (second view) have been omitted for clarity. Close Rh1···F5,11 approaches have been highlighted in red. Selected bond lengths [Å] and angles [°], where Cent is the centroid of C1–C2 and Cent' the centroid of C6–C7: Rh1–P1, 2.2713(6); Rh1–P2, 2.2716(6); Rh1–C1, 2.221(2); Rh1–Cent, 2.10956(18); Rh1–C2, 2.214(2); C1–C2, 1.365(4); Rh1–C6, 2.211(2); Rh1–Cent', 2.10578(18); Rh1–C7, 2.217(2); C6–C7, 1.366(4); Rh1–F5, 3.0546(15); Rh1–F11, 3.0926(15); P1–Rh1–P2, 83.37(2); P1–Rh1–C1, 104.81(7); P2–Rh1–C6, 106.08(7); C1–Rh1–C6, 65.70(9); P1–Rh1–C6, 169.10(7); P1–Rh1–C7, 150.44(7); P2–Rh1–C1, 171.77(7); P2–Rh1–C2, 145.04(7). A similar distortion from square-planarity was present in all structures obtained containing this cation, with a pitching-distorted η^2,η^2-NBD fragment and close Rh1···F5,11 approaches (~3.05-3.15 Å).

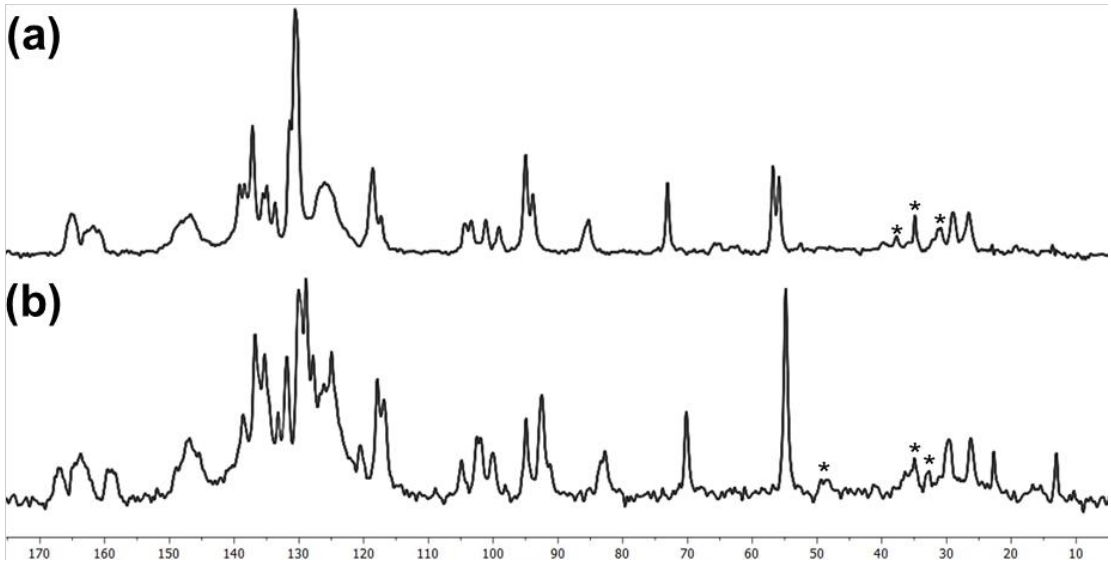


Figure 3.3.4: $^{13}C\{^{1}H\}$ SSNMR (100.66 MHz, 298 K, ν = 10 kHz) spectra of 'empty' morph **13-II**$_{SCSC}$ as generated by loss of CH_2Cl_2 from **13-I** (**a**), and pentane-containing morph **13-III** (**b**). * denote spinning side-bands.

Other differences between these $^{13}C\{^{1}H\}$ SSNMR spectra, *i.e.* the discrepant appearance of the $[BAr^F_4]^-/C_6F_5$ region (δ > 100), suggested a change in packing pattern between these two morphs. We will revisit this observation in the proceeding Section. $^{19}F\{^{1}H\}$ SSNMR spectroscopic data were collected but proved impossible to deconvolute despite the use of multiple MAS speeds (ν = 6, 8, 10 kHz). $^{19}F\{^{1}H\}$ SSNMR was therefore of little use as a characterising technique, and will not re-enter the discussion.

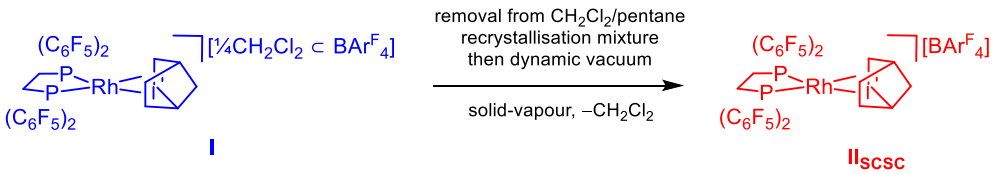
The pitching distortion described above appeared not to have been retained on the timescales of solution-phase NMR spectroscopy (CD_2Cl_2, 298 K). A single ^{1}H NMR resonance was resolved for alkene CH (δ_H 5.40). For each of the *ortho*-, *meta*-, and *para*-^{19}F positions, single $^{19}F\{^{1}H\}$ NMR resonances were also resolved (δ_F –130.0 [br. d, $^3J_{FF}$ ~ 19 Hz], –155.8 [br. dd, $^3J_{FF}$ = 20.7 Hz, $^3J_{FF}$' ~ 15 Hz], –141.9 [t br. t, $^3J_{FF}$ ~ 21 Hz, $^4J_{FF}$ ~ 19 Hz] respectively). These observations suggested the cationic fragment to be fluxional in solution. This fluxionality did not freeze out upon cooling to 185 K, at which only broadening and some upfield movement of the alkene CH (δ_H 5.31) resonance were noted, alongside significant broadening in the *ortho*-^{19}F resonance (δ_F –129.9) not seen at the *meta*- and *para*-^{19}F positions, perhaps indicative of some weak interaction between *ortho*-F and the metal centre as suggested by the solid-state structure.

Evidence for some form of pitching distortion was available, however, by $^{13}C\{^{1}H\}$ SSNMR spectroscopy (**Figure 3.3.4**): resonances corresponding to the η^2,η^2-NBD alkene ^{13}C atoms were seen to be split (**13-II**$_{SCSC}$: δ 93.9, 95.0 (~110 Hz dispersion); **13-III**: δ 93.2, 95.6 (~240 Hz)). These values chimed with the chemical shift for this position observed in CD_2Cl_2 solution (δ 92.8), the solid-state signal dispersion evoking the distinctly inequivalent chemical environments of each pair of alkene ^{13}C atoms (C1,6; C2,7).

SMOMs **13-II**$_{SCSC}$ and **13-III** which had been exposed to an atmosphere of H_2 (1 bar, 298 K, 10 minutes) were deployed as solid-gas 1-butene isomerisation catalysts with success.[a] However, no significant performance differences were observed between the two solvent morphs. As such, we were not able to confirm a structure-activity relationship between these two variant structures of SMOM **13**.

*3.3.2 CH_2Cl_2-Containing Morph **13-I**: A Single-Crystal to Single-Crystal Solvent De-Encapsulation*

In the previous Section, we discussed how the use of different solvents determined which morph of SMOM **13** was obtained during recrystallisation, and how the CH_2Cl_2-containing morph (**13-I**) underwent loss of its encapsulated solvent once removed from its CH_2Cl_2/pentane recrystallisation mixture and exposed to dynamic vacuum (**Scheme 3.3.2**). We also showed how the parent structure **13-I** and the daughter structure **13-II**$_{SCSC}$ were dissimilar. Here, we will discuss the SC-SC de-encapsulation proceeding from CH_2Cl_2-containing **13-I** to 'empty' **13-II**$_{SCSC}$ in greater detail.



Scheme 3.3.2: SC-SC loss of CH_2Cl_2 from crystals of CH_2Cl_2-containing morph, **13-I**.

[a] See Chapter 2, Sections 2.4.2 and 2.4.7, for the deployment of pre-hydrogenated SMOM **13-II**$_{SCSC}$ (as simply 'SMOM **13**') under heterogeneous continuous flow conditions.

All attempts to reintroduce CH_2Cl_2 vapours into crystals of **13-II**$_{SCSC}$ thus formed without dissolving were unsuccessful. This suggested an irreversibly gated process, due to the closure of cross-structural pores and collapse of structural void spaces (**Figure 3.3.5**). Gated adsorption/desorption phenomena have been reported for numerous systems where flexible substituents penetrate into channels, namely certain permeable MOFs[121–126] and metalloenzymes[127] capable of gas and volatile trafficking.

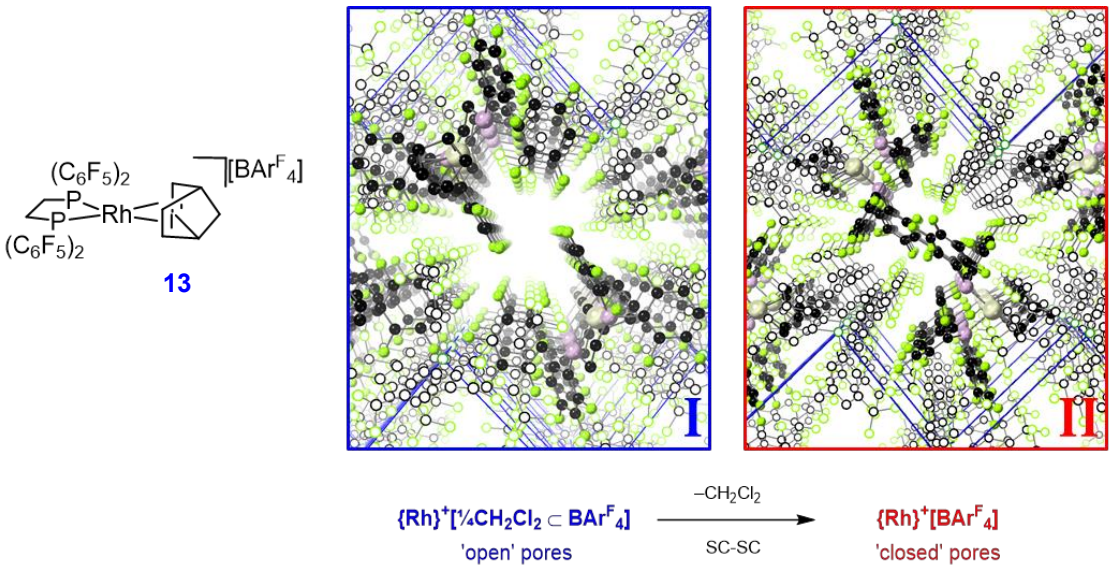


Figure 3.3.5: Extended ball-and-stick structures of the CH_2Cl_2-containing morph **I** (**left**) and 'empty' morph **II**$_{SCSC}$ (**right**) of SMOM **13** oriented along the *x*-direction. In the former case, CH_2Cl_2 sites have been omitted in order to exaggerate the narrow pores interconnecting each solvent site. Layers of proximal $[BAr^F{}_4]^-$ anions are highlighted with blue B-B 'bonds'.

The absence of pentane in the bulk solution-phase ^{1}H NMR spectra of **13-II**$_{SCSC}$ or of larger crystals of **13-I** (*vide supra*), its absence in powders of **13-II**$_{SCSC}$ by $^{13}C\{^1H\}$ SSNMR spectroscopy, and the resistance to loss of solvent by crystals of pentane-containing **13-III** altogether evidenced that pentane was *not* present in samples of **13-I** as obtained from CH_2Cl_2/pentane in significant quantities. This is important to note as the solid-state structures of **13-I** and **13-III** are similar (recall **Figure 3.3.1**) and were difficult to tell apart by *sc*-XRD unit cell checks. The metrics of all the morphs of SMOM **13** discussed in this section are summarised in **Table 3.3.1**.

Structure	S.G.	a (Å)	b (Å)	c (Å)	α (°)	β (°)	γ (°)	R_{int} (%)
13-I	$P\bar{1}$	12.3599(2)	14.0345(3)	20.4886(4)	85.648(2)	81.526(2)	80.998(2)	3.24
13-II	$P\bar{1}$	12.1327(5)	14.8905(6)	19.6485(8)	98.126(3)	102.350(4)	99.011(3)	2.58
13-II$_{SCSC}$	$P\bar{1}$	12.1404(2)	14.8801(3)	19.6360(3)	98.105(2)	102.364(2)	99.003(2)	2.38
13-III	$P\bar{1}$	12.3695(5)	13.9884(5)	20.5021(6)	85.173(3)	81.140(3)	80.922(3)	2.36

Table 3.3.1: Selected crystal metrics for morphs of SMOM **13** discussed in this chapter. S.G. = space group.

Compared to the *sc*-XRD diffraction data for **13-II$_{SCSC}$**, only a slight improvement in data quality was noted for the recrystallised **13-II** (R_{int} 2.38% *versus* 2.58%), indicating particularly favourable maintenance of crystallinity across the SC-SC transformation. Consistent with structural response to loss of encapsulated solvent, **13-II$_{SCSC}$** possessed a smaller unit cell volume than **13-I** (-2.9%), and a π-π stacking interaction was again observed between the same dpfppe C_6F_5 group (C8) and one $[BAr^F_4]^-$ Ar^F group (intercentroid distance ~4.32 Å, +5.6%), maintained despite the solid-state shifting of both anions and cations (**Figure 3.3.6**).

We have already described how $^{13}C\{^1H\}$ SSNMR data collected for powders of **13-II$_{SCSC}$** and **13-III** indicated the absence of CH_2Cl_2 in the former (expected δ ~53.8) and the presence of pentane in the latter (δ 14.3, 24.0); these data were shown in **Figure 3.3.4**. Other differences between these $^{13}C\{^1H\}$ SSNMR spectra, *i.e.* the architecture of the $[BAr^F_4]^-/C_6F_5$ region (δ > 100), were ascribed to a change in packing pattern between these two morphs, now confirmed by *sc*-XRD studies. These observations aligned with those made in Sections 3.2.3 and 3.2.6, on modifications to the $[BAr^F_4]^-$ region (δ 115-140) upon the solid-gas exposure of iridium-containing SMOMs [(^{i}Pr-PONOP)Ir(η^2-propene)][BAr^F_4] (**35**) and [(^{i}Pr-PONOP)Ir(η^2-ethene)][BAr^F_4] (**38**) to H_2 in the solid-state.

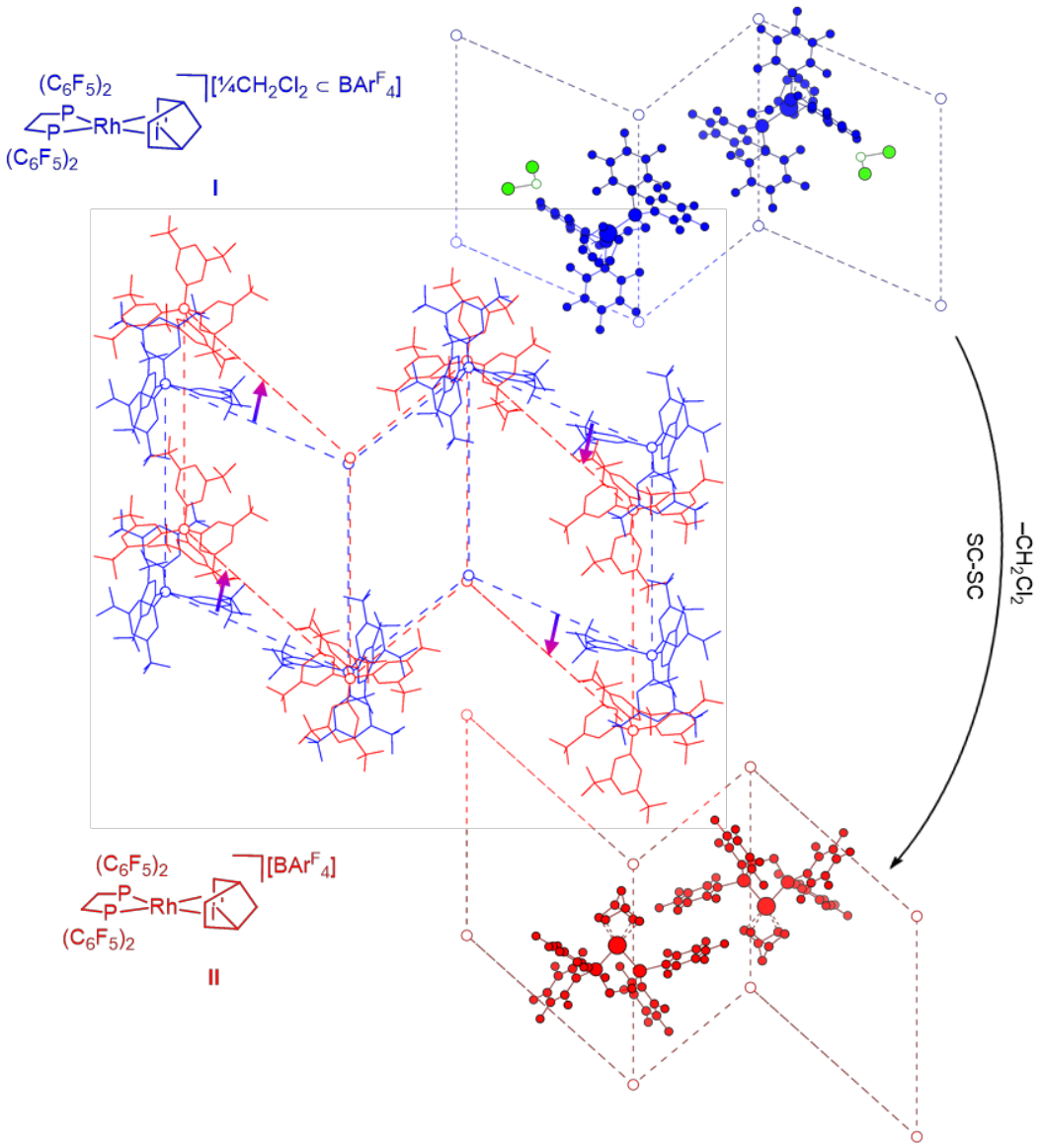


Figure 3.3.6: Hexagonal-prismatic packing motifs of the solid-state structures of **13-I** (blue) and **13-II**$_{SCSC}$ (red) viewed along the *x*-direction. (**middle**) Overlaid $[BAr^F_4]^-$ anions as wireframes, with some removed for clarity and arrows added to indicate the shifting direction of the anionic array; (**top** and **bottom**) Cationic fragments as ball-and-stick, CH_2Cl_2 in green. In both cases B–B 'bonds' are included as dashed lines.

3.4 Conclusion

In this chapter, two remarkable SC-SC transformations were described, each proceeding with a shift in the packing pattern of anions and cations (periodic structure-shifting, 'PSS'). One proceeded from a PONOP-bound iridium(I)-propene SMOM (**35**) and was induced by oxidative *cis*-addition of H_2; the other proceeded from a perfluorophenyl-bearing P_2-type SMOM (**13–I**) co-crystallised with CH_2Cl_2 and induced by vacuum-assisted, irreversible, 'gated' loss of the encapsulated CH_2Cl_2 from the structure. Both of these, although proceeding from quite chemically different materials, were understood to benefit from a plastic, flexible array of $[BAr^F_4]^-$ anions, capable of fluid-like responses to stimuli[a] and of undergoing significant solid-state movements in a concerted fashion, with maintenance of crystallinity despite shifting structure.

The protective/arresting nature of the solid-state was used to (reversibly) produce alkene-dihydrides in the solid-state from alkene complexes **35** and **38** at 298 K without over-hydrogenation, unavoidable in solution at the same temperature. Reflecting the importance of structure in determining reactivity, a recrystallised form of the ethene-dihydride (**42**$_{xtal}$) did *not* undergo solid-gas reductive elimination of H_2 due to a structural locking feature not present in the structures of its *in situ*-generated counterparts.

3.5 References

[1] A. J. Martínez-Martínez, C. G. Royle, S. K. Furfari, K. Suriye, A. S. Weller, *ACS Catalysis* **2020**, *10*, 1984–1992.

[2] F. M. Chadwick, N. Olliff, A. S. Weller, *Journal of Organometallic Chemistry* **2016**, *812*, 268–271.

[3] H. Salem, L. J. W. Shimon, Y. Diskin-Posner, G. Leitus, Y. Ben-David, D. Milstein, *Organometallics* **2009**, *28*, 4791–4806.

[4] M. Feller, E. Ben-Ari, M. A. Iron, Y. Diskin-Posner, G. Leitus, L. J. W. Shimon, L. Konstantinovski, D. Milstein, *Inorganic Chemistry* **2010**, *49*, 1615–1625.

[5] L. Schwartsburd, M. A. Iron, L. Konstantinovski, E. Ben-Ari, D. Milstein, *Organometallics* **2011**, *30*, 2721–2729.

[6] M. Feller, Y. Diskin-Posner, L. J. W. Shimon, E. Ben-Ari, D. Milstein, *Organometallics* **2012**, *31*, 4083–4101.

[7] A. Kumar, T. Zhou, T. J. Emge, O. Mironov, R. J. Saxton, K. Krogh-Jespersen, A. S. Goldman, *Journal of the American Chemical Society* **2015**, *137*, 9894–9911.

[8] F. Liu, A. S. Goldman, *Chemical Communications* **1999**, 655–656.

[9] S. Gu, R. J. Nielsen, K. H. Taylor, G. C. Fortman, J. Chen, D. A. Dickie, W. A. Goddard, T. B. Gunnoe, *Organometallics* **2020**, *39*, 1917–1933.

[10] X. Zhang, S.-B. Wu, X. Leng, L. W. Chung, G. Liu, Z. Huang, *ACS Catalysis* **2020**, 6475–6487.

[a] Compare the 'solution-like' heterogeneous catalysis described in Chapter 2, Section 2.4.9, where it was postulated that the $[BAr^F_4]^-$ anion adopted a role similar to a weakly-coordinating solvent in its facilitation of solid-gas catalytic 1-butene isomerisation.

[11] L. P. Press, A. J. Kosanovich, B. J. McCulloch, O. v Ozerov, *Journal of the American Chemical Society* **2016**, *138*, 9487–9497.

[12] H. Ito, M. Muromoto, S. Kurenuma, S. Ishizaka, N. Kitamura, H. Sato, T. Seki, *Nature Communications* **2013**, *4*, 2009.

[13] M. Albrecht, M. Lutz, A. L. Spek, G. van Koten, *Nature* **2000**, *406*, 970–974.

[14] D. Braga, F. Grepioni, M. Polito, M. R. Chierotti, S. Ellena, R. Gobetto, *Organometallics* **2006**, *25*, 4627–4633.

[15] A. I. McKay, T. Krämer, N. H. Rees, A. L. Thompson, K. E. Christensen, S. A. Macgregor, A. S. Weller, *Organometallics* **2017**, *36*, 22–25.

[16] S. D. Pike, F. M. Chadwick, N. H. Rees, M. P. Scott, A. S. Weller, T. Krämer, S. A. Macgregor, *Journal of the American Chemical Society* **2015**, *137*, 820–833.

[17] A. J. Martínez-Martínez, C. G. Royle, S. K. Furfari, K. Suriye, A. S. Weller, *ACS Catalysis* **2020**, *10*, 1984–1992.

[18] A. I. McKay, A. J. Martínez-Martínez, H. J. Griffiths, N. H. Rees, J. B. Waters, A. S. Weller, T. Krämer, S. A. Macgregor, *Organometallics* **2018**, *37*, 3524–3532.

[19] P. Kissel, D. J. Murray, W. J. Wulftange, V. J. Catalano, B. T. King, *Nature Chemistry* **2014**, *6*, 774–778.

[20] O. S. Bushuyev, A. Tomberg, T. Friščić, C. J. Barrett, *Journal of the American Chemical Society* **2013**, *135*, 12556–12559.

[21] T. Sasaki, S. Sakamoto, S. Takamizawa, *Crystal Growth & Design* **2019**, *19*, 5491–5493.

[22] S. Libri, M. Mahler, G. Mínguez Espallargas, D. C. N. G. Singh, J. Soleimannejad, H. Adams, M. D. Burgard, N. P. Rath, M. Brunelli, L. Brammer, *Angewandte Chemie International Edition* **2008**, *47*, 1693–1697.

[23] I. J. Vitórica-Yrezábal, G. Mínguez Espallargas, J. Soleimannejad, A. J. Florence, A. J. Fletcher, L. Brammer, *Chemical Science* **2013**, *4*, 696–708.

[24] A. J. Martínez-Martínez, N. H. Rees, A. S. Weller, *Angewandte Chemie International Edition* **2019**, *58*, 16873–16877.

[25] D. Morales-Morales, C. G. M. Jensen, *The Chemistry of Pincer Compounds*, Elsevier, **2011**.

[26] A. Johnson, C. G. Royle, C. N. Brodie, A. J. Martínez-Martínez, S. B. Duckett, A. S. Weller, *Inorganic Chemistry* **2021**, *60*, 13903–13912.

[27] S. M. Chapp, N. D. Schley, *Inorganic Chemistry* **2020**, *59*, 7143–7149.

[28] D. H. Woodmansee, M.-A. Müller, M. Neuburger, A. Pfaltz, *Chemical Science* **2010**, *1*, 72–78.

[29] M. R. Gyton, T. M. Hood, A. B. Chaplin, *Dalton Transactions* **2019**, *48*, 2877–2880.

[30] F. M. Chadwick, N. H. Rees, A. S. Weller, T. Krämer, M. Iannuzzi, S. A. Macgregor, *Angewandte Chemie International Edition* **2016**, *55*, 3677–3681.

[31] M. D. Walter, P. S. White, *New Journal of Chemistry* **2011**, *35*, 1842–1854.

[32] M. Rubio, A. Suárez, D. del Río, A. Galindo, E. Álvarez, A. Pizzano, *Organometallics* **2009**, *28*, 547–560.

[33] D. W. Price, M. G. B. Drew, K. K. (Mimi) Hii, J. M. Brown, *Chemistry – A European Journal* **2000**, *6*, 4587–4596.

[34] K. Tanoue, M. Yamashita, *Organometallics* **2015**, *34*, 4011–4017.

[35] Y. Segawa, M. Yamashita, K. Nozaki, *Organometallics* **2009**, *28*, 6234–6242.

[36] Y. Segawa, M. Yamashita, K. Nozaki, *Journal of the American Chemical Society* **2009**, *131*, 9201–9203.

[37] M. Hasegawa, Y. Segawa, M. Yamashita, K. Nozaki, *Angewandte Chemie International Edition* **2012**, *51*, 6956–6960.

[38] T. Yano, Y. Moroe, M. Yamashita, K. Nozaki, *Chemistry letters* **2008**, *37*, 1300–1301.

[39] A. Friedrich, R. Ghosh, R. Kolb, E. Herdtweck, S. Schneider, *Organometallics* **2009**, *28*, 708–718.

[40] F. M. Chadwick, A. I. McKay, A. J. Martinez-Martinez, N. H. Rees, T. Krämer, S. A. Macgregor, A. S. Weller, *Chemical Science* **2017**, *8*, 6014–6029.

[41] M. Henn, V. Deáky, S. Krabbe, M. Schürmann, M. H. Prosenc, S. Herres-Pawlis, B. Mahieu, K. Jurkschat, *Zeitschrift für anorganische und allgemeine Chemie* **2011**, *637*, 211–223.

[42] J. Campos, S. Kundu, D. R. Pahls, M. Brookhart, E. Carmona, T. R. Cundari, *Journal of the American Chemical Society* **2013**, *135*, 1217–1220.

[43] X. L. Luo, R. H. Crabtree, *Journal of the American Chemical Society* **1990**, *112*, 6912–6918.

[44] T. J. Hebden, K. I. Goldberg, D. M. Heinekey, X. Zhang, T. J. Emge, A. S. Goldman, K. Krogh-Jespersen, *Inorganic Chemistry* **2010**, *49*, 1733–1742.

[45] E. A. K. Spearing-Ewyn, N. A. Beattie, A. L. Colebatch, A. J. Martinez-Martinez, A. Docker, T. M. Boyd, G. Baillie, R. Reed, S. A. Macgregor, A. S. Weller, *Dalton Transactions* **2019**, *48*, 14724–14736.

[46] M. Findlater, K. M. Schultz, W. H. Bernskoetter, A. Cartwright-Sykes, D. M. Heinekey, M. Brookhart, *Inorganic Chemistry* **2012**, *51*, 4672–4678.

[47] G. J. Kubas, C. J. Unkefer, B. I. Swanson, E. Fukushima, *Journal of the American Chemical Society* **1986**, *108*, 7000–7009.

[48] C. Bianchini, S. Moneti, M. Peruzzini, F. Vizza, *Inorganic Chemistry* **1997**, *36*, 5818–5825.

[49] H. v Nanishankar, S. Dutta, M. Nethaji, B. R. Jagirdar, *Inorganic Chemistry* **2005**, *44*, 6203–6210.

[50] M. A. Salomon, T. Braun, I. Krossing, *Dalton Transactions* **2008**, 5197–5206.

[51] K. M. Schultz, K. I. Goldberg, D. G. Gusev, D. M. Heinekey, *Organometallics* **2011**, *30*, 1429–1437.

[52] R. N. Perutz, S. Sabo-Etienne, *Angewandte Chemie International Edition* **2007**, *46*, 2578–2592.

[53] E. M. Titova, E. S. Osipova, E. S. Gulyaeva, V. N. Torocheshnikov, A. A. Pavlov, G. A. Silantyev, O. A. Filippov, E. S. Shubina, N. v Belkova, *Journal of Organometallic Chemistry* **2017**, *827*, 86–95.

[54] W. J. Oldham, A. S. Hinkle, D. M. Heinekey, *Journal of the American Chemical Society* **1997**, *119*, 11028–11036.

[55] C. Ammann, F. Isaia, P. S. Pregosin, *Magnetic Resonance in Chemistry* **1988**, *26*, 236–238.

[56] K. J. Jonasson, A. v Polukeev, R. Marcos, M. S. G. Ahlquist, O. F. Wendt, *Angewandte Chemie International Edition* **2015**, *54*, 9372–9375.

[57] C. Y. Tang, A. L. Thompson, S. Aldridge, *Journal of the American Chemical Society* **2010**, *132*, 10578–10591.

[58] N. Phillips, C. Y. Tang, R. Tirfoin, M. J. Kelly, A. L. Thompson, M. J. Gutmann, S. Aldridge, *Dalton Transactions* **2014**, *43*, 12288–12298.

[59] C. J. Stevens, R. Dallanegra, A. B. Chaplin, A. S. Weller, S. A. Macgregor, B. Ward, D. McKay, G. Alcaraz, S. Sabo-Etienne, *Chemistry – A European Journal* **2011**, *17*, 3011–3020.

[60] H. C. Johnson, C. L. McMullin, S. D. Pike, S. A. Macgregor, A. S. Weller, *Angewandte Chemie International Edition* **2013**, *52*, 9776–9780.

[61] J. Yang, P. S. White, C. K. Schauer, M. Brookhart, *Angewandte Chemie International Edition* **2008**, *47*, 4141–4143.

[62] R. H. Crabtree, H. Felkin, G. E. Morris, *Journal of Organometallic Chemistry* **1977**, *141*, 205–215.

[63] R. H. Crabtree, H. Felkin, T. Fillebeen-Khan, G. E. Morris, *Journal of Organometallic Chemistry* **1979**, *168*, 183–195.

[64] R. H. Crabtree, P. C. Demou, D. Eden, J. M. Mihelcic, C. A. Parnell, J. M. Quirk, G. E. Morris, *Journal of the American Chemical Society* **1982**, *104*, 6994–7001.

[65] C. Mazet, S. P. Smidt, M. Meuwly, A. Pfaltz, *Journal of the American Chemical Society* **2004**, *126*, 14176–14181.

[66] S. J. Roseblade, A. Pfaltz, *Accounts of Chemical Research* **2007**, *40*, 1402–1411.

[67] C. Cheng, B. G. Kim, D. Guironnet, M. Brookhart, C. Guan, D. Y. Wang, K. Krogh-Jespersen, A. S. Goldman, *Journal of the American Chemical Society* **2014**, *136*, 6672–6683.

[68] S. D. Pike, A. L. Thompson, A. G. Algarra, D. C. Apperley, S. A. Macgregor, A. S. Weller, *Science* **2012**, *337*, 1648–1651.

[69] A. J. Martínez-Martínez, B. E. Tegner, A. I. McKay, A. J. Bukvic, N. H. Rees, G. J. Tizzard, S. J. Coles, M. R. Warren, S. A. Macgregor, A. S. Weller, *Journal of the American Chemical Society* **2018**, *140*, 14958–14970.

[70] T. N. Drebushchak, E. v Boldyreva, *Zeitschrift für Kristallographie - Crystalline Materials* **2004**, *219*, 506–512.

[71] A. Gionda, G. Macetti, L. Loconte, S. Rizzato, A. M. Orlando, C. Gatti, L. lo Presti, *RSC Advances* **2018**, *8*, 38445–38454.

[72] H.-Y. Zhuo, H.-F. Su, Z.-Z. Cao, W. Liu, S.-A. Wang, L. Feng, G.-L. Zhuang, S.-C. Lin, M. Kurmoo, C.-H. Tung, D. Sun, L.-S. Zheng, *Chemistry – A European Journal* **2016**, *22*, 17619–17626.

[73] K. F. Bowes, I. P. Clark, J. M. Cole, M. Gourlay, A. M. E. Griffin, M. F. Mahon, L. Ooi, A. W. Parker, P. R. Raithby, H. A. Sparkes, M. Towrie, *CrystEngComm* **2005**, *7*, 269–275.

[74] A. B. Chaplin, J. C. Green, A. S. Weller, *Journal of the American Chemical Society* **2011**, *133*, 13162–13168.

[75] D. Braga, *Chemical Reviews* **1992**, *92*, 633–665.

[76] A. J. Bukvic, A. L. Burnage, G. J. Tizzard, A. J. Martínez-Martínez, A. I. McKay, N. H. Rees, B. E. Tegner, T. Krämer, H. Fish, M. R. Warren, S. J. Coles, S. A. Macgregor, A. S. Weller, *Journal of the American Chemical Society* **2021**, *143*, 5106–5120.

[77] Z. Huang, P. S. White, M. Brookhart, *Nature* **2010**, *465*, 598–601.

[78] T. N. Hoheisel, S. Schrettl, R. Marty, T. K. Todorova, C. Corminboeuf, A. Sienkiewicz, R. Scopelliti, W. B. Schweizer, H. Frauenrath, *Nature Chemistry* **2013**, *5*, 327–334.

[79] J. Sun, J. Abbenseth, H. Verplancke, M. Diefenbach, B. de Bruin, D. Hunger, C. Würtele, J. van Slageren, M. C. Holthausen, S. Schneider, *Nature Chemistry* **2020**, *12*, 1054–1059.

[80] K. A. Reid, D. C. Powers, *Chemical Communications* **2021**, *57*, 4993–5003.

[81] D. Braga, S. L. Giaffreda, F. Grepioni, A. Pettersen, L. Maini, M. Curzi, M. Polito, *Dalton Transactions* **2006**, 1249–1263.

[82] Y. Miyamoto, S. Takamizawa, *Dalton Transactions* **2015**, *44*, 5688–5691.

[83] B. Cockayne, B. Lent, J. S. Abell, I. R. Harris, *Journal of Materials Science* **1973**, *8*, 871–875.

[84] H. Wenbo, Y. Duorong, X. Dong, Z. Nan, Y. Wentao, L. Mingguo, T. Xutang, S. Suoying, J. Minhua, *Journal of Crystal Growth* **1993**, *133*, 71–74.

[85] P. S. Hariharan, C. Pan, S. Karthikeyan, D. Xie, A. Shinohara, C. Yang, L. Wang, S. P. Anthony, *Dyes and Pigments* **2020**, *174*, 108067.

[86] K. T. Aust, *Journal of Crystal Growth* **1972**, *13–14*, 57–61.

[87] F. Dominé, T. Lauzier, A. Cabanes, L. Legagneux, W. F. Kuhs, K. Techmer, T. Heinrichs, *Microscopy Research and Technique* **2003**, *62*, 33–48.

[88] Y. Uchida, G. Weinberg, G. Lehmpfuhl, *Microscopy Research and Technique* **1992**, *20*, 406–412.

[89] M. D. Walter, P. S. White, C. K. Schauer, M. Brookhart, *Journal of the American Chemical Society* **2013**, *135*, 15933–15947.

[90] M. Findlater, W. H. Bernskoetter, M. Brookhart, *Journal of the American Chemical Society* **2010**, *132*, 4534–4535.

[91] W. H. Bernskoetter, S. K. Hanson, S. K. Buzak, Z. Davis, P. S. White, R. Swartz, K. I. Goldberg, M. Brookhart, *Journal of the American Chemical Society* **2009**, *131*, 8603–8613.

[92] E. G. Lundquist, K. Folting, W. E. Streib, J. C. Huffman, O. Eisenstein, K. G. Caulton, *Journal of the American Chemical Society* **1990**, *112*, 855–863.

[93] S. Park, M. Brookhart, *Journal of the American Chemical Society* **2012**, *134*, 640–653.

[94] I. Göttker-Schnetmann, D. M. Heinekey, M. Brookhart, *Journal of the American Chemical Society* **2006**, *128*, 17114–17119.

[95] S. Gruber, M. Neuburger, A. Pfaltz, *Organometallics* **2013**, *32*, 4702–4711.

[96] E. Piras, F. Läng, H. Rüegger, D. Stein, M. Wörle, H. Grützmacher, *Chemistry – A European Journal* **2006**, *12*, 5849–5858.

[97] E. J. Lawrence, V. S. Oganesyan, G. G. Wildgoose, A. E. Ashley, *Dalton Transactions* **2013**, *42*, 782–789.

[98] E. Clot, O. Eisenstein, T. Dubé, J. W. Faller, R. H. Crabtree, *Organometallics* **2002**, *21*, 575–580.

[99] A. García-Camprubí, M. Martín, E. Sola, *Inorganic Chemistry* **2010**, *49*, 10649–10657.

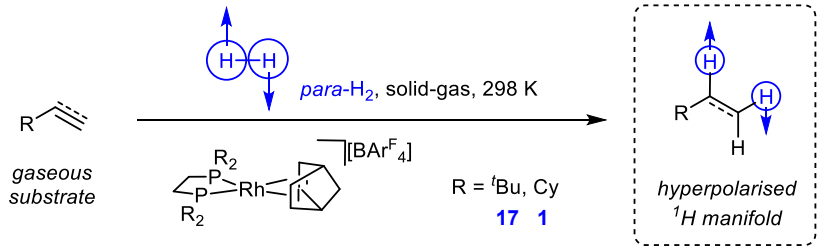
[100] B. S. Omar, J. Mallah, M. Ataya, B. Li, X. Zhou, S. Malakar, A. S. Goldman, F. Hasanayn, *Inorganic Chemistry* **2018**, *57*, 7516–7523.

[101] A. L. Spek, *Utrecht University: The Netherlands* **2005**.
[102] A. L. J. Spek, *Journal of Applied Crystallography* **2003**, *36*, 7–13.
[103] D. Braga, F. Grepioni, *Chemical Society Reviews* **2000**, *29*, 229–238.
[104] C. Murali, M. S. Shashidhar, R. G. Gonnade, M. M. Bhadbhade, *Chemistry – A European Journal* **2009**, *15*, 261–269.
[105] C. Schumacher, D. E. Crawford, B. Raguž, R. Glaum, S. L. James, C. Bolm, J. G. Hernández, *Chemical Communications* **2018**, *54*, 8355–8358.
[106] A. Bacchi, P. Pelagatti, *Chemical Communications* **2016**, *52*, 1327–1337.
[107] D. Braga, F. Grepioni, L. Maini, M. Polito, in *Molecular Networks* (Ed.: M.W. Hosseini), Springer Berlin Heidelberg, Berlin, Heidelberg, **2009**, pp. 87–95.
[108] D. P. Fairlie, B. Bosnich, *Organometallics* **1988**, *7*, 936–945.
[109] A. S. C. Chan, C.-C. Pai, T.-K. Yang, S.-M. Chen, *Journal of the Chemical Society, Chemical Communications* **1995**, 2031–2032.
[110] G. E. M. Crisenza, O. O. Sokolova, J. F. Bower, *Angewandte Chemie International Edition* **2015**, *54*, 14866–14870.
[111] M. Mantina, A. C. Chamberlin, R. Valero, C. J. Cramer, D. G. Truhlar, *The Journal of Physical Chemistry A* **2009**, *113*, 5806–5812.
[112] C. González-Rodríguez, R. J. Pawley, A. B. Chaplin, A. L. Thompson, A. S. Weller, M. C. Willis, *Angewandte Chemie International Edition* **2011**, *50*, 5134–5138.
[113] H.-J. Drexler, S. Zhang, A. Sun, A. Spannenberg, A. Arrieta, A. Preetz, D. Heller, *Tetrahedron: Asymmetry* **2004**, *15*, 2139–2150.
[114] B. Zupančič, B. Mohar, M. Stephan, *Advanced Synthesis & Catalysis* **2008**, *350*, 2024–2032.
[115] L. Carreras, J. Benet-Buchholz, A. Franconetti, A. Frontera, P. W. N. M. van Leeuwen, A. Vidal-Ferran, *Chemical Communications* **2019**, *55*, 2380–2383.
[116] R. Meijboom, A. Muller, A. Roodt, *Acta Crystallographica Section E* **2005**, *61*, m1283–m1285.
[117] M. J. Atherton, K. S. Coleman, J. Fawcett, J. H. Holloway, E. G. Hope, A. Karaçar, L. A. Peck, G. C. Saunders, *Journal of the Chemical Society, Dalton Transactions* **1995**, 4029–4037.
[118] R. J. Kulawiec, E. M. Holt, M. Lavin, R. H. Crabtree, *Inorganic Chemistry* **1987**, *26*, 2559–2561.
[119] K. Stanek, B. Czarniecki, R. Aardoom, H. Rüegger, A. Togni, *Organometallics* **2010**, *29*, 2540–2546.
[120] J. Emerson-King, I. Prokes, A. B. Chaplin, *Chemistry – A European Journal* **2019**, *25*, 6317–6319.
[121] D. P. van Heerden, V. J. Smith, H. Aggarwal, L. J. Barbour, *Angewandte Chemie International Edition* **2021**, *60*, 13430–13435.
[122] S. Horike, S. Shimomura, S. Kitagawa, *Nature chemistry* **2009**, *1*, 695.
[123] S. Henke, R. A. Fischer, *Journal of the American Chemical Society* **2011**, *133*, 2064–2067.
[124] A. Grigoropoulos, G. F. S. Whitehead, N. Perret, A. P. Katsoulidis, F. M. Chadwick, R. P. Davies, A. Haynes, L. Brammer, A. S. Weller, J. Xiao, M. J. Rosseinsky, *Chemical Science* **2016**, *7*, 2037–2050.
[125] J. A. Mason, J. Oktawiec, M. K. Taylor, M. R. Hudson, J. Rodriguez, J. E. Bachman, M. I. Gonzalez, A. Cervellino, A. Guagliardi, C. M. Brown, P. L. Llewellyn, N. Masciocchi, J. R. Long, *Nature* **2015**, *527*, 357–361.
[126] X. Sun, Y. Ma, J. Zhao, D.-S. Li, G. Li, L. Zhang, Y. Liu, *Dalton Transactions* **2018**, *47*, 13158–13163.
[127] L. J. Murray, S. J. Lippard, *Accounts of Chemical Research* **2007**, *40*, 466–474.

4 Solid-Gas Catalytic Hydrogenation-Polarisation of Alkenes and Alkynes (SMOM-PHIP)

4.1 Introduction

The phenomenon of *para*-hydrogen induced polarisation (PHIP) by means of catalytic hydrogenation is well established in the solution-phase,[1,2] occurring due to the perturbation of the normal Boltzmann population of nuclear spin states – a full theoretical and practical background of this phenomenon is provided in Section 1.4. The potential applications of PHIP in medical imaging had already been discussed. With this in mind, we set about translating this chemistry to the gas phase using SMOM catalysts (*e.g.* **Scheme 4.1.1**), hoping to generate hyperpolarised, gaseous hydrocarbons to signpost the route towards inhalable[3] medical contrast agents for probing the functions of the mammalian lung – a low-density, constantly-shifting organ with a large number of tissue-gas interfaces that responds poorly to traditional MRI techniques.[4]



Scheme 4.1.1: The general concept: solid-gas *para*-hydrogen induced polarisation (PHIP) of gaseous alkenes/alkynes in the presence of SMOM pre-catalysts **1** and **17**.

Although not the first time PHIP has been accomplished under heterogeneous conditions,[5–9] this chapter details the first time gas-phase PHIP has been accomplished with discrete organometallic catalysts and for the first time at ambient temperature, while also operating at relatively low pressures (no higher than 3.5 bar-absolute in total). As in Chapter 2, SMOMs of formula $[(P_2)Rh(\eta^2,\eta^2\text{-NBD})][BAr^F{}_4]$ (P_2 = dcpe = $Cy_2P(CH_2)_2PCy_2$ (**1**) and dtbpe = $^tBu_2P(CH_2)_2P^tBu_2$ (**17**)) were used as successful proofs-of-concept – in this case, for the solid-gas hydrogenation-polarisation of unsaturated substrates under NMR batch conditions.

4.2 Synthesis and Characterisation of a Target Propene Complex

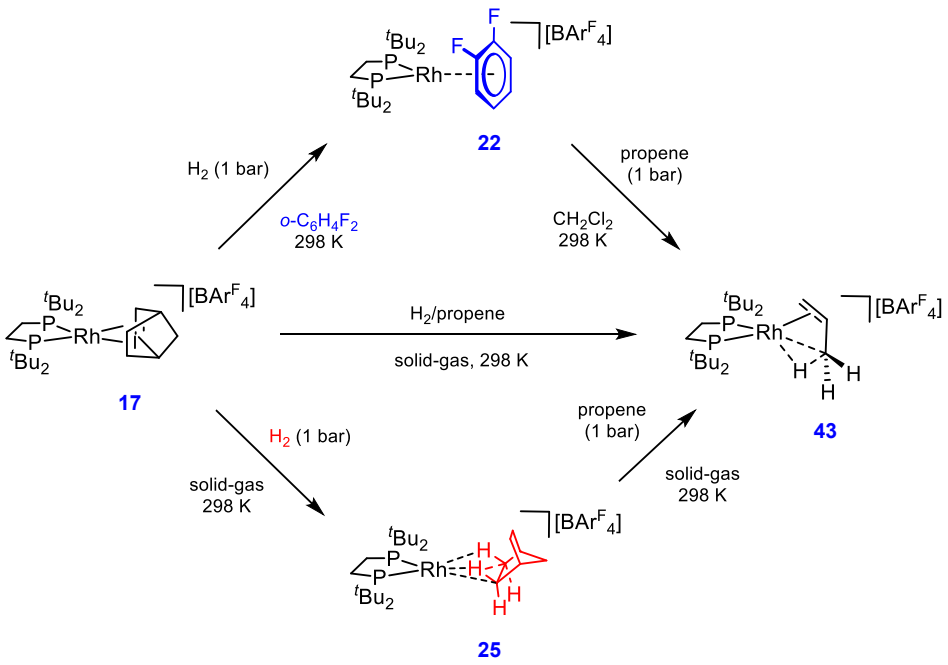
Of the limited number of gaseous *mono*-alkenes available under ambient conditions, propene was selected as the first target for solid-gas PHIP. Ethene and 2-butene (both *cis* and *trans* isomers) constitute inappropriate targets due to the symmetry about the double bond,[a] and 1-butene and *iso*-butene, with relatively high boiling points (−7.0 and −6.3 °C respectively at 1.013 atm),[10] were initially discounted due to potential problems with condensation at raised pressures. C_4 linear *mono*-alkenes were also avoided due to the potentially complicating aspect of catalytic isomerisation, the very property exploited in Chapter 2.

Essential to the understanding of the behaviours of these SMOMs in the presence of H_2 and propene gases are the respective propene complexes $[(P_2)Rh(\eta^2\text{-propene})][BAr^F_4]$ (P_2 = $Cy_2P(CH_2)_2PCy_2$ (dcpe), **28**; $^tBu_2P(CH_2)_2P^tBu_2$ (dtbpe), **43**). Complex **28** has been previously reported, generated in the solid-state by action of propene gas on $[(dcpe)Rh(\sigma\text{-NBA})][BAr^F_4]$ (**2**) in a single-crystal to single-crystal (SC-SC) transformation. Additionally, *bis*-propene complex $[(dcpe)Rh(\eta^2\text{-propene})_2][BAr^F_4]$ (**44**) has also been reported, generated by recrystallising **28** from CH_2Cl_2/pentane under a propene atmosphere at −20 °C, or *in situ* by stirring a CD_2Cl_2 solution of the 1,2-difluorobenzene complex (**21**) under a propene atmosphere.[11]

In the case of P_2 = dtbpe, both solution and solid-gas routes lead to the formation of *mono*-propene complex **43** (**Scheme 4.2.1**), a consequence of the greater steric bulk of the ^{t}Bu groups. Stirring a CH_2Cl_2 solution of 1,2-difluorobenzene complex **22** under a propene atmosphere lead to the formation of a sherry-coloured solution. Layering this propene-saturated solution with pentane at 298 K generated orange crystalline plates of *mono*-propene complex **43** in high yield (95%).

In the *absence* of a propene atmosphere at room temperature, CH_2Cl_2 solutions of **43** decomposed to the solvent-activated product (**24**),[b] in a similar manner to the related *n*-butenes complex (**27**). Therefore, all solution-phase NMR experiments on species **43** were conducted at 185 K, with CD_2Cl_2 vacuum-distilled over the solid samples with the assistance of liquid N_2.

[a] See Introduction (Section 1.4.3).
[b] A dimer of formula $[(dtbpe)Rh(\mu\text{-}CH_2)(\mu\text{-}Cl)_2Rh(dtbpe)][BAr^F_4]_2$, described in Section 2.2.5.



Scheme 4.2.1: Solid-gas and solution-phase routes to *mono*-propene complex **43**.

Treating crystalline η^2,η^2-NBD SMOM **17** sequentially with H_2 and then propene gas generated complex **43** *in situ*, albeit not in an SC-SC fashion. *sc*-XRD studies conducted on crystallites of **17** thus exposed to H_2 and propene revealed few Bragg peaks in the product and none beyond ~3.0 Å, indicating substantial loss of long-range order, certainly insufficient for any acceptable structural solution.

The identity of *mono*-propene complex [(dtbpe)Rh(η^2-propene)][BAr^F_4] (**43**) as generated by both solid-state and solution-phase routes was confirmed by solution-phase and solid-state NMR spectroscopy, elemental microanalysis, and *sc*-XRD studies (on material recrystallised from solution). Crystals of **43**[a] and amorphous **43** produced *in situ* by the solid-gas route were both taken in CD_2Cl_2 at 185 K, and were indistinguishable by solution-phase NMR spectroscopic methods. Integrated relative to [BAr^F_4]$^-$, ^{1}H NMR resonances corresponding to a propene ligand were located in a 1:1:1:3 integral ratio (**Figure 4.2.1**). No evidence was available for free propene that might have indicated the accessibility of a hypothetical, solution-unstable *bis*-propene complex in the solid-state, in analogy to complex **44**.

[a] Crystals of **43** could be obtained by taking amorphous material as generated by the solid-gas route, dissolving it in CH_2Cl_2 and layering with pentane at 253 K *or* by taking **43** as generated *in situ* by the solution route and layering the (propene-saturated) reaction mixture with pentane at 298 K. Both routes generated crystalline **43** in high purity and yield.

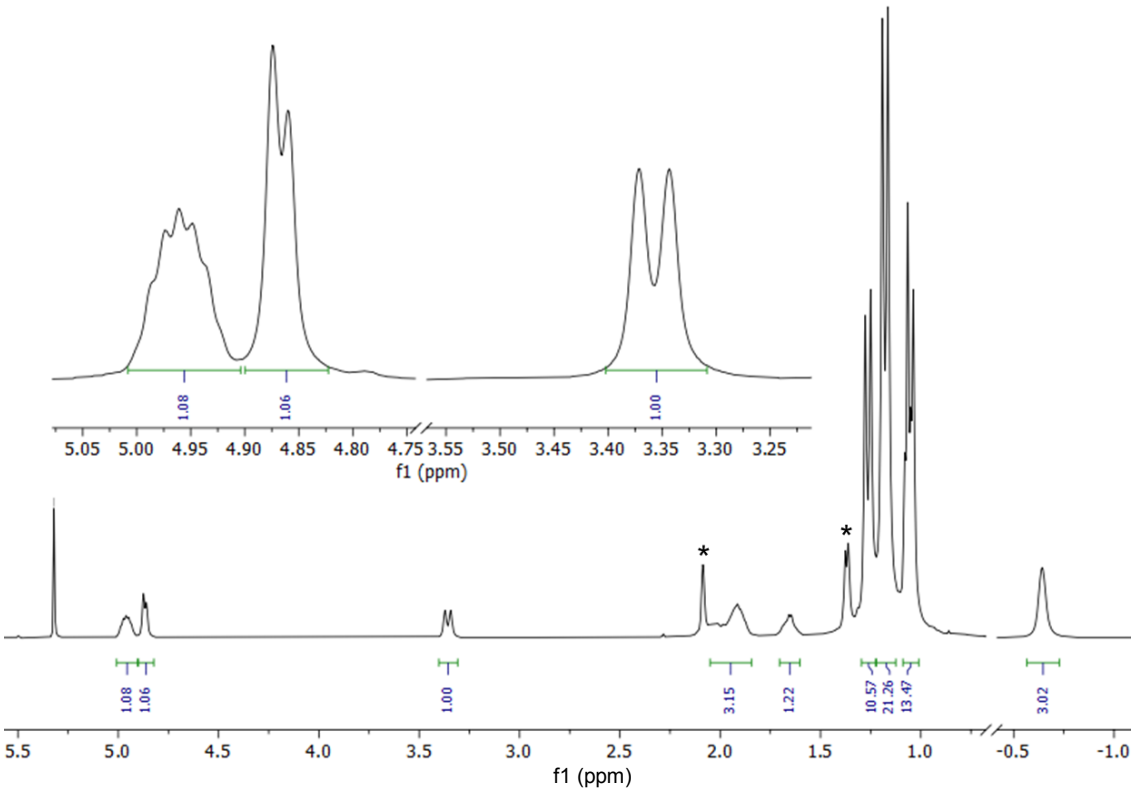


Figure 4.2.1: ^{1}H NMR (500.23 MHz, CD_2Cl_2, 185 K) spectrum of *mono*-propene complex **43** as generated *via* the solid-gas route. * indicates recalcitrant NBA.

Typical for an agostically-associated CH_3 group,[11,12] the corresponding 3 H-integrating resonance occurred markedly upfield, at δ −0.64, as a broad singlet. This compared well to the agostic CH_3 resonance of the dcpe variant [(dcpe)Rh(η^2-propene)][BAr^F_4] (**28**),[11] observed at δ −0.02 (CD_2Cl_2, 193 K). Resonances associated with the alkene CH positions also occurred at similar chemical shifts: δ 3.36 (*cf.* 3.55; **28**), 4.87 (*cf.* 4.54), and 4.96 (*cf.* 4.84). However, unlike complex **28**, *cis*, *trans*, and geminal coupling patterns were resolved in **43**, suggesting that the increased steric constraint of the dtbpe ligand reduced the conformational freedom of the propene ligand and/or increased the barrier to a 1,3-hydride shift.

Both propene complexes (**28** and **43**) exhibited relatively broad $^{31}P\{^{1}H\}$ spectra, with doublets resolved for ^{31}P *trans* to C=C ($^{1}J_{PRh}$ ~ 160 Hz) and *trans* to agostic CH_3 ($^{1}J_{PRh}$ ~ 220 Hz), with no ^{31}P-^{31}P coupling resolved even at low temperature. Near-identical coupling constants to these (162, 220 Hz) were measured for [(dtbpe)Rh(η^2-*cis*-2-butene)][BAr^F_4] (**27**) in Chapter 2 (see the Experimental, Section 5.13.13).

Variable-temperature solid-state NMR (VT-SSNMR) spectroscopy was conducted on powders of solid-state *in situ*-generated **43** (**Figure 4.2.2a**). In common with the dcpe variant **28**,[11] broadness at ambient temperature gave way to complexity at low temperature. One broad ^{31}P environment at 298 K divided clearly into two environments below 200 K, in agreement with the solid-state structure (*vide infra*) and the solution-phase $^{31}P\{^{1}H\}$ NMR spectrum. Similarly, $^{13}C\{^{1}H\}$ SSNMR data collected at 298 K revealed no useful information in the intermediate region (δ 45–110) where the alkene carbons would be expected. Cooling to 175 K allowed these carbons to be resolved, as complex resonances at δ ~70 and ~100, comparing well to the solution-phase (δ 74.8, 96.2). It is apparent from these observations that some fluxionality on the propene fragment was frozen out at low temperatures – tentatively, libration and/or isomerisation.[a] We will return to the concept of a C1–C3 exchange mechanism later (Section 4.4.4), where observations of C1–C3 H/D-scrambling in a d_2-propene intermediate will be detailed.

Crystals of *mono*-propene complex **43** as obtained *via* the solution route were interrogated by *sc*-XRD (**Figure 4.2.3**), crystallising in the enantiomorphic[b] space group of $P4_12_12$ with one formula unit of CH_2Cl_2 in the unit cell, with an octahedral (O_h) packing of anions about cationic fragments. The solid-state structure of the *mono*-propene dcpe variant **28**, as reportedly obtained *via* SC-SC exposure of σ-NBA complex **2** to propene gas, included propene coordination isomers as ~1:1 superpositions and preserved the centrosymmetric[c] space group $P\bar{1}$ of precursor complexes **1** and **2**.[11] In this work, **43** demonstrated no clear disorder on its propene moiety. Propene carbon atom identities in **43** were unambiguous, with clearly differentiated C···C (1.24(3) *versus* 1.50(3) Å) and Rh···C distances (2.177(14), 2.086(14) *versus* 2.343(18) Å). Metrics obtained from the previous report of the SC-SC structure of **28** compared well,[11] with freely refined Rh···C distances of 2.24/2.30(2), 2.14/2.15(2), and 2.29/2.31(3) Å, and C···C distances of 1.240/1.239(9) and 1.359/1.361(9) Å (both superposed components), but were overall less clearly differentiated in this previous report, indicating the possibility of further unresolved disorder.

[a] See Introduction (Section 1.2.1) and Chapter 2 (Section 2.3.2) for isomerisation *via* 1,3-hydride shift (π-allyl hydride mechanism).
[b] Such space groups lack a symmetry element that change the 'handedness' of the object. A Flack parameter of 0.03(2) ≈ 0 was obtained for a crystal of complex **43**, indicating enantiopure material.
[c] Such space groups possess a point of inversion.

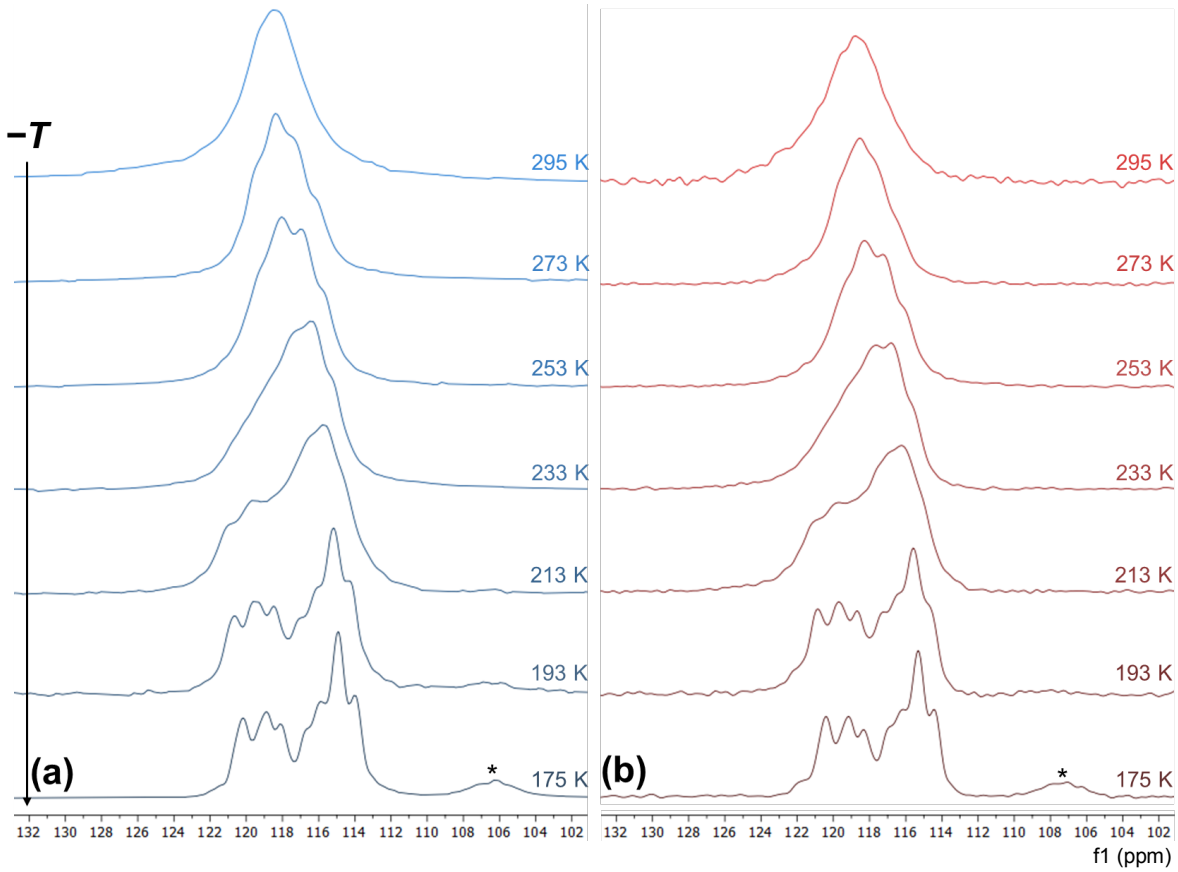


Figure 4.2.2: $^{31}P\{^{1}H\}$ VT-SSNMR (162.03 MHz, ν = 10 kHz) of (**a**) solid-state *in situ*-generated (**b**) crushed recrystallised solution-generated *mono*-propene complex **43**. * indicates an unknown species.

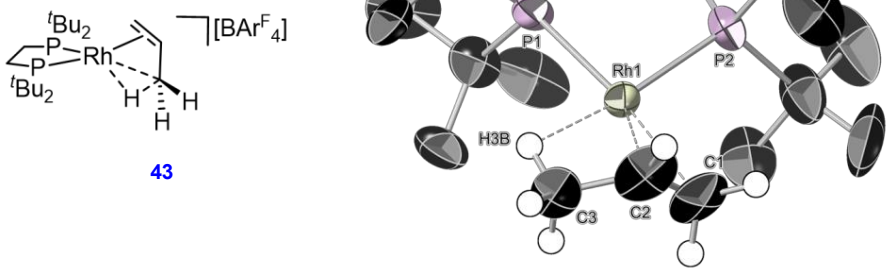


Figure 4.2.3: Cationic fragment [(dtbpe)Rh(η^2-propene)]$^+$ from the solid-state structure of [(dtbpe)Rh(η^2-propene)][BAr$^F_4$] (**43**), as obtained through CH_2Cl_2/pentane recrystallisation of the complex as produced by the solid-gas route. 50% displacement ellipsoids. Anions and H atoms omitted for clarity, except calculated positions on the propene moiety. Selected bond lengths (Å) and angles (deg), where Cent is the centroid of C1–C2: Rh1–P1, 2.281(3); Rh1–P2, 2.253(3); Rh1–C1, 2.177(14); Rh1–Cent, 2.0395(9); Rh1–C2, 2.086(14); C1–C2, 1.24(3); Rh1–C3, 2.343(18); C2–C3, 1.50(3); P1–Rh1–P2, 87.67(14); P1–Rh1–H3B, 90.42(11); P2–Rh1–Cent, 108.02(10); C1–C2–C3, 120(2).

The relative simplicity of the crystal structure of **43** collected at 110 K (*i.e.* only one propene component; **Figure 4.2.3**) compared to the complexity of the $^{31}P\{^{1}H\}$ VT-SSNMR spectroscopic information at 175 K (**Figure 4.2.2a**) suggested that more than one coordination isomer was generated by the solid-gas route before recrystallisation. We sought to investigate this possibility by undertaking VT-SSNMR studies on powdered samples of *recrystallised* propene complex **43** down to 175 K, although no significant differences in the SSNMR data were noted between the *in situ* (**Figure 4.2.2a**) and recrystallised solid-state samples (**Figure 4.2.2b**). The discrepancy between SSNMR and *sc*-XRD data may be attributed to either unresolved disorder in the solid-state structure, noting the suboptimal quality of the structural data (R_1 ~ 8.9%), or to a phase transition occurring between the *sc*-XRD and SSNMR collection temperatures of 110 and 175 K respectively. Unfortunately, temperatures *below* 175 K were not practically accessible by VT-SSNMR, and temperatures *above* 110 K for *sc*-XRD data collection yielded structural data of insufficient quality to be useful (little diffraction beyond ~2.0 Å), which in itself may be indicative of disorder.

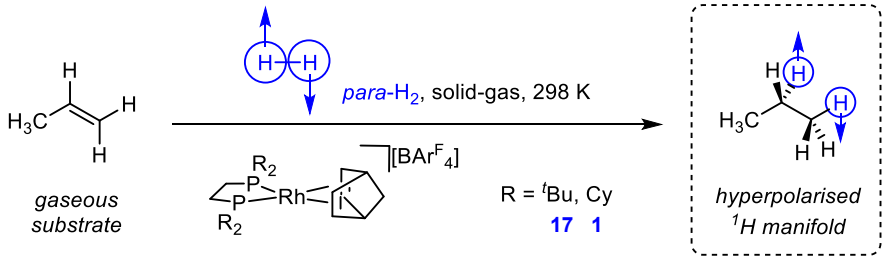
The corresponding propyne complex was also approached, as this gas also constituted a target for solid-gas PHIP. However, the simple propyne complex was not generated by either solid-gas or solution-phase exposure routes; the nature of the actual products obtained will be discussed below (Section 4.4).

4.3 Solid-Gas Hydrogenation-Polarisation of Propene by Precursor NBD SMOMs

Samples of the appropriate η^2,η^2-NBD SMOM (**1** or **17**, 2 mg) were loaded into NMR tubes fitted with Young's taps. For H_2 pre-activation, the samples were first exposed to H_2 (1 bar) for 10 minutes at 298 K. The tube atmosphere was then evacuated and repressurised with propene (1 bar), and connected to a *para*-hydrogen generator outputting at a pressure of 3.5 bar-absolute. The tap was opened for three seconds before sealing. The tube was then disconnected from the generator, shaken vigorously, and promptly introduced to the NMR probe (~3-5 additional seconds), whereupon NMR experiments began immediately.

Single-scan gas-phase ^{1}H NMR spectra were obtained every 6-10 seconds with an inverse ^{1}H-sensitivity probe, with a 45° pulse angle to take maximum advantage of any enhancement achieved by PASADENA.[a] To avoid probe saturation, namely on the first scan, low receiver gains were used throughout – typically 1.0, and no higher than 16.0.[b] Variations on this procedure made use of different propene/*para*-H_2 pressures, masses of catalyst, and a pre-cooling step for *in situ para*-enrichment (see Section 4.3.3).

The employment of SMOMs 1 or 17 as solid-gas PHIP pre-catalysts (**Scheme 4.3.1**) was highly successful under NMR batch conditions. Partially-negative lineshapes (PNLs) corresponding to both the CH_2 (C2) and CH_3 (C1,3) propane positions were observed. An exemplar experiment utilising precursor SMOM 17 is given in **Figure 4.3.1**, with initial enhancement factors of up to ~700 and ~800 respectively, falling to ~40 and ~30 after ~100 seconds.



Scheme 4.3.1: Solid-gas PHIP of propene gas by pre-catalyst SMOMs 1 or 17.

The evolving lineshapes and intensities observed in **Figure 4.3.1** were a complex result of progressive hydrogenation-polarisation (the first scan represents only ~20% conversion, or TON_{app} ~ 20), progressive relaxation of hyperpolarised propane (introducing a 'normal', low-intensity resonance coincident with the PNL), progressive catalyst deactivation, progressive 'reorthoisation' of the *para*-H_2 atmosphere by the SMOM catalyst,[c] and imperfect pulse angles, as inhomogeneous magnetic fields are present at the extremities of the coil.

[a] See Introduction (Section 1.4.2).
[b] Normal solution-phase acquisitions typically use a receiver gain of >90.
[c] See Introduction (Section 1.4.3, *Competitive 'reorthoisation'*). *Ortho*-H_2 becomes visible over the course of these experiments as a broad singlet ~0.5 ppm upfield from the propene CH_2 resonance (this would not be visible on the scale presented in **Figure 4.3.1**).

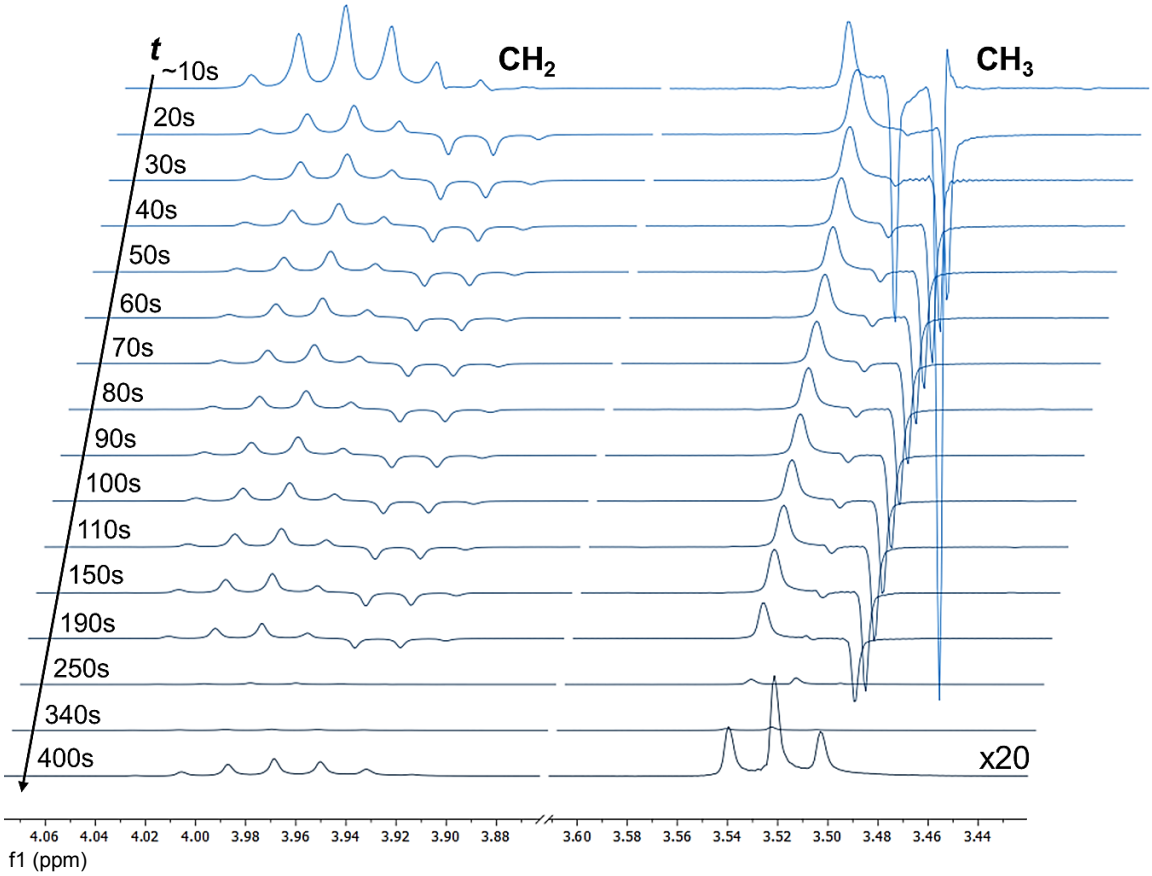


Figure 4.3.1: Exemplar sequential gas-phase ^{1}H NMR spectra (400.12 MHz, 45° pulse angle, 1.0 receiver gain) of propene solid-gas hydrogenation-polarisation at 298 K. Conditions: propene (1 bar) + *para*-H_2 atmosphere (3.5 bar-absolute) in the presence of H_2-preactivated SMOM **17** (2 mg, finely ground). The final scan (t ~ 400 s, ~100% conversion) has been zoomed by a factor of 20. Time is measured from the initial exposure of the sample to the *para*-H_2 source.

Probe saturation and initial operation of ALTADENA instead of PASADENA[a] may both have accounted for the anomalous PNLs observed in the initial scan, noting that some hydrogenation was assumed to have initially occurred *outside* the strong magnetic field of the NMR probe, in the brief <10 seconds of time that elapsed before the sample was inserted.

Out of SMOMs **1** and **17**, complex **17** produced the strongest and most persistent enhancement and was highly amenable to recharging. On one experiment, on the *second* charge of propene/*para*-H_2, SMOM **17** produced initial enhancement factors of ~470 (CH_2) and ~440 (CH_3), and ~20 and ~14 after ~100 seconds.

[a] See Introduction (Section 1.4.2) for details on this important distinction.

The initial enhancement factors produced by *cyclo*-hexyl-bearing SMOM **1** on the *first* charge were somewhat weaker (up to ~500) than those observed for *tert*-butyl-bearing SMOM **17** (up to ~800) and thereafter dropped off precipitously, such that negligible enhancement was observed after ~100 seconds as well as upon the introduction of the second charge of *para*-H_2/propene, concomitant with a severely reduced rate of solid-gas hydrogenation. This loss of activity, which was not reversed by exposure to a fresh charge of *para*-H_2/propene, suggested a deactivation product *other* than an alkene complex such as the 1,3-butadiene complex [(dcpe)Rh(η^4-C_4H_6)][BAr^F_4] (**18**), which was discovered in Chapter 2 to recover its catalytic activity upon exposure to H_2. This deactivation product was instead suggested to be the Ar^F-coordinated zwitterion [(dcpe)Rh(η^6-Ar^F-BAr^F_3)] (**32**; *vide infra*). Due to the advantage in terms of PHIP response strength and persistence of precursor SMOM **17** *versus* SMOM **1**, the remainder of this Section will focus on catalytic systems based on {(dtbpe)Rh}[BAr^F_4].

Samples of single-crystalline SMOM **17** which had *not* been ground into powders were tested, in order to probe the influence of crystallite size on PHIP response. Fine (>50 μm) samples of macrocrystalline SMOM **17** deployed under NMR batch conditions also gave rise to hyperpolarised ('*HP*'-)propane, albeit with a much-reduced PHIP response compared to ground samples: initial enhancement factors of ~80 (CH_2) and ~33 (CH_3) were measured. This is consistent with a predominantly surface/near-surface process, linking a faster hydrogenation reaction to a stronger PHIP response, and mirroring results discussed in Chapter 2.[a] Variation of both *para*-H_2 (1.0-3.5 bar-absolute onto 1.0 bar propene) and propene (0.25-3.0 bar onto 3.5 bar-absolute *para*-H_2) pressures gave rise to optimal PHIP responses with pre-catalyst SMOM **17** when pressures of 1.0 bar (propene) and 3.5 bar-absolute (*para*-H_2)[b] were used. Higher propene pressures gave rise to lower rates of %-conversion, with only ~9% conversion measured after 10 seconds at 3.0 bar propene and 1.0 bar-absolute *para*-H_2 (*cf.* ~20% at 1.0 bar). Disappointing initial enhancement factors were measured at this pressure (~6.0 (CH_2) and ~2.3 (CH_3)), suggesting surface-site saturation at higher propene pressures, although it is not clear why such little enhancement under these conditions was observed.

[a] Section 2.4.4, where ground samples of SMOM **17** outperformed fine crystalline samples in catalytic solid-gas 1-butene isomerisation.
[b] Overall system pressure 3.5 bar-absolute, as *para*-hydrogen was introduced at this pressure into the tube containing substrate gas.

Lower pressures of both propene and *para*-H_2 also gave rise to reduced initial PHIP responses, with almost none registered for 0.25 bar propene at 3.5 bar-absolute *para*-H_2. Lower *para*-H_2 pressures resulted in more sluggish solid-gas hydrogenation reactions, with correspondingly weak-to-non-existent PHIP responses.

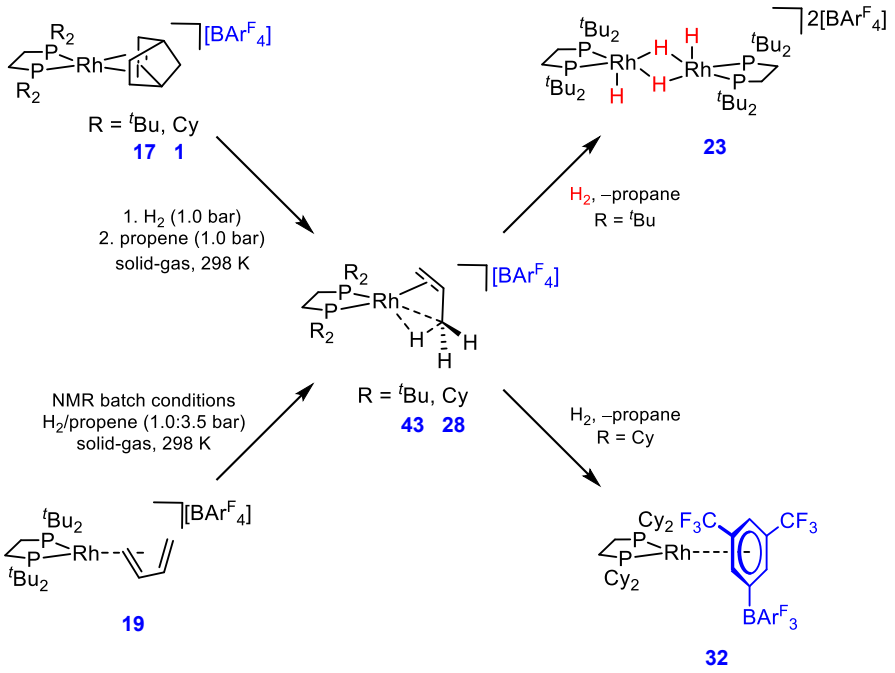
In addition to pre-hydrogenated η^2,η^2-NBD SMOM **17**, catalysts based upon {(dtbpe)Rh}[BAr^F_4] that did *not* require H_2 pre-activation were also deployed. *Ex situ*-synthesised, single-crystalline, powdered samples of 1,3-butadiene complex **19**[12] and *mono*-propene complex **43** were both used to good effect, generally giving rise to approximately equal or superior initial enhancement factors, persistent PHIP effects, and rechargeability compared to H_2-preactivated SMOM **17**. Where pre-hydrogenated SMOM **17** typically generated initial enhancement factors of ~500-700 (CH_2) and ~600-800 (CH_3), falling to 8-12 and 12-16 after ~100 seconds, pre-catalyst *mono*-propene complex **43** registered ~610- and ~850-fold enhancement initially, falling to ~13 and ~17, and pre-catalyst 1,3-butadiene complex **19** registered ~750 and ~1,000, falling to ~17 and ~22. Both SMOMs **19** and **45** were amenable to recharges of *para*-H_2/propene in a similar manner to SMOM **17**. The reason for the superior PHIP response of 1,3-butadiene SMOM **19** cannot be due to discrepancies in structure-type as all three SMOMs (**17**, **19**, **43**) possessed similar O_h-type structures.[a] The explanation may instead have lain with an initial absence of crystallite deformation that may have occurred with pre-hydrogenation,[b] or a discrepancy in the time between *para*-H_2 exposure and insertion. All three SMOMs would be expected to form the same propene complex (**43**) under NMR batch conditions.

4.3.1 Deactivation Routes of Propene Hydrogenation-Polarisation Catalytic Systems

In order to assess the deactivation products of these hydrogenation-polarisation catalytic systems, CD_2Cl_2 was distilled over post-catalytic material from catalytic systems derived from SMOMs **1** (dcpe-type), **17**, **19** and **43** (all dtbpe-type) after which NMR spectroscopic interrogation took place at 183 K.

[a] See Section 2.2.4.
[b] Compare Section 2.4.6.

Post-catalytic material derived from SMOM **1** was unambiguously identified as Ar^F-coordinated zwitterion **32** (**Scheme 4.3.2**), whose solution-phase NMR characterising information matched that reported previously.[13] Indicative of symmetry-breaking on the η^6-bound $[BAr^F_4]^-$ anion, six ^{1}H NMR resonances were located in the aromatic region (δ 7.19, 7.53, 7.59, 7.66, 7.71; 1:3:1:1:6 integral ratio, where the 3 and 6 H resonances corresponded to the unbound Ar^F rings); additionally, a broad resonance at $\delta \sim 92$ was located by $^{31}P\{^1H\}$ NMR spectroscopy, which sharpened and split into two resonances (δ 91.0, 92.0) upon warming to 223 K. No evidence for hydrides was obtained by solution spectroscopic methods. By $^{31}P\{^1H\}$ SSNMR spectroscopy, a broad resonance at $\delta \sim 94$ (zwitterion **32**)[14–16] was present in the majority (~80%), alongside a similarly broad unidentified resonance at $\delta \sim 72$ (~20%). The broadness of these SSNMR resonances evidenced a loss of long-range order across the catalytic process (compare Section 2.4.6).



Scheme 4.3.2: Proposed deactivation routes for SMOM pre-catalyst η^2,η^2-NBD complexes **1** and **17**, also *ex situ*-prepared 1,3-butadiene complex **19** and *mono*-propene complex **43**, under propene PHIP NMR batch conditions (propene/*para*-H_2 atmosphere 1.0+3.5 bar, solid-gas, 298 K).

Congruent with observations made in Chapter 2, no analogous Ar^F-coordinated zwitterion was observed for post-catalytic material derived from the {(dtbpe)Rh}$[BAr^F_4]$-containing SMOMs.

Instead, consistent with the pale yellow colouration of the post-catalytic material, the Rh(III) bridging hydride [(dtbpe)Rh(H)(μ-H)]$_2$[BAr$^F_4$]$_2$ (**23**)[12] was evidenced by solution-phase NMR spectroscopy at 183 K according to its characteristic ^{1}H-hydridic (δ −27.5, −4.69) and ^{31}P{^{1}H} (δ 121.7, 122.3; $^1J_{PRh}$ ~ 180 Hz) NMR resonances.

In Chapter 2, we noted that a ^{31}P{^{1}H} SSNMR resonance of δ ~120 was generated upon prolonged solid-gas hydrogenation of η^2,η^2-NBD complex **17** (72 hours at 1.0 bar); also *n*-butenes complex **27** (rapid, <60 seconds), and butadiene complex **19** (rapid, <60 seconds). This approximately matched the chemical shift observed for recrystallised dihydride **23** (see Experimental).[12] Recall that crushed samples of recrystallised **23** proved inactive in solid-gas 1-butene isomerisation (Section 2.3.3), although samples of hydride generated *in situ* from 1,3-butadiene complex **19** (see footnote, p. 86) proved active in this regard. It is possible that any hydride **23** produced as the 'deactivation' product of solid-gas PHIP may have been an active hydrogenation catalyst, albeit insufficiently productive to produce any distinguishable enhancement response.

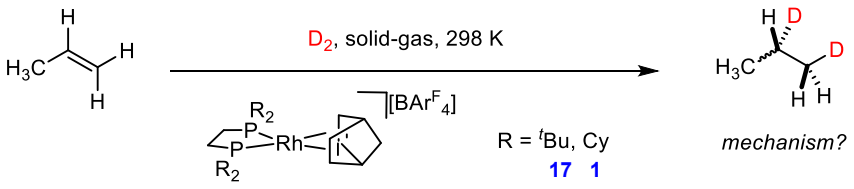
This stark difference in the identity of the deactivation product between dcpe- and dtbpe-type SMOMs again highlights the importance of the electron-donating and sterically-constraining capacity of the chelate, with the more powerfully electron-donating[17–19] and more constraining dtbpe respectively favouring oxidation to Rh(III) and *dis*-favouring coordination of bulky [BAr$^F_4$]$^-$, compared to dcpe.

In previous studies, the rapidity with which [BAr$^F_4$]$^-$ coordination to {(dcpe)Rh}$^+$ occurred was dependent on the size of the σ-coordinated hydrocarbon fragment. [(dcpe)Rh(σ-NBA)][BAr$^F_4$] (**2**) has been reported to persist for months in the solid-state at 298 K without formation of Ar^F-coordinated zwitterion **32**.[13] The lifetime of the σ-propane complex under a flushing N_2 atmosphere was reportedly assessed as ~30 minutes at 294 K, although in its solid-state synthesis (1.0 bar H_2, 180 seconds, 298 K) zwitterion **32** was co-produced in the majority (~70:30),[14] indicating that the presence of an H_2 atmosphere *accelerated* the loss of σ-bound alkanes and subsequent Ar^F-coordination. This is consistent with our findings of relatively rapid deactivation under high H_2 pressures in PHIP catalytic systems derived from pre-catalyst SMOM **1**.

Attempts to reactivate catalytic systems derived from pre-catalyst SMOM **1** by exposing post-batch material to higher pressures of propene (2.0 bar, ~4 hours, 298 K) in the absence of H_2 were not successful, indicating that the formation of zwitterion **32** in the solid-state was practically irreversible. However, there was a degree of success in this strategy for inactive post-batch material derived from pre-catalyst SMOM **17**: some restoration in activity was observed, with initial enhancement factors of ~44 (CH_2) and ~110 (CH_3) measured, indicating that some degree of reactivation was possible. As discussed, hydride **23** thus formed may have been active for propene hydrogenation-polarisation, albeit weaker than propene complex **43**.

4.3.2 Solid-Gas Propene Hydrogenation: Mechanistic Investigations with D_2

We were interested to probe the nature of propene hydrogenation reaction – principally, whether direct, pairwise[a] addition of H_2 occurred. We reasoned that D_2, in substitution for H_2, would act as a mechanistic probe: if only 1,2-d_2-propane was generated, this would be indicative of strict pairwise addition (**Scheme 4.3.3**), eliminating the possibility of any elimination-reinsertion reactions from alkyl-hydride intermediates that might have given rise to over-deuteration or H/D scrambling. Pairwise addition, as demonstrated by SMOMs **1** and **17**, has also been reported for rhodium on titania.[20,21] Due to the strong initial PHIP response obtained from the *HP*-propane produced by both pre-catalyst η^2,η^2-NBD SMOMs tested (**1** and **17**), as discussed in the previous Section, we suspected a straightforwardly pairwise addition mechanism, in line with previous reports.[21,22]



Scheme 4.3.3: Solid-gas catalytic deuterogenation of propene by pre-catalyst SMOMs **17** or **1** as a mechanistic probe.

[a] Both ^1H nuclei incorporated into the product molecule are derived from the same *para*-H_2 molecule under *pairwise* conditions.

Samples of SMOM (1 or 17, 2 mg) were loaded into NMR tubes fitted with Young's taps. The samples were first pre-activated by exposing to H_2 (1.0 bar) for 10 minutes at 298 K, before evacuation and repressurisation with propene (1.0 bar). The tubes were then partially immersed in liquid N_2 in order to freeze the propene atmosphere before a pressure of D_2 (1.0 bar) was introduced. The tubes were thawed and the contents monitored by gas-phase ^{1}H NMR until near-complete conversion to propane (>99.5%, TON_{app} ~ 110) was achieved. In common with observations that SMOM 1 was initially a substantially more active PHIP catalyst than SMOM 17, the atmosphere of propene was more rapidly deuterogenated in the presence of SMOM 1, with 98% conversion exceeded after 90 seconds. SMOM 17 required 180 seconds to exceed 98% conversion. The atmospheres of the tubes were then frozen with liquid N_2. Excess D_2 was removed under dynamic vacuum before thawing, whereupon gaseous hydrocarbons were distilled over CD_2Cl_2.

Both SMOMs 1 and 17 produced atmospheres of exclusively 1,2-d_2-propane, unambiguously identified by ^{1}H, ^{2}H, and ^{13}C{^{1}H} solution-phase NMR spectroscopic studies, with evidence for neither over-deuteration nor H/D scrambling. By ^{2}H NMR spectroscopy (**Figure 4.3.2a**,**b**), two resonances were resolved, at δ 0.90 and 1.32, corresponding to CH_2D and CHD positions respectively, in a 1:1 integral ratio. The observed coupling patterns were completely consistent with 1,2-d_2-propane: both geminal and vicinal ^{1}H-^{2}H coupling were resolved ($^2J_{HD}$ = 2.0 Hz, $^3J_{HD}$ = 1.1 Hz), in addition to vicinal ^{2}H-^{2}H coupling ($^3J_{DD}$ ~ 0.2 Hz). By ^{13}C{^{1}H} NMR spectroscopy (**Figure 4.3.2c**), only three resonances were resolved, in the region δ 15.8-16.6: a singlet, corresponding to the CH_3 position, and two 1:1:1 trinomial triplets, corresponding to the CHD and CH_2D positions ($^1J_{CD}$ = 19.6 and 19.0 Hz, respectively), with the latter slightly downfield (confirmed by HSQC studies). By ^{1}H NMR spectroscopy (**Figure 4.3.2d**,**e**), three resonances were resolved, with coupling patterns in agreement with the ^{2}H NMR data. The integral ratio between the two ^{1}H NMR resonances was shy of the excepted 1:5 by almost 40%. Given the absence of evidence for over-deuteration, we suggest this discrepancy was due to deuterons affecting the relaxation times of adjacent protons,[23] and unoptimised experimental conditions in relation to this. However, the lineshapes observed by ^{1}H NMR spectroscopy remained important pieces of evidence, consistent with other sources of NMR data.

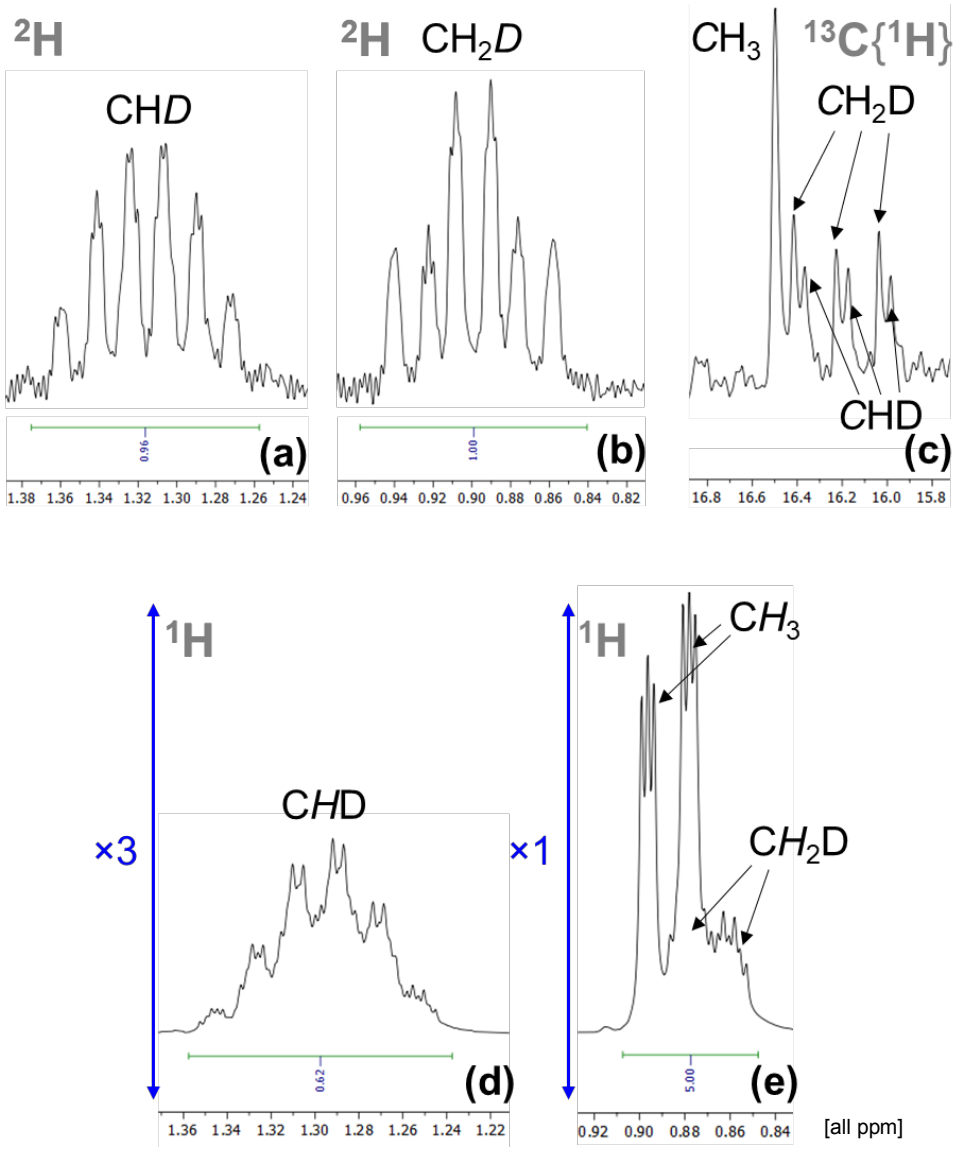


Figure 4.3.2: Selected NMR data for a CD_2Cl_2 solution of 1,2-d_2-propane, produced by the catalytic deuterogenation of propene by pre-catalyst SMOM 1. (**a**) and (**b**): Sections of ^{2}H NMR spectrum (61.42 MHz, 298 K). (**c**) Section of $^{13}C\{^1H\}$ NMR spectrum (100.62 MHz, 298 K). (**d**) and (**e**) Sections of unoptimised ^{1}H NMR spectrum (400.12 MHz, 298 K); (**d**) is zoomed by a factor of three relative to (**e**).

These deductions must be considered with some caution. Where the NMR-scale hydrogenation-polarisation reactions were conducted at a pressure of approximately 3.5 bar-absolute, these NMR-scale deuterogenation reactions were not precisely pressure-controlled – note that the D_2 atmosphere was introduced when the NMR tube was partially immersed in liquid N_2, to keep the already-present propene atmosphere frozen. The total pressure of the NMR tube when thawed and warmed to 298 K would have been approximately 4-6 bar-absolute.

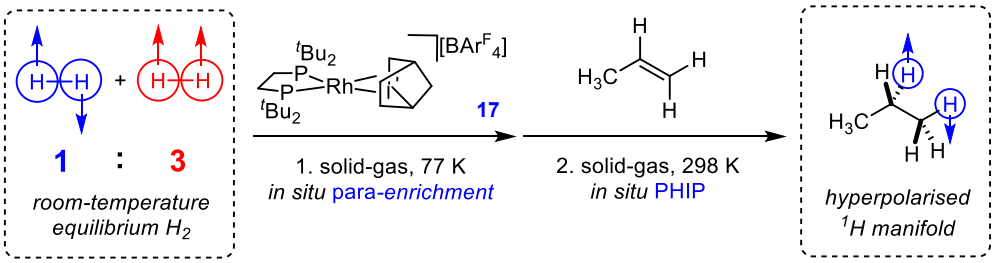
4.3.3 *Solid-Gas PHIP with Normal H_2: A Demonstration of* In Situ Para-*Enrichment*

As briefly discussed in the Introduction (Section 1.4.3), catalysts capable of reversibly binding and releasing H_2 should be capable of encouraging equilibration of any non-equilibrium mixture of *ortho* and *para*-H_2, due to the formation of an H_2-bound intermediate where the ^{1}H nuclei become inequivalent and the singlet and triplet states may mix, inducting relaxation and loss of spin cohesion.

We have already noted that pre-catalyst SMOM **17** was capable of *para*-H_2 'reorthoisation' (see footnote *c*, p. 186). The equilibrium proportion of *ortho*:*para* at 298 K is ~3:1 (so-called 'normal' H_2), corresponding to the spin-state degeneracies.[24,25] As the temperature is lowered, assuming an appropriate catalyst is present to induce spin-state interconversion, the proportion of *para*-H_2 approaches totality.

We reasoned that any catalyst capable of 'reorthoising' *para*-H_2 at *high* temperature must be capable of the reverse (*i.e. para*-enrichment) at *low* temperature, under cryogenic conditions which favoured a higher proportion of *para*-H_2 in an equilibrium mixture. Given that *para*-H_2 is NMR-silent, we opted to use the solid-gas hydrogenation-polarisation of propene as a tell-tale for successful *para*-enrichment.

Using SMOM **17** as a proof-of-concept, the procedure described in Section 4.3 was repeated with 'normal' H_2 (3.5 bar-absolute) and an additional step (**Scheme 4.3.4**): once disconnected from the H_2 source, the tube was immediately immersed in liquid N_2 for ten seconds, removed from the liquid N_2 and allowed to thaw for a further five seconds, and introduced to the spectrometer before gas-phase ^{1}H NMR data acquisition began as before.



Scheme 4.3.4: PHIP using 'normal' H_2, taking advantage of *in situ para*-enhancement by pre-catalyst SMOM **17**.

Enhanced PNLs indicative of PHIP were visible (**Figure 4.3.3**), albeit only for a short time: the effect was present solely for the first scan, whereafter the hydrogenation proceeded in the same fashion as the control experiment (without pre-cooling, no PNLs nor enhancements on the incipient propane peaks were observed). By this method, the *para*-enrichment was clearly incomplete, due to the presence of a significant *ortho*-H_2 peak ~0.5 ppm upfield from the propene CH_2 resonance.

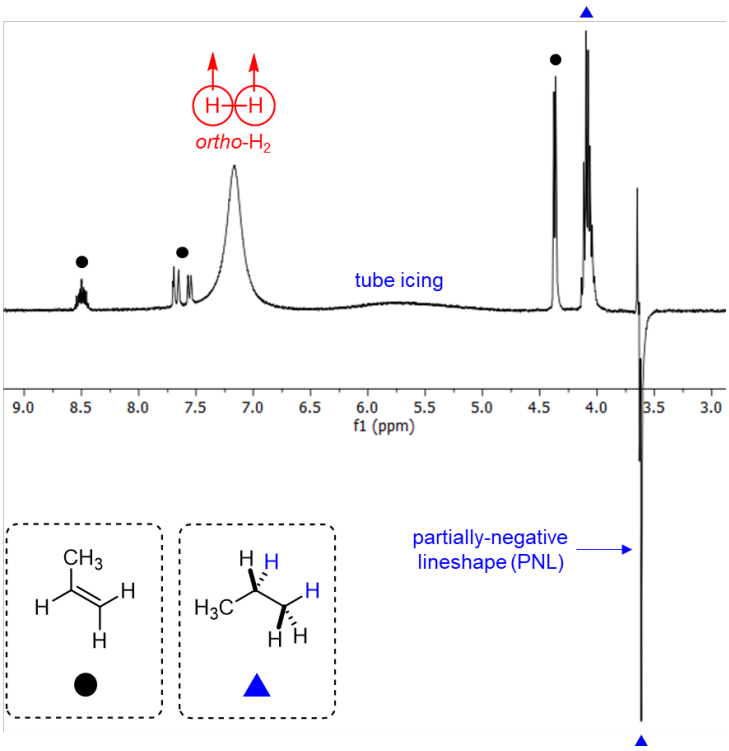


Figure 4.3.3: Exemplar initial gas-phase ^{1}H NMR spectra (400.12 MHz, 45° pulse angle, 16.0 receiver gain) of propene solid-gas hydrogenation-polarisation. Conditions: propene (1 bar) + H_2 atmosphere (3.5 bar-absolute) in the presence of H_2-preactivated SMOM **17** (2 mg, finely ground), with a pre-cooling step in liquid N_2.

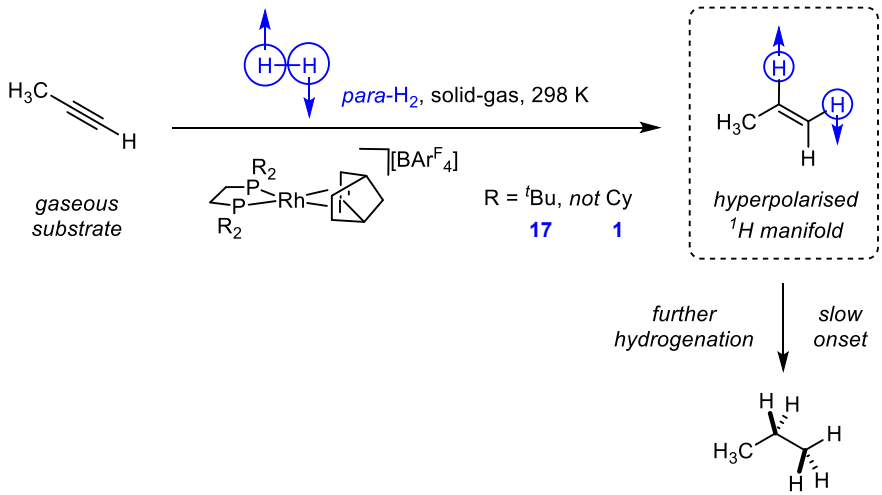
Nonetheless, on the first scan, at ~15% conversion (TON_{app} ~ 15), enhancement factors of ~14.0 (CH_2) and ~2.4 (CH_3) were estimated from the |*z*| spectrum, despite the absence of an obvious PNL in the propane CH_2 position. Repeated attempts at this procedure produced variable results, with the degree of initial PHIP highly dependent on cooling and thawing times. Nevertheless, deployment of 'normal' H_2 as a PHIP agent was demonstrably possible, showing unequivocally that solid-gas PHIP may be conducted on the small-scale without the expensive necessity of a *para*-H_2 generator.

4.4 Solid-Gas Semihydrogenation-Polarisation of Propyne by Precursor NBD SMOMs

Relatively fast spin-lattice relaxation times (T_1) present a challenging obstacle if these hyperpolarised gases are to be used as contrast agents.[a] In a healthy adult, the average breathing period is between 3-5 seconds, somewhat longer than the T_1 of hyperpolarised C_{sp3}–^{1}H, approximately one second at ambient pressure.[3,20,26,27] Potential ways of extending this T_1 time have already been discussed in the Introduction[a] where the methods of selective deuteration and reversible dissolution were mentioned.

Targeting a hyperpolarised gas that would possess a longer gas-phase T_1 time and therefore be better suited for the purpose of an inhalable contrast agent, we opted to focus on the production of *HP*-propene gas from propyne, due to its more limited freedom of rotation compared to *HP*-propane.[3,28,29]

The procedure detailed in Section 4.3 was repeated, substituting a propene atmosphere for one of propyne (1.0 bar) (**Scheme 4.4.1**). As we shall see, exposure of pre-catalyst SMOMs **1** and **17** to propyne did not generate the corresponding alkyne complexes.

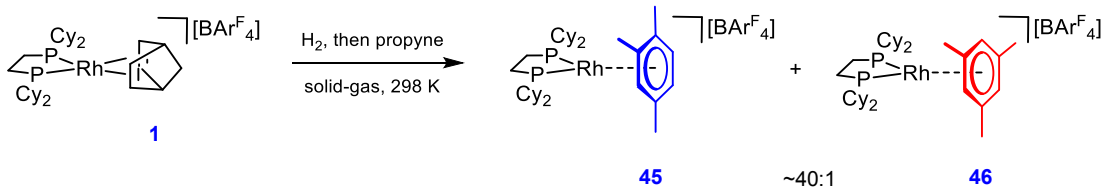


Scheme 4.4.1: Solid-gas PHIP of propyne gas by pre-catalyst SMOM **17**.

[a] See Introduction (Section 1.4.5).

4.4.1 *Solid-State Cyclotrimerisation of Propyne by Precursor NBD SMOM 1*

Pre-catalyst SMOM 1 failed to generate significant PHIP response with an H_2 pre-activation step and *para*-H_2/propyne.[a] The 1,2,4-trimethylbenzene complex [(dcpe)Rh(η^6-*o*,*p*-$C_6H_3(CH_3)_3$)][BAr^F_4] (**45**) was formed in the solid-state in ~98% purity upon exposure of *in situ*-generated [(dcpe)Rh(σ-NBA)][BAr^F_4] (**2**) to propyne gas (**Scheme 4.4.2**), through cyclotrimerisation of the alkyne. Similarly to the solid-gas synthesis of propene complex **43** described in Section 4.2, this solid-gas reaction also failed to maintain crystallinity, generating arene complex **45** as an amorphous pale orange solid.



Scheme 4.4.2: Propyne trimerisation by pre-hydrogenated SMOM 1 in the solid-state, primarily generating 1,2,4-trimethylbenzene complex **45**, in addition to a small minority of mesitylene complex **46**.

Solution-phase ^{1}H and ^{31}P{^{1}H} NMR spectroscopic data for this major cyclotrimerisation product accorded unambiguously with coordinated 1,2,4-trimethylbenzene (**45**), and with the 1,3,5-isomer [(dcpe)Rh(η^6-*m*,*m*-$C_6H_3(CH_3)_3$)][BAr^F_4] for the minor product in ~2% proportion (η^6-mesitylene; **46**).

Three arene resonances were located by ^{1}H NMR spectroscopy: a singlet at δ 6.04, and two doublets at δ 5.88 and 6.25 (each $^3J_{HH}$ = 6.4 Hz, linked by COSY), in a 1:1:1 integral ratio relative to [BAr^F_4]$^-$. The corresponding methyl singlets were located at δ 2.23, 2.26, and 2.33, in a 3:3:3 integral ratio. Low-intensity singlets were resolved at δ 2.30 and 6.31, indicating the presence of the 1,3,5 isomer (**46**; ~2%). Both isomers were visible by ^{31}P{^{1}H} NMR spectroscopy, at δ 96.7 ($^1J_{PRh}$ = 202 Hz, ~98%) and δ 95.3 ($^1J_{PRh}$ = 203 Hz, ~2%), respectively. Reacting 1,2-difluorobenzene complex **21** with propyne in CH_2Cl_2 at 298 K yielded an almost identical cyclotrimerisation product distribution.

[a] Ongoing experiments are exploring the possibility of *limited* propyne pre-exposure times for this system, with some early success.

CH_2Cl_2 solutions of the trimethylbenzene complexes resulting from solid-gas or solution-phase propyne cyclotrimerisation routes were layered with pentane at 298 K to yield low-quality[a] (R_1 ~ 10.0%) pale orange crystals of 1,2,4-trimethylbenzene complex 45 (**Figure 4.4.1**). These were of insufficient quality for a discussion of bond distances and angles to be appropriate, and served only to confirm connectivity.

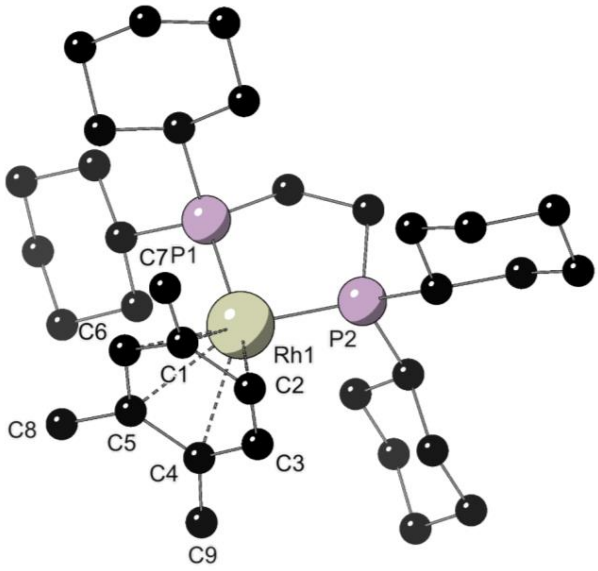
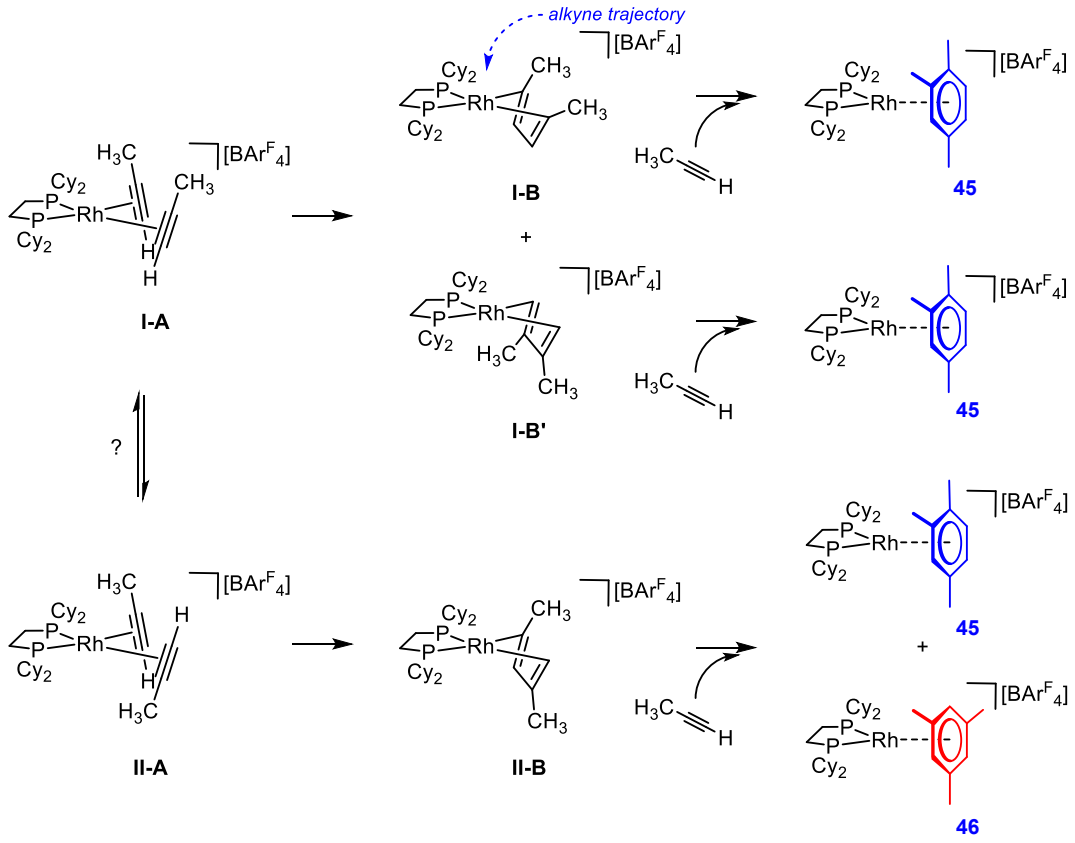


Figure 4.4.1: Preliminary solid-state structure of 45 (one of two symmetry independent cationic fragments; one 1,2,4-trimethylbenzene coordination isomer) as recrystallised from CH_2Cl_2/pentane. Anions and H atoms omitted for clarity. Atoms are represented isotropically due to the low quality of the structural information (R_1 ~ 10.0%).

Metal-catalysed alkyne trimerisation is a powerful method for synthesising polysubstituted arenes.[30,31] In the case of terminal alkynes, regioselectivity in homotrimerisation has often favoured the 1,2,4-isomer. Extensive experimental and computational evidence supports the presence of metallacyclopentadiene intermediates;[32–34] a plausible mechanism has been provided in **Scheme 4.4.3**. In this instance, the fact that this alkyne cyclotrimerisation reaction occurred readily in the solid-state is remarkable in itself. To the knowledge of the author, this marks the first instance of solid-gas alkyne trimerisation to yield an arene complex in the solid-state.

[a] The low quality of these crystals may have been due to co-crystallisation with the small proportion of the similar mesitylene complex 46, compromising long-range order. They were also noted to have been twinned.



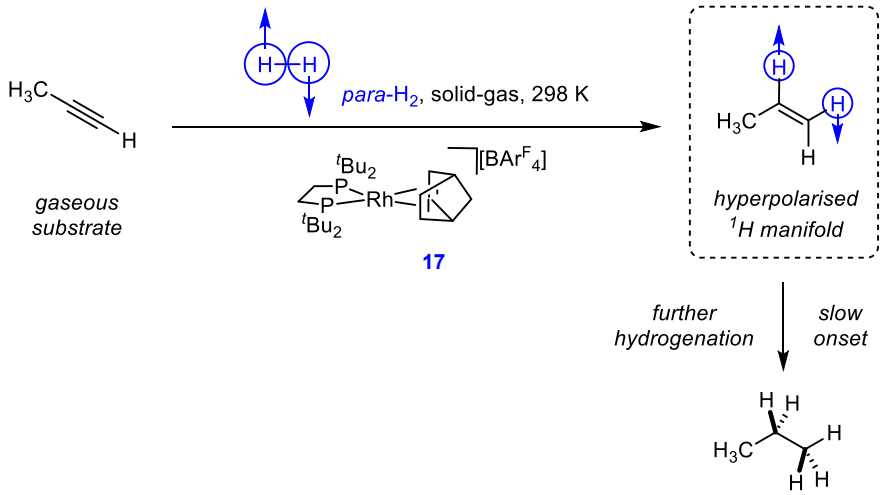
Scheme 4.4.3: A plausible mechanism for the cyclotrimerisation of propyne by {(dcpe)Rh}[BAr$^F_4$] in the solid-state to yield a trimethylbenzene complex.

On a purely statistical basis, 1,2,4-regioselectivity is already highly favourable. 12 permutations of this isomerism are possible given a random distribution of three CH_3 groups on an arene ring, and only two permutations for the 1,3,5-isomer. Two possible metallacyclopentadienes (**I-B** and **I-B'**) give rise to entirely 1,2,4-selectivity; the third (**II-B**) possibly yields both.

On a steric basis, as originally proposed by Wakatsuki and co-workers in their work with the {CpCo^I} fragment,[35] one might expect the formation of **I-B'** to be disfavoured – due to the proximity of the alkyl groups in the transition state – or perhaps the formation of **45** from **II-B** to be disfavoured, since the required orientation of the third propyne molecule for 1,2,4-selectivity would also result in increased steric clash. However, recent studies have emphasised the importance of Curtin-Hammett selectivity[33] – for example, although **I-A** may be less thermodynamically stable than **II-A**, it may form the corresponding metallacyclopentadiene (**I-B** or **I-B'**) more rapidly.

4.4.2 Solid-Gas Semihydrogenation-Polarisation of Propyne by Precursor NBD SMOM 17

Samples of pre-catalyst SMOM 17 proved to be active in the catalytic semihydrogenation-polarisation of propyne gas (**Scheme 4.4.4**), albeit effective for one charge only (**Figure 4.4.2**). A superior PHIP response was measured when the pre-catalyst SMOM had *not* been pre-hydrogenated.



Scheme 4.4.4: Solid-gas PHIP of propyne gas by pre-catalyst SMOM 17.

Accounting for ~6% conversion to propene on the first scan (t ~ 10 seconds; TON_{app} ~ 6-8), determined by reverse extrapolation of the propyne CH_3 |z| integral and comparison to the final (~100% relaxed) scan, initial enhancement factors of ~20 (propene CH_3, C3), ~50 (propene CH_2, C1), and ~180 (propene CH, C2) were estimated. Enhancement at C3 was observed despite no incorporation of a polarised proton at this site *via* a straightforward semihydrogenation of the triple bond – spin-order transfer *via* J-coupling[36] and/or C1-C3 scrambling on coordinated propene (*vide infra*) may have accounted for this.

Perhaps unsurprisingly, the most significantly enhanced resonance (propene CH, C2) derived its only proton from *para*-H_2. This position was *not* involved in the major 1,3-hydride shift that precipitated the C1-C3 scrambling discussed below; such scrambling would have led to some degree of spin-order dilution by encouraging scrambling with positions that had not been directly hyperpolarised.

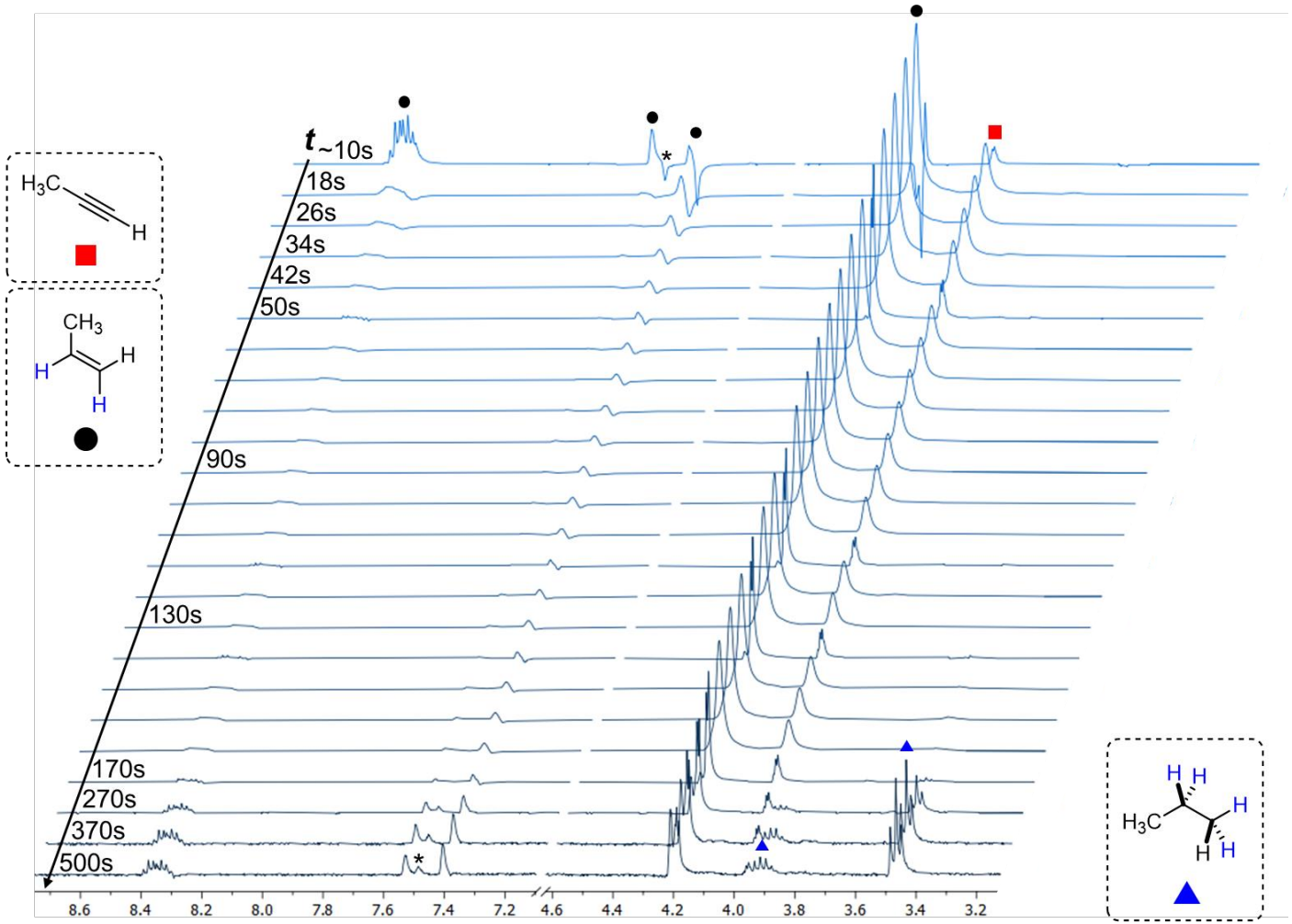


Figure 4.4.2: Exemplar sequential gas-phase ^{1}H NMR spectra (400.12 MHz, 45° pulse angle, 1.0 receiver gain) of propyne solid-gas hydrogenation-polarisation at 298 K. Conditions: propyne (1 bar, 10 minutes' pre-exposure) + *para*-H_2 atmosphere (3.5 bar-absolute) in the presence of pre-catalyst SMOM 17 (2 mg, finely ground). Time is measured from the initial exposure of the sample to the *para*-H_2 source. The resonance marked * is thought to correspond to allene.

The appearance of fully-hydrogenated propane only much later in the experiment suggested that propyne outcompeted propene for coordination to the metal, such that only once a significant reservoir of propene gas had built up did propene hydrogenation become significant. No enhancement in the latterly-generated propane resonances was observed, presumably due to a heavily depleted *para*-H_2 atmosphere due to catalytic reorthoisation by this stage.

The late-emerging peak marked with an asterisk in **Figure 4.4.2** was thought to correspond to allene, which in solution is known to observe a similar ^{1}H NMR chemical shift to propene's alkene protons (δ 4.68 *versus* ~5.0 and ~5.8, $CDCl_3$, 298 K).[37,38] This resonance may also have been visible as a shoulder on a PNL observed in the first scan, also marked with an asterisk. No alkyne/allene isomerisation was observed in a propyne atmosphere above pre-hydrogenated SMOM 17 in the *absence* of H_2, arguing against the operation of an alkyne-allene isomerisation mechanism proceeding *via* a π-propargyl hydride[39] in analogy to the π-allyl hydride mechanism, suggesting a hydride insertion-elimination mechanism. Since this tentatively-assigned allene constituted only a very small proportion of the C_3H_4 atmosphere, even by the final scan (~500 seconds), we can assume that alkyne-allene isomerisation did not play a significant part in the PHIP process.

On the initial scan, the resonance corresponding to propyne CH (C1) demonstrated a partially negative lineshape (not clearly visible in **Figure 4.4.2**; see **Figure 4.4.3**). We suggest this PNL was due to either direct incorporation of protons from *para*-H_2 by reversible C–H activation and hydride insertion-elimination, or indirectly *via* SABRE,[a] with spin-order transfer from a hyperpolarised metal hydride/σ-H_2 complex to the C_{sp}-H of a coordinated alkyne. We will attempt to differentiate between the possibilities of SABRE and hydride insertion-elimination in the following Section. One propene CH_2 signal (δ ~7.42) was more significantly polarised throughout the experiment than the other (δ ~7.56) with the exception of the first scan, where the enhancement factors of each methylene signal were comparable. The resonance at δ ~7.56 is then presumably the proton located *E* to methine CH, directly correlating with no protons incorporated from *para*-H_2.

[a] Signal Amplification by Reversible Exchange – see Introduction (Section 1.4.4).

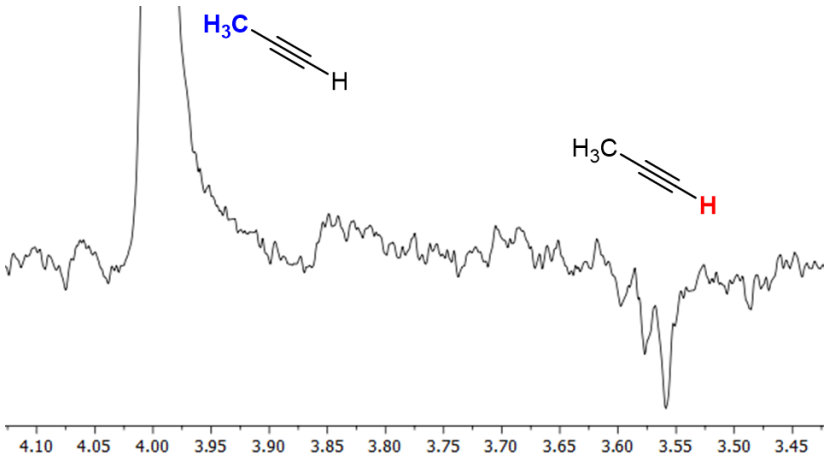


Figure 4.4.3: Zoomed section of the initial scan in **Figure 4.4.2** (1.0 Hz apodised), showing the low-intensity PNL corresponding to the propyne CH resonance.

Solution-phase NMR spectroscopic studies conducted on post-catalytic material[a] and also on samples of pre-hydrogenated SMOM **17** exposed only to propyne both evidenced the formation of 1,2,4-trimethylbenzene complex [(dtbpe)Rh(η^6-*o*,*p*-$C_6H_3(CH_3)_3$)][BAr^F_4] (**47**) in the solid-state. Indicative of protons in the *ortho* and *meta* positions, a roofed pair of ^{1}H NMR doublets was resolved, at δ 6.00 and 6.31 ($^3J_{HH}$ = 6.6 Hz, linked by COSY) in addition to a singlet at δ 5.99, in a 1:1:1 integral ratio, relative to [BAr^F_4]$^-$. Three further singlets were noted at δ 2.19, 2.24 and 2.42 in a 3:3:3 integral ratio, corresponding to the arene CH_3 groups. A simple doublet was observed by ^{31}P{^{1}H} NMR spectroscopy, at δ 116.4 ($^1J_{PRh}$ = 209 Hz).

Proportions of **47** as generated in the solid-state varied between ~85-90% by solution-phase ^{31}P{^{1}H} NMR integrals, alongside the alternative 1,3,5-isomer [(dtbpe)Rh(η^6-*m*,*m*-$C_6H_3(CH_3)_3$)][BAr^F_4] (**48**; ~3%), unreacted precursor η^2,η^2-NBD complex **17** (~5%), and an unknown complex observed at δ 96.9 ($^1J_{PRh}$ = 175 Hz, ~3-6%) by solution-phase ^{31}P{^{1}H} NMR spectroscopy. Assignment of 1,3,5-isomer **48** was made on the basis of its similar ^{31}P{^{1}H} NMR chemical shift and coupling constant (δ 115.2, $^1J_{PRh}$ = 212 Hz) to 1,2,4-isomer **47**, as well its two ^{1}H NMR signals occurring at δ 2.33 and 6.24 in a ~3:1 integral ratio (~3-6% relative to peaks corresponding to **47**).

[a] CD_2Cl_2 was vacuum-transferred over solid-state samples with liquid N_2, thereafter warming to 185 K and then to 298 K, to ascertain the stability of the mixture. No changes were noted after two hours at 298 K.

The unknown complex observed by $^{31}P\{^{1}H\}$ NMR spectroscopy at δ 96.9 was tentatively assigned as either an enyne[40–45] complex (arising from alkyne C–H activation), given its similar chemical shift and coupling constant to 1,3-butadiene complex **19** (δ 97.8, $^{1}J_{PRh}$ = 173 Hz),[12] or to a cyclobutadiene[46,47] complex (arising from metallacyclopentadiene elimination). ESI-MS analysis of this material revealed mass peaks at *m*/*z* 541.2598 (100% relative intensity) and 501.2288 (~5%). The former corresponded to either arene isomers **47** and **48** (calc. 541.2594), the latter to a complex with a mass/charge ratio equal to {(dtbpe)Rh}$^{+}$ plus *two* equivalents of propyne (calc. 501.2281). This accords with both an enyne and a cyclobutadiene as the identity of the unknown complex, although due to its low concentration neither can be declared with certainty. Attempts to recrystallise these mixtures yielded only pseudocrystalline material,[a] and attempts to increase the purity of the arene complex by longer exposures to propyne were unsuccessful.

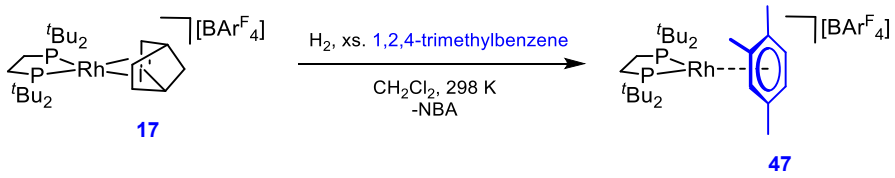
Propyne cyclotrimerisation was also approached in solution. By exposing labile[48] 1,2-difluorobenzene complex **22** in CD_2Cl_2 solution to a propyne atmosphere, the proportion of 1,2,4-trimethylbenzene complex **47** thus generated increased to ~99%, with only ~1% 1,3,5-isomer **48** measured by $^{31}P\{^{1}H\}$ NMR integrals. No evidence was available for any other dimer- or trimer-isation product. This improvement in selectivity, against both the 1,3,5-isomer and any n = 2 product(s), likely came as a result of the absence of a constricting solid-state microenvironment, which in tandem with the relatively crowded coordination sphere of {(dtbpe)Rh}$^{+}$ may have favoured the formation of these minor products.

The absence of PHIP response observed for pre-catalyst SMOM **1** suggested that the catalytically inert trimethylbenzene complexes **45** and **46** formed too rapidly for significant hydrogenation-polarisation to take place, perhaps due to the less sterically constrained active site of SMOM **1** compared to **17**. SMOM **17**, however, when pre-hydrogenated and exposed to propyne, did not exclusively generate cyclotrimerisation products in the solid-state. It therefore became necessary to independently synthesise a corresponding trimethylbenzene complex (*i.e.* **47**) and prove its catalytic inactivity.

[a] While precipitating into well-defined blocks reminiscent of crystals, this material diffracted X-rays poorly, giving rise to no Bragg peaks beyond ~2.0 Å, suggesting a material with limited long-range order. Different crystallisation solvent systems (*i.e.* 1,2-difluorobenzene/hexane, THF/hexane) yielded no improvement in crystallographic data quality.

4.4.3 *Synthesis and Testing Independently-Synthesised 1,2,4-Trimethylbenzene Complex* **47**

The 1,2,4-trimethylbenzene complex **47** discussed above, suspected to be a deactivation product in the solid-gas hydrogenation of propyne by pre-catalyst SMOM **17**, was synthesised independently in order to unambiguously confirm its catalytic inactivity. Precursor SMOM **17** was taken in CH_2Cl_2 solution in the presence of a large excess of 1,2,4-trimethylbenzene (**Scheme 4.4.5**).



Scheme 4.4.5: Independent solution-phase synthesis of 1,2,4-trimethylbenzene complex **47**.

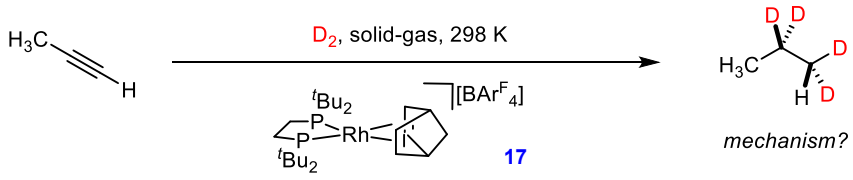
After exposure to an atmosphere of H_2 (1.0 bar) for ten minutes at 298 K, a colour change from deep to pale orange was noted. The solution was then frozen with liquid N_2, the atmosphere of H_2 was evacuated, and the thawed contents of the flask were layered with hexane at 298 K to give rise to pale orange crystalline plates of arene complex **47**.

Solution-phase ESI-MS and NMR characterisation matched with that of the material obtained *via* the solid-state route in the previous Section. *sc*-XRD data obtained from the crystals of **47** thus obtained were of insufficient quality for publication and served only to confirm connectivity, due to the combination of a large unit cell (12,131.4 $Å^3$) and poor diffraction below 1.0 Å (see Experimental for this Chapter, Section 5.15.2 for an isotropic representation of the solid-state structure).

Taking finely-ground powders of independently-synthesised **47** with normal H_2 (3.5 bar-absolute) and propyne (1.0 bar) produced some evidence for hydrogenation, albeit with extremely slow turnover: after 60 minutes by gas-phase ^1H NMR spectroscopy only ~10% conversion to propene was recorded (TON_{app} ~ 10), confirming this complex to be almost catalytically inactive relative to pre-catalyst SMOM **17**. Indeed, repeating this experiment with *para*-H_2 produced no visible PHIP response.

4.4.4 *Solid-Gas Propyne Hydrogenation: Mechanistic Investigations with D_2*

As in Section 4.3.2, we were interested to probe the nature of propyne hydrogenation reaction with D_2 – principally, whether straightforward, pairwise addition of *para*-H_2 occurred (**Scheme 4.4.6**). Given the positive result concerning propyne semihydrogenation-polarisation by pre-catalyst SMOM **17** above, this Section will consider SMOM **17**. After the observation of a hyperpolarised alkyne C_{sp}–H position (**Figure 4.4.3**), we were also curious to determine whether SABRE was taking place or reversible hydride insertion-elimination that may have led to this curious negative lineshape.



Scheme 4.4.6: Solid-gas catalytic deuterogenation of propyne by pre-catalyst SMOM **17** as a mechanistic probe.

Finely-ground SMOM **17** (2 mg) was loaded into an NMR tube fitted with Young's tap, and first exposed to H_2 (1.0 bar) for 10 minutes at 298 K before evacuation and repressurisation with propyne (0.5 bar). The tube was then partially immersed in liquid N_2 in order to freeze the propyne atmosphere before a pressure of D_2 (1.0 bar) was introduced. The tube was thawed and its contents were monitored by gas-phase ^{1}H NMR until near-complete conversion to the alkane (>99.5%, TON_{app} ~ 55) was achieved, after approximately 200 seconds. The atmosphere of the tube was then frozen with liquid N_2 and excess D_2 was removed under dynamic vacuum before thawing and distilling any gaseous hydrocarbons into CD_2Cl_2.

Under these NMR-scale conditions, the solid-gas deuterogenation reaction proved difficult to control for only semi-deuterogenation. We therefore decided instead to pursue complete deuterogenation and to spectroscopically inspect the alkane product, using the knowledge that the propene→propane deuterogenation step occurred in a straightforwardly pairwise fashion, without over-deuteration or scrambling as deduced in Section 4.3.2.

In contrast, with propyne as a substrate, the C1-C3 scrambling product 1,2,2,3-d_4-propane was evidenced by ^{1}H, ^{2}H, and ^{13}C{^{1}H} NMR spectroscopy (**Figure 4.4.4**), in addition to 1,1,2,2-d_4-propane. No evidence for over-deuteration was noted, suggesting that the hyperpolarised propyne C_{sp}–H position was a result of SABRE rather than insertion-elimination. C1-C3 scrambling *via* a 1,3-hydride shift also explained the enhancement at propene CH_3 (C3) upon propyne semihydrogenation-polarisation, a position that would not normally receive any protons from *para*-H_2 upon straightforward semihydrogenation of the triple bond.

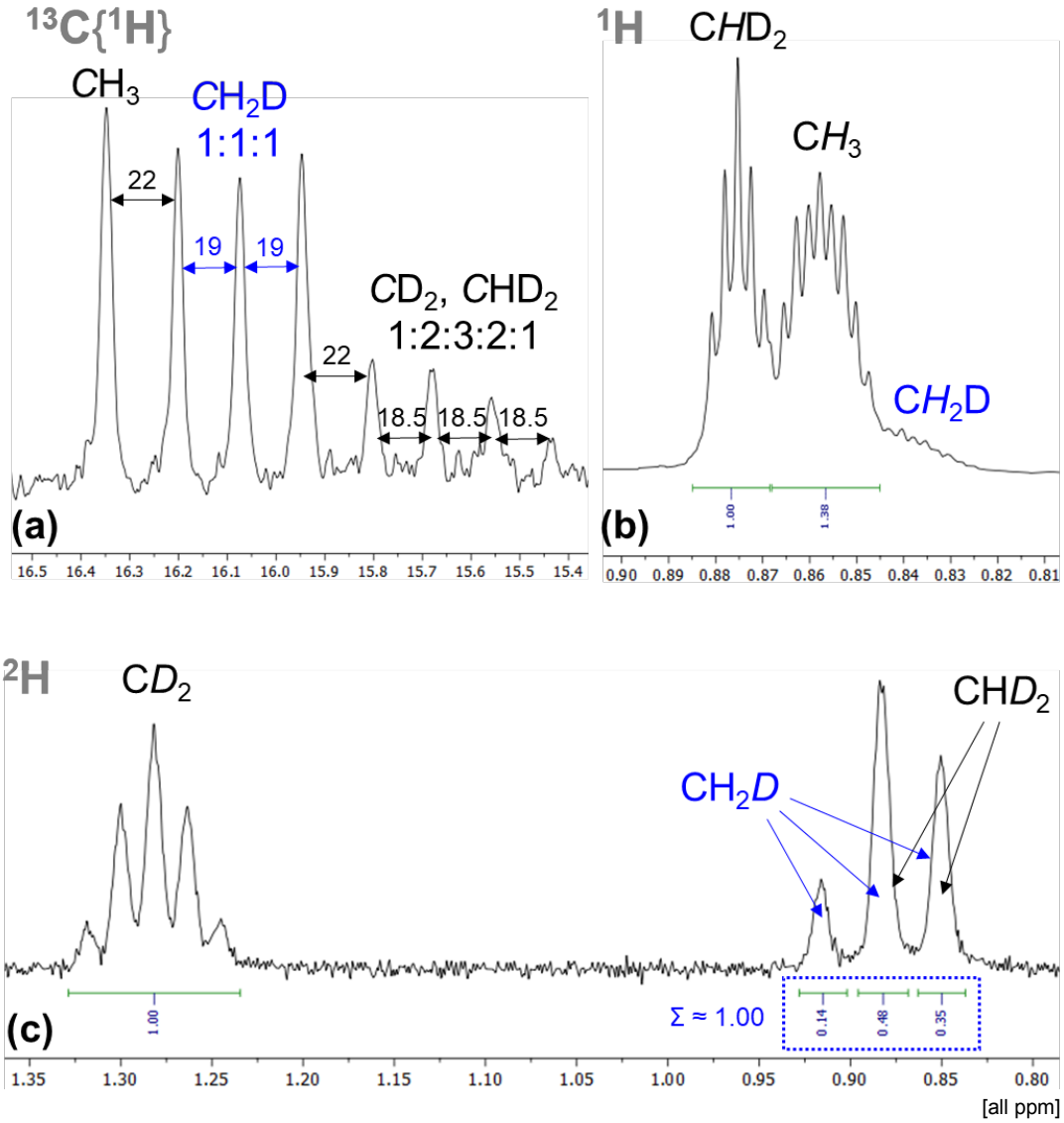


Figure 4.4.4: Selected NMR data for a CD_2Cl_2 solution of a mixture of 1,1,2,2-d_4-propane and 1,2,2,3-d_4-propane, produced by the catalytic deuterogenation of propyne by pre-catalyst SMOM 17. (**a**) Section of ^{13}C{^{1}H} NMR spectrum (100.62 MHz, 298 K). (**b**) Section of unoptimised ^{1}H NMR spectrum (400.12 MHz, 298 K). (**c**) ^{2}H NMR spectrum (61.42 MHz, 298 K). Peaks consistent with C1-C3 scrambling product 1,2,2,3-d_4-propane are highlighted in blue.

By $^{13}C\{^{1}H\}$ NMR spectroscopy (**Figure 4.4.4a**), eight d_4-propane peaks were resolved in the region δ 15.4–16.4. By measuring the intervening frequencies, these peaks were assigned as a singlet (*i.e.* CH_3), a 1:1:1 trinomial triplet ($^{1}J_{CD}$ = 19.0 Hz, *i.e.* CH_2D and/or CHD), and apparently a 1:2:3:2:1 trinomial quintet ($^{1}J_{CD}$ = 18.5 Hz, *i.e.* CHD_2 and/or CD_2). The presence of such a triplet eliminates the possibility of pure 1,1,2,2-d_4-propane, which would be expected to generate only a singlet and a trinomial quintet. This strongly suggested the operation of some H/D scrambling mechanism capable of producing carbon atoms bound to only one deuteron (CHD or CH_2D) in the alkane product. We must consider the possibility of multiplets overlapping (see Section 4.3.2) or being too low-intensity to be resolved, hence the resolution of only one trinomial quintet in this instance.

By ^{1}H NMR spectroscopy (**Figure 4.4.4b**), only resonances in the methyl region δ 0.8–1.0 were resolved. No resonance was resolved at δ ~1.3, where the C2 CH_2 would be expected.[49] This eliminates the possibility of any H/D scrambling involving the C2 position, consistent with C1–C3 H/D scrambling *only*, *via* a π-allyl hydride mechanism (an effective 1,3-hydride shift).[11] The two highest-intensity manifolds were successfully modelled as belonging to the CH_3 and CHD_2 groups of 1,1,2,2-d_4-propane, with identical coupling constants to those seen in 1,2-d_2-propane (Section 4.3.2; $^{2}J_{HD}$ = 2.0 Hz [geminal], $^{3}J_{HD}$ = 1.1 Hz [vicinal]). While the integrals of these two manifolds seemed far from the expected ratio of 1:3, we have already discussed how the presence of deuterons affects the relaxation rates of adjacent protons.[23] A third, lower-intensity resonance was also resolved; the only reasonable assignment of this was the remaining methyl isotopomer CH_2D, also evidencing C1–C3 scrambling, or possibly over-deuteration at C3.

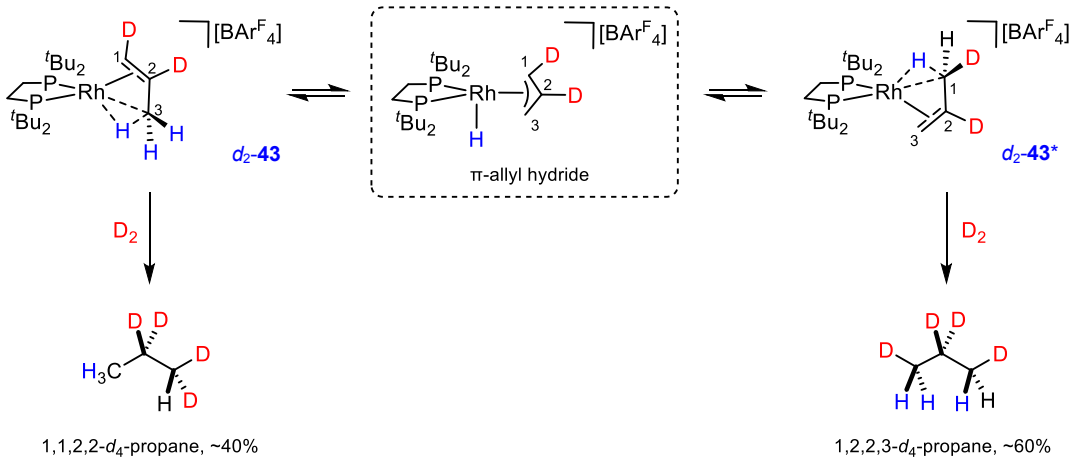
By ^{2}H NMR spectroscopy (**Figure 4.4.4c**), two resonances in a 1:1 integral ratio were resolved at δ 0.88 and 1.28, consistent with the C1/C3 and C2 positions respectively. Since no ^{1}H NMR resonance at δ_H ~1.3 was resolved, the C2 position must have been fully deuterated (as CD_2). Therefore, the ^{2}H NMR 1:1 integral ratio eliminates the possibility of any over-deuteration (or indeed under-deuteration) during the solid-gas deuterogenation reaction, such that only tetradeutero-isotopomers n_D = 4 were formed.

The ^{2}H NMR resonance at δ 1.28 (C2 CD_2) was successfully modelled as a binomial quintet, consistent with the presence of four protons in vicinal positions ($^{3}J_{HD}$ = 1.1 Hz) and none in geminal positions, presumably broadened somewhat by vicinal ^{2}H-^{2}H coupling (as in Section 4.3.2). The resonance at δ 0.88 was not the simple binomial doublet that might have been expected from C1 CHD_2 (1,1,2,2-d_4-propane). Analysis of the sub-integrals (0.14, 0.48, 0.35) suggested the superposition of a binomial doublet and *either* a binomial doublet (*i.e.* 0.14, [0.14+0.34], 0.35) or a binomial triplet (*i.e.* 0.14, [0.20+0.28], [0.20+0.14]), with geminal ^{1}H-^{2}H coupling constants ($^{2}J_{HD}$ ~ 2 Hz). The former seems impossible, as the presence of a second doublet in the methyl region would contradict the previous discussion[a] and there seems no physically feasible way in which to generate a second doublet at this position. The latter is possible (as 2 × CH_2D), and is consistent with the idea of C1-C3 scrambling of a rhodium-bound 1,2-d_2-propene intermediate to yield 2,3-d_2-propene (**Scheme 4.4.7**).

From the sub-integrals measured in the methyl region,[b] we can infer that 1,1,2,2-d_4-propane was generated in a ~40% proportion *versus* its scrambling product 1,2,2,3-d_4-propane in a ~60% proportion (see **Scheme 4.4.7**, which assumes *cis*-selective hydrogenation of alkyne to alkene[50]). If the deuterogenation of propene by SMOM **17** occurred in a straightforwardly pairwise fashion, as in Section 4.3.2, then the introduction of complexity must have occurred *before* this step, *i.e.* by isomerisation of a hypothetical [(dtbpe)Rh(η^2-1,2-d_2-propene)]$^+$ intermediate, consistent with the scrambling previously observed[11] in [(dcpe)Rh(η^2-3,3,3-d_3-propene)]$^+$ discussed in the Introduction (Section 1.2.1).

The high proportion of isomerisation product 1,2,2,3-d_4-propane indicated that C1-C3 scrambling was facile on the d_2-propene intermediate (d_2-**43**), occurring at a rate comparable to the subsequent deuterogenation step. This aligns with the observations made in Chapter 2, of {(dtbpe)Rh}[BAr$^{F}_{4}$]-containing SMOM **17** being a powerful solid-gas catalyst for alkene isomerisation, also proceeding *via* a π-allyl hydride intermediate.

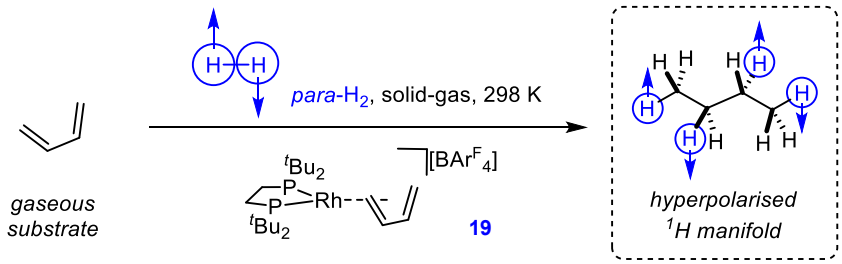
[a] It has already been deduced that the C2 position was fully deuterated and only n_D = 4 isotopomers were present. As such, only a binomial doublet (CH_2D) *or* triplet (CH_2D) was possible in the methyl region.
[b] Binomial doublet [0.20+0.20] (CH_2D), Σ = 0.40, plus triplet [0.14+0.28+0.14] (2 × CH_2D), Σ = 0.56, *i.e.* ~40:60.



Scheme 4.4.7: Proposed C1-C3 H/D scrambling mechanism for the catalytic deuterogenation of propyne gas by pre-catalyst SMOM **17**, envisioning a 1,2-d_2-propene-bound intermediate vulnerable to reversible allylic C–H activation *via* a π-allyl hydride (an effective 1,3-hydride shift).

4.5 Solid-Gas Hydrogenation-Polarisation of 1,3-Butadiene

Reasoning that a *bis*-alkene might constitute another possible route to a hyperpolarised alkene while avoiding cyclotrimerisation, 1,3-butadiene gas was also tested under NMR batch conditions. The procedure detailed in Section 4.3 was repeated, substituting propene for 1,3-butadiene (1.0 bar), and utilising the 1,3-butadiene complexes for both dcpe[11] (**18**) and dtbpe[12] (**19**) as pre-catalysts without pre-hydrogenation steps (**Scheme 4.5.1**). While reports of heterogeneous hydrogenation-polarisation of 1,3-butadiene have been made,[9,51,52] operating temperatures of <100 °C have not been achieved. Here, we show that the hydrogenation-polarisation of 1,3-butadiene can occur at ambient temperature using SMOM pre-catalysts.



Scheme 4.5.1: Solid-gas PHIP of 1,3-butadiene gas by SMOM **19**.

Under NMR batch conditions, only resonances corresponding to 1,3-butadiene and *HP*-butane gases were initially recognised with pre-catalyst SMOM **19** (**Figure 4.5.1**); turnover with pre-catalyst SMOM **18** was only slight by comparison, so this catalytic system will not be discussed further. Accounting for ~10% conversion on the first scan (t ~ 10 seconds; TON_{app} ~ 10), determined by reverse extrapolation of the 1,3-butadiene methine CH |z| integral, initial enhancement factors of ~16 (butane CH_2) and ~12 (butane CH_3) were estimated for the catalytic system derived from SMOM **19**.

The higher initial enhancement factor for the internal CH_2 resonance once again reflected the higher proportion of incorporated protons arising from *para*-H_2. However, the magnitudes of these enhancement factors were somewhat low, especially compared to the hydrogenation-polarisation of propene (Section 4.3) or the semihydrogenation-polarisation of propyne (Section 4.4). The reason for this may lie in this system's selectivity for butane over any butene, the production of which must have required *two* consecutive hydrogenation steps *without* release of an intermediate butene, a delay that may have permitted loss of spin cohesion and release of butane with a low proportion of non-Boltzmann product (*HP*-butane).

It is possible that the hydrogenation of any bound butene as produced from 1,3-butadiene occurred more rapidly than it could be substituted for 1,3-butadiene, hence the system's selectivity for butane over any butene. Resonances corresponding to butene[53,54] appeared only gradually, in small quantities; it is not clear which butene isomer a minor emergent resonance in the alkene region (δ ~6.00) corresponded to.

Over the course of the experiment, the sample was observed to turn a pale orange, and subsequent charges observed a reduced capacity for hydrogenation, without a PHIP response. Solution-phase NMR spectroscopy on post-batch material evidenced the dimeric Rh(III) hydride, **23**, as in Section 4.3.1. Exposure of 1,3-butadiene complex **19** even to low pressures of H_2 (1.0 bar) is known to rapidly yield this hydride.[12]

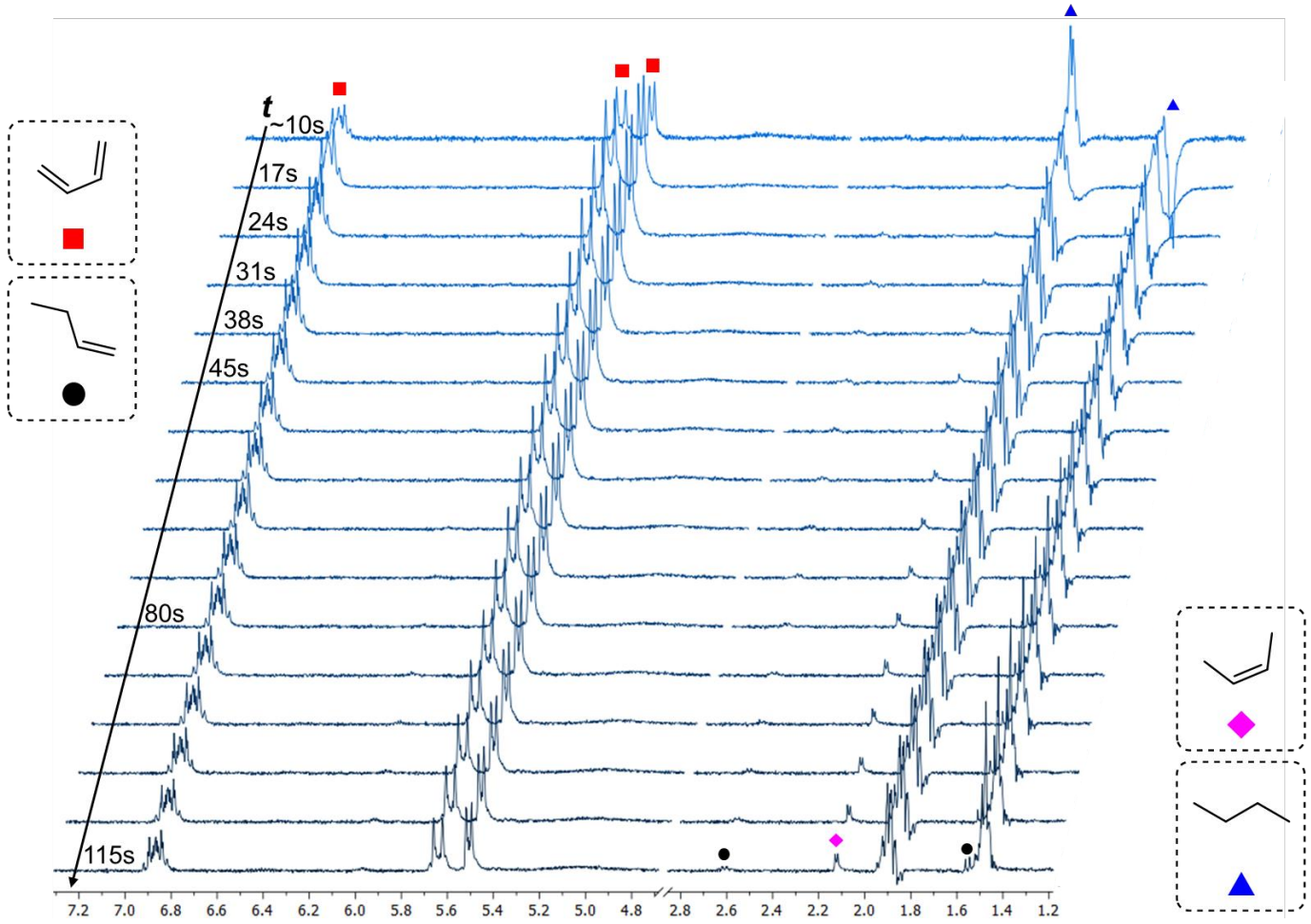
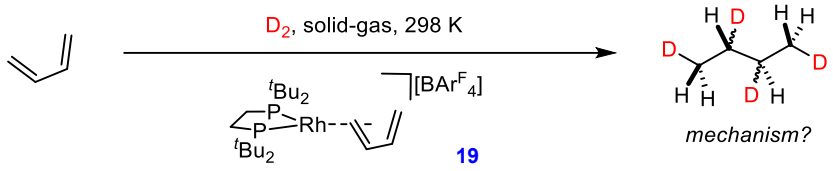


Figure 4.5.1: Exemplar sequential gas-phase ^{1}H NMR spectra (400.12 MHz, 45° pulse angle, 1.0 receiver gain) of 1,3-butadiene solid-gas hydrogenation-polarisation at 298 K. Conditions: 1,3-butadiene (1 bar) + *para*-H_2 atmosphere (3.5 bar-absolute) in the presence of SMOM **19** (2 mg, finely ground). Time is measured from the initial exposure of the sample to the *para*-H_2 source. Note that some minor resonances have not been assigned as they are either obscured or too weak to be assigned unambiguously. The first scan (~10s) has been upscaled to compensate for receiver saturation.

4.5.1 *Solid-Gas Hydrogenation of 1,3-Butadiene: Mechanistic Investigations with D_2*

Noting that the hydrogenation-polarisation protocol succeeded in generating a powerful PHIP enhancement response with propyne but *not* 1,3-butadiene, we were again interested to probe the nature of hydrogenation reaction – principally, whether straightforward addition of H_2 occurred (**Scheme 4.5.2**), without isomerisation and concomitant C1-C3 H/D scrambling as discussed in Section 4.4.4. Once again, due to the positive response of pre-catalyst SMOM **19** in the hydrogenation-polarisation of 1,3-butadiene, only pre-catalyst SMOM **19** will be discussed in this Section.



Scheme 4.5.2: Solid-gas catalytic deuterogenation of 1,3-butadiene by SMOM **19** as a mechanistic probe.

Finely-ground SMOM **19** (2 mg) was loaded into an NMR tube fitted with Young's tap, and first exposed to H_2 (1.0 bar) for 10 minutes at 298 K before evacuation and repressurisation with 1,3-butadiene (0.5 bar). The tube was then partially immersed in liquid N_2 in order to freeze the butadiene atmosphere before a pressure of D_2 (1.0 bar) was introduced. The tube was thawed and its contents were monitored by gas-phase ^{1}H NMR until near-complete conversion (>99.5%, TON_{app} ~ 55) was achieved, after approximately five minutes. The atmosphere of the tube was then frozen with liquid N_2 and excess D_2 was removed under dynamic vacuum before thawing and distilling any gaseous hydrocarbons into CD_2Cl_2.

Significant evidence for isomerisation/scrambling was obtained by solution-phase ^{1}H, ^{2}H, and ^{13}C{^{1}H} NMR spectroscopy (**Figure 4.5.2**). By ^{13}C{^{1}H} NMR spectroscopy (**Figure 4.5.2a**), multiple peaks were resolved in the region δ 13.0-14.2. By measuring the intervening frequencies, these peaks were assigned as a singlet (*i.e.* CH_3) and a 1:1:1 trinomial triplet ($^1J_{CD}$ = 19.0 Hz, *i.e.* CH_2D). Other peaks closer to the baseline may have indicated a 1:2:3:2:1 trinomial quintet ($^1J_{CD}$ ~ 18.5 Hz, *i.e.* CHD_2).

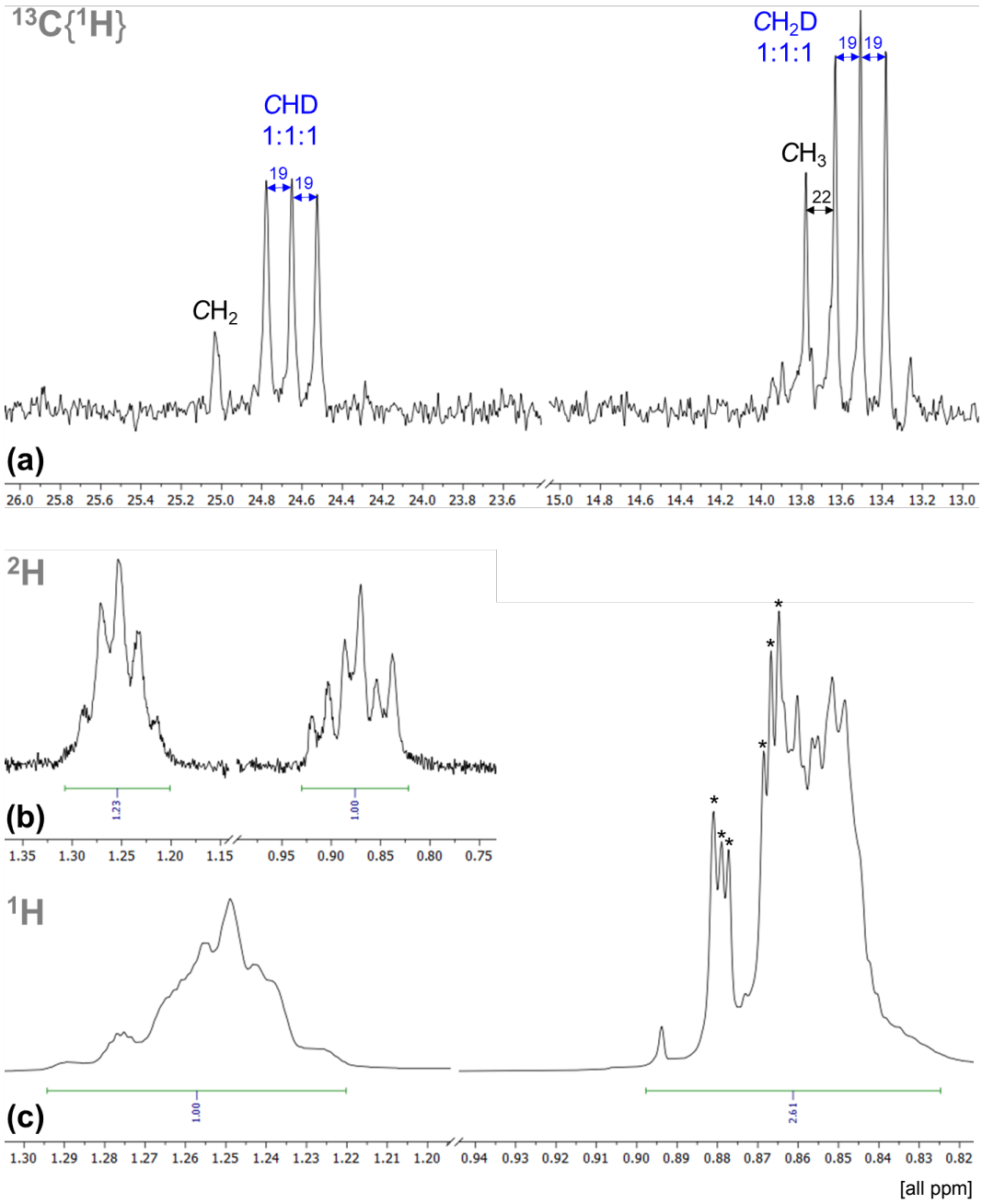


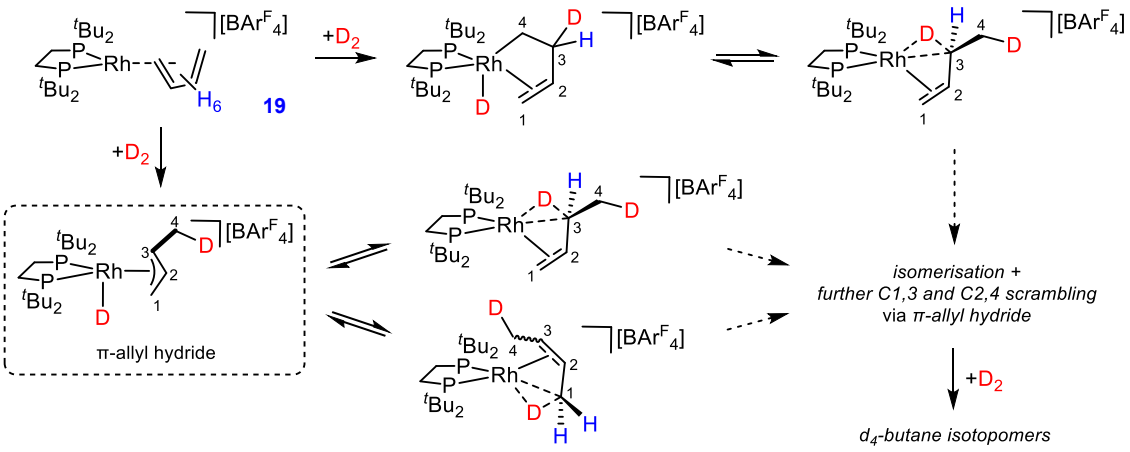
Figure 4.5.2: Selected NMR data for a CD_2Cl_2 solution of a mixture of various isomers of d_4-butane, produced by the catalytic deuterogenation of 1,3-butadiene by SMOM **19**. (**a**) Sections of $^{13}C\{^1H\}$ NMR spectrum (100.62 MHz, 298 K). (**b**) Sections of ^2H NMR spectrum (61.42 MHz, 298 K). (**c**) Section of unoptimised ^1H NMR spectrum (600.09 MHz, 298 K).

In the $^{13}C\{^1H\}$ NMR region δ 24.0–25.4, a singlet (*i.e.* CH_2) and a 1:1:1 trinomial triplet ($^1J_{CD}$ = 19.0 Hz, *i.e.* CHD) were resolved. Already, evidence is available for isomerisation: strict production of 1,2,3,4-d_4-propane would be expected to generate solely trinomial triplets by $^{13}C\{^1H\}$ NMR spectroscopy in both regions δ 24.0–25.4 (methylene) and δ 13.0–14.2 (methyl).

By ^{2}H NMR spectroscopy (**Figure 4.5.2b**), a triplet of doublets (δ 0.88) and a multiplet (δ 1.25) were resolved. The former is consistent with a -CHDCH$_2$*D* moiety, containing the expected vicinal ($^{2}J_{HD}$ = 2.0 Hz) and geminal ($^{2}J_{HD}$ = 1.1 Hz) coupling constants. Both lineshapes were somewhat broad and misshapen: a pure isotopomer was likely not present, consistent with the ^{13}C{^{1}H} NMR spectrum. It is not clear whether the unequal ^{2}H NMR integrals are indicative of ^{2}H over-incorporation or unequal ^{2}H distribution as a result of H/D scrambling.

By ^{1}H NMR spectroscopy (**Figure 4.5.2c**), complex manifolds were resolved at δ 0.86 and 1.25, once again inconsistent with a pure isotopomer. The peaks marked with asterisks were successfully linked by HSQC with the *C*H$_3$ singlet in **Figure 4.5.2a**, containing the expected coupling constants for a -CHDC*H*$_3$ moiety ($^{3}J_{HH}$ = 7.4 Hz, $^{3}J_{HD}$ = 1.1 Hz [geminal], with no $^{2}J_{HD}$ ~ 2 Hz [vicinal]).

Taken together, NMR evidence incontrovertibly revealed H/D-scrambling at the methyl (C1,4) *and* methylene (C2,3) positions. A plausible scrambling mechanism is presented in **Scheme 4.5.3**, proceeding *via* the same π-allyl hydride intermediate as proposed for the C1,3 scrambling observed during the deuterogenation of propyne (Section 4.4.4).



Scheme 4.5.3: A mechanism for the emergence of various isotopomers during the deuterogenation of 1,3-butadiene by SMOM **19**.

4.6 Conclusions

In this chapter, SMOMs 1 and 17 (and derivatives thereof) were successfully deployed as pre-catalysts for the solid-gas *para*-hydrogen induced polarisation (PHIP) of various gaseous unsaturated hydrocarbons – namely, a *mono*-alkene (propene), an alkyne (propyne) and a *bis*-alkene (1,3-butadiene) – and the factors affecting this PHIP response were explored in detail. For the hydrogenation-polarisation of propene, NMR enhancement factors of up to ~1,000 were achieved in the hyperpolarised products. Reflecting the results of Chapter 2, the *tert*-butyl-bearing SMOM 17 resisted deactivation to a greater degree than *cyclo*-hexyl-bearing SMOM 1, allowing for a prolonged PHIP response over multiple charges of alkene. Remarkably, it was also shown that a PHIP experiment could be conducted *without* the use of enriched *para*-hydrogen, when an atmosphere of normal hydrogen was first pre-cooled with liquid N_2 in the presence of the catalyst.

The mechanisms of the solid-gas hydrogenation reactions were elucidated with the assistance of D_2 gas. Evidence was available for isomerisation *via* a π-allyl hydride intermediate during the deuterogenation of propyne and 1,3-butadiene. Cyclotrimerisation of propyne by SMOMs was demonstrated in the solid-state, generating the corresponding 1,2,4-trimethylbenzene complexes (45, 47) in overwhelming majorities.

4.7 References

[1] S. B. Duckett, N. J. Wood, *Coordination Chemistry Reviews* **2008**, *252*, 2278–2291.

[2] S. B. Duckett, C. J. Sleigh, *Progress in Nuclear Magnetic Resonance Spectroscopy* **1999**, *34*, 71–92.

[3] K. v Kovtunov, A. S. Romanov, O. G. Salnikov, D. A. Barskiy, E. Y. Chekmenev, I. v Koptyug, *Tomography* **2016**, *2*, 49–55.

[4] M. Wielpütz, H.-U. Kauczor, *Diagnostic and interventional radiology* **2012**, *18*, 344.

[5] I. v Skovpin, V. v Zhivonitko, I. v Koptyug, *Applied Magnetic Resonance* **2011**, *41*, 393–410.

[6] K. v Kovtunov, V. v Zhivonitko, I. v Skovpin, D. A. Barskiy, I. v Koptyug, in (Ed.: L.T. Kuhn), Springer Berlin Heidelberg, Berlin, Heidelberg, **2013**, pp. 123–180.

[7] K. V. Kovtunov, I. E. Beck, V. I. Bukhtiyarov, I. V. Koptyug, *Angewandte Chemie International Edition* **2008**, *47*, 1492–1495.

[8] V. v Zhivonitko, K. v Kovtunov, I. E. Beck, A. B. Ayupov, V. I. Bukhtiyarov, I. v Koptyug, *The Journal of Physical Chemistry C* **2011**, *115*, 13386–13391.

[9] K. v Kovtunov, D. A. Barskiy, O. G. Salnikov, A. K. Khudorozhkov, V. I. Bukhtiyarov, I. P. Prosvirin, I. v Koptyug, *Chemical Communications* **2014**, *50*, 875–878.

[10] Air Liquide, **2017**.

[11] F. M. Chadwick, A. I. McKay, A. J. Martinez-Martinez, N. H. Rees, T. Krämer, S. A. Macgregor, A. S. Weller, *Chemical Science* **2017**, *8*, 6014–6029.

[12] A. J. Martínez-Martínez, C. G. Royle, S. K. Furfari, K. Suriye, A. S. Weller, *ACS Catalysis* **2020**, *10*, 1984–1992.

[13] S. D. Pike, F. M. Chadwick, N. H. Rees, M. P. Scott, A. S. Weller, T. Krämer, S. A. Macgregor, *Journal of the American Chemical Society* **2015**, *137*, 820–833.

[14] A. J. Bukvic, A. L. Burnage, G. J. Tizzard, A. J. Martínez-Martínez, A. I. McKay, N. H. Rees, B. E.

Tegner, T. Krämer, H. Fish, M. R. Warren, S. J. Coles, S. A. Macgregor, A. S. Weller, *Journal of the American Chemical Society* **2021**, *143*, 5106–5120.

[15] A. I. McKay, A. J. Bukvic, B. E. Tegner, A. L. Burnage, A. J. Martínez-Martínez, N. H. Rees, S. A. Macgregor, A. S. Weller, *Journal of the American Chemical Society* **2019**, *141*, 11700–11712.

[16] A. J. Martínez-Martínez, B. E. Tegner, A. I. McKay, A. J. Bukvic, N. H. Rees, G. J. Tizzard, S. J. Coles, M. R. Warren, S. A. Macgregor, A. S. Weller, *Journal of the American Chemical Society* **2018**, *140*, 14958–14970.

[17] A. D. Wilson, A. J. M. Miller, D. L. DuBois, J. A. Labinger, J. E. Bercaw, *Inorganic Chemistry* **2010**, *49*, 3918–3926.

[18] C. A. Tolman, *Journal of the American Chemical Society* **1970**, *92*, 2953–2956.

[19] D. Martin, D. Moraleda, T. Achard, L. Giordano, G. Buono, *Chemistry – A European Journal* **2011**, *17*, 12729–12740.

[20] K. v Kovtunov, M. L. Truong, D. A. Barskiy, O. G. Salnikov, V. I. Bukhtiyarov, A. M. Coffey, K. W. Waddell, I. v Koptyug, E. Y. Chekmenev, *The Journal of Physical Chemistry C* **2014**, *118*, 28234–28243.

[21] O. G. Salnikov, K. v Kovtunov, D. A. Barskiy, A. K. Khudorozhkov, E. A. Inozemtseva, I. P. Prosvirin, V. I. Bukhtiyarov, I. v Koptyug, *ACS Catalysis* **2014**, *4*, 2022–2028.

[22] R. Zhou, E. W. Zhao, W. Cheng, L. M. Neal, H. Zheng, R. E. Quiñones, H. E. Hagelin-Weaver, C. R. Bowers, *Journal of the American Chemical Society* **2015**, *137*, 1938–1946.

[23] K. Akasaka, T. Imoto, S. Shibata, H. Hatano, *Journal of Magnetic Resonance (1969)* **1975**, *18*, 328–343.

[24] K. v Kovtunov, I. v Koptyug, M. Fekete, S. B. Duckett, T. Theis, B. Joalland, E. Y. Chekmenev, *Angewandte Chemie International Edition* **2020**, *59*, 17788–17797.

[25] J. Y.-C. Chen, Y. Li, M. Frunzi, X. Lei, Y. Murata, R. G. Lawler, N. J. Turro, *Philosophical Transactions of the Royal Society A: Mathematical, Physical and Engineering Sciences* **2013**, *371*, 20110628.

[26] D. B. Burueva, A. S. Romanov, O. G. Salnikov, V. v Zhivonitko, Y.-W. Chen, D. A. Barskiy, E. Y. Chekmenev, D. W. Hwang, K. v Kovtunov, I. v Koptyug, *The Journal of Physical Chemistry C* **2017**, *121*, 4481–4487.

[27] B. Joalland, N. M. Ariyasingha, H. R. Younes, S. Nantogma, O. G. Salnikov, N. v Chukanov, K. v Kovtunov, I. v Koptyug, J. G. Gelovani, E. Y. Chekmenev, *Chemistry – A European Journal* **2021**, *27*, 2774–2781.

[28] R. E. D. McClung, *eMagRes* **2007**.

[29] A. E. Khudozhitkov, S. S. Arzumanov, D. I. Kolokolov, D. Freude, A. G. Stepanov, *Physical Chemistry Chemical Physics* **2020**, *22*, 5976–5984.

[30] Y. Shibata, K. Tanaka, *Synthesis* **2012**, *44*, 323–350.

[31] D. L. J. Broere, E. Ruijter, *Synthesis* **2012**, *44*, 2639–2672.

[32] K. Yoshida, I. Morimoto, K. Mitsudo, H. Tanaka, *Chemistry letters* **2007**, *36*, 998–999.

[33] Ò. Torres, M. Fernàndez, À. Díaz-Jiménez, A. Pla-Quintana, A. Roglans, M. Solà, *Organometallics* **2019**, *38*, 2853–2862.

[34] T. Konno, K. Moriyasu, R. Kinugawa, T. Ishihara, *Organic & Biomolecular Chemistry* **2010**, *8*, 1718–1724.

[35] Y. Wakatsuki, O. Nomura, K. Kitaura, K. Morokuma, H. Yamazaki, *Journal of the American Chemical Society* **1983**, *105*, 1907–1912.

[36] S. Bär, T. Lange, D. Leibfritz, J. Hennig, D. von Elverfeldt, J.-B. Hövener, *Journal of Magnetic Resonance* **2012**, *225*, 25–35.

[37] Z.-Y. Cao, Y. Zhang, C.-B. Ji, J. Zhou, *Organic Letters* **2011**, *13*, 6398–6401.

[38] J. Bielefeld, S. Mannhaupt, M. Schmidtmann, S. Doye, *Synlett* **2019**, *30*, 967–971.

[39] H. Werner, P. Schwab, N. Mahr, J. Wolf, *Chemische Berichte* **1992**, *125*, 2641–2650.

[40] W. Weng, C. Guo, R. Çelenligil-Çetin, B. M. Foxman, O. v Ozerov, *Chemical Communications* **2006**, 197–199.

[41] T. M. Hood, A. B. Chaplin, *Dalton Transactions* **2020**, *49*, 16649–16652.

[42] L. Rubio-Pérez, R. Azpíroz, A. Di Giuseppe, V. Polo, R. Castarlenas, J. J. Pérez-Torrente, L. A. Oro, *Chemistry – A European Journal* **2013**, *19*, 15304–15314.

[43] A. M. Geer, A. Julián, J. A. López, M. A. Ciriano, C. Tejel, *Chemistry – A European Journal* **2018**, *24*, 17545–17556.

[44] A. M. Geer, A. Julián, J. A. López, M. A. Ciriano, C. Tejel, *Chemistry – A European Journal* **2014**, *20*, 2732–2736.

[45] M. Schäfer, J. Wolf, H. Werner, *Dalton Transactions* **2005**, 1468–1481.

[46] N. v Shvydkiy, E. A. Trifonova, A. M. Shved, Y. v Nelyubina, D. Chusov, D. S. Perekalin, A. R. Kudinov, *Organometallics* **2016**, *35*, 3025–3031.

[47] D. S. Perekalin, N. v Shvydkiy, Y. v Nelyubina, A. R. Kudinov, *Chemistry – A European Journal* **2015**, *21*, 16344–16348.

[48] S. D. Pike, M. R. Crimmin, A. B. Chaplin, *Chemical Communications* **2017**, *53*, 3615–3633.

[49] T. Zuschneid, H. Fischer, T. Handel, K. Albert, G. Häfelinger, *Zeitschrift für Naturforschung B* **2004**, *59*, 1153–1176.

[50] R. R. Schrock, J. A. Osborn, *Journal of the American Chemical Society* **1976**, *98*, 2143–2147.

[51] D. A. Barskiy, K. v Kovtunov, A. Primo, A. Corma, R. Kaptein, I. v Koptyug, *ChemCatChem* **2012**, *4*, 2031–2035.

[52] A. Svyatova, E. S. Kononenko, K. v Kovtunov, D. Lebedev, E. Yu. Gerasimov, A. v Bukhtiyarov, I. P. Prosvirin, V. I. Bukhtiyarov, C. R. Müller, A. Fedorov, I. v Koptyug, *Catalysis Science & Technology* **2020**, *10*, 99–104.

[53] F. Rekhroukh, L. Estevez, S. Mallet-Ladeira, K. Miqueu, A. Amgoune, D. Bourissou, *Journal of the American Chemical Society* **2016**, *138*, 11920–11929.

[54] M. Shiramizu, F. D. Toste, *Angewandte Chemie International Edition* **2012**, *51*, 8082–8086.

5 Experimental

Some of the material in this Section pertaining to Chapter 2 has been adapted from the reference;[1] the relevant material was also authored by the author of this work.

5.1 General Methods and Reagents

All manipulations, unless otherwise stated, were performed under an inert atmosphere of argon or N_2 using standard Schlenk techniques on a dual vacuum/inlet manifold or by employment of an MBraun glovebox. Evacuation refers to a pressure equal or lower than 10^{-2} mbar, measured with a vacuum gauge and display fitted to a Schlenk line. Glassware was dried in an oven at 130-150 °C overnight prior to use. All solvents intended for air-sensitive chemistry underwent three freeze-pump-thaw cycles prior to use. *n*-pentane, *n*-hexane, THF, and CH_2Cl_2 were dried using an MBraun SPS-800 solvent purification system, and stored over activated molecular sieves (3 Å). CD_2Cl_2 was dried by stirring over CaH_2 overnight before vacuum distillation and stored over activated molecular sieves (3 Å). 1,2-difluorobenzene and fluorobenzene were stirred over Al_2O_3 for two hours before stirring over CaH_2 overnight, followed by vacuum distillation. CD_3CN was distilled over a small amount of P_2O_5. C_6D_6, 1,5-cyclooctadiene (COD) and 2,5-norbornadiene (NBD) were purchased from Sigma-Aldrich/Merck and distilled over freshly cut small pieces of sodium metal. Neat 1-butene and *iso*-butene were supplied by CK Special Gases Ltd. (UK) and used as received. *Cis*-2-butene and *trans*-2-butene (2% balanced with N_2) were supplied by Air Liquide (UK) and used as received. Gas lecture bottles of D_2, HD, ethene, propene, propyne, 1-butene, *iso*-butene, and 1,3-butadiene, in addition to samples of 1,2-dibromoethene, 1,2,4-trimethylbenzene, trimethylamine-borane (TMAB), 1,3-butadiene (15 wt% in hexanes), and chelating *bis*-phosphines unless otherwise stated were purchased from Sigma-Aldrich/Merck and used as received. $RhCl_3{\cdot}(H_2O)_n$ and $IrCl_3{\cdot}(H_2O)_n$ were purchased from Precious Metals Online Ltd. and used as received.

(*R*)-MaxPhos·HBF_4 and *bis*-phosphonium salts [(dcyppp)H_2][BF_4] and [(dcyppb)H_2][BF_4] (dcyppp = 1,3-bis(di-*cyclo*-pentylphosphino)propane; dcyppb = 1,4-bis(di-*cyclo*-pentylphosphino)butane) were purchased from STREM and used as received. Na[BAr^F_4],[2] ^{i}Pr-PONOP,[3,4] [Rh(η^2,η^2-NBD)$_2$][BAr^F_4],[5] [Ir(η^2,η^2-COD)$_2$][BAr^F_4],[6] 1,2- (dtbpe)[7] and 1,4-bis(di-*tert*-butylphosphino)ethane (dtbpb),[8] 1,2-bis(di-*tert*-butylphosphino)amine (dtbpa),[9] [RhCl(η^2,η^2-COD)$_2$]$_2$,[10] [RhCl(η^2,η^2-NBD)]$_2$,[11] and SMOMs **1**, **7**;[12] **4**, **5**, **6**;[13] **8**;[14] and **11**[15] were synthesised according to reported protocols.

5.2 Solution-Phase NMR Spectroscopic Data

Solution-phase NMR data were collected on either a Bruker Avance III NMR spectrometer (equipped with a 11.75 T magnet), a Bruker Avance III HD nanobay NMR spectrometer (equipped with a 9.4 T magnet), or a Bruker Avance III HD wide-bore NMR spectrometer (equipped with a 14.1 magnet) at the specified temperatures. The temperature for NMR experiments was externally calibrated to observe the chemical-shift separation between the OH and CH_3 resonances in methanol. Non-deuterated solvents and gas-phase samples were locked to standard external neat CD_2Cl_2 or 10% fluorobenzene in C_6D_6 sample solutions. $^{31}P\{^1H\}$ NMR spectra were referenced externally to 85% H_3PO_4 in D_2O. All chemical shifts (δ) are quoted in ppm and coupling constants (J) in Hz. T_1 spin-lattice relaxation times were measured by the standard inversion-recovery pulse technique. Spin simulations were conducted using MestReNova (11.0.2-18153 to 14.1.2-25024, ©2016-2020 MestreLab Research).

5.3 Solid-State NMR Spectroscopic Data

Solid-state NMR samples were prepared in an argon- or N_2-filled glovebox, by pre-loading 35-75 mg of the finely crushed crystalline sample in question into a zirconia solid-state rotor. *In situ* solid-gas transformations made use of either custom glassware for capping under a flow of gas,[16] or took place inside Young's flasks, purged with argon or N_2 before the rotor was capped inside an argon- or N_2-filled glovebox.

Solid-state NMR spectra were obtained on a Bruker Avance III HD spectrometer equipped with a 9.4 T magnet, operating at 100.56 MHz (^{13}C) or 161.89 MHz (^{31}P), with a MAS rate (ν) of 10 kHz. For $^{13}C\{^{1}H\}$ CP/MAS SSNMR, a sequence with a variable X-amplitude spin-lock pulse[17] and spinal64 proton decoupling was used. 4500 transients were acquired using a contact time of 2.5 ms, an acquisition time of 25 ms (2048 data points zero-filled to 32 K) and a recycle delay of 2.0 s. All $^{13}C\{^{1}H\}$ spectra were referenced to adamantane where the upfield methane resonance was taken to be δ 29.5 ppm[18] on a scale secondarily referenced to $SiMe_4$, δ 0.0. Relaxation times for ^{1}H and contact time for $^{31}P\{^{1}H\}$ CP/MAS, $^{13}C\{^{1}H\}$ CP/MAS, and FSLG-HETCOR NMR experiments were optimised for each compound as appropriate. The temperature for variable-temperature SSNMR experiments was calibrated externally using $PbNO_3$.

5.4 Gas-Phase ^{1}H NMR Spectroscopic Data and Solid-Gas PHIP

Gas phase ^{1}H NMR spectra were obtained using either a Bruker Avance III NMR spectrometer (equipped with a 11.75 T magnet) or a Bruker Avance III HD nanobay NMR spectrometer (equipped with a 9.4 T magnet). Pressurisation of medium-wall NMR tubes (2 mL) fitted with Teflon controlled atmosphere valves using the appropriate gaseous substrate was achieved by evacuation and backfilling at the appropriate pressure using custom glassware detailed in previous work.[16] The spectrometer was pre-locked and pre-shimmed to a separate sample of CD_2Cl_2 or 10% difluorobenzene in C_6D_6 solution before NMR study of the of the hydrocarbon gas in question.

Para-hydrogen was supplied by a bespoke generator at the University of York Centre for Hyperpolarisation in Magnetic Resonance (CHyM) to a maximum pressure of ~3.5 bar-absolute. PHIP experiments were initiated by pressurising a sample of catalyst or pre-catalyst inside an NMR tube fitted with a Young's tap firstly with substrate gas at a given pressure, and secondly with *para*-H_2 at a given pressure, with the supply of H_2 opened for no more than three seconds to prevent departure of substrate gas. The NMR tube was then sealed and promptly removed from the supply, shaken vigorously, and introduced to the probe (inverse ^{1}H-sensitivity probe).

At this point, single-scan gas-phase ^{1}H NMR experiments at specified pulse angles and receiver gains took place in sequence.

5.5 Mass Spectrometric Data

(Chapters 2 and 3) Electrospray ionisation mass spectrometry (ESI-MS) was carried out using a Bruker MicrOTOF instrument directly connected to a modified Innovative Technology glovebox.[19] The spectrometer was calibrated using a mixture of tetra-alkylammonium bromides $[N(C_nH_{2n+1})_4]Br$ (n = 2–8, 12, 16, and 18). Samples were diluted to a concentration of (at most) 10^{-6} mol dm^{-3} before mass spectrometry. Samples were typically acquired with a 4 μL min^{-1} flow rate, a 0.4 bar nebuliser gas pressure, a flow of argon at 333 K with a 4 L min^{-1} flow rate to act as a drying gas, a capillary voltage of 4.5 kV, and an exit voltage of 60 V. (Chapters 3 and 4) ESI-MS were recorded by Karl Heaton at the University of York on a Bruker compact® time-of-flight mass spectrometer.

5.6 Scanning Electron Microscopic Data

(Chapter 2) Scanning electron microscopy (SEM) was performed using a Carl Zeiss Merlin-Analytical instrument, with an operating voltage of 3.0 kV, and carried out by Dr Dana-Georgiana Crivoi at the University of Oxford. The samples were prepared by adding the material directly onto the carbon tape, under an atmosphere of argon. The samples were analysed without metal or carbon coating. Energy dispersive X-ray spectroscopy (EDX) was carried out on a Carl Zeiss Merlin-Analytical instrument with an operating voltage of 3.0 kV. (Chapter 3) Scanning electron microscopy (SEM) was performed using a JEOL JSM-7800F Prime Field Emission instrument, with an operating voltage of 1.0 kV, and carried out by Dr Claire Brodie at the University of York. The samples were prepared by adding the material directly onto the carbon tape, under an atmosphere of air. The samples were carbon-coated by vapour deposition before SEM analysis.

5.7 Powder X-Ray Diffractometric Data

(Chapter 2 only) Powder X-ray diffraction data were collected on a PANAnalytical X'Pert Pro Diffractometer in scanning mode using Cu K_α radiation (α_1 = 1.540598 Å, α_2 = 1.54426 Å, weighted average = 1.541847 Å). Scans were recorded between 2θ = 3.0–80°, with step size 0.017° and scan step-time 26.67 s. The samples were mounted on stainless steel holders that gave rise to peaks at 2θ = 43.36, 44.29, and 50.51° (the identity of these peaks were verified by recording a blank prior to analysis; see text).

5.8 Gas Chromatographic Data

(Chapter 2 only) Analyses by gas chromatography (GC) for the alkene gas mixtures (either from batch or flow experiment) were performed using a Shimadzu GC-2014 gas chromatograph equipped with a Flame Ionization Detector (FID) and a Restek alumina (BOND MAPD) capillary column (50 m × 0.53 mm × 10.0 μm) using a gas sampling loop (50 μL). To obtain gaseous sample aliquots, the loop was opened for a period of 60 seconds, and the contents passed *via* the Restek alumina column at a constant temperature of 80 °C (oven operating temperature), 9.57 mL min^{-1} operating flow rate, and 60.0 split ratio. Hydrogen and helium were passed through an on-stream O_2 and moisture trap. Sampling from catalytic runs under flow conditions were done by injection of a gas aliquot (50 μL) onto the gas chromatograph using an automated gas sampling valve every 15 min. Gas flow rates are reported as measured at 298 K and atmospheric pressure. External calibration using unique butene samples proved comparable GC response factors for the butene isomers analysed in this study with reproducible GC traces.

5.9 Elemental/CHN Microanalysis

Elemental microanalyses were carried out by Dr Stephen Boyer of London Metropolitan University (Chapters 2 and 3) and Dr Graeme McAllister of the University of York (Chapters 3 and 4).

5.10 Protocol for Solid-Gas Batch Experiments: Gas Analysis Sample Preparation

(Chapter 2) Gas samples from batch experiments corresponding to neat gas reagents and/or gas mixtures were diluted ~100-fold with argon gas before being analysed by gas chromatography using a custom glassware heavy wall ampoule (V ~ 50 mL) fitted with tubing/Teflon valves (**Figure 5.10.1**).

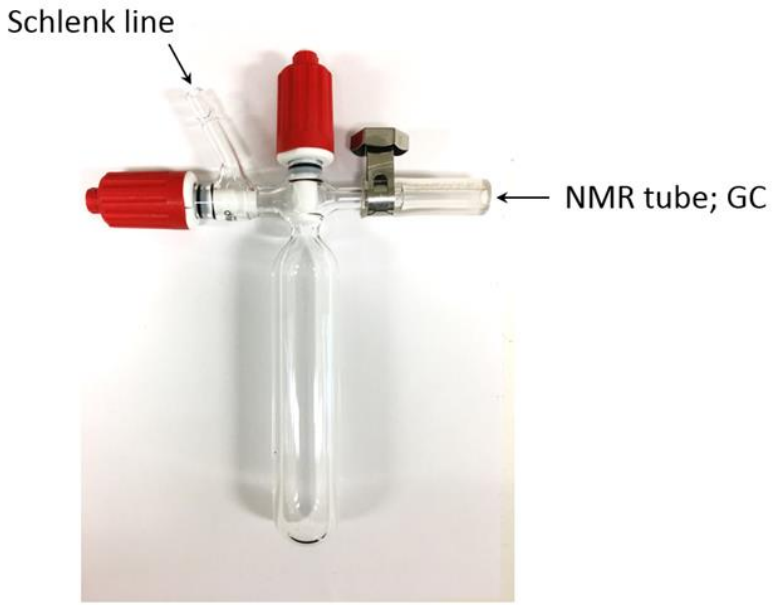


Figure 5.10.1: Custom ampoule (V ~ 50 mL) employed for gaseous sample dilution prior to GC analysis from batch experiments.

The ampoule was fitted with a medium-wall NMR tube with a controlled atmosphere Teflon valve (2 mL), containing the gas sample to be analysed, using the tubing adaptor. With the valve on the NMR tube closed at first, the ampoule was evacuated and filled with argon gas to a pressure of 1.5 bar and closed. Then, the ampoule was half-submerged in liquid nitrogen and the NMR tube was opened for 5 min allowing the gas mixture to condense inside the half-submerged ampoule. At this point, the NMR tube gas closed, and the ampoule was warmed up to room temperature to give an approximately 100-fold dilution of the gas mixture balanced with argon. The ampoule was then fitted to the sampling valve on the chromatograph using the tubing adaptor. An aliquot of 50 µL was then injected using the automated sampling valve and analysed by GC as described before. This protocol proved to give reproducible and consistent results.

5.11 Protocol for Solid-Gas Batch Experiments: 75 mL-Scale Reactor

A single crystal of SMOM 17 (~1 mg) was placed inside a ~75 mL reactor vessel fitted with two Young's taps, the second of these in turn connected to a junction where an NMR tube adapter and a third Young's tap were fitted (**Figure 5.11.1**). The vessel was evacuated and placed under a pressure of H_2 (1 bar) for 45 min, after which the H_2 was evacuated and replaced with 1-butene (1.4 bar). Every 24 hours, an aliquot of gas was removed into a high-pressure NMR tube fitted with a Young's tap, to be analysed by gas-phase ^{1}H NMR and gas chromatography. After this, the atmosphere of butene was removed and recharged.

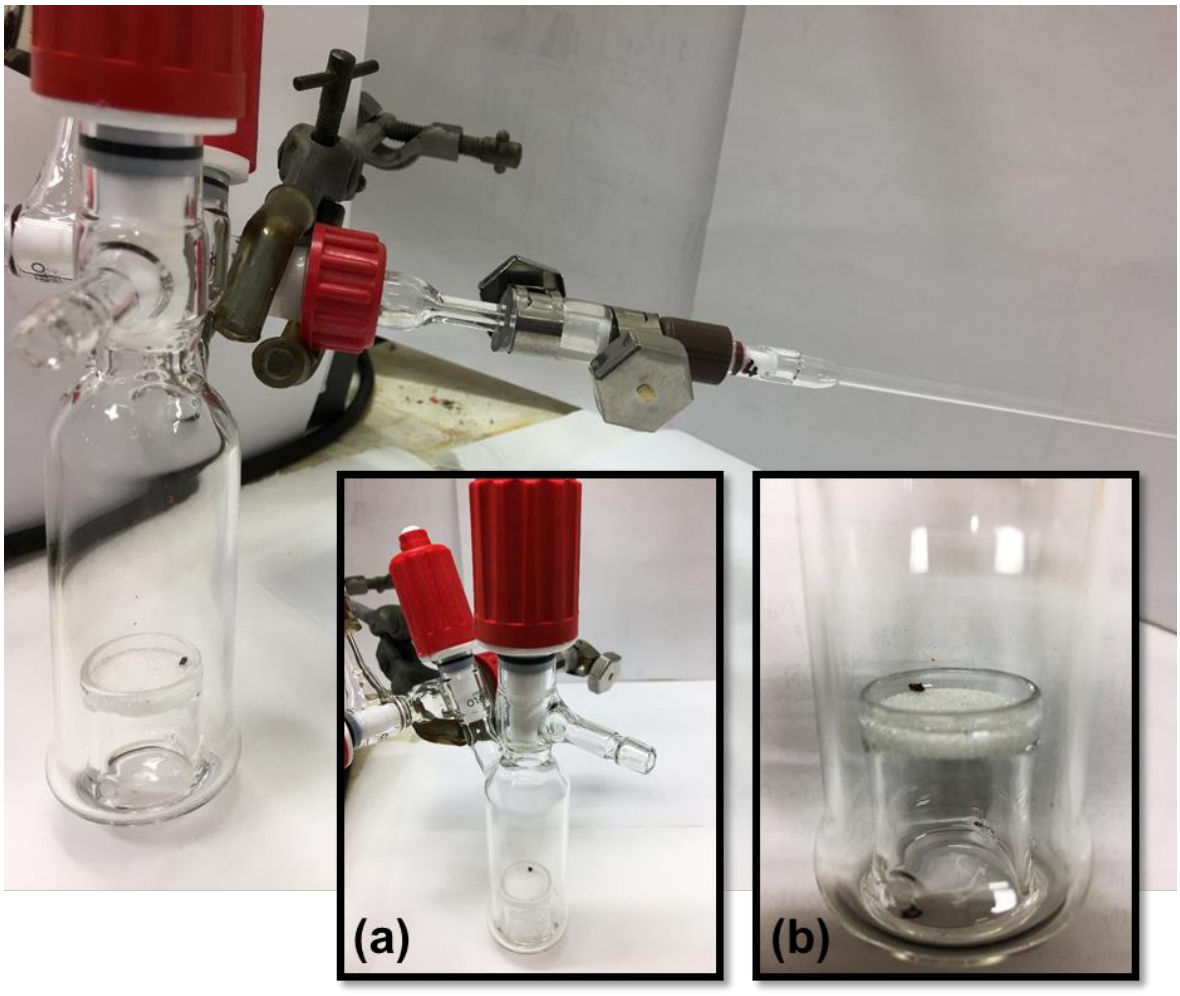


Figure 5.11.1: Custom reactor vessel (V ~ 75 mL), with high-pressure NMR tube fitted. (**a**) Detail of the reactor vessel; (**b**) close-up of mounted single-crystal of SMOM 17.

5.12 Protocol for Solid-Gas Continuous Flow Experiments

(Chapter 2) Samples were prepared by loading an appropriate amount of each catalyst/pre-catalyst supported with inert glass wool inside a stainless-steel column (thickness Ø 6.35 mm, internal diameter 4.0 mm, and length *L* 20.0 cm, **Figure 5.12.1**), inside a glovebox under an argon atmosphere. The inert glass wool support prevented the catalyst from dislodging from the column and improved its dispersion.



Figure 5.12.1: Stainless steel column fitted with gas-tight valves where the catalyst/pre-catalyst was packed before the catalytic runs under continuous gas flow conditions. This column was fitted to the continuous gas flow reactor using the upper and lower gas-tight two-way Swagelok valves.

The catalyst or pre-catalyst was first crushed in a glass vial and then filtered through a 150-micron Endecott sieves. The fine powder was then ground further. An initial plug of glass wool (~100 mg) was compacted within the column using a metal rod and then moved back up the column by approximately 2 cm (**Figure 5.12.2**, **A**). A small amount of glass wool (~30 mg) was placed at the top of the column and the powder was added to this (**B**), which was then compacted lightly on top of the initial glass wool plug (**C**). This was repeated 5-7 times depending on the desired catalyst loading (**D**).

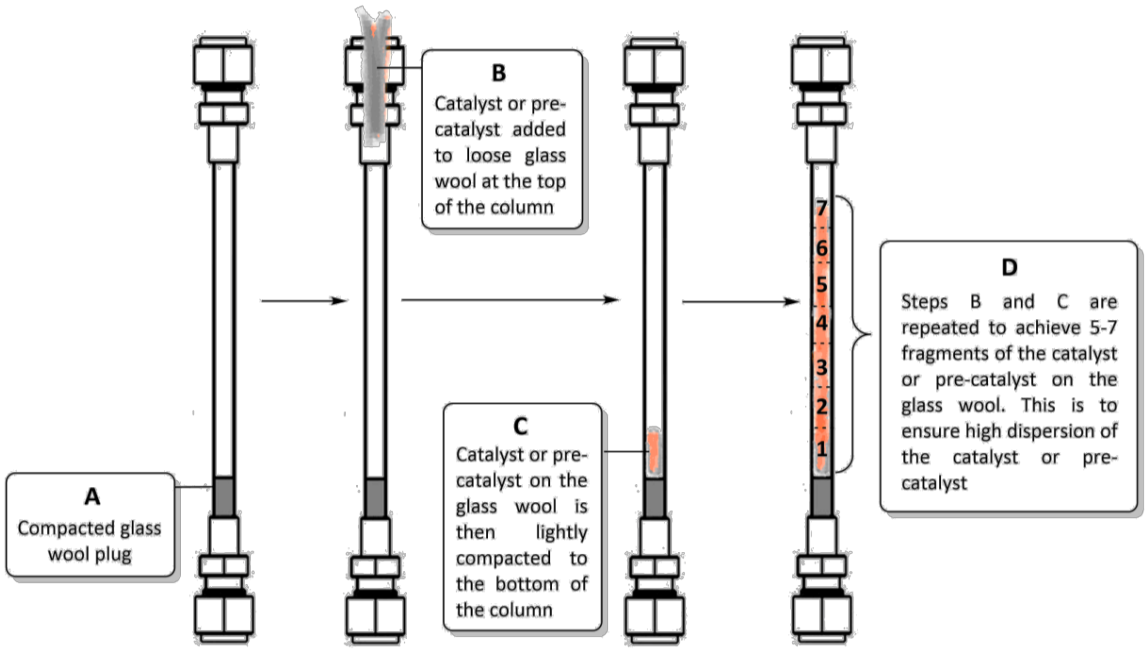


Figure 5.12.2: Packing of the stainless-steel column loaded with either the catalyst or pre-catalyst catalytic runs under continuous gas flow conditions. The initial glass wool plug (**A**) was followed by the addition of the catalyst or pre-catalyst on glass wool at the top of the column (**B**). The sample was then lightly compacted (**C**) and repeated in small fragments (**D**) to pack the column with the desired amount of catalyst or pre-catalyst.

Once the column was charged with the supported catalyst/pre-catalyst, it was sealed using the two-way Swagelok gas-tight valves, fitted at each end (as **Figure 5.12.1**). The pre-loaded column was then fitted to a bespoke continuous gas reactor using the Swagelok valves. Gas flow *into* the column (**Figure 5.12.3**, **A**) was controlled with a Brooks Delta Smart II mass-flow meters setup (**Figure 5.12.4**). Gas flow *out* of the column, charged with the corresponding catalyst or pre-catalyst, passed through a loop fitted with a pressure regulator (permitting column pressurisation to $p \leq 2$ bar; **Figure 5.12.3**, **B**). Gas aliquots were sampled and analysed every 15 minutes by GC as described above. Flow rates passing through the loop and thereafter vented were confirmed using an Ellutia 7000 flowmeter.

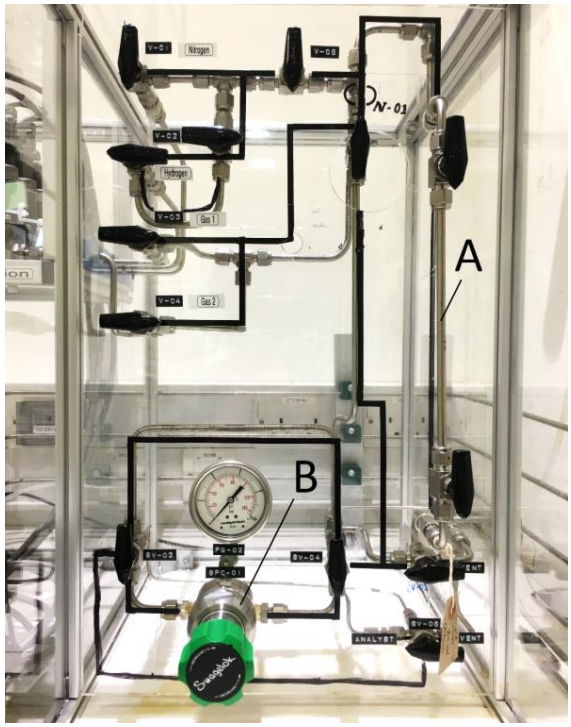


Figure 5.12.3: Bespoke continuous solid-gas flow reactor setup fitted with the pre-loaded stainless-steel column (**A**) containing the catalyst or pre-catalyst, during a catalytic run. Note that the N_2 and H_2 feeds are closed whereas the gas 1 (1-butene) and gas 2 (isobutene) feeds are open and set to pass *via* the column (**A**). The outflow is set to pass *via* the loop, fitted with a regulator (**B**) to allow H_2 pressurisation, and into the gas chromatograph, 'analyst'.

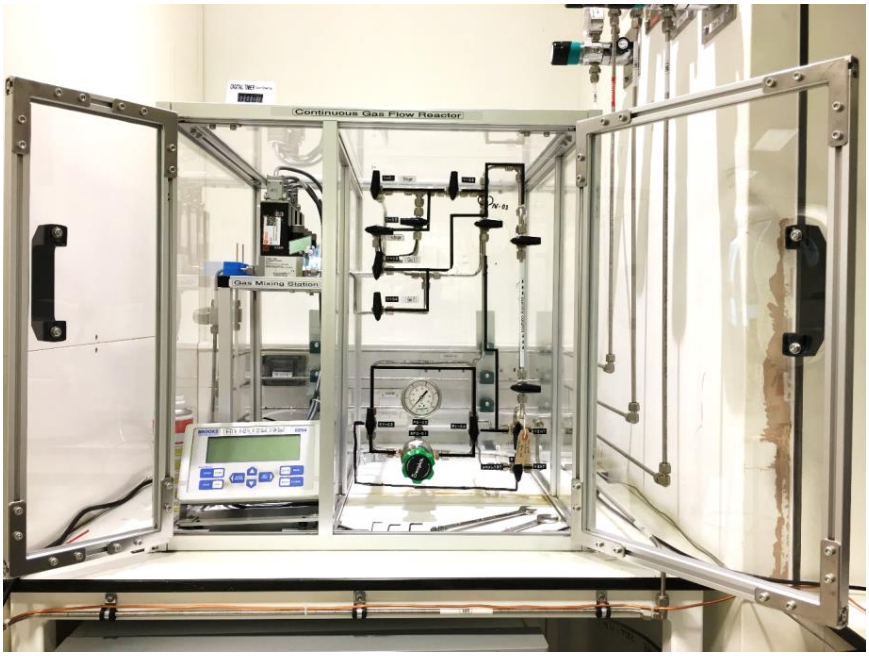


Figure 5.12.4: Bespoke continuous gas flow reactor setup, dormant, fitted with a dummy column: full cabinet view. The mass-flow meters are visible in the leftmost compartment.

After fitting the packed column into the flow reactor under a 50 mL min^{-1} flow of N_2, tightening all relevant connections, and opening the two-way Swagelok valves at each end of the column, the column was then (1) purged with neat N_2 gas, (2) the pre-catalyst was pre-activated with neat H_2 gas (if needed) and (3) the catalytic run was started. **Figure 5.12.5** contains a simplified diagram of the flow-reactor setup.

(1) *Neat N_2 purging* – After the column containing the catalyst or pre-catalyst was fitted to the continuous gas flow reactor, the column was purged with neat N_2 gas at 50 mL min^{-1} for 10 min. The N_2 flow passing through the column was immediately vented, bypassing the regulated loop setup. Simultaneously, the substrate diluted gas mixture at their target flow rates were mixed and made to bypass the column, *via* the regulated loop and the GC before venting. After this time, and before the catalytic run started, the N_2 and substrate gas mixture flows were stopped.

(2) *Pre-activation with H_2 gas* (only for pre-catalysts that require pre-activation with H_2 gas before a catalytic run) – H_2 at 100 mL min^{-1} was passed through the system *via* the column and the regulated loop before venting for 5 min, before pressurisation of the system with H_2 to 1 bar for 10 minutes, using the regulator setup. Then, the pressure was carefully released and the H_2 flow stopped. A flow of N_2 at 50 mL min^{-1} was resumed and passed *via* the column and the loop before venting for 10 minutes, in order to remove any remaining H_2 gas before the catalytic run was started.

(3) *Addition of substrate diluted gas mixtures* – After the column was charged, fitted, purged with N_2 gas, activated with H_2 gas, and purged with N_2 once again, the substrate diluted gas mixtures at the target flow rate(s) were passed through the column, *via* the regulated loop and the gas chromatograph before venting (after the gas chromatograph), for the relevant on-stream time(s). Gas aliquots were taken of the outflow and analysed by GC every 15 minutes *via* the automatic sampling loop installed in the chromatograph as described above.

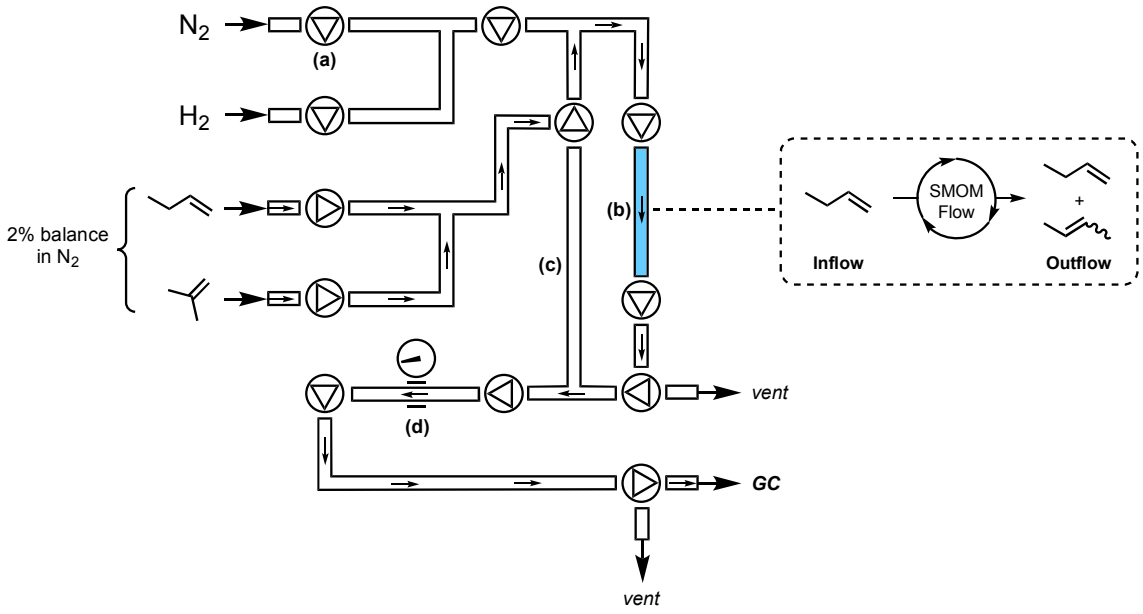
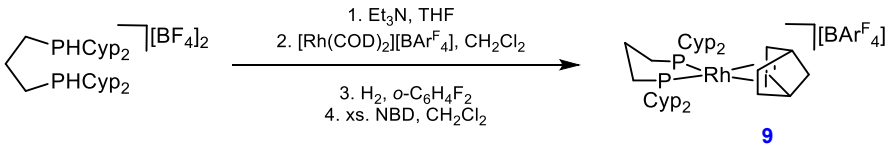


Figure 5.12.5: Simplified schematic of the flow reactor setup, shown operating under gas-flow conditions: a butenes (1-butene + *iso*-butene) gas mixture passing *via* a pre-loaded column, over active catalyst, to be analysed *via* gas chromatography. (**a**) A gas-tight Swagelock valve. (**b**) Stainless steel column pre-loaded with catalyst/pre-catalyst dispersed on glass wool, fitted at each end with gas-tight Swagelock valves. (**c**) Column bypass. (**d**) Regulated loop, intended to establish a pressure of H_2 during hydrogenation of pre-catalyst. Reproduced from Section 2.4.

5.13 Synthetic Procedures: Chapter 2

*5.13.1 Synthesis of [(dcyppp)Rh(η²,η²-NBD)][BAr$^F_4$] (dcyppp = Cyp$_2$P(CH$_2$)$_3$PCyp$_2$), **9***



9

[(dcyppp)H$_2$][BF$_4$]$_2$ (47 mg, 85 μmol; dcyppp = Cyp$_2$P(CH$_2$)$_3$PCyp$_2$) was dissolved in THF (2 mL). With stirring, a solution of Et$_3$N in THF (0.48 mL, 5% by volume, 170 μmol) was introduced, and stirring was continued for 3 hours at 298 K. After this time, pentane (2 mL) was introduced to precipitate [Et$_3$NH][BF$_4$], and the solution was transferred *via* filter cannula into a second flask, already containing [Rh(η²,η²-COD)$_2$][BAr$^F_4$] (100 mg, 85 μmol) dissolved in CH$_2$Cl$_2$ (5 mL).

The resulting mixture was allowed to stir at 298 K for a further hour, over which time the initially dark red solution turned a deep orange, after which all volatiles were removed *in vacuo* to give an orange solid. Once evaporated to dryness, the solid was dissolved in 1,2-difluorobenzene (2 mL). The contents were frozen with liquid N_2 before the flask was evacuated and repressurised with H_2 (1 bar). After thawing, the solution was stirred at room temperature for 1 hour, over which time the initially orange solution darkened significantly, before all volatiles were again removed *in vacuo*. To the resulting brown residue, CH_2Cl_2 (2 mL) was added to dissolve it. With stirring at 298 K, neat norbornadiene (NBD; 0.1 mL, 983 μmol) was added, and stirring was continued for a further 90 minutes before transfer of the resulting deep orange-red solution to an appropriate crystallisation vessel *via* filter cannula and layering with pentane at 298 K. Dark orange crystals of [(dcyppp)Rh(η^2,η^2-NBD)][BAr^F_4] (**9**; 106 mg, 92%) were obtained after 48 hours. Despite the high quality of these crystals, no satisfactory structural solution was obtained.

^{1}H NMR (400 MHz, CD_2Cl_2, 298 K) δ 1.36–2.20 (multiple peaks, $\sum$ = 44 H; dcyppp + NBD CH_2), 4.09 (m, 2 H; bridgehead CH), 5.19 (vq, J = 2.2 Hz, 4 H; alkene CH), 7.56 (s, 4 H; [BAr^F_4]$^-$ *p*-H), 7.72 (br. m, 8 H; [BAr^F_4]$^-$ *o*-H).

^{13}C{^{1}H} NMR (100.64 MHz, CD_2Cl_2, 298 K) δ 18.6 (m; PCH_2), 22.0 (dt, $^2J_{CP}$ = 3.4 Hz, $^3J_{CRh}$ = 2.4 Hz; PCH_2CH_2), 26.2 (vt, J = 5.0 Hz; Cyp), 26.9 (vt, J = 3.9 Hz; Cyp), 29.8 (s; Cyp), 31.1 (br. vt, J ~ 2.0 Hz; Cyp), 38.0 (m; PCH Cyp), 55.4 (br. m; bridgehead CH), 71.3 (m; NBD CH_2), 82.4 (vdt, J = 6.6 Hz, J' = 4.5 Hz; alkene CH), 118.0 (septet, $^3J_{CF}$ = 3.9 Hz; [BAr^F_4]$^-$ *p*-C_{aryl}), 125.2 (q, $^1J_{CF}$ = 272.5 Hz; [BAr^F_4]$^-$ CF_3), 129.4 (qq, $^2J_{CF}$ = 31.4 Hz, $^4J_{CF}$ = 2.9 Hz; [BAr^F_4]$^-$ C_{aryl}-CF_3), 135.4 (s; [BAr^F_4]$^-$ *o*-C_{aryl}), 162.3 (q, $^1J_{CB}$ = 49.9 Hz (^{11}B), 16.6 Hz (^{10}B); [BAr^F_4]$^-$ *i*-C_{aryl}).

^{31}P{^{1}H} NMR (162 MHz, CD_2Cl_2, 298 K) δ 12.1 (d, $^1J_{PRh}$ = 146.8 Hz).

^{19}F{^{1}H} NMR (376.5 MHz, CD_2Cl_2, 298 K) δ –62.9.

^{11}B{^{1}H} NMR (128.39 MHz, CD_2Cl_2, 298 K) δ –6.63.

Elemental analysis found (calculated) for $C_{62}H_{62}BF_{24}P_2Rh$: C, 51.65 (51.76); H, 4.16 (4.34).

ESI-MS (CH_2Cl_2) *m*/*z* found (calculated) for $C_{30}H_{50}P_2Rh$ [M]$^+$: 575.2436 (575.2437).

*5.13.2 Synthesis of [(dcyppb)Rh(η²,η²-NBD)][BAr^F_4] (dcyppb = Cyp₂P(CH₂)₄PCyp₂), **10***

In a similar procedure to that described in Section 5.13.1, [(dcyppp)H_2][BF_4]$_2$ was substituted for [(dcyppb)H_2][BF_4]$_2$ (48 mg, 85 μmol), ultimately yielding bright orange crystals of [(dcyppb)Rh(η^2,η^2-NBD)][BAr^F_4] (**10**; 104 mg, 90%) amenable to *sc*-XRD.

^{1}H NMR (400 MHz, CD_2Cl_2, 298 K) δ 1.41–2.14 (multiple peaks, $\sum$ = 46 H; dcyppb + NBD CH_2), 4.03 (s, 2 H; bridgehead CH), 4.98 (br. m, 4 H; alkene CH), 7.56 (s, 4 H; $[BAr^F_4]^-$ *p*-H), 7.72 (br. m, 8 H; $[BAr^F_4]^-$ *o*-H).

^{13}C{^{1}H} NMR (100.64 MHz, CD_2Cl_2, 298 K) δ 17.4 (m; PCH_2), 24.1 (vt, J = 2.5 Hz; PCH_2CH_2), 26.4 (vt, J = 4.8 Hz; Cyp), 26.7 (vt, J = 3.6 Hz; Cyp), 29.7 (s; Cyp), 31.5 (br. vt, J ~ 1.6 Hz; Cyp), 37.3 (m; PCH Cyp), 54.6 (br. m; bridgehead CH), 70.2 (m; NBD CH_2), 78.9 (vdt, J = 7.0 Hz, J' = 4.5 Hz; alkene CH), 118.0 (septet, $^{3}J_{CF}$ = 3.9 Hz; $[BAr^F_4]^-$ *p*-C_{aryl}), 125.1 (q, $^{1}J_{CF}$ = 272.4 Hz; $[BAr^F_4]^-$ CF_3), 129.4 (qq, $^{2}J_{CF}$ = 31.5 Hz, $^{4}J_{CF}$ = 2.8 Hz; $[BAr^F_4]^-$ C_{aryl}-CF_3), 135.4 (s; $[BAr^F_4]^-$ *o*-C_{aryl}), 162.3 (q, $^{1}J_{CB}$ = 50.0 Hz (^{11}B), 16.8 Hz (^{10}B); $[BAr^F_4]^-$ *i*-C_{aryl}).

^{31}P{^{1}H} NMR (162 MHz, CD_2Cl_2, 298 K) δ 23.2 (d, $^{1}J_{PRh}$ = 150.6 Hz).

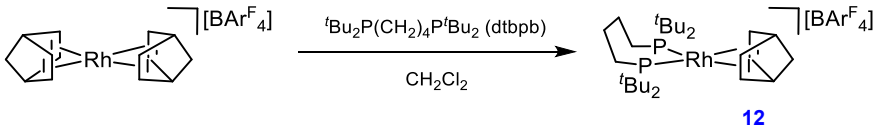
^{19}F{^{1}H} NMR (376.5 MHz, CD_2Cl_2, 298 K) δ –62.9 (Ar^F-CF_3).

^{11}B{^{1}H} NMR (128.39 MHz, CD_2Cl_2, 298 K) δ –6.64 ($BAr^F_4^-$).

Elemental analysis found (calculated) for $C_{63}H_{64}BF_{24}P_2Rh$: C, 52.11 (52.08); H, 4.32 (4.44).

ESI-MS (CH_2Cl_2) *m*/*z* found (calculated) for $C_{31}H_{52}P_2Rh$ $[M]^+$: 589.2662 (589.2594).

*5.13.3 Synthesis of [(dtbpb)Rh(η²,η²-NBD)][BAr$^F_4$] (dtbpb = ^{t}Bu$_2$P(CH$_2$)$_4$P^{t}Bu$_2$), **12***



12

Adapted from the procedure for the synthesis of [(dtbpp)Rh(η^2,η^2-NBD)][BAr^F_4] (dtbpp = ^{t}Bu$_2$P(CH$_2$)$_3$P^{t}Bu$_2$; **11**) given in the reference.[15] A solution of dtbpb[8] = ^{t}Bu$_2$P(CH$_2$)$_4$P^{t}Bu$_2$ in pentane (0.10 mol dm^{-3}, 1.4 mL, 0.140 mmol) was introduced to a stirred solution of [Rh(η^2,η^2-NBD)$_2$][BAr^F_4] (161 mg, 0.140 mmol) in CH_2Cl_2 (10 mL) at 298 K. After one hour, the solution was concentrated *in vacuo* by ~50% before it was transferred *via* cannula to an appropriate crystallisation vessel and layered with pentane, producing deep red crystals of [(dtbpb)Rh(η^2,η^2-NBD)][BAr^F_4] (**12**; 100 mg, 51%) after 48 hours.

^{1}H NMR (400.1 MHz, CD_2Cl_2, 298 K) δ 1.38 (d, 36 H, $^{3}J_{HP}$ = 12.4 Hz; ^{t}Bu), 1.55–1.90 (various, $\sum$ = 12 H; dtbpb CH_2 + NBD), 5.04 (m, 4 H; alkene CH), 7.55 (s, 4 H; $[BAr^F_4]^-$ *p*-H), 7.71 (s, 8 H; $[BAr^F_4]^-$ *o*-H).

^{13}C{^{1}H} NMR (125 MHz, CD_2Cl_2, 298 K) δ 17.7 (m; dtbpb CH_2), 23.2 (br. m; dtbpb CH_2), 30.8 (br. m; ^{t}Bu CH_3), 38.7 (m; ^{t}Bu C_Q), 51.5 (m; bridgehead CH), 63.3 (NBD CH_2), 66.6 (m; alkene CH), 117.9 (septet, $^{3}J_{CF}$ = 3.8 Hz; $[BAr^F_4]^-$ *p*-C_{aryl}), 127.8 (q, $^{1}J_{CF}$ = 272.4 Hz; $[BAr^F_4]^-$ CF_3), 128.5 (qq, $^{2}J_{CF}$ = 30.6 Hz, $^{4}J_{CF}$ = 2.6 Hz; $[BAr^F_4]^-$ C_{aryl}-CF_3), 134.8 (s; $[BAr^F_4]^-$ *o*-C_{aryl}), 161.7 (q, $^{1}J_{CB}$ = 49.9 Hz; $[BAr^F_4]^-$ *i*-C_{aryl}).

^{31}P{^{1}H} NMR (161.9 MHz, CD_2Cl_2, 298 K) δ 34.5 ($^{1}J_{PRh}$ = 152 Hz).

^{19}F{^{1}H} NMR (376.5 MHz, CD_2Cl_2, 298 K) δ –62.8.

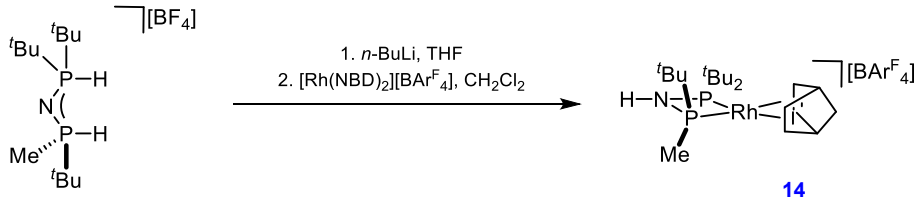
$^{11}B\{^{1}H\}$ NMR (128.4 MHz, CD_2Cl_2, 298 K) δ –6.61.

Elemental analysis found (calculated) for $C_{59}H_{64}BF_{24}P_2Rh$: C, 50.32 (50.42); H, 4.62 (4.59).

ESI-MS (CH_2Cl_2) *m/z* found (calculated) for $C_{27}H_{52}P_2Rh$ $[M]^+$: 541.2572 (541.2594).

*For the synthesis of SMOM [(dpfppe)Rh(η²,η²-NBD)][BAr$^F_4$] (**13**; dpfppe = (C$_6$F$_5$)P(CH$_2$)$_2$P(C$_6$F$_5$)$_2$), please see the Experimental for Chapter 3 (Section 5.14).*

5.13.4 Synthesis of [((R)-MaxPhos)Rh(η²,η²-NBD)][BAr$^F_4$] (MaxPhos = HN(P^{t}Bu$_2$)(P^{t}BuMe)), **14**



14

(*R*)-MaxPhos·HBF$_4$ (94 mg, 268 μmol) was introduced to a flame-dried Schlenk flask and dissolved in anhydrous THF (5 mL), before cooling to −78 °C and dropwise addition of *n*-BuLi in hexanes (0.17 mL, 1.6 M, 266 μmol). The reaction mixture was stirred for 30 minutes before addition of anhydrous EtOH (0.1 mL) and removal of all volatiles *in vacuo* to leave behind a colourless oil. CH_2Cl_2 was then introduced (2 mL) and the reaction mixture was transferred dropwise into a second Schlenk flask, containing stirred [Rh(η²,η²-NBD)$_2$][BAr$^F_4$] (308 mg, 268 μmol) in CH_2Cl_2 (5 mL) to produce an immediate colour change from red to light orange. After 30 minutes, the resulting solution was concentrated *in vacuo* by ~50% and layered with pentane at 298 K. This gave red crystals of [((*R*)-MaxPhos)Rh(η²,η²-NBD)][BAr$^F_4$] (**14**; 305 mg, 87%), after 48 hours.

^{1}H NMR (400 MHz, CD_2Cl_2, 298 K) δ 1.11 (d, $^3J_{HP}$ = 16.5 Hz, 9 H; ^{t}Bu), 1.30 (overlapping d, $^3J_{HP}$ = 14.9 Hz, 15.2 Hz, 18 H; ^{t}Bu), 1.58 (dd, $^2J_{HP}$ = 7.2 Hz, $^3J_{HRh}$ = 1.2 Hz, 3 H; PCH$_3$), 1.72 (m, 2 H; NBD CH$_2$), 3.68 (br. s, 1 H; NH), 4.22 (m, 2 H; bridgehead CH), 5.48 (m, 2 H; alkene CH), 5.69 (m, 1 H; alkene CH), 5.88 (m, 1 H; alkene CH), 7.57 (s, 4 H; [BAr$^F_4$]$^-$ *p*-H), 7.73 (q, $^4J_{HF}$ = 2.2 Hz, 8 H; [BAr$^F_4$]$^-$ *o*-H).

$^{13}C\{^{1}H\}$ NMR (100.64 MHz, CD_2Cl_2, 298 K) δ 14.7 (dd, $^1J_{CP}$ = 17.5 Hz, $^2J_{CRh}$ = 2.1 Hz; PCH$_3$), 26.2 (d, $^2J_{CP}$ = 6.2 Hz; ^{t}Bu CH$_3$), 29.0 (overlapping d, $^2J_{CP}$ = 6.7 Hz, 6.5 Hz; ^{t}Bu CH$_3$), 35.8 (ddd, $^1J_{CP}$ = 25.6 Hz, $^2J_{CRh}$ ~ 2.5 Hz, $^3J_{CP}$ ~ 1.5 Hz; ^{t}Bu C$_Q$), 38.9 (overlapping dd, $^1J_{CP}$ ~ 11.6 Hz, $^2J_{CRh}$ ~ 2 Hz; ^{t}Bu C$_Q$), 56.7 (vq, *J* ~ 1.5 Hz; NBD CH$_2$), 57.2 (vq, *J* ~ 1.5 Hz; bridgehead CH), 72.2 (m; NBD CH$_2$), 85.0 (m; alkene CH), 89.5 (dd,

J = 10.5 Hz, J' = 6.0 Hz; alkene CH), 92.0 (dd, J = 9.6 Hz, J' = 6.5 Hz; alkene CH), 118.0 (septet, $^4J_{CF}$ = 3.9 Hz; $[BAr^F_4]^-$ *p*-C_{aryl}), 125.1 (q, $^1J_{CF}$ = 272.6 Hz; $[BAr^F_4]^-$ CF_3), 129.3 (qq, $^2J_{CF}$ = 31.5 Hz, $^4J_{CF}$ = 2.9 Hz; $[BAr^F_4]^-$ C_{aryl}-CF_3), 135.3 (s; $[BAr^F_4]^-$ *o*-C_{aryl}), 162.2 (q, $^1J_{CB}$ = 50.0 Hz (^{11}B), 16.8 Hz (^{10}B); $[BAr^F_4]^-$ *i*-C_{aryl}).

$^{31}P\{^1H\}$ NMR (162 MHz, CD_2Cl_2, 298 K) δ 57.9 (dd, $^1J_{PRh}$ = 141 Hz, $^2J_{PP}$ = 53 Hz), 81.6 (dd, $^1J_{PRh}$ = 138 Hz, $^2J_{PP}$ = 53 Hz).

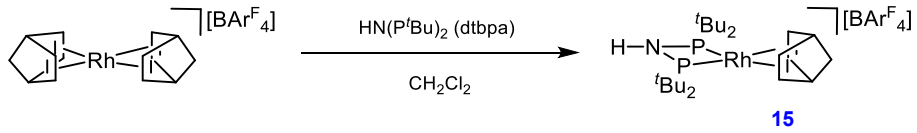
$^{19}F\{^1H\}$ NMR (376.5 MHz, CD_2Cl_2, 298 K) δ –62.8.

$^{11}B\{^1H\}$ NMR (128.39 MHz, CD_2Cl_2, 298 K) δ –6.60.

Elemental analysis found (calculated) for $C_{52}H_{52}BF_{24}NP_2Rh$: C, 47.40 (47.22); H, 3.84 (3.96); N, 1.05 (1.06).

ESI-MS (CH_2Cl_2) *m/z* found (calculated) for $C_{20}H_{39}NP_2Rh$ $[M]^+$: 458.1607 (458.1607) [*sic*].

5.13.5 *Synthesis of [(dtbpa)Rh(η²,η²-NBD)][BAr$^F_4$] (dtbpa = HN(P^{t}Bu$_2$)$_2$), **15***



15

$HN(P^tBu)_2$ was synthesised according to an existing protocol as a micro-crystalline white solid.[9] $[Rh(\eta^2,\eta^2\text{-NBD})_2][BAr^F_4]$ (100 mg, 87 μmol) and dtbpa (27 mg, 87 μmol) were introduced to separate Young's flasks and each dissolved in CH_2Cl_2 (2 × 2 mL). With stirring, the phosphine-CH_2Cl_2 solution was transferred *via* cannula to the CH_2Cl_2 solution of $[Rh(\eta^2,\eta^2\text{-NBD})_2][BAr^F_4]$, resulting in a colour change from red to bright orange, and stirring was continued for a further 60 minutes. The resulting solution was concentrated *in vacuo* by ~50%, transferred to an appropriate crystallisation vessel, and layered with pentane at 298 K to give red crystals of $[(dtbpa)Rh(\eta^2,\eta^2\text{-NBD})][H_2O \subset BAr^F_4]$ (**15** ; 106 mg, 88%) amenable to *sc*-XRD studies after 48 hours. It is not known whether the H_2O present in the structure co-crystallised due to serendipitous moisture in the solvent, or was absorbed by the structure when exposed to air, in a similar manner to CH_2Cl_2/xenon gas into the related $[(Cy_2PCH_2PCy_2)Rh(\eta^2,\eta^2\text{-NBD})][BAr^F_4]$.[20]

^1H NMR (400 MHz, CD_2Cl_2, 298 K) δ 1.39 (d, $^3J_{HP}$ = 14.5 Hz, 36 H; ^{t}Bu CH_3), 1.67 (s, 2 H; NBD CH_2), 3.81 (br. s, 1 H; NH), 4.22 (br. m, 2 H; bridgehead CH), 5.52 (m, 4 H; alkene CH), 7.57 (s, 4 H; $[BAr^F_4]^-$ *p*-H), 7.73 (q, $^4J_{HF}$ = 2.2 Hz, 8 H; $[BAr^F_4]^-$ *o*-H).

$^{13}C\{^1H\}$ NMR (100.64 MHz, CD_2Cl_2, 298 K) δ 30.2 (vt, $^2J_{CP}$ = 2.7 Hz; ^{t}Bu CH_3), 39.7 (vt, J = 5.6 Hz; ^{t}Bu C_Q), 56.5 (s; bridgehead CH), 71.2 (m; NBD CH_2), 84.1 (m; alkene CH), 118.0 (septet, $^4J_{CF}$ = 3.8 Hz; $[BAr^F_4]^-$ *p*-C_{aryl}), 125.2 (q, $^1J_{CF}$ = 272.4 Hz; $[BAr^F_4]^-$ CF_3), 129.4 (qq, $^2J_{CF}$ = 31.5 Hz, $^4J_{CF}$ = 2.8 Hz; $[BAr^F_4]^-$ C_{aryl}-CF_3), 135.3 (s; $[BAr^F_4]^-$ *o*-C_{aryl}), 162.3 (q, $^1J_{CB}$ = 50.0 Hz (^{11}B), 16.7 Hz (^{10}B); $[BAr^F_4]^-$ *i*-C_{aryl}).

$^{31}P\{^{1}H\}$ NMR (162 MHz, CD_2Cl_2, 298 K) δ 82.7 (d, $^{1}J_{PRh}$ = 138.4 Hz).

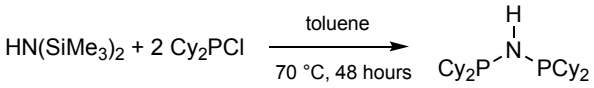
$^{19}F\{^{1}H\}$ NMR (376.5 MHz, CD_2Cl_2, 298 K) δ –62.8.

$^{11}B\{^{1}H\}$ NMR (128.39 MHz, CD_2Cl_2, 298 K) δ –6.61.

Elemental analysis found (calculated) for $C_{55}H_{57}BF_{24}NP_2Rh$: C, 48.24 (48.44); H, 4.17 (4.21); N, 0.97 (1.03).

ESI-MS (CH_2Cl_2) m/z found (calculated) for $C_{23}H_{45}NP_2Rh$ $[M]^+$: 500.2039 (500.2077).

5.13.6 *Syntheses of $HN(PCy_2)_2$ (dcpa) and $[(dcpa)Rh(\eta^2,\eta^2\text{-NBD})][BAr^F{}_4]$, **16***



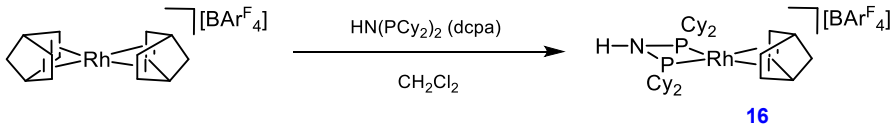
The procedure for the synthesis of this *bis*-phosphine amide $HN(PCy_2)_2$ (dcpa) was adapted from an existing protocol.[21] $HN(SiMe_3)_2$ (0.5 mL, 2.39 mmol) was introduced to a stirred toluene (15 mL) solution of Cy_2PCl (1.05 mL, 4.77 mmol). After stirring for 48 hours at 70 °C, all volatiles were removed *in vacuo* to yield a fine white powder, dcpa (960 mg, 98%), which at this stage was sufficiently pure (by solution-phase NMR spectroscopy) to proceed with synthesis of the SMOM.

^{1}H NMR (400 MHz, C_6D_6, 298 K) δ 1.16–1.50 (multiple resonances, $\sum$ = 24 H; Cy $PCH_2CH_2CH_2$ + $PCH_2CH_2CH_2CH_2$), 1.59–1.87 (multiple resonances, $\sum$ = 16 H; Cy PCH_2CH_2), 1.92 (d, $^{2}J_{HP}$ = 11.8 Hz, 4 H; PCH_2). *N.B.: N-H not resolved.*

$^{13}C\{^{1}H\}$ NMR (100.64 MHz, C_6D_6, 298 K) δ 27.1 (s; PC_3C), 27.5 (vt, $^{3}J_{CP}$ = 3.6 Hz; PC_2C), 27.6 (vt, $^{2}J_{CP}$ = 6.1 Hz; PCC), 28.3 (vt, $^{3}J_{CP}$ = 4.2 Hz; PC_2C), 29.5 (vt, $^{2}J_{CP}$ = 8.8 Hz; PCC), 38.5 (vt, $^{1}J_{CP}$ = 6.0 Hz; PC).

$^{31}P\{^{1}H\}$ NMR (162 MHz, C_6D_6, 298 K) δ 61.9.

Elemental analysis found (calculated) for $C_{24}H_{45}NP_2$: C, 70.23 (70.38); H, 10.96 (11.07); N, 3.27 (3.42).



16

$[Rh(\eta^2,\eta^2\text{-NBD})_2][BAr^F{}_4]$ (141 mg, 122 μmol) and dcpa (50 mg, 122 μmol) were introduced to separate Young's flasks and each dissolved in CH_2Cl_2 (2 × 2 mL). With stirring, the phosphine-CH_2Cl_2 solution was transferred *via* cannula to the CH_2Cl_2 solution of $[Rh(\eta^2,\eta^2\text{-NBD})_2][BAr^F{}_4]$. This resulted in a colour change from red to bright orange, and stirring was continued for a further 60 minutes.

The resulting bright red solution was concentrated *in vacuo* by ~50%, transferred to an appropriate crystallisation vessel, and layered with pentane at 275 K to give orange-red crystals of [(dcpa)Rh(η^2,η^2-NBD)][BAr^F_4] (**16**; 160 mg, 95%) after seven days.

^{1}H NMR (400 MHz, CD_2Cl_2, 298 K) δ 1.15–1.39 (multiple resonances, $\sum$ = 20 H; Cy CH_2), 1.69 (s, 2H; NBD CH_2), 1.71–1.95 (multiple resonances, $\sum$ = 24 H; Cy CH + CH_2), 3.48 (m, 1 H; NH), 4.20 (br. m, 2 H; bridgehead CH), 5.66 (br. m, 4 H; alkene CH), 7.56 (s, 4 H; [BAr^F_4]$^-$ *p*-H), 7.72 (br. m, 8 H; [BAr^F_4]$^-$ *o*-H).

^{13}C{^{1}H} NMR (100.64 MHz, CD_2Cl_2, 298 K) δ 26.1 (s; PC_3C), 26.7 (vt, $^3J_{CP}$ = 5.5 Hz; PC_2C), 27.0 (vt, $^2J_{CP}$ = 7.0 Hz; PC*C*), 28.3 (vt, $^3J_{CP}$ = 4.2 Hz; PC_2C), 38.9 (vt, $^1J_{CP}$ = 10.4 Hz; P*C*), 57.0 (d br. m, J ~ 1.5 Hz; bridgehead CH), 72.1 (m; NBD CH_2), 89.1 (dt, J = 6.0 Hz, J' = 5.5 Hz; alkene CH), 117.9 (septet, $^4J_{CF}$ = 3.9 Hz; [BAr^F_4]$^-$ *p*-C_{aryl}), 125.1 (q, $^1J_{CF}$ = 272.3 Hz; [BAr^F_4]$^-$ CF_3), 129.4 (qq, $^2J_{CF}$ = 31.4 Hz, $^4J_{CF}$ = 3.0 Hz; [BAr^F_4]$^-$ C_{aryl}–CF_3), 135.2 (s; [BAr^F_4]$^-$ *o*-C_{aryl}), 162.2 (q, $^1J_{CB}$ = 49.9 Hz (^{11}B), 16.6 Hz (^{10}B); [BAr^F_4]$^-$ *i*-C_{aryl}).

^{31}P{^{1}H} NMR (162 MHz, CD_2Cl_2, 298 K) δ 62.1 (d, $^1J_{PRh}$ = 136.8 Hz).

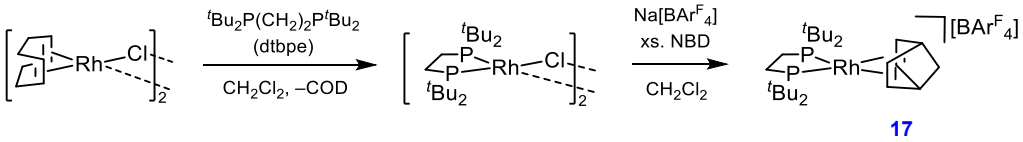
^{19}F{^{1}H} NMR (376.5 MHz, CD_2Cl_2, 298 K) δ –62.9.

^{11}B{^{1}H} NMR (128.39 MHz, CD_2Cl_2, 298 K) δ –6.60.

Elemental analysis found (calculated) for $C_{63}H_{65}BF_{24}NP_2Rh$: C, 51.57 (51.55); H, 4.48 (4.46); N, 0.97 (0.95).

ESI-MS (CH_2Cl_2) *m/z* found (calculated) for $C_{31}H_{53}NP_2Rh$ [M]$^+$: 604.2676 (604.2703) (also detected *m/z* 921.5083 (~3% relative intensity), corresponding to [$(dcpa)_2Rh$]$^+$ (calculated 921.5104)).

*5.13.7 Synthesis of [(dtbpe)Rh(η²,η²-NBD)][BAr^F_4] (dtbpe = $^tBu_2P(CH_2)_2P^tBu_2$), **17***



[(η^2,η^2-COD)RhCl]$_2$ (100 mg, 203 μmol) and dtbpe (129 mg, 406 μmol) were introduced to separate Schlenk flasks and separately dissolved in CH_2Cl_2 (10 mL each). The dtbpe solution was then dropwise added to the [(η^2,η^2-COD)RhCl]$_2$ solution *via* cannula. The reaction mixture was then allowed to stir at room temperature for 60 min before all volatiles were removed *in vacuo*. The resulting dark orange crude was washed with cold hexanes (3 × 10 mL) and dried *in vacuo*. The resulting orange solid was dried *in vacuo* for 12 hours to give [(dtbpe)RhCl]$_2$ (170 mg, 186 μmol, 92%). [(dtbpe)RhCl]$_2$ was used without further purification. Spectroscopic data of this product matched with reported values.[22]

In separate Schlenk flasks, $[(dtbpe)RhCl]_2$ (50 mg, 55 μmol) and $Na[BAr^F_4]$ (97 mg, 109 μmol) were dissolved in CH_2Cl_2 (10 mL each). NBD (0.1 mL, 983 μmol, ~9.0 eq.) was added to the stirred $Na[BAr^F_4]$ solution *via* syringe, before the orange $[(dtbpe)RhCl]_2$ solution was added dropwise *via* cannula; upon addition, a deep red colour was observed. The reaction mixture was stirred for 30 min at room temperature, and the contents were concentrated *in vacuo* to a volume of 2.5 mL to give a claret-coloured solution. The mixture was then filtered *via* cannula, and the filtrate was layered with pentane at 298 K to give red crystalline plates of $[(dtbpe)Rh(\eta^2,\eta^2\text{-NBD})][BAr^F_4]$ (17; 120 mg, 79%) amenable to *sc*-XRD studies after 7 days.

^{1}H NMR (400.1 MHz, CD_2Cl_2, 298 K) δ 1.29 (d, 36 H, $^3J_{HP}$ = 13.0 Hz; ^{t}Bu), 1.75 (s, 2 H; NBD CH_2), 1.82 (m, 4 H; dtbpe CH_2), 4.19 (m, 2 H; bridgehead CH), 5.54 (m, 4 H; alkene CH), 7.56 (s, 4 H; $[BAr^F_4]^-$ *p*-H), 7.72 (s, 8 H; $[BAr^F_4]^-$ *o*-H).

^{13}C{^{1}H} NMR (100.6 MHz, CD_2Cl_2, 298 K) δ 23.1 (m; dtbpe CH_2), 30.7 (vdd, J ~ 2.5 Hz; ^{t}Bu CH_3), 38.5 (ddd, $^1J_{CP}$ = 8.4 Hz, $^2J_{CRh}$ = 6.3 Hz, $^3J_{CP}$ = 1.2 Hz; ^{t}Bu C_Q), 55.0 (m; bridgehead CH), 71.2 (NBD CH_2), 81.1 (m; alkene CH), 118.1 (septet, $^3J_{CF}$ = 3.8 Hz; $[BAr^F_4]^-$ *p*-C_{aryl}), 125.1 (q, $^1J_{CF}$ = 272.4 Hz; $[BAr^F_4]^-$ CF_3), 129.6 (qq, $^2J_{CF}$ = 30.6 Hz, $^4J_{CF}$ = 2.6 Hz; $[BAr^F_4]^-$ C_{aryl}-CF_3), 135.3 (s; $[BAr^F_4]^-$ *o*-C_{aryl}), 162.3 (q, $^1J_{CB}$ = 49.4 Hz; $[BAr^F_4]^-$ *i*-C_{aryl}).

^{13}C{^{1}H} SSNMR (100.6 MHz, 10 kHz spin rate, 298 K) δ 20.8 (dtbpe CH_2), 28–39 (^{t}Bu CH_3 + C_Q), 54.0 (NBD CH_2), 67.9 (bridgehead CH), 72.2 (alkene CH), 85.5 (alkene CH), 116–137 ($[BAr^F_4]^-$), 162.9 ($[BAr^F_4]^-$ *i*-C_{aryl}).

^{13}C{^{1}H} SSNMR (100.6 MHz, 10 kHz spin rate, 158 K) δ 19.9 (dtbpe CH_2), 23–39 (^{t}Bu CH_3 + C_Q), 53.9 (NBD CH_2), 67.2 (bridgehead CH), 70.6 (alkene CH), 86.3 (alkene CH), 116–137 ($[BAr^F_4]^-$), 162.4 ($[BAr^F_4]^-$ *i*-C_{aryl}).

^{31}P{^{1}H} NMR (161.9 MHz, CD_2Cl_2, 298 K) δ 84.0 ($^1J_{PRh}$ = 154 Hz).

^{31}P{^{1}H} SSNMR (161.9 MHz, 10 kHz spin rate, 298 K) δ 77.7 (d+d, $^1J_{PRh}$ ~ 140 Hz).

^{31}P{^{1}H} SSNMR (161.9 MHz, 10 kHz spin rate, 183 K) δ 75.1 (br. d+d, $\nu_{½}$ ~ 300 Hz).

^{31}P{^{1}H} SSNMR (161.9 MHz, 10 kHz spin rate, 158 K) δ 75.0 (br. d+d, $\nu_{½}$ ~ 325 Hz).

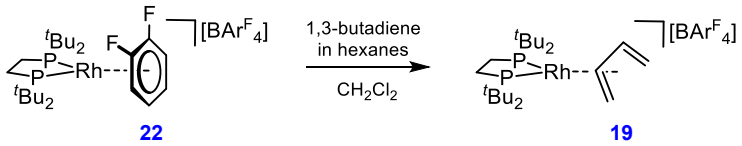
^{19}F{^{1}H} NMR (376.5 MHz, CD_2Cl_2, 298 K) δ –62.8.

^{11}B{^{1}H} NMR (128.4 MHz, CD_2Cl_2, 298 K) δ –6.60.

Elemental analysis found (calculated) for $C_{57}H_{60}BF_{24}P_2Rh$: C, 49.77 (49.73); H, 4.44 (4.39).

ESI-MS (CH_2Cl_2) *m*/*z* found (calculated) for $C_{25}H_{49}P_2Rh$ $[M]^+$: 514.2394 (514.2414).

5.13.8 *Synthesis of [(dtbpe)Rh(η⁴-1,3-butadiene)][BAr$^F_4$], **19***



22 **19**

Powdered crystalline complex **17** (25 mg, 18 μmol) was introduced to a Young's flask and dissolved in 1,2-difluorobenzene (2 mL). The solution was frozen with liquid N_2 and the flask was evacuated before re-pressurisation with H_2 (1.0 bar). After thawing and 30 minutes of stirring at 298 K, all volatiles were removed *in vacuo* to give the 1,2-difluorobenzene adduct [(dtbpe)Rh(η^6-1,2-diflurobenzene)][BAr$^F_4$] (**22**, *vide infra* for independent synthesis) as an orange solid. This was then dissolved in CH_2Cl_2 (2 mL), and a solution of 1,3-butadiene in hexanes (0.5 mL, ~15 wt%, ~1,000 μmol) was introduced with stirring. Stirring was continued for a further two hours, over which time the solution turned a deep red, before all volatiles were removed *in vacuo*. The product was then redissolved in CH_2Cl_2 (2 mL) and layered with hexane to give dark purple crystals of [(dtbpe)Rh(η^4-C_4H_6)][BAr$^F_4$]·CH_2Cl_2 (**19**·CH_2Cl_2; 17 mg, 72%) after 48 hours, amenable to *sc*-XRD studies. 1,3-butadiene complex **19** degraded in CH_2Cl_2 over time to give unknown products, and, unlike the parent η^2,η^2-NBD complex **17**, was sensitive to moist air.

Hydrogenation of a ~2 mg sample of crushed η^2,η^2-NBD complex **17** in a high-pressure NMR tube fitted with a Young's tap (controlled atmosphere valve; H_2 (1.0 bar), 45 min) followed by evacuation and pressurisation with 1-butene (1.0 bar) at 70 °C for 48 hours generated 1,3-butadiene complex **19** (~95%), confirmed through ^{1}H and ^{31}P{^{1}H} NMR spectroscopic analysis of the resulting solid dissolved in CD_2Cl_2.

^{1}H NMR (400 MHz, CD_2Cl_2, 298 K) δ 1.18 (d, 18 H, $^3J_{HP}$ = 13.6 Hz; ^{t}Bu), 1.40 (d, 18 H, $^3J_{HP}$ = 13.6 Hz; ^{t}Bu), 2.02 (m, 4 H; dtbpe CH_2), 2.71 (dm, 2 H, $^3J_{HH}$ = 14.8 Hz; alkene CH), 4.73 (m, 2 H; alkene CH), 5.52 (m, 2 H; alkene CH), 7.56 (s, 4 H; [BAr$^F_4$]$^-$ *p*-H), 7.72 (br. m, 8 H; [BAr$^F_4$]$^-$ *o*-H).

^{13}C{^{1}H} NMR (100.6 MHz, CD_2Cl_2, 298 K) δ 24.3 (m; dtbpe CH_2), 30.2 (s; ^{t}Bu CH_3), 31.6 (s; ^{t}Bu CH_3), 38.8 (m; ^{t}Bu C_Q), 61.9 (q, J = 5.5 Hz; alkene CH_2), 101.8 (d, J = 5.8 Hz; alkene CH), 118.0 (m; [BAr$^F_4$]$^-$ *p*-C_{aryl}), 125.1 (q, $^1J_{CF}$ = 273.5 Hz; [BAr$^F_4$]$^-$ CF_3), 129.4 (qq, $^2J_{CF}$ = 31.4 Hz, $^4J_{CF}$ = 2.8 Hz; [BAr$^F_4$]$^-$ C_{aryl}-CF_3), 135.3 (s; [BAr$^F_4$]$^-$ *o*-C_{aryl}), 162.3 (q, $^1J_{CB}$ = 49.9 Hz (^{11}B); [BAr$^F_4$]$^-$ *i*-C_{aryl}).

^{13}C{^{1}H} SSNMR (100.6 MHz, 10 kHz spin rate, 298 K) δ 23.2 (dtbpe CH_2), 29.2 (^{t}Bu CH_3), 37.9 (^{t}Bu C_Q), 58.9 (alkene CH_2), 61.5 (alkene CH_2), 99.3 (alkene CH), 101.4 (alkene CH), 115–137 ([BAr$^F_4$]$^-$), 163.9 ([BAr$^F_4$]$^-$ *i*-C_{aryl}).

^{31}P{^{1}H} NMR (161.9 MHz, CD_2Cl_2, 298 K) δ 97.8 (br. d, $^2J_{PRh}$ = 173 Hz).

$^{31}P\{^{1}H\}$ SSNMR (161.9 MHz, 10 kHz spin rate, 298 K) δ 95.5 (s) ($\nu_{½}$ = 400 Hz).

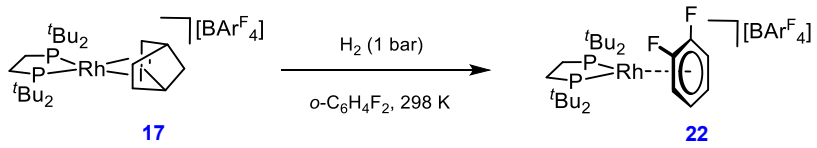
$^{19}F\{^{1}H\}$ NMR (376.5 MHz, CD_2Cl_2, 298 K) δ –62.9.

$^{11}B\{^{1}H\}$ NMR (128.9 MHz, CD_2Cl_2, 298 K) δ –6.61.

ESI-MS (CH_2Cl_2) *m/z* found (calculated) for $C_{29}H_{46}P_2Rh$ $[M]^+$: 475.2145 (475.2124).

Elemental analysis found (calculated) for $C_{54}H_{58}BF_{24}P_2Rh$: C, 48.79 (48.45); H, 4.45 (4.37).

5.13.9 *Independent Synthesis of [(dtbpe)Rh(η⁶-difluorobenzene)][BAr$^F_4$], 22*



17 22

Powdered crystalline complex 17 (25 mg, 18 μmol) was introduced to a Young's flask and dissolved in 1,2-difluorobenzene (2 mL). The solution was frozen with liquid N_2 before the flask was evacuated and pressurised with H_2 (1 bar). After thawing and 30 min of stirring at room temperature (the reaction mixture lightened significantly to a bright orange), the solution was layered with pentane to give the 1,2-difluorobenzene complex 22 as orange crystals (17 mg, 68%) after 24 hours.

^{1}H NMR (400 MHz, CD_2Cl_2, 298 K) δ 1.25 (d, 36 H, $^{3}J_{HP}$ = 13.6 Hz; ^{t}Bu), 1.78 (d, $^{2}J_{PP}$ = 13.4 Hz, 4 H; dtbpe CH_2), 6.41 (br. m, 2 H; difluorobenzene), 6.86 (m, J = 5.0 Hz, J' = 3.1 Hz, 2 H; difluorobenzene), 7.58 (s, 4 H; $[BAr^F_4]^-$ *p*-H), 7.74 (s, 8 H; $[BAr^F_4]^-$ *o*-H).

$^{13}C\{^{1}H\}$ NMR (100.6 MHz, CD_2Cl_2, 298 K) δ 24.1 (m; dtbpe CH_2), 30.3 (s; ^{t}Bu CH_3), 38.7 (dm, $^{1}J_{CP}$ = 19.1 Hz; ^{t}Bu C_Q), 91.5 (m; difluorobenzene), 95.4 (br. m; difluorobenzene), 118.1 (septet, $^{3}J_{CF}$ = 3.7 Hz; $[BAr^F_4]^-$ *p*-C_{aryl}), 123.1 (d, $^{1}J_{CF}$ = 420.3 Hz; difluorobenzene C-F), 125.2 (q, $^{1}J_{CF}$ = 272.6 Hz; $[BAr^F_4]^-$ CF_3), 129.5 (qq, $^{2}J_{CF}$ = 31.7 Hz, $^{4}J_{CF}$ = 3.0 Hz; $[BAr^F_4]^-$ C_{aryl}-CF_3), 135.4 (s; $[BAr^F_4]^-$ *o*-C_{aryl}), 162.4 (q, $^{1}J_{CB}$ = 50.0 Hz; $[BAr^F_4]^-$ *i*-C_{aryl}).

$^{31}P\{^{1}H\}$ NMR (161.9 MHz, CD_2Cl_2, 298 K) δ 117.7 ($^{1}J_{PRh}$ = 206 Hz).

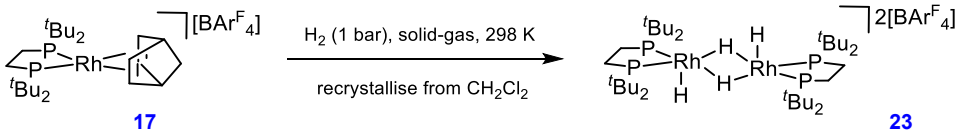
$^{19}F\{^{1}H\}$ NMR (376.5 MHz, CD_2Cl_2, 298 K) δ –141.2 (1,2-difluorobenzene), –62.8 ($[BAr^F_4]^-$).

$^{11}B\{^{1}H\}$ NMR (128.4 MHz, CD_2Cl_2, 298 K) δ –6.60.

ESI-MS (CH_2Cl_2) *m/z* found (calculated) for $C_{24}H_{44}F_2P_2Rh$ $[M]^+$: 535.1974 (535.1936).

Elemental analysis found (calculated) for $C_{56}H_{56}BF_{26}P_2Rh$: C, 48.03% (48.09%); H, 4.13% (4.04%).

5.13.10 *Synthesis of {[(dtbpe)RhH(μ-H)]$_2$}[BAr$^F{}_4$]$_2$, 23*



17 **23**

Crushed crystalline **17** (25 mg, 18 μmol) was introduced to a Young's flask before the flask was evacuated and repressurised with H_2 (1.0 bar), forming complex **25** *in situ* (*vide infra*). After 24 hours, the material had yellowed significantly: the flask was evacuated (p < 10^{-2} mbar, 5 min) and H_2 (1.0 bar) was reintroduced; this was repeated after an additional 24 hours. After a third 24-hour period (~72 hours in total), the resulting bright yellow solid was dissolved in CH_2Cl_2 (1 mL) for crystallisation. This solution was immediately frozen with liquid N_2, before the headspace was evacuated and re-pressurised with H_2 (1 bar) to prevent dehydrogenation and formation of a C-Cl activated complex (*vide infra*) upon thawing.

Crystallisation was carried out at 2 °C, providing bright yellow crystals of {[(dtbpe)RhH(μ-H)]$_2$}[BAr$^F{}_4$]$_2$ (**23**; 19 mg, 73%), after six hours. The supernatant was removed *via* cannula under pressure of H_2. Once removed from the solvent mixture, the crystals survived indefinitely under an atmosphere of argon, and were not sensitive to vacuum. Dissolution of crystalline **23** in CD_2Cl_2 and immediate NMR interrogation at 183 K produced spectra comparable to the amorphous material produced after 72 hours under H_2 without a recrystallisation step. The solution-phase NMR spectroscopic information given below corresponds to this method.

This complex was also accessible from the 1,3-butadiene complex: a crushed crystalline sample of **19** (~25 mg, ~20 μmol) was introduced to a Young's flask before the flask was evacuated and repressurised with H_2 (1 bar). A yellow solid was generated almost immediately; NMR studies conducted on the resulting solid at 183 K after 20 minutes under H_2 confirmed quantitative conversion to dihydride **23**.

This material was also prepared *in situ* for solid-state NMR spectroscopic studies (crystalline dihydride **23** was studied by solid-state NMR separately). A 4.0 mm zirconia solid-state rotor was packed with ~25 mg of **17** (~20 μmol).

Left unsealed, the rotor was introduced to H_2 (1.0 bar) for 50 min, followed by evacuation and a second charge of H_2 (1.0 bar) for 16 hours. The rotor was capped under a flow of H_2 before solid-state NMR spectroscopic studies were undertaken (SSNMR data provided below). The dihydride could also be accessed in the solid-state from the 1,3-butadiene complex **19**, requiring just 10 minutes' exposure to H_2.

Due to the tendency of this species to slowly degrade in solution, coupled with its generally poor solubility, a clean solution-phase $^{13}C\{^1H\}$ spectrum could not be achieved. Such a tendency to degrade also prevented the acquisition of reliable elemental microanalysis data.

^{1}H NMR (400 MHz, CD_2Cl_2, 298 K) δ 1.36 (d, 36 H, $^3J_{HP}$ = 12.8 Hz; ^{t}Bu), 2.23 (d, 4 H, $^2J_{HP}$ = 12.0 Hz; dtbpe CH_2), 7.56 (s, 4 H; $[BAr^F_4]^-$ *p*-H), 7.72 (s, 8 H; $[BAr^F_4]^-$ *o*-H), *Rh-H poorly resolved.*

^{1}H NMR (400 MHz, CD_2Cl_2, 183 K) δ –27.6 (br. d, $^1J_{HRh}$ ~ 48 Hz, 2 H; terminal Rh-H), –4.70 (br. tt, $^1J_{HRh}$ ~ 30 Hz, $^2J_{HP}$ ~ 65 Hz, 2 H; bridging Rh-H), 1.17 (br. d, $^3J_{PH}$ ~ 9 Hz, 18H; ^{t}Bu), 1.27 (br. d, $^3J_{PH}$ ~ 8 Hz, 18 H; ^{t}Bu), 2.00 (br. s, 2 H; dtbpe CH_2), 2.12 (br. s, 2 H; dtbpe CH_2), 7.52 (s, 4 H; $[BAr^F_4]^-$ *p*-H), 7.70 (s, 8 H; $[BAr^F_4]^-$ *o*-H).

$^1H\{^{31}P\}$ NMR (400 MHz, CD_2Cl_2, 183 K) δ –27.6 (br. d, $^1J_{HRh}$ ~ 48 Hz, 2 H; terminal Rh-H), –4.70 (br. tt, $^1J_{HRh}$ ~ 30 Hz, $^2J_{HH}$ ~ 25 Hz, 2 H; bridging Rh-H), 1.18 (s, 18 H; ^{t}Bu), 1.27 (s, 18 H; ^{t}Bu), 2.00 (br. s, 2 H; dtbpe CH_2), 2.12 (br. s, 2 H; dtbpe CH_2), 7.52 (s, 4 H; $[BAr^F_4]^-$ *p*-H), 7.70 (s, 8 H; $[BAr^F_4]^-$ *o*-H).

$^{13}C\{^1H\}$ SSNMR (100.6 MHz, 10 kHz spin rate, 298 K) δ 22.3 (dtbpe CH_2), 29.1 (^{t}Bu CH_3), 37.6 (^{t}Bu C_Q), 117–136 ($[BAr^F_4]^-$), 161.8 ($[BAr^F_4]^-$ *i*-C_{aryl}).

$^{31}P\{^1H\}$ NMR (161.9 MHz, CD_2Cl_2, 298 K) δ 123.0 (dm, $^2J_{PRh}$ ~ 108 Hz, $^2J_{PP'}$ ~ 20 Hz).

$^{31}P\{^1H\}$ NMR (161.9 MHz, CD_2Cl_2, 183 K) δ 121.9 (dm, $^2J_{PRh}$ ~ 108 Hz, $^2J_{PP'}$ ~ 20 Hz).

$^{31}P\{^1H\}$ SSNMR (161.9 MHz, 10 kHz spin rate, 298 K) δ 117.7 (br. d, $^1J_{PRh}$ ~ 180 Hz).

$^{19}F\{^1H\}$ NMR (376.5 MHz, CD_2Cl_2, 298 K) δ –62.8.

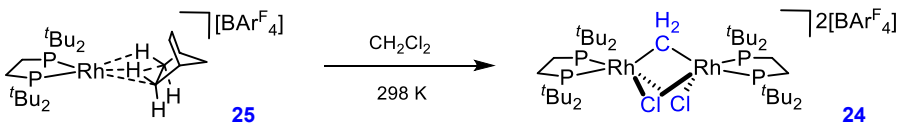
$^{19}F\{^1H\}$ NMR (376.5 MHz, CD_2Cl_2, 183 K) δ –62.2.

$^{11}B\{^1H\}$ NMR (128.4 MHz, CD_2Cl_2, 298 K) δ –6.63.

$^{11}B\{^1H\}$ NMR (128.4 MHz, CD_2Cl_2, 183 K) δ –6.87.

ESI-MS (CH_2Cl_2) *m/z* found (calculated) for $C_{36}H_{84}P_4Rh_2$ $[M]^{2+}$: 423.1853 (423.1811).

*5.13.11 Synthesis of [(dtbpe)Rh(μ-CH$_2$)(μ-Cl)$_2$Rh(dtbpe)][BAr$^F_4$]$_2$, **24***



Crushed complex **17** (~5 mg) was introduced to an NMR tube fitted with a Young's tap. The tube was evacuated and repressurised with H_2 (1.0 bar) for 45 min at 298 K to give σ-NBA complex **25** *in situ* (*vide infra*) before the H_2 atmosphere was evacuated and the tube was backfilled with argon. CH_2Cl_2 (~0.5 mL) was then introduced. The solution was left for 48 hours before quantitative conversion to pale yellow complex **24** was obtained, observed *via* $^{31}P\{^1H\}$ NMR spectroscopy; initially, a broad doublet in the $^{31}P\{^1H\}$ NMR was visible at δ 120.3 ppm ($^1J_{PRh}$ ~ 220 Hz). The solution of **24** thus obtained was layered with pentane inside the NMR tube at 298 K, yielding pale yellow crystals of CH_2Cl_2-activated complex **24** amenable to *sc*-XRD studies after seven days. Complex **24** was also obtained from the decomposition of dihydride **23** in CH_2Cl_2 at 298 K, as well as from the *n*-butenes complex **27** (*vide infra*).

^1H NMR (400 MHz, CD_2Cl_2, 298 K) δ 1.42 (d, 18 H, $^3J_{HP}$ = 14.9 Hz; ^{t}Bu), 1.50 (d, 18 H, $^3J_{HP}$ = 14.2 Hz; ^{t}Bu), 1.94 (m, 2 H; dtbpe CH_2), 2.18 (s, 2 H; bridging CH_2), 2.32 (m, 2 H; dtbpe CH_2), 7.56 (s, 4 H; $[BAr^F_4]^-$ *p*-H), 7.71 (s, 8 H; $[BAr^F_4]^-$ *o*-H).

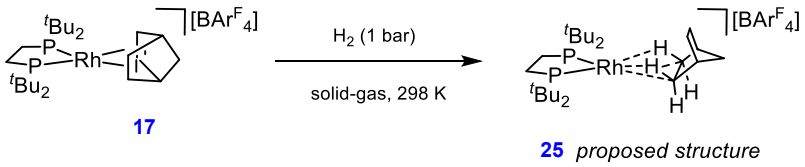
$^{31}P\{^1H\}$ NMR (162 MHz, CD_2Cl_2, 298 K) δ 98.0 (br. d, $^1J_{PRh}$ ~ 150 Hz).

$^{19}F\{^1H\}$ NMR (376.5 MHz, CD_2Cl_2, 298 K) δ –62.8.

$^{11}B\{^1H\}$ NMR (128.39 MHz, CD_2Cl_2, 298 K) δ –6.65.

ESI-MS (CH_2Cl_2) *m/z* found (calculated) for $C_{37}H_{82}P_4Rh_2Cl_2$ $[M]^{2+}$: 463.1460 (463.1422).

5.13.12 In Situ *Solid-State Synthesis of [(dtbpe)Rh(σ-NBA)][BAr$^F_4$], 25*



17 **25** *proposed structure*

A 4.0 mm zirconia solid-state rotor was packed with ~25 mg of **17** (~20 μmol). Left unsealed, the rotor was exposed to H_2 (1 bar) for 50 minutes before the rotor was capped under a flow of H_2 and solid-state NMR studies were immediately undertaken. Note that due to the poor area of contact between the packed material and the H_2 atmosphere, hydrogenation *in situ* took longer than under NMR batch conditions (as in Section 2.3.2) where only 10 minutes was necessary for near-quantitative conversion of the precursor η^2,η^2-NBD complex **17** to the σ-NBA complex **25**.

This material could also be prepared by an *ex situ* solid-gas methodology, from finely powdered complex **17**, by reaction with H_2 gas (1.0 bar) for 20 min at 298 K in a Young's flask. This claret-coloured material is sensitive to moist air and does not survive in solution, even at 183 K, giving C-Cl activation products in CH_2Cl_2 (*vide infra*) or the arene adduct (*vide infra*) in 1,2-difluorobenzene.

In addition to a colour change from red to a darker red-brown, crystals of **17** exposed to H_2 were observed to fracture and burst upon hydrogenation. Crystals for *sc*-XRD studies were harvested from intact parts of otherwise split crystals, but diffraction was poor across all *t* considered (*t* = 2, 5, 10, 30 and 60 min) and no diffraction data could be acquired for the postulated *σ*-NBA complex **25** (see Section 2.3.2).

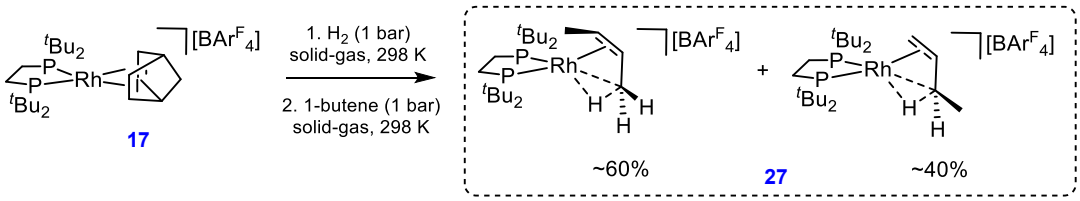
$^{31}P\{^1H\}$ SSNMR (161.9 MHz, 10 kHz spin rate, 298 K) δ 125.8 (vt, $^1J_{PRh}$ ~ 190 Hz).

$^{31}P\{^1H\}$ SSNMR (161.9 MHz, 10 kHz spin rate, 158 K) δ 119.3 (br. s, $\nu_{½}$ ~ 400 Hz).

$^{13}C\{^1H\}$ SSNMR (100.6 MHz, 10 kHz spin rate, 298 K) δ 22.4 (dtbpe CH_2), 29.3 (^{t}Bu CH_3), 36.4 (^{t}Bu C_Q), 117–136 ($[BAr^F_4]^-$), 162.6 ($[BAr^F_4]^-$ *i*-C_{aryl}).

$^{13}C\{^1H\}$ SSNMR (100.6 MHz, 10 kHz spin rate, 158 K) δ 22.0 (dtbpe CH_2), 29.1 (^{t}Bu CH_3), 36.1 (^{t}Bu C_Q), 114–140 ($[BAr^F_4]^-$), 161.5 ($[BAr^F_4]^-$ *i*-C_{aryl}).

5.13.13 In Situ *Solid-Gas Synthesis of [(dtbpe)Rh(η²-n-butenes)][BAr$^F_4$], 27*



Crystalline complex **17** (~2 mg) was introduced to a high-pressure NMR tube fitted with a Young's tap (controlled atmosphere valve), before the tube was evacuated and pressurised with H_2 (1.0 bar) to form *σ*-NBA complex **25** *in situ*. After 45 minutes, the NMR tube was again evacuated and repressurised with 1-butene gas (1.0 bar) for 48 hours. The resulting air-sensitive orange crystals of [(dtbpe)Rh(*η*²-*n*-butenes)][BAr^F_4] (**27**) included solid-state proportions of ([(dtbpe)Rh(*η*²-*cis*-2-butene)][BAr^F_4], ~60%) and ([(dtbpe)Rh(*η*²-1-butene)][BAr^F_4] (~40%). These proportions were ascertained from *sc*-XRD studies and confirmed by solution-phase NMR spectroscopy.

Samples for SSNMR spectroscopic analysis were prepared *in situ*. A 4.0 mm zirconia solid-state rotor was packed with ~25 mg of **17** (~20 μmol). Left unsealed, the rotor was introduced to H_2 (1.0 bar) for 50 min, followed by evacuation and repressurisation with 1-butene (1.0 bar) for 48 hours, and sealing of the rotor under a flow of 1-butene gas. Due to the critical importance of these NMR data to the discussion in Section 2.3.2, some relevant spectra not already included in the text are also provided below pictorially.

^{1}H NMR (400 MHz, CD_2Cl_2, 183 K) δ 0.05 (br. s, 0.4 H; agostic CH*), 0.41 (br. s, 3.6 H; agostic $CH_3^{\dagger}$), 1.06 (d, $^{3}J_{HP}$ = 13.8 Hz, *c.* 7 H; ^{t}Bu*), 1.19 (vdd, $^{3}J_{HP}$ = 13.2 Hz, *c.* 22 H; ^{t}Bu†), 1.27 (d, $^{3}J_{HP}$ = 13.6 Hz, *c.* 7 H; ^{t}Bu*), 1.45 (br. t, $^{3}J_{HH}$ ~ 5.5 Hz, 1.2 H; $CH_3^{\star}$), 1.65–2.02 (m, ∑ = 4.0 H; dtbpe $CH_2^{\star\dagger}$), 2.09 (br. s, 0.4 H; allylic non-agostic CH*), 3.37 (d, $^{3}J_{HH}$ = 14.0 Hz, 0.4 H; alkene CH*), 4.74 (m, 0.4 H; alkene CH*), 4.86 (d, *J* = 7.5 Hz, 0.4 H; alkene CH*), 7.53 (s, 4 H; $[BAr^F_4]^-$ *p*-H), 7.71 (s, 8 H; $[BAr^F_4]^-$ *o*-H). *Alkene CH† is obscured by the* protio-*solvent, confirmed by COSY experiments.*

^{13}C{^{1}H} NMR (100.6 MHz, CD_2Cl_2, 183 K) δ 11.2 (d, $^{2}J_{CRh}$ = 4.8 Hz; agostic $CH_n^{\star}$), 13.3 (br. s†), 18.0 (s; 1-butene CH_3), 20.2 (br. m†), 25.5 (br. m†), 29.7 (m; ^{t}Bu CH_3), 35.9 (d, $^{1}J_{CP}$ ~ 19 Hz; ^{t}Bu $C_Q^{\dagger}$), 36.2 (d, $^{1}J_{CP}$ ~ 18 Hz; ^{t}Bu $C_Q^{\star}$), 36.4 (d, $^{1}J_{CP}$ ~ 18 Hz; ^{t}Bu $C_Q^{\star}$), 37.5 (d, $^{1}J_{CP}$ ~ 18 Hz; ^{t}Bu $C_Q^{\star}$), 37.9 (d, $^{1}J_{CP}$ ~ 18 Hz; ^{t}Bu $C_Q^{\star}$), 38.2 (d, $^{1}J_{CP}$ ~ 19 Hz; ^{t}Bu $C_Q^{\dagger}$), 90.2 (alkene C*), 90.3 (alkene C†), 90.4 (alkene C*), 117.2 (br. sept, $^{3}J_{CF}$ ~ 4 Hz; $[BAr^F_4]^-$ *p*-C_{aryl}), 124.1 (q, $^{1}J_{CF}$ = 272.6 Hz; $[BAr^F_4]^-$ CF_3), 128.3 (qm, $^{2}J_{CF}$ ~ 30 Hz; $[BAr^F_4]^-$ C_{aryl}–CF_3), 134.3 (s; $[BAr^F_4]^-$ *o*-C_{aryl}), 161.5 (q, $^{1}J_{CB}$ ≈ 50 Hz (^{11}B); $[BAr^F_4]^-$ *i*-C_{aryl}).

* corresponds to [(dtbpe)Rh(1-butene)][BAr^F_4] (~40%); † corresponds to [(dtbpe)Rh(*cis*-2-butene)][BAr^F_4] (~60%). All ^{1}H NMR resonances are scaled according to $[BAr^F_4]^-$ aryl C-H integrals normalised to 8H:4H.

^{13}C{^{1}H} SSNMR (100.6 MHz, 10 kHz spin rate, 298 K) δ 10–40 (dtbpe), 115–140 ($[BAr^F_4]^-$), 163 ($[BAr^F_4]^-$ *i*-C_{aryl}).

^{13}C{^{1}H} SSNMR (100.6 MHz, 10 kHz spin rate, 183 K) δ 10–40 (dtbpe), 88.3 (alkene C), 88.9 (alkene C), 90.5 (alkene C), 115–140 ($[BAr^F_4]^-$), 163 ($[BAr^F_4]^-$ *i*-C_{aryl}).

^{31}P{^{1}H} NMR (161.9 MHz, CD_2Cl_2, 183 K) δ 112.9 (dd, $^{2}J_{PRh}$ = 162 Hz, $^{3}J_{PP}$ = 16 Hz; P *trans* to π*), 114.4 (dd, $^{2}J_{PRh}$ = 162 Hz, $^{3}J_{PP}$ = 16 Hz; P *trans* to π†), 114.9 (dd, $^{2}J_{PRh}$ = 220 Hz, $^{3}J_{PP}$ = 16 Hz; P *trans* to σ†), 116.2 (dd, $^{2}J_{PRh}$ = 205 Hz, $^{3}J_{PP}$ = 15 Hz; P *trans* to σ*).

^{31}P{^{1}H} SSNMR (161.9 MHz, 10 kHz spin rate, 298 K) δ 113.9 (m, $\nu_{½}$ = 200 Hz).

^{31}P{^{1}H} SSNMR (161.9 MHz, 10 kHz spin rate, 183 K) δ 111.1 (br. s, $\nu_{½}$ = 600 Hz).

^{19}F{^{1}H} NMR (376.5 MHz, CD_2Cl_2, 298 K) δ –62.8.

^{19}F{^{1}H} NMR (376.5 MHz, CD_2Cl_2, 183 K) δ –62.2.

^{11}B{^{1}H} NMR (128.4 MHz, CD_2Cl_2, 298 K) δ –6.63.

^{11}B{^{1}H} NMR (128.4 MHz, CD_2Cl_2, 183 K) δ –6.87.

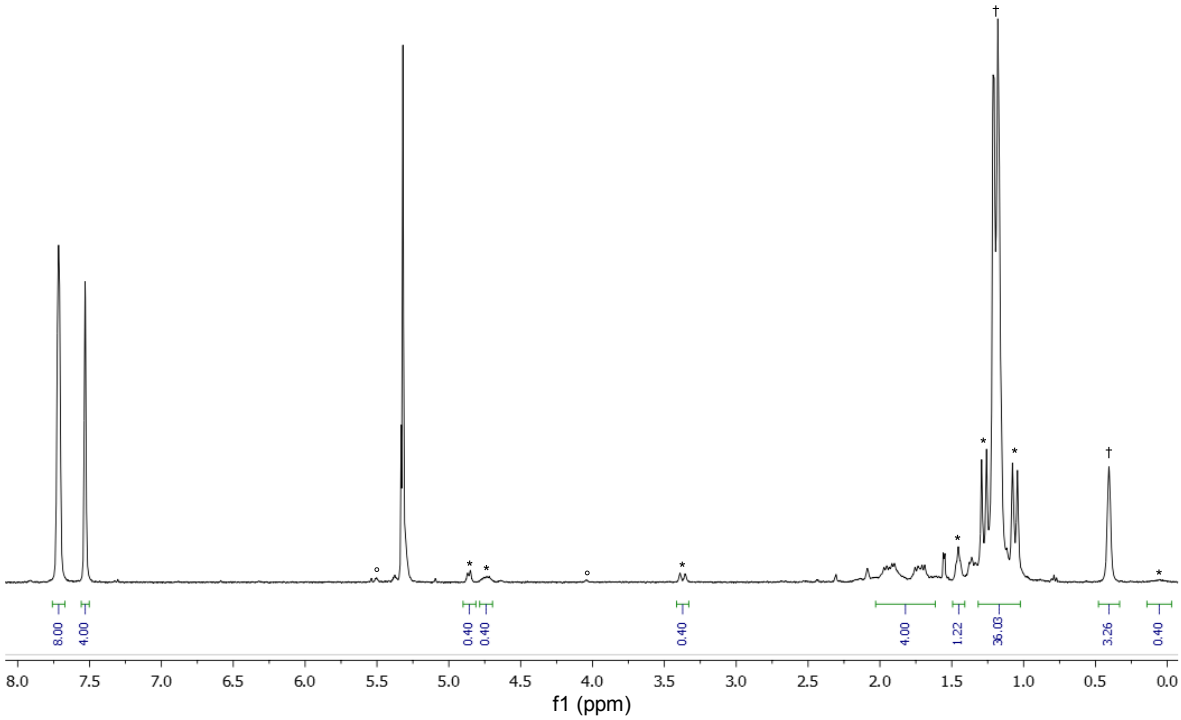


Figure 5.13.1: ^{1}H NMR spectrum of complex 27 (400. MHz, 183 K, CD_2Cl_2). *corresponds to [(dtbpe)Rh(1-butene)][BAr^F_4] (~40%); †corresponds to [(dtbpe)Rh(*cis*-2-butene)][BAr^F_4] (~60%); °corresponds to unreacted 17 (<4%).

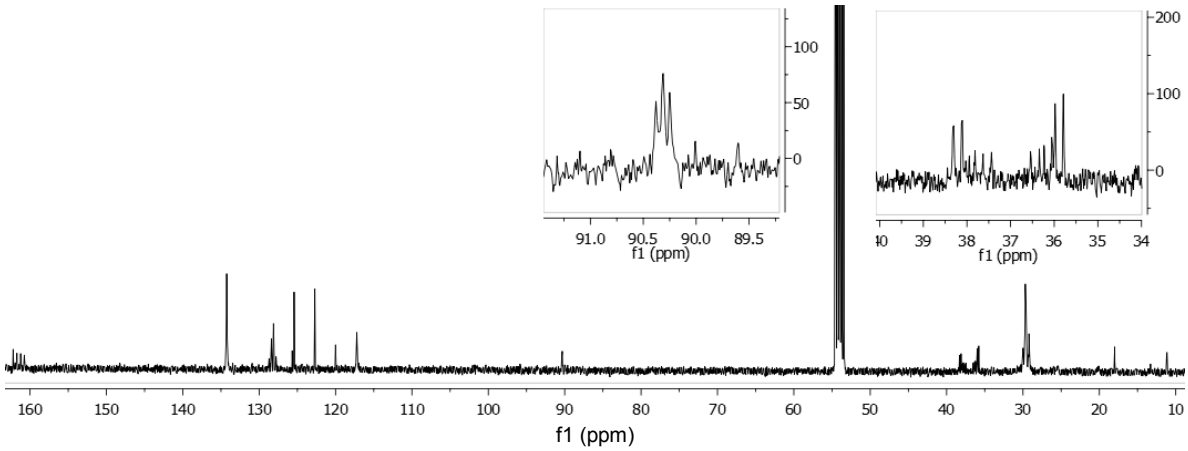


Figure 5.13.2: $^{13}C\{^{1}H\}$ NMR spectrum of complex 27 (100.6 MHz, 183 K, CD_2Cl_2).

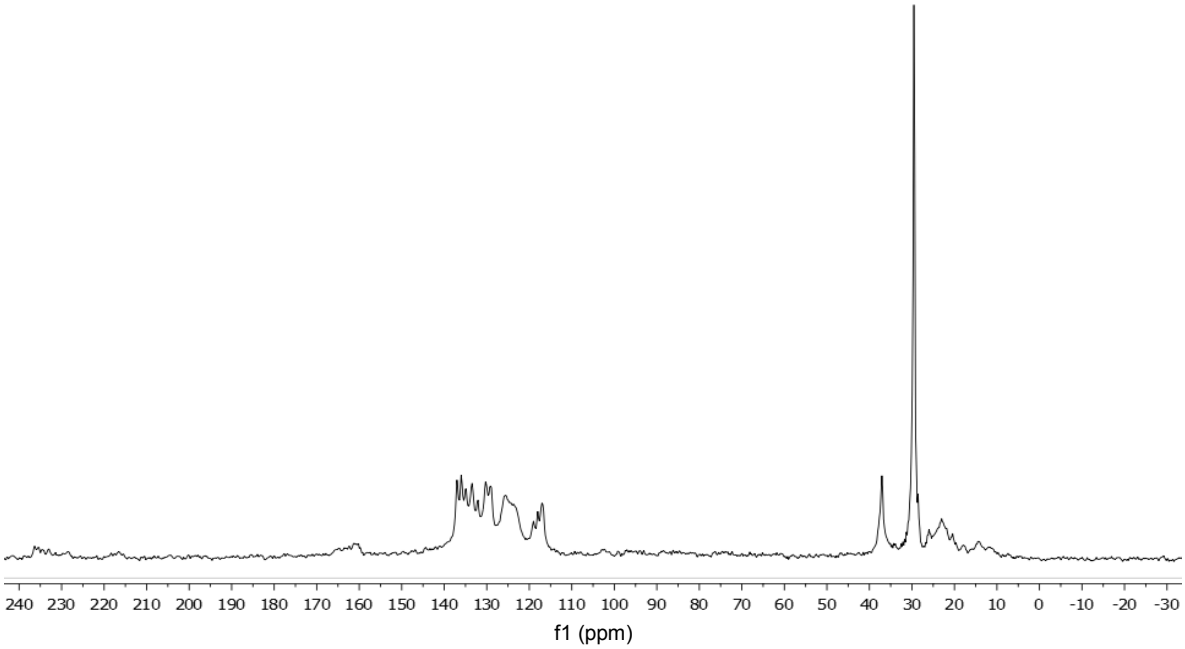


Figure 5.13.3: $^{13}C\{^{1}H\}$ SSNMR spectrum of complex **27** (100.6 MHz, 298 K, ν = 10 kHz) prepared *in situ* from σ-NBA complex **25**.

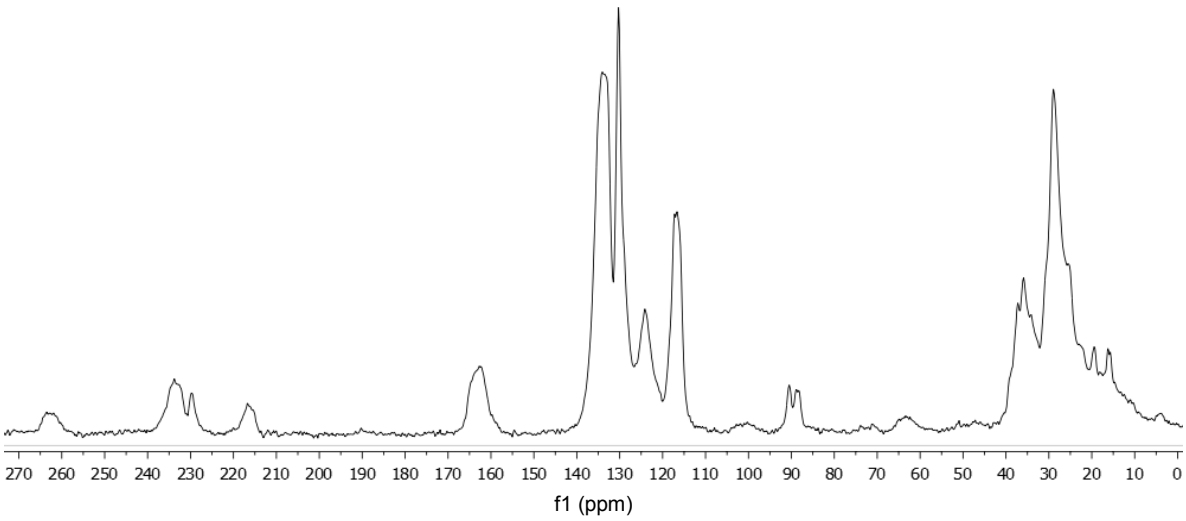


Figure 5.13.4: $^{13}C\{^{1}H\}$ SSNMR spectrum of complex **27** (100.6 MHz, 183 K, ν = 10 kHz) prepared *in situ* from σ-NBA complex **25**.

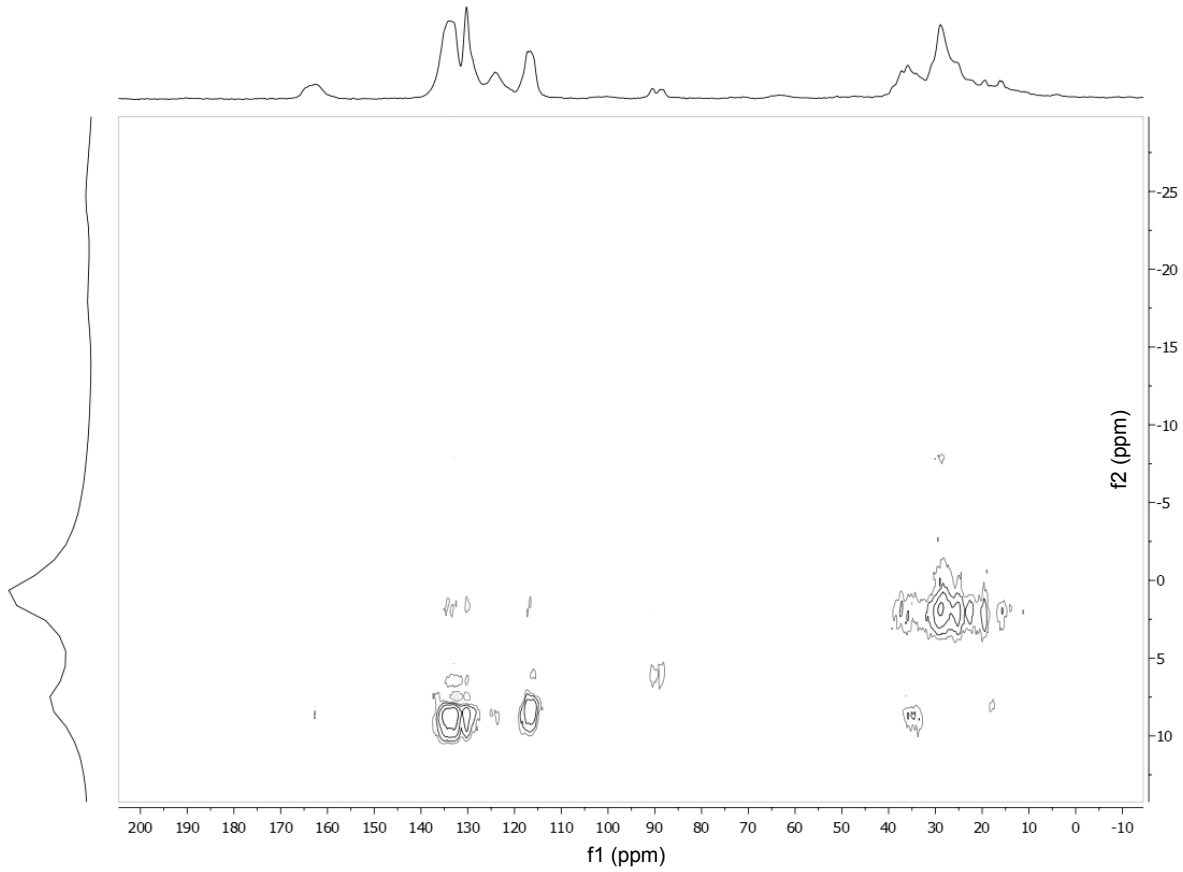


Figure 5.13.5: $^{13}C/^{1}H$ SSNMR HETCOR spectrum of complex 27 (ν = 10 kHz, 183 K) prepared *in situ* from σ-NBA complex 25.

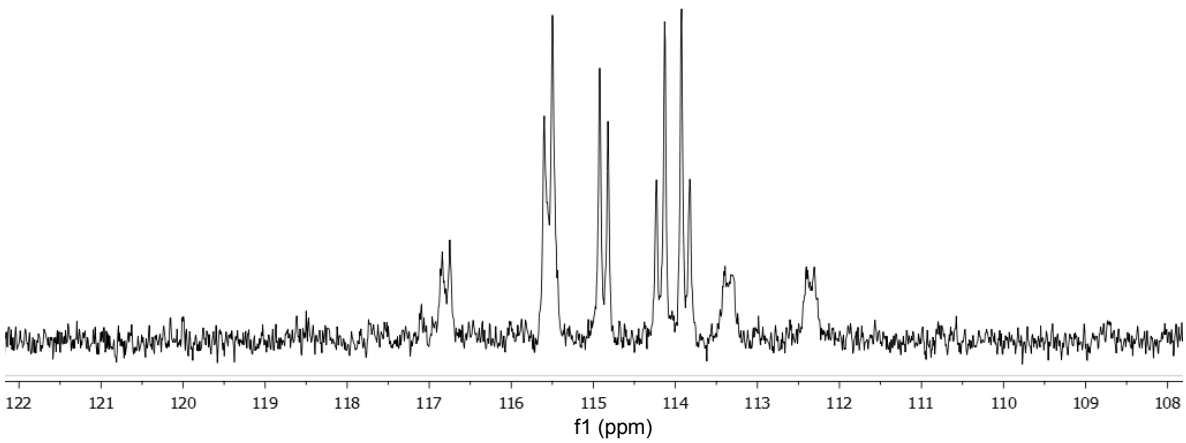
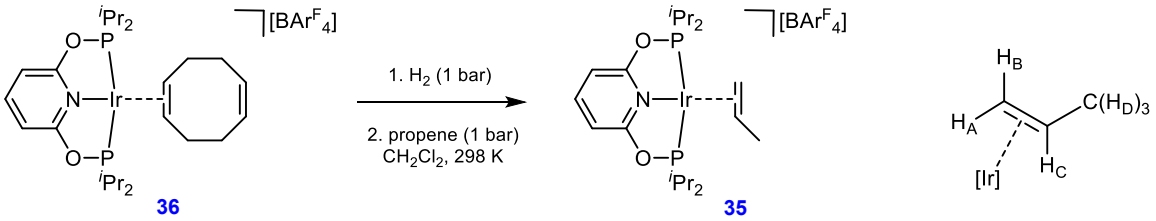


Figure 5.13.6: $^{31}P\{^{1}H\}$ NMR spectrum of complex 27 (161.9 MHz, 183 K, CD_2Cl_2).

5.14 Synthetic Procedures: Chapter 3

5.14.1 *Synthesis of [(ⁱPr-PONOP)Ir(η²-propene)][BAr$^F_4$], 35*



Complex **36** (100 mg, 66 μmol) was introduced to a Young's flask and dissolved in CH_2Cl_2 (5 mL). The solution was frozen with liquid N_2 and the headspace of the flask evacuated before repressurising with H_2 (1.0 bar), thawing, and stirring under H_2 at 298 K for seven days,[a] over which time the initially orange-red solution turned a very pale golden-yellow. The solution was again frozen with liquid N_2, the headspace was evacuated, and the solution allowed to thaw before a pressure of propene gas (1.0 bar) was introduced with vigorous stirring. Four further charges of propene atmosphere were introduced every five minutes, after which the reaction was stirred at 298 K for a further 24 hours. Over this time, the reaction mixture was freeze-pump-thawed with liquid N_2 three times, and a colour change from pale golden-yellow to bright orange was observed. All volatiles were then removed *in vacuo* to yield an amorphous orange solid, which was then redissolved in 1,2-difluorobenzene (2 mL) and transferred *via* cannula to an appropriate crystallisation vessel where it was layered with pentane at 298 K, yielding bright orange crystals of [(ⁱPr-PONOP)Ir(η^2-propene)][BAr$^F_4$] (**35**; 90 mg, 94%) amenable to *sc*-XRD studies after two weeks.

Note that recrystallisation of **35**, when carried out from CH_2Cl_2/pentane at 298 K, generated large crystals of the CH_2Cl_2-containing structure [(ⁱPr-PONOP)Ir(η^2-propene)][CH_2Cl_2 ⊂ BAr$^F_4$] (**35**·CH_2Cl_2; 90 mg, 95%). While both sets of crystals were amenable to *sc*-XRD studies, solid-gas reactivity and solid-state NMR spectroscopic studies proceeded only for the non-solvent-containing structure. Aside from a signal corresponding to CH_2Cl_2 (δ_H 5.33), the NMR data provided below were identical for both structures.

[a] This extensive hydrogenation time, compared to that of the *in situ* NMR-scale synthesis of 'tetrahydride' **37** (*vide infra*) was employed to combat the formation of a poorly-characterised Ir(III) bridging-COD dimer as a hydrogenation intermediate, which appeared to only form readily as a contaminant on these larger scales (>20 mg) and *not* on the NMR-scale (1-5 mg).

^{1}H NMR (500.23 MHz, CD_2Cl_2, 298 K) δ 1.13 (m, $^{3}J_{HH}$ ~ $^{3}J_{HP}$ ~ 7.0 Hz, 12 H; ^{i}Pr CH_3), 1.37 (m, $^{3}J_{HH}$ ~ 6.5 Hz, $^{3}J_{HP}$ ~ 7.0 Hz, 12 H; ^{i}Pr CH_3), 1.72 (d, $^{3}J_{HDHC}$ = 5.8 Hz, 3 H; H_D), 2.57 (br. septet, $^{3}J_{HP}$ ~ 7.0 Hz, 2 H; ^{i}Pr CH), 2.77 (septet, $^{3}J_{HP}$ = 7.2 Hz, 2 H; ^{i}Pr CH), 3.08 (d, $^{3}J_{HAHC}$ = 7.5 Hz, 1 H; H_A), 3.40 (dt, $^{3}J_{HBHC}$ = 10.6 Hz, $^{3}J_{HP}$ = 6.3 Hz, 1 H; H_B), 4.33 (ddqt, $^{3}J_{HCHD}$ = 5.8 Hz, $^{3}J_{HCHA}$ = 7.5 Hz, $^{3}J_{HCHB}$ = 10.6 Hz, $^{3}J_{HP}$ ~ 5.5 Hz, 1 H; H_C), 6.92 (d, $^{3}J_{HH}$ = 8.2 Hz, 2 H; heterocyclic C3,5), 7.56 (s, 4 H; $[BAr^F_4]^-$ *p*-H), 7.71 (br. m, 8 H; $[BAr^F_4]^-$ *o*-H), 7.95 (br. tt, $^{3}J_{HH}$ = 8.2 Hz, $^{5}J_{HP}$ ~ 1.0 Hz, 1 H; heterocyclic C4).

^{13}C{^{1}H} NMR (125.80 MHz, CD_2Cl_2, 298 K) δ 16.3 (vt, $^{2}J_{CP}$ = 2.9 Hz; ^{i}Pr CH_3), 16.4 (s; ^{i}Pr CH_3), 16.8 (s; ^{i}Pr CH_3), 17.8 (vt, $^{2}J_{CP}$ = 2.0 Hz; ^{i}Pr CH_3), 23.9 (s; alkene CH_3), 30.5 (vt, $^{1}J_{CP}$ = 14.3 Hz; ^{i}Pr CH), 31.4 (vt, $^{1}J_{CP}$ = 13.7 Hz; ^{i}Pr CH), 42.6 (s; alkene CH_2), 54.8 (s; alkene CH), 103.2 (vt, $^{3}J_{CP}$ = 2.7 Hz; heterocyclic C3,5), 117.9 (septet, $^{4}J_{CF}$ = 4.0 Hz; $[BAr^F_4]^-$ *p*-C_{aryl}), 124.9 (q, $^{1}J_{CF}$ = 272.6 Hz; $[BAr^F_4]^-$ CF_3), 129.2 (qq, $^{2}J_{CF}$ = 31.5 Hz, $^{4}J_{CF}$ = 3.0 Hz; $[BAr^F_4]^-$ C_{aryl}-CF_3), 135.2 (m; $[BAr^F_4]^-$ *o*-C_{aryl}), 145.4 (s; heterocyclic C4), 162.1 (q, $^{1}J_{CB}$ = 49.9 Hz (^{11}B); $[BAr^F_4]^-$ *i*-C_{aryl}), 164.2 (vt, $^{2}J_{CP}$ = 3.5 Hz; heterocyclic C2,6).

^{13}C{^{1}H} SSNMR (100.66 MHz, 10 kHz spin rate, 298 K) δ 13–20 (^{i}Pr CH_3), 23.0 (alkene CH_3), 23.3 (alkene CH_3), 29.7 (^{i}Pr CH), ~32.0 (^{i}Pr CH), 42.9 (alkene CH_2), 44.8 (alkene CH_2), 56.6 (alkene CH), 57.4 (alkene CH), 102.9 (heterocyclic C3,5), 117.7–120.0 ($[BAr^F_4]^-$ *p*-C_{aryl}), 121–140 ($[BAr^F_4]^-$), 143.6 (heterocyclic C4), 144.0 (heterocyclic C4), 162–167 ($[BAr^F_4]^-$ *i*-C_{aryl}), 165.2 (heterocyclic C2,6).

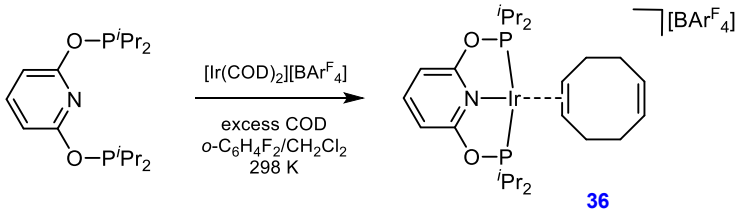
^{31}P{^{1}H} NMR (202.49 MHz, CD_2Cl_2, 298 K) δ 188.6.

^{31}P{^{1}H} SSNMR (162.03 MHz, 10 kHz spin rate, 298 K) δ 189.5 (d, $^{2}J_{PP'}$ ~ 310 Hz), 194.1 (d, $^{2}J_{PP'}$ ~ 310 Hz).

ESI-MS (CH_2Cl_2) *m/z* found (calculated) for $C_{20}H_{37}IrNO_2P_2$ $[M]^+$: 578.1930 (578.1923).

Elemental analysis found (calculated) for $C_{52}H_{49}BF_{24}IrNO_2P_2$: C, 43.10 (43.35); H, 3.39 (3.43); N, 0.85 (0.97).[a]

5.14.2 *Synthesis of [(^{i}Pr-PONOP)Ir(η^2-COD)][BAr$^F_4$], 36*



[Ir(η^2,η^2-COD)$_2$][BAr^F_4] (100 mg, 79 μmol) was introduced to a Young's flask and dissolved in CH_2Cl_2 (2 mL) before the addition of neat COD (50 μL, 410 μmol). A solution of ^{i}Pr-PONOP (27 mg, 79 μmol) in 1,2-difluorobenzene (0.2 mL) was added dropwise to the stirred solution of [Ir(η^2,η^2-COD)$_2$][BAr^F_4] at 298 K, inducing a colour change from rusty pink to bright orange.

[a] For sample free of CH_2Cl_2.

The mixture was stirred for an additional 60 minutes before transfer to an appropriate crystallisation vessel and layering with pentane at 298 K to give [(^{i}Pr-PONOP)Ir(η^2-COD)][BAr$^F_4$] (**36**; 107 mg, 90%) as large orange-red crystals amenable to *sc*-XRD studies after two weeks.

^{1}H NMR (400 MHz, CD_2Cl_2, 298 K) δ 1.26 (m, 24 H; ^{i}Pr CH_3), 1.89 (m, 2 H; COD Ir-C_{sp2}H-$C_{sp3}H_2$), 2.20 (m, 2 H; COD Ir-C_{sp2}H-C_{sp3}H$_2$-$C_{sp3}H_2$), 2.49 (m, 4 H; COD Ir-C_{sp2}H-$C_{sp3}H_2$ + Ir-C_{sp2}H-C_{sp3}H$_2$-$C_{sp3}H_2$), 2.56 (septet, $^3J_{HH}$ = 7.2 Hz, 4 H; ^{i}Pr CH), 4.45 (br. m, 2 H; bound alkene CH), 5.68 (t, $^3J_{HH}$ = 3.7 Hz, 2 H; spectator alkene CH), 6.90 (d, $^3J_{HH}$ = 8.2 Hz, 2 H; heterocyclic C3,5), 7.57 (s, 4 H; [BAr$^F_4$]$^-$ *p*-H), 7.73 (br. m, 8 H; [BAr$^F_4$]$^-$ *o*-H), 7.93 (t, $^3J_{HH}$ = 8.2 Hz, 1 H; heterocyclic C4).

^{13}C{^{1}H} NMR (100.64 MHz, CD_2Cl_2, 298 K) δ 16.3 (s; ^{i}Pr CH_3), 17.2 (vt, $^2J_{CP}$ = 2.4 Hz; ^{i}Pr CH_3), 31.0 (vt, $^1J_{CP}$ = 13.2 Hz; ^{i}Pr CH), 31.9 (s; COD Ir-C_{sp2}-C_{sp3}-C_{sp3}), 36.8 (vt, J = 3.2 Hz; COD Ir-C_{sp2}-C_{sp3}), 65.3 (s; bound alkene CH), 102.8 (vt, $^3J_{CP}$ = 2.3 Hz; heterocyclic C3,5), 117.9 (septet, $^4J_{CF}$ = 4.0 Hz; [BAr$^F_4$]$^-$ *p*-C_{aryl}), 125.0 (q, $^1J_{CF}$ = 272.6 Hz; [BAr$^F_4$]$^-$ CF_3), 129.3 (qq, $^2J_{CF}$ = 31.5 Hz, $^4J_{CF}$ = 2.9 Hz; [BAr$^F_4$]$^-$ C_{aryl}-CF_3), 130.0 (s; spectator alkene CH), 135.2 (s; [BAr$^F_4$]$^-$ *o*-C_{aryl}), 146.3 (s; heterocyclic C4), 162.2 (q, $^1J_{CB}$ = 49.8 Hz (^{11}B); [BAr$^F_4$]$^-$ *i*-C_{aryl}), 164.5 (vt, $^2J_{CP}$ = 2.8 Hz; heterocyclic C2,6).

^{31}P{^{1}H} NMR (162 MHz, CD_2Cl_2, 298 K) δ 184.4.

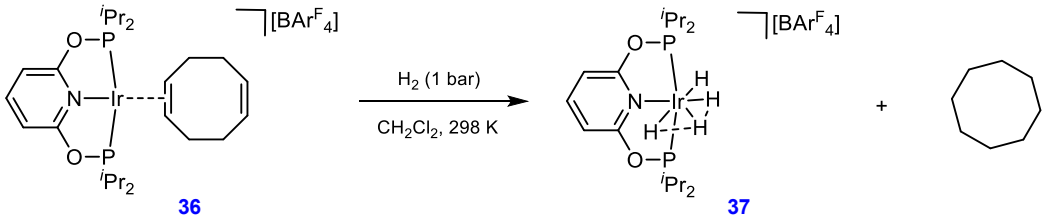
^{19}F{^{1}H} NMR (376.5 MHz, CD_2Cl_2, 298 K) δ –62.8.

^{11}B{^{1}H} NMR (128.39 MHz, CD_2Cl_2, 298 K) δ –6.63.

Elemental analysis found (calculated) for $C_{57}H_{55}BF_{24}IrNO_2P_2$: C, 45.27 (45.43); H, 3.56 (3.68); N, 0.89 (0.93).

ESI-MS (CH_2Cl_2) *m/z* found (calculated) for $C_{25}H_{43}IrNO_2P_2$ [M]$^+$: 644.2426 (644.2394).

5.14.3 In Situ *NMR-Scale Synthesis of [(^{i}Pr-PONOP)IrH$_4$][BAr$^F_4$], 37*



36 **37**

36 (~2 mg, ~2 μmol) was introduced to a thick-walled NMR tube fitted with a Young's tap (controlled atmosphere valve) and dissolved in CD_2Cl_2 (0.4 mL). The contents of the tube were frozen with liquid N_2, the headspace was evacuated, and the tube was repressurised with H_2 (1.0 bar). Upon thawing to 298 K and shaking, the solution turned from orange to a pale golden-yellow, generating cyclooctane and the non-classical 'tetrahydride' [(^{i}Pr-PONOP)IrH$_4$][BAr$^F_4$] (**37**) *in situ*.

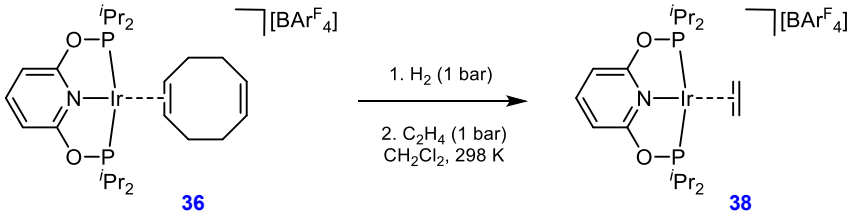
Ethene complex **38**, propene complex **35**, and pure samples of dihydride **39** ($^{13}C\{^1H\}$ NMR data) also constituted valid starting-points for the *in situ* synthesis of **37** by a similar method, also *via* solution-phase hydrogenation in CD_2Cl_2 at 298 K. In the absence of an H_2 atmosphere, solutions of **37** slowly dehydrogenated to yield the dihydride **39**. Spin-lattice relaxation time (T_1) measurements on the hydride position were carried out by the inversion-recovery method using standard 180°-θ-90° pulse sequence:[23,24] 119 ± 8 ms (295 K) and 38 ± 1 ms (253 K) under a pressure of H_2 (1.5 bar).

^1H NMR (400 MHz, CD_2Cl_2, 298 K) δ −8.75 (br. s, 4 H; Ir-*H*), 1.20 (m, 18 H; ^{i}Pr CH_3), 1.70 (br. s, 6 H; ^{i}Pr CH_3), 2.45 (m, 4 H; ^{i}Pr CH), 6.87 (d, $^3J_{HH}$ = 8.1 Hz, 2 H; heterocyclic C3,5), 7.56 (s, 4 H; $[BAr^F_4]^-$ *p*-H), 7.72 (br. m, 8 H; $[BAr^F_4]^-$ *o*-H), 7.83 (t, $^3J_{HH}$ = 8.1 Hz, 1 H; heterocyclic C4). *Liberated cyclooctane at δ 1.52.*

$^{31}P\{^1H\}$ NMR (162 MHz, CD_2Cl_2, 298 K) δ 181.2 (s).

$^{13}C\{^1H\}$ NMR (150.91 MHz, CD_2Cl_2, 298 K) δ 17.3 (s; ^{i}Pr CH_3), 17.7 (br. vt, $^2J_{CP}$ ~ 3 Hz; ^{i}Pr CH_3), 31.3 (vt, $^1J_{CP}$ = 15.8 Hz; ^{i}Pr CH), 103.9 (s; heterocyclic C3,5), 117.9 (septet, $^4J_{CF}$ = 4.0 Hz; $[BAr^F_4]^-$ *p*-C_{aryl}), 125.0 (q, $^1J_{CF}$ = 272.6 Hz; $[BAr^F_4]^-$ CF_3), 129.3 (qq, $^2J_{CF}$ = 31.5 Hz, $^4J_{CF}$ = 2.9 Hz; $[BAr^F_4]^-$ C_{aryl}-CF_3), 135.2 (s; $[BAr^F_4]^-$ *o*-C_{aryl}), 145.3 (s; heterocyclic C4), 161.1 (s; heterocyclic C2,6), 162.2 (q, $^1J_{CB}$ = 49.8 Hz (^{11}B); $[BAr^F_4]^-$ *i*-C_{aryl}).

5.14.4 *Synthesis of [(^{t}Pr-PONOP)Ir(η^2-ethene)][BAr$^F_4$], **38***



36 **38**

36 (100 mg, 66 μmol) was introduced to a Young's flask and dissolved in CH_2Cl_2 (5 mL). The solution was frozen with liquid N_2 and the headspace of the flask was evacuated before repressurising with H_2 (1.0 bar), thawing, and stirring under H_2 at 298 K for seven days, over which time the initially orange-red solution turned a very pale golden-yellow. The solution was again frozen with liquid N_2, the headspace was evacuated, and the solution allowed to thaw before a pressure of ethene gas (1.0 bar) was introduced with vigorous stirring. Four further charges of ethene atmosphere were introduced every five minutes, after which the reaction was stirred at 298 K for a further 24 hours.

Over this time, the reaction mixture was freeze-pump-thawed with liquid N_2 three times, and a colour change from pale golden-yellow to bright red was observed. The reaction mixture was then concentrated *in vacuo* by ~50%, and transferred *via* cannula to an appropriate crystallisation vessel where it was layered with pentane at 275 K, yielding bright red crystals of [(^{i}Pr-PONOP)Ir(η^2-ethene)][BAr^F_4] (**38**; 90 mg, 95%) amenable to *sc*-XRD studies after two weeks.

^{1}H NMR (399.74 MHz, CD_2Cl_2, 298 K) δ 1.19–1.28 (overlapping resonances, Σ = 24 H; ^{i}Pr CH_3), 2.72 (septet, $^3J_{HH}$ = 7.1 Hz, 4 H; ^{i}Pr CH), 3.09 (t, $^3J_{HP}$ = 3.3 Hz, 4 H; ethene), 6.93 (d, $^3J_{HH}$ = 8.2 Hz, 2 H; heterocyclic C3,5), 7.56 (s, 4 H; [BAr^F_4]$^-$ *p*-H), 7.72 (br. m, 8 H; [BAr^F_4]$^-$ *o*-H), 7.98 (tt, $^3J_{HH}$ = 8.2 Hz, $^5J_{HP}$ = 0.9 Hz, 1 H; heterocyclic C4).

^{13}C{^{1}H} NMR (100.51 MHz, CD_2Cl_2, 298 K) δ 16.5 (s; ^{i}Pr CH_3), 17.1 (vt, $^2J_{CP}$ = 2.4 Hz; ^{i}Pr CH_3), 30.7 (vt, $^1J_{CP}$ = 14.6 Hz; ^{i}Pr CH), 37.3 (br. t, $^2J_{CP}$ ~ 1 Hz; ethene), 103.5 (vt, $^3J_{CP}$ ~ 3 Hz; heterocyclic C3,5), 117.9 (septet, $^4J_{CF}$ = 4.0 Hz; [BAr^F_4]$^-$ *p*-C_{aryl}), 124.9 (q, $^1J_{CF}$ = 272.6 Hz; [BAr^F_4]$^-$ CF_3), 129.2 (qq, $^2J_{CF}$ = 31.5 Hz, $^4J_{CF}$ = 3.0 Hz; [BAr^F_4]$^-$ C_{aryl}-CF_3), 135.2 (m; [BAr^F_4]$^-$ *o*-C_{aryl}), 144.7 (s; heterocyclic C4), 162.1 (q, $^1J_{CB}$ = 49.9 Hz (^{11}B); [BAr^F_4]$^-$ *i*-C_{aryl}), 163.7 (s; heterocyclic C2,6).

^{13}C{^{1}H} SSNMR (100.66 MHz, 10 kHz spin rate, 298 K) δ 13.3–18.0 (^{i}Pr CH_3), 30.2 (^{i}Pr CH), 32.1 (^{i}Pr CH), 38.4 (ethene), 103.1 (heterocyclic C3,5), 103.6 (heterocyclic C3,5), 117.7 ([BAr^F_4]$^-$ *p*-C_{aryl}), 118.5 ([BAr^F_4]$^-$ *p*-C_{aryl}), 122–138 ([BAr^F_4]$^-$), 143.7 (heterocyclic C4), 159.5–168.0 ([BAr^F_4]$^-$ *i*-C_{aryl} + heterocyclic C2,6).

^{31}P{^{1}H} NMR (161.82 MHz, CD_2Cl_2, 298 K) δ 191.8.

^{31}P{^{1}H} SSNMR (162.03 MHz, 10 kHz spin rate, 298 K) δ 193.7 (d, $^2J_{PP'}$ ~ 300 Hz), 194.3 (d, $^2J_{PP'}$ ~ 300 Hz).

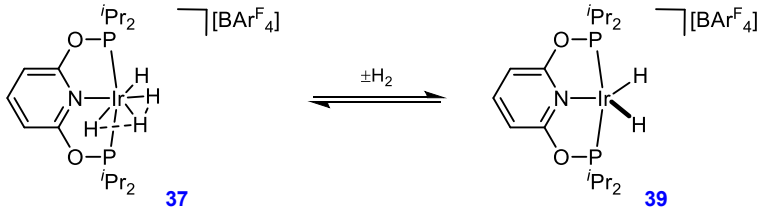
^{19}F{^{1}H} NMR (376.13 MHz, CD_2Cl_2, 298 K) δ –62.8.

^{11}B{^{1}H} NMR (128.39 MHz, CD_2Cl_2, 298 K) δ –6.63.

ESI-MS (CH_2Cl_2) *m*/*z* found (calculated) for $C_{19}H_{35}IrNO_2P_2$ [M]$^+$: 564.1627 (564.1772).

Elemental analysis found (calculated) for $C_{51}H_{47}BF_{24}IrNO_2P_2$: C, 42.96 (42.93); H, 3.32 (3.32); N, 0.94 (0.98).

5.14.5 *Synthesis of [(^{i}Pr-PONOP)IrH$_2$][BAr$^F_4$], **39***



37 **39**

Samples of **37** as generated in Section 5.14.3 *in situ* were refrozen with liquid N_2 and the headspaces of the tubes were evacuated; upon thawing, the dihydride **39** slowly formed over the course of 3-6 hours, encouraged by further freeze-pump-thaw cycles. Pure samples of dihydride **39** were obtained by removing all volatiles (including liberated cyclooctane) *in vacuo*, leaving behind dihydride **39** as an oily orange solid. Spin-lattice relaxation time (T_1) measurements on the hydride position were carried out by the inversion-recovery method using standard 180°-θ-90° pulse sequence:[23,24] 1870 ± 10 ms (295 K).

^{1}H NMR (500.23 MHz, CD_2Cl_2, 298 K) δ −19.85 (br. s, 2 H; Ir-*H*), 1.15 (vq, $^3J_{HH}$ = 7.1 Hz, $^3J_{HP}$ ~ 8 Hz, $^3J_{HP}$' ~ 9 Hz, 12 H; ^{i}Pr CH_3), 1.32 (vq, $^3J_{HH}$ = 6.8 Hz, $^3J_{HP}$ ~ 8 Hz, $^3J_{HP}$' ~ 9 Hz 12 H; ^{i}Pr CH_3), 2.67 (br. septet, $^3J_{HH}$ ~ 7 Hz, 4 H; ^{i}Pr CH), 6.89 (d, $^3J_{HH}$ = 8.2 Hz, 2 H; heterocyclic C3,5), 7.56 (s, 4 H; $[BAr^F_4]^-$ *p*-H), 7.71 (br. m, 8 H; $[BAr^F_4]^-$ *o*-H), 7.82 (t, $^3J_{HH}$ = 8.2 Hz, 1 H; heterocyclic C4).

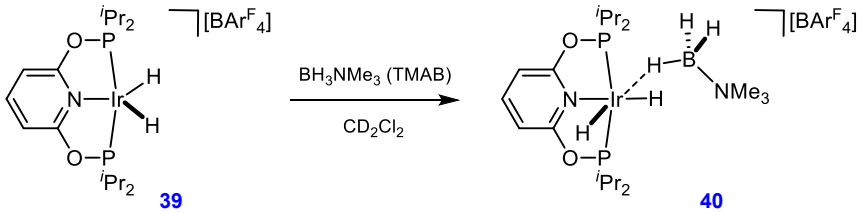
^{31}P{^{1}H} NMR (202.49 MHz, CD_2Cl_2, 298 K) δ 183.3 (br.).

^{31}P{^{1}H} NMR (242.93 MHz, 1,2-difluorobenzene, 298 K) δ 186.5 (br.).

^{13}C{^{1}H} NMR (150.91 MHz, CD_2Cl_2, 298 K) δ 17.3 (s; ^{i}Pr CH_3), 18.0 (br. vt, $^2J_{CP}$ ~ 2 Hz; ^{i}Pr CH_3), 30.5 (vt, $^1J_{CP}$ = 14.5 Hz; ^{i}Pr CH), 103.8 (s; heterocyclic C3,5), 117.9 (septet, $^4J_{CF}$ = 4.0 Hz; $[BAr^F_4]^-$ *p*-C_{aryl}), 125.0 (q, $^1J_{CF}$ = 272.6 Hz; $[BAr^F_4]^-$ CF_3), 129.3 (qq, $^2J_{CF}$ = 31.5 Hz, $^4J_{CF}$ = 2.9 Hz; $[BAr^F_4]^-$ C_{aryl}-CF_3), 135.2 (s; $[BAr^F_4]^-$ *o*-C_{aryl}), 145.0 (s; heterocyclic C4), 161.6 (s; heterocyclic C2,6), 162.2 (q, $^1J_{CB}$ = 49.8 Hz (^{11}B); $[BAr^F_4]^-$ *i*-C_{aryl}).

ESI-MS (CH_2Cl_2) *m/z* found (calculated) for $C_{17}H_{33}IrNO_2P_2$ $[M]^+$: 538.1604 (538.1616); ~60% relative intensity for $[(^i$Pr-PONOP)Ir$]^+$: 536.1460 (536.1459); ~5% relative intensity for $[(^i$Pr-PONOP)Ir$(N_2)]^+$: 564.1403 (564.1521).

5.14.6 *Synthesis of [(^{i}Pr-PONOP)IrH$_2$(σ-H$_3$BNMe$_3$)][BAr$^F_4$], **40***



39 **40**

36 (10 mg, ~7 μmol) was introduced to a thick-walled NMR tube fitted with a Young's tap (controlled atmosphere valve) and dissolved in CH_2Cl_2 (0.4 mL). The contents of the tube were frozen with liquid N_2, the headspace was evacuated, and the tube was repressurised with H_2 (1.0 bar). Upon thawing and shaking, the solution turned from orange to a pale golden-yellow, generating non-classical 'tetrahydride' **37** *in situ*.

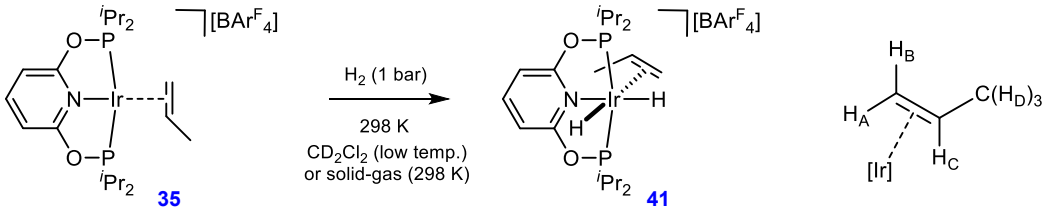
After this, all volatiles were removed *in vacuo*, leaving behind the dihydride **39** as an oily orange solid. Trimethylamine-borane (TMAB; 0.5 mg, 7 μmol) was introduced to the tube, and the comingled solids were dissolved in CD_2Cl_2 (0.4 mL), generating a colourless solution which was interrogated by solution-phase NMR spectroscopy. The contents of the NMR tube were layered with pentane at 298 K to yield colourless crystals of [(ⁱPr-PONOP)IrH$_2$(σ-H_3BNMe_3)][BAr$^F_4$] (**40**) after one week, amenable to *sc*-XRD studies. Complex **40** was manufactured in too limited a quantity for reliable microanalysis.

^{1}H NMR (399.74 MHz, CD_2Cl_2, 298 K) δ −20.00 (br. td, $^2J_{HP}$ = 17.3 Hz, $^2J_{HH}$ ~ 6 Hz, 1 H; Ir-*H*), −15.91 (td, $^2J_{HP}$ = 12.0 Hz, $^2J_{HH}$ = 5.7 Hz, 1 H; Ir-*H*), −2.20 (br. s, 3 H; BH_3), 0.88 (vq, $^3J_{HH}$ = 6.9 Hz, $^3J_{HP}$ ~ 8 Hz, 6 H; ⁱPr CH_3), 1.10 (m, $^3J_{HH}$ = 6.9 Hz, $^3J_{HP}$ ~ 10 Hz, 6 H; ⁱPr CH_3), 1.36 (m, $^3J_{HH}$ = 7.9 Hz, $^3J_{HP}$ ~ 10.5 Hz, 6 H; ⁱPr CH_3), 1.48 (m, $^3J_{HH}$ = 6.9 Hz, $^3J_{HP}$ ~ 6 Hz, 6 H; ⁱPr CH_3), 2.56 (br. m, 2 H; ⁱPr CH), 2.62 (s, 9 H; NMe_3), 2.84 (septet, $^3J_{HH}$ = 6.9 Hz, 2 H; ⁱPr CH), 6.75 (d, $^3J_{HH}$ = 8.2 Hz, 2 H; heterocyclic C3,5), 7.56 (s, 4 H; [BAr$^F_4$]$^-$ *p*-H), 7.71 (br. m, 8 H; [BAr$^F_4$]$^-$ *o*-H), 7.69 (t, $^3J_{HH}$ = 8.2 Hz, 1 H; heterocyclic C4).

^{31}P{^{1}H} NMR (161.82 MHz, CD_2Cl_2, 298 K) δ 179.8.

^{11}B{^{1}H} NMR (128.25 MHz, CD_2Cl_2, 298 K) δ –6.63 ([BAr$^F_4$]$^-$), −14.7 (σ-H_3BNMe_3).

5.14.7 *Synthesis of [(ⁱPr-PONOP)IrH$_2$(η^2-propene)][BAr$^F_4$], **41***



35 (5 mg, ~4 μmol) was introduced to an NMR tube fitted with a Young's tap (controlled atmosphere valve) and dissolved in CD_2Cl_2 (0.4 mL). The resulting red solution was frozen with liquid N_2 before the headspace of the tube was evacuated and repressurised with H_2 (1.0 bar). As it thawed (*i.e.* <u>while still cold</u> to prevent over-hydrogenation to **37**), the NMR tube was shaken vigorously until the solution decolourised before being immediately refrozen with liquid N_2 and the headspace evacuated. The tube was closed and allowed to thaw to 298 K before solution-phase NMR spectroscopy was undertaken. A mixture of products was observed, the vast majority composed of *cis*-[(ⁱPr-PONOP)IrH$_2$(η^2-propene)][BAr$^F_4$] (**41**), alongside a minority of 'tetrahydride' **37** (~2%).

41 was relatively stable in the *absence* of an H_2 atmosphere in solution at 298 K, only slowly losing H_2 over the course of 3-6 hours to regenerate **35**. **41** was also obtained *via* a solid-gas route, monitored by SSNMR spectroscopy. A 4.0 mm zirconia solid-state rotor was packed with ~25 mg of **35** (~17 μmol). Left unsealed, the rotor was introduced to H_2 (1.0 bar) for 15 min inside a Young's flask before the system was gently purged with argon and the rotor was capped promptly inside an argon-filled glovebox. Note that attempts to obtain a solid-state structure of **41** by recrystallisation of CH_2Cl_2 solutions were not successful, as any single-crystalline material obtained suffered from a large unit cell (18,135.9 Å^3), poor crystal quality, high monodirectional mosaicity, and the absence of a straightforward structural solution ($\alpha \approx \beta \approx \gamma \approx 90°$), as discussed in the text.

^{1}H NMR (600.09 MHz, CD_2Cl_2, 298 K) δ −16.50 (t, $^2J_{HP}$ = 10.0 Hz, 1 H; Ir-*H*), −11.64 (t, $^2J_{HP}$ = 18.3 Hz, 1 H; Ir-*H*), 0.85 (br. m, 6 H; ^{i}Pr CH_3), 1.13 (br. m, 6 H; ^{i}Pr CH_3), 1.29 (br. m, 6 H; ^{i}Pr CH_3), 1.46 (br. m, 6 H; ^{i}Pr CH_3), 1.72 (d, $^3J_{HH}$ = 5.9 Hz, 3 H; H_D), 2.63 (br. m, 2 H; ^{i}Pr CH), 2.73 (br. s, 2 H; ^{i}Pr CH), 3.56-3.68 (br., multiple resonances, 2 H; H_A + H_B), 4.84 (br. s, 1 H; H_C), 6.83 (br. d, $^3J_{HH}$ = 8.0 Hz, 2 H; heterocyclic C3,5), 7.56 (s, 4 H; $[BAr^F{}_4]^-$ *p*-H), 7.70–7.76 (overlapping 8 H singlet + 1 H triplet, $^3J_{HH}$ = 8.0 Hz; $[BAr^F{}_4]^-$ *o*-H + heterocyclic C4).

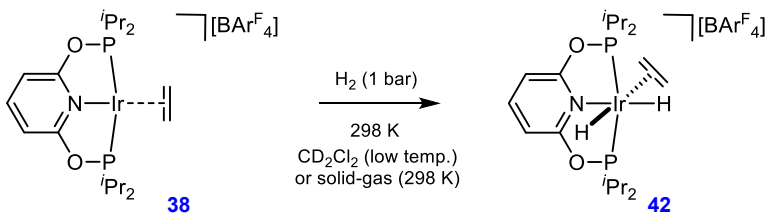
^{13}C{^{1}H} NMR (150.91 MHz, CD_2Cl_2, 298 K) δ 15.3 (br. s; ^{i}Pr CH_3), 17.1 (br. s; ^{i}Pr CH_3), 17.2 (br. s; ^{i}Pr CH_3), 19.5 (br. s; ^{i}Pr CH_3), 21.2 (s; alkene CH_3), 28.5 (br. vt, $^1J_{CP}$ ~ 15 Hz; ^{i}Pr CH), 30.9 (br. s; ^{i}Pr CH), 62.0 (s; alkene CH_2), 82.5 (s; alkene CH), 103.9 (s; heterocyclic C3,5), 117.9 (septet, $^4J_{CF}$ = 4.0 Hz; $[BAr^F{}_4]^-$ *p*-C_{aryl}), 124.9 (q, $^1J_{CF}$ = 272.6 Hz; $[BAr^F{}_4]^-$ CF_3), 129.2 (qq, $^2J_{CF}$ = 31.5 Hz, $^4J_{CF}$ = 3.0 Hz; $[BAr^F{}_4]^-$ C_{aryl}-CF_3), 135.2 (m; $[BAr^F{}_4]^-$ *o*-C_{aryl}), 144.8 (s; heterocyclic C4), 160.3 (br. s; heterocyclic C2,6), 162.1 (q, $^1J_{CB}$ = 49.9 Hz (^{11}B); $[BAr^F{}_4]^-$ *i*-C_{aryl}).

^{13}C{^{1}H} SSNMR (100.66 MHz, 10 kHz spin rate, 298 K) δ 13.0-19.3 (^{i}Pr CH_3), 20.0 (alkene CH_3), 21.1 (alkene CH_3), 28.2-33.7 (^{i}Pr CH), 59.2 (alkene CH_2), 61.8 (alkene CH_2), 77.9 (alkene CH), 84.5 (alkene CH), 104.5 (heterocyclic C3,5), 105.1 (heterocyclic C3,5), 117.0–120.5 ($[BAr^F{}_4]^-$ *p*-C_{aryl}), 120.5–141.0 ($[BAr^F{}_4]^-$), 144.3 (heterocyclic C4), 161.2 (heterocyclic C2,6), 162-167 ($[BAr^F{}_4]^-$ *i*-C_{aryl}).

^{31}P{^{1}H} NMR (161.82 MHz, CD_2Cl_2, 298 K) δ 168.2 (br. d, $^2J_{PP'}$ ~ 320 Hz), 170.0 (br. d, $^2J_{PP'}$ ~ 320 Hz).

^{31}P{^{1}H} SSNMR (162.03 MHz, 10 kHz spin rate, 298 K) δ 169-178 (multiple signals).

5.14.8 *Synthesis of [(^{i}Pr-PONOP)IrH$_2$(η^2-ethene)][BAr$^F{}_4$], **42***



In situ solution-phase and solid-state[a] samples of ethene-dihydride **42** were obtained in a similar method to Section 5.14.7, substituting propene complex **35** for ethene complex **38**. Crystals of ethene-dihydride $\mathbf{42}_{xtal}$ were obtained by first taking finely powdered single-crystalline **38** (10 mg, ~7 μmol) in a Young's flask and dissolving it CH_2Cl_2 (0.5 mL). The contents of the flask were then frozen with liquid N_2 before the headspace was evacuated and repressurised with H_2 (1.0 bar). As it thawed (*i.e.* while still cold to prevent over-hydrogenation to **37**), the flask was shaken vigorously until the solution decolourised before immediately refreezing with liquid N_2 and evacuating the headspace, repressurising with argon upon thawing. The resulting pale-yellow solution was layered with pentane at 275 K to give single-crystalline $\mathbf{42}_{xtal}$ as large colourless blocks after 12 hours, which could be easily separated by hand from the minority of **38** (small orange blocks) reformed through elimination of H_2.

Note that **42** was relatively stable in solution at 298 K in the *absence* of an H_2 atmosphere, slowly losing H_2 over the course of 6-12 hours to regenerate **38**. Crystalline $\mathbf{42}_{xtal}$ was obtained in too limited a quantity for reliable microanalysis.

^{1}H NMR (600.09 MHz, CD_2Cl_2, 298 K) δ −16.30 (t, $^{2}J_{HP}$ = 10.2 Hz, 1 H; Ir-*H*), −9.56 (t, $^{2}J_{HP}$ = 17.6 Hz, 1 H; Ir-*H*), 0.89 (m, 6 H; ^{i}Pr CH_3), 1.13 (m, 6 H; ^{i}Pr CH_3), 1.24 (m, 6 H; ^{i}Pr CH_3), 1.42 (m, 6 H; ^{i}Pr CH_3), 2.59 (m, 4 H; ^{i}Pr CH), 3.49 (m, 4 H; CH_2CH_2), 6.83 (d, $^{3}J_{HH}$ = 8.2 Hz, 2 H; heterocyclic C3,5), 7.56 (s, 4 H; $[BAr^F_4]^-$ *p*-H), 7.71 (br. m, 8 H; $[BAr^F_4]^-$ *o*-H), 7.78 (t, $^{3}J_{HH}$ = 8.2 Hz, 1 H; heterocyclic C4).

^{13}C{^{1}H} NMR (150.91 MHz, CD_2Cl_2, 298 K) δ 15.2 (s; ^{i}Pr CH_3), 17.0 (s; ^{i}Pr CH_3), 17.4 (vt, $^{2}J_{CP}$ = 4.3 Hz; ^{i}Pr CH_3), 19.1 (vt, $^{2}J_{CP}$ = 5.6 Hz; ^{i}Pr CH_3), 28.4 (vt, $^{1}J_{CP}$ = 15.8 Hz; ^{i}Pr CH), 29.9 (vt, $^{1}J_{CP}$ = 14.5 Hz; ^{i}Pr CH), 57.8 (s; ethene), 103.9 (vt, $^{3}J_{CP}$ ~ 2 Hz; heterocyclic C3,5), 117.9 (septet, $^{4}J_{CF}$ = 4.0 Hz; $[BAr^F_4]^-$ *p*-C_{aryl}), 124.9 (q, $^{1}J_{CF}$ = 272.5 Hz; $[BAr^F_4]^-$ CF_3), 129.2 (qq, $^{2}J_{CF}$ = 31.5 Hz, $^{4}J_{CF}$ = 3.0 Hz; $[BAr^F_4]^-$ C_{aryl}-CF_3), 135.2 (m; $[BAr^F_4]^-$ *o*-C_{aryl}), 145.0 (s; heterocyclic C4), 160.6 (s; heterocyclic C2,6), 162.2 (q, $^{1}J_{CB}$ = 49.9 Hz (^{11}B), 16.9 (^{10}B); $[BAr^F_4]^-$ *i*-C_{aryl}).

^{13}C{^{1}H} SSNMR (100.66 MHz, 10 kHz spin rate, 298 K) δ 14.7 (^{i}Pr CH_3), 16.8 (^{i}Pr CH_3), 18.1 (^{i}Pr CH_3), 26.5 (^{i}Pr CH), 28.2 (^{i}Pr CH), 30.5 (^{i}Pr CH), 57.7 (ethene), 103.4 (heterocyclic C3,5), 116.0–119.5 ($[BAr^F_4]^-$ *p*-C_{aryl}), 120.0–137.5 ($[BAr^F_4]^-$), 143.4 (heterocyclic C4), 161.4 (heterocyclic C2,6), 163.2 ($[BAr^F_4]^-$ *i*-C_{aryl}).

^{31}P{^{1}H} NMR (242.96 MHz, CD_2Cl_2, 298 K) δ 169.1 ($^{2}J_{PP'}$ ~ 320 Hz), 169.3 ($^{2}J_{PP'}$ ~ 320 Hz).

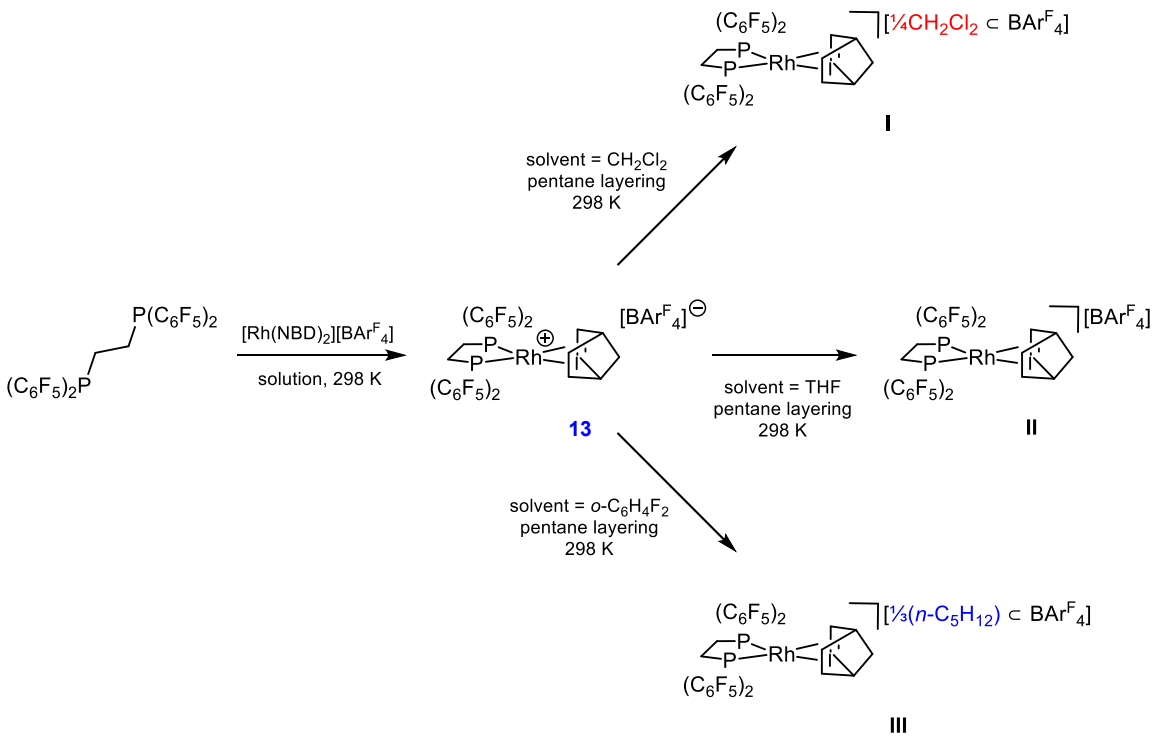
^{31}P{^{1}H} SSNMR (162.03 MHz, 10 kHz spin rate, 298 K) δ 168.9 (d, $^{2}J_{PP'}$ ~ 340 Hz), 172.7 (d, $^{2}J_{PP'}$ ~ 340 Hz).

[a] A longer SSNMR in-rotor hydrogenation time (1 bar, 298 K) of ~45 minutes was necessary in this case.

5.14.9 *Synthesis of [(dpfppe)Rh(η²,η²-NBD)][BAr$^F_4$] Morphs (**13-I,II,III**; dpfppe = (C$_6$F$_5$)$_2$P(CH$_2$)$_2$P(C$_6$F$_5$)$_2$)*

Introduced to separate Young's flasks, 1,2-bis[bis(pentafluorophenyl)phosphino]ethane (*dpfppe*; 33 mg, 43 μmol) and [Rh(η^2,η^2-NBD)$_2$][BAr$^F_4$] (50 mg, 43 μmol) were dissolved in the relevant solvent (2 × 1 mL CH_2Cl_2, 1,2-difluorobenzene or THF). With stirring at 298 K, the dpfppe solution was transferred to the [Rh(η^2,η^2-NBD)$_2$][BAr$^F_4$] solution dropwise *via* cannula, yielding a bright orange solution, and stirring was continued for one hour before the contents were layered with pentane at 298 K.

This yielded large orange prismatic crystals after 24 hours (yields obtained 70 mg (90%, CH_2Cl_2), 72 mg (92%, 1,2-difluorobenzene), 76 mg (97%, THF)). Use of CH_2Cl_2 as the solvent generated the CH_2Cl_2-containing morph **{Rh}[¼CH$_2$Cl$_2$ ⊂ BAr$^F_4$]** (**13-I**) whereas use of THF generated the non-solvent-containing morph **{Rh}[BAr$^F_4$]** (**13-II**), and use of 1,2-difluorobenzene generated the pentane-containing morph **{Rh}[⅓-(*n*-pentane) ⊂ BAr$^F_4$]** (**13-III**).



Aside from co-crystallised solvent (see proceeding Section), these structures were indistinguishable *via* solution-phase NMR spectroscopy (*vide infra*). The assignment of n_{DCM} ~ ¼ in **13-I** was an approximation based upon the most reasonable refinement of the solid-state structure; this value of n_{DCM} would be expected to give rise to a *protio*-CH_2Cl_2 integral of 0.50 H. No pentane was detected in the bulk solution-phase ^{1}H NMR spectra of **13-I**, **13-II**, or **13-II**$_{SCSC}$ (*vide infra*). The SC-SC de-encapsulation of CH_2Cl_2 from **13-I** is discussed in the proceeding Section. $n_{pentane}$ ~ ⅓ in **13-III** was informed by solution NMR spectroscopic studies as well as reasonable solid-state refinement. Crystals of **13-III** of any size (including finely ground powders) were not observed to lose pentane, since subsequent exposures to dynamic vacuum did not significantly alter the integral ratio of the pentane resonances by bulk solution-phase ^{1}H NMR spectroscopy. Pentane resonances were detected at δ 0.86 (CH_3), 1.22 (CH_2), and 1.27 (CH_2), with the latter two overlapping, giving rise to two groups of resonances in a ~1:1 integral ratio. $n_{pentane}$ ~ ⅓ would be expected to give rise to pentane resonances of integral ~2.0:2.0 H – integrals in the ranges 1.74-1.86 H and 1.87-1.99 H were noted. The solid-state structures of **13-I** and **13-III**, notwithstanding encapsulated solvent molecules, are very similar and could not be easily told apart by *sc*-XRD unit cell checks.

^{1}H NMR (400 MHz, CD_2Cl_2, 298 K) δ 1.91 (s, 2 H; NBD CH_2), 2.95 (m, 4 H; dpfppe CH_2), 4.21 (br. m, 2 H; bridgehead CH), 5.40 (br. m, 4 H; alkene CH), 7.55 (s, 4 H; $[BAr^F_4]^-$ *p*-H), 7.71 (br. quintet, $^4J_{HF}$ ~ 2.3 Hz, 8 H; $[BAr^F_4]^-$ *o*-H). *protio*-CH_2Cl_2 detected at δ 5.33; pentane detected at δ 0.86 (CH_3), 1.22 (CH_2), 1.27 (CH_2).

^{13}C{^{1}H} NMR (100.64 MHz, CD_2Cl_2, 298 K) δ 28.5 (vt, J ~ 24 Hz; dpfppe CH_2), 56.3 (s; bridgehead CH), 72.6 (vq, J ~ 3.5 Hz; NBD CH_2), 92.8 (vq, J ~ 4 Hz; olefinic CH), 102.2 (br. m; C_6F_5 *i*-C_{aryl}), 118.0 (septet, $^4J_{CF}$ = 4.0 Hz; $[BAr^F_4]^-$ *p*-C_{aryl}), 125.1 (q, $^1J_{CF}$ = 272.4 Hz; $[BAr^F_4]^-$ CF_3), 129.4 (qq, $^2J_{CF}$ = 31.5 Hz, $^4J_{CF}$ = 2.8 Hz; $[BAr^F_4]^-$ C_{aryl}-CF_3), 135.4 (s; $[BAr^F_4]^-$ *o*-C_{aryl}), 139.1 (br. dt, $^1J_{CF}$ = 259.0 Hz, J' ~ 15 Hz; C_6F_5 *o*-C_{aryl}), 145.2 (br. dt, $^1J_{CF}$ = 265.1 Hz, J' ~ 14 Hz; C_6F_5 *p*-C_{aryl}), 147.1 (br. dm, $^1J_{CF}$ = 249.2 Hz; C_6F_5 *m*-C_{aryl}), 162.3 (q, $^1J_{CB}$ = 49.8 Hz (^{11}B), 16.7 Hz (^{11}B); $[BAr^F_4]^-$ *i*-C_{aryl}).

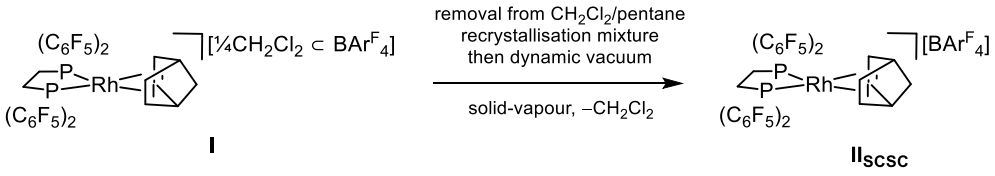
^{31}P{^{1}H} NMR (162 MHz, CD_2Cl_2, 298 K) δ 20.9 (d, $^1J_{PRh}$ = 169.0 Hz).

^{19}F{^{1}H} NMR (376.5 MHz, CD_2Cl_2, 298 K) δ –155.8 (br. dd, $^3J_{FF}$ = 20.7 Hz, $^3J_{FF}$' ~ 15 Hz; C_6F_5 *m*-F), –141.9 (t br. t, $^3J_{FF}$ ~ 21 Hz, $^4J_{FF}$ ~ 19 Hz; C_6F_5 *p*-F), –130.0 (br. d, $^3J_{FF}$ ~ 19 Hz; C_6F_5 *o*-F), –63.0 ($[BAr^F_4]^-$).

ESI-MS (CH_2Cl_2) *m*/*z* found (calculated) for $C_{33}H_{12}F_{20}P_2Rh$ $[M]^+$: 952.9117 (952.9144).

Elemental analysis found (calculated) for $C_{65}H_{24}BF_{44}P_2Rh$ (empty **13-II**): C, 43.13 (42.98); H, 1.16 (1.33); $C_{67.5}H_{30}BF_{44}P_2Rh$ (pentane-containing **13-III**): C, 43.61 (43.76); H 1.47 (1.63).

5.14.10 SC-SC Reactivity of [(dpfppe)Rh(η²,η²-NBD)][BAr$^F_4$] (13) Morphs



Once removed from the solvent mixture used to crystallise it and exposed to dynamic vacuum (p < 10^{-2} mbar, 10 minutes), smaller crystals (less than *ca.* 1 mm × 1 mm × 1 mm, or finely ground powders) of **13-I** lost CH_2Cl_2 rapidly and irreversibly in a single-crystal to single-crystal (SC-SC) fashion to generate the non-solvent-containing ('empty') morph **13-II**$_{SCSC}$. Loss of CH_2Cl_2 was confirmed by *sc*-XRD (unit cell checks on multiple individual crystals) and bulk solution-phase NMR, where no *protio*-CH_2Cl_2 was evidenced by ^{1}H NMR spectroscopy (**Figure 5.14.1**), expected at δ 5.33. All attempts to reintroduce CH_2Cl_2 vapours into crystals of **13-II**$_{SCSC}$ without dissolving were unsuccessful, indicating an irreversible process.

Larger crystals of **13-I** (greater than *ca.* 2 mm × 2 mm × 2 mm) resisted loss of CH_2Cl_2 after exposure to dynamic vacuum, with evidence for the retention of some *protio*-CH_2Cl_2 by ^{1}H NMR spectroscopy. After exposing a large crystal of **13-I** (*ca.* 3 mm × 2 mm × 1 mm) to dynamic vacuum (p < 10^{-2} mbar) for 60 minutes in total, a resonance at δ 5.33 was observed, integrating to 0.36 H relative to the adjacent NBD alkene CH peak, fixed to 4.00 H (**Figure 5.14.2**). Prolonged exposure to dynamic vacuum (8 hours in total) lead to the further diminishment of this resonance, to 0.21 H. The absence of pentane in the bulk solution-phase ^{1}H NMR spectra of **13-II**$_{SCSC}$ (**Figure 5.14.1**) or larger crystals of **13-I** as detailed above, and the resistance to depassivation of crystals of **13-III** as obtained from 1,2-difluorobenzene/pentane, altogether suggest that pentane was not present in samples of **13-I** as obtained from CH_2Cl_2/pentane in significant quantities (*i.e.* it did not co-crystallise alongside CH_2Cl_2).

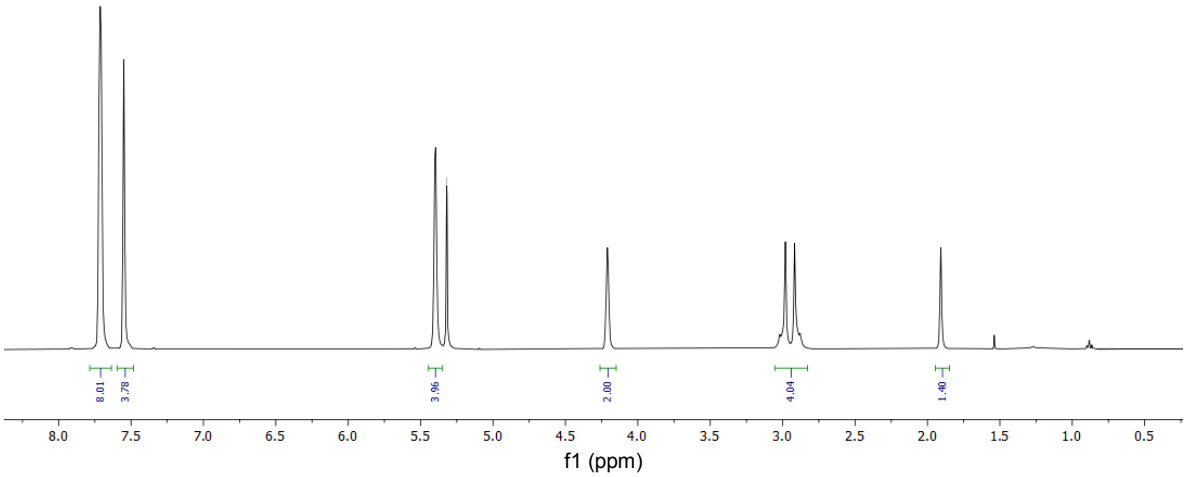


Figure 5.14.1: ^{1}H NMR spectrum (400 MHz, CD_2Cl_2, 298 K) of non-solvent-containing morph **13-II**$_{SCSC}$.

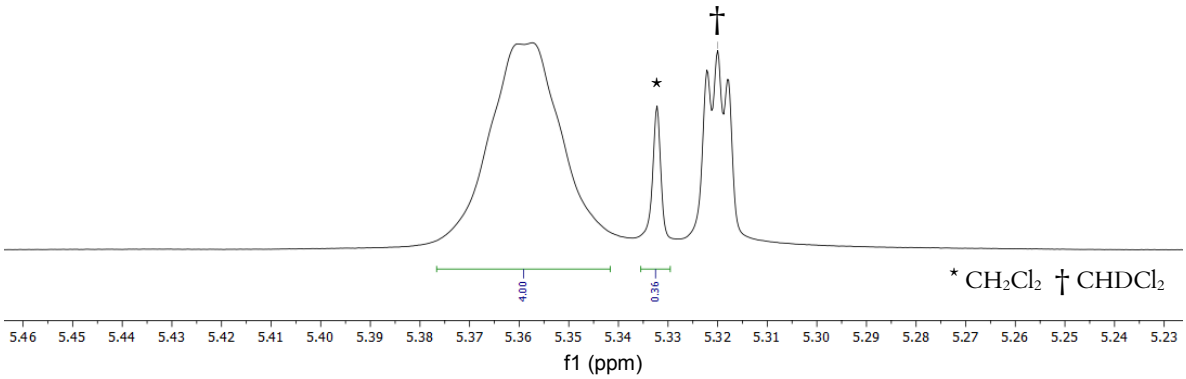


Figure 5.14.2: Zoomed ^{1}H NMR (400 MHz, CD_2Cl_2, 298 K) spectrum of a large crystal of **13-I** (*ca.* 3 mm × 2 mm × 1 mm) exposed to dynamic vacuum, showing *protio*-CH_2Cl_2 at δ 5.33 (NBD alkene CH at δ 5.36 with integral fixed to 4.0 H). The integral of 0.36 H corresponds to *ca.* 0.2 formula units; according to the crystal structure with assigned n_{DCM} ~ ¼, an integral of 0.50 H (0.25 formula units) would be expected.

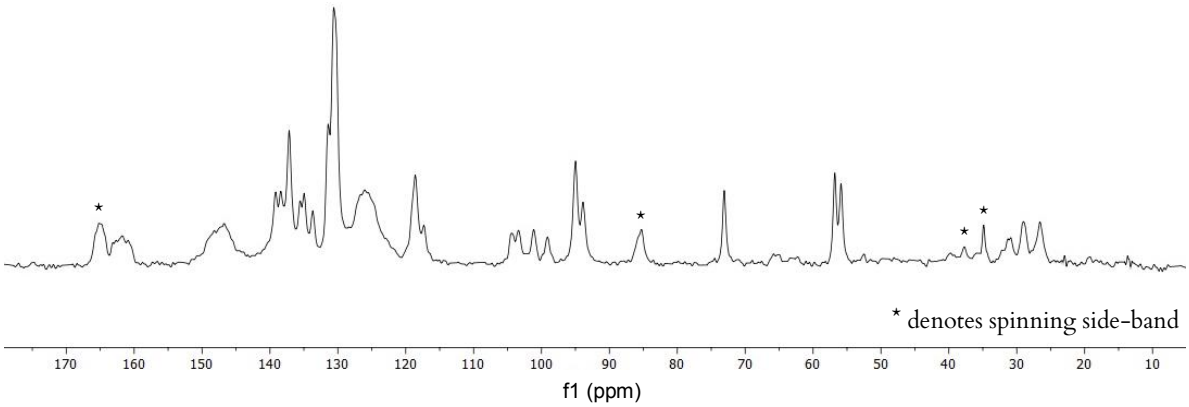


Figure 5.14.3: ^{13}C{^{1}H} SSNMR (100.66 MHz, 298 K, ν = 10 kHz) spectrum of empty morph **13-II**$_{SCSC}$.

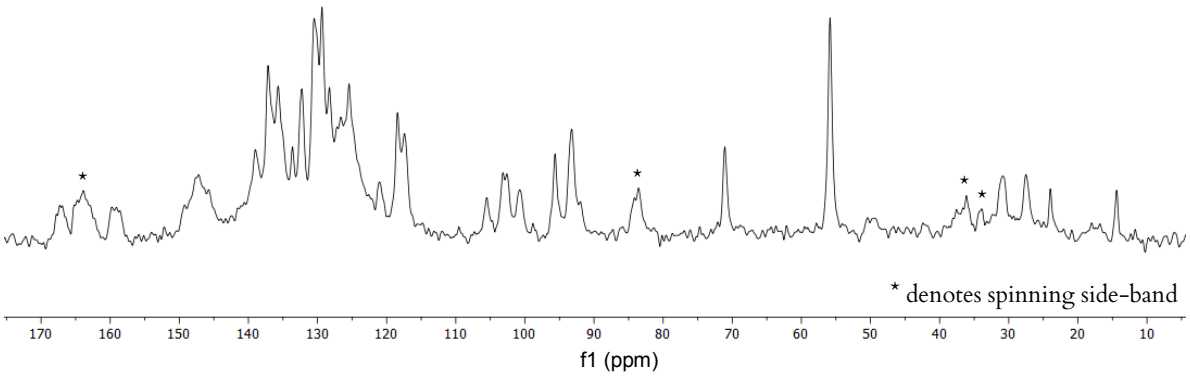
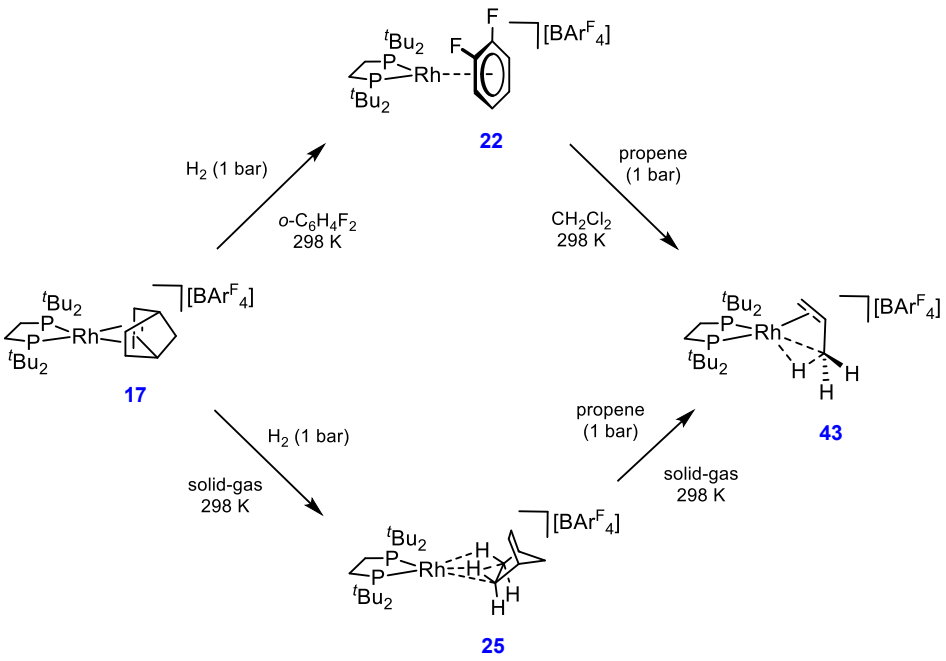


Figure 5.14.4: $^{13}C\{^{1}H\}$ SSNMR (100.66 MHz, 298 K, ν = 10 kHz) spectrum of **13-III**.

5.15 Synthetic Procedures: Chapter 4

*5.15.1 Synthesis of [(dtbpe)Rh(η²-propene)][BAr$^F_4$], **43***



Powdered crystalline **17** (25 mg, 18 μmol) was introduced to a Young's flask and dissolved in 1,2-difluorobenzene (2 mL). The solution was frozen with liquid N_2 and the flask was evacuated before re-pressurisation with H_2 (1.0 bar). After thawing and 30 minutes of stirring at 298 K, all volatiles were removed *in vacuo* to give the 1,2-difluorobenzene adduct [(dtbpe)Rh(η^6-1,2-diflurobenzene)][BAr$^F_4$] (**22**) *in situ* as an orange solid. This was then dissolved in CH_2Cl_2 (2 mL).

The resulting deep orange solution was refrozen with liquid N_2 and the headspace evacuated ($p < 10^{-2}$ mbar) before the solution was allowed to thaw under a static vacuum. The flask was then repressurised with a charge of propene (1.0 bar), sealed, and shaken vigorously. This process was repeated twice more, until a headspace pressure of ~1.0 bar was maintained. The solution was stirred at 298 K for 30 minutes, over which time the solution became a slightly lighter red-orange colour. After this time had elapsed, was concentrated *in vacuo* by ~50% (thus also removing the propene atmosphere but still leaving much excess propene dissolved) and repressurised under N_2 before layering with pentane at 298 K, yielding [(dtbpe)Rh(η^2-propene)][BAr^F_4] (**43**; 23 mg, 95%) as orange-red plates amenable to *sc*-XRD analysis.

Propene complex **43** was also accessible *via* a solid-gas route: finely ground **17** (~10 mg, ~7 μmol) was introduced to an NMR tube fitted with a Young's tap and exposed to H_2 (1.0 bar) for 15 minutes (darkening from red to deep reddish-brown), before evacuation ($p < 10^{-2}$ mbar) and repressurisation with propene gas (1.0 bar), rapidly generating a pale orange powder. Solution-phase NMR spectroscopic characterisation of this solid was undertaken in CD_2Cl_2 at 185 K, the requisite solvent distilled over the solid under vacuum ($p < 10^{-4}$ mbar) with the assistance of liquid N_2. Propene complex **43**, in absence of a propene atmosphere, decomposed rapidly in CD_2Cl_2 solution at 298 K to give the C–Cl-activated species **24** (Section 5.13.11),[a] hence no solution-phase NMR data is provided here at 298 K. Solution-phase NMR data for crystalline **43** as produced by the solution-phase method above was indistinguishable to that acquired for **43** obtained *via* the solid-gas route, provided below. Elemental microanalysis data could be obtained for crystalline **43**, but due to the solution-phase instability of **43** at 298 K, no ESI-MS data were obtained.

^{1}H NMR (500.23 MHz, CD_2Cl_2, 185 K) δ −0.64 (s, 3 H; propene CH_3), 1.05 (d, $^3J_{HP}$ = 13.6 Hz, 9 H; ^{t}Bu CH_3), 1.18 (d, $^3J_{HP}$ = 13.6 Hz, 18 H; ^{t}Bu CH_3), 1.26 (d, $^3J_{HP}$ = 13.6 Hz, 9 H; ^{t}Bu CH_3), 1.66 (br., 1 H; dtbpe CH_2), 1.84–2.05 (br., 3 H; dtbpe CH_2), 3.36 (d, $^3J_{HH}$ = 14.0 Hz, 1 H; propene CH_2), 4.87 (d, $^3J_{HH}$ = 7.0 Hz, 1 H; propene CH_2), 4.96 (br. m, $^3J_{HH}$ = 14.0 Hz, $^3J_{HH}$' = 7.0 Hz, $^3J_{HH}$" ≈ 5.0 Hz), 7.53 (s, 4H; [BAr^F_4]$^-$ *p*-H), 7.71 (s, 8H; [BAr^F_4]$^-$ *o*-H). Recalcitrant NBA observed at δ 1.07, 1.37, 2.09.

^{13}C{^{1}H} NMR (125.80 MHz, CD_2Cl_2, 185 K) δ 10.4 (br. d, J ≈ 8 Hz; propene CH_3), 20.1 (br.; dtbpe CH_2), 25.4 (br.; dtbpe CH_2), 29.1 (d, $^2J_{CP}$ = 33 Hz; ^{t}Bu CH_3), 29.7 (d, $^2J_{CP}$ = 34 Hz; ^{t}Bu CH_3), 36.1 (d, $^1J_{CP}$ = 19 Hz; ^{t}Bu C_Q), 36.7 (d, $^1J_{CP}$ = 20 Hz; ^{t}Bu C_Q), 37.4 (d, $^1J_{CP}$ = 21 Hz; ^{t}Bu C_Q), 37.9 (d, $^1J_{CP}$ ≈ 22 Hz; ^{t}Bu C_Q), 74.8 (s; propene CH_2), 96.2 (s; propene CH), 117.9 (septet, $^4J_{CF}$ = 4.0 Hz; [BAr^F_4]$^-$ *p*-C_{aryl}), 124.9 (q, $^1J_{CF}$ = 272.6 Hz;

[a] Note that **43** was sufficiently stable at 298 K in CH_2Cl_2 in the *presence* of a large excess of dissolved propene such that crystallisation under these conditions was possible (see preceding paragraph).

$[BAr^F{}_4]^-$ CF_3), 129.2 (qq, $^2J_{CF}$ = 31.5 Hz, $^4J_{CF}$ = 3.0 Hz; $[BAr^F{}_4]^-$ C_{aryl}-CF_3), 135.2 (m; $[BAr^F{}_4]^-$ *o*-C_{aryl}), 162.1 (q, $^1J_{CB}$ = 49.9 Hz (^{11}B); $[BAr^F{}_4]^-$ *i*-C_{aryl}). Recalcitrant NBA observed at δ 29.1, 35.9, 37.8.

$^{13}C\{^1H\}$ SSNMR* (100.6 MHz, 10 kHz spin rate, 175 K) δ 20-40 (dtbpe + recalcitrant NBA), 71.5–78.0 (alkene CH_2), 95.3 (alkene CH), 96.7 (alkene CH), 115–140 ($[BAr^F{}_4]^-$), 160–168 ($[BAr^F{}_4]^-$ *i*-C_{aryl}).

$^{31}P\{^1H\}$ NMR (202.53 MHz, CD_2Cl_2, 185 K) δ 112.3 (br. d, $^2J_{PRh}$ ≈ 160 Hz; P *trans* to π), 116.4 (br. d, $^2J_{PRh}$ ≈ 210 Hz; P *trans* to σ-CH_3).

$^{31}P\{^1H\}$ SSNMR* (161.9 MHz, 10 kHz spin rate, 298 K) δ 118.5 (br. s, $\nu_{½}$ ~ 650 Hz).

$^{31}P\{^1H\}$ SSNMR* (161.9 MHz, 10 kHz spin rate, 175 K) δ 114.9 (m, $\nu_{½}$ ~ 600 Hz), 119.0 (m, $\nu_{½}$ ~ 600 Hz).

Elemental analysis found (calculated) for $C_{53}H_{57}BF_{24}P_2Rh$: C 47.79 (47.98); H 4.42 (4.41).

*pertains to material obtained *in situ* by the solid-state route, although SSNMR data pertaining to recrystallised material was indistinguishable by this method (see text).

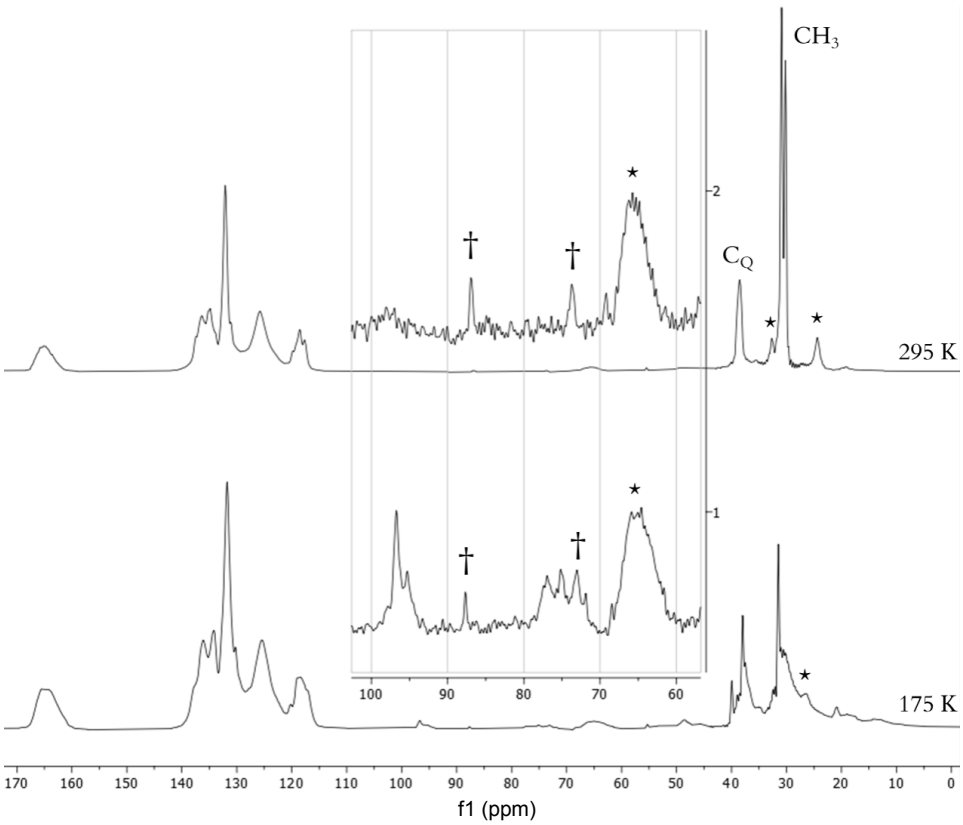


Figure 5.15.1: $^{13}C\{^1H\}$ VT-SSNMR (100.66 MHz, ν = 10 kHz) spectrum of *in situ*-generated propene complex **43** with a zoomed insert of the region δ ~60–100. *indicates spinning side-bands. †indicates unreacted **17** (~4%).

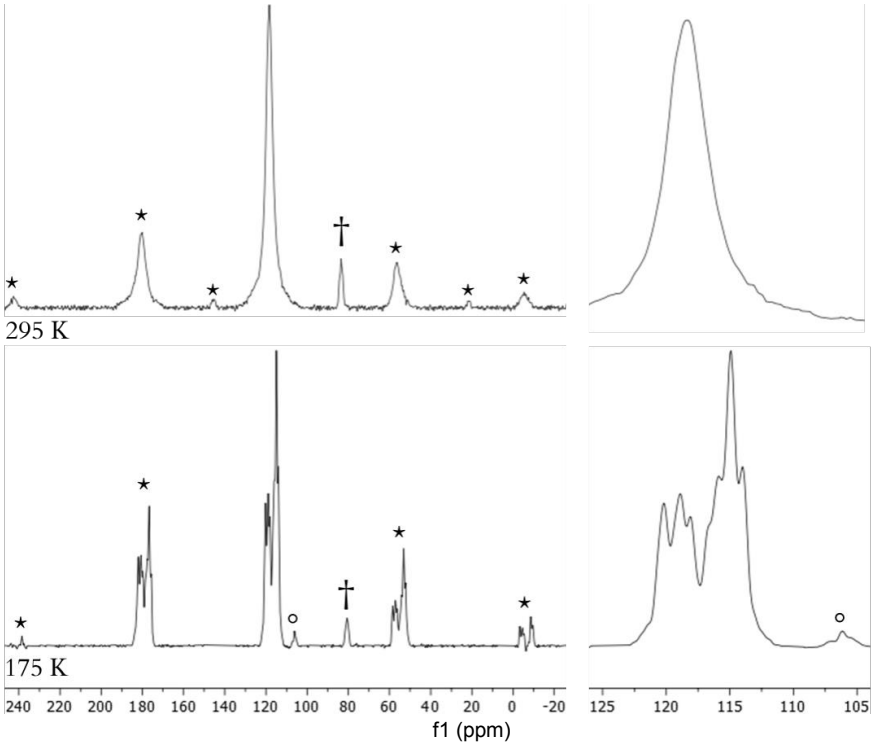
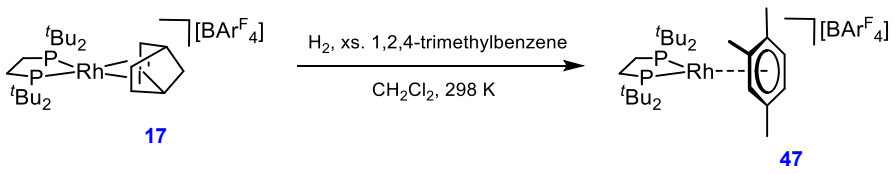


Figure 5.15.2: $^{13}C\{^{1}H\}$ VT-SSNMR (162.03 MHz, ν = 10 kHz) spectrum of *in situ*-generated propene complex **43**. *indicates spinning side-bands. †indicates unreacted **17** (~4%). °indicates an unknown contaminant.

5.15.2 Independent Solution-Phase Syntheses of [(dtbpe)Rh(η⁶-1,2,4-trimethylbenzene)][BAr$^{F}_{4}$], 47



17 (50 mg, 36 μmol) was taken in a Young's flask and dissolved in CH_2Cl_2 (5 mL), to which 1,2,4-trimethylbenzene (0.1 mL, ~730 μmol, ~20 eq.) was added. The solution was frozen with liquid N_2 and the flask was evacuated and repressurised with H_2 (1.0 bar) before thawing and stirring at 298 K for 5 minutes, over which time the initially dark orange solution lightened. After this, the solution was refrozen with liquid N_2, the H_2 atmosphere was removed under dynamic vacuum and replaced with argon, and the solution was thawed, thereafter layering with hexane to yield pale orange plates, [(dtbpe)Rh(η^6-1,2,4-trimethylbenzene)][BAr$^{F}_{4}$] (**47**; 44 mg, 87%) after 16 hours.

sc-XRD data obtained from crystals of **47** obtained by this method were of insufficient quality for a satisfactory structural solution, serving only to confirm connectivity (**Figure 5.15.3**), due to the combination of a large unit cell (12,131.4 Å^3) and poor diffraction below ~1.0 Å. Attempts to achieve higher-quality crystals were not successful.

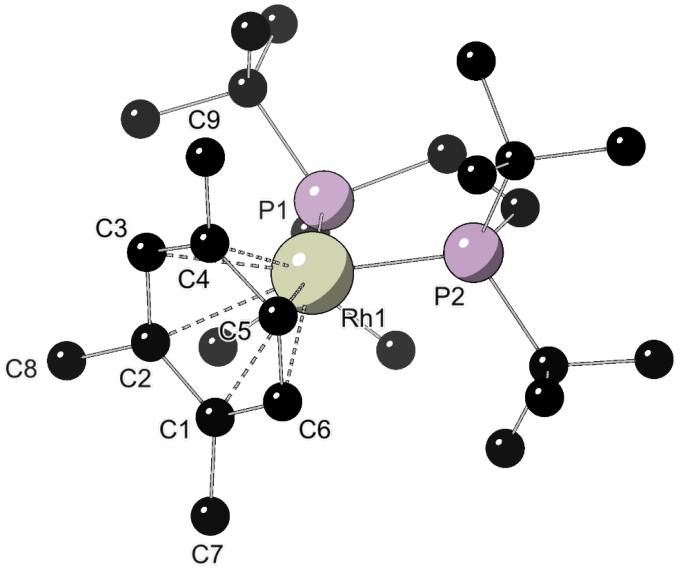


Figure 5.15.3: Solid-state structure of **47** (one of two symmetry independent cationic fragments) as recrystallised from CH_2Cl_2/pentane. Anions and H atoms omitted for clarity. Atoms are represented isotropically due to the low quality of the structural information (R_1 ~ 10.0%).

^{1}H NMR (500.23 MHz, CD_2Cl_2, 298 K) δ 1.20 (d, $^3J_{HP}$ = 3.8 Hz, 18 H; ^{t}Bu CH_3), 1.23 (d, $^3J_{HP}$ = 3.8 Hz, 18 H; ^{t}Bu CH_3), 1.48 (br., 2 H; dtbpe CH_2), 1.90 (br., 3 H; dtbpe CH_2), 2.19 (s, 3 H; arene CH_3), 2.24 (s, 3 H; arene CH_3), 2.41 (s, 3 H; arene CH_3), 5.98 (s, 1 H; arene CH), 5.99 (d, $^3J_{HH}$ = 6.5 Hz, 1 H; arene CH), 6.31 (d, $^3J_{HH}$ = 6.5 Hz, 1 H; arene CH), 7.53 (s, 4H; $[BAr^F{}_4]^-$ *p*-H), 7.71 (s, 8H; $[BAr^F{}_4]^-$ *o*-H).

^{13}C{^{1}H} NMR (150.91 MHz, CD_2Cl_2, 298 K) δ 18.7 (s; arene CH_3), 19.8 (s; arene CH_3), 20.7 (s; arene CH_3), 23.9 (m; dtbpe CH_2), 30.5 (m; ^{t}Bu CH_3), 38.1 (m; ^{t}Bu C_Q), 38.6 (m; ^{t}Bu C_Q), 92.5 (m; arene CH), 98.2 (m; arene CH), 102.1 (arene CH), 117.9 (septet, $^4J_{CF}$ = 4.0 Hz; $[BAr^F{}_4]^-$ *p*-C_{aryl}), 120.1 (m; arene C_Q), 121.9 (m; arene C_Q), 123.8 (m; arene C_Q), 124.9 (q, $^1J_{CF}$ = 272.6 Hz; $[BAr^F{}_4]^-$ CF_3), 129.2 (qq, $^2J_{CF}$ = 31.5 Hz, $^4J_{CF}$ = 3.0 Hz; $[BAr^F{}_4]^-$ C_{aryl}-CF_3), 135.2 (m; $[BAr^F{}_4]^-$ *o*-C_{aryl}), 162.1 (q, $^1J_{CB}$ = 49.9 Hz (^{11}B); $[BAr^F{}_4]^-$ *i*-C_{aryl}).

^{31}P{^{1}H} NMR (242.95 MHz, CD_2Cl_2, 298 K) δ 116.3 (d, $^1J_{PRh}$ = 208.5 Hz).

ESI-MS (CH_2Cl_2) *m*/*z* found (calculated) for $C_{27}H_{52}P_2Rh$ $[M]^+$: 541.2598 (541.2594).

Elemental analysis found (calculated) for $C_{59}H_{64}BF_{24}P_2Rh$: C 50.40 (50.45); H 4.51 (4.59).

5.16 Single-Crystal X-ray Diffractometric Data

Single-crystal X-ray diffraction data were collected (ω-scans) on (Chapters 2 and 3) Oxford Diffraction/Agilent SuperNova diffractometers with Cu-K_α (λ = 1.54184 Å) radiation equipped with an N_2 gas Oxford Cryosystems Cryostream unit at the University of Oxford Chemical Crystallography Service, or (Chapters 3 and 4) at the University of York. Diffraction images from raw frame data were reduced using CrysAlisPro. The structures were solved using SHELXT[25] and refined to convergence on F^2 and against all independent reflections by full-matrix least-squares using SHELXL[26] in combination with the GUI OLEX2[27] program. All non-hydrogen atoms were refined anisotropically; hydrogen atoms were geometrically placed unless otherwise stated (see specific details for each molecular structure in the text) and allowed to ride on their parent atoms. In several structures some of the CF_3 groups on the $[BAr^F_4]^-$ anions were disordered and modelled over two domains, and restrained to maintain sensible geometries. Distances and angles were calculated using the full covariance matrix. Selected crystallographic data and refinement data are summarized in the text. Many of the structures provided in Chapter 2 have already been published;[1,15] those which have not are summarised in the tables on the following pages, in addition to the unreported structures detailed in Chapters 3 and 4.

In situ X-ray diffractometry on the I19 EH2 beamline[28] at the Diamond Light Source was carried out similarly to specifications outlined in greater detail previously.[29,30] Sample crystals of **35** were glued to sample mounts (mitogen M2-L25SP-30) with minimal glue in an argon-filled glovebox and subsequently secured within a 1 mm quartz capillary. The assembly was then connected to the gas cell, which has a self-sealing quick connect valve to ensure retention of inert atmosphere. *In situ* solid-state structures were collected on a four circle Newport diffractometer equipped with a Pilatus 300K detector with synchrotron-source Ag-edge radiation (λ = 0.4859 Å). The cell was first evacuated and a test structure collected before backfilling with H_2 (2.0 bar) at 275 K. A collection strategy consisting of four phi and omega sweeps was used to obtain structures before and after H_2 addition.

Chapter 2	**10**	**14**	**15**·H_2O
Formula	$C_{63}H_{64}BF_{24}P_2Rh$	$C_{52}H_{51}BF_{24}NP_2Rh$	$C_{55}H_{59}BF_{24}NOP_2Rh$
M	1452.80	1321.69	1381.69
Crystal System	Triclinic	Triclinic	Tetragonal
Space group	$P\bar{1}$	$P1$	$P4_32_12$
T [K]	150.00(18)	150.01(10)	110.00(10)
a [Å]	12.6572(3)	10.6593(2)	13.18250(10)
b [Å]	12.6577(3)	14.1454(3)	13.18250(10)
c [Å]	19.6534(3)	18.7920(3)	33.8825(4)
α [°]	89.042(2)	82.650(2)	90
β [°]	89.055(2)	87.227(2)	90
γ [°]	87.211(2)	87.341(2)	90
V [Å^3]	3144.14(12)	2804.57(9)	5888.04(11)
Z	2	2	4
ρ_{calc} [g cm^{-3}]	1.535	1.565	1.559
μ [mm^{-1}]	3.674	4.060	3.907
2θ range [°]	6.992 to 152.496	4.746 to 154.504	7.196 to 141.89
Reflns collected	38417	52269	12255
R_{int}	0.0265	0.0222	0.0241
Compl. 67.684°	100%	100%	99.9%
Data/restr/param	12988/620/953	22060/648/1627	5483/408/482
R_1 [$I > 2\sigma(I)$]	0.0361	0.0386	0.0280
wR_2 [all data]	0.0935	0.1073	0.0690
GoF	1.037	1.015	1.048
Larg. pk/hole [eÅ^{-3}]	0.64/–0.46	1.29/–0.56	0.40/–0.55

Table 5.16.1: Selected crystallographic and refinement data.

Chapter 3	**35** (150 K)	**35** (298 K)	**35**·CH_2Cl_2
Formula	$C_{52}H_{49}BF_{24}IrNO_2P_2$	$C_{52}H_{49}BF_{24}IrNO_2P_2$	$C_{52.5}H_{50}BCl_{0.93}F_{24}IrNO_2P_2$
M	1440.87	1440.57	1480.15
Crystal System	Triclinic	Triclinic	Monoclinic
Space group	$P\bar{1}$	$P\bar{1}$	$C2/c$
T [K]	150.00(10)	298.00(14)	150.00(10)
a [Å]	12.0828(2)	12.3216(4)	16.8546(2)
b [Å]	12.3637(2)	12.5391(4)	19.4509(2)
c [Å]	20.0374(3)	20.1903(4)	35.6895(3)
α [°]	102.6640(10)	77.466(2)	90
β [°]	100.4020(10)	79.734(2)	90.9030(10)
γ [°]	90.1870(10)	89.951(3)	90
V [Å^3]	2869.67(8)	2994.02(15)	11698.9(2)
Z	2	2	8
ρ_{calc} [g cm^{-3}]	1.668	1.598	1.681
μ [mm^{-1}]	6.108	5.854	6.391
2θ range [°]	7.336 to 142.046	7.228 to 142.15	7.342 to 142.292
Reflns collected	53008	21278	39294
R_{int}	0.0198	0.0219	0.0261
Compl. 67.684°	100%	99.7%	99.8%
Data/restr/param	10985/482/888	11325/641/927	11199/459/888
R_1 [$I > 2\sigma(I)$]	0.0190	0.0292	0.0302
wR_2 [all data]	0.0477	0.0770	0.0719
GoF	1.061	1.036	1.102
Larg. pk/hole [eÅ^{-3}]	0.76/–0.70	0.74/–0.94	0.55/–0.85

Table 5.16.2: Selected crystallographic and refinement data.

Chapter 3	**36**	**38**	**40**
Formula	$C_{57}H_{55}BF_{24}IrNO_2P_2$	$C_{51}H_{47}BF_{24}IrNO_2P_2$	$C_{52}H_{57}B_2F_{24}IrN_2O_2P_2$
M	1506.97	1426.84	1473.75
Crystal System	Triclinic	Monoclinic	Monoclinic
Space group	$P\bar{1}$	$P2_1/c$	$P2_1/n$
T [K]	150.0(2)	109.95(10)	150.05(10)
a [Å]	12.9568(2)	12.13239(18)	12.54330(10)
b [Å]	13.0286(2)	12.03382(19)	26.5647(2)
c [Å]	19.6838(3)	38.8564(5)	19.1920(2)
α [°]	73.7910(10)	90	90
β [°]	73.9640(10)	96.4744(14)	109.0180(10)
γ [°]	83.3290(10)	90	90
V [Å^3]	3063.82(8)	5636.82(14)	6045.89(10)
Z	2	4	4
ρ_{calc} [g cm^{-3}]	1.634	1.681	1.619
μ [mm^{-1}]	5.751	6.213	5.813
2θ range [°]	7.106 to 152.404	7.334 to 142.388	7.46 to 142.664
Reflns collected	86798	21720	93686
R_{int}	0.0384	0.0311	0.0443
Compl. 67.684°	100%	99.6%	99.9%
Data/restr/param	12726/657/941	10688/505/859	11637/390/881
R_1 [$I > 2\sigma(I)$]	0.0333	0.0387	0.0260
wR_2 [all data]	0.0869	0.0783	0.0624
GoF	1.051	1.160	1.031
Larg. pk/hole [eÅ^{-3}]	1.51/–0.40	0.78/–0.80	0.94/–1.28

Table 5.16.3: Selected crystallographic and refinement data.

Chapter 3	**41*** (I19)[a]	**41**$_{SCSC}$ (I19)[b]	**42**$_{xtal}$
Formula	$C_{52}H_{51}BF_{24}IrNO_2P_2$	$C_{52}H_{51}BF_{24}IrNO_2P_2$	$C_{51}H_{49}BF_{24}IrNO_2P_2$
M	1442.88	1442.90	1428.86
Crystal System	Monoclinic	Triclinic	Triclinic
Space group	$C2/c$	$P\bar{1}$	$P\bar{1}$
T [K]	275	275	149.9(2)
a [Å]	38.540(3)	12.5277(19)	13.3544(4)
b [Å]	12.7865(9)	12.8255(17)	13.3678(4)
c [Å]	23.894(2)	19.5074(17)	16.1642(5)
α [°]	90	104.711(10)	88.586(2)
β [°]	99.035(8)	100.421(11)	82.217(2)
γ [°]	90	90.094(12)	85.800(2)
V [Å^3]	11628.6(16)	2977.8(7)	2851.04(15)
Z	8	2	2
ρ_{calc} [g cm^{-3}]	1.646	1.600	1.664
μ [mm^{-1}]	0.931	0.909	6.142
2θ range [°]	3.092 to 28.116	2.942 to 28.122	6.63 to 134.16
Reflns collected	49397	25916	26472
R_{int}	0.1461	0.1259	0.0278
Compl. 67.684°	99.4%	98.7%	100%
Data/restr/param	6040/675/898	6154/972/969	10181/422/855
R_1 [$I > 2\sigma(I)$]	0.0944	0.1497	0.0321
wR_2 [all data]	0.2370	0.4191	0.0831
GoF	1.114	1.596	1.058
Larg. pk/hole [eÅ^{-3}]	1.92/-0.63	2.71/-1.11	0.93/-0.49

Table 5.16.4: Selected crystallographic and refinement data.

[a] This structure is the second (intermediate/metastable) on-beamline structure in the SC-SC-SC transformation sequence originating from the solid-gas hydrogenation of crystalline propene complex **35**, discussed in Section 3.2.4.
[b] This structure is the third on-beamline structure in the same sequence. Both I19 datasets given here are *preliminary* structural solutions, and both give clear indications of an equatorial-to-axial rearrangement.

Chapter 3	**13-I**	**13-II**	**13-II$_{SCSC}$**
Formula	$C_{65.25}H_{24.5}BCl_{0.5}F_{44}P_2Rh$	$C_{65}H_{24}BF_{44}P_2Rh$	$C_{65}H_{24}BF_{44}P_2Rh$
M	1837.73	1816.50	1816.50
Crystal System	Triclinic	Triclinic	Triclinic
Space group	$P\bar{1}$	$P\bar{1}$	$P\bar{1}$
T [K]	150.00(10)	150.00(10)	150.01(12)
a [Å]	12.3599(2)	12.1327(5)	12.1404(2)
b [Å]	14.0345(3)	14.8905(6)	14.8801(3)
c [Å]	20.4886(4)	19.6485(8)	19.6360(3)
α [°]	85.648(2)	98.126(3)	98.105(2)
β [°]	81.526(2)	102.350(4)	102.364(2)
γ [°]	80.998(2)	99.011(3)	99.003(2)
V [Å^3]	3466.88(12)	3368.1(2)	3365.85(11)
Z	2	2	2
ρ_{calc} [g cm^{-3}]	1.760	1.791	1.792
μ [mm^{-1}]	4.097	4.030	4.033
2θ range [°]	7.932 to 154.526	6.994 to 142.176	4.684 to 153.178
Reflns collected	65818	24398	50803
R_{int}	0.0324	0.0238	0.0258
Compl. 67.684°	99.9%	99.9%	100%
Data/restr/param	14565/301/1101	12778/877/1214	13995/666/1158
R_1 [$I > 2\sigma(I)$]	0.0350	0.0315	0.0331
wR_2 [all data]	0.1029	0.0792	0.0892
GoF	1.061	1.041	1.034
Larg. pk/hole [eÅ^{-3}]	0.96/–0.41	0.58/–0.42	1.30/–0.65

Table 5.16.5: Selected crystallographic and refinement data.

Chapters 3 and 4	**13–III**	**43**
Formula	$C_{66.67}H_{28.01}BF_{44}P_2Rh$	$C_{54}H_{60}BCl_2F_{24}P_2Rh$
M	1840.60	1411.58
Crystal System	Triclinic	Tetragonal
Space group	$P\bar{1}$	$P4_12_12$
T [K]	150.00(10)	110.00(10)
a [Å]	12.3695(5)	13.15540(10)
b [Å]	13.9884(5)	13.15540(10)
c [Å]	20.5021(6)	69.8799(5)
α [°]	85.173(3)	90
β [°]	81.140(3)	90
γ [°]	80.922(3)	90
V [Å^3]	3454.7(2)	12093.7(2)
Z	2	8
ρ_{calc} [g cm^{-3}]	1.769	1.551
μ [mm^{-1}]	3.938	4.593
2θ range [°]	7.312 to 142.458	6.838 to 133.182
Reflns collected	24767	105812
R_{int}	0.0236	0.0712
Compl. 67.684°	99.9%	100%
Data/restr/param	13080/434/1168	10698/1004/966
R_1 [$I > 2\sigma(I)$]	0.0359	0.0889
wR_2 [all data]	0.1038	0.1970
GoF	1.020	1.171
Larg. pk/hole [eÅ^{-3}]	0.73/–0.49	1.01/–0.94

Table 5.16.6: Selected crystallographic and refinement data.

5.17 References

[1] A. J. Martínez-Martínez, C. G. Royle, S. K. Furfari, K. Suriye, A. S. Weller, *ACS Catalysis* **2020**, *10*, 1984–1992.

[2] A. J. Martínez-Martínez, A. S. Weller, *Dalton Transactions* **2019**, *48*, 3551–3554.

[3] H. Salem, L. J. W. Shimon, Y. Diskin-Posner, G. Leitus, Y. Ben-David, D. Milstein, *Organometallics* **2009**, *28*, 4791–4806.

[4] A. Johnson, C. G. Royle, C. N. Brodie, A. J. Martínez-Martínez, S. B. Duckett, A. S. Weller, *Inorganic Chemistry* **2021**, *60*, 13903–13912.

[5] E. Molinos, S. K. Brayshaw, G. Kociok-Köhn, A. S. Weller, *Dalton Transactions* **2007**, 4829–4844.

[6] D. H. Woodmansee, M.-A. Müller, M. Neuburger, A. Pfaltz, *Chemical Science* **2010**, *1*, 72–78.

[7] K.-R. Pörschke, C. Pluta, B. Proft, F. Lutz, C. Krüger, *Zeitschrift für Naturforschung B* **1993**, *48*, 608.

[8] K. Wurst, J. Strähle, *Zeitschrift für Naturforschung B* **1993**, *48*, 425–430.

[9] J. S. Ritch, T. Chivers, D. J. Eisler, H. M. Tuononen, *Chemistry – A European Journal* **2007**, *13*, 4643–4653.

[10] G. Giordano, R. H. Crabtree, R. M. Heintz, D. Forster, D. E. Morris, *Inorganic Syntheses* **1979**, *19*, 218–220.

[11] E. W. Abel, M. A. Bennett, G. Wilkinson, *Journal of the Chemical Society (Resumed)* **1959**, 3178–3182.

[12] S. D. Pike, F. M. Chadwick, N. H. Rees, M. P. Scott, A. S. Weller, T. Krämer, S. A. Macgregor, *Journal of the American Chemical Society* **2015**, *137*, 820–833.

[13] A. J. Martínez-Martínez, B. E. Tegner, A. I. McKay, A. J. Bukvic, N. H. Rees, G. J. Tizzard, S. J. Coles, M. R. Warren, S. A. Macgregor, A. S. Weller, *Journal of the American Chemical Society* **2018**, *140*, 14958–14970.

[14] A. I. McKay, T. Krämer, N. H. Rees, A. L. Thompson, K. E. Christensen, S. A. Macgregor, A. S. Weller, *Organometallics* **2017**, *36*, 22–25.

[15] S. K. Furfari, B. E. Tegner, A. L. Burnage, L. R. Doyle, A. J. Bukvic, S. A. Macgregor, A. S. Weller, *Chemistry – A European Journal* **2021**, *27*, 3177–3183.

[16] F. M. Chadwick, A. I. McKay, A. J. Martinez-Martinez, N. H. Rees, T. Krämer, S. A. Macgregor, A. S. Weller, *Chemical Science* **2017**, *8*, 6014–6029.

[17] O. B. Peersen, X. L. Wu, I. Kustanovich, S. O. Smith, *Journal of Magnetic Resonance, Series A* **1993**, *104*, 334–339.

[18] W. L. Earl, D. L. Vanderhart, *Journal of Magnetic Resonance (1969)* **1982**, *48*, 35–54.

[19] A. T. Lubben, J. S. McIndoe, A. S. Weller, *Organometallics* **2008**, *27*, 3303–3306.

[20] A. J. Martínez-Martínez, N. H. Rees, A. S. Weller, *Angewandte Chemie International Edition* **2019**, *58*, 16873–16877.

[21] J. S. Ritch, T. Chivers, K. Ahmad, M. Afzaal, P. O'Brien, *Inorganic Chemistry* **2010**, *49*, 1198–1205.

[22] M. T. Whited, A. J. Kosanovich, D. E. Janzen, *Organometallics* **2014**, *33*, 1416–1422.

[23] X. L. Luo, R. H. Crabtree, *Journal of the American Chemical Society* **1990**, *112*, 6912–6918.

[24] R. H. Crabtree, D. G. Hamilton, *Journal of the American Chemical Society* **1986**, *108*, 3124–3125.

[25] G. Sheldrick, *Acta Crystallographica Section A* **2015**, *71*, 3–8.

[26] G. Sheldrick, *Acta Crystallographica Section C* **2015**, *71*, 3–8.

[27] O. v Dolomanov, L. J. Bourhis, R. J. Gildea, J. A. K. Howard, H. Puschmann, *Journal of Applied Crystallography* **2009**, *42*, 339–341.

[28] H. Nowell, S. A. Barnett, K. E. Christensen, S. J. Teat, D. R. Allan, *Journal of Synchrotron Radiation* **2012**, *19*, 435–441.

[29] A. I. McKay, A. J. Bukvic, B. E. Tegner, A. L. Burnage, A. J. Martínez-Martínez, N. H. Rees, S. A. Macgregor, A. S. Weller, *Journal of the American Chemical Society* **2019**, *141*, 11700–11712.

[30] A. J. Bukvic, A. L. Burnage, G. J. Tizzard, A. J. Martínez-Martínez, A. I. McKay, N. H. Rees, B. E. Tegner, T. Krämer, H. Fish, M. R. Warren, S. J. Coles, S. A. Macgregor, A. S. Weller, *Journal of the American Chemical Society* **2021**, *143*, 5106–5120.

This page intentionally left blank.

6 Future Directions

This short section of the thesis is intended for the discussion of further lines of inquiry for all three research-based chapters (2-4), which could be undertaken in the future given more time for wider and deeper understandings of these areas of research.

6.1 Chapter 2: Future Directions for Solid-Gas Catalytic Alkene Isomerisation

Due to the exceptionally wide range of SMOM catalyst lifetimes, turnover frequencies and *cis*/*trans* selectivities discussed in this Chapter obtained only by subtle variation of the chelate, further exploration of this chemical space is warranted to gain a wider understanding of the factors influencing productivity and lifetime. The P_2N_1-type systems (**14**-**16**) described at the end of the chapter represent a 'taste' of this direction, making use of a ligand system departing from the P_2C_n paradigm and producing a set of on-stream characteristics significantly divergent from the P_2C_2-type systems, chiefly SMOMs **1** and **17**.

This exploration process has the ultimate aim of prolonged (>100 hours) on-stream lifetimes and high isomer selectivity. Bulkier R-groups (*e.g.* 1-adamantyl)[1] or different anions (*e.g.* **Figure 6.1.1**)[2,3] may be entertained to prevent deactivation, either by physical deformation or by chemical quenching (avoiding the solid-state formation of a bridging hydride or an Ar^F-complex). Introducing the $\{(P_2)Rh\}^+$ catalytic nuclei into a MOF-like framework[4] may improve physical and chemical stability for SMOM-flow.

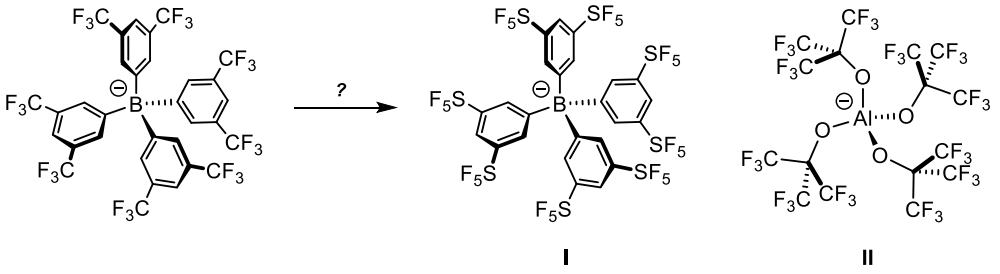


Figure 6.1.1: Alternative weakly-coordinating anions: Mecking's anion (**I**) and Krossing's anion (**II**).

6.2 Chapter 3: Future Directions for Single-Crystal to Single-Crystal Transformations with Shifts in Periodic Structure

In pursuit of high-quality *sc*-XRD data, *in situ* SC-SC hydrogenation studies were limited to the propene complex **35**, and were not undertaken in this Chapter for the also-approached ethene (**38**), η^2-1-butene (not included), and η^2-1,3-butadiene (not included) complexes which, in addition to the η^2-COD complex **36** discussed as a synthetic intermediate, all exhibited a degree of SC-SC hydrogenation behaviour. Given more time and potentially given further collaboration with the Diamond Light Source, the solid-gas chemistry of these species may be explored more thoroughly, building up a suite of Ir(I)-centred SMOMs, each with SC-SC chemistry. Marrying the concepts of pincer-bound Ir(I) and fluorinated ligands found in this Chapter, a ligand platform bearing fluorinated aromats[5] may also be a fruitful line of inquiry.

6.3 Chapter 4: Future Directions for Solid-Gas Hydrogenation-Polarisation

The SMOM-PHIP project is already moving in the direction of solid-gas flow conditions, intended to avoid issues of relaxed product build-up, *para*-hydrogen 'reorthoisation' by the SMOM catalyst, and early time-point probe saturation/detection under NMR batch conditions. PHIP substrates more complex than hydrocarbons may be tested such as haloalkenes, intended to mimic flurane-type anaesthetics[6] and/or give rise to non-^{1}H gas-phase hyperpolarisation.

6.4 References

[1] L. Chen, P. Ren, B. P. Carrow, *Journal of the American Chemical Society* **2016**, *138*, 6392–6395.
[2] D. Langford, I. Göttker-Schnetmann, F. P. Wimmer, L. A. Casper, P. Kenyon, R. F. Winter, S. Mecking, *Organometallics* **2019**, *38*, 2710–2713.
[3] I. Krossing, I. Raabe, *Angewandte Chemie International Edition* **2004**, *43*, 2066–2090.
[4] A. Grigoropoulos, A. I. McKay, A. P. Katsoulidis, R. P. Davies, A. Haynes, L. Brammer, J. Xiao, A. S. Weller, M. J. Rosseinsky, *Angewandte Chemie International Edition* **2018**, *57*, 4532–4537.
[5] Z. Huang, P. S. White, M. Brookhart, *Nature* **2010**, *465*, 598–601.
[6] B. Joalland, N. M. Ariyasingha, H. R. Younes, S. Nantogma, O. G. Salnikov, N. v Chukanov, K. v Kovtunov, I. v Koptyug, J. G. Gelovani, E. Y. Chekmenev, *Chemistry – A European Journal* **2021**, *27*, 2774–2781.